

DTIC FILE COPY

AD-A220 870

AGARD-CP-463

AGARD-CP-463

AGARD

ADVISORY GROUP FOR AEROSPACE RESEARCH & DEVELOPMENT

7 RUE ANCELLE 92200 NEUILLY SUR SEINE FRANCE

AGARD CONFERENCE PROCEEDINGS No.463

Computational Methods for Aerodynamic Design (Inverse) and Optimization

DISTRIBUTION STATEMENT A

Approved for public release
Distribution Unlimited

DTIC
ELECTE
APR 25 1990
S D

NORTH ATLANTIC TREATY ORGANIZATION



DISTRIBUTION AND AVAILABILITY
ON BACK COVER

90 04 24 043

AGARD-CP-463

NORTH ATLANTIC TREATY ORGANIZATION
ADVISORY GROUP FOR AEROSPACE RESEARCH AND DEVELOPMENT
(ORGANISATION DU TRAITE DE L'ATLANTIQUE NORD)

AGARD Conference Proceedings No.463
COMPUTATIONAL METHODS FOR AERODYNAMIC DESIGN (INVERSE)
AND OPTIMIZATION



Accession For	
NTIS CRA&I	<input checked="" type="checkbox"/>
DTIC TAB	<input type="checkbox"/>
Unannounced	<input type="checkbox"/>
Justification	
By	
Distribution	
Availability Codes	
Dist	Avail and/or Special
A-1	

Papers presented and discussions held at the Specialists' Meeting of the Fluid Dynamics Panel
in Loen, Norway, 22-23 May 1989.

THE MISSION OF AGARD

According to its Charter, the mission of AGARD is to bring together the leading personalities of the NATO nations in the fields of science and technology relating to aerospace for the following purposes:

- Recommending effective ways for the member nations to use their research and development capabilities for the common benefit of the NATO community;
- Providing scientific and technical advice and assistance to the Military Committee in the field of aerospace research and development (with particular regard to its military application);
- Continuously stimulating advances in the aerospace sciences relevant to strengthening the common defence posture;
- Improving the co-operation among member nations in aerospace research and development;
- Exchange of scientific and technical information;
- Providing assistance to member nations for the purpose of increasing their scientific and technical potential;
- Rendering scientific and technical assistance, as requested, to other NATO bodies and to member nations in connection with research and development problems in the aerospace field.

The highest authority within AGARD is the National Delegates Board consisting of officially appointed senior representatives from each member nation. The mission of AGARD is carried out through the Panels which are composed of experts appointed by the National Delegates, the Consultant and Exchange Programme and the Aerospace Applications Studies Programme. The results of AGARD work are reported to the member nations and the NATO Authorities through the AGARD series of publications of which this is one.

Participation in AGARD activities is by invitation only and is normally limited to citizens of the NATO nations.

The content of this publication has been reproduced directly from material supplied by AGARD or the authors.

The annotation on some of the illustrations is not as clear as desirable. These illustrations have been printed as supplied, in order not to delay publication.

Published March 1990

Copyright © AGARD 1990
All Rights Reserved

ISBN 92-835-0542-5



Printed by Specialised Printing Services Limited
40 Chigwell Lane, Loughborough, Essex IG10 3TZ

PREFACE

Computational Fluid Dynamics (CFD) play an increasingly important role in the aerodynamic design of flight vehicles. The main reasons for this are the rapid developments in computer hardware and solution algorithms in combination with the increasing requirements (and potential) for improving aerodynamic quality and reducing design cycle time and cost.

The objective of the aerodynamic design of flight vehicles can be described as to shape the external geometry of the various parts of a configuration in such a way that they will exhibit given aerodynamic characteristics while satisfying a large number of geometric and other, for instance, structural constraints. CFD can serve this purpose in different ways. In a broad sense two categories of aerodynamic design methodology utilizing CFD may be distinguished.

One category utilizes analysis type CFD methods in an heuristic/empirical cut-and-try type of process. In this kind of process the role of CFD is to predict the aerodynamic characteristics of a configuration (or part thereof) of given geometry provided by the designer.

The second category of CFD-based methods addresses the problem of design for given aerodynamic characteristics in a more direct sense. Examples are "inverse" methods which provide the detailed geometry required to generate a given pressure distribution and methods utilizing numerical optimization techniques to obtain the geometry that minimizes, subject to constraints, a given aerodynamic objective function such as drag, load distribution, etc.

It can be argued that this second category of methods in particular offers unique possibilities of which there is no equivalent in experimental aerodynamics. It is, therefore, perhaps somewhat surprising that the design type of CFD methods appear to receive relatively little attention as compared to the analyses type of methods.

It is this observation that led the Fluid Dynamics Panel to organize a Specialist Meeting on the subject of "Computational Methods for Aerodynamic Design (Inverse) and Optimization". This volume collects the papers presented at the Specialists' Meeting and the concluding Round Table Discussion.

For the sake of statistics it is mentioned that of the 33 papers offered to the Program Committee 23, (including invited papers) could be accommodated within the time frame available.

These 23 papers were ordered into 4 sessions:

- Invited and Survey Papers (3 papers)
- Inverse Methods — Airfoils and Wings (5 papers)
- Inverse Methods — Turbomachinery (6 papers)
- Numerical Optimization Techniques (9 papers)

In alphabetical order of country of origin there was/were

1 paper from Belgium
3 papers from France
5 papers from Germany
3 papers from Italy
3 papers from The Netherlands
1 paper from Portugal
1 paper from Turkey
1 paper from UK
5 papers from USA

It is finally remarked that the Technical Evaluation Report on the meeting is available as AGARD Advisory Report No.267.

PREFACE

Les Calcul en Dynamique des Fluides (CDF) joue en rôle de plus en plus important dans la conception aérodynamique des véhicules aériens. Les principales raisons pour ceci sont, les progrès rapides qui ont été réalisés dans le domaine du matériel informatique et des algorithmes de résolution, ainsi que la demande (et le potentiel) croissants en ce qui concerne l'amélioration de la qualité aérodynamique et la réduction du coût et de la durée du cycle d'étude.

La conception aérodynamique des véhicules aériens a pour objectif de former la géométrie externe des différents éléments d'une configuration donnée de telle manière qu'ils présentent un certain nombre de caractéristiques aérodynamiques données, tout en respectant un nombre important de contraintes géométriques et autres, parmi lesquelles de contraintes structurelles. Le CDF peut servir à cette fin, et de différentes façons. De manière générale, on distingue deux catégories de méthodologies pour la conception aérodynamique faisant appel au CDF.

La première utilise des méthodes analytiques dans un procédé heuristique/empirique du type à expérimentation systématique. Le rôle du CDF dans ce type de procédé est de prévoir les caractéristiques aérodynamiques de tout ou partie d'une configuration d'une géométrie donnée, fournie par le concepteur.

La deuxième catégorie de méthode permet d'aborder d'une façon plus directe le problème de la conception en fonction de caractéristiques aérodynamiques données. Parmi les exemples de ces méthodes, on peut citer les méthodes inverses qui donnent la géométrie détaillée nécessaire pour une distribution de pression donnée, et les méthodes qui font appel à des techniques d'optimisation numériques, afin d'obtenir une géométrie, laquelle, sous réserve de certaines contraintes, permet de minimiser une fonction distincte aérodynamique donnée, telle que la traînée, la répartition des charges etc.

On peut dire que cette deuxième catégorie de méthodes en particulier, offre des possibilités uniques, qui ne trouvent aucun équivalent dans le domaine de l'aérodynamique expérimentale. Il est donc, quelque peu surprenant que les types de méthode CDF pour la conception suscitent relativement peu d'intérêt en comparaison des types de méthode pour l'analyse

Cette constatation a amené le Panel de la Dynamique des Fluides à organiser une réunion de spécialistes sur le thème de "Les méthodes de calcul pour la conception aérodynamique (méthodes inverses) et l'optimisation". Le présent volume est un recueil des communications présentées lors de la réunion de spécialistes et de la table ronde tenue en fin de séance.

Par égard pour les statistiques, nous tenons à signaler que sur les 33 communications proposées au comité du programme, 23 (dont celles réalisées à la demande expresse du comité) ont pu être présentées dans le temps imparti.

Ces 23 communications ont été présentées en 4 séances:

Communications présentées sur invitation et communications présentant l'état de l'art (3 communications)
Méthodes inverses -- Profils aérodynamiques et voilures (5 communications)
Méthodes inverses -- les turbomachines (6 communications)
Techniques d'optimisation numériques (9 communications)

La liste des communications par pays d'origine et par ordre alphabétique s'établit comme suit:

1 communication de la Belgique
3 communications de la France
5 communications de l'Allemagne Fédérale
3 communications de l'Italie
3 communications du Pays Bas
1 communication du Portugal
1 communication de la Turquie
1 communication du Royaume Uni
5 communications des Etats Unis

En conclusion, il est à noter que le rapport d'évaluation technique pour cette réunion, est disponible sous la forme du rapport consultatif de l'AGARD No.267.

AGARD FLUID DYNAMICS PANEL

Chairman: Mr D.H. Peckham
Superintendent AE2 Division
Royal Aerospace Establishment
R 141 Building
Farnborough, Hants GU14 6TD
United Kingdom

Deputy Chairman: Dr W.J. McCroskey
Senior Staff Scientist
US Army Aero Flightdynamics
Directorate — Mail Stop N258-1
NASA Ames Research Center
Moffett Field, CA 94035-1099
United States

PROGRAMME COMMITTEE

Professor Ir J.W. Slooff (Chairman)
National Aerospace Laboratory, NLR
Anthony Fokkerweg 2
1059 Amsterdam
The Netherlands

Mr L.H. Ohman
Head, High Speed Aerodynamics Lab.
National Aeronautical Establishment
National Research Council
Montreal Road
Ottawa, Ontario K1A 0R6
Canada

M. l'Ing. en Chef B. Masure
STCAN/BA
26 Bd Victor
75015 Paris
France

Dr W. Schmidt
Deputy Director — Dornier 328 Program
Dornier GmbH, EY
Postfach 1420
D-7990 Friedrichshafen 1
Federal Republic of Germany

Professor D. Papailiou
Department of Mechanical Engineering
University of Patras
Rio 26001
Patras
Greece

Professor M. Onorato
Dipartimento di Ingegneria Aeronautica
e Spaziale
Politecnico di Torino
C.so Duca degli Abruzzi 24
10129 Torino
Italy

Professor H. Norstrud
Division of Hydro- and Gas Dynamics
Norwegian Institute of Technology
N-7034 Trondheim
Norway

Dr K.L. Kushman
Chief, Facility Division
AEDC/DOTR — Mail Code RF
Arnold AFB, TN 37389-5000
United States

PANEL EXECUTIVE

Mail from Europe:
Mr M.C. Fischer
AGARD/OTAN
7 rue Ancelle
92200 Neuilly sur Seine, France

Mail from US and Canada:
Mr M.C. Fischer
AGARD/NATO
APO New York 09777

Tel (1) 4738 5775 — Telex 610176 (France)
Telefax (1) 4738-5799

CONTENTS

	Page
PREFACE (English)	iii
PREFACE (French)	iv
AGARD FLUID DYNAMICS PANEL	v
	Reference

SESSION I - INVITED & SURVEY PAPERS

Chairman: J.W.Slooff

PROGRESS IN INVERSE DESIGN AND OPTIMIZATION IN AERODYNAMICS by H.Sobiechzy	1
AEROFOIL DESIGN TECHNIQUES by A.J.Bocci	2
AERODYNAMIC DESIGN TECHNIQUES AT DLR INSTITUTE FOR DESIGN AERODYNAMICS by H.Koster, C.H.Rohardt, K.F. rtorstmann and R.Radespiel	3

SESSION - INVERSE METHODS - AIRFOILS AND WINGS

Chairman: K.L.Kushman

INVERSE DESIGN OF AIRFOIL CONTOURS: CONSTRAINTS, NUMERICAL METHODS AND APPLICATIONS by G.Volpe	4
AN EFFICIENT AIRFOIL DESIGN METHOD USING THE NAVIER-STOKES EQUATIONS by J.B.Malone, J.C.Narramore and L.N.Sankar	5
AN ITERATIVE PROCEDURE FOR THE DESIGN OF PRESSURE-SPECIFIED THREE-DIMENSIONAL CONFIGURATIONS AT SUBSONIC AND SUPERSONIC SPEEDS BY MEANS OF A HIGHER-ORDER PANEL METHOD by L.Fornasier	6
A SYSTEM FOR TRANSONIC WING DESIGN WITH GEOMETRIC CONSTRAINTS BASED ON AN INVERSE METHOD by F.J.Brandma and J.M.J.Fray	7
A FAST COLLOCATION METHOD FOR TRANSONIC AIRFOIL DESIGN by S.De Ponte, M.Boffadossi and C.Mantegazza	8

SESSION-III - INVERSE METHODS - TURBOMACHINERY, INTAKES, DUCTS

Chairman: B.Masure

SUBSONIC AND TRANSONIC BLADE DESIGN BY MEANS OF ANALYSIS CODES by R.A.van den Braembussche, O.Leonard and L.Nekmouche	9
A COMPUTATIONAL DESIGN METHOD FOR SHOCK FREE TRANSONIC CASCADES AND AIRFOILS by T.A.Cetinkaya, I.S.Akmandor and A.S.Üçer	10
INVERSE COMPUTATION OF TRANSONIC INTERNAL FLOWS WITH APPLICATION FOR MULTI-POINT-DESIGN OF SUPERCRITICAL COMPRESSOR BLADES by E.Schmidt and F.Klimetzek	11
UNE METHODE INVERSE POUR LA DETERMINATION D'AUBES DE TURBOMACHINES by O.P.Jacquotte	12

APPLICATION OF AN INVERSE METHOD TO THE DESIGN OF A RADIAL-INFLOW
TURBINE

by J.E.Borges

13

NUMERICAL METHOD FOR DESIGNING 3D TURBOMACHINERY BLADE ROWS

by L.Zannetti, R.Larocca and R.Marsillo

14

SESSION IV — NUMERICAL OPTIMIZATION

Chairman: W.Schmidt

AERODYNAMIC OPTIMIZATION BY SIMULTANEOUSLY UPDATING FLOW
VARIABLES AND DESIGN PARAMETERS

by M.H.Rizk

15

CONSTRAINED SPANLOAD OPTIMIZATION FOR MINIMUM DRAG OF MULTI-
LIFTING SURFACE CONFIGURATIONS

by R.F.van den Dam

16

NUMERICAL OPTIMIZATION OF TARGET PRESSURE DISTRIBUTIONS FOR
SUBSONIC AND TRANSONIC AIRFOIL DESIGN

by J.A.van Egmond

17

A TOOL FOR AUTOMATIC DESIGN OF AIRFOILS IN DIFFERENT OPERATING
CONDITIONS

by L.Ghielmi, R.Marazzi and A.Baron

18

DEFINITIONS DE PROFILS ET DES PALES D'HELICOPTERE PAR OPTIMISATION
NUMERIQUE

par J.Reneaux et M.Allongue

19

AERODYNAMIC DESIGN BY OPTIMIZATION

by K.W.Bock

20

OPTIMISATION NUMERIQUE DE VOILURES EN REGIME TRANSSONIQUE

by D.Destarac, J.Reneaux et D.Gisquet

21

AIRFOIL DESIGN VIA CONTROL THEORY

by A.Jameson

22

OPTIMIZATION OF AERODYNAMIC DESIGNS USING COMPUTATIONAL FLUID
DYNAMICS

by D.H.Huddleston and C.W.Martin

23

TECHNICAL EVALUATOR'S REMARKS/ROUND TABLE DISCUSSION

RTD

PROGRESS IN INVERSE DESIGN AND OPTIMIZATION IN AERODYNAMICS

by

Helmut Sobieczky
DLR Institute for Theoretical Fluid Mechanics
Bunsenstrasse 10
D-3400 Göttingen
Federal Republic of Germany

Summary

Aerodynamic design has been developed to an advanced state of the art: Inverse methods allow for strong control of aerodynamic airfoil or wing performance so that optimization strategies are no longer beyond practical use and knowledge bases can be established for the implementation in "aerodynamic expert systems". This paper reviews some recent steps into this direction.

Introduction

Twenty years ago an AGARD conference publication¹ marked the date of renewed interest in an important field of fluid mechanics: Transonic flow. Among other progress, one of the reasons was that important results were presented for systematically designed airfoil flows without a recompression shock at design conditions. These have been found by Nieuwland, and progress also in wind tunnel experiments now allowed the conclusion that such flows actually would be of practical interest. Systematic use was made by the fact that compressible gasdynamics allows for a linearization of the basic model equation if the roles of independent (2D space coordinates x, y) and dependent variables (velocity components u, v) are switched. Every approach to gain insight in particular flow problems by this change of roles was called a use of "the Hodograph Method". In contrast to the linear model equations, an airfoil boundary value problem in the hodograph plane (u, v) is nonlinear and therefore did not easily allow for the construction of practical airfoil flows. Results were termed as obtained "indirectly", because the classical "inverse" problem - to prescribe the velocity or pressure distribution and obtain a transonic airfoil shape - was still not solved twenty years ago.

During the seventies and early eighties, knowledge of basic analytical models, as well as the resulting indirect methods and the availability of larger computers allowed for the development of a number of computer programs to design shock-free transonic airfoils². In addition, faster flow analysis methods with viscous effects already taken into account, were used for the direct design approach by successive shape variations. Design methods, termed "indirect" and "direct" became available but finally also the step from indirect to "inverse" techniques completed methodology as a toolbox available today for the aerodynamic designer³.

This present review is not quite restricted to transonic flows but, because of the author's interest, mainly addressing this speed regime.

It starts with the observation that today the hodograph transformation has some renewed value for phenomena understanding: refined mathematical modelling is necessary to define a knowledge base for future design and optimization concepts. A few of the successful developments in the field of inverse airfoil and wing design methods published during the past 5 years will be mentioned.

Design methods are suitable for optimization strategy development, as well as the availability of inexpensive flow analysis codes, to be run many times on carefully varied geometrical boundary conditions. Geometry generation is a large topic on its own so it will be mentioned here only as a basic component for optimization.

Aside from the world of supercomputing numerics and facilities we witness the rapid progress in modern workstation computer development. New possibilities arise to make use of accumulated aerodynamic experience, input for "expert design systems" within the technology of artificial intelligence.

Value of the Hodograph Transformation

Mapped Phenomena

Early transonic flow research was successfully exploiting the fact that two-dimensional compressible flow modelling yields linear equations for velocity potential or stream function. A variety of attempts to describe flow singularities was partly successful by solving complex problems and partly not so successful because some approaches to arrive at solutions rather confused the aerodynamicist than simplified the task to design practically useful flow examples. Today we have renewed interest in hodograph solutions for different reasons: Rapid desk-top computers with interactive graphics allow for a direct evaluation, easier understanding and application of such solutions. One complex of questions is related to the nature and sensitivity of supercritical airfoil flows without or with tolerably weak recompression shocks. Model solutions of a simple analytic structure describe supersonic bubbles embedded in subsonic flows. These well understood flow components and their mappings in the hodograph plane may draw continuous interest because they may be used to support heuristic models to be implemented in global design and optimization goals.

One example is our task to use the hodograph of supercritical airfoil flow fields for practical design modification tools: Fig. 1 shows the result of an airfoil flow analysis, mapped to hodograph variables. Here we use the Prandtl-Meyer function (depending only on the local Mach Number) and the flow angle. Earlier

studies in this special hodograph allowed for a rheoelectric flow analogy ("Rheograph")¹; today we use this knowledge base to develop simplified models for an expert system. The figure shows the flow in the physical and in the rheograph plane. The role of the characteristics within the supersonic field is crucial for sensitivity to off-design perturbations.

Analytical particular solutions valid in the near-sonic domain help to clarify the appearance of shocks in slightly perturbed shock-free flows. Test cases for numerical methods are easily defined by exact local solutions². Fig. 2 shows a model for a cusped indentation to the sonic line of a local supersonic field wetting a smoothly curved airfoil contour. Such indentations are observed in experiments and refined analysis calculations of airfoil flows with very flat supersonic bubbles, if the lift or the Mach number is slightly below design conditions (Fig. 3b).

Laminar flow control (LFC) technology research in the transonic regime has stressed the importance of very refined knowledge of local (inviscid) flow structure because of its influence on the appearance of viscous instabilities. In W. Pfenniger's work³ the role of the hodograph is outlined as a tool for a knowledge base about laminar flow control. The quality of local supersonic flow bubble shapes is found crucial for design pressure (Fig. 3a) distribution as well as for sensitivity to off design perturbations (Fig. 3b):

"At the design point with transonic potential flow the supersonic bubble should be regular without concave indentations, which precipitate off-design shock formation. For this purpose, the supersonic zone, where the surface curvature increases continuously, must decelerate progressively faster to sonic velocity, followed by a steep subsonic rear pressure rise with suction.

The upper surface nose contour is characteristic to airfoils with a far upstream pressure minimum; it decisively influences the entire flow of the upper surface supersonic zone. The on-design hodograph streamline of the upper surface decelerates continuously over a wide range of flow inclination angles (i.e., upper surface slope angles) from the pressure minimum to the flat rooftop".

It is exactly such detailed knowledge about the phenomena crucial for airfoil performance which should be made available by new techniques to evaluate model solutions, mappings and graphic display.

Fictitious Gas Concept: a Link between Direct and Inverse Design Methods

A detailed knowledge of local flow phenomena is undoubtedly the best prerequisite for successful configuration design. Hodograph mappings have laid ground for the nearly - direct "Fictitious Gas" design concept⁴, which has resulted in a number of efficient computer codes to redesign given 2D or 3D configurations to be shock-free^{5,6}.

Aerodynamicists have also developed their own applications of the concept, which can be implemented in nearly every analysis code. However, it takes creativity and the courage for non-standard approaches to make full use of the idea which still seems to have the potential to help gaining a better understanding of unresolved mixed type flow phenomena. Starting with shock-free redesigns to finally arrive at aerodynamically optimized 3D configurations seems both relatively easy and economical, see some examples in review⁷.

Indirect Design Methods

Because of rapid progress in direct computational fluid dynamics within the past years there are only very few new methods for solving the hodograph equations with boundary conditions resulting from an indirect design approach. One method seems interesting from a numerical point of view:

The work of C. Mavriplis¹⁰ is an attempt at combining the hodograph formulation and spectral methods to create an efficient analytical/numerical method for designing two-dimensional transonic flow. Spectral methods were chosen for their efficiency and accuracy. They are an extension of the classical separation of variable methods, capable of approximating smooth solutions with exponential convergence. An iterative numerical procedure involving a Chebyshev-Fourier pseudo-spectral method is constructed for the solution of two-dimensional shockless transonic potential flow in the hodograph plane.

Inverse Design of Airfoil and Wings

The classical inverse problem of aerodynamics is posed by specifying the pressure distribution around an airfoil or wing and determining the geometry of this airfoil or wing that realizes this pressure distribution as solution. For incompressible flow past airfoils this classical problem was solved by Lighthill¹¹. Compressible flows, especially in the mixed-subsonic/supersonic regime, did not allow for reasonably precise solutions until perhaps a decade ago.

Today, with the help of faster and larger computers, iterative procedures allow for the solution of nonlinear model equations as well as nonlinear boundary value problems. The latter are a crucial part of inverse problems and results at first were obtained for potential flow models. Volpe and Melnik¹² have developed a method for airfoils in flows with Mach numbers up to the transonic regime. Interesting insight into the structure of transonic flows can be gained with results from this method:

Specification of shock-free pressure distributions on airfoils in too high Mach numbers results in flows where indeed the surface pressure distribution is shock-free, but a strong recompression shock wave terminates a part of the supersonic bubble within the flowfield (Fig. 4), resulting in strong wave drag and presumably a very unstable behavior of this flow near the design condition. We may ask how to avoid such unwelcome results without having to investigate the flow field above the airfoil contour and checking the integrated airfoil drag. A simple answer results from knowledge of the hodograph mapping: The undesirable airfoil property of such a "hanging shock" is compatible only with a part of the airfoil surface being concave in the supersonic region. This fact allows to impose an additional constraint on surface curvature.

Other inverse potential flow methods are proposed by Daripa¹³ and for multielement airfoils in incompressible flow by Siladic and Carey¹⁴.

M. Drela¹⁵ developed a new design/analysis method for airfoils and cascades. It solves the Euler equations and allows for viscous interaction by a coupling with a boundary layer method.

S. Takanashi¹⁶ uses the transonic integral equation to develop an iterative design procedure utilizing various reliable analysis codes.

Because of the attractiveness of these methods, they are described here in more detail, reproducing some convincing results for airfoils and wings designed.

M. Drela's Design Method using the Euler Equations

This design/analysis method is based on a novel discretization and solution technique for the steady Euler equations. The discretization is based on an intrinsic grid in which one set of coordinate lines corresponds to streamlines and hence there is no convection across the corresponding faces of the conservation cells. This type of coordinate system is very attractive for the steady-state Euler equations. Both the continuity and energy equations are replaced by the simple conditions of constant mass flux and stagnation enthalpy in each streamtube, thus reducing the number of unknowns per grid node from four to two. With conventional finite-volume discretization, all four equations and four unknowns per grid node must be retained in general, and only the energy equation can be eliminated in the special case of constant upstream total enthalpy.

The key feature of the present discretization scheme which permits inverse solutions to be performed is that since the streamline grid evolves as part of the solution, the airfoil shape (which is defined by two particular streamlines) can evolve as well. In the discrete equations, it is as easy to specify that the surface pressure match some given distribution as it is to specify that the surface streamlines match the airfoil shape.

The boundary conditions for the analysis code deal with the direct problem. A body geometry was prescribed, and the flow field and surface pressures were a result of a calculation. An alternative to this procedure is the inverse problem, where surface pressures are prescribed and geometry is calculated as a result. A straightforward implementation of this idea is to replace the fixed-wall boundary condition with the condition that the wall pressure at each grid node on the body surface equal some specified value.

In addition to the full-inverse formulation, the program implementing the algorithms also handles the mixed-inverse formulation, where the pressure is prescribed on part of airfoil, and the geometry is prescribed on the rest. This can in fact be considered a generalization of both the direct and full-inverse formulations, since either the prescribed-pressure or the prescribed-geometry parts can in principle encompass the whole airfoil. The ability to mix the two formulations in arbitrary proportions is an extremely useful feature which gives the designer much more overall control over both the aerodynamic and geometric properties of the airfoil than is present with either formulation alone.

Some test cases involve the RAE 2822 supercritical airfoil. They are compared with experiment to demonstrate the accuracy of the turbulent integral boundary-layer formulation for transonic flow with and without shock-induced separation. The design case demonstrates the redesign of the suction side of the 2822 airfoil using the mixed-inverse design option, see Fig. 5. This redesign eliminates wave drag and yields a 21% predicted drag reduction from the original 2822 drag.

S. Takanashi's Design Method using the Transonic Integral Equation

A practical design method is presented for three-dimensional transonic wings with prescribed pressure distributions. The method is based on an iterative "residual-correction" concept. The residual, defined as the difference between the computed and the prescribed pressure distributions at each iteration step, is determined by the use of an existing direct analysis code for a transonic wing with or without the body. The wing geometry correction to compensate for the residual can be approximately obtained from the inverse solution code developed in the present study. The inverse (correction) problem is mathematically reduced to a Dirichlet-boundary value problem that is solved here by the aid of the transonic integral equation method.

The advantage of the iterative residual-correction procedure approach is that only minimal effort in developing the geometry correction code is needed to compensate for the pressure residual, while an analysis code is retained in its original form and can be treated solely as a "black box". As a result, the analysis code can be easily replaced whenever a more advanced code becomes available.

The basic procedure of iteration for the wing design is described in the following. 1) the flowfield is solved for an initial wing by a direct analysis code that provides the initial pressure distribution; and 2) the inverse correction corresponding to the pressure difference between the actually computed pressure at the first step and a specified pressure distribution. As long as the higher-order terms in the transonic integral equation are small, the calculated geometry difference can provide a good approximation of the exact amount of correction for the initial wing geometry. Thus, a new wing geometry is obtained that, in turn, can be used as the second set of input data to the analysis code. The same process is repeated until convergence is achieved in the sense that the calculated pressure distribution agrees with the prescribed one within a specified amount of tolerance.

This procedure requires neither restrictions on the formulation nor a numerical solution scheme for the analysis code. The only requirement is that the flow solver calculates the pressure distribution on the cor-

rected wing surface, since the design code is completely independent of the analysis code. Therefore, any analysis code for a three-dimensional transonic wing with or without a body can be employed using the procedure. FLO-22 was at first used as a direct code for the nonconservative infinite difference equations derived from the three-dimensional transonic full potential equations.

A transonic swept-wing design for a transport airplane was attempted. The target pressure distribution chosen here is characterized by its particular isobar pattern. That is, the specified chordwise pressure distributions are the same at any span station between the wing root and tip, so that the straight line isobar pattern is realized over the entire wing surface (Fig. 6).

The design method recently has been coupled also with a Navier-Stokes code¹⁷. Results for viscous airfoil design have been obtained using the 2D analysis code HSFOL; an example is shown in Fig. 7.

Aerodynamic Optimization

This paper deals, in the previous part, with inverse design procedures. Hodograph models and indirect design concepts are considered a theoretical background and basic toolbox for development of practical inverse methods. The ultimate goal of either approach is the ability to find shapes which perform "optimally" in a certain range of missions. An optimum may include many abilities beyond aerodynamic performance, here we constrain the large amount of practically important parameters to the group within the discipline "aerodynamics" but we do this knowing that aerodynamic design does not play the most important role in global design/optimization of a new airplane project. Optimization, both just aerodynamic or in other disciplines like structures, require a suitable parameterization of the shapes to be designed. It is therefore the basic discipline of geometry which turns out to be a key tool for optimization, utilizing direct or inverse design methods.

Using aerodynamic knowledge for geometry parameterization

Learning from test cases evolving from hodograph models, inverse and direct design studies, we develop a knowledge base about the regions of high aerodynamic sensitivity on configuration surfaces. This is true especially in the transonic regime, here the surfaces wetted by supersonic flow are most important. Mixed direct-inverse operation like the one in Drela's Euler code mentioned above are therefore of high practical value. Such an approach may implement the best features of subsonic aerodynamics on the main portion of the whole configuration, but allow for modifications within the supersonic domain. Initial geometries as an input to design/optimization cycles should therefore consist of accurately, i.e. analytically defined surfaces, but allowing for local shape deformations analog to elastic variable geometry devices on actual configurations.

Based on this concept the author's geometry generator code E88¹⁸ has been created as a tool for design aerodynamics. Input wing sections to be blended arbitrarily along wing span allow an a-priori selection of airfoils known to be suitable for the desired range of operation. Spline supports of these basic sections may be situated densely where the contour is fixed, but only a few support points are located within the contour portion which is allowed to vary. Fig. 8 shows such sections: the single supports on the upper surface are to be moved vertically like jacks of a flexible wall in a wind tunnel. Use of a reliable analysis code to determine aerodynamic response to a support location change, the definition of an objective function to be minimized and an optimizer complete the software for aerodynamic optimization.

Cosentino and Holst²⁰ have used a version of the abovementioned geometry generator to be coupled with a potential flow wing analysis code, wing optimization was performed using lift-over-drag ratio as objective function. Fig. 8 shows three generating sections at wing root, break and tip with three movable spline supports each. This gives nine parameters in total to be varied in a gradient method optimization strategy. Here the fact is stressed that aerodynamic knowledge allows us to create shapes with many fixed but only a few, but crucially important, movable parameters, located in areas where the flow is influenced most effectively. Fig. 8 shows a selected span station with pressure distribution before and after the optimization process.

The number of parameters for shape variation can be further reduced if geometric changes can be expressed by suitable functions controlled by fewer parameters than the number of moveable spline supports. We drive the use of aerodynamic knowledge further if we recognize results from the fictitious gas design procedure²¹: Initial geometries in a fictitious flow yield the sonic bubble and the domain to be modified in a second step of the (non-fictitious) calculation. The modification is a difference bump within this sonic bubble, its local amplitude being proportional to the local bubble height, as can be verified by simple continuity considerations. Modelling a bump function between the calculated sonic points on wing sections and calibrating its amplitude using the extent of the bubble results in a one-step method to modify a given wing to become a nearly shock-free one. Since we have learned that reducing shocks on otherwise already acceptable designs may bring the configuration very close to an optimum aerodynamic efficiency, this method²¹ seems attractive for arbitrary three-dimensional configurations, utilizing a fictitious gas version of an analysis code capable to analyze such configurations.

The Use of Known Flow Fields for Configuration Optimization

The main problem of aerodynamic optimization - compared to optimization in other disciplines - is the relatively costly evaluation of an objective function, like aerodynamic efficiency or the differences to a target pressure distribution. Integration of the whole flow field at each iteration usually cannot be avoided but there are applications to use selected parts of just one flow field, either known as a basic flow element or computed just once for all following purposes.

Revived interest in hypersonic aerodynamics asks for optimum performance lifting bodies in this speed regime, even with many details of flow physics still neglected or just crudely modeled. The concept of supersonic waveriders²² dates back thirty years ago, when the application of flow elements with oblique shocks and sharp edged delta wings allowed for a complete description of wing geometry compatible with a known supersonic field plus the bow shock. These examples were and still are valuable test cases for experiments in supersonic and hypersonic wind tunnels. In addition today, we may develop new numerical algorithms to evaluate more sophisticated model generation, like the Euler and time-averaged Navier Stokes equations, using examples with known (inviscid) flow and shocks.

Configuration optimization also finds a field of suitable case studies because we may evaluate lift and drag, possibly utilizing boundary layer methods and however little existing experience in hypersonic flow transition. Bowcutt et al.²³ use conical flow fields to be cut out by a body leading edge and determining the lower body surface producing lift. The upper surface is cylindrical in undisturbed flow or produces additional lift by utilizing an also known Prandtl-Meyer expansion flow. Parametric variation of the leading edge shape allows for a fast determination of the aerodynamic characteristics including friction drag from a boundary layer method. Corda and Anderson²⁴ extend this concept by using non-conical axisymmetric flows for body generation, again just the leading edge intersecting with the shock determines the body and the flow. Leading edge shape parameters are varied and a simplex method is used to optimize lift over drag (Fig. 9). Resulting body shapes, for the chosen leading edges, may be of rather academic value only, (Fig. 10), but they provide an excellent data base for the development of more general supersonic and hypersonic design and optimization strategies, as well as - in combination with geometry and CFD grid generators - for an analysis of flows past more applied configurations.

Evolution Theory for Aerodynamic Optimization

The purpose of the two previous subsections was to demonstrate the goal of aerodynamic knowledge, to reduce the number of design parameters, by using classes of shapes or flow fields. In cases where this knowledge base is still insufficient, the number of design variables may have to be high at least for a first orientation.

As the number of design variables increases, or as variables become coupled, the efficiency of a gradient search method is reduced. In addition, gradient search methods are quite complex to implement. Misegades²⁵ suggested the use of evolution theory as an alternative approach. Evolution theory is a very simple method that can be used with any number of variables, which do not have to be completely independent of one another. In addition, evolution theory is insensitive to step functions in the processing function and to local minima and maxima.

Gregg and Misegades²⁶ presented a wing optimization method based on evolution theory and making use of multitasking, one of the options to use multiple processors for a single job, executed on a Cray XMP computer with multiple CPUs. While total CPU time is not decreased by multitasking, elapsed time can be substantially reduced to improve turnaround time.

Toward Aerodynamic Expert Design Systems

Aerodynamic engineers are accumulating expertise in the field of CFD, design aerodynamics and in many practical fields related to and resulting from their work, they become experts. Reviewing progress in the field of aerodynamic design and optimization, one cannot oversee recent developments in the field of Artificial Intelligence (AI), i.e. in the study of how to make computers perform tasks that currently have to be done, or are better done, by human beings. An approach to be successful in this direction, is the development of software formulated with concepts of Expert Systems (ES).

The coupling of AI/ES with CFD was generally outlined and demonstrated for aerodynamic turbocomponent design by S.S. Tong²⁷. This new field has begun to spark development of new programming languages, because a problem still obstructing applications of AI to CFD and aerodynamics is the lack of powerful, portable, fully supported and well documented developmental software. With the current worldwide interest in AI, it is expected that much more commercial AI related software will soon be available.

However, it is evident, that an Expert Design System will be just as good as the knowledge bases used to build the system. Necessity to extract knowledge bases from experts seems difficult because of obvious human reasons. A new interdisciplinary world of Aerospace Sciences and Computer Science with many open problems but also exciting possibilities opens so that it is certainly not unrealistic to expect progress in the development of aerodynamic Expert Design Systems in the near future.

Conclusion

This article reviews progress in a field of design aerodynamics. Results to model fluid dynamic phenomena are used to illustrate the value of hodograph mappings for a better understanding of flow structure. Numerical methods for inverse airfoil and wing design are available now to give viscous flow results up to high accuracy. Aerodynamic optimization should take advantage from a refined understanding of flow phenomena; the number of design parameters to vary surfaces can so be reduced to arrive at faster optimization procedures. Finally, the new direction of coupling Artificial Intelligence with Aerodynamic Design may use much of the recent progress in systematic design and optimization developments.

References

- 1 Transonic Aerodynamics.
AGARD CP 35 (1968)

- 2 Sobieczky, H., Seebass, A. R.
Supercritical Airfoil and Wing Design
Ann. Rev. Fluid Mech. 16, (1984)
- 3 Slooff, J.W.
Computational Procedures In Transonic Aerodynamic Design.
Applied Computational Transonic Aerodynamics,
AGARD-AG-266, (1982)
- 4 Sobieczky, H.
Related Analytical, Analog and Numerical Methods In Transonic Airfoil Design.
AIAA paper 79-1566 (1980)
- 5 Sobieczky, H.
Exakte Loesungen der Ebenen Gasdynamischen Gleichungen in Schallnaehe.
Zeitschr. Flugwiss. 19 No. 5, (1971)
- 6 Pfennlinger, W., Viken, J.K., Chandra, S., Vemuru, C.S., Volpe, G.
All Laminar SC LFC Airfoils with Natural Laminar Flow in the Region of the Main Wing Structure.
AIAA paper 86-2625 (1986)
- 7 Sobieczky, H., Fung, K.-Y., Seebass, A.R., Yu, N.J.
New Method for Designing Shock-free Transonic Configurations.
AIAA Journal Vol. 17 No. 7, (1979)
- 8 Dullkravich, D. S. (Ed.)
1. Int. Conf. on Inverse Design and Optimization In Engg. Sciences
Conf. Proc. Univ of Texas at Austin, (1984)
- 9 Sobieczky, H.
Research In Inverse Design and Optimization in Germany.
Appl. Mech. Rev., Vol. 41, No. 6 (1988)
- 10 Mavriplis, C., Harris, W.L.
A Spectral Hodograph Method for Shockless Transonic Two-Dimensional Flow.
AIAA paper 86-1796 (1986)
- 11 Lighthill, M.J.,
A Method of Two-Dimensional Aerodynamic Design.
R&M 2112, Aeronautical Research Council, London, England, (1945)
- 12 Volpe, G., Melnik, R.E.
The Design of Transonic Airfoils by a Well-posed Inverse Method.
Int. Conf. In Inverse Design Concepts In Engg. Science, Austin (1984)
- 13 Daripa, P.
On Inverse Airfoil Design.
AIAA paper 88-2573 (1988)
- 14 Siladic, M., Carey, G.F.
Extension of Inverse Design Techniques for Multicomponent Airfoils.
AIAA Journal, Vol. 26 No.6, (1988)
- 15 Drela, M.
Two-dimensional Transonic Aerodynamic Design and Analysis using the Euler Equations.
Massachusetts Inst. of Technology Ph. D. Thesis, (1985)
- 16 Takanashi, S.
Iterative Three-Dimensional Transonic Wing Design Using Integral Equations.
Journal of Aircraft, Vol. 22, pp. 655-660 (1985)
- 17 Hirose, N., Takanashi, S., Kawal, N.
Transonic Airfoil Design Procedure Utilizing a Navier-Stokes Analysis Code.
AIAA Journal, Vol. 25 No. 3, (1987)
- 18 Sobieczky, H.
Geometry Generation for Transonic Design.
Recent Advances In Numerical Methods In Fluids, Vol. 4, Ed. W.G. Habashi, Swansea: Pineridge Press, (1985)
- 19 Sobieczky, H.
Analytical Surfaces and Grids.
In: AGARDograph No. 309, Three Dimensional Grid Generation, H. Yoshihara (Ed.), (1988)
- 20 Cesentino, G.B., Holst, T.L.
Numerical Optimization Design of Advanced Transonic Wing Configurations.
Journal of Aircraft, Vol. 23, pp.192-199, (1986)
- 21 Zhu, Z., Sobieczky, H.
An Engineering Approach for Nearly Shock-free Wing Design.
Acta Aeron. et Astron. Sinica, Vol. 8 No.7 (1987)

- 22 Nonweiler, T.R.F.,
Aerodynamic Problems of Manned Space Vehicles.
Journal of the Royal Aeronautical Society, Vol. 63, pp. 521-538, (1959)
- 23 Bowcult, K.W., Anderson, J.D., Capriotti, D.
Viscous Optimized Hypersonic Waveriders.
AIAA paper 87-0272, (1987)
- 24 Corda, S., Anderson, J. D.
Viscous Optimized Hypersonic Waveriders Designed from Axisymmetric Flow Fields.
AIAA paper 88-0369, (1988)
- 25 Misegades, K.P.,
Optimization of Multielement Airfoils.
Project report 1980-5, Van Karman Institute (1980)
- 26 Gregg, R.D., Misegades, K.P.
Transonic Wing Optimization Using Evolution Theory.
AIAA paper 87-0520, (1987)
- 27 Tong, S.S.,
Design of Aerodynamic Bodies using Artificial Intelligence/Expert System Technique.
AIAA paper 85-0112, (1985)

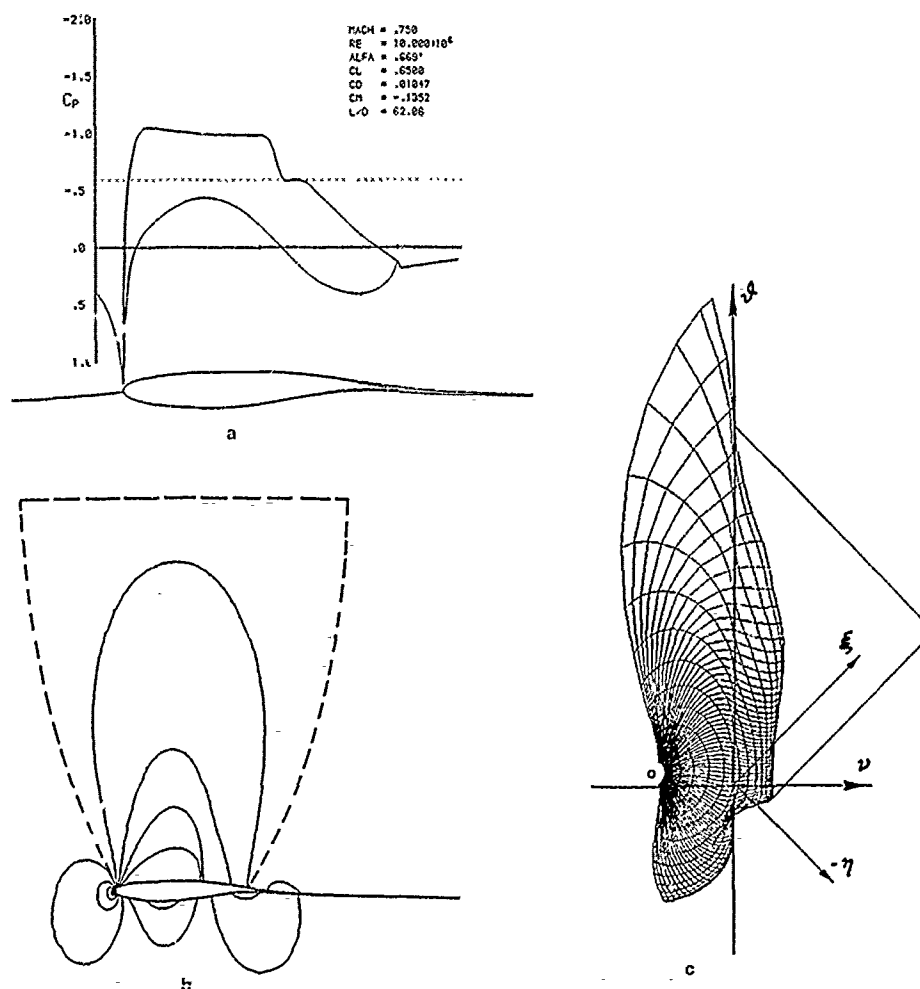


Fig. 1: Supercritical airfoil at optimum aerodynamic efficiency,
Euler code plus viscous analysis (Ref. 15), (a).
Iso-Machlines and selected flow section (b).
Hodograph mapping (Ref. 4) of selected flow section (c).

Fig. 2: Breakdown of shock-free supercritical flow wetting a smoothly curved wall: Analytical model using transonic similarity solutions (Ref. 5): Cusped sonic line separates subsonic flow (with Iso-Machlines) and supersonic flow (with characteristics drawn)

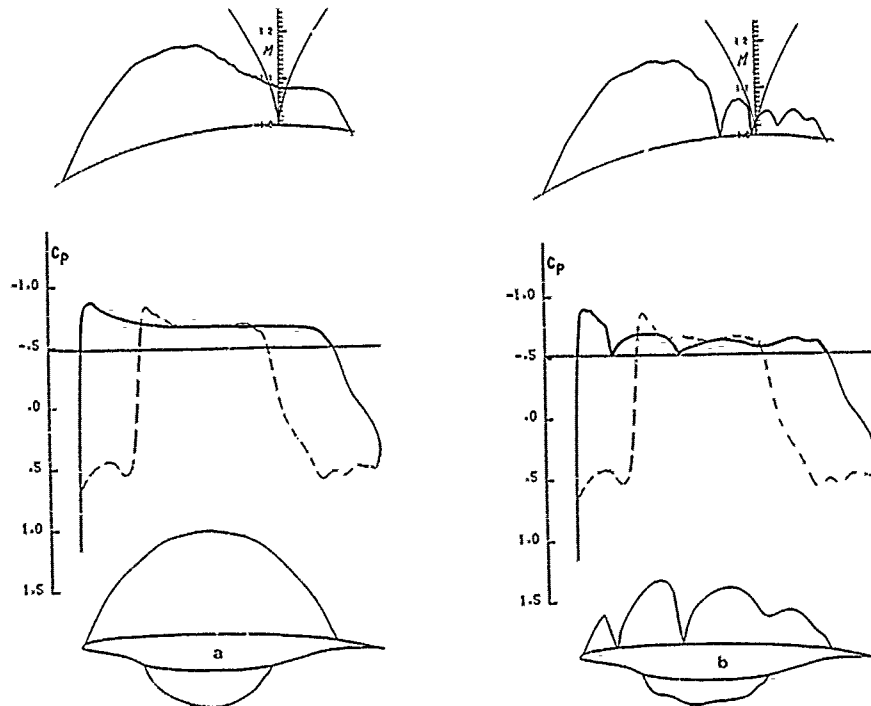
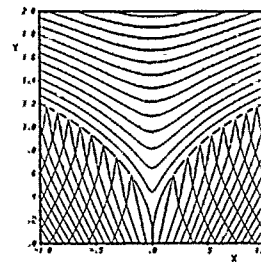
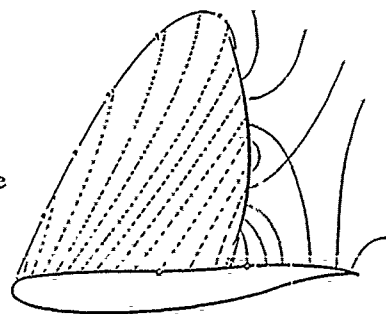


Fig. 3: Laminar Flow Control Airfoil flow (Ref. 6):
Design conditions (a): Mach = 0.783, $c_l = 0.522$.
Off design cond. (b): Mach = 0.772, $c_l = 0.493$.
Sonic lines, Supersonic hodograph mapping.

Fig. 4: Quality of transonic flow field around an airfoil with shock-free surface pressure but a strong shock in the flow field. Supersonic 'expansion' characteristics, Sonic and subsonic Iso-Machlines.



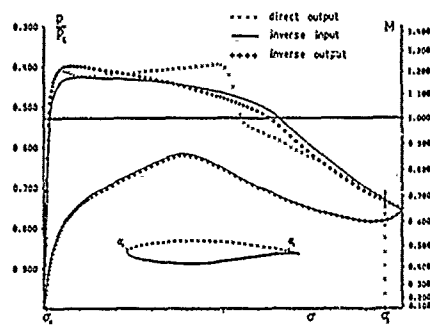


Fig. 5: Mixed Redesign of RAE 2822 airfoil,
(Ref. 15).

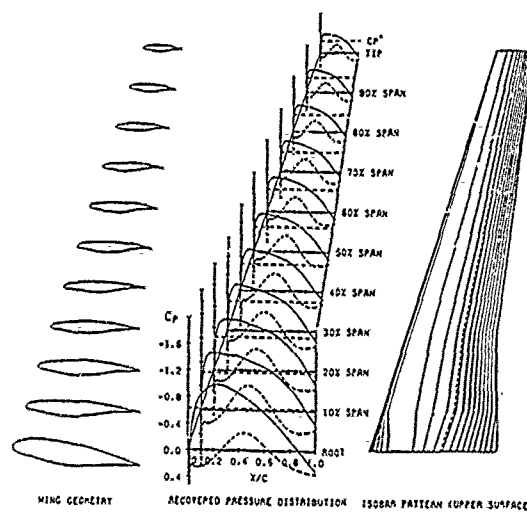


Fig. 6: Inverse Design of a shock-free wing (Ref. 16):
Transonic integral equation plus FLO22 wing analysis.
Mach = 0.74, CL = 0.6492, CD = 0.0123; inviscid flow.

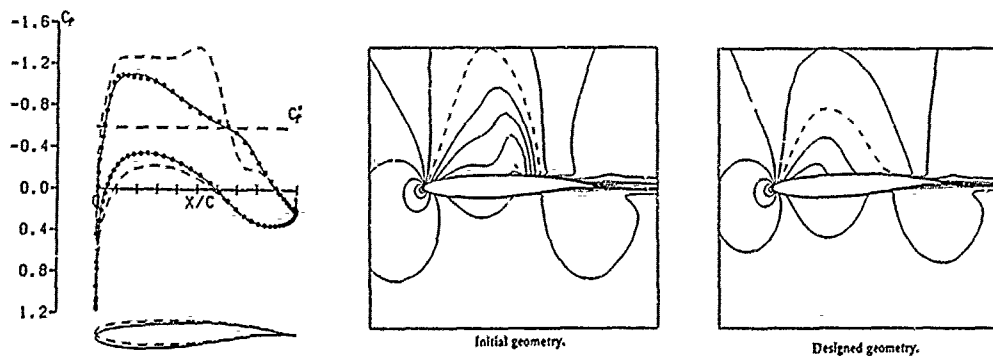


Fig. 7: Viscous Inverse Design of a shock-free airfoil (Ref. 17):
Transonic integral equation plus 2D Navier Stokes code.

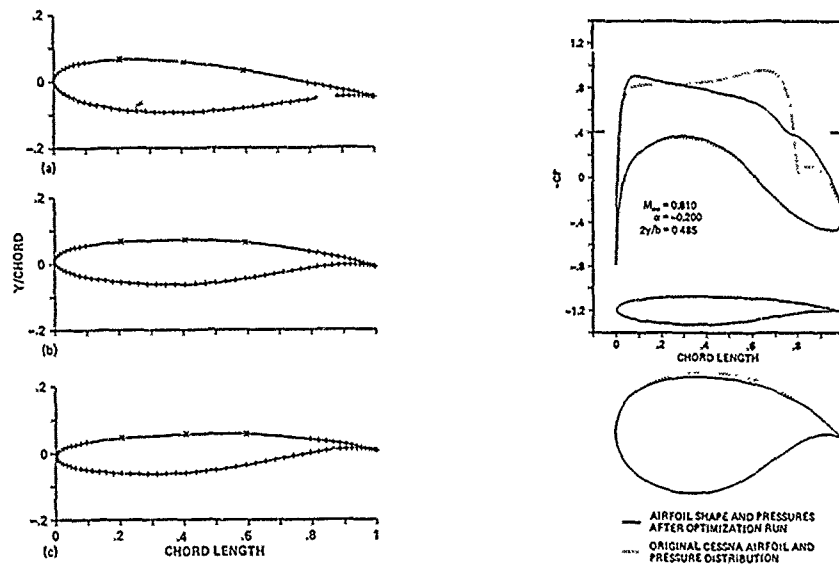


Fig. 8: Transonic wing optimization using parameterized geometry (Ref. 20). Movable spline supports for wing root, midspan and tip sections. Comparison of section pressures before and after optimization

Fig. 9: Typical optimization history for waverider design (Ref. 24).

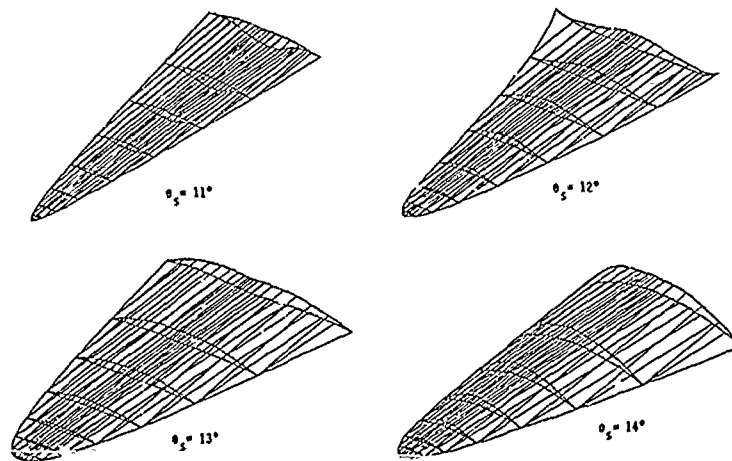
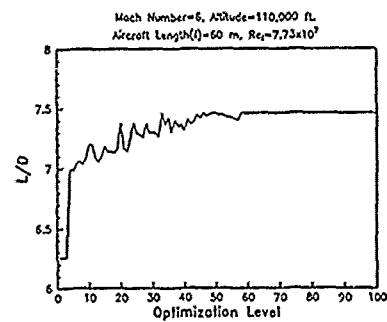


Fig. 10: Optimized waverider shapes using conical flow fields generated by cones with different semiangles θ_s (Ref. 23).

AEROFOIL DESIGN TECHNIQUES

A J Bocci
Aircraft Research Association Limited
Manton Lane, Bedford, MK41 7PF, England

SUMMARY

Various aerofoil design exercises carried out at ARA over the years are described, concentrating on the part played by the inverse methods. The design of an aerofoil suitable for the wing of a combat aircraft research model was successful in meeting a number of performance requirements but the inverse supercritical method used gave an unsatisfactory intermediate profile and off-design calculations were necessary to resolve the problem. In a research exercise involving the design of an aerofoil suitable for the wing of a

transport aircraft to take advantage of full-scale Reynolds number, the inverse supercritical method used produced changes to the geometry in an opposite sense to those finally required. It is suggested that the difficulties with the inverse supercritical methods arose because appropriate design target pressures were not known and because viscous effects were not included in the methods. Subsequent designs of laminar flow aerofoils and high-speed propeller blade aerofoils are described. For these cases, a technique was used involving a subcritical method, with progressive adjustment of target pressures until a geometry arose with suitable flow development according to a viscous supercritical method, with little use of supercritical inverse methods.

1 INTRODUCTION

A fair amount of experience in aerofoil design for various applications has been gained at ARA over the years. The applications have included combat aircraft wings, transport aircraft wings with either largely turbulent flow or extensive regions of laminar flow, and propeller blades. Usually, the work has consisted of design research exercises aimed at advancing the state of the art but the work has sometimes had direct practical application, notably in the case of aerofoils for propeller blades. The more academic investigations have focused on a primary design point but off-design performance and practical constraints have been taken into account in the more applied investigations. The flows of interest have almost invariably included supercritical regions and shock waves, particularly at the primary design point; these have a major influence on the aerofoil performance. This paper will review various aerofoil design exercises carried out at ARA and comment on the techniques used.

Up until around 1970 it was customary in the UK to carry out aerofoil design work using subcritical methods and then to investigate the performance of the aerofoil in wind tunnel tests. Inverse subcritical methods were available for the design work, giving the aerofoil geometry for a prescribed flow distribution. With the advent of 'supercritical' aerofoils it was necessary to develop greater understanding of the relationship between surface geometry and supercritical flow development, the relationship differing from that in subcritical flow conditions.

The approach adopted in the UK to designing the early supercritical aerofoils was to combine such understanding with an assessment of the likely supercritical flow development implied by the subcritical methods. Elsewhere such aerofoils were developed using supercritical inverse methods for shock-free flows (eg Refs 1,2) although the methods were very difficult to use. Also, supercritical aerofoils of the type proposed by R T Whitcomb were developed by, presumably, empirically modifying the geometry on the basis of experimental evidence; mathematical expressions for the profiles of such aerofoils are given in Ref 3.

In recent years, methods for calculating viscous supercritical flows about aerofoils have been developed and are in routine use. The methods are sufficiently accurate that it is now no longer always considered essential to confirm the performance of the aerofoil by carrying out wind tunnel tests. The majority of such methods involve analysis of the flow for a given geometry but inverse versions of some of the methods have been developed. When the latter became available it was hoped that a more flexible approach to supercritical aerofoil design would be possible. However, experience at ARA with two inverse supercritical methods showed up fundamental problems in their use. These were not necessarily a consequence of deficiencies in the methods themselves but, rather, of uncertainties as to what pressures should be prescribed to correspond to an achievable geometry in the supercritical region and result in an aerofoil with the required viscous flow development and overall performance. As a result of such experience, a relatively conservative design approach has been adopted at ARA, with less emphasis on the use of inverse supercritical methods.

In this paper, two aerofoil design exercises will be considered which illustrate the problems which arose in using the inverse supercritical methods. These exercises involved the design of a combat wing aerofoil and an assessment of the performance improvement which could be expected from a transport wing aerofoil designed for full-scale Reynolds number. In subsequent sections, examples of more recent aerofoils designed for laminar flow wings and the blades of advanced propellers will be described more briefly, with an indication of the techniques used.

The methods used in the various aerofoil design exercises considered here were taken from the following.

- (a) Inviscid subcritical Weber theory (analysis and inverse), Ref 4. In this method, solutions for thickness and camber are linearly superimposed and only aerofoils with sharp trailing edges can be dealt with.
- (b) 'DES2D', an inviscid small perturbation (TSP) method (analysis and inverse), Ref 5. This method was developed at ARA. The inverse capability applies aft of a fixed leading edge region, with a regular

updating of the surface geometry during the calculation iterations. A normal velocity related to the prescribed tangential velocity by the vorticity equation and thus defines the surface slope and, hence, the profile.

- (c) TSPVISC, a viscous transonic small perturbation (TSP) method (analysis), Ref 6. This method was developed at the RAE; the inviscid component is believed to be a slight improvement on DES2D.
- (d) G+K, the Bauer, Garabedian and Korn inviscid supercritical method (analysis), Ref 2.
- (e) The Traner design method, Ref 7, as programmed at ARA (analysis and inverse). A G + K analysis solution is coupled to an inverse solution with Dirichlet boundary conditions on the aerofoil surface, in an iterative process, to provide a design version of G + K. The detailed velocity distribution around the leading edge must be prescribed and there is an option of specifying a fixed trailing edge thickness.
- (f) VGK a viscous coupled version of G + K (analysis), Ref 8.
- (g) Jameson an inviscid method capable of providing solutions for cases with both subsonic and supersonic free streams (analysis), Ref 9.

Also some results are shown which were obtained using,

- (h) BVGK, a development of VGK which includes various second order viscous effects and provides a more accurate solution (analysis), Ref 10. This method became available after the design exercises considered here were complete.

The Weber subcritical method provides approximate solutions to the incompressible potential flow equation, with appropriate compressibility corrections included. The supercritical methods provide solutions to the compressible potential flow equation, by finite difference techniques involving field grids. The inverse methods were subject to comprehensive checks to ensure that the correct geometry was retrieved on specifying surface pressures obtained from the analysis mode solution, including supercritical cases with shocks.

Aside from the above comments, the details of the methods used are not discussed in this paper.

In the next section, some general characteristics of supercritical aerofoils will be described, to set the scene. The combat wing aerofoil design exercise is discussed in section 3 and the high Reynolds number design exercise in section 4. The laminar flow and propeller blade aerofoils are described in sections 5 and 6, respectively.

2 SUPERCRITICAL AEROFOIL FEATURES

Broadly speaking, the design of supercritical aerofoils involves geometric shaping to control the flow development such as to maximise lift or thickness/chord at a given Mach number, subject to constraints on wave drag and viscous drag, and the avoidance of significant flow separation. Typical features of the flow development and geometry of a supercritical aerofoil are sketched in Figs 1(a), (b), including some terminology commonly used. The flow development shown, with an isentropic recompression ahead of a weak shock, is actually representative of a drag-rise cruise point on a transport aircraft wing. The flow development would be different at other conditions, or on aerofoils for different applications.

A primary aerofoil parameter is thickness/chord. At the condition shown, the maximum velocity due to thickness alone may be near to sonic, and the thickness/chord which gives this velocity reduces as the freestream Mach number increases. The thickness form tends to be cusped towards the trailing edge, with a low included angle and some base thickness. The base thickness is limited by the need to avoid excess base drag.

The term 'rooftop' refers to a region of roughly constant, near-maximum velocity on either surface. A near-sonic rooftop would occur on the upper surface at a lower incidence but it is restricted to a region just downstream of the shock in the supercritical condition shown. The steep pressure rise over the aft part of the upper surface commences at the end of the rooftop.

The combined effect of an extensive rooftop and the cusped thickness form is to give appreciable rear loading, with a concave lower surface over the rear of the aerofoil. The rooftop extent is constrained by the need to avoid excess viscous drag and/or flow separation due to the steepness and magnitude of the aft pressure rise. This is alleviated by the effects of the low included angle at the trailing edge and the base thickness, which tend to reduce the trailing edge pressure towards the freestream value. The aft pressure rise reduces with increasing freestream Mach number and so the corresponding rooftop extent increases. The combination of thickness/chord, thickness form and rooftop extent at the condition shown determines the steepness and magnitude of the lower surface aft pressure rise, and this should be constrained to avoid viscous penalties.

Consider next the supercritical flow development. Over the supercritical region the surface curvature generates expansion waves which reflect from the sonic line as compression waves. If the supersonic velocity is constant the curvature is such that there is an exact balance between the rate at which expansion waves are generated at the surface and the rate at which compression waves arrive at the surface. Increased curvature towards the leading edge together with reduced curvature, or flattening, over the main supercritical region gives a trend to a higher peak suction followed by a recompression. The recompression occurs because the incoming compression waves originating near the leading edge over-ride the reduced expansion from the flatter region. The shock strength depends on the total surface slope change between the sonic point on the nose and the shock position, as a measure of the net expansion in the supercritical region.

The peak suction level may need to be constrained to avoid excess wave drag at lower Mach numbers, where the shock is located well forward on the chord. If the surface curvature over the main supercritical region is too low, the recompression may break down into a further forward, stronger shock. If the region of low surface curvature is followed by sufficiently high surface curvature at the end of the rooftop, there may be a supercritical expansion to a second shock. The resulting aft pressure rise may then give viscous penalties.

It is apparent from the above comments that the aerofoil design has a strong dependence on viscous effects. Hence Reynolds number is an important parameter. Also, the accuracy of representation of viscous effects in the theoretical methods could affect the quality of the design achieved. Only inviscid inverse methods were available for the design exercises discussed here but the inviscid designs were examined using viscous supercritical methods. Some reassessment of the earlier designs by the more recently available BVSK supercritical viscous method is included here.

3 COMBAT WING AEROFOIL

This exercise represented an early (1973) attempt to use the newly-available TSP supercritical theory for aerofoil design. The aerofoil was intended to form the basis of the swept wing of a combat aircraft research model which was to be manufactured and tested in the ARA 9'x8' (2.74m x 2.43m) transonic wind tunnel. The design requirements of the aerofoil were translated from those of the 3-D wing using simple sweep concepts. The design requirements, the test performance achieved and the final aerofoil geometry are shown in Fig 2. It can be seen that the design requirements comprise three separation boundary points at $M=0.5$, 0.7 and 0.75 , high lift, and a drag rise point at $M=0.75$, $C_L=0.0$. The aerofoil design and test Reynolds number was 3.5×10^6 , for consistency with the 3-D wing test conditions. Only a brief description of the overall design exercise will be given, the main intention being to discuss the use of the DES2D program to develop the aerofoil geometry to meet the high lift requirement at $M=0.75$. The design exercise is described in more detail in Ref 11.

The starting point for the work was an existing aerofoil of about 8% thickness/chord, derived from an earlier wing of similar planform. The first design steps included incorporation of a drooped leading edge profile, taken from a separate aerofoil which had demonstrated good high lift characteristics at $M=0.5$, and a modification to the forward lower surface to weaken an excessively strong shock wave which was predicted at low lift, to ensure that the drag rise requirement would be met. The lower surface problem was partly a consequence of the introduction of the drooped leading edge, and the modification resulted in an increase in thickness/chord to just over 10%. Also, a blunt trailing edge of 1% thickness/chord was introduced, in an attempt to avoid the possibility of premature flow separation at the trailing edge, at the relatively low design Reynolds number. At this stage of its development, a calculation using the DES2D program indicated that at high lift at $M=0.75$ an excessively strong shock was to be expected on the upper surface and that extensive redesign of much of the upper surface would be required if the separation boundary requirement was to be met.

The next step taken was to 'key' the upper surface geometry to that of the Korn aerofoil (Ref 2), an aerofoil which was believed to feature a desirable upper surface supercritical flow development at $M=0.75$. A design calculation was performed at $M=0.75$ using subcritical Weber theory, with target upper surface pressures similar to those calculated for the Korn aerofoil using the same theory. The pressures are shown in Fig 3(a), with the aerofoil at this stage of its development referred to as aerofoil A. The minor differences in pressures over the supercritical region were partly a consequence of keeping the geometry of the leading edge and much of the lower surface unchanged in the design calculation. It was necessary to remove the thick trailing edge from aerofoil A to enable the Weber theory to cope. The subcritical theory cannot, of course, predict the true supercritical flow development; the exercise was purely for matching purposes. The intention was to go at least part of the way towards a suitable upper surface geometry and then to use the DES2D supercritical method to refine the design.

Fig 3(b) shows that the shock strength was still high on aerofoil A (with the thick trailing edge reintroduced) according to DES2D, at a lift coefficient $\Delta C_L \approx 0.1$ below the target. Attempts were made to weaken the shock by specifying the design target pressures shown. However, all that could be achieved, despite repeated attempts, were the pressures corresponding to aerofoil B. This was felt to be an improvement on aerofoil A in that the shock was slightly weaker, despite the re-expansion ahead of the shock. A check calculation on aerofoil B at $M=0.7$ suggested that the design was reasonably consistent with the separation boundary requirement at that Mach number but that the flow development at a Mach number intermediate between 0.7 and 0.75 would be worth investigating. The result of a DES2D calculation at $M=0.73$ is shown in Fig 3(c) and it is clear that the supercritical flow development has broken down into a two-shock system. Design target pressures which removed the second supercritical region were then specified, as shown, and the program successfully converged to this target. Following some mild smoothing of the blend between the fixed leading edge shape and the rest of the aerofoil, this defined the final geometry.

During the course of the final design iterations, the lower surface geometry had remained fixed, as well as the leading edge geometry. The changes to the upper surface left the overall thickness/chord almost unchanged but the trailing edge thickness/chord had increased to about 1.4%. It was assumed that any increment in drag due to the base thickness would be small enough to be ignored in a combat aircraft context but the lack of control over base thickness was felt to be an undesirable feature of the design approach followed.

Having completed the design it was necessary to check that the aerofoil would meet the design targets. For the high lift point at $M=0.5$ and the zero lift point at $M=0.75$ the G+K method was used because the shock was located fairly close to the leading edge in both cases and TSP methods typically fail to provide an adequate prediction of suction peaks around the leading edge. Allowances for viscous effect were estimated, partly, on the basis of similar calculations for other tested aerofoils. At $M=0.7$, 0.75 the high lift performance was assessed using TSPVISC. Predicted pressures at $M=0.75$ are shown in Fig 4(a)

compared with those subsequently obtained in the experiment, over a range of incidences approaching the separation boundary. The likely performance was inferred from the predicted shock strength and boundary layer development. The supercritical flow development and shock strength are quite well predicted by the theory but there are substantial differences in pressures between theory and experiment over the aft part of the aerofoil, presumably due, in part, to inadequate modelling of thick base effects, and this implies that the predicted boundary layer development was incorrect. However, it was concluded from the above checks that the aerofoil would meet this and other design targets and reference to fig 2 shows that this proved to be the case.

Pressures at $M=0.75$ calculated by the subsequently developed BVGK method are compared with experiment, at the same values of C_l , in Fig 4(b) and it can be seen that the comparison over the aft part of the aerofoil, in particular, is much improved compared with TSPVISC. The remaining differences are as likely to be a consequence of inadequacies in the experiment as in the theory. It is interesting to note that the BVGK calculations predict the onset of flow separation at the foot of the shock and this is consistent with examination of the experimental data, which suggest that the aerofoil exhibits predominantly 'class A' separation characteristics (see Ref 12) over a range of Mach numbers. This is presumably the major reason for the satisfactory prediction of performance using methods with inadequate representations of viscous effects. Nowadays, a method such as BVGK can be used to predict aerofoil performance characteristics with much greater confidence. Note that had the design exercise stopped with aerofoil B, the influence of the viscous flow development would have been greater and the performance would have been more difficult to predict with the methods available at the time.

Looking back on the design exercise, it appears probable that the target supercritical peak suction and recompression, shock strength and position for aerofoil B, shown in Fig 3(b), were inconsistent with a possible surface geometry. The recompression required a flatter upper surface aft of the fixed leading edge and so higher curvature was needed around the shock position to match the original profile further aft, and this implied a stronger shock. The supercritical flow development on the final aerofoil shown in Figs 4(a), (b) suggests that associating the target recompression with a further forward shock position would have proved more successful. This was not obvious at the time, off-design calculations being necessary to resolve the problem.

4 TRANSPORT WING AEROFOIL

It is common practice to design transport aircraft wings to achieve acceptable performance in wind tunnel tests and then to extrapolate the test data to predict the performance at full-scale Reynolds number. Almost invariably, a performance increment, a consequence of the thinner viscous layers, is predicted. Another approach would be to design from the start to take advantage of the thinner viscous layers, although considerable confidence in techniques for extrapolation of the wind tunnel data, or tests at appreciably higher tunnel Reynolds numbers than available at present, would be required before going ahead with an aircraft project designed on such a basis. The exercise discussed here concerns a theoretical attempt to quantify what performance increment could be expected of a 2-D aerofoil from such an approach. The work was carried out shortly after the VGK and Tranen programs became available at ARA (1978), these methods being used rather than the TSP methods since their improved accuracy was felt to be necessary. Also, the option of fixing trailing edge thickness was an attractive feature of the Tranen program.

A research aerofoil of relatively advanced aerodynamic standard (although not an optimum design) was selected as a datum and a new aerofoil was designed for a representative full-scale Reynolds number, subject to certain constraints adopted in an attempt to maintain some consistency in aerodynamic standard. The datum aerofoil was a theoretical design of about 12% thickness/chord, with a nominal cruise point $M=0.75$, $C_l \approx 0.7$. At this condition the flow featured an isentropic recompression ahead of the shock, and viscous layers which were judged to remain attached and likely to contribute little or no excess viscous drag at a Reynolds number of 6.0×10^6 , according to a VGK calculation with transition assumed close to the leading edge on both surfaces. The base thickness was about 0.5% chord. The Reynolds number assumed is typical of tests on 5 inch (127mm) chord models in the ARA 18 inch x 8 inch (457mm x 203mm) 2-D wind tunnel. Pressures on the datum aerofoil at the cruise point are included in Fig 9, which will be discussed later. The aim in the design exercise was to increase lift for a given thickness/chord, by extending the upper surface rooftop and moving the shock downstream by a similar distance. The constraints adopted were that the shock strength, viscous flow development and pitching moment of the full-scale design should be similar to those of the datum aerofoil and that the leading edge suction peak should not be exceeded.

In redesigning the datum aerofoil, the identical base thickness was retained. In the calculations referred to below, the base thickness was included in the geometries used for the VGK and BVGK calculations but was removed from the geometries used for the Weber calculations because of the sharp trailing edge requirement.

An initial aerofoil shape was obtained by using Weber theory to redesign the upper surface to give an extended rooftop. The target rooftop extension was adjusted until, at a representative full-scale Reynolds number of 35.0×10^6 , the boundary layer development towards the trailing edge matched that of the datum aerofoil at the lower Reynolds number, according to VGK. The intention was to go most of the way towards a suitable upper surface geometry using the subcritical theory and then to refine the design using the Tranen program. It was found that simply extending the rooftop had no effect on the shock position, which remained the same as on the datum aerofoil, and it appeared that it would be necessary to use the supercritical inverse method to move the shock downstream.

For the Tranen calculations, displacement surface geometries were used so that the inviscid pressures were not too different from what would be given by a viscous calculation. The starting point for the redesign was a GVK calculation on a displacement surface geometry given by smoothing the VGK boundary layer displacement thicknesses and adding these to the initial shape. Fig 5 shows pressures given by this calculation and by a calculation for a shape which arose from several loops through the Tranen program, compared with the design target. The design target pressures on the upper surface were chosen to be the

same as for the initial shape apart from the downstream shift of the pressure rise corresponding to the shock. On the lower surface, the design target pressures were chosen in line with the pitching moment requirement. Also, the lower surface adverse pressure gradient was expected to result in a match of the viscous flow development of the datum aerofoil in that region, at the higher Reynolds number.

It appears from Fig 5 that the Tranen program has functioned satisfactorily as an inverse of G&K, apart from the fact that the suction peak close to the leading edge is higher than specified. The reason for this may be inferred from the comparison of aerofoil displacement surface geometries in Fig 6, plotted to an expanded scale to illustrate the differences clearly. The calculation has moved the shock aft by increasing the surface curvature downstream of the original shock position. The surface slope is similar at the new shock position, since a similar shock strength is required. The net result is that the surface further forward is tilted down, giving increased curvature where the surface blends with the leading edge and, hence, a higher suction peak. It is probable that an upper surface geometry could not be found which corresponded precisely to the target pressures.

The technique adopted for arriving at the final shape involved the use of Weber theory. For this purpose it was necessary to define a sharp trailing edge version of the Tranen design geometry and this was done by removing displacement thicknesses as well as the base thickness. For convenience, the displacement thicknesses which had been added to the initial shape were used, although these took no account of the changed pressures. Fig 7 shows the results of Weber calculations which were then carried out for the initial and Tranen designs.

The pressure distributions in Fig 7 are, again, unrealistic in the supercritical region. However, the differences between the pressure are qualitatively what might have been expected of the displacement surface geometries already seen in Fig 6. The 'wriggle' in the pressures for the Tranen design originated in the choice of the design target shock pressure rise. The difference in suction levels towards the end of the rooftop suggested that differences in upper surface boundary layer development towards the trailing edge would be expected in viscous flow conditions. It was essential to control this feature but it was felt that this could not be done, adequately, by continuing to use the supercritical method to refine the flow development on the displacement surface geometry. The design work was continued using the Weber theory, with target pressures progressively adjusted until what was thought to be a suitable flow development was given by VGK.

Fig 8 shows the final geometry compared with the earlier shapes, with the coordinates shifted to match at the trailing edge. Figs 9(a), (b) show pressures on the datum and final aerofoils given by VGK and by later calculations using BVGK. It was found that a reduced peak suction and a lower rate of supercritical recompression were required on the final aerofoil, to give a shock of similar strength to that on the datum aerofoil, at the further aft position. The BVGK pressures differ in detail from those given by VGK but show similar trends between the two aerofoils. The pitching moments are not given but were very similar for the two aerofoils, according to both methods.

The viscous standard of the datum and final aerofoils was compared on the basis of the development of the calculated boundary layer incompressible shape parameter H . Figs 9(a), (b) include variations of this parameter approaching the trailing edge on the upper surface and around the maximum value on the lower surface and it can be seen that the values compare closely between the two aerofoils according to both VGK and BVGK. In view of the improved prediction of viscous effects expected of BVGK, the comparison of skin friction C_f is of interest, as a more direct indication of how close the flow is to separation. Variations of C_f are included in Fig 9(b) and it can be seen that the values are reasonably consistent on the upper surfaces of both aerofoils but there are appreciable differences on the lower surface, a result to be expected for flows with similar values of H (not close to separation) and a factor of 6 difference in Reynolds number.

The lift increment from designing for full-scale Reynolds number was assessed to be over 10% according to the VGK comparisons, with the constraints adopted, but this assessment clearly depends on the accuracy of the viscous representation. The later BVGK calculations confirm the VGK assessment, apart from possible consequences of any changes to the lower surface which might be desirable in the light of the C_f comparison.

Referring back to Fig 8, it is noteworthy that the inverse supercritical method changed the upper surface of the initial geometry in an opposite sense to the changes required for the final geometry. This occurred because the choice of supercritical target pressures was not quite appropriate and because viscous effects were not allowed for adequately by using the displacement surface geometry. The experience gained in this design exercise, and in the combat wing aerofoil design exercise discussed earlier, has led to a reluctance at ARA to attempt to make significant changes to the supercritical flow development using the inverse supercritical methods. Instead, the approach adopted in more recent aerofoil design exercises has been to get to know the effects of geometric changes on flow development, using inverse methods in subcritical conditions, mostly, and by using mathematical expressions or drawing, as appropriate, to define the profiles. The next two sections contain brief descriptions of aerofoils designed more recently at ARA using this approach.

5 LAMINAR FLOW AEROFOILS

Fig 10 shows geometries and pressures for two research aerofoils designed to maintain significant runs of laminar flow on both upper and lower surfaces in conditions corresponding to cruise. The NLF aerofoil was representative of the outer wing of a possible executive jet aircraft, with a Reynolds number of 10.0×10^6 assumed. The suction aerofoil was representative of the outer wing of a possible medium sized civil transport aircraft, with a Reynolds number of 35.0×10^6 assumed. The sweep was taken to be about 20° in both cases. Flow conditions on the 2-D aerofoils were related to 3-D using simple sweep concepts. The design pressures were used in conjunction with sheared or tapered wing finite difference boundary layer methods, with transition predicted according to various simple criteria and 3-D stability analysis. Transition position has a strong dependence on Reynolds number and so it was necessary to use the flight values in the calculations.

The pressures on the NLF aerofoil were given by a VGK calculation. Both Weber theory and the Tranen program were used in the design of the profile, with the Tranen program particularly useful in controlling the pressure gradients over most of the forward parts of both surfaces. This was necessary to constrain the amplification of instabilities in the laminar boundary layer velocity profile, both in the streamline direction (Tollmien-Schlichting) and in the cross-flow direction, and thus delay the onset of transition to turbulent flow. The detailed leading edge shape was important in avoiding both attachment line contamination and transition due to cross-flow in the favourable pressure gradients immediately aft of the leading edge. It was found difficult to control the detailed leading edge shape in design calculations using the Tranen program, and empirical modification of the shape by drawing was resorted to.

Similar techniques were used in the design of the suction profile. The pressures were given by a G+K calculation for the displacement surface geometry, the boundary layers being extremely thin at the high Reynolds number, with laminar flow assumed to be maintained to a far-aft chordwise position on both surfaces. The extent of laminar flow assumed was reasonable because the specified suction quantities could be increased until transition was avoided, according to the transition prediction methods. The pressures were chosen to minimise the suction quantities required to maintain laminar flow, with little or no wave drag.

Pressure distributions at two slightly different freestream Mach numbers are shown in Fig 10(b) and either of these could be regarded as representative of cruise conditions. Pressure gradients over the laminar flow regions are either very steep or near zero. These features minimise the tendency to cross-flow transition, and suction is mainly necessary to constrain the amplification of instabilities in the streamline direction. Higher suction is needed in the shock-free case due to the increased amplification of the streamline instabilities in the adverse pressure gradient. In the higher Mach number case, the favourable pressure gradient is more suited to maintaining laminar flow but it would be difficult to delay transition beyond the shock position.

The Tranen program was used to smooth the supercritical flow development, which was very susceptible to slight surface unevenness in the supercritical flow region, particularly in the shock-free case. The program was also used to define the shape required to give the lower surface pressures away from the leading edge. The very small leading edge radius was necessary to avoid attachment line contamination, and cross-flow transition close to the leading edge. It was found essential to define the leading edge shape, and the blend with the rest of the profile, by drawing.

Note that the two aerofoils considered here are very specialised, although not necessarily optimised, for the different applications. If changes in such parameters as sweep or Reynolds number were required, the effects of changes to transition position in the NLF case, or suction quantities in the suction case, would need to be included in the design process. Optimising such aerofoils for project applications could be a substantially more laborious process than for turbulent flow aerofoils and more straightforward design techniques than were used for the cases considered here would be desirable.

6 PROPELLER BLADE AEROFOILS

Propellers incorporating the ARA-D series of aerofoil sections are fitted to a number of commuter aircraft. The design of these aerofoils has been described in Refs 13, 14 and this will not be repeated here, except to say that the aerofoils are intended to operate at significantly higher lift coefficients than NACA series 16 or 65, traditionally used in propeller blades. This means that it is possible to produce propellers with reduced blade chord and hence weight, higher take-off thrust and improved climb and cruise efficiency. Alternatively, the aerodynamic advantages can be exchanged for reduced tip speed and thus noise.

Selected sections from the ARA-D/A series are shown in Fig 11(a). These are essentially identical to the ARA-D series for values of thickness/chord less than 10% but the thicker sections have been modified slightly to reduce upper surface super-velocities at the higher aircraft cruise speeds which are becoming more common. The high camber levels of the sections are apparent and these are mainly intended for the purpose of improving take-off performance. A camber factor, referred to as K1, is applied to the tip sections to improve the high Mach number performance, since blade onset Mach numbers at the tip can be close to sonic, even for relatively low cruise speed aircraft. The camber factor also varies from unity across the complete radius of a typical blade, for structural reasons and in order to produce smooth blade surfaces when the aerofoil sections are stacked. The complete ARA-D/A series is, like the ARA-D series, defined by simple mathematical expressions which give the complete profile, of regular and smooth shape, once the thickness/chord and camber factor are specified.

The ARA-D/A aerofoil sections are well suited to propellers designed for aircraft cruise speeds up to about $M=0.6$. For higher cruise speed cases the sections provide acceptable performance when thickness and camber are reduced, and the spinner is shaped to slow the onset flow over the thicker sections towards the root. However, the aerofoils were not optimised for such conditions and Fig 11(b) shows a selection of profiles from a new series, referred to as ARA-D/S, which were designed to maintain high values of lift/drag up to higher Mach numbers than ARA-D/A.

Pressures on ARA-D/S aerofoils of 2%, 10% and 20% thickness/chord (t/c), representative of tip, inboard and root stations, respectively, on the blade of a high-speed propeller are shown in Figure 12. The 2-D freestream Mach numbers correspond to the helical Mach numbers on the advancing blade, possibly including some reduction due to spinner shaping for the thicker sections. The lift coefficients are around those for peak lift/drag at the given Mach number, as would be expected to occur on a blade designed for maximum aerodynamic efficiency.

The pressures for the 2% t/c case in Fig 12(a), at a supersonic freestream Mach number, were calculated using the inviscid Jameson method. The pressures for the 10% t/c and 20% t/c cases were calculated using VGK and extensive runs of laminar flow were indicated at the relatively low Reynolds numbers of 3.0 and

2.0×10^6 , respectively, assumed for the calculations. These Reynolds numbers are representative of cruise conditions on the blades of the high-speed rotors planned for application to medium-sized transport aircraft.

The 2% t/c aerofoil comprises circular arc components blended smoothly to a nose shape defined by drawing, with the aerofoil geometry optimised to minimise wave drag at supersonic speeds, according to the theory.

The 10% t/c and 20% t/c aerofoils have similar nose radii, trailing edge included angles and base thicknesses to the corresponding ARA D/A aerofoils, and the surface curvatures vary smoothly along the chord. These aerofoils were designed in subcritical conditions using Weber theory, with the base thicknesses removed from the geometries, and the supercritical viscous flow development was checked using VGK. The separate design of thickness and camber was a convenient feature of the Weber theory in view of the geometric constraints on thickness form. However, the design of the thicker aerofoil presented difficulties due to limitations on accuracy arising from the linearised basis of the theory. It can be seen from Figs 12(b), (c) that it was possible to define aerofoils with relatively advanced supercritical flow development by this approach. The rooftop extents were chosen such that, at the relatively low Reynolds numbers assumed, well-attached flow was predicted by VGK calculations with transition assumed to occur close to the leading edge on both surfaces. This is a conservative assumption which allows for possible in-service deterioration of the blade surfaces.

ARA-D/S aerofoils of intermediate thickness/chord vary smoothly in geometry and pressures between the key 2% t/c, 10% t/c and 20% t/c aerofoils. A means of varying camber for an aerofoil of given thickness/chord is necessary for application to propeller blades, and this is introduced by interpolating geometries between the ARA-D/S aerofoil, of nominally zero camber, and the ARA-D/A aerofoil of camber factor unity. The interpolated camber level is defined by a K1 factor, as for the ARA-D/A aerofoils.

In addition to enabling a practical blade geometry to be defined, the camber variation introduces the possibility of optimising the section geometries in the interests of the overall performance of the propeller. Taking the 10% t/c case as an example, Fig 13(a) shows pressures on ARA-D/A and ARA-D/S aerofoils at nominal cruise conditions, and on an interpolated geometry at an interpolated Mach number. The geometric definition of the ARA-D/A and ARA-D/S aerofoils ensures that the intermediate geometry is regular and smooth, as can be seen from the pressures. The lift/drag characteristics also interpolate smoothly, as can be seen from Fig 13(b). This means that if the Mach numbers on the propeller blade in cruise are not high enough to require the full ARA-D/S performance, interpolated sections of higher camber than ARA-D/S can be used, in the interests of take-off/climb performance. The ARA-D/S aerofoils are currently being used by Dowty Rotol Ltd in the design of blades for high speed propellers. The geometric constraints, adopted in the interests of ensuring a smooth variation across the blade and blending with ARA-D/A aerofoils, placed some limitations on the scope for detailed refinement of the individual aerofoils. Even so, the aerofoils feature advanced supercritical flow development, and performances in line with requirements.

CONCLUDING REMARKS

- 1 The general features of supercritical aerofoils representative of a drag-rise cruise point on a transport aircraft wing have been discussed. The importance of viscous effects to the design was emphasised and the dependence of the supercritical flow development on surface curvature was described.
- 2 Various aerofoil design exercises carried out at ARA, involving the use of both subcritical and supercritical inverse methods, have been reviewed. The inverse methods used were inviscid but the designs were examined using viscous supercritical methods.
- 3 A combat wing aerofoil design exercise was successful in meeting a number of target performance requirements. However, use of an inverse supercritical method gave an unsatisfactory intermediate profile and off-design calculations were necessary to resolve the problem.
- 4 A transport wing aerofoil design exercise involved assessing the performance increment to be expected from designing to take advantage of full-scale Reynolds number. Viscous effects were particularly important in this exercise but it was felt that these could not be controlled adequately using an inviscid inverse supercritical method, which produced changes to the upper surface geometry opposite to those finally found to be required. An approximate inverse subcritical method was used to produce the final geometry, involving progressive adjustment of the target pressures until a geometry was achieved with a suitable flow development according to the viscous supercritical theory.
- 5 The reasons for achieving incorrect intermediate geometries using the inverse supercritical methods could be inferred from the relationship between surface curvature and supercritical flow development. Unfortunately, target pressures which satisfy this relationship are not known, in general.
- 6 Laminar flow aerofoils have been designed subsequent to the above exercises and the use of the inverse supercritical methods was limited to design of the lower surface and smoothing the supercritical pressures. The leading edge shape is particularly important for such profiles but the inverse methods were inadequate for this purpose and it was necessary to resort to drawing. The design of such profiles is particularly laborious, since effects on transition must be included in the iterations, and improved techniques would be desirable.
- 7 A new series of aerofoils suitable for the blades of high-speed propellers has been developed recently and is described briefly here. The geometries were mostly designed by the iterative technique involving the approximate subcritical theory. The geometric constraints, and the means of varying the camber level, were included in the interests of practical application.

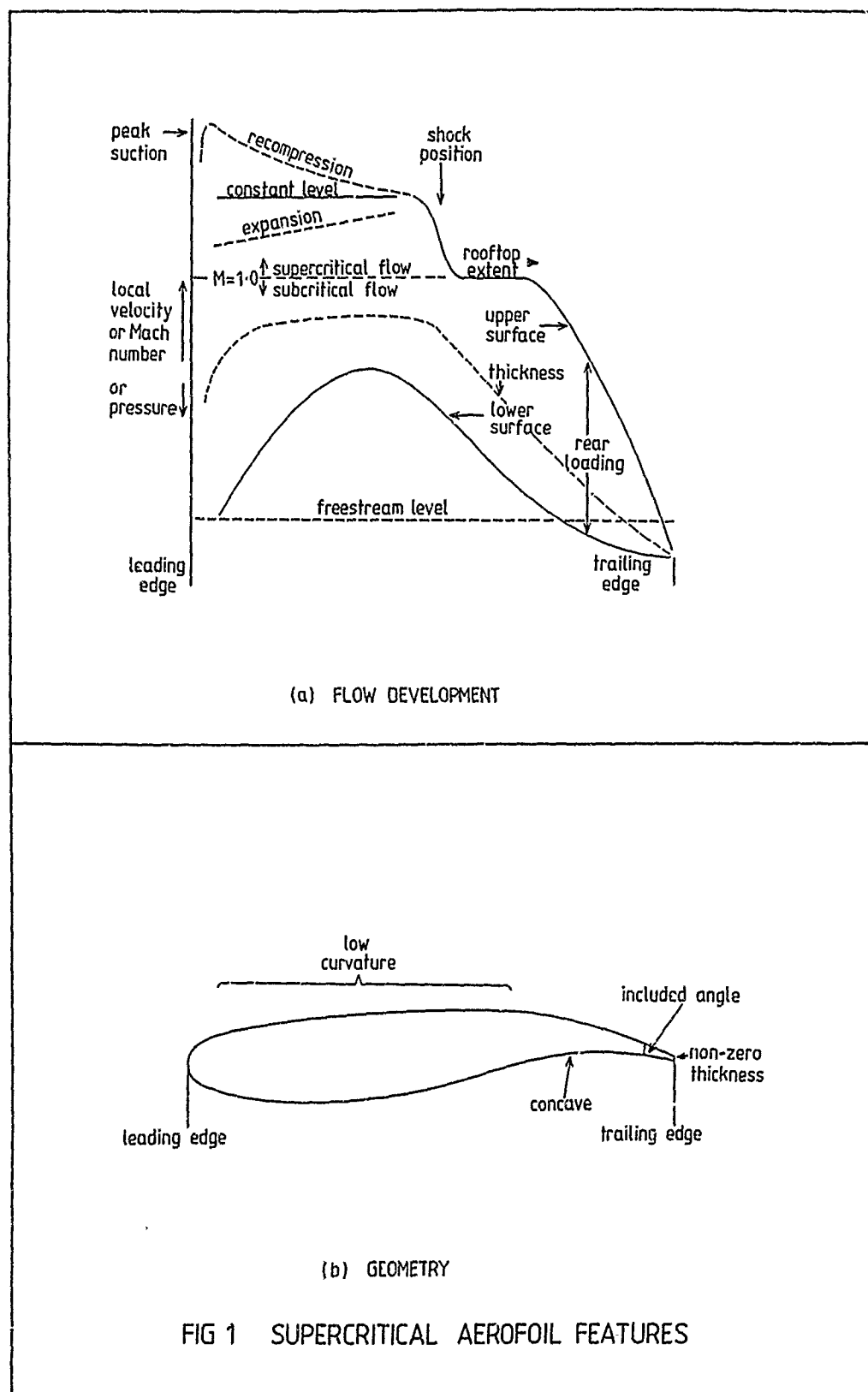
- 8 Finally, it is felt from experience of such design exercises that it is necessary to understand the effects of geometric changes on both the supercritical and viscous flow development. Inverse supercritical methods are unlikely to be entirely suitable for such work unless the supercritical flow/geometry relationship is allowed for and unless viscous effects are included.

ACKNOWLEDGEMENT

The combat wing aerofoil and suction aerofoil design exercises were carried out under contract to the Procurement Executive, Ministry of Defence. The NLF design exercise was part of a program of work involving laminar flow investigations carried out under contract to BAe (Hatfield). The propeller blade aerofoils were designed under contract to Dowty Rotol Ltd, partly supported by the Department of Trade and Industry. The author wishes to thank these organisations for the support received.

REFERENCES

- 1 G Y Nieuwland, Theoretical Design of Shock-free Transonic Flow around Aerofoil Sections, Aerospace Proc. 1966, RAES/ICAS Congress VI
- 2 F Bauer, P Garabedian, D Korn, A Theory of Supercritical Wing Sections with Computer Programs and Examples, Lecture Notes in Economics and Mathematical Systems No 66 published by Springer-Verlag 1972.
- 3 R T Whitcomb, UK Patent Specification 1406826, Filed 1972 in UK.
- 4 R C Lock, B J Powell, C C L Sells, P G Wilbey, The Prediction of Aerofoil Pressure Distributions for Subcritical Viscous Flows (Section 3 - Development of a New Approximate Method for Inviscid Flow), AGARD CP35, 1968, Paper no 12.
- 5 M J Langley, Numerical Methods for Two-Dimensional and Axisymmetric Transonic Flows, ARA Memo 143, 1973.
- 6 A F Jones, M C P Firmin, Unpublished work at the RAE.
- 7 T L Tranen, A Rapid Computer Aided Transonic Airfoil Design Method, AIAA Paper no 74-501, 1974.
- 8 M R Collyer, R C Lock, Prediction of Viscous Effects in Steady Transonic Flow past an Aerofoil, Aeronautical Quarterly Vol 30, 1979.
- 9 A Jameson, Iterative Solution of Transonic Flows over Airfoils and Wings, including Flows at Mach 1, Communications on Pure and Applied Mathematics Vol XXVII, pp 283-309.
- 10 P R Ashill, R F Wood, D J Weeks, An Improved, Semi-Inverse Version of the Viscous Garabedian and Korn method, RAE TR87002, 1987.
- 11 M J Langley, A Harris, A J Bocci, The Design and Measured Performance of Aerofoil M62/5, RAE 1330(U), ARA Report No 49, 1977.
- 12 H H Pearcey, J Osborne, A B Haines, The Interaction between Local Effects at the Shock and Rear Separation - a Source of Significant Scale Effects in Wind Tunnel Tests on Aerofoils and Wings, AGARD CP35, 1968, Paper no 11.
- 13 A J Bocci, A New Series of Aerofoil Sections suitable for Aircraft Propellers, Aeronautical Quarterly Vol 28, 1977.
- 14 A J Bocci, Advances in the Aerodynamic Design of Propeller Blades, ARA Memo 241, 1982.



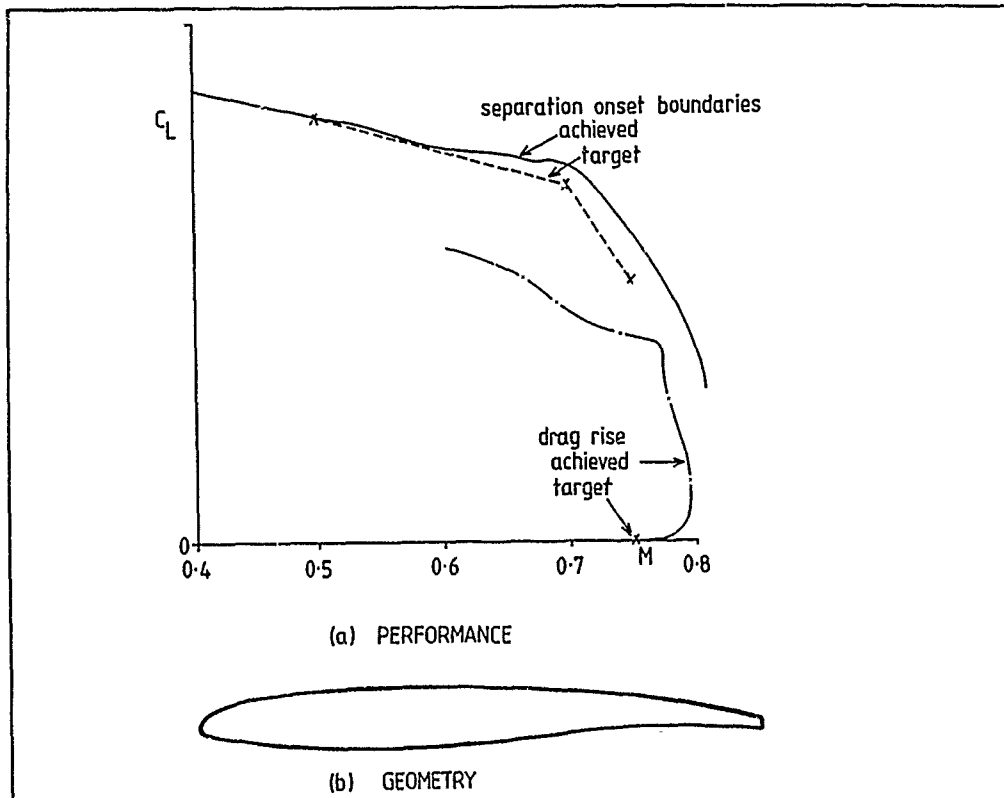


FIG 2 COMBAT WING AEROFOIL

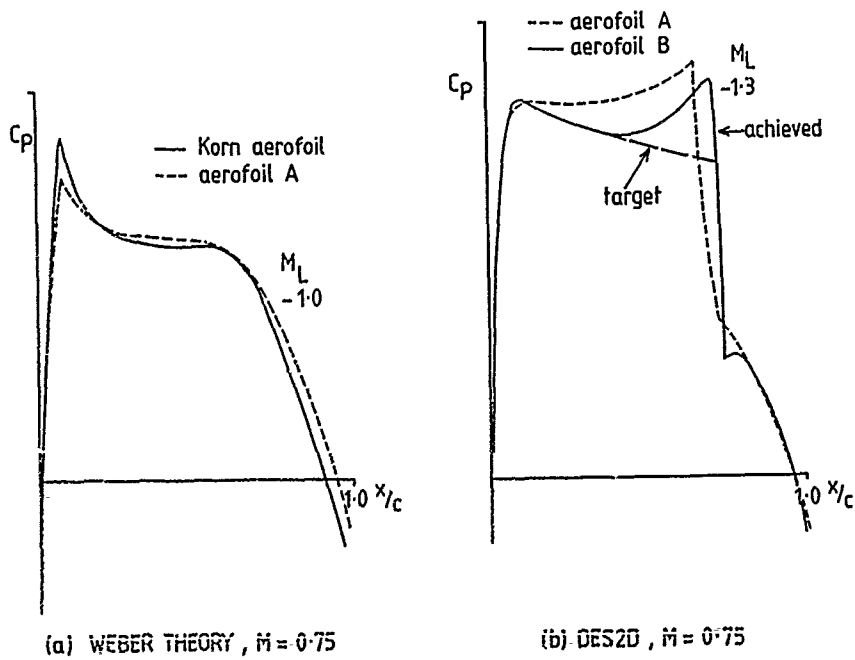


FIG 3 COMBAT WING AEROFOIL DESIGN STAGES

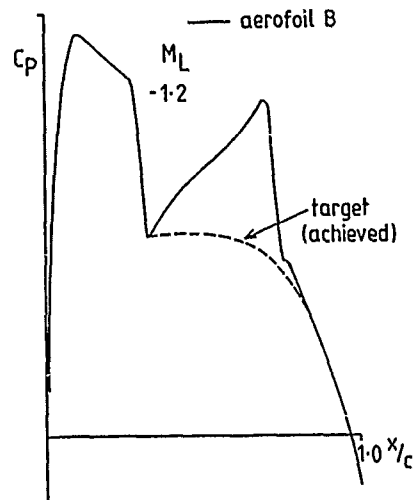
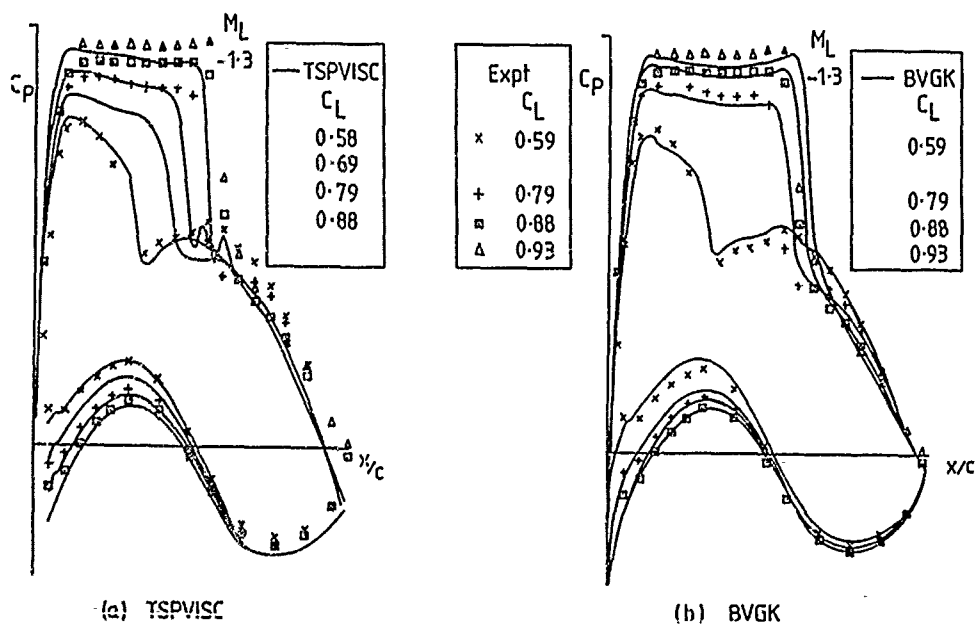
(c) DES2D, $M = 0.73$

FIG3(cont) COMBAT WING AEROFOIL DESIGN STAGES

FIG 4 COMBAT WING AEROFOIL, THEORY-EXPERIMENT, $M = 0.75$

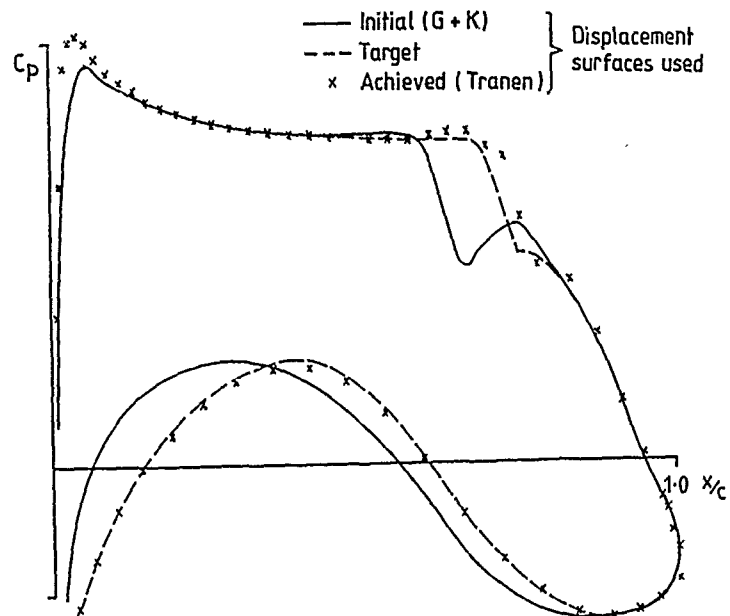


FIG 5 HIGH REYNOLDS NUMBER AEROFOIL
TRANEN DESIGN $M \approx 0.75$

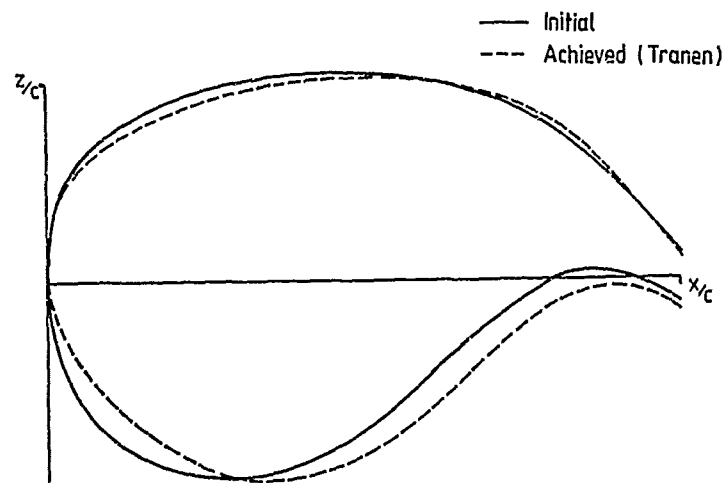


FIG 6 DISPLACEMENT SURFACE GEOMETRIES (EXPANDED SCALE)

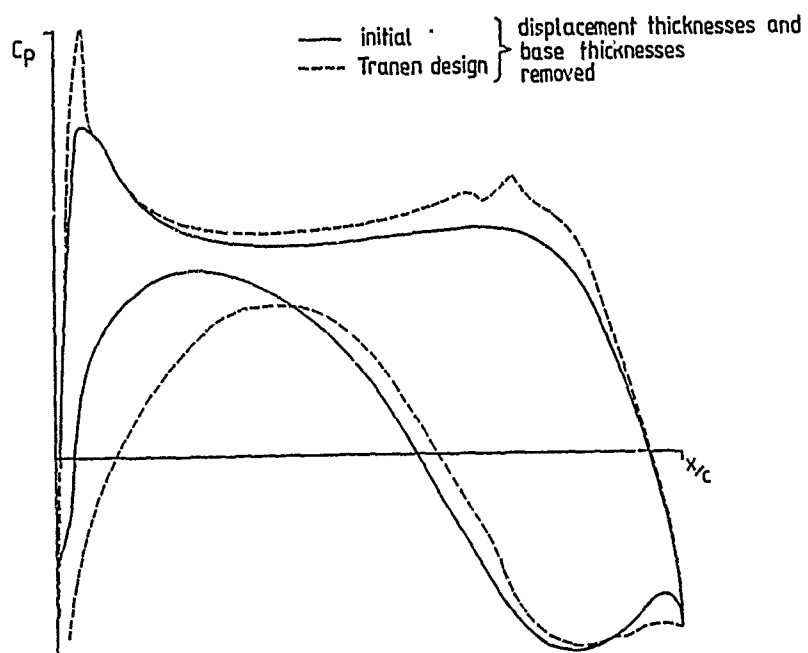
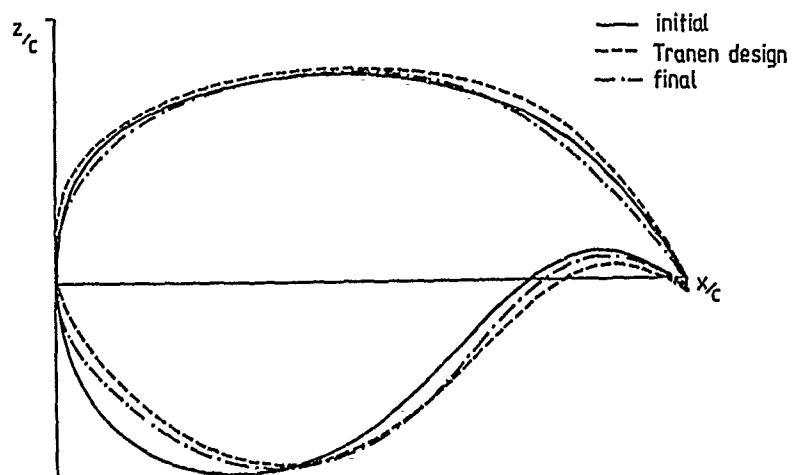
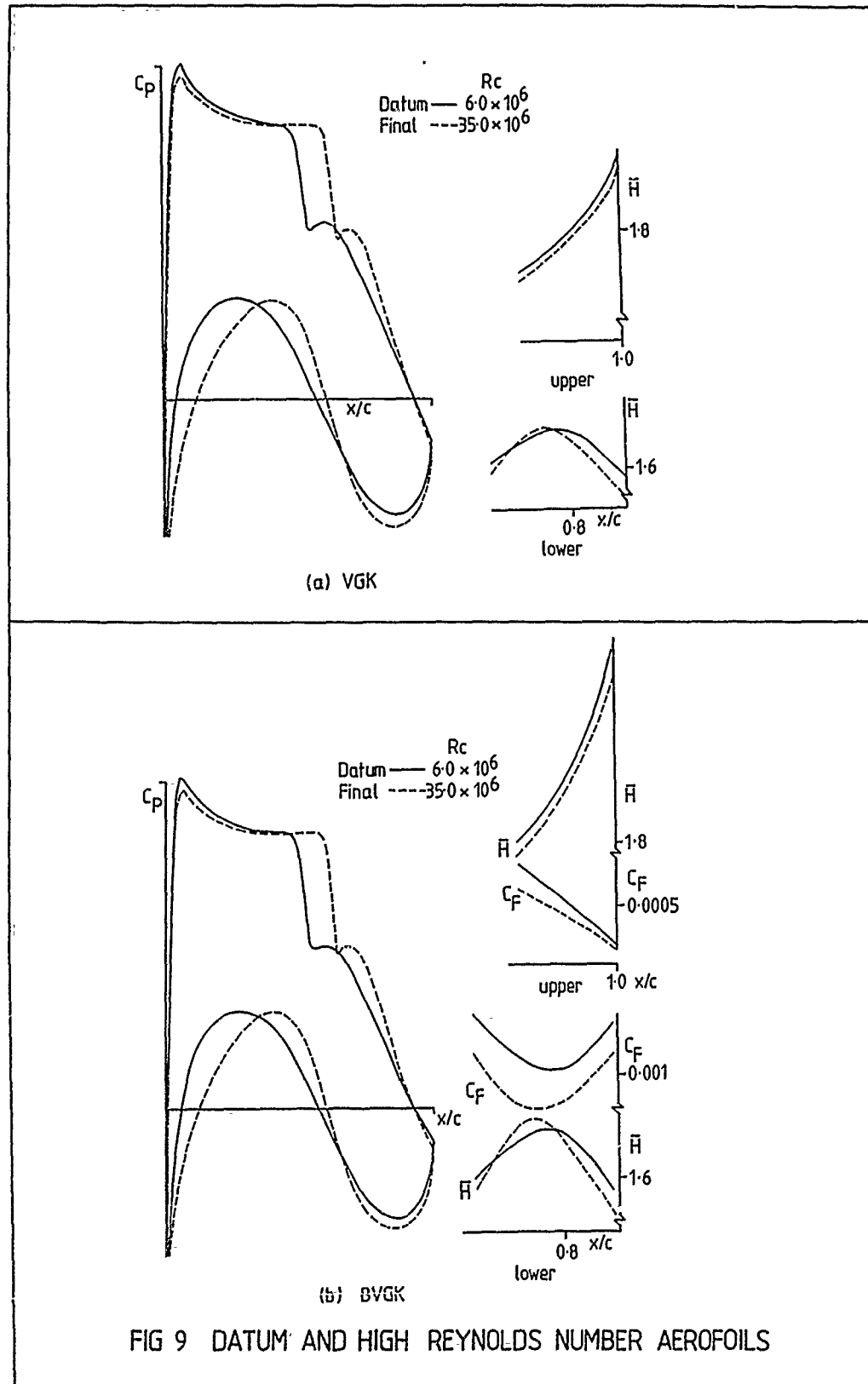
FIG 7 WEBER THEORY $M \approx 0.75$ 

FIG 8 GEOMETRIES (EXPANDED SCALE)



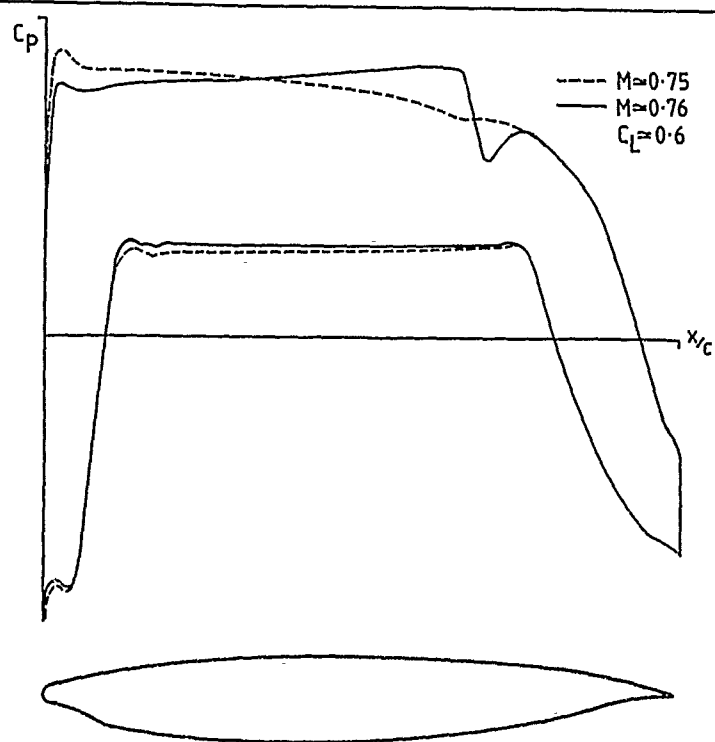
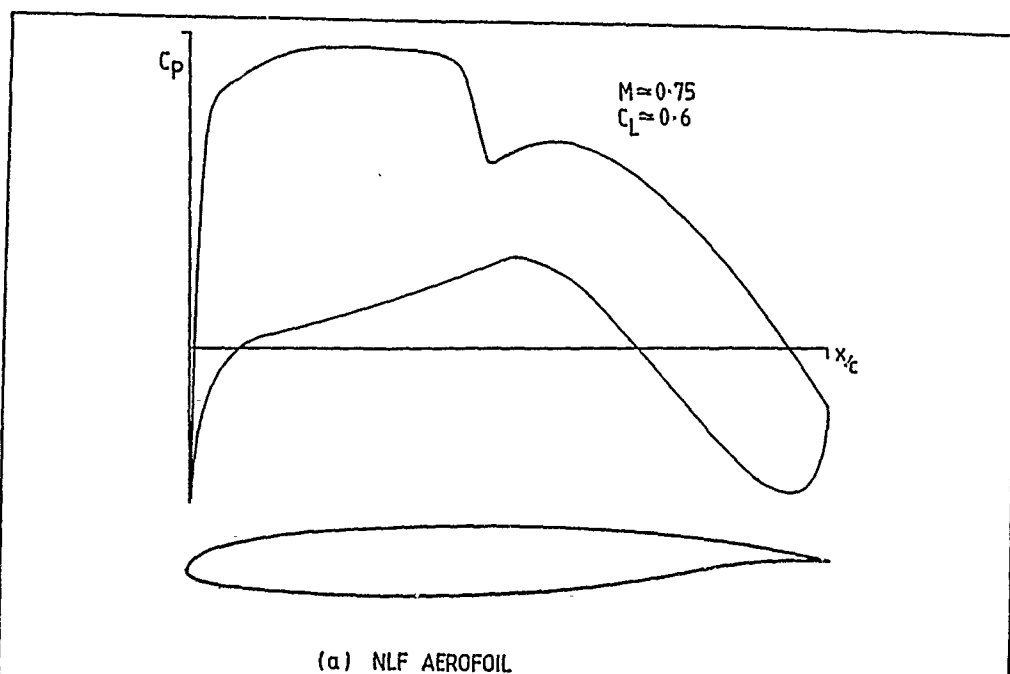
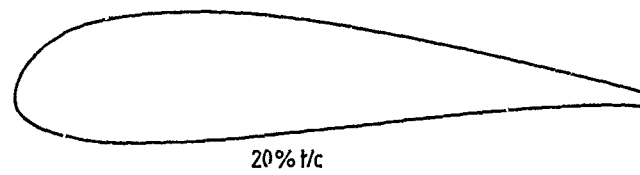
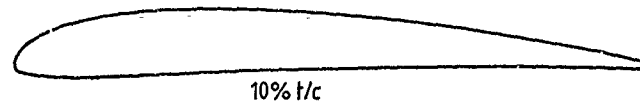
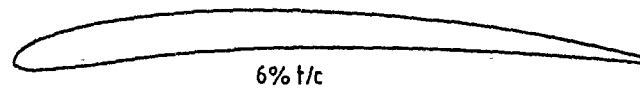
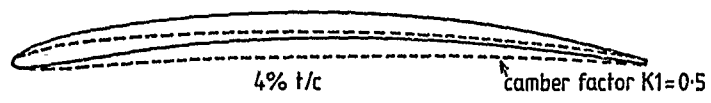
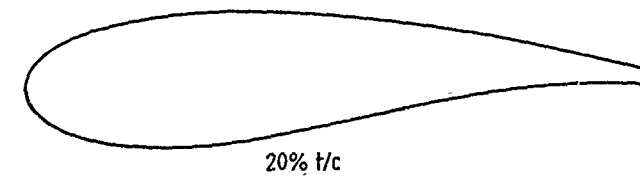
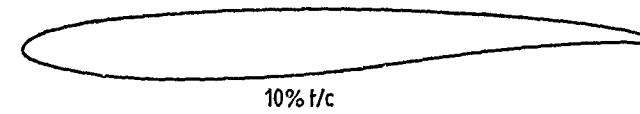
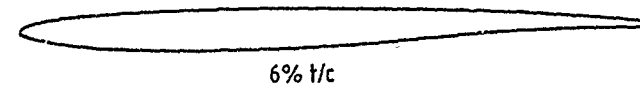
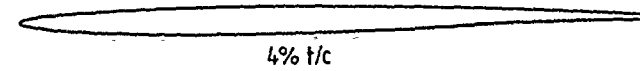
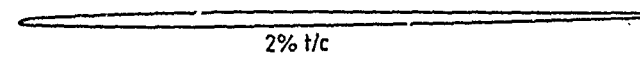


FIG 10 LAMINAR FLOW AEROFOILS
GEOMETRY AND PRESSURES



(a) ARA - D/A



(b) ARA - D/S

FIG 11 PROPELLER BLADE AEROFOILS

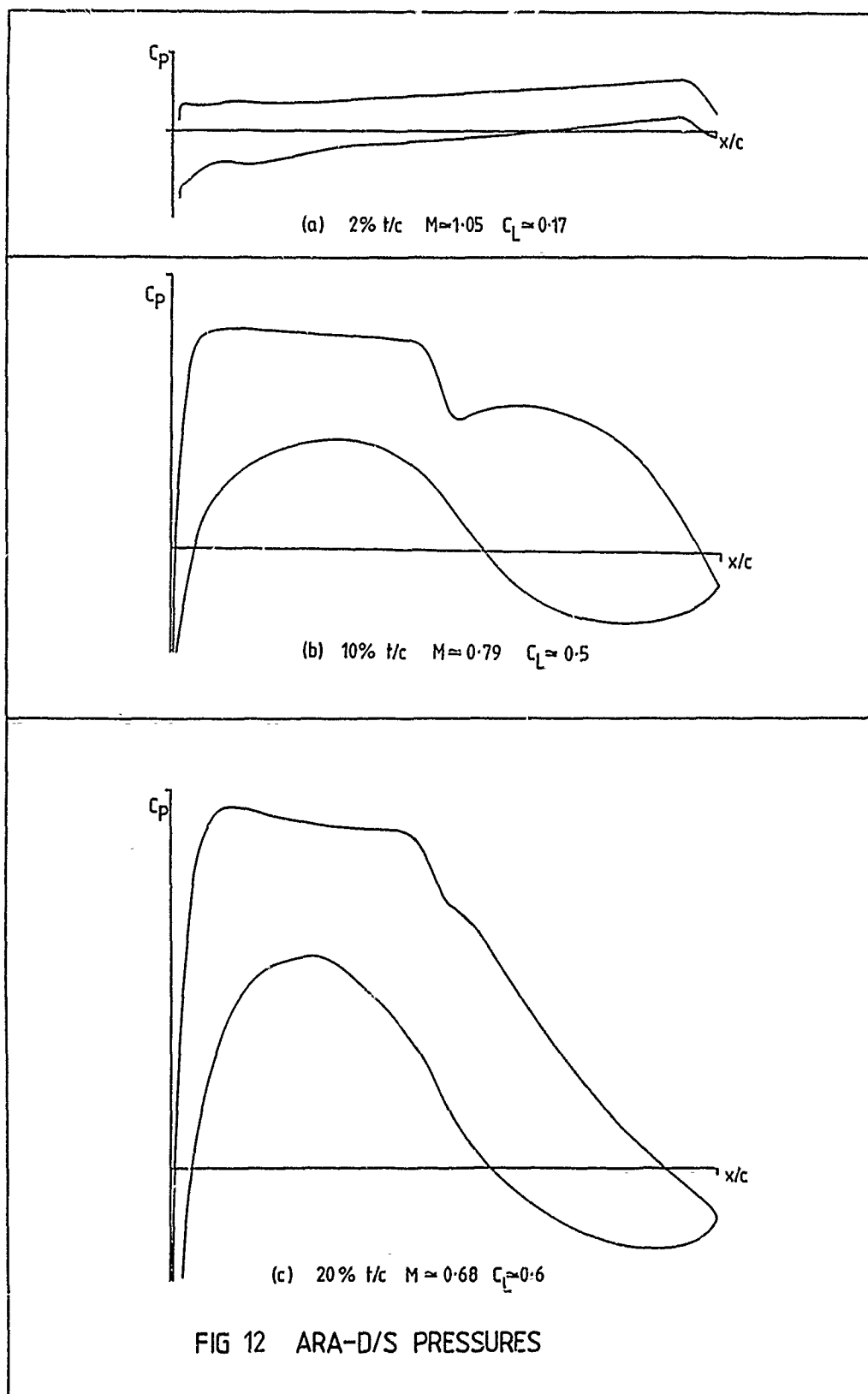
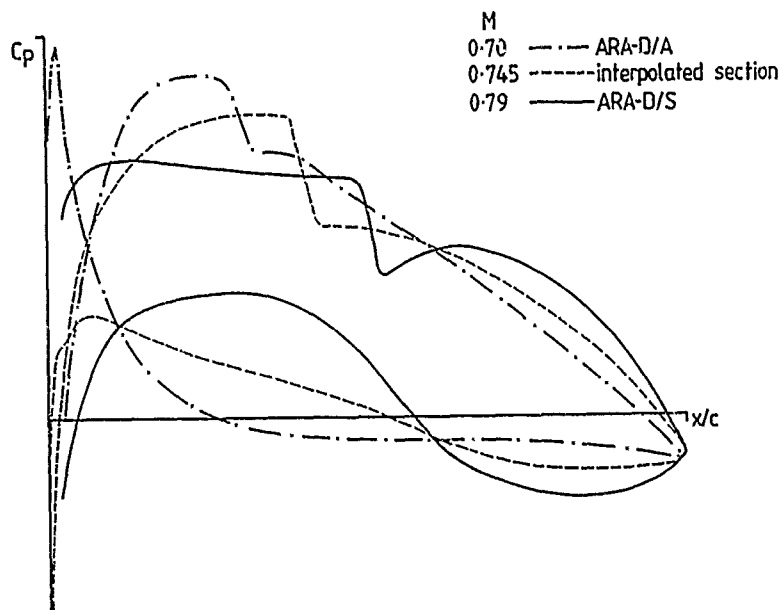
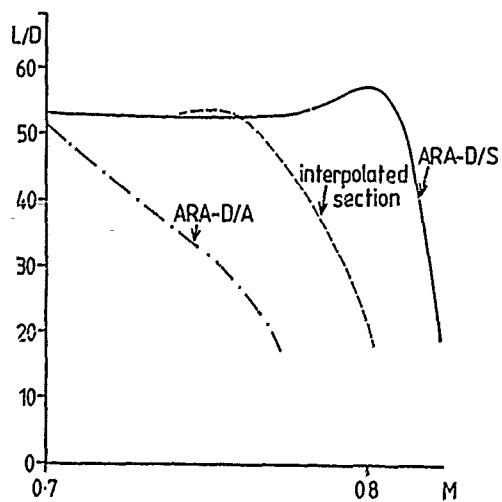


FIG 12 ARA-D/S PRESSURES

(a) C_p Variation, $C_L \approx 0.5$ (b) LIFT/DRA3, $C_L \approx 0.5$ FIG 13 10% t/c PERFORMANCE, ARA-D/A \rightarrow ARA-D/S

AERODYNAMIC DESIGN TECHNIQUES AT DLR INSTITUTE FOR DESIGN AERODYNAMICS

by

H. Köster, G.-H. Rohardt, K.-H. Horstmann, R. Radespiel

Deutsche Forschungsanstalt für Luft- und Raumfahrt e.V. (DLR)
Institut für Entwurfsaerodynamik
D-3300 Braunschweig, Flughafen, Germany

SUMMARY

Some general remarks about aerodynamic design are given first. Then, a short survey of the design methods used here including the basic ideas and, particularly, an improvement of the design method of McFadden for supercritical airfoils are presented. Also, an overview is given of the analysis methods in use at the DLR Institute for Design Aerodynamics.

Design procedures, which use the forementioned design and analysis methods, are explained in detail. With these procedures, several designs of airfoils and nacelles have been performed. Results of selected design examples are discussed.

NOTATIONS

c	chord length of nacelle, airfoil chord, speed of sound
c_D	drag coefficient of airfoils
c_{D0}	zero lift drag coefficient of airfoils
c_{DW}	wave drag coefficient of nacelle and airfoils
c_L	lift coefficient of airfoils
$c_{L \max}$	maximum lift coefficient of airfoils
c_H	pitching moment coefficient of airfoils
c_p	pressure coefficient
$c_{p \min}$	minimum pressure coefficient
c_p^*	critical pressure coefficient
\dot{m}	mass flow through nacelle
M	Mach number
Q, u	velocity
Q_{PU}, Q_{PL}	upper and lower limit M_1 and M_0 of transitional function
r	radius of nacelle, coordinate inside unit circle
Re	Reynolds number
s	arc length along airfoil contour
$V(M)$	transitional function
x, y	rectangular coordinate system airfoil
x, z	rectangular coordinate nacelle
α, α_{LP}	angle of attack
α^*	angle of attack relativ to zero lift for velocity specification in design mode
ε	area ratio of the streamtube of the flow through the nacelle
ε_1	amount of additional artificial viscosity
w	circumferential angle
θ	angle in circumferential direction of nacelle
Φ	reduced flow potential

1. INTRODUCTION

One of the main tasks in aircraft industry is to develop products for new applications or with an increased efficiency for better achieving economic results to withstand the large competition among producers and among users. For this purpose, aerodynamics can contribute with new or better suited shapes for those parts which are surrounded by the flowing fluid. The design of well suited shapes is an old difficult problem in aerodynamics because of its mathematical difficulties. Therefore a lot of work is spent on developing better design calculation methods or at least procedures with which successful aerodynamic designs can be realized. In the last 15 years, the Institute for Design Aerodynamics has been involved in a number of design tasks in the area of airfoils and wings. It started with the development of an airfoil for a sailplane of the "Akademische

Fliegergruppe" of the Technical University in Braunschweig. This sailplane has won the world championship 1978 in the FAI-15m class. The institute has gained a lot of experiences in the following years in designing laminar airfoils for sailplanes and many of the german modern sailplanes are equipped with these airfoils [1]. For the transonic range two rear-loading airfoils have been developed [2] of which the latter one was the basis for the F4-wing which was tested in all important european transonic windtunnels as a standard test wing [3,4]. Since then, additional transonic airfoils have been designed and investigated [5,6,7]. In cooperation with the Dornier company several airfoils for an advanced propeller for commuter aircraft have been designed and some of them tested in the windtunnel [8]. The manufactured propeller revealed improved performance when tested in flight [9]. Also a cooperation with the MBB company on the field of helicopter rotor airfoil development has been started in 1981 which showed successful results as we shall see below [10,11,12]. Laminar airfoils for commuter and transport aircraft have become more and more important. This fact has stimulated design work on this type of airfoils. In the course of this work three laminar airfoils have been designed partly in cooperation with aircraft industrie [13-17]. For basic research on transition prediction several gloves for a general aviation [18] and a transport type aircraft wing section have been developed and tested. As the design procedures for laminar airfoils showed good results, they have been extended on the development of a laminar flow nacelle for Airbus Industrie of which some results are shown below [19].

This paper gives a brief survey of the used design and analysis methods and describes in short some of the procedures used for the design of the different types of airfoils and nacelle contours. For one of the design methods, an improvement developed at the institute is also presented. Some design examples complete this paper.

2. AERODYNAMIC DESIGN

2.1 General remarks

For the design process four essential parts are necessary

- detailed and accurate description of the design requirements
- design methods for providing the basic shape
- analysis methods to confirm the design and estimate the off-design performance
- experience how to use and to combine results from design and analysis methods to do a successful design, e.g. the development of certain design procedures which may be different from task to task but which have the same components.

In the following paper, the latter three points will be discussed. Although the design requirements should be provided by the customer, and one may argue that they are therefore out of discussion, their impact on the result is very strong and some statements are necessary. Only reasonable and feasible requirements can lead to a successful design. Therefore, permanent discussions between design engineer and customer are necessary to clarify the problems and to end up in design requirements as accurate as possible.

2.2 Design methods

For designing airfoil and fan cowl contours a low speed design method for airfoils according to Eppler and Somers [20] has been employed. This method is based on a conformal mapping procedure. The flow around the airfoil is mapped into a flow around a circle. The circle is split into segments. For each segment an angle of attack α^* has to be chosen. The calculation of the airfoil contour then implies that the velocity is constant in each segment at the chosen value of α^* .

The velocity decrease at the rear part of the airfoil can be defined by a set of parameters and the closure condition is automatically realized. It should be pointed out that this unusual way of specifying the velocity distribution enables the user to take different design points into account.

As a method for designing supercritical airfoils the artificial viscosity method of McFadden has been used [21]. It is a design mode of the wellknown analysis code of Bauer, Garabedian, Korn, Jameson [22,23] in which the full potential equation is solved and the exterior to the airfoil is conformally mapped into the interior of the unit circle (Fig. 1). The code solves the inverse design problem by an iteration process in which the actual pressure distribution calculated with the use of additional artificial viscosity is compared with the desired one and a correction to the estimated airfoil is made until the airfoil shape has converged.

It should be mentioned that further design methods have been used in the past. One of these is the method of elliptic continuation of Sobieczky and Eberle [24,25], with which some transonic airfoils for basic research have been developed. The other one is the method of Carlson [26] who also solves the full potential equation but, in contrary to Bauer, Garabedian, Korn, Jameson, by using cartesian coordinates. Both methods need an initial airfoil which is then changed. For solving future design problems in the field of airfoils the method of Giles and Drela [27] have to be taken into account.

2.3 Improvement of the design code of McFadden

In subsonic flow, the airfoils designed with the original McFadden code do exhibit the target pressure distribution. However, if there are supersonic regions in the target distributions, the calculated pressure distributions from the designed airfoils are in general different from the prescribed ones above all near the shock waves (Fig. 2) [28].

Therefore, this method was investigated in more detail in cooperation between DLR and INTA [29] in order to suppress or, at least, diminish as far as possible the discrepancies between the analysis and the design code. One result of these investigations will be given here in short.

The iterative process developed in the original code seems to converge very well for subsonic flows. In contrast, for transonic flows some problems may appear. They are due to the presence of shock waves, that is, to the presence of large gradients in the derivative of $\Phi(s, w)$ which may cause a logarithmic singularity.

The problem can be avoided on coarse grids because the artificial viscosity inherent in the finite differences scheme smoothes the shock wave. This effect allows the process to converge even in the case of transonic flow. For modelling the flow accurately, we need to use fine grids. In that case, converged results are obtained by adding an artificial viscosity to the potential equation with the form:

$$\varepsilon_1 \cdot \Delta w \cdot \frac{\partial}{\partial w} [V(M) \cdot \Phi_{ww}]$$

The factor ε_1 is included for changing the amount of artificial viscosity to be used, and $V(M)$ is a smooth function of the local Mach number with the shape shown in Fig. 3. In [21], it is suggested to use $QPL = 0.85$ and $QPU = 0.95$ as boundary values for this function.

The main problem to be solved concerns the discrepancies between the analysis and the design code, which are due to the use of the added artificial viscosity. Fig. 4 shows, that the artificial viscosity does not only influence the flow field in the supersonic area and at the shock wave, but also far away from it depending on the values given to the input parameters QPL and QPU . The influence of these parameters is shown in Fig. 5.

There are a couple of reasons indicating that, away from the shock, the added artificial viscosity is overestimated. First, it should not be necessary to use any additional artificial viscosity at subsonic points near the sonic line. On the other hand the value of the artificial viscosity does not need to be so high as it originally is in most of the supersonic zone, where the gradient of Φ_w is small enough. An improved function $V(M)$ should therefore satisfy the following conditions:

- be zero in the whole subsonic region,
- be large enough in the supersonic area and near the shock wave,
- falling to zero on the sonic line.

The fact of using a first order retarded differences scheme for Φ_{ww} at all supersonic points introduces an error in the potential equation of the form:

$$\Delta w \cdot \max [(u^2 - c^2), 0] \cdot \Phi_{www}$$

that gives the idea of using the new function

$$\max [M^2 - 1, 0]$$

of which an example is displayed in Fig. 6. In this way, the difference between the analysis and the design codes becomes smaller.

The new artificial viscosity is

$$\varepsilon_1 \cdot \Delta w \cdot \max [(M^2 - 1), 0] \cdot \Phi_{www}$$

instead of the original one

$$\varepsilon_1 \cdot \Delta w \cdot \frac{\partial}{\partial w} [V(M) \cdot \Phi_{ww}]$$

The velocity distribution derived from the analysis of the KORN1 airfoil with the BGKJ-code ($M = 0.75$, $c_L = 0.629$) in Fig. 7, has been used as input data for the improved design code.

The flow over the redesigned airfoil was then again computed using the BGKJ-code and is presented in Fig. 8. It is shown that the results obtained with the modified code are essentially equal to the input data in the subsonic region and also, the input data could nearly be reached in the supersonic part. These calculations indicate very clearly that by using the artificial viscosity only inside the supersonic field deviations outside of it can be avoided and that the new artificial viscosity which is concentrated on areas with large pressure gradients gives a good agreement with the input data. When using the original smooth design pressure distribution of the Korn1 airfoil and carrying out the same procedure as in the example before nearly the same behaviour is obtained. The modified code yields a much better result (Fig. 9).

The third example, Fig. 10, shows an input pressure distribution with a prescribed shock obtained from an analysis run including the effect of boundary layer displacement thickness. The airfoil designed with the modified code yields a result which is nearly the same as the input data. It has also been found that the thickness at the trailing edge of the designed airfoil was almost the same as the thickness of the boundary layer displacement thickness at that point.

2.4 Analysis methods

For verifying designed shapes and estimating their off-design behaviour it is convenient to use well proved and reliable analysis methods which are also numerical stable and easy to handle and which have been checked against experiments and other methods. Essentially two methods are employed for flows around airfoils without significant separation. In the case of incompressible and lower subsonic flows the analysis part of the computer program of Eppler/Somers [20] has been chosen. It is originally a higher order panel method for incompressible flow which has been extended by Radebeil [30] to subsonic flow by introducing a combination of two different compressibility rules. For transonic flow the well-known Bauer/Garabedian/Korn/Jameson method [22,23] is employed which is based on a finite difference approximation of the full potential equation in a transformed mesh to fulfill the exact boundary conditions. In both methods viscous effects are taken into account by adding the boundary layer displacement thickness to the airfoil contour during the iteration process. The calculation of laminar and turbulent compressible and incompressible boundary layers has been performed with the integral method of Walz [31,32], method II, which is based on the numerical integration of the integral equations of momentum and energy. The friction drag is obtained by integrating the local shear stresses whereas the pressure drag is calculated after a proposal of Pretsch [33] by application of the momentum law around the airfoil. For estimation of the laminar-turbulent boundary layer transition the method of Granville [34] is used in which a relation between an average shape parameter and the Reynolds number based on momentum thickness between the point of neutral stability [35] and the transition location is employed. For laminar airfoils at high Reynolds numbers, the transition location prediction method based on the stability theory of laminar boundary layers is used. This method defines transition by a certain limiting amplification exponent or N-factor of the laminar boundary layer. Transition is predicted if the limiting N-factor is exceeded by the calculated amplification values. The method is described in detail in [36].

For the analysis of the transonic inviscid flow around isolated nacelles an extension of the three-dimensional DFVLR Euler code CEVCATS is used. This code is based on a cell-vertex finite-volume scheme for the three-dimensional Euler equations. The scheme uses central differences for the calculation of the flux balances and therefore artificial dissipative terms are used to damp high-frequency oscillations in the solution. Steady state solutions are obtained using a Runge-Kutta time stepping scheme. The scheme is analysed in detail in [37,38]. The extension of CEVCATS for the calculation of nacelle flows is described in [39].

The code uses a computational domain, which is divided into three blocks as sketched in Fig. 11. In the streamwise direction an H-type grid topology is used whereas a polar grid is used in the circumferential direction. In the present version of the code the grid is rotationally symmetric and the core jet is simulated by a cylindrical body. The total number of grid points is around 56000. Although characteristic boundary conditions are applied at all inflow/outflow boundaries of the computational domain for a proper convergence behaviour to the steady state, the code accurately reproduces the mass flow into the inlet of the nacelle as specified by input.

For the calculation of laminar and turbulent compressible boundary layers around the nacelle outer contour, the integral method according to Rotta [40] has been used. The method is also based on the numerical integration of the integral equations for momentum and energy and can be used for axisymmetric or plane flows. In the axisymmetric case both external and internal flows can be calculated.

The use of an axisymmetric boundary layer code is certainly justified under cruise conditions where the angle of attack is less than 1.5° . For the take-off case, however, a much larger angle of attack has been specified and three-dimensional boundary layers within the inlet are expected. In this case the result of an axisymmetric boundary layer code is of less value.

The transition location of the laminar boundary layer into a turbulent one is also computed by means of the forementioned stability theory of laminar boundary layers.

For applying this 2D transition location prediction procedure it is necessary to investigate the influence of 3D effects due to an axisymmetric geometry on the laminar boundary layer. This has been done in [41] with the Rotta method [40]. The main result of [41] is, that for a relative nacelle radius $r/c \geq 0.5$ the differences of the boundary layer parameters between the axisymmetric flow and the 2D flow are negligible.

Using the present Euler code for the inviscid flow around the nacelle a direct integration of the pressure drag is not possible for two reasons:

- The contour of the nacelle is not closed as shown in Figure 11.
- Usually, the pressure drag is a small value which is obtained from large integrands. Therefore, a direct integration of the pressure drag is not very accurate.
- The present Euler code does not account for the pressure drag due to viscous-inviscid interaction.

On the other hand, it is possible to calculate the sum of pressure drag and friction drag of the outer flow around the nacelle from the stagnation point at the leading edge to the trailing edge from the boundary layer results at the trailing edge according to Squire and Young [42]. Hence, it is possible to estimate the drag increment between nacelles with laminar and turbulent flow.

Furthermore, the wave drag due to shock waves in transonic flow is neglected in the Squire/Young formula. Experiences with transonic airfoils indicate, that the wave drag is negligible in comparison with the viscous drag if the Mach number upstream of the shock does not exceed $M_1 = 1.15$. At higher Mach numbers, where the local Mach number M_1 upstream of the shock wave is larger, the wave drag c_{DW} is estimated by subtracting the pressure drag at a lower Mach number without shock waves from that at the high Mach number.

3. DESIGN PROCEDURES

By means of the analysis and design methods described in the preceding chapters, the following design procedures have been proved advantageous for the design of airfoil shapes for different purposes.

3.1 Sailplane airfoils

When designing airfoils for sailplanes at least two design conditions have to be taken into account: the circular climb at low speed, low Reynolds number and high lift coefficient and the distance flight at high speed, higher Reynolds number and lower lift coefficient. Such a design task can be carried out, with some experience, using the calculation system of Eppler and Somers [20] if the boundary layer method in the analysis part is accompanied with a reliable and accurate method to determine laminar-turbulent boundary layer transition location. The Eppler design code is well suited for the design of laminar airfoils because both design points can be taken into account in a simple manner. The angles of attack related to the design points can be used as input data α^* (see chapter 2.2) of the design code.

The same technique can be used for subsonic airfoils if the Mach numbers in the flow field are not too high, i.e. for airfoils for low and medium speed general aviation and commuter aircraft and for propellers.

3.2 Helicopter airfoils

The flow around helicopter rotor blades is very different, depending on circumferential location of the blades and the flight conditions. Therefore, the blade sections have to be designed for high lift coefficients at low Mach numbers, for low drag at medium lift coefficients and Mach numbers and for low drag at low lift coefficients and high Mach numbers. In all cases the pitching moment coefficient should be small.

It has been proved that a combination of the Eppler's design code and the transonic Bauer/Garabedian/Korn analysis method is very efficient for such a multiple objective design. The different steps in the complicated design process for such airfoils are:

1. Choice of a prescribed velocity distribution or change of a velocity distribution used in a step before.
2. Calculation of airfoil contour and aerodynamic coefficients at main design objectives by means of the subsonic code of Eppler and Somers.
3. Reiteration of step 1 and 2 until the desired subsonic airfoil characteristics are obtained.
4. Calculation of the transonic behaviour at all design objectives by means of the Bauer/Garabedian/Korn III method.
5. Reiteration of step 1 to 4 until the desired subsonic and transonic behaviour is obtained.

As both codes are unable to calculate separated flow regions they cannot predict the maximum lift coefficient $c_{l, \max}$. Comparison of measurements and calculation of similar airfoil types have shown that the following auxiliary criterions can be used for the estimation of $c_{l, \max}$ values. At Mach number of $M = 0.3$ $c_{l, \max}$ is reached when the pressure coefficient at the calculated separation point is equal zero. At $M = 0.4$ either the above separation criterion or a limiting maximum local Mach number of 1.4 was used. Maximum lift coefficient at $M = 0.5$ was estimated by limiting the local Mach number just ahead of the shock pressure rise to a value of 1.4.

Some essential results of helicopter rotor blade airfoils designed with this procedure will be presented in the following. A 9% thick airfoil, DM-H1, showed the expected zero lift drag vs. Mach number (Fig. 12) but the comparison of the measured and calculated drag polar at $M = 0.7$ seemed not to be satisfying for lift coefficients larger than 0.4 (Fig. 13). An oil-flow pattern indicated that a turbulent separation bubble was the reason for this behaviour which could not be detected by the analysis method used here. As a consequence, the Mach number and shock strength on the upper side (Fig. 14) was reduced in order to avoid such separation bubbles. The experimental results of the improved airfoil, DM-H3, given in Fig. 15 and 16, reveal the increase in the drag rise Mach number as well as the improvement of the drag polar at $M = 0.75$.

The measured and calculated minima of the pressure coefficient for the 12% thick airfoil DM-H2 at $M = 0.4$ differ from each other at large lift coefficients, Fig. 17, indicating that the expected maximum lift coefficient could not be realized. The transonic calculation gives no indication of a shock in contrast to the experiment. The lack of the transonic calculation in this case may be caused by a insufficient number of grid points which leads to a wrong boundary layer calculation shifting the predicted maximum lift coefficient to a higher value. To increase the maximum lift coefficient the small local supersonic flow field has to be extended (Fig. 18), using a higher contour curvature near the end of the supersonic region and corresponding changes of curvature up- and downstream. This modification influences, of course, the aerodynamic characteristics at other operational points. Windtunnel experiments confirmed the increased maximum lift coefficient of the modified airfoil DM-H4, Fig. 19.

These two examples may demonstrate that in such a design process, the reliability of the analysis methods is of decisive importance. Therefore, it is necessary for such cases to use methods which are able to calculate wave drag more accurately and to deal with separated flows like separation bubbles behind shocks, laminar separation bubbles or trailing edge separation. One can expect that the methods of Drela and Giles [43] in which a panel method for incompressible flow and an Euler method for compressible flow is combined with an inverse boundary layer method can fulfill these requirements.

This design procedure can be completed with the improved McFadden code especially for designing supercritical airfoils or changing parts of them as can be shown in the following example for a helicopter tail rotor blade airfoil. On the upper and lower sides of this airfoil supersonic areas appear at the outer part of the advancing blade which cannot be avoided because of other requirements. Fig. 20 shows the pressure distribution of the initial airfoil. The design aim was to reduce the wave drag. Fig. 21 compares the inviscid flow velocity distributions of the initial airfoil and the target distribution in the supersonic areas for use in the McFadden design code. The result presented in Fig. 22 indicates very clearly the improvement of the pressure distribution and wave drag.

This described design procedure has also been used successfully in the development of high subsonic and transonic laminar airfoils for transport aircraft [16,17]. Here, the laminar-turbulent transition location prediction has been carried out by means of the forementioned stability theory of laminar boundary layer (e^N -procedure [36]) which yields more reliable results for high Reynolds numbers.

3.3 Design of a nacelle with natural laminar flow on the fan cowl

For the design of a natural laminar flow nacelle three main flight conditions have to be taken into account. Cruise conditions are characterised by high Mach number, low angle of attack and a medium mass flow ratio ϵ which is defined by the relation of the inlet stream tube area at infinity and the highlight area of the nacelle. At take-off conditions low Mach number, high angle of attack and high mass flow ratio are present. At landing conditions the parameters are similar except of the mass flow ratio, which is very low.

The design of the nacelle contour has been done iteratively by means of the methods described in chapter 2. It has to be mentioned that the subsonic code of Eppler/Somers is valid for 2D flow only and the pressure distribution for three-dimensional transonic flow around a nacelle may be quite different from that of the low speed airfoil.

Nevertheless, the angle of attack in the design code can be chosen, so that the stagnation points on the low speed airfoil and on the transonic nacelle coincide. Then, the flows around the nose of airfoil and nacelle behave very similar and the input parameters of the airfoil design code can be systematically used to change the transonic behaviour of the nacelle. With some experience the flow around the nacelle can be effectively influenced by changing the input of the low-speed code.

The different steps in the design process are:

1. Choice of a velocity distribution taking into account the 2D subsonic and the 3D transonic calculation of a given nacelle contour or of an iteration step before.
2. Calculation of nacelle contour by means of the 2D subsonic design code.
3. Reiteration of step 1 and 2 until the desired pressure distribution characteristics in the different design points are obtained.
4. Calculation of the 3D transonic inviscid pressure distribution at the design points by the Euler code.
5. Reiteration of step 1 to 4 until a desired transonic pressure distribution is obtained.
6. Calculation of boundary layer characteristics by means of the Rotta-method and prediction of lamina-turbulent transition by means of a stability code.
7. Reiteration of step 1 to 6 until the design objectives are fulfilled as good as possible.

Some of the nacelle contours designed in this way are shown in Figure 23. The contours LN1A to LN1D show the modifications from the complete adverse outside pressure distribution of a conventional nacelle to a typical natural laminar flow pressure distribution with a slight pressure drop up to 60% of chord length, Figure 24. Thus, the maximum thickness is increased from 7.4% to 9.6% and the location of maximum thickness is shifted downstream.

Another important design point is the take-off case with low Mach number and high angle of attack. Figure 25 shows, that the inside pressure peak at the $\theta = 180^\circ$ section can be reduced by a careful design. From LN1D to LN1 the contour curvature is decreased in the supersonic region and increased behind it, resulting in a reduced supersonic expansion.

4. CONCLUSIONS

In order to perform the different design tasks successfully, the following essential conditions have to be fulfilled:

- Detailed and accurate description of reasonable and feasible design requirements
- Both reliable design methods and efficient and validated analysis methods have to be available
- Physically established efficient design procedures have to be developed for different tasks using suitable design and analysis methods

On the basis of these principles a number of design tasks for industry and research have been carried out with good success.

These tasks, of which some results have been shown, comprise the design of:

- Laminar airfoils for sailplanes (sailplane industry)
- Supercritical airfoils (basic research)
- Propeller airfoils (Dornier TNT Experimental)
- Helicopter rotor blade airfoils (MBB BO-108)
- Laminar airfoils for high Reynolds numbers (Dornier, gloves for LFU-205 and ATTAS research aircrafts, Airbus 310 type aircraft)
- Natural laminar flow nacelle (Airbus Industrie, A320 type aircraft)

5. REFERENCES

- [1] Körner, H., Redeker, G.: Recent airfoil developments at DFVLR. Proc. of the 13th ICAS Congress, Seattle, Wa., 1982.
- [2] Redeker, G., Müller, R.: Design and experimental verification of two supercritical airfoils. DGLR/GARTEUR 6 Symposium on "Transonic Configurations", Bad Harzburg, 1978, DGLR-No. 78-075.
- [3] Redeker, G., Schmidt, N.: Design and experimental investigations of a wing for a transonic transport aircraft. DGLR/GARTEUR 6 Symposium on "Transonic Configurations", Bad Harzburg, 1978, DGLR-No. 78-85.

- [4] Redeker, G., Schmidt, N., Müller, R.: Design and experimental verification of a transonic wing for a transport aircraft. AGARD-CP-285 (1980), pp. 13-1 to 13-14.
- [5] Wichmann, G.: Entwurf eines Basisprofils für einen schwach gepfeilten Tragflügel. Teil 1: Theoretischer Profilentwurf für den transsonischen Geschwindigkeitsbereich. DFVLR-FB 84-19 (1984).
- [6] Redeker, G.; Wichmann, G., Oelker, H.-Chr.: Application of Elliptic Continuation Method for Transonic Airfoil Design and Experimental Verification. Proceedings of the International Conference on Inverse Design Concepts in Engineering Sciences (ICIDES), pp. 241-265, Austin, Texas (1984).
- [7] Redeker, G., Wichmann, G., Oelker, H.-Chr.: Aerodynamic investigations on an adaptive airfoil for a transonic transport aircraft. Proceedings of the 14th ICAS Congress, Toulouse, France, (1984), pp. 868-880.
- [8] Horstmann, K.H., Köster, H., Quast, A.: Entwicklung von vier Profilen für einen Experimentalpropeller in der Leistungsklasse 750 PS. DGLR-Jahrbuch 1982, S. 67-1 bis 67-23, (1983).
- [9] Zimmer, H., Hoffmann, R., Horstmann, K.H.: Investigation of modern General Aviation propellers. AGARD-CP-366, pp. 16-1 to 16-14, (1984).
- [10] Horstmann, K.H., Köster, H., Polz, G.: Development of two airfoil sections for helicopter rotor blades. Z. Flugwiss. (1983), 2, pp. 82-90.
- [11] Horstmann, K.H., Köster, H., Polz, G.: Improvement of two blade sections for helicopter rotors. 10th Europ. Rotorcraft Forum, The Hague/Netherlands, 1984.
- [12] Polz, G., Schinke, D.: New aerodynamic rotor blade design at MBB. 13th European Rotorcraft Forum, Arles, France, 1987.
- [13] Somers, D.M., Horstmann, K.H.: Design of medium-speed, natural-laminar-flow airfoil for commuter aircraft application. DFVLR-IB (1985).
- [14] Redeker, G., Horstmann, K.H., Köster, H., Quast, A.: Investigations on high Reynolds-number laminar flow airfoils. Proc. of the 15th ICAS Congress, London 1986, pp. 73-85. Journ. of Aircraft, Vol. 25, pp. 583-590, 1988.
- [15] Körner, H., Horstmann, K.H., Köster, H., Quast, A., Redeker, G.: Laminarization of Transport Aircraft Wings - A German View. AIAA-Paper 87-0085 (1987).
- [16] Köster, H., Müller, R.: Bestimmung des N-Faktors im Transsonischen Windkanal Braunschweig (TWB) anhand von Druckverteilungs- und Umschlagpunktmessungen und dem Sally-Verfahren. 6. DGLR-Fach-Symposium: Strömung mit Ablösung, Braunschweig, (1988), DGLR Bericht 88-05, pp. 77-92.
- [17] Köster, H.: Druckverteilungs- und Nachlaufmessungen am Profil DFVLR-LC2 im Transsonischen Windkanal Braunschweig. DFVLR-IB (1988).
- [18] Horstmann, K.H., Quast, A., Redeker, G.: Flight and windtunnel investigations on boundary layer transition at Reynolds numbers up to 10^7 . Proc. of the 16th ICAS Congress, Jerusalem, 1988, pp. 979-986.
- [19] Radespiel, R., Horstmann, K.H., Redeker, G.: Feasibility study on the design of a laminar flow nacelle. AIAA-Paper 89-0640 (1989).
- [20] Eppler, R., Somers, D.M.: A computer program for the design and analysis of low-speed airfoils. NASA TM 80210 (1980).
- [21] McFadden, G.B.: An Artificial Viscosity Method for the Design of Supercritical Airfoils. NASA-CR-158840 (1979).
- [22] Bauer, F., Garabedian, P., Korn, D., Jameson, A.: Supercritical Wing Sections II. Lecture Notes in Economics and Math. Syst., Vol. 108 (1975). Springer, Berlin/Heidelberg/New York.
- [23] Bauer, F., Garabedian, P., Korn, D.: Supercritical Wing Sections III. Lecture Notes in Economics and Math. Syst., Vol. 150 (1977). Springer, Berlin/Heidelberg/New York.
- [24] Eberle, A.: Profilloptimierung für transsonische Strömung mittels der Methode der finiten Elemente und Charakteristiken. MBB Rep. UFE 1362(0), (1977).
- [25] Sobieczky, H., Yu, N.J., Fung, K.J., Sebass, A.R.: A new method for designing shock-free transonic configurations. AIAA-78-1114 (1978).
- [26] Carlson, L.A.: Transonic airfoil analysis and design using cartesian coordinates. Journ. Aircraft, Vol. 13, (1976) pp. 349-356.

- [27] Giles, M.M., Drela, M.: Two-dimensional transonic aerodynamic design method. AIAA Journal, Vol. 25, pp. 1199-1206, 1987.
- [28] Monge, F.: Transonic Airfoil Design Using an Optimized McFadden Program, Preliminary Study. INTA Technica N/221/510/85.029 (1985).
- [29] Monge, F., Köster, H.: Improvement of a design code for airfoils at transonic regime. Proceedings of the Second International Conference on Inverse Design Concepts and Optimization in Engineering Sciences (ICIDES II), pp. 507-530, University Park, PA, USA (1987), see also DGLR Jahrbuch 1987 I, pp. 180-189.
- [30] Radespiel, R.: Erweiterung eines Profilberechnungsverfahrens im Hinblick auf Entwurfs- und Nachrechnungen von Laminarprofilen für Verkehrsflugzeuge. DFVLR IB (1981).
- [31] Walz, A.: Strömungs- und Temperaturgrenzschichten. Verlag G. Braun, Karlsruhe, 1966.
- [32] Rohardt, C.H.: Erweiterung eines Nachrechnungsverfahrens für zweidimensionale Strömungen durch ein leistungsfähiges Grenzschichtverfahren. DFVLR-IB (1983).
- [33] Pretsch, J.: Zur theoretischen Berechnung des Profilwiderstandes. Jahrbuch 1938 d. deutschen Luftfahrtforschung, 8. 160-181.
- [34] Granville, P.S.: The calculation of the viscous drag of bodies of revolution. David Taylor Model Basin Report 849, (1953).
- [35] Schlichting, H.: Boundary-Layer Theory. 7. Edition, McGraw-Hill Book Company, New York (1979).
- [36] Redeker, G., Horstmann, K.H.: Die Stabilitätsanalyse als Hilfsmittel beim Entwurf von Laminarprofilen. DGLR-Ber. 86-03, (1986), S. 317-331.
- [37] Rossow, C.: Berechnung von Strömungsfeldern durch Lösung der Euler-Gleichungen mit einer Finite-Volumen Diskretisierungsmethode. DFVLR-IB (1987).
- [38] Rossow, C., Kroll, N., Radespiel, R., Scherr, S.: Investigation of the accuracy of finite volume methods for 2- and 3-dimensional flows. In AGARD CP 437, pp. 14.1-11, Lissabon, Mai 1988 on Validation of Computational Fluid Dynamics.
- [39] Radespiel, R.: Calculation of the Flow around Powered High Bypass Ratio Nacelles Using an Euler Code. DFVLR IB (1987).
- [40] Rotta, J.-C.: FORTRAN IV - Rechenprogramm für Grenzschichten bei kompressiblen und achsensymmetrischen Strömungen. DLR FB 71-51, (1971).
- [41] Wichmann, G.: Einfluß der Rotationssymmetrie auf die Grenzschichtentwicklung der Außenströmung bei gondelähnlichen Konfigurationen. DFVLR IB (1987).
- [42] Squire, H.B., Young, A.D.: The Calculation of the Profile Drag of Aerofoils. RAE Rpt. No. 1838, (1937).

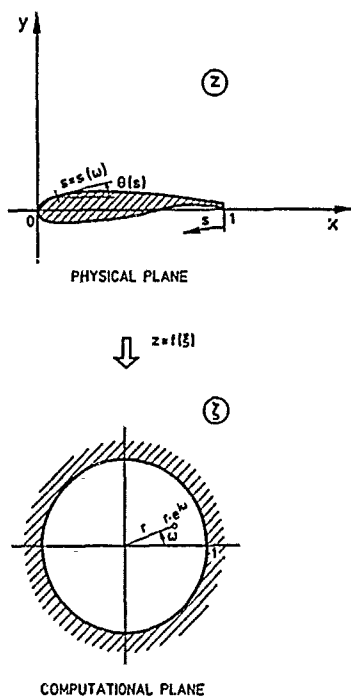


Fig. 1 Mapping of the airfoil

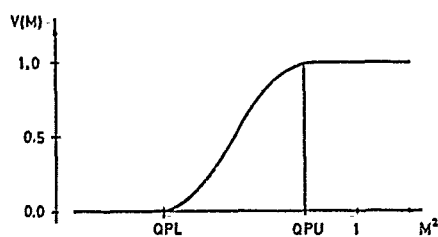
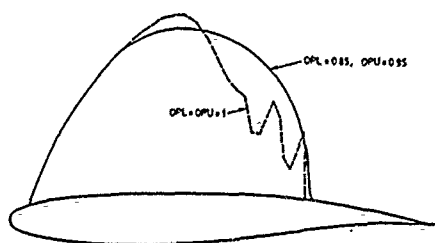
Fig. 3 Transitional function $V(M)$ 

Fig. 5 Effect of QPL and QPU on the sonic line of KORN1 airfoil

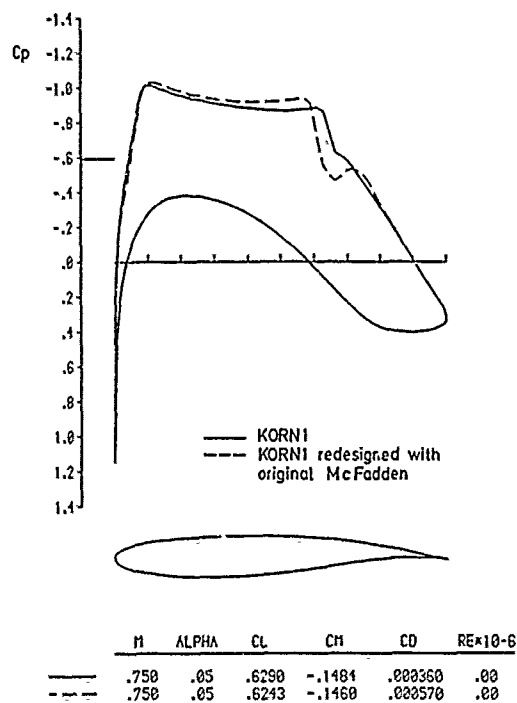


Fig. 2 Pressure distributions of KORN1 airfoil and the airfoil redesigned with the original McFadden code

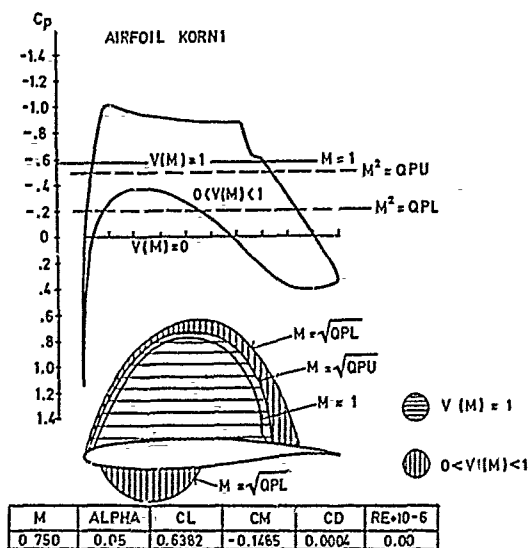


Fig. 4 Artificial viscosity influence domain of KORN1 airfoil

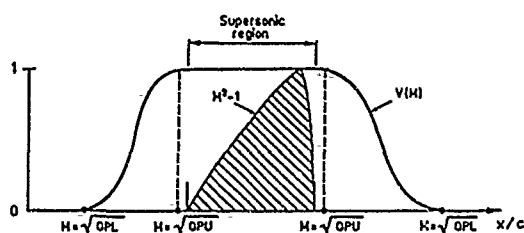


Fig. 6 Example of the new function in the artificial viscosity term

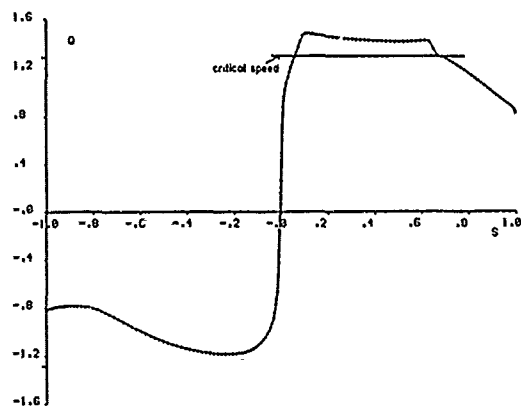


Fig. 7 Non-smooth input speed distribution derived from analysis calculation of airfoil KORN1

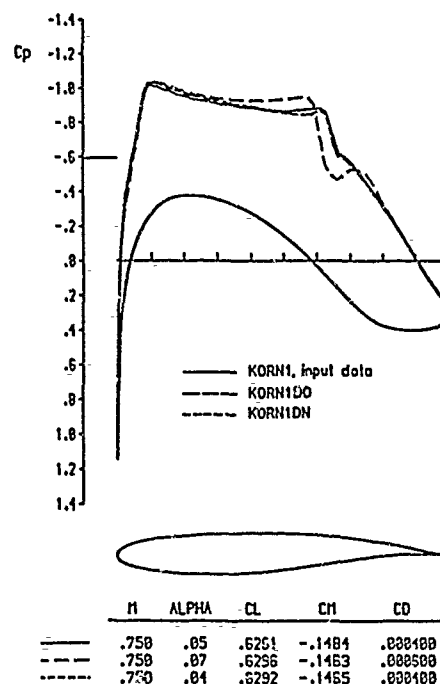
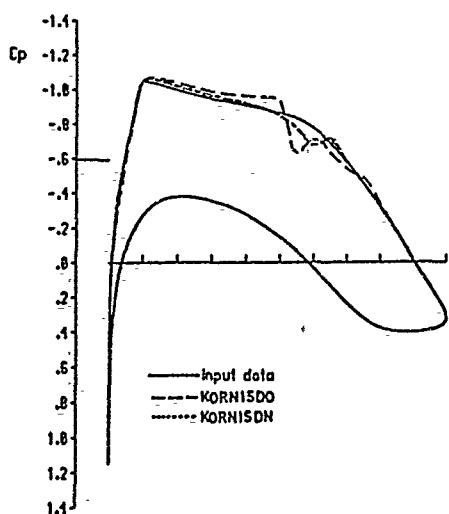
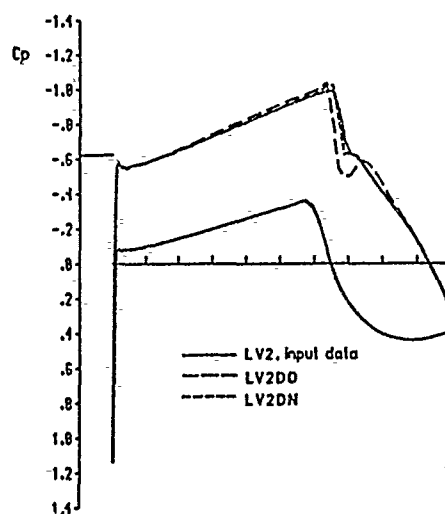


Fig. 8 Airfoil KORN1: Comparison of the pressure distributions of the airfoils designed with the original and modified McFadden code (non-smoothed input speed distribution)



	M	ALPHA	CL	CM	CD
————	.750	.05	.6290	.0020	.002000
- - - - -	.750	.08	.6297	-.1435	.002500
· · · · ·	.750	.05	.6294	-.1431	.002500

Fig. 9 Airfoil KORN1S: Comparison of the pressure distributions of the airfoils designed with the original and modified McFadden code (smooth input speed distribution)



	M	ALPHA	CL	CM	CD
=====	.741	-.06	.5996	-.1656	.000300
-----	.741	.09	.5980	-.1633	.000100
-----	.741	.04	.5981	-.1648	.000100

Fig. 10 Airfoil DFVLR-LV2: Comparison of the pressure distributions of the airfoils designed with the original and modified McFadden code

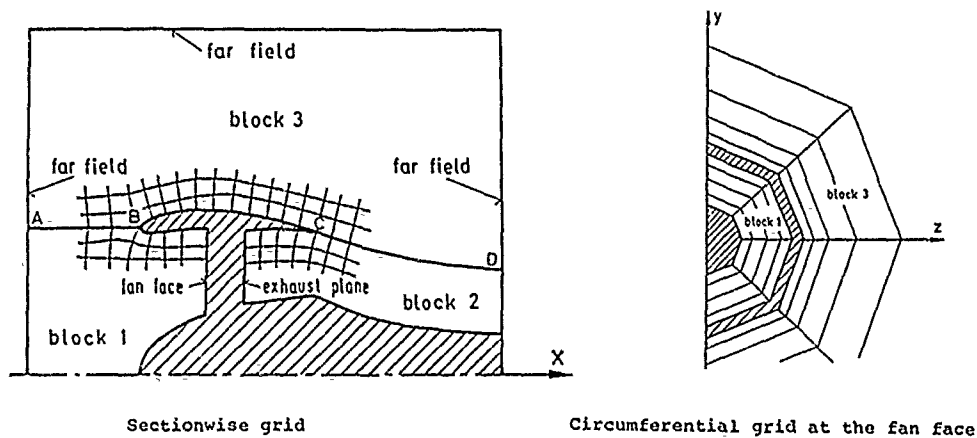


Fig. 11 Grid structure for high bypass nacelle configurations

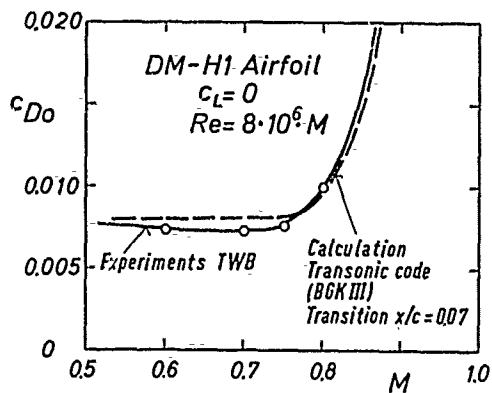


Fig. 12 Comparison of measured and calculated zero lift drag coefficients of the airfoil DM-H1

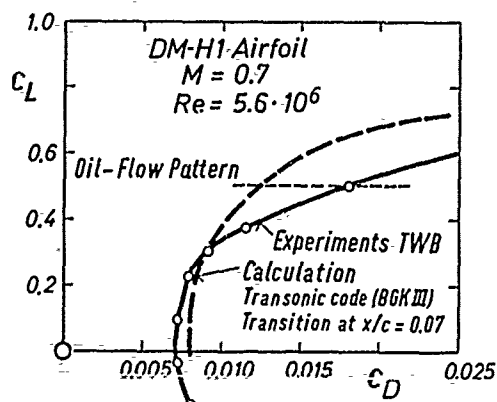
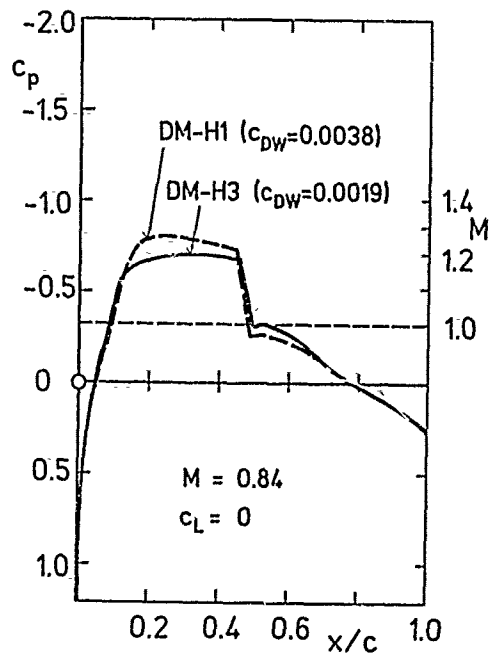
Fig. 13 Comparison of measured and calculated drag polars of the airfoil DM-H1 at $M = 0.7$ 

Fig. 14 Upper surface pressure distributions calculated by the BGK III-method

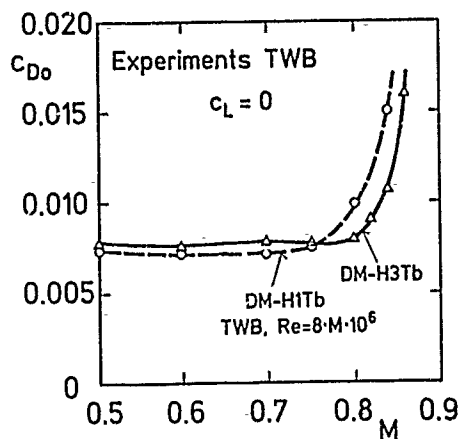


Fig. 15 Zero lift drag coefficients of several airfoils with thickness to chord ratio $t/c = 0.09$

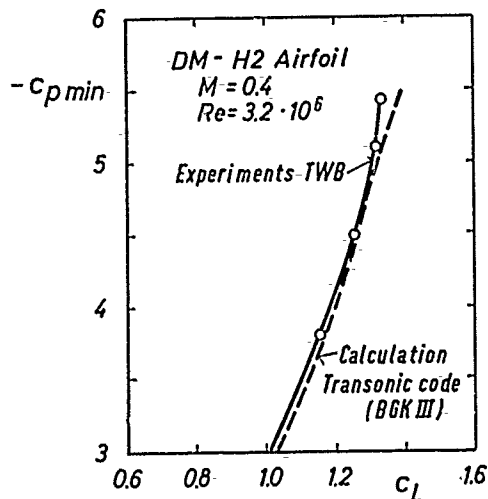


Fig. 17 Comparison of measured and calculated minimum pressure coefficient of the airfoil DM-H2

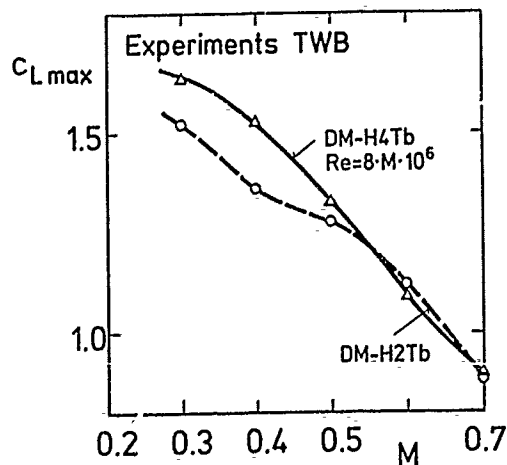


Fig. 19 Maximum lift coefficients of several airfoils with thickness to chord ratio $t/c = 0.12$

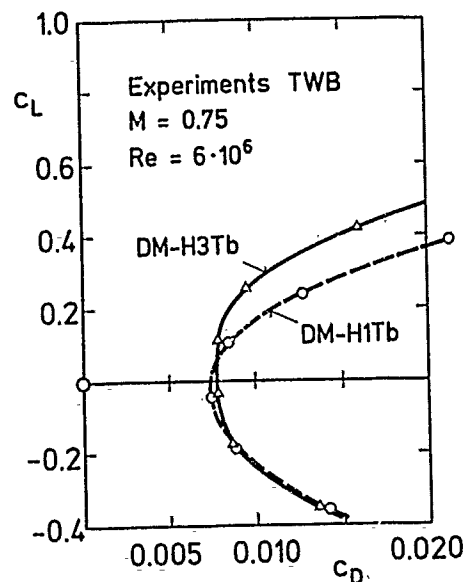


Fig. 16 Drag polars of the airfoils DM-H1 Tb and DM-H3 Tb

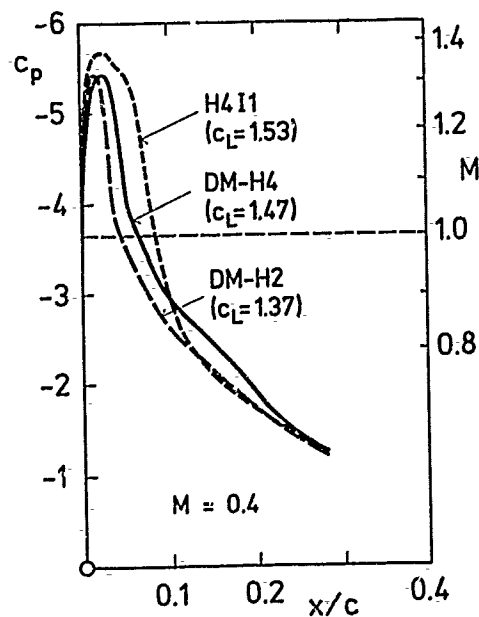


Fig. 18 Upper surface pressure distributions of several airfoils calculated with the BGK III-method

$M = .800$ $\alpha/p = -.85$ $Re = 3.3 \times 10^6$
 $C_L = .261$ $C_D = .01759$ $C_M = -.090$

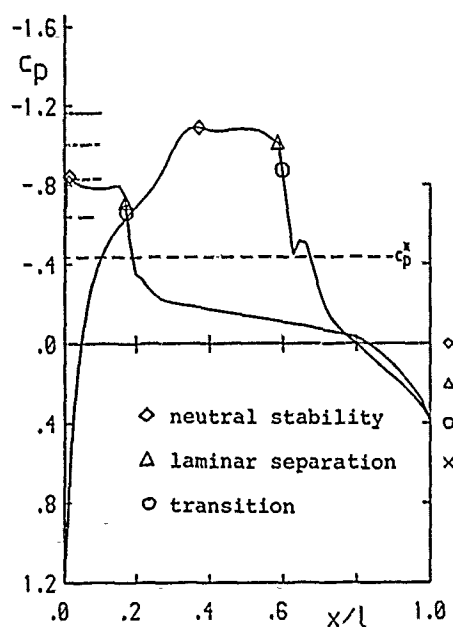


Fig. 20 Pressure distribution airfoil A

$M = .800$ $\alpha/p = -.85$ $Re = 3.3 \times 10^6$
 $C_L = .267$ $C_D = .01501$ $C_M = -.090$

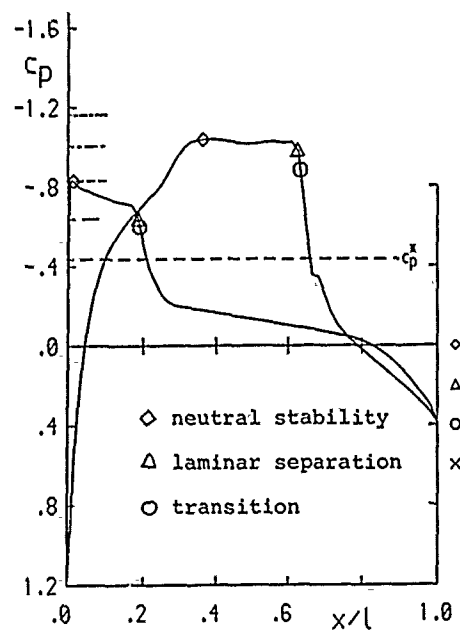


Fig. 22 Pressure distribution airfoil B

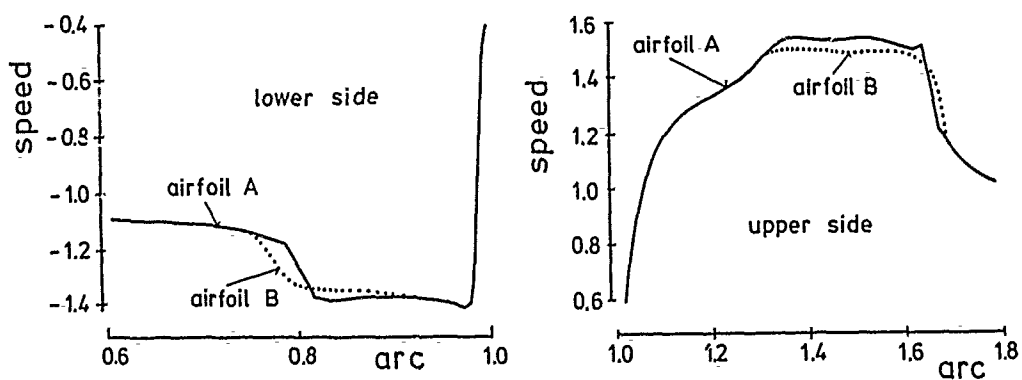


Fig. 21 Input speed distribution airfoil A and B

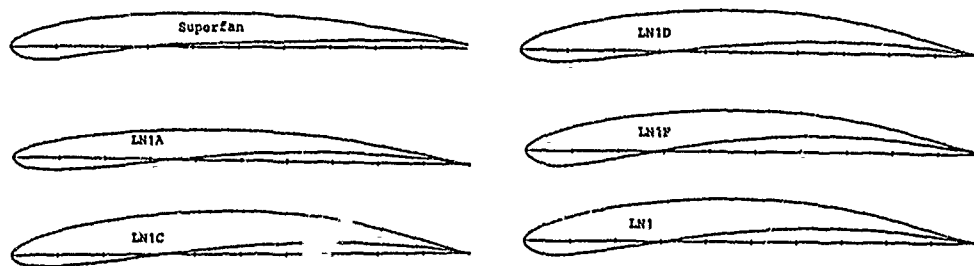


Fig.23: Nacelle contours at various stages of the design process

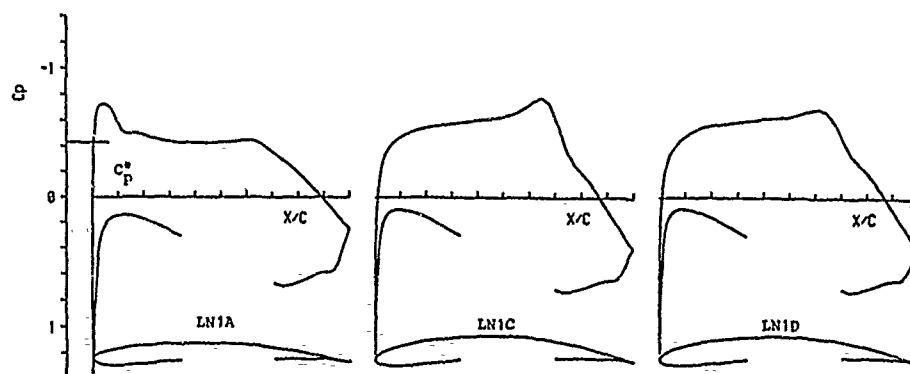


Fig.24: Pressure distribution for axisymmetric flow around nacelles in cruise, $M_\infty = 0.8$, $\epsilon = 0.76$

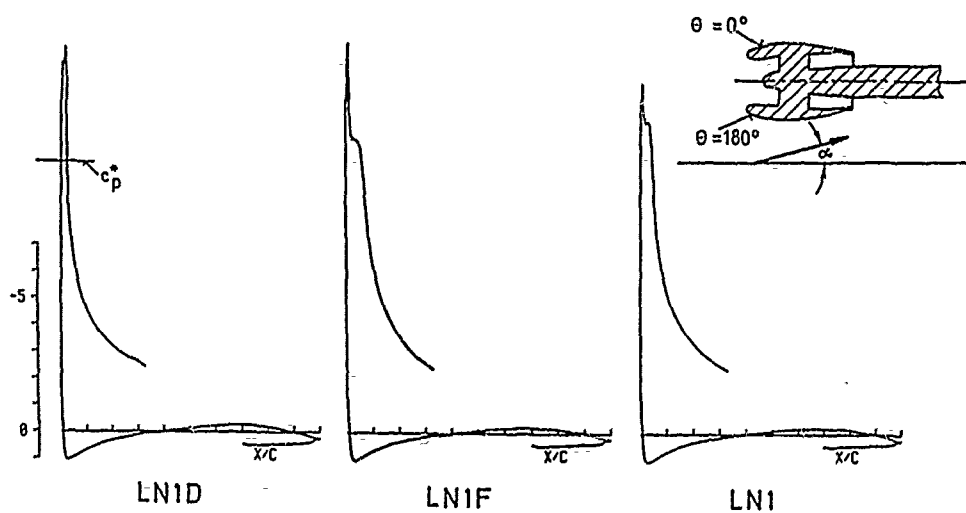


Fig.25: Pressure distribution on nacelle sections $\theta = 180^\circ$ at $M_\infty = 0.25$, $\alpha = 18^\circ$, $\epsilon = 1.4$

INVERSE DESIGN OF AIRFOIL CONTOURS:
CONSTRAINTS, NUMERICAL METHOD, AND APPLICATIONS

by
G. Volpe
Senior Staff Scientist
GRUMMAN CORPORATE RESEARCH CENTER
Mail Stop A08-35
Bethpage, New York 11714
U.S.A.

SUMMARY

The classical problem of constructing an airfoil profile that corresponds to an arbitrarily prescribed speed distribution is discussed and recast here in a form suitable for transonic applications. The problem, in general, is not well posed unless the specified speed distribution satisfies certain constraints. Thus, a solution exists only if the speed distribution contains a sufficient number of free parameters with values that can be adjusted in order to satisfy the constraints. This paper discusses the nature of the constraints and proposes several strategies for introducing the necessary freedom in the speed distribution. The computational method described in this paper determines the values of the parameters as part of the solution. It is based on the numerical solution of the full potential equation in conservation form with Dirichlet-type boundary conditions by a multigrid-ADI scheme. The general applicability and the accuracy of the numerical method are illustrated by several examples.

1. INTRODUCTION

The problem of designing airfoil profiles has aroused considerable theoretical interest for well over half a century because of the tremendous, practical implications. The aerodynamic performance of an aircraft can be greatly enhanced by tailoring the airfoil to its specific commercial or military requirements. An aircraft design usually calls for the wing profile to exhibit specified lift and/or drag characteristics, a particular lift distribution, or a specific velocity distribution that would provide a measure of control on the behavior of the boundary layer. In these cases, the airfoil design problem is reduced to the specification of a desired speed or pressure distribution.

Mangler¹ and Lighthill² discussed this "inverse" problem of airfoil theory for the case of incompressible flow and proposed various analytical solutions. Their methodology was refined and adapted for application on large and small computers by successive researchers.^{3,7} However, the difficulty in extending the methodology developed for incompressible flow to the transonic regime eventually gave rise to a number of alternate methods. In a pure inverse-type method of airfoil design -- such as those of Mangler and Lighthill -- the speed (or pressure) distributions desired on the surface of the profile are specified along with the magnitude and direction of the free stream. In contrast to the direct problem in which the shape of the airfoil profile is specified and the surface speed is computed through a solution of a Neumann-type problem, the inverse problem does not necessarily have a solution. A solution to the inverse problem exists only if a certain constraint between the free-stream speed and the surface speed is satisfied. In incompressible flow, which can be described by Laplace's equation, this can easily be shown and the constraint can be expressed in closed form. If, in addition, it is required that the airfoil profile be closed (or have a particular trailing edge thickness), two additional constraints appear. They can also be expressed in closed form for incompressible flow. The existence of these constraints has been known since the work of Mangler and Lighthill, and Woods has extended the analysis to subcritical compressible flows of a Karman-Tsien-type gas. The work of these authors indicated that a specified surface speed distribution had to be altered in such a manner as to satisfy the three constraints in order to guarantee a solution. In their methods, as in the refinements that followed,^{4,7} the approach was to prescribe the surface speed distributions with three free parameters whose values were to be adjusted to satisfy the three constraints.

An obvious advantage of inverse methods is the control the designer has over the force characteristics of the airfoil profile and over the boundary layer development on its surface, a control gained through the pressure (speed) distribution that is specified. This control can still be retained when making the changes that might be necessary to satisfy the constraints. The introduction of the three free parameters can be arranged such that an "ideal" speed distribution is modified only over selected segments of the airfoil surface. Desired characteristics of a speed distribution (e.g., "rooftops," Stratford-type pressure recovery, rear or front loading) can be retained with little or no modifications.

The formulation of an inverse method at supercritical speeds has been problematic because of the lack of closed-form expressions for the three constraints. The existence of constraints for the transonic design problem was intuitively true because the incompressible design problem was a subset of the more general compressible problem. The lack of a clear understanding of the nature of the first constraint was the main source of the difficulties. A number of alternate approaches to airfoil design were thus developed, each approach having its particular advantages and disadvantages. A number of methods, such as those of Hicks et al.,⁸ Davis,⁹ McFadden,¹⁰ Tranen,¹¹ and Carlson¹² can be classified as "direct" methods. In these methods the solutions (pressure and/or force characteristics) for the flow over some arbitrary initial airfoil contour are compared with a desired set of values for the pressure distribution or forces. The differences between the "target" and "current" characteristics are used in some rational way to modify the airfoil profile in the hope of reducing these differences. The process obviously has to be iterated. One advantage of such methods is that a realistic airfoil profile is always obtained at every step of the iteration. The biggest disadvantage, however, is the lack of a guarantee that the iteration will converge with the differences between computed and target values reduced to arbitrarily small levels. The question of the existence of an airfoil solution for a particular "target" pressure distribution is skirted in these methods and, in fact, they will not

converge for arbitrarily prescribed pressure distributions that do not satisfy the three constraints. This approach to airfoil design is best suited to applications where the target pressure distribution is a "small" modification of the one computed over the initial profile.

Another approach pioneered by Sobieczky¹³ is built around the concept of the fictitious gas in regions of supersonic flow. This approach is ideally suited to the redesign of an existing contour in a way that the new contour will have shock-free flow. This technique is much easier to implement than hodograph methods for the design of shock-free airfoils such as those of Garabedian and Korn (see Ref. 14) and Boerstel.¹⁵ In neither of these classes of methods does the user have control of the pressure distribution, however. Such control can be exercised only with an inverse method.

A formulation of the inverse problem for airfoil design at transonic speeds was finally given by Volpe and Melnik.¹⁶ They devised a method in which the first constraint could be satisfied by treating the value of the free-stream speed as a free parameter that is determined as part of the solution of the Dirichlet problem. Alternatively, the target surface speed distribution could be scaled keeping the free-stream speed fixed. The two options are equivalent in practice since the quantity of interest is the ratio of the surface to free-stream speed. The discovery of a mean by which the first constraint might be satisfied essentially completed the extension of the methodology of Mangic and Lighthill to transonic flow. In the method described in this paper, three free parameters are adjusted numerically to drive the values of the free-stream speed and trailing edge gap dimensions to prescribed values. The trailing edge parameters are introduced in such a way that each mainly affects only one of the constraints. This permits the formulation of a diagonal-type iterative scheme in which the three parameters can be determined from three uncoupled one-dimensional relaxation methods. The result is a robust method for the design of airfoils that generate speed distributions in close approximation to an arbitrarily prescribed ideal.

2. FORMULATION OF THE INVERSE DESIGN PROBLEM

The problem being addressed is the construction of the airfoil profile, which has a surface speed distribution, q_0 , equal to some desired function, F , everywhere along its arc length, s . This is to be measured clockwise around the airfoil contour starting at the lower surface trailing edge point. The airfoil's coordinates, x, y , can be parameterized as functions of s . A feature of practical airfoil contours is that the trailing edge be either closed or have a very small gap. Thus, a requirement on the to-be-determined airfoil is that the upper and lower surface trailing edge points be separated by prescribed distances Δx and Δy . The horizontal gap, Δx , is usually set to zero, while the vertical gap, Δy , is set to zero (a closed airfoil) or to a small positive number. The free stream is also defined by prescribing values for the free-stream velocity q_∞ , temperature, and pressure (or density). These in turn determine the free-stream Mach Number, M_∞ . In incompressible flow, of course, it is only necessary to specify the velocity in order to identify the free stream uniquely. Our formulation applies in its entirety if we specify a surface-pressure distribution instead of a surface speed since the two are uniquely related. Formally, then, the problem is to determine the airfoil profile of a specified trailing edge thickness corresponding to the speed distribution

$$\frac{q_0}{q_\infty} = F(s/s_{\max}) \quad (1)$$

Without loss of generality, s_{\max} can be set equal to one; q_0 is taken as positive in the clockwise direction around the airfoil. The strategy followed is to iteratively modify some initial contour until the desired speed distribution, q_0 , is achieved. This initial contour can be mapped into the unit circle by the unique conformal transformation

$$\frac{dz}{d\zeta} = \left[1 - \frac{1}{\zeta}\right](1-\epsilon) e^{(P+iQ)} \quad (2)$$

where $z = x + iy$ and $\zeta = re^{i\omega}$ are the coordinates in the physical and mapped planes, respectively, and $\epsilon\pi$ is the included trailing edge angle. This equation can be separated into its real and imaginary parts. Thus, on $r = 1$,

$$\frac{ds}{d\omega} = \left[2 \sin \frac{\omega}{2}\right](1-\epsilon) e^P \quad (3)$$

$$\theta = \frac{1}{2} (1+\epsilon)(\pi-\omega) - \frac{\pi}{2} + Q \quad (4)$$

where θ is the local slope of the airfoil. Q is the Fourier series

$$Q = \sum_{n=0}^N (A_n \sin n\omega - B_n \cos n\omega) \quad (5)$$

and P is its conjugate series. Because θ is known as a function of s , the coefficients of the series can be found by standard Fourier analysis as described in Ref. 4. With this mapping procedure, the leading terms of the series are related to the trailing edge gap ($\Delta x, \Delta y$) by

$$\begin{aligned} A_1 &= -\left(\frac{\Delta x}{2\pi}\right) \sin B_0 - \left(\frac{\Delta y}{2\pi}\right) \cos B_0 + (1-\epsilon) \\ B_1 &= -\left(\frac{\Delta x}{2\pi}\right) \cos B_0 + \left(\frac{\Delta y}{2\pi}\right) \sin B_0 \end{aligned} \quad (6)$$

In the case of incompressible flow, if q_0 were defined in terms of the circle plane coordinate, w , then the airfoil contour corresponding to q_0 could be constructed immediately. The complex potential, w , for the incompressible flow past the circle (to which the unknown airfoil is mapped) is

$$w = q_\infty \left(\zeta e^{-i\alpha} + \frac{e^{i\alpha}}{\zeta} \right) + i\Gamma \log \zeta \quad (7)$$

where α is the angle of attack of the free stream and Γ is the circulation around the circle. The value of Γ is obtained by requiring that the velocity $\frac{dw}{d\zeta}$ be zero at the point on the circle corresponding to the airfoil's trailing edge. Now

$$\frac{dw}{dz} = \left| \frac{dz}{d\zeta} \right| = \left| \frac{dw}{d\zeta} \right| \left| \frac{d\zeta}{dz} \right|^{-1} \quad (8)$$

and, in the physical plane, $\left| \frac{dw}{dz} \right| = q_0$. The right hand side of Eq. (8) is then completely known as a function of w . Using Eq. (3) and (5) the coefficients of the series of the transformation can be evaluated. Once $\frac{dz}{d\zeta}$ has been expressed as a trigonometric series in w , the airfoil coordinates, z , are found by integration.

If q_0 is prescribed as a function of arc length, s , some iteration will be required in this procedure since $\left| \frac{dw}{dz} \right|$, which is needed in Eq. (8), will not be known as a function of w until after $s(w)$ is found. However, the design of the airfoil is still a straightforward process.

For compressible flow of a perfect gas, the flow past the circle cannot be expressed in closed form. However, it can be computed numerically, and a similar iterative procedure can be formulated for compressible flow.

Specifically, the procedure will be as follows: An initial airfoil contour is mapped into the unit circle and the flow around the circle is solved subject to the conditions on the circle boundary that the tangential speed be the required total speed. The passage from $q_0(s)$ to $q_0(w)$ is done using the current $s(w)$. In this flow the circle boundary is not necessarily a streamline and the departure of the boundary from a streamline can be used to find a correction to the aircraft contour. Using the new metric the process can then be repeated.

The following sections will describe a numerical scheme for computing the compressible flow in the circle plane and a method for updating the airfoil contour.

3. TRANSONIC FLOW FIELD SOLUTION

The infinite flow field around a unit circle can be transformed into the finite region inside the circle. The modulus of the transformation of the physical plane, z , to the inside of the circle is then written as

$$h = \frac{1}{r^2} \left| \frac{dz}{d\zeta} \right| \quad (9)$$

$dz/d\zeta$ is, of course, the quantity we seek since it describes the transformation of the unknown airfoil profile into the circle. It should be recalled that the transformation is conformal everywhere except at the airfoil's trailing edge where the metric $h=0$.

The flow in the circle plane is assumed to be governed by the continuity equation

$$\frac{\partial}{\partial w} (\rho U) + r \frac{\partial}{\partial r} (\rho V) = 0 \quad (10)$$

U and V are the transformed circle plane velocity components in the r and w directions, respectively. For irrotational flow they can be expressed as gradients of a potential function ϕ ; thus

$$U = \phi_w, \quad V = r\phi_r \quad (11)$$

As long as shock waves in the flow remain of moderate strength, the above assumptions will not introduce significant errors in the flow solution. The density, ρ , is found from the speed of sound, a , through the relation

$$\rho = (M_\infty^2 a_\infty^2)^{1/(\gamma-1)}$$

where γ is the ratio of specific heats. In turn, a can be evaluated through the energy relation

$$a^2 = a_0^2 - \frac{\gamma-1}{2} (u^2 + v^2)$$

Here a_0 is the stagnation speed of sound and u and v are the velocity components in the physical plane. These are related to the components in the circle plane by

$$u = \frac{rU}{h}, \quad v = \frac{rV}{h} \quad (12)$$

We see that the flow within the circle cannot be computed if h is not known; the assumed initial shape for the airfoil provides the initial estimate for h . In the limit of M_∞ going to zero, equation (10) reduces to Laplace's equation. Then, the solution for the flow within the circle is independent of the mapping metric h , and it is given by Eq. (7).

The mapping introduces singularities at infinity, but they can be removed by subtracting from the potential its behavior in the far field. As discussed by Ludford,¹⁷ the solution in the far field is made up of a uniform stream plus a circulatory component. The potential functions describing these terms are known. Thus, we can define a reduced potential function.

$$G = \phi - q_\infty \left(r + \frac{1}{r} \right) \cos(\omega + \alpha) - E \tan^{-1} \left[\sqrt{1 - M_\infty^2} \tan(\omega + \alpha) \right] \quad (13)$$

where E is a circulation constant. This reduced potential is continuous and single valued everywhere.

At infinity ($r=0$) $G=G_\infty$, a constant that can be set at zero in direct (Neumann) problems, but which must be determined as part of the solution in inverse (Dirichlet) problems by extrapolating from the interior of the flow field.

For the direct (analysis) problem, q_∞ is usually set to unity and the boundary conditions demand that $v=0$ at the surface. The solution for the flow field is computed numerically by discretizing the flow field in conservation form along a polar coordinate mesh. The set of difference equations that approximates equation (10) is solved for the discrete values of the reduced potential, G , at the nodes of the computational mesh by an approximate factorization multigrid scheme similar to the one described by Jameson.¹⁸ The value of the circulation constant, E , is determined from the Kutta condition, which requires that u be finite at the trailing edge. Since $h=0$ at the trailing edge, U must be made to vanish at this point. In this direct problem the surface speed $q_0(s)=q(s)$ is computed from the potential function G .

For the inverse design problem the boundary conditions at $r=1$ are imposed on u rather than v . Using the known functional relation between s and ω for the current contour, the target speed distribution q_0 can then be expressed as a function of ω . Then, at the boundary in the circle plane we set $u_0=u(\omega)$ equal to $q_0(s(\omega))$. Of course, this would be true if h were the true mapping metric; in general, it is not. Hence, the boundary is not necessarily a streamline of the flow. In other words, v is not necessarily zero at the boundary. The flow field is computed subject to the boundary condition $u_0=q_0(s(\omega))$ at $r=1$ by a numerical scheme identical to the one used for the direct problem. The Dirichlet boundary conditions are implemented by integrating q_0 around the airfoil to find the reduced potential G at the boundary points using Eq. (11-13). A constant of integration G_0 can be prescribed arbitrarily. The numerical problem that has boundaries at both $r=0$ and $r=1$ is well posed since the value at the inner boundary, G_∞ , is determined as part of the solution. The circulation constant is determined by integrating u_0 around the full boundary. In general, in the Dirichlet problem there is a net mass flow emitted from the boundary. To allow for this, a source term $\sigma \log r$ is subtracted from the potential leading to a new reduced potential, \bar{G} , defined by

$$G = \bar{G} + \sigma \log r$$

The far-field boundary condition will then have the additional term

$$\frac{\sigma}{2} \log [1 - M_\infty^2 \sin^2(\omega + \alpha)]$$

The source term has a role similar to that of the circulation term for the Neumann problem. The value of σ is determined by setting V equal to zero at the trailing edge. The introduction of the source term guarantees compatibility of surface and far-field boundary conditions during the iteration process. This source term vanishes as the design process converges to its final contour.

A non-zero normal velocity v will, in general, be computed on the circle boundary. This can be used to modify the original airfoil contour.

4. CONTOUR MODIFICATION

A non-zero normal velocity v at the circle boundary implies that the actual streamline is (to first order) rotated from the boundary by an angle of magnitude

$$\delta\theta = \tan^{-1} \left(-\frac{v}{u} \right) \quad (14)$$

The mapping of a new streamline contour, \tilde{z} , to the unit circle is accomplished by a mapping similar to Eq. (2)

$$\frac{dz}{d\zeta} = \left(1 - \frac{1}{\zeta}\right) (1 - \bar{\zeta})_0 (\bar{P} + i\bar{Q})$$

which implies relations similar to Eq. (4) and (5). Letting

$$\bar{Q} = \sum_{n=0}^N (\bar{A}_n \sin n\omega - \bar{B}_n \cos n\omega)$$

and $A'_n = \bar{A}_n - A_n$ and $B'_n = \bar{B}_n - B_n$, it follows that

$$\delta\theta = \frac{1}{2} \delta\epsilon(\pi - \omega) = \sum_{n=0}^N (A'_n \sin n\omega - B'_n \cos n\omega) \quad (15)$$

where

$$\delta\epsilon = \frac{1}{\pi} (\delta\theta_1 - \delta\theta_{2N})$$

$\delta\theta_1$ and $\delta\theta_{2N}$ are the values of $\delta\theta$ at the two sides of the trailing edge point. Since $\delta\theta$ is known as a function of ω , A'_n and B'_n can be evaluated by a standard Fourier analysis of Eq. (15). The new components of the series of the transformation, \bar{A}_n and \bar{B}_n , can be formed. The new derivative of the arc length, $d\bar{s}/d\omega$, is calculated, in turn, as well as

$$\frac{dx}{d\omega} = -\frac{d\bar{s}}{d\omega} \cos \bar{\theta}, \quad \frac{dy}{d\omega} = -\frac{d\bar{s}}{d\omega} \sin \bar{\theta}$$

The actual ordinates of the new airfoil contour are then obtained by integration. This new airfoil provides a new approximation for the metric h and a new relation $s(\omega)$, which are needed to set up a new Dirichlet problem in the circle plane. This process can be repeated until a desired tolerance in the maximum value of v/u is reached. At this point the tangential velocity is equal to the total target speed prescribed on the surface, and the target speed will have been modified appropriately to satisfy the constraints.

5. CONSTRAINTS IN INCOMPRESSIBLE FLOW

The question that must be asked at this point is whether an airfoil solution exists for an arbitrarily prescribed speed distribution. For incompressible flow, Mangler and Lighthill showed that, in fact, a solution exists only if certain integral constraints are satisfied by q_0 , and this can be demonstrated as follows.

Since a lifting flow over a circle can be reduced to the non-lifting, symmetric flow as shown in Ref. 2 and 19, it is sufficient to consider the nonlifting case in order to simplify the discussion. The mapping between the z and ζ planes must have the form

$$z = \zeta + \sum_{n=0}^{\infty} a_n \zeta^{-n}$$

if the flow in the far field is to remain unscaled. Here, the a_n 's are complex constants. Therefore,

$$\frac{dz}{d\zeta} = 1 - \sum_{n=1}^{\infty} n a_n \zeta^{-(n+1)}$$

From Eq. (7), we see that

$$\frac{dw}{d\zeta} = q_{\infty} \left(1 - \frac{1}{\zeta^2}\right)$$

Hence, combining the last two equations, we find that

$$\frac{dw}{dz} = \left(1 + \sum_{n=2}^{\infty} b_n \zeta^{-n}\right) \quad (16)$$

Since $(dw/dz) = q_0 e^{-i\theta}$, it follows that

$$\log \left| \frac{q_0}{q_{\infty}} \right| = \sum_{n=2}^{\infty} h_n \zeta^{-n} \quad (17)$$

As pointed out by Lighthill and Thwaites, $\log|q_0/q_{\infty}|$ is an analytic function in the domain outside the circle (it fails to be analytic at stagnation points on the circle where $q_0 = 0$). Therefore, it can be expanded in a Fourier series on the circle itself. However, from Eq. (17) we see that the series cannot have terms of zero or first order. In fact, q_0 must be such that

$$\int_0^{2\pi} \log \left| \frac{q_0}{q_\infty} \right| \frac{1}{\sin \omega} \cos \omega \, d\omega = 0 \quad (18)$$

These are the three integral constraints that the prescribed speed distribution must satisfy for an airfoil solution to exist. These three constraints have arisen from the requirements that the airfoil be closed and from the imposition of a value on the free stream. It can be safely assumed that similar constraints exist also at supercritical speeds. The above discussion indicates that the prescribed speed distribution should contain, in general, three adjustable parameters to guarantee that the constraints may be satisfied. Thus, the surface speed distribution should be prescribed in the form

$$\frac{q_0}{q_\infty} = F(S/S_{\max}; p_1, p_2, p_3) \quad (19)$$

where p_1 , p_2 , and p_3 are the three parameters that are found as part of the solution. For compressible flow ($M_\infty \neq 0$), Eq. (18) is no longer an adequate expression for the constraints. One must then formulate alternative means of evaluating the parameters while still ensuring that the constraints are satisfied. The particular functional forms chosen to introduce the parameters will, of course, affect the class of airfoil solutions that can be obtained. These will be discussed later.

6. AN ALTERNATE LOOK AT THE CONSTRAINTS

In order to formulate a well-posed inverse design procedure which would be valid at compressible speeds, the nature of the constraints must be re-examined since the above-derived closed form expressions are valid only for incompressible flow. It is logical to do this in the context of the computational method that has been outlined. The two constraints that arose because of the required trailing edge gap are of a geometrical nature. Hence, one can set up a procedure in which, by monitoring the trailing edge gap size, the target speed can be modified in order to drive the gap's dimensions to its specified values. The first constraint creates a problem because there is no single, physical quantity that reflects the constraint. This first condition is a statement of "compatibility" between the prescribed surface speed and the free-stream speed. If the latter is also being prescribed, as is usually the case, the surface speed prescription has to be modified for the constraint to be satisfied. If the free-stream speed is not specified, in the case of incompressible flow its value can be found from Eq. (18). In the absence of a closed-form expression, which would be valid at compressible speeds, the problem is to define a procedure whereby either the surface speed or the free-stream speed might be changed to bring about "compatibility."

Let us consider the incompressible flow over a circle again. As mentioned earlier, it will be sufficient to consider the nonlifting symmetric flow. The general solution for the flow on the outside of a circle of unit radius can be represented in the form

$$G = a_0 + a_1 r \cos \omega + \sum_{n=1}^N \frac{b_n}{r^n} \cos n\omega$$

N being a sufficiently large number.

This is the most general solution to Laplace's equation that yields a uniform free-stream flow in the far-field ($r \rightarrow \infty$). Hence

$$\frac{\partial G}{\partial r} = \left(a_1 - \frac{b_1}{r^2}\right) \cos \omega - \sum_{n=2}^N n \frac{b_n}{r^{n+1}} \cos n\omega \quad (20)$$

and

$$\frac{1}{r} \frac{\partial G}{\partial \omega} = -\left(a_1 + \frac{b_1}{r^2}\right) \sin \omega - \sum_{n=2}^N \frac{nb_n}{r^{n+1}} \sin n\omega \quad (21)$$

It follows that the total velocity

$$q = \left(G_r - \frac{1}{r} G_\omega\right) e^{-i\omega}$$

must be of the form

$$q = a_1 - \sum_{n=2}^N b'_n \zeta^{-n} \quad (22)$$

In the far field, as $\zeta \rightarrow \infty$, $q = q_\infty$. Hence, $a_1 = q_\infty$ and

$$q = q_\infty - \sum_{n=2}^N b'_n \zeta^{-n} \quad (23)$$

which reflects the result expressed in Eq. (17). Thus, if the flow over the circle is determined with the condition that $q = q_0(\omega)$ on the boundary $r = 1$, we see that when we expand $q_0(\omega)$ in a series

$$q_0(\omega) = c_0 + \sum_{n=1}^N c_n e^{-in\omega} \quad (24)$$

restrictions on q_0 immediately arise, echoing the constraints described by Lighthill and Mangler. In particular, we see that $c_0 = q_\infty$, the first constraint. Also, we see that $c_1 = 0$, implying two additional restrictions on the speed, since c_1 is a complex constraint. For the rest of this section we will concentrate on the first constraint.

It is interesting to note that Eq. (23) can be factored into the form

$$q = q_\infty \left(1 - \frac{1}{\zeta^2}\right) \left[1 - \sum_{n=2}^N b_n \zeta^{-n}\right] \quad (25)$$

Since the first part on the right-hand side of this expression represents the solution for the flow over the unit circle, the expression in brackets formally gives the mapping $|dz/dz|$ which generates the airfoil corresponding to $q=q_0(\omega)$ (assuming q_0 satisfies the constraints).

At this point it should be mentioned that a proper speed distribution for an airfoil should contain at least one zero corresponding to the leading edge stagnation point, and two zeroes if the trailing edge is not cusped. Hence, the zeroes of q should match the zeroes of the flow over the circle if the metric is to be free of singularities with the possible exception of the trailing edge.

In the procedure described in the previous sections, the airfoil's contour is to be found by successively modifying some starting profile. The modifications are to be guided by the solution of a Dirichlet problem. Consider now such a Dirichlet problem in the case of incompressible flow. Boundary conditions are now imposed on the tangential velocity and can be expressed as $\frac{\partial G}{\partial \omega} = g(\omega)$. Expanding $g(\omega)$ in a trigonometric series, one obtains

$$\left(\frac{\partial G}{\partial \omega}\right)_{r=1} = c'_0 + \sum_{n=1}^N c'_n \sin \omega. \quad (26)$$

A comparison of Eq. (26) and (21) leads to $N+1$ conditions for the constant a_1 and the N Fourier coefficients b_n . However, c'_0 is identically zero since

$$\int_0^{2\pi} \frac{\partial G}{\partial \omega} d\omega = 0$$

Thus, there are really only N -conditions, and a_1 -- the term representing the free stream -- can be specified!

Having determined the values of the b 's, the speed normal to the boundary can be found from Eq. (20). The total speed on the boundary, as anywhere else in the flow field, must have the form given in Eq. (22). Thus, the solution to the Dirichlet problem yields a flow in which the free stream, and the speed on any closed path that can be drawn within the flow field are automatically compatible; there is no "first" constraint. Not all paths are of interest, however. Only the contours that pass through branch (stagnation) points of the flow can yield airfoil-like profiles. The location of the stagnation points of the flow computed from the solution of the Dirichlet problem depends on the value assigned to the free-stream term, a_1 . Regardless of the value assigned to a_1 , an airfoil contour can be traced from the stagnation points, but the speed distribution on the contour is not necessarily equal to the one prescribed, or even close to it. The first constraint has been removed at the expense of retaining control over the speed on the airfoil, which is an undesirable result.

If the circle boundary were to be truly a streamline, G_ω would be identically equal to the sought after total speed. If the branch points of the flow were to be on the circle boundary, it would be reasonable to expect that the streamline passing through them would be "close" to the circle and the total speed on the streamline would be "close" to G_ω . The contour-perturbation process described above may have a chance to work in such a situation. This "closeness" can be brought about by choosing a_1 in such a way that the branch points do fall exactly on the circle boundary. Since points where G_ω is already zero are already specified, it is natural to enforce these points to be the stagnation points of the flow. This is guaranteed by forcing G_ω to be zero at these two points by appropriately choosing values for the free stream and for the mass-flow term, a . Since the formulation already called for a to be chosen in such a way as to make $G_\omega=0$ at the trailing edge, the procedure just outlined has reinstated the constraint between the free stream and the prescribed surface speed. The advantage consists in the fact that the constraint is now satisfied by making $G_\omega=0$ at the leading edge stagnation point rather than through an integral relation. This new approach to the constraints generates a profile with a speed distribution that automatically satisfies the integral expression without invoking it explicitly. In this new procedure, as in the classical one, the free-stream speed can be kept at a specified value by introducing free parameters in the specified surface speed, as in Eq. (16); p_1 in Eq. (16) can be adjusted to return a_1 to its desired value.

In summary, an airfoil design procedure that satisfies the first constraint and is equivalent to the Mangler/Lighthill method can be formulated as follows. The design strategy calls for the computation of a flow field about a circle on which the boundary conditions are that the tangential velocity u (equivalent to G_ω in incompressible flow) is set equal to the target speed distribution $q_0(\omega; p_1)$ (we are still neglecting trailing edge closure). At convergence, u must be equal to q_0 . If we adjust the value of p_1 in such a way that $v = 0$ at the point on the circle where $u = 0$, this point will be a stagnation point for the flow. Hence, the streamline representing an airfoil-like contour must pass through that point. The speed distribution along that streamline is not equal to the target speed, but it automatically satisfies the free-stream speed constraint. The mapping metric, h , can then be updated as described above. It is worth mentioning, at this point, that setting $v=0$ where $u=0$ ensures that the

ratio expressed in Eq. (14) remains finite at all times. With the new metric one can set up another Dirichlet problem that has a streamline passing closer to the circle and the speed along it will be closer to the target speed. If one repeats this process until the circle itself becomes a streamline, the speed distribution on the streamline will then be equal to the specified target and will satisfy the constraint. Hence, adjusting p_1 in such a way that $v = 0$ at $u = 0$ at all times leads to the design of the airfoil that corresponds to $q_0(\omega; p_1)$, and the value of p_1 is the value that ensures satisfaction of the free-stream speed constraint.

This technique for satisfying the constraint can be applied at supercritical speeds as well as for incompressible flow. The constraints imposed by the trailing edge closure requirements can be accounted for by monitoring the trailing edge gap during the iteration process and adjusting the two additional parameters, p_2 and p_3 in Eq. (16).

7. ENFORCEMENT OF CONSTRAINTS

The discovery of a method that ensures that the first constraint can be satisfied at compressible speed opens the way to the formulation of schemes whereby the necessary freedom can be introduced in the speed distribution. For the remainder of this paper, it will be assumed that the target speed is of the form

$$\frac{q_0}{q_\infty} = f_1(s; p_1) [f_0(s) + f_2(s; p_2) + f_3(s; p_3)] \quad (27)$$

where $f_0(s)$ represents the ideal target speed distribution that, in practice, is usually a tabulated function. The functions f_1 , f_2 , and f_3 are introduced to modify the ideal target in order to satisfy the three constraints. In general, it is desirable to localize the effect of f_1 , f_2 , and f_3 so that the resulting surface speed will be close to the ideal speed distribution, $f_0(s)$, over most of the airfoil surface. Since in transonic flow it is not possible to relate p_1 , p_2 , and p_3 to the three constraints in closed form, a numerical search for the parameters must be made. The search is greatly facilitated by choosing f_1 , f_2 , and f_3 in such a way that each significantly affects only one of the constraints. We would then have three one-dimensional searches for p_1 , p_2 , and p_3 . In Ref. 20 the sensitivity of a designed airfoil contour to various changes in the target speed distribution is reported. These results have guided the definition of f_1 , f_2 , and f_3 in Eq. (27). Three separate schemes have been tried, but they hardly exhaust the number of possibilities and many more can be constructed.

Satisfaction of the first constraint is guaranteed by adjustment of p_1 . By definition, f_1 causes a scaling of surface speed (q_0/q_∞). In scheme 1, we choose $f_1 = p_1$, which results in a scaling that is uniform along the airfoil. In this case we could consider p_1 as a scaling on either q_0 or q_∞ . In the latter case we would essentially have q_∞ floating, and it would be determined as part of the solution. As discussed above, the value of p_1 is chosen to guarantee that the specified leading edge stagnation point will truly be a branch point of the flow.

Control over Δy , the vertical separation between the upper and lower surface trailing edge points, can be exercised by defining

$$f_2 = p_2 \sin\left(\frac{8}{3}\omega\right), \quad \omega \leq \frac{3}{4}\pi \quad (28)$$

Outside this range f_2 is zero. Here, we are substituting the ordinate ω in the computational plane for the arc length s . It is more convenient to use ω rather than s , and the formulation of the problem is not affected by this substitution. The function f_3 is the hardest to define. The horizontal separation between the two trailing edge points, Δx , is affected primarily by the location of the leading edge stagnation point. As shown in Ref. 20, a small shift in this stagnation point along the surface of the airfoil, on the order of 2% of the chord length, can alter the horizontal gap by 5-6%. It should be pointed out that a 2% shift in the stagnation point along the surface is hardly noticeable when viewed as a shift along the chord. In order to maintain a loose coupling among p_1 , p_2 , and p_3 , the shift must be accomplished without altering the local velocity gradients. This can be accomplished by shifting the functional dependence of q_0 on s locally, near the leading edge. Thus, we let

$$f_3(s) = f_0(s') - f_0(s)$$

with

$$s' = s - p_3 h(s)$$

where

$$h(s) = \frac{1}{2} [1 - \cos\left(\frac{\pi}{\Delta s}(s - s_T + 2\Delta s)\right)] \quad , \quad s_T - 2\Delta s \leq s \leq s_T + \Delta s$$

$$= 0 \quad , \quad s_T - \Delta s \leq s \leq s_T - \Delta s$$

$$= \frac{1}{2} [1 + \cos\left(\frac{\pi}{\Delta s}(s - s_T + \Delta s)\right)] \quad , \quad s_T + \Delta s \leq s \leq s_T + 2\Delta s$$

Elsewhere, $h(s)$ is zero. The point s_T denotes the location where $f_0(s)$ is zero in the leading edge region and Δs is some appropriate distance, typically 2.5% of the total arc length. This form for f_3 shifts the leading edge stagnation point smoothly without introducing any "wiggles" in the target speed

distribution and, in addition, has hardly any effect on the values of p_1 and p_2 . This form for f_3 is common to all the three schemes we have tried.

A second scheme for modifying the target distribution uses a different definition for f_2 in Eq. (27). The expression given in Eq. (28) alters the target speed distribution only on the lower surface of the airfoil. It would, therefore, be unsatisfactory if we were trying to design a symmetric airfoil. An alternative form for f_2 is

$$\begin{aligned} f_2 &= p_2 \left[1 - \frac{\omega}{\omega_1} \right] \quad , \quad \omega \leq \omega_1 \\ &= p_2 \left[\frac{2\pi - \omega}{\omega_1} - 1 \right] \quad , \quad \omega \geq 2\pi - \omega_1 \end{aligned} \quad (29)$$

This function symmetrically alters the magnitude of the speed in the neighborhood of the trailing edge. In our computational scheme, the speed takes on opposite signs on the upper and lower surfaces, accounting for the sign difference between the two parts of Eq. (29); ω_1 is typically taken as $\pi/3$. A third scheme is formulated by substituting for $f_1 = p_1$ in scheme 1 the function

$$f_1 = \sqrt{1 + p_1 \sin^2\left(\frac{\omega}{2}\right)}$$

which concentrates the scaling in the front half of the airfoil.

Regardless of which scheme is used, the three parameters are adjusted periodically during the solution of the Dirichlet problem that precedes each contour modification. At the end of every sweep of the flow field, q_0 and σ are determined by forcing v to be zero both at the leading edge point where u is zero and at the trailing edge. The factor p_1 is then adjusted to scale q_0 back to its specified value, and the flow field is swept again. The value of the normal component of velocity at the leading edge stagnation point, v , goes to zero quite fast (due to the continuous resetting of p_1). When v is below a given tolerance (typically 10^{-2} - 10^{-6}), estimates are made of the values that A_1 and B_1 , the first-order terms of the series in Eq. (5), would have if the airfoil were modified at that stage. These values are compared with the values they should have for the airfoil to have the desired trailing edge gap dimensions, as given by Eq. (5). The differences between the current and desired values, δA_1 and δB_1 , are then used to change p_2 and p_3 , respectively. The change in p_2 is made proportional to δA_1 , and the change in p_3 is proportional to $(-\delta B_1)$. Since p_1 is introduced as a multiplier, a change in the surface boundary conditions due to a new p_1 can be transmitted through the entire flow field by scaling the entire potential field. Using this procedure we can update p_1 after each multigrid sweep of the flow field without seriously affecting the convergence rate of the numerical scheme. This procedure is not possible with p_2 and p_3 ; therefore, they are updated infrequently. However, the method of false position can be used to accelerate convergence of p_2 and p_3 . The flow field is assumed to be converged when all the residuals at all the flow field node points are below a specified tolerance, and v at the leading edge stagnation point together with δA_1 and δB_1 are below their respective tolerances. At this point the airfoil contour is modified and another Dirichlet problem is set up. There is no need to analyze the new airfoil contour with this procedure. A direct analysis is made at the very end of the calculation just to check our results.

To ensure convergence of the design process, it is necessary to under-relax the changes to the contour shape. Thus, only a fraction of the changes suggested by Eq. (14) is actually taken in the early design cycles. After several contour modifications the factor can be increased. The tangential velocity $u(\omega)$ at the boundary, which is interpolated from the desired $q_0 = F(s)$, is also under-relaxed when a new design cycle is started.

8. RESULTS

A considerable number of airfoil contours have been designed by the method over a wide range of speed (or pressure) distributions including cases in which shock waves were present in the flow field. All the examples that will be presented in this section have been computed on a mesh containing 192 points in the circumferential direction and 32 points in the radial direction. Five mesh levels were used in the multigrid sequence. In each case the angle of incidence of the designed contour was set at zero. In the present formulation the angle of attack can be specified; different choices for the angle result in different orientations of an otherwise identical contour within the given coordinate system.

A strong test of the system is illustrated in the redesign of the Korn airfoil using as a target the pressure distribution computed on the profile at $M_\infty = 0.750$, $\alpha = 0.5^\circ$. At these flow conditions a shock is present in the flow on the upper surface as can be seen in Fig. 1. Using the distribution given by the circles in Fig. 1 and using the NACA 0012 airfoil as a starting contour (see Fig. 2), the Korn airfoil is recovered exactly in about a dozen iterations of the airfoil shape. A measure of the convergence rate of the procedure is given by Fig. 3 which gives the maximum value of $|v/u|$ at each cycle. The program was run through 30 cycles, but, usually, no changes in the shape can be noticed once the maximum value of $|v/u|$ has been reduced below 0.01. The pressure distribution computed on the redesigned profile is given by the solid line in Fig. 1, and it is practically identical to the specified target (the symbols). Obviously, since the target was a direct solution for the flow over a known profile, it satisfied the three constraints of the inverse problem, and it should have generated an airfoil solution without need of modifications. The actual values computed for the three parameters were (scheme 1 was used in this example): $p_1 = 1.000023$, $p_2 = 0.000040$, and $p_3 = -0.000668$, all well within the specified numerical tolerances. The slight differences near the shock are due to the fact that values for the target distribution were computed by central difference formulas at midpoints of the mesh, while the values associated with the recomputed profile were computed at node points. The Korn profile

is recovered exactly, without any "wiggles." In Fig. 4 the slope distribution of the computed profile in the leading edge region is compared with the values of the original contour. Even in the vicinity of the shock, the redesigned profile is as smooth as the original Korn airfoil, as can be seen in Fig. 5. An interesting exercise is to use the pressure distribution in Fig. 1 as the target for designing airfoils at a free-stream Mach number other than 0.75. This was tried with free-stream Mach numbers of 0.730 and 0.770. As the results of Fig. 5 and 6 show, the recompression through the shock implied by the target distribution can no longer be achieved over a smooth profile. Thus, even though the "modified" target distributions for these two cases differ only slightly (see Fig. 6) from the original target; the designed airfoil profiles have dramatically different upper surfaces. As Fig. 5 shows, the profile designed for $M_\infty = 0.730$ has a convex (to the flow) corner underneath the shock, while the profile obtained for $M_\infty = 0.770$ has a concave corner at that point. This is consistent with expectations. For the $M_\infty = 0.730$ case, the specified shock is too strong. The opposite is true for the case at $M_\infty = 0.770$. The vertical extent of the supersonic regions in these several cases is of some interest as can be noticed in Fig. 7. The corners for the designs in Fig. 5 are real features of the airfoil solutions and are not due to numerical inaccuracies.

Evidence for the equivalence between the present design procedure and the one described for incompressible flow can be generated by trying to design a profile using as a target speed the distribution obtained by the analysis at a low Mach number of a known profile, which we will call q_1 , multiplied by some arbitrary factor, p . Since q_1 automatically satisfies Eq. (19), (pq_1) cannot satisfy the constraints. Straightforward application of Eq. (19) suggests that, for a contour to exist, either q_∞ must be scaled by the same factor, or p must be scaled back to one. The numerical procedure described in this paper accomplishes this same result as shown in Fig. 8. The Korn airfoil was analyzed at $M_\infty = 0.100$, $\alpha = 1.7^\circ$ and the resulting speed distribution was scaled to provide a target. The scaling factor was assigned a value in the range of $0.2 < q_\infty < 2$. As was expected, using the above-mentioned Scheme 1, the multiplier was scaled back to one in each case. As can be seen in Fig. 8 the scaling is accomplished almost entirely within the first design cycle -- before any airfoil updates. Also, as expected, the resulting profile was the Korn airfoil.

These examples demonstrate the robustness and self-consistency of the numerical scheme. The remaining examples illustrate the use of the various schemes for satisfying the constraints in the design of airfoils. Rarely, if ever, pressure distributions with shocks in the flow field are prescribed. At supercritical speeds, "shockless" airfoils are usually the goal. A reasonable target might be the distribution depicted by the symbols in Fig. 9. The free-stream Mach number in this case is 0.800, and, again, the exercise is to design a closed airfoil using scheme 1 to make any necessary changes in the target distribution. The modified target speed distribution is given by the solid line in Fig. 9.

The shift in the location of the stagnation point should be noticed in this figure. The shift is achieved smoothly and makes it possible to close the x-gap in the airfoil. The designed airfoil is depicted in Fig. 10 along with the computed pressure distribution. This pressure distribution is the result of a direct solution of the flow field over the designed airfoil contour, and it agrees to three decimal places with the pressure distribution that corresponds to the target speed distribution (the solid line in Fig. 9). This airfoil solution is obtained regardless of the airfoil contour initially prescribed to start the iteration procedure. In Fig. 11 the designed airfoil contour is compared with four different starting shapes: the Korn airfoil, the NACA 0012, the NACA 0002, and, finally, a "needle" -- two straight lines joined at the trailing edge and at the leading edge tangent to a semicircle of radius equal to 0.25% of the chord.

It is satisfying to note that the values of p_1 , p_2 , and p_3 are identical regardless of the starting shape (i.e., the modified target speed distribution is the same in all cases). Apparently, by decoupling the three parameters, we have ensured that only a single set of values exists that satisfies the three constraints. It is possible that, if the three parameters had been coupled, more than one set of values might exist that would satisfy the constraints. Even though we have no formal proof of this, decoupling appears to guarantee a unique solution as well as making the search simpler and faster. The convergence rate of the method for the various "starter" profiles is given in Fig. 12, which depicts the maximum value of $|v/u|$ as a function of design cycles. Again, after 10-12 cycles it is difficult to distinguish any changes in the airfoil shape. Typically, we run the code to a level where the maximum $|v/u|$ is 0.001 or smaller. A converged solution generally requires 4-5 min. on a Cray-1M computer and about 20 min. on the IBM 308; machine.

The pressure distribution depicted in Fig. 10 appears to have very desirable features; in particular, the "plateau" region on the upper surface suggests the absence of a shock. However, a very large drag ($C_D = 0.0232$) is present even at the design point. If we look at the Mach number contours in Fig. 13, we see that, while there is no shock at the airfoil surface itself, a very strong shock is present off the surface. The contours represent increments of 0.01 in Mach number, and only contours for values greater than the free stream are shown. At off-design conditions, the shock reaches the surface. Several authors have observed this feature. A smooth recompression along the surface does not necessarily mean that the flow field is shockless. Thus, the airfoil shown in Fig. 10 is impractical because of its high drag.

A truly shockless closed airfoil is depicted in Fig. 14, along with the computed pressure distribution (i.e., modified target) and the original, unmodified target. Note the low computed drag ($C_D = 0.0005$) of this airfoil. The computed isomach pattern in Fig. 15 shows that the flow over this airfoil is truly shock free, and at off-design points only a weak shock develops. This case was computed using scheme 2 described above. It should also be noted that in this case the modifications made to the ideal target pressure distribution are considerably larger than those that resulted in the previous case. The changes on the lower surface reflect mostly the effect of f_2 , as given by Eq. (29). An example of an airfoil designed using scheme 3 is shown in Fig. 16. Note, in this case again, the very low value for the drag and the considerable lift coefficient. The modifications to the ideal target that should be noticed apart from the scaling are concentrated near the trailing edge.

A very interesting profile designed to an unusual pressure distribution is depicted in Fig. 17. The

airfoil was designed for laminar flow (remember that the present method is purely inviscid) to a distribution devised by Pfenninger¹¹ for $M_\infty = 0.766$. It is only one of a series of airfoils designed for such purposes. The scheme used was scheme 1. Since the ideal pressure distribution was based on the considerable personal experience of its designer, minor modifications were needed to generate the airfoil solution. The computed Mach number contours are depicted in Fig. 18. Notice the shallowness of the supersonic region as compared to its length. This airfoil exhibits very low drag for a considerable range of flow conditions around its design point.

As mentioned earlier, the method will generate airfoil contours of arbitrary trailing edge thickness. The contour shown in Fig. 19 has a trailing edge thickness equal to 2% of its chord. Like the previous example, this represents an interesting design that, in addition to front loading, has a long and shallow supersonic flow region. A final set of examples depicts airfoils designed at a moderate free-stream Mach number ($M_\infty = 0.675$). All were designed to have a trailing edge thickness equal to 1% of the chord. The two examples shown in Fig. 20 and 21 were designed to original target pressure distributions that differed only in the leading edge region. The resulting airfoils both have a substantial thickness -- maximum values are 12.5% and 13.7% of the chord, respectively. The contour in Fig. 22 is not as thick (11% of chord), but it generates considerably more lift. The very shallow supersonic region present on this profile at its design point is of interest in Fig. 23.

9. CONCLUSIONS

An inverse method for the design of airfoils for supercritical applications has been described in this paper. The problem imposes constraints on the speed distribution to which the airfoil is to be designed. An effort has been made to illustrate the most elusive of the constraints -- the one relating the target surface speed to the free-stream speed -- and to interpret it within the context of the numerical scheme presented. All the constraints on the speed are accounted for in our formulation. The method is, therefore, well posed both theoretically and numerically. It is also quite general in the sense that the ideal specified speed distribution, represented by $f_0(s)$, is general, and an airfoil solution will always be found by modifying the target speed in order to satisfy the constraints. Also, the initial airfoil contour needed to start the procedure need not be close to the final contour to achieve convergence.

The particular forms proposed for f_1 , f_2 , and f_3 are by no means exhaustive or even necessarily best. They do, however, provide the freedom needed to satisfy the constraints automatically, without user intervention, and to introduce only a loose coupling among their respective multipliers -- making their evaluation simpler and computationally cost-effective. Other forms for f_2 and f_3 are, of course, possible, although the search for p_1 , p_2 , and p_3 might be more difficult. Most alternative formulations for introducing free parameters will probably require a multidimensional search for the parameters. Techniques exist, however, for optimizing this search. Also, following the approaches of Arlinger, Strand, and Polito, it would be possible to develop formulations that would keep changes to a minimum. Additional free parameters could conceivably be introduced to prevent crossovers of the upper and lower surfaces of the airfoil, a possibility not ruled out by the present formulation. In its present form, however, the approach presented is a reliable and efficient method for the design of airfoil profiles of given trailing edge thicknesses at transonic speeds.

REFERENCES

1. Mangler, W., "Die Berechnung eines Tragflügelprofils mit Vorgeschiebener Druckverteilung," Jahrbuch 1938 Deutsche Luftfahrtforschung.
2. Lighthill, M.J., "A New Method of Two-Dimensional Aerodynamic Design," R&M 2112, Aeronautical Research Council, London, England, 1945.
3. Woods, L.C., "Airfoil Design in Two-Dimensional Subsonic Compressible Flow," R&M 2845, Aeronautical Research Council, London, England, March 1952.
4. Van Ingen, J.L., "A Program for Airfoil Section Design Utilizing Computer Graphics," Agard Short Course Notes, 1969.
5. Arlinger, B., "An Exact Method of Two-Dimensional Airfoil Design," TN67, Saab, Sweden, 1970.
6. Strand, T., "Exact Method of Designing Airfoils with Given Velocity Distribution in Incompressible Flow," *J. Aircraft*, Vol. 10, 1973, pp. 651-659.
7. Polito, L., "Un Metodo Esatto per il Progetto di Profili Alari in Corrente Incompressibile Avanti un Prestabilito Andamento della Velocità sul Contorno," Università degli Studi di Pisa, Pisa, Italy, Rept. 42, 1974.
8. Hicks, R.M., Vanderplaats, G.N., Murman, E.M., and King, R.R., "Airfoil Section Drag Reduction at Transonic Speeds by Numerical Optimization," NASA TMX-73097, Feb. 1976.
9. Davis, W.M., "Technique for Developing Design Tools from the Analysis Methods of Computational Aerodynamics," AIAA Paper 79-1529, 1979.
10. McFadden, G.N., "An Artificial Viscosity Method for the Design of Supercritical Airfoils," Research and Development Report C00-3077-158, Courant Inst Math Sci, New York University, July 1979.
11. Tranen, T.L., "A Rapid Computer Aided Transonic Airfoil Design Method," AIAA Paper 74-501, 1974.
12. Carlson, L.A., "Transonic Airfoil Analysis and Design Using Cartesian Coordinates," *J. Aircraft*, Vol. 13, 1976, pp. 369-356.

13. Sobieczky, M., Fung, K.Y., and Seebass, A.R., "A New Method for Designing Shock-free Transonic Configurations," AIAA Paper 78-1114, 1978.
14. Bauer, F., Garabedian, P., and Korn, D., "Supercritical Wing Sections," Springer Verlag, 1972.
15. Boerstel, J.W., and Muizing, G.H., "Transonic Shock-Free Airfoil Design by an Analytic Hodograph Method," AIAA Paper 74-439, 1974.
16. Volpe, G., and Melnik, R.E., "The Role of Constraints in the Inverse Design Problem for Transonic Airfoils," AIAA Paper 81-1233, 1981.
17. Ludford, G.S., "The Behavior at Infinity of the Potential Function of a Two-Dimensional Subsonic Compressible Flow," J. of Mathematical Physics, Vol. 30, 1951, pp. 117-130.
18. Jameson, A., "Acceleration of Transonic Potential Flow Calculations on Arbitrary Meshes by the Multiple Grid Method," AIAA Paper 79-1458, 1979.
19. Thwaites, B., "Incompressible Aerodynamics," Oxford University Press, 1960.
20. Volpe, G., "The Inverse Design of Closed Airfoils in Transonic Flow," AIAA Paper 83-504, 1983.
21. Pfenniger, W., Viken, J.K., Vemuru, C.S., and Volpe, G., "All Laminar SC LFC Airfoils with Natural Laminar Flow in the Region of the Main Wing Structure," AIAA Paper 86-2625, 1986.

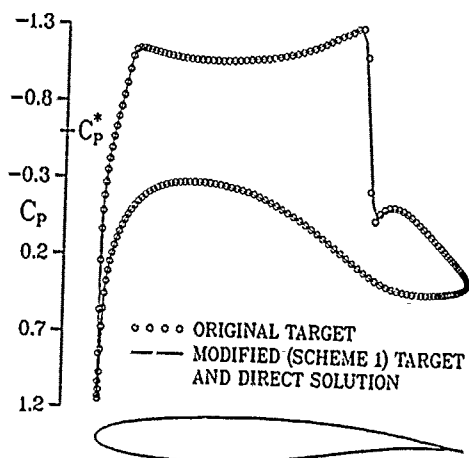


Fig. 1 Target pressure distribution (computed on Korn airfoil at 0.5°); redesigned Korn airfoil and direct solution: $M_\infty = 0.750$, $\alpha = 0^\circ$, $C_L = 0.8334$, $C_D = 0.0063$

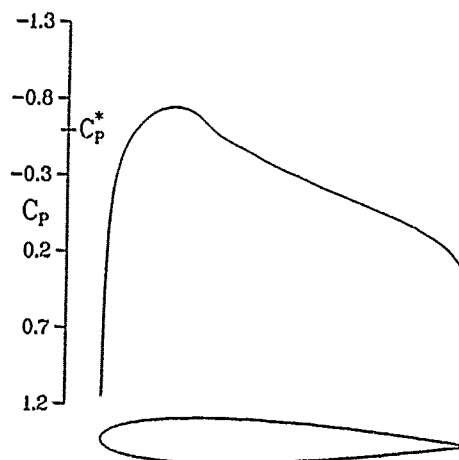


Fig. 2 Starter airfoil contour (NACA 0012) and computed pressure distribution: $M_\infty = 0.750$, $\alpha = 0^\circ$, $C_L = 0.0$, $C_D = 0.0001$

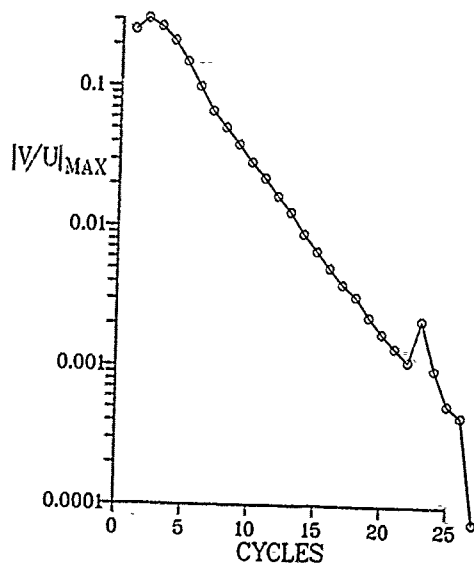


Fig. 3 Convergence history of maximum velocity ratio; Korn airfoil redesign; $M_\infty = 0.750$, $\alpha = 0^\circ$

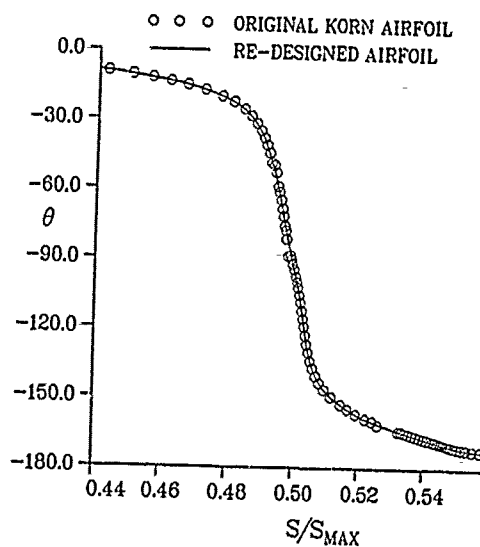


Fig. 4 Computed and actual slope distribution for Korn airfoil design in leading edge region

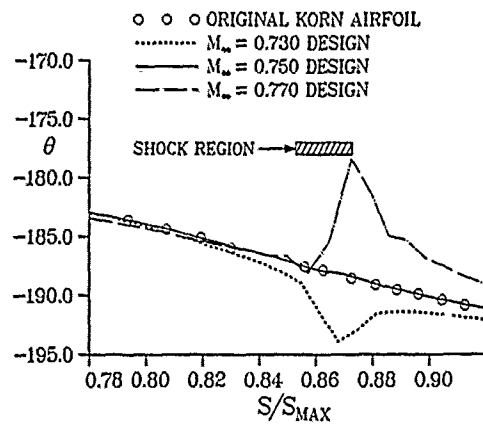


Fig. 5 Slope distribution in shock wave region for Korn airfoil, and for airfoils designed to Korn pressure distribution in Fig. 1 at various free-stream mach numbers

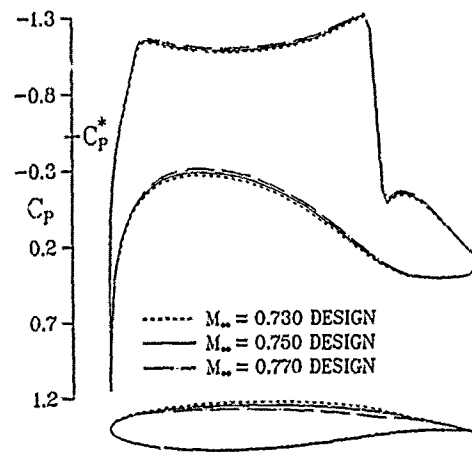


Fig. 6 Direct solutions (modified target distributions) for airfoils designed to Korn pressure distribution from Fig. 1; $\alpha = 0^\circ$;
 $M_\infty = 0.770$: $C_L = 0.8359$, $C_D = 0.0026$
 $M_\infty = 0.750$: $C_L = 0.8334$, $C_D = 0.0063$
 $M_\infty = 0.770$: $C_L = 0.8316$, $C_D = 0.0167$

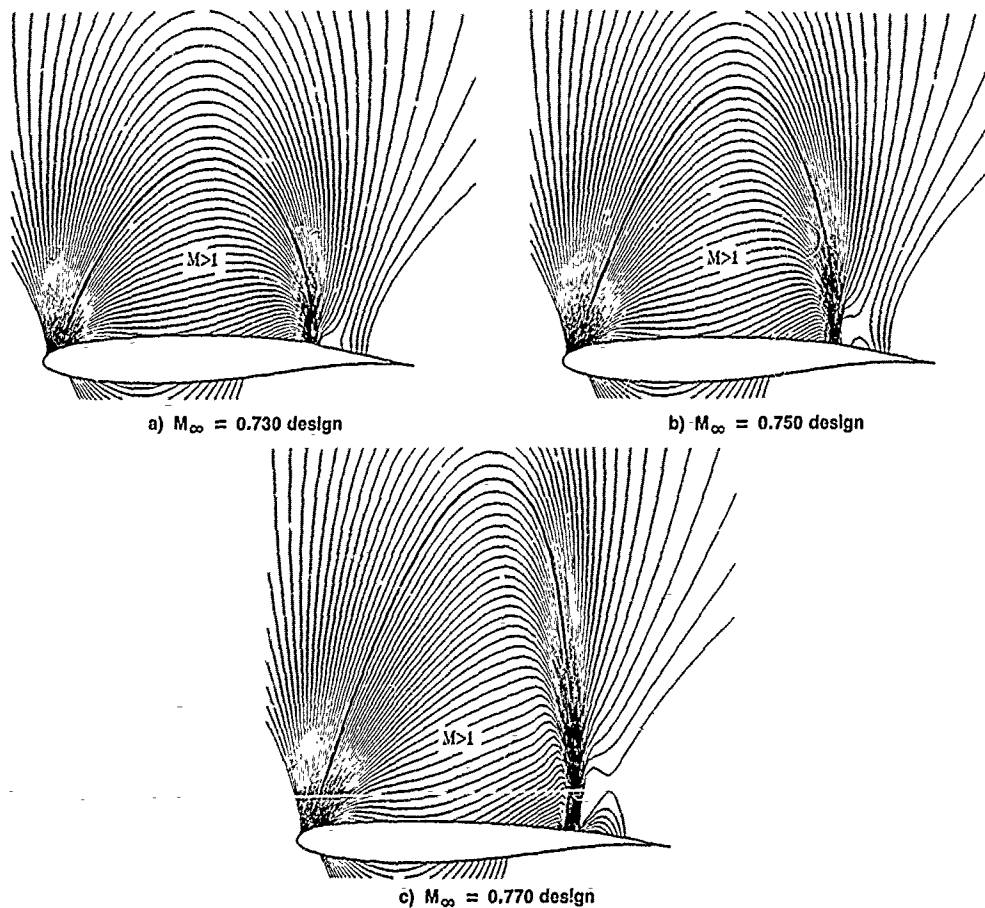


Fig. 7 Design point isomachs for airfoils designed to Korn pressure distributions from Fig. 6; $\alpha = 0^\circ$; contours shown at 0.01 intervals

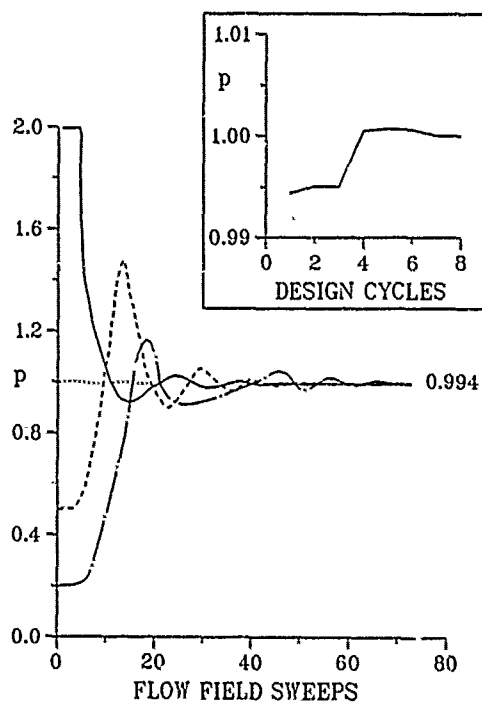


Fig. 8 Convergence history of scale factor for Korn airfoil design; $M_\infty = 0.100$

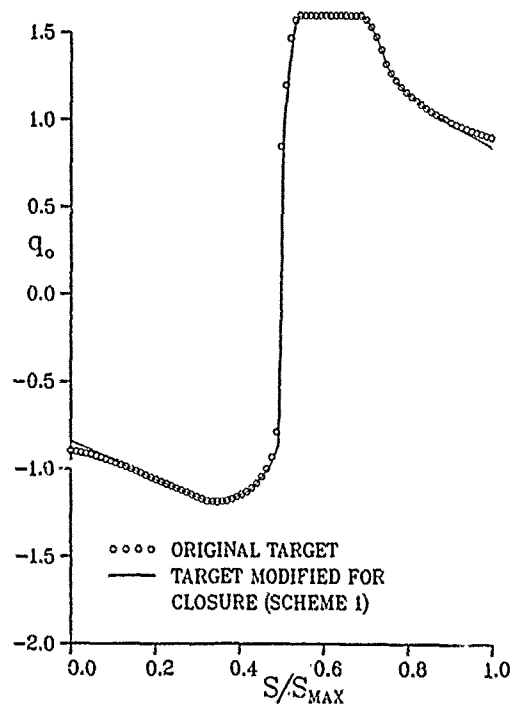


Fig. 9 Original and modified target speed distributions; "shockless" case, $M_\infty = 0.800$, $\alpha = 0^\circ$

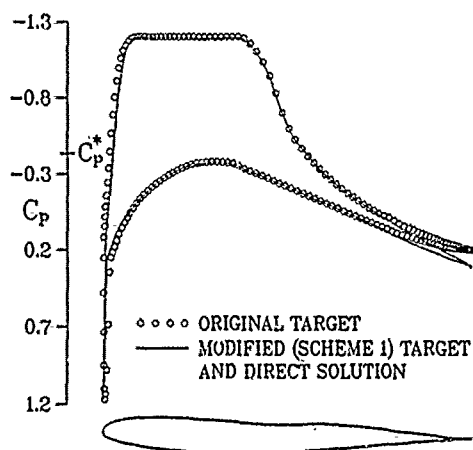


Fig. 10 Designed contour, original target and computed pressure distribution; "shockless" case, $M_\infty = 0.800$, $\alpha = 0^\circ$, $C_L = 0.4801$, $C_D = 0.0232$

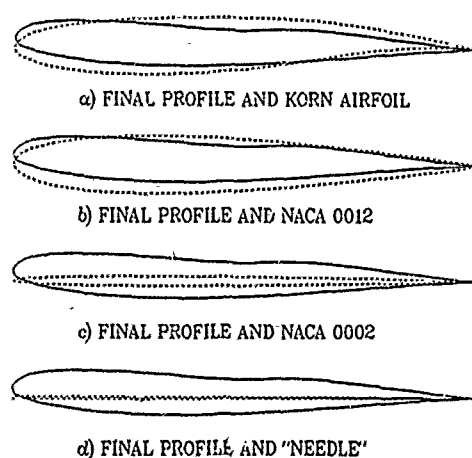


Fig. 11 Final airfoil profile (solid line) compared with starting profiles (dashed line)

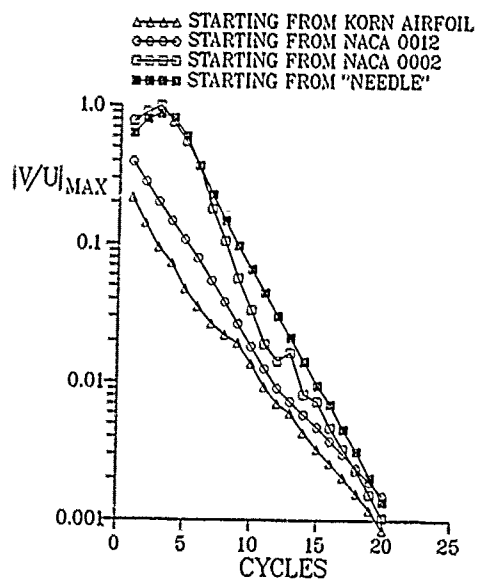


Fig. 12 Convergence history of maximum surface velocity ratio for various starter profiles; "shockless" case, $M_\infty = 0.800$, $\alpha = 0^\circ$

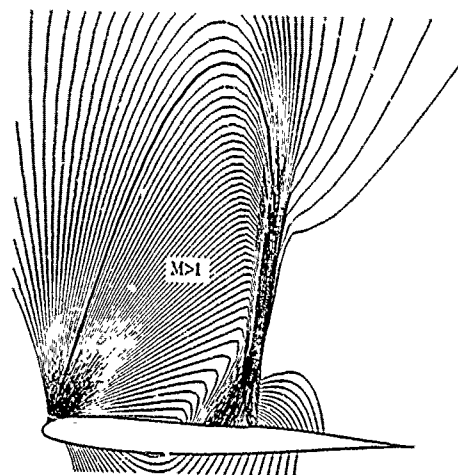


Fig. 13 Design point isomachs; "shockless" case, $M_\infty = 0.800$, $\alpha = 0^\circ$; contours shown at 0.01 intervals beginning with $M = 0.810$

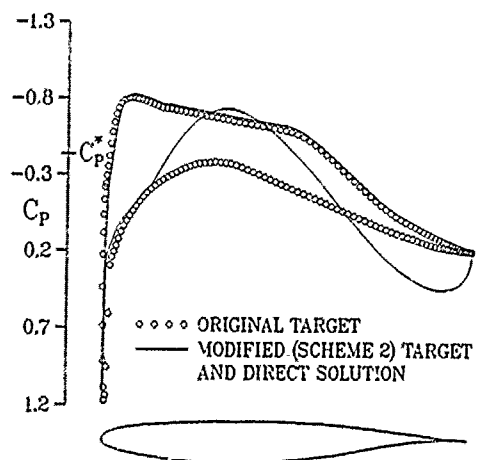


Fig. 14 Designed contour, original target and computed pressure distribution; case 2, $M_\infty = 0.800$, $\alpha = 0^\circ$, $C_L = 0.2673$, $C_D = 0.0005$

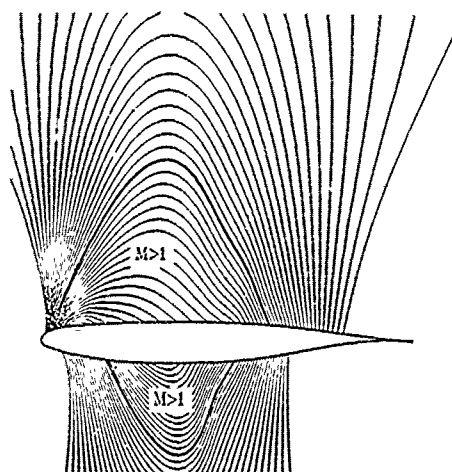


Fig. 15 Design point isomachs; case 2, $M_\infty = 0.800$, $\alpha = 0^\circ$; contours shown at 0.01 intervals beginning with $M = 0.810$

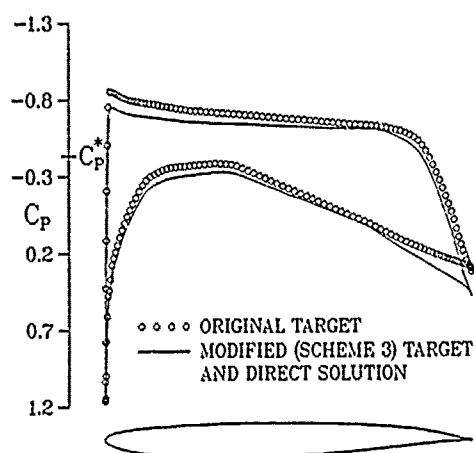


Fig. 15 Designed contour, original target and computed pressure distribution; case 3, $M_\infty = 0.800$, $\alpha = 0^\circ$, $C_L = 0.4972$, $C_D = 0.0002$

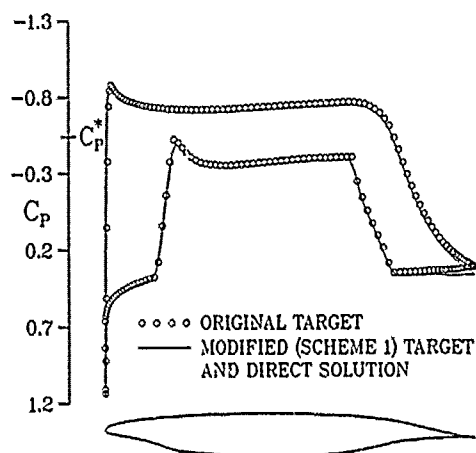


Fig. 17 Designed contour, original target and computed pressure distribution; case LFC1, $M_\infty = 0.766$, $\alpha = 0^\circ$, $C_L = 0.5166$, $C_D = 0.0001$

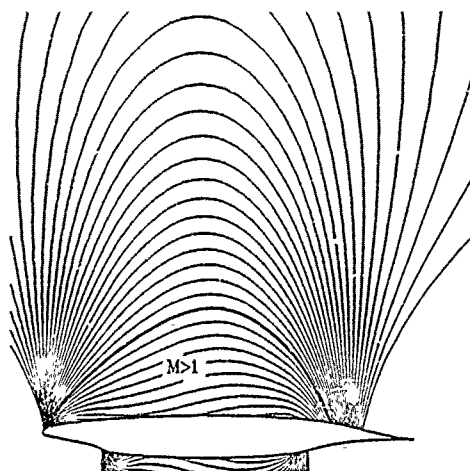


Fig. 18 Design point isomachs; case LFC1, $M_\infty = 0.766$, $\alpha = 0^\circ$; contours shown at 0.01 intervals beginning with $M = 0.770$

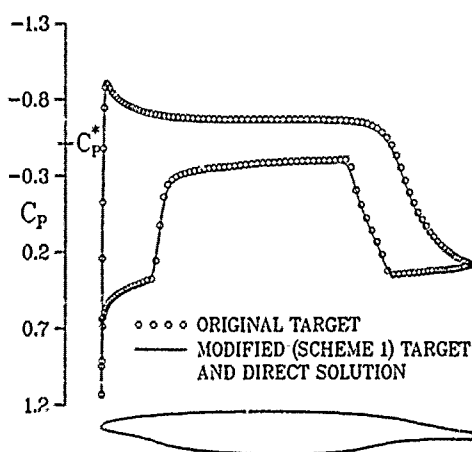


Fig. 19 Designed contour, original target, and computed pressure distribution; case LFC2, 2% trailing edge thickness; $M_\infty = 0.775$, $\alpha = 0^\circ$, $C_L = 0.4805$, $C_D = 0.0001$

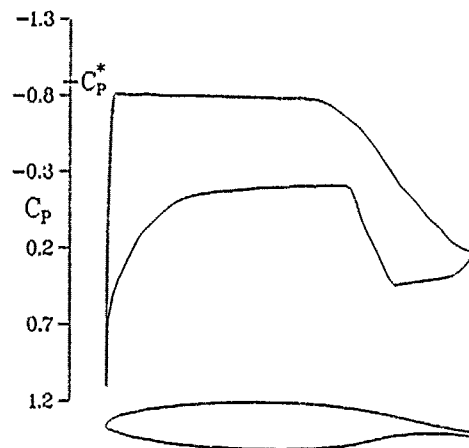


Fig. 20 Designed contour and computed pressure distribution; case AMSS-8, 12.5% maximum thickness, 1% trailing edge thickness; $M_\infty = 0.675$, $\alpha = 0^\circ$, $C_L = 0.6121$, $C_D = 0.0001$

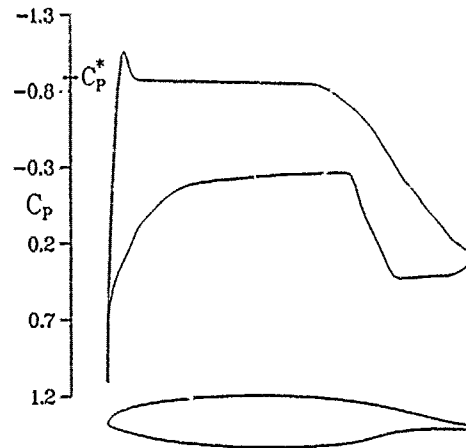


Fig. 21 Designed contour and computed pressure distribution; case AMSS-10, 13.7% maximum thickness, 1% trailing edge thickness; $M_\infty = 0.675$, $\alpha = 0^\circ$, $C_L = 0.6190$, $C_D = 0.0001$

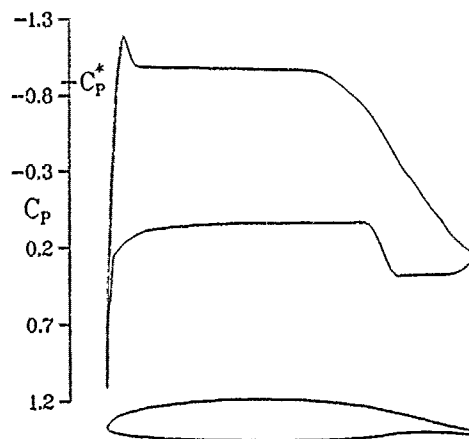


Fig. 22 Designed contour and computed pressure distribution; case AMSS-11, 11.0% maximum thickness, 1% trailing edge thickness; $M_\infty = 0.675$, $\alpha = 0^\circ$, $C_L = 0.8540$, $C_D = 0.0001$

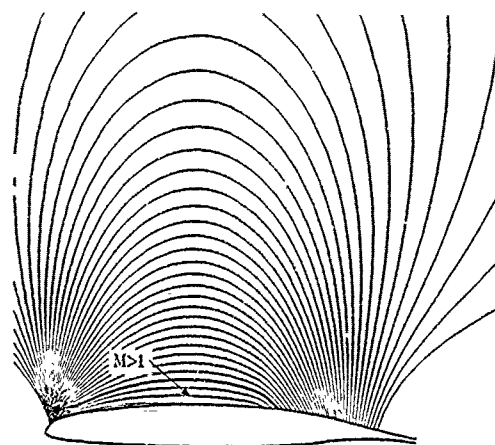


Fig. 23 Design point isomachs; case AMSS-11, $M_\infty = 0.675$, $\alpha = 0^\circ$; contours shown at 0.01 intervals beginning with $M = 0.680$

AN EFFICIENT AIRFOIL DESIGN METHOD USING THE NAVIER-STOKES EQUATIONS

by

J.B. Malone and J.C. Narramore
Bell Helicopter Textron, Inc.
P.O. Box 482, MS 012681-14
Fort Worth, Texas 76101
U.S.A.

and

L.N. Sankar
School of Aerospace Engineering
Georgia Institute of Technology
Atlanta, Georgia 30332
U.S.A.

SUMMARY

An airfoil design procedure is described that has been incorporated into an existing 2-D Navier-Stokes airfoil analysis method. The resulting design method, an iterative procedure based on a residual-correction algorithm, permits the automated design of airfoil sections with prescribed surface pressure distributions. This paper describes the inverse design method and the technique used to specify target pressure distributions. It presents several example problems to demonstrate application of the design procedure. It shows that this inverse design method develops useful airfoil configurations with a reasonable expenditure of computer resources.

NOTATION

a_∞	speed of sound
C_L	airfoil section lift coefficient
C_M	airfoil section moment coefficient
C_p	local pressure coefficient
C_{p_0}	pressure coefficient at location of peak Mach number
$C_{p_{TE}}$	trailing edge pressure coefficient
$C_{p_{t,c}}$	target (t) or computed (c) pressure coefficient
e	total energy per unit volume
H	boundary layer energy form parameter
I	identity matrix
k	thermal conductivity
K	coefficient in generalized recovery distribution equation
M_0	peak Mach number
M_2	Mach number aft of shock wave
M_∞	freestream Mach number
n	coefficient in generalized acceleration region equation
p	surface pressure
P_0	pressure at peak Mach number
P_2	pressure aft of the shock wave
q	heat transfer rate
q_c	computed speed distribution
q_t	target speed distribution
Re	Reynolds number
S	aerodynamic surface ordinate value
S_a	airfoil surface length measured from stagnation point
S_0	location of peak Mach number on airfoil surface
t	time coordinate
T	temperature
TE/c	trailing edge thickness-to-chord ratio
u	instantaneous x component of velocity
v	instantaneous y component of velocity
x, y	cartesian coordinates
ϕ	coefficient in generalized recovery distribution equation
Δ	shock strength effective wedge angle
Δ_t	specified time-step factor
γ	ratio of specific heats
ϵ_E	artificial dissipation coefficient, explicit factor
ϵ_I	artificial dissipation coefficient, implicit factor
μ	coefficient of dynamic viscosity
μ_R	roughness parameter for transition criterion
μ_T	turbulent eddy viscosity
ρ	density

τ shear stress
 ξ, η coordinates in transformed plane

1. INTRODUCTION

The aerodynamic design of aircraft components is often carried out by means of one of the following four approaches. a) "cut and-try" analysis, b) indirect methods, c) optimization techniques, and d) inverse design techniques. The cut-and-try approach consists of multiple applications of direct aerodynamic analysis methods. The design engineer specifies a geometry, and then uses the computed flowfield to guide further changes to the geometry definition. This approach to aerodynamic design is time consuming, and usually requires considerable expertise to produce optimum configurations. Unlike the cut-and-try method, the latter three design techniques are far more automated, requiring fewer "engineer-in-the-loop" interactions to achieve specific design goals. These automated design methods can reduce the overall engineering effort and calendar time for developing aircraft components and configurations that have favorable aerodynamic performance or aerodynamic interference characteristics. A variety of different analytical and numerical design algorithms has been developed, and Sloof has summarized a number of the most successful methods in Reference 1.

Automated design methods of the "design-to-pressure" type are normally used to generate aerodynamic geometries that have favorable surface pressure distributions at given freestream conditions. For example, high speed aircraft lifting surface geometries that generate "shock-free" or "weak-shock" flow fields are usually sought in order to minimize wave drag performance penalties. Obviously, the use of these automated design methods requires that the aerodynamicist can specify, a priori, the desired pressure distributions for a particular application.

By far the majority of aerodynamic design procedures are based upon potential-flow Computational Fluid Dynamic (CFD) methods.^{1,2-5} Although it is likely that potential-flow design procedures will continue to be used as the "workhorses" in industry due to their reasonable computer-resource requirements, there is now an increasing interest in developing similar design procedures that use higher-order CFD methods such as the Euler equations⁶⁻⁸ and the Reynolds-averaged Navier-Stokes equations.⁹ If used during the design process, these higher order CFD methods help the aerodynamicist to account for the occurrence of rotational flow effects, vortical flow field structures, and a number of significant viscous effects such as flow separations and strong shock/boundary-layer interactions.

In Reference 10, Garabedian and McFadden described an inverse aerodynamic design procedure based on a residual-correction algorithm. Their design method, which we will refer to here as the GM method, can be used to generate aerodynamic surfaces with prescribed surface pressure distributions. They demonstrated their design method by incorporating it into a 3-D, compressible-flow, full potential equation (FPE) aerodynamic analysis code.

In Reference 11, Malone et al presented a modified Garabedian McFadden(MGM) residual-correction design algorithm that removed some limitations of the original GM technique. These authors applied the new MGM design method, also using FPE aerodynamic analysis codes as a basis, to airfoil, axisymmetric nacelle inlet, and 3-D nacelle inlet design problems. Most recently, Hazarika and Sankar¹² used an FPE CFD method to apply the MGM procedure to the design of blended wing-body configurations.

This paper describes the first use of the MGM residual-correction design algorithm coupled with a 2-D Navier-Stokes solution procedure. It describes the 2-D Navier-Stokes computational procedure, the MGM design algorithm, the implementation of the design procedure, and the technique used to define target pressure distributions, and also presents the results of several sample design problems.

2. NAVIER-STOKES SOLUTION PROCEDURE

2.1 Mathematical Formulation

The two-dimensional Navier-Stokes procedure used in the present work was originally developed by Sankar and Tang,¹³ and later extended by Huff and Sankar.¹⁴ Their method solves the Reynolds-averaged form of the full Navier-Stokes equations, which are given below for a cartesian coordinate system.

$$Q_t + F_x + G_y = R_x + S_y \quad (1)$$

where

$$Q = [p, \rho u, \rho v, e]^T \quad (2a)$$

$$F = [\rho u, \rho u^2 + p, \rho uv, u(e+p)]^T \quad (2b)$$

$$G = [\rho v, \rho uv, \rho v^2 + p, v(e+p)]^T \quad (2c)$$

$$R = [0, \tau_{xx}, \tau_{xy}, u\tau_{xx} + v\tau_{xy} - q_x]^T \quad (2d)$$

$$S = [0, \tau_{xy}, \tau_{yy}, u\tau_{xy} + v\tau_{yy} - q_y]^T \quad (2e)$$

$$\tau_{xx} = 2/3 \mu (2u_x - v_y) \quad (2f)$$

$$\tau_{yy} = 2/3 \mu (2 v_y - u_x) \quad (2g)$$

$$\tau_{xy} = \mu (u_y + v_x) \quad (2h)$$

$$q_x = -k T_x \quad (2i)$$

$$q_y = -k T_y \quad (2j)$$

$$p = (\gamma - 1) [\epsilon - .5 \rho (u^2 + v^2)] \quad (2k)$$

In Equations 1 and 2, $[Q]$ is the vector of conserved flow variables. The vectors $[F]$ and $[G]$ are the inviscid flux vectors in the x and y coordinate directions, respectively. Also, the vectors $[R]$ and $[S]$ are the viscous flux terms in the corresponding cartesian coordinate directions.

Equations 1 and 2 are solved in a generalized, body-fitted coordinate system, after the equations are first non-dimensionalized in a manner consistent with that of Reference 15. That is, the time coordinate is scaled by l/a_∞ , where l is an arbitrary reference length (here taken as $l = 1$). The coordinate dimensions are likewise scaled by l . The fluid density is scaled by ρ_∞ , while the cartesian velocity components are each scaled by a_∞ . The energy and the fluid pressure are both scaled by the term, $\rho_\infty a_\infty^2$. Finally, the viscosity, μ , is scaled by its freestream value, μ_∞ .

Then, after the appropriate coordinate transformations have been performed, Equation 1 can be rewritten in a strong-conservation form as follows:

$$Q_t + F_\xi + G_\eta = M_\infty Re^{-1} (R_\xi + S_\eta) \quad (3)$$

where the vectors, Q , F , G , R , and S are transformed quantities, given by:

$$Q = Q/J \quad (4a)$$

$$F = (\xi_t Q + \xi_x F + \xi_y G)/J \quad (4b)$$

$$G = (\eta_t Q + \eta_x F + \eta_y G)/J \quad (4c)$$

$$R = (\xi_t Q + \xi_x R + \xi_y S)/J \quad (4d)$$

$$S = (\eta_t Q + \eta_x R + \eta_y S)/J \quad (4e)$$

$$\xi = \xi(x, y, t) \quad (4f)$$

$$\eta = \eta(x, y, t) \quad (4g)$$

and the Jacobian, J , is given by

$$J = \xi_x \eta_y - \eta_x \xi_y \quad (4h)$$

2.2 Numerical Solution Procedure

The techniques used to solve Equation 3 are given in References 13 through 15, and readers interested in specific details should refer to those publications. Here we present only a brief description of the Navier-Stokes solution procedure

The Navier-Stokes system of equations given by Equation 3 is solved on a structured mesh by means of a finite-difference technique. The system of equations is integrated in time with the implicit Beam-Warming¹⁶ ADI algorithm. Second-order finite-difference expressions are used for spatial derivatives, while first-order differences are used for temporal terms. A combination of second- and fourth-order artificial dissipation is added for numerical stability. Then, if we let $()^n$ represent a quantity evaluated at the n th time level, the resulting factored equation can be expressed as follows:

$$[I + \Delta t (\delta_\xi A - \epsilon_1 J^{-1} \delta_{\xi\xi} J)] [I + \Delta t (\delta_\eta B - \epsilon_1 J^{-1} \delta_{\eta\eta} J)] \Delta Q^{n+1} = R_n \quad (5a)$$

where

$$R_n = [- (\delta_\xi F^n + \delta_\eta G^n) + \delta_\xi R^n + \delta_\eta S^n + D^n] \Delta t \quad (5b)$$

$$D^n = \epsilon_2 J^{-1} [\delta_{\xi\xi\xi} (QJ) + \delta_{\eta\eta\eta} (QJ)] \Delta \xi^4 \Delta \eta^4 \quad (5c)$$

$$A = \partial F / \partial Q \quad (5d)$$

$$B = \partial G / \partial Q \quad (5e)$$

$$\Delta Q^{n+1} = Q^{n+1} - Q^n \quad (5f)$$

The Navier-Stokes code¹³ that was developed to solve Equations 5 can be used as a time-accurate procedure, or as a variable time-stepping algorithm to speed calculations where a steady-state solution exists. For time-accurate calculations, the value of Δt is held constant throughout the computational mesh. For computations that are not time-accurate, the value of Δt is set proportional to a spatially variable quantity, Δt_v , where

$$\Delta t_v = \Delta t_f (1.0 + (\text{abs}(J))^5)^{-1} \quad (6)$$

Finally, some observations are made about the manner in which several of the terms are modeled in the present solution procedure. The artificial dissipation terms used on the implicit side of Equation 5a are second order so that the tridiagonal ADI formulation will remain unchanged. The explicit dissipation shown in Equation 5c is a blended combination of second- and fourth-order terms. The contribution of each of these terms throughout the computational mesh is controlled by a pressure-gradient switching function devised by Jameson and described in Reference 15. And, as indicated in Equation 5b, the procedure models the viscous stress terms in an explicit manner by keeping these terms on the right hand side of the equation. This explicit treatment of the viscous terms reduces the computational effort required and normally provides stable calculations for moderate- to high-Reynolds-number flows.¹³

2.3 Turbulence Modeling

For the present work, the Baldwin-Lomax¹⁷ algebraic eddy viscosity model was used to simulate turbulent flowfield effects. In this model, the eddy viscosity, μ_T , replaces the dynamic viscosity, μ , given in Equations 2f through 2h. Values of μ_T are then computed throughout the mesh with a two-layer formulation. This formulation is related to the Cebeci-Smith turbulence model, but does not require an accurate determination of the boundary-layer edge location. A complete description of the turbulence model formulation is given in the cited reference.

2.4 Computational Grid

The computational grid used in the present application is a C-Grid topology. The grid is generated algebraically with the sheared-parabolic technique of Jameson.¹³ An example of this type of computational mesh is shown in Figure 1. For the present design applications, this type of algebraic grid generation procedure is desirable because it is extremely fast and computationally efficient.

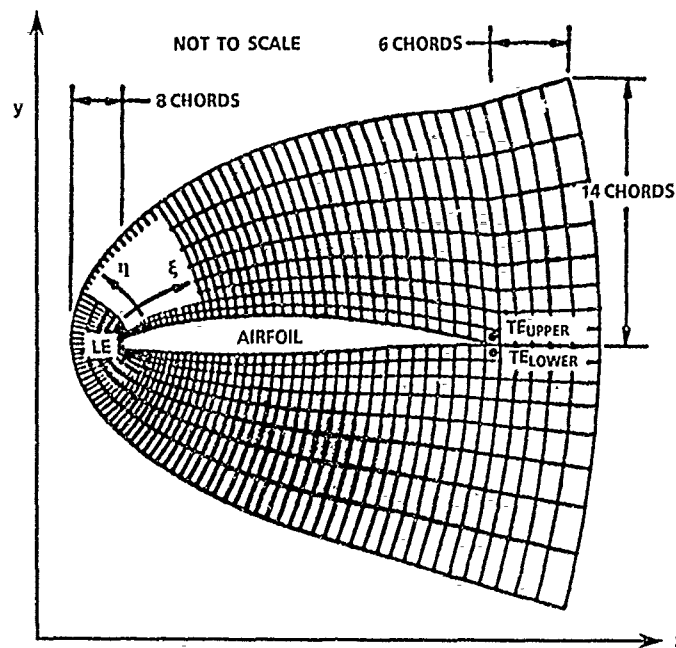


Figure 1. Sheared Parabolic Grid

2.5 Boundary Conditions

The present solution procedure treats the boundary conditions in an explicit manner, assigning them values at each iteration after the flow variables have been updated in the interior of the computational domain. Then the boundary conditions applied at the outer edges of the computational domain are divided into three different regions: the airfoil surface, the wake, and the freestream boundary.

At the airfoil surface, the velocity components are set to zero for viscous flow calculations. In addition, the density and pressure are extrapolated from values at interior mesh points. The extrapolation for pressure is obtained from a second-order expression through the use of a $\partial p / \partial n = 0$ criterion. Then the energy values at the airfoil surface are computed with the updated surface values of velocity, density, and pressure. Along the wake cut, values of density, velocity, and energy are averaged across the cut by the use of values just above and below the boundary points. And finally, at the outer boundary, freestream conditions are assumed, so that Δq_{n+1} is taken as zero along this boundary.

3. MGM DESIGN PROCEDURE

The MGM design method can be classified as a residual-correction technique, in which the residuals are the difference between the desired pressure or speed distribution and the computed distribution. Over the past decade a number of residual-correction methods have been developed, such as the "wavy-wall" approach of Davis.¹⁸ The methods differ primarily in the manner in which changes in residual are related to changes in surface shape. The MGM algorithm itself consists of an auxiliary PDE that is solved for incremental changes in surface coordinates during each design cycle. The final aerodynamic shape is approached in a stepwise fashion through a cyclical iteration between the flow solver and the MGM algorithm.

3.1 Mathematical Formulation

For two-dimensional configurations, the MGM auxiliary equation is given by

$$F_0 S_t + F_1 S_{xt} + F_2 S_{xxt} = Q^2 + F_3 Q_x^2 \quad (7)$$

where the coefficients F_0 , F_1 , F_2 , and F_3 are constants chosen to produce a stable iterative process, and $Q^2 = \text{residual} = q_t^2 - q_c^2$. As q_c approaches q_t , the right-hand side of Equation 7 vanishes, and the aerodynamic surface stops varying with time, t .

Figure 2 shows how the MGM algorithm is typically incorporated into existing flow solution procedures. The computed surface velocities are normally obtained from partially converged numerical solutions to the flow equations under consideration at a given value of time, t . The flow equations may be solved in either a time-accurate or variable time-stepping manner. Note that the time coordinate in Equation 7 is not equivalent to the time coordinate in the flow solver, but rather is a pseudo-time coordinate used to interpret the PDE as an expression relating a change in coordinate value, S , to a change in the residual, Q , as follows:

$$S_t = \Delta S / \Delta t = \Delta S$$

where we have chosen $\Delta t = 1$. Equation 7 can then be written as:

$$F_0 \Delta S + F_1 (\Delta S)_x + F_2 (\Delta S)_{xx} = Q^2 + F_3 Q_x^2 \quad (8)$$

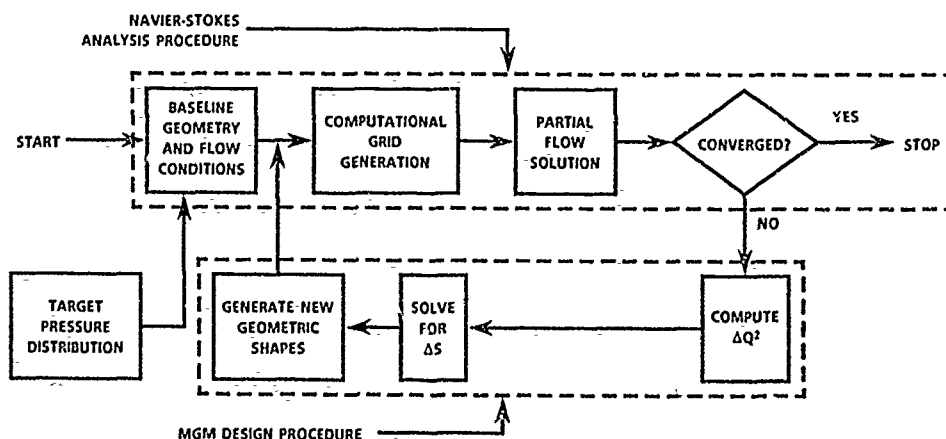
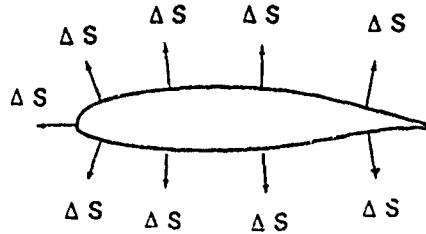


Figure 2. Implementation of the MGM 2-D Inverse Design Algorithm

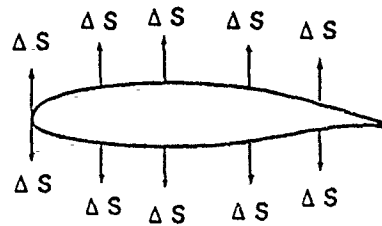
The present inverse design procedure is formulated in a manner similar to that of the original GM scheme, but with several important differences. In the MGM method, the auxiliary equation is solved directly in the physical domain, rather than in the computational domain, as was done in Reference 10. Additionally, whereas the GM method was recommended for use only on a portion of the airfoil surface, excluding the leading and trailing edges, and then only with an increase in the airfoil thickness away from some thinner starting configuration, the MGM design algorithm was

developed as an airfoil design method through which arbitrary changes to the complete airfoil geometry could be generated, including situations where modifications to the leading-edge shape are required. This capability helps to eliminate the need for a starting configuration that is close in shape to the final designed airfoil shape.

A further difference is shown in Figure 3, where the surface perturbations generated with the MGM procedure are interpreted as changes in the coordinate direction perpendicular (y direction) to the longitudinal axis of the geometry (x direction). This choice for the movement of the surface coordinates (which differs from the original GM method) leads to smoother leading-edge geometry and eliminates chordwise stretching of the airfoil.



a. Original Garabedian-McFadden Method



b. Modified Garabedian-McFadden Method

Figure 3. Schematic of Geometry Perturbations for Original and Modified (MGM) Design Algorithms

3.2 Numerical Solution Procedure

We solve the auxiliary PDE by writing finite difference expressions for each term of Equation 8. The computational grid used to solve this equation is the same grid used for the fluid-dynamic equations, which, for the present Navier-Stokes solver, is an algebraically generated C-grid topology (Figure 1). Of course, Equation 8 is solved only along the airfoil surface, so that only the grid-line clustering in the x or streamwise direction is of importance.

Then, under the assumption that there are a total of N computational points on the airfoil surface, Equation 8 is written for each of these points, i, where $1 < i < N$. A typical equation evaluated at the ith point on the surface is

$$A_i \Delta Y_{i+1} + B_i \Delta Y_i + C_i \Delta Y_{i-1} = R_i \quad (9)$$

Here the coefficients A_i , B_i , and C_i are evaluated by means of standard finite difference expressions, and ΔY_i is the incremental change in surface coordinate, ΔS , at the ith computational point. The use of the Y coordinate here results from the direction chosen for incrementing the airfoil surface. First-order, accurate, spatially upwind derivatives are used to discretize the $(\Delta Y)_x$ terms, while second-order accurate expressions are used to model the $(\Delta Y)_{xx}$ terms.

For points on the airfoil upper surface, the following expressions are obtained:

$$A_i = -2F_2/((x_{i+1} - x_i)(x_{i+1} - x_{i-1})) \quad (10a)$$

$$B_i = F_0 + F_1/(x_i - x_{i-1}) + 2F_2/((x_{i+1} - x_i)(x_i - x_{i-1})) \quad (10b)$$

$$C_i = -F_1/(x_i - x_{i-1}) - 2F_2/((x_i - x_{i-1})(x_{i+1} - x_i)) \quad (10c)$$

$$R_i = Q_i^2 + F_3(Q_i - Q_{i-1}) \quad (10d)$$

For points on the airfoil lower surface, similar expressions are derived:

$$A_i = -F_1/(x_i - x_{i+1}) - 2F_2/((x_{i+1} - x_i)(x_{i+1} - x_{i-1})) \quad (11a)$$

$$B_i = F_0 + F_1/(x_i - x_{i+1}) + 2F_2/((x_{i+1} - x_i)(x_i - x_{i-1})) \quad (11b)$$

$$C_i = -2F_2/((x_i - x_{i-1})(x_{i+1} - x_{i-1})) \quad (11c)$$

$$R_i = -Q_i^2 + F_3(Q_i - Q_{i+1}) \quad (11d)$$

Since Equations 10 and 11 are written in physical coordinates, the finite difference expressions are normally derived for non-uniform grid-point distributions in the x , or streamwise, direction. Hence the difference terms in the denominators are not usually equal to each other. This formulation will be referred to here as "Design Option No. 1."

During the derivation of Equations 10 and 11, the change in sign between slope and curvature is accounted for so that the coefficients F_0 , F_1 , and F_2 are assumed to be positive constants. That is, during consideration of the appropriate proportionality to take between the slope and the source term, $F_1(\Delta S)_x \approx Q$, F_1 should be positive (locally) if $(\Delta S)_x$ and Q are positive. However, for the curvature term, $(\Delta S)_{xx}$, for the case where the airfoil upper surface has a positive value of the source term, Q , the airfoil should be thickened locally. This leads to a negative curvature (increase in thickness on the upper surface) and a negative F_2 term, so that the product, $F_2(\Delta S)_{xx}$, will have the same sign as Q . The opposite observation is true for the airfoil lower surface. This change in sign for the curvature term is accounted for in Equations 10 and 11 so that the factor F_2 is also considered a positive number.

Special treatment is used in the evaluation of Equation 9 at the leading edge, where an ambiguity arises as to the direction in which to apply the upwind derivatives, especially for non-zero angle-of-attack conditions. To eliminate this problem, the leading edge point is constrained to move as the average of both the upper and lower surface points located just downstream of the leading edge point. This constraint is treated implicitly by the replacement of the coefficients in Equation 9 with the following expressions

$$A_i \approx -0.5 \quad (12a)$$

$$B_i \approx +1.0 \quad (12b)$$

$$C_i \approx -0.5 \quad (12c)$$

$$R_i \approx 0.0 \quad (12d)$$

Thus, the leading edge is free to translate vertically, allowing for relative angle-of-attack adjustments to occur naturally

Equation 9 is evaluated at each point, i , around the airfoil surface, leading to a system of equations with N unknowns, the ΔY_i values. Note that at each point on the aerodynamic surface, ΔY_i is coupled to values at neighboring points. The resulting equations form a tridiagonal system that is solved for values of ΔY_i by means of the well-known Thomas algorithm.¹⁹

After Equation 9 is solved for a value of ΔY_i , the new surface coordinates are obtained from the relationship

$$Y_i^{\text{new}} = Y_i^{\text{old}} + \Delta Y_i, \text{ for } i = 1 \text{ to } N \quad (13)$$

This completes one design cycle.

4. IMPLEMENTATION OF DESIGN PROCEDURE

The MGM design procedure has been incorporated into the previously described 2-D Navier-Stokes procedure. The resulting computer program is referred to as the MGM2D code. One of the desirable features of the MGM residual-correction algorithm is that relatively few changes to an aerodynamic analysis code can convert it into an analysis/design procedure. In this respect, the MGM algorithm is similar to optimization methods used for aerodynamic design,²⁰ in that the existing aerodynamic analysis method is treated very much like a "black box." Several of the computer program features are discussed in the following paragraphs.

4.1 Trailing-Edge Crossover

The present MGM2D procedure permits the design of complete airfoil surfaces, including the leading-edge and trailing-edge regions. However, some choices of target pressure distributions may lead to trailing-edge crossover, and hence to an unrealistic configuration. Therefore an artifice is used in the MGM2D code so that the trailing edge thickness can be controlled by the program user. If the geometry is driven to a "fish-tail" configuration (trailing-edge crossover), a linear wedge is removed from the airfoil section such that the resulting trailing-edge thickness equals a user determined value. In applying the wedge technique, surface modifications are made equally to both the upper and lower surfaces. These modifications are linearly varying from zero at the leading edge to a maximum of one-half the desired trailing edge thickness at the airfoil trailing edge. If no crossover occurs on the airfoil surface, the designed geometry remains as produced by the MGM algorithm. It has been demonstrated that this technique can give some measure of control over the potential manufacturability of airfoil configurations generated by automated design procedures.²¹

4.2 Calculation of Target Velocity Distributions

Previous FPE applications of the MGM design procedure¹¹ used an expression for q^2 as a function of C_p that is derived from isentropic flow relationships. This expression is

$$q^2 = \{1 - [(C_p(\gamma - 1)/2)M_\infty^2 + 1]^{(\gamma-1)/\gamma} - 1/2M_\infty^2\} \quad (14)$$

Equation 14 is also used in the present Navier-Stokes design method to convert computed and target surface pressure coefficient distributions into equivalent velocity distributions. However, these are non-physical velocity distributions, since the numerical boundary conditions used in the present numerical formulation are actually $u = v = 0$. Nevertheless, the "pseudo-velocity" function given by Equation 14 has proven to be effective in the current applications of the MGM inverse design procedure. That is, the airfoil geometry perturbations computed during each design iteration are in the correct direction to generate either increases or decreases in local velocity as dictated by the source term, Q .

In addition to Equation 14, an alternate function has been used to convert C_p distributions to q^2 distributions. This function is obtained from Equation 2k through the use of the definition of pressure coefficient and the boundary condition $\partial p/\partial n = 0$. The resulting expression is given by

$$q^2 = 2\rho[e - (.5(\gamma - 1)M_\infty^2 C_p + 1)/(\gamma(\gamma - 1))] \quad (15)$$

where the quantities e and ρ are evaluated along the first grid line above the airfoil surface. The velocity distribution given by Equation 15 is then considered to be a physical velocity evaluated just above the surface of the airfoil. Preliminary comparisons of airfoil designs generated with either Equation 14 or Equation 15 show little difference in the convergence rate of the design algorithm. However, this alternate expression is described here for the sake of completeness.

4.3 Alternate Difference Expressions of the Auxilliary Equation

Near the airfoil leading edge, computational grid points are clustered to permit accurate modeling of the rapid changes that occur in flowfield properties in this region. The use of these non-uniform, physical, x -coordinate spacings in the denominators of Equations 10 and 11 therefore leads to large values of the A_i , B_i , and C_i coefficients near the airfoil leading edge. The coefficients in these equations are often of the order of 10^6 or 10^7 , whereas the residual terms, R_i , are of the order of 10^{-1} . Consequently, the solution obtained for Equation 9 tends to produce surface perturbations, ΔY_i , that modify the rearward portion of the airfoil more rapidly than the forward portion, regardless of the local magnitude of the source term, Q_i .

Of course, for many applications this characteristic may be perfectly acceptable. However, to speed convergence of the design procedure for cases that have converged everywhere except in the leading-edge region, an alternate interpretation of Equation 9 is used. In the alternate approach, the auxilliary equation is considered to be solved in the computational domain where the grid spacing is uniform and equal to unity ($\Delta\xi = \Delta\eta = 1$), but the correction to the airfoil surface is still applied normal to the airfoil chordline. With this option, referred to here as "Design Option No. 2," the individual left-hand-side terms of the tridiagonal matrix are of the order of unity. The resulting surface corrections that are computed tend to be maximum wherever the source terms are greatest, including the leading-edge area when the source terms in that region so dictate. Experience to date with the design method indicates that the nonuniform grid spacing option should be used initially, followed by the uniform spacing option to accomplish final surface modifications when required.

4.4 Design Convergence Considerations

As in other iterative inverse design methods or design procedures based on optimization methods, formal convergence criteria are somewhat arbitrary. That is, the design engineer usually decides case by case how close the new airfoil must come to achieving the target pressure goals. Also, as mentioned previously, the target pressures themselves may not always produce a manufacturable airfoil geometry. For these reasons, the design engineer should be able to monitor the progress of the design method while it is generating a new airfoil shape.

The MGM2D code has been structured to facilitate its use as a multistep procedure, allowing the design engineer to monitor the results of each step before proceeding with a subsequent computer submittal. Of primary concern to the engineer are data that measure the "closeness" of the current computed pressures to the targets. Therefore the following computer program output is provided at user-determined intervals:

- a) location and value of the maximum source term, Q
- b) computed and target C_p values corresponding to maximum Q
- c) average Q value around the airfoil surface
- d) average $\Delta C_p = \text{rms}(C_{p_t} - C_{p_c})$ around the airfoil surface

In addition, the distributions of x/c_t , Q_i , ΔY_i , and Y_i , together with values of computed and target C_p 's, are displayed at each computation grid point on the airfoil surface.

The MGM2D user can also control the maximum number of iterations per program execution, the number of ADI iterations between surface geometry updates, and the maximum value of ΔY_i permitted along the airfoil. The importance of the first item mentioned is obvious. The second item allows the user some measure of control over the accuracy of the computed C_p values. Each sequence of ADI iterations defines one design cycle, and the more iterations used per design

cycle, the better will be the approximation of C_p for the current airfoil geometry. The latter item permits the program user to control the speed of the design process by limiting the magnitude of the airfoil surface updates. This control can also be used to limit any possible adverse effects that might arise from the inadvertent use of inappropriately low values of F_0, F_1, F_2 , or F_3 .

5. TARGET PRESSURE SELECTION

One approach to selecting an appropriate target pressure distribution is described in Reference 22. This method is incorporated into a computerized aerodynamic design and analysis system called ADAM. The approach taken in the ADAM transonic airfoil design methodology is to assume generalized equations for the target velocity distribution along the perimeter of the airfoil. Advantages stem from the fact that there exists a series of expressions with a small number of coefficients that may be varied to determine the velocity distribution that will best satisfy the lift, drag, and pitching moment requirements at the design point conditions. These parameters may be systematically varied to produce families of velocity distribution curves from which the best velocity distribution to satisfy the design requirements may be selected. This approach can significantly reduce the effort required to determine the appropriate input to an inverse design code.

5.1 Velocity Distribution Equations

The transonic design method evaluates families of velocity distributions to determine which distribution on the airfoil will best satisfy the performance requirements. On the upper and lower surface of the airfoil, the velocity distribution is divided into an acceleration region with one equation, a deceleration region with a second equation, and a shock pressure jump between them if the flow in the acceleration region becomes sonic. These three regions are indicated schematically in Figure 4.

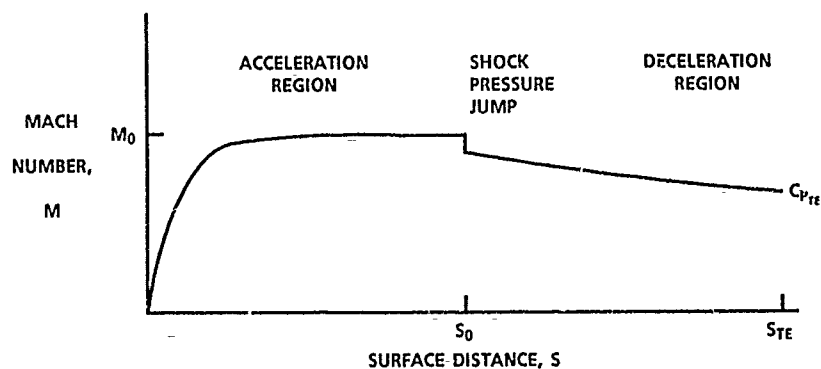


Figure 4. Parametric Equations Define the Mach Number Distribution along the Surface of an Airfoil

5.2 Acceleration Region

The pressure distribution in the acceleration region is of the form

$$C_p = C_{p_s} + (C_{p_0} - C_{p_s}) [1 - (1 - S_a/S_0)^n] \quad (16)$$

where

$$C_{p_s} = [(1 + 0.2 M_\infty^2)^{1/2} - 1] / 0.7 M_\infty^2 \quad (17)$$

As Figure 5 shows, increasing the value of n in this equation drives the Mach number to a rooftop distribution, and allows for airfoils with different nose radii.

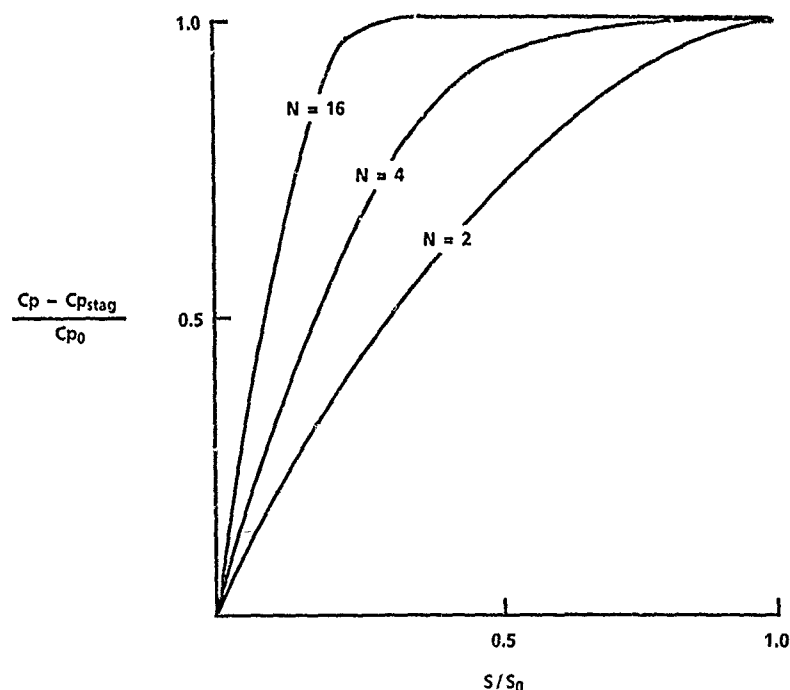
5.3 Shock Pressure Rise

If the peak Mach number, M_0 , is greater than one, a shock will form at the start of the pressure recovery. Yoshiara²³ indicates that the pressure behind the shock on an airfoil may be estimated by a value that is halfway between the pressure associated with sonic flow behind an oblique shock and an oblique shock detachment. Then an effective wedge angle can be established for the pressure rise through the shock. The wedge angle is

$$\Delta = 0.5 (\Delta^* + \Delta_{\max}) \quad (18)$$

Using small angle assumptions (M_0 close to 1.0), the sonic wedge angle may be approximated²⁴ by

$$\Delta^* = 0.296 (M_0^2 - 1)^{3/2} / M_0^2 \quad (19)$$

Figure 5. Effect of n on Acceleration Region Distribution

and the detachment wedge angle by

$$\Delta_{\max} = 0.3208 (M_o^2 - 1)^{3/2} / M_o^2 \quad (20)$$

The pressure rise through the shock is approximated by

$$\begin{aligned} p_2/p_1 = 1 &+ \gamma M_o^2 \Delta / \beta + \gamma M_o^2 \beta^{-4} [(\gamma + 1) M_o^4 - 4 \beta^2] \Delta^2 / 4 \\ &+ \gamma \beta - 7 M_o^2 [(\gamma + 1)^2 M_o^8 / 32 - (7 + 12\gamma - 3\gamma^2) M_o^6 / 24 \\ &+ 3(\gamma + 1) M_o^4 / 4 - M_o^2 + 2/3] \Delta^3 + \dots \end{aligned} \quad (21)$$

where

$$\beta = (M_o^2 - 1)^{1/2}$$

and the Mach number behind the shock wave as a function of the wedge angle can be determined by

$$M^2 = [M_o^2 (6P_j + 1) - 5(P_j^2 - 1)] / P_j(P_j + 6) \quad (22)$$

where

$$P_j = p_2/p_1$$

5.4 Deceleration Region

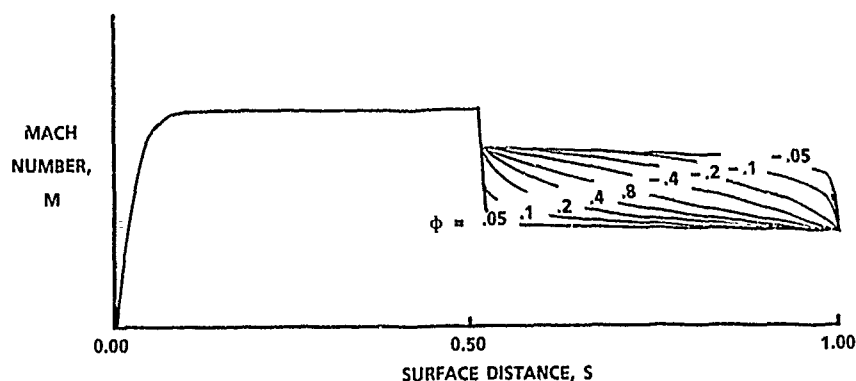
In the deceleration region, the Mach number is of the form

$$M = M_2 [1 + K(S_n - S_o) / (1 - S_o)]^{-\phi} \quad (23)$$

This equation was developed by F. X. Wortmann²⁵ to produce a constant form parameter in the turbulent boundary layer. Notice that the parameters S_o , ϕ , and K may be varied to produce an infinite number of velocity distributions. In Figure 6 the value of ϕ is varied to produce a family of pressure recovery distributions.

The pressure distribution on the surface as a function of the Mach number is

$$C_p = \{[(1 + 0.2M_\infty^2) / (1 + 0.2M^2)]^{7/2} - 1\} / 0.7M_\infty^2 \quad (24)$$

Figure 6. Effect of ϕ on Pressure Recovery System

5.5 Integrated Performance Results

The pressure distributions on the upper and lower airfoil surface may be integrated numerically for lift and pitching moment on each surface:

$$C_L = C_{p_{TE}} - \int_0^{S_0} C_p dS - \int_{S_0}^1 C_p dS \quad (25)$$

and

$$C_M = \int_0^{S_0} (C_p S - 0.25 C_p) dS + \int_{S_0}^1 (C_p S - 0.25 C_p) dS - 0.25 C_{p_{TE}} \quad (26)$$

The friction drag is calculated by means of the Squire-Young drag method in conjunction with the Walz²⁶ compressible boundary layer theory. The Squire-Young drag method can be expressed as

$$C_D = 20_{TE} (V_{TE} / V_\infty)^\lambda \quad (27a)$$

where

$$\lambda = (H_{12TE} + 5) / 2 \quad (27b)$$

The Walz boundary layer method is also used to calculate the separation location. The transition location is determined by a method of Eppler²⁷ that allows the effective roughness of the surface to be varied. The transition criterion assumes that transition has occurred if

$$\ln Re_0 > 18.4 H_{32} - 21.74 - 0.36 (\mu_R - 1) \quad (28)$$

In addition a capability to set the transition point at or before a given location is available.

5.6 Perturbations to the Pressure

The pressure distribution on the upper and lower surface of the airfoil can be defined by five parameters through the use of this method. However, in the design of airfoil sections with practical leading and trailing edge shapes, the simple pressure distribution produced by this method may have to be perturbed slightly to generate realistic input values. One area in which perturbations to the basic pressure distribution may be important is the trailing edge region. Without viscous effects the pressure at the trailing edge would recover to the stagnation pressure. However, this pressure rise is alleviated by the growth of the boundary layer as it nears the trailing edge of the airfoil. The pressure distribution in this area usually experiences a small rise. Figure 7 shows a typical pressure distribution that is generated through the design method. An interactive modification of this pressure can be performed and the pressure distribution can be modified, as shown in Figure 8, to produce a realistic trailing edge pressure distribution.

6. RESULTS

We now present three design problems to illustrate the application of the MGM2D airfoil analysis/design code. The first problem demonstrates that target pressure distributions corresponding to a known airfoil geometry can be used to recover the target geometry starting from some arbitrary baseline configuration that is not "close" (thickness, camber,

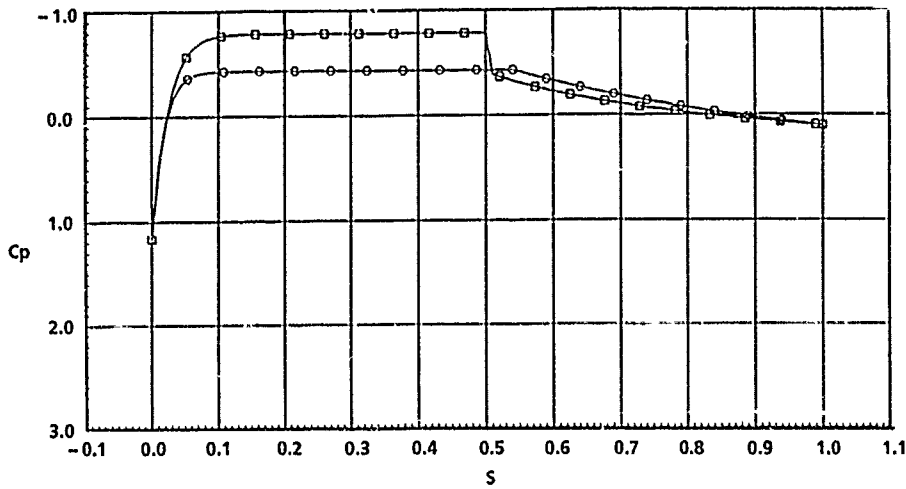


Figure 7. Typical Airfoil Pressure Distributions Generated with the Velocity Function Method

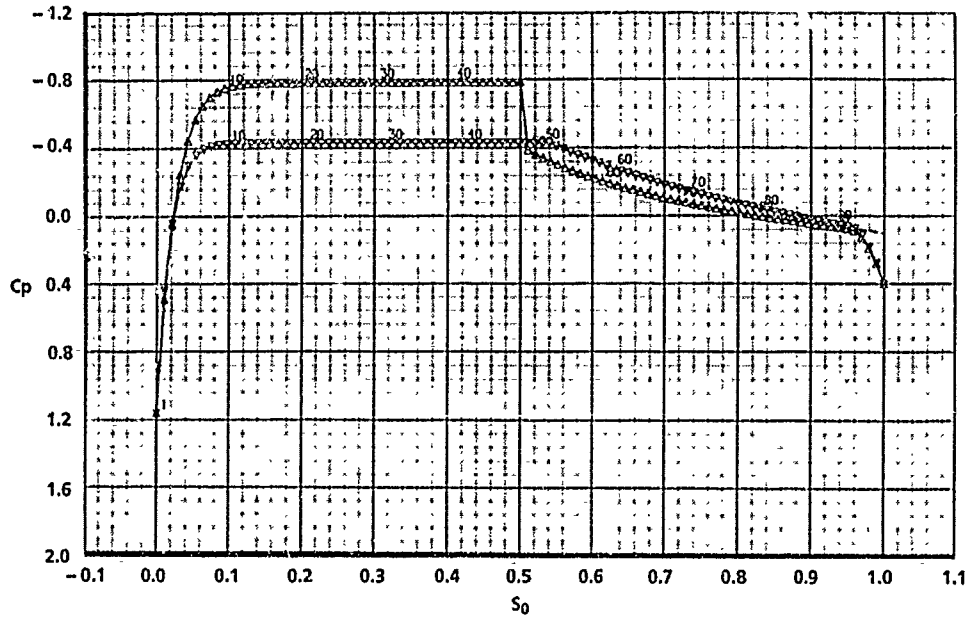


Figure 8. Typical Trailing Edge Pressure Recovery

etc.) to the target geometry. The second example is similar to the first, but also demonstrates that the MGM2D algorithm can be used to design airfoils even when the baseline leading-edge region requires significant changes. The third example was chosen to solve a specific airfoil design problem where the target pressures were generated with the ADAM system and correspond to certain desired lift and moment coefficients.

Several parameters were held constant for each of the sample problems. These parameters and their respective values are

- 1) Grid size = 157 wrap-around (ξ), 58 normal (η)
- 2) Nodes in wake region = 31
- 3) Grid clustering normal to airfoil surface = .00005 chord lengths
- 4) $\epsilon_E = 5.0$, $\epsilon_I = 20.0$
- 5) Time-steps between geometry perturbations = 50
- 6) Variable time-stepping option, $\Delta t_r = 0.5$, and $F_3 = 0$

6.1 Design Case No. 1

For Case No. 1, the MGM2D code was used in the analysis mode to compute the surface pressures corresponding to an NACA 64A010 airfoil at $M_\infty = 0.8$, $\alpha = 9^\circ$, and $Re = 6,500,000$. Two thousand iterations (time-steps) were required to reduce the correction (Equation 5f) five orders of magnitude. It should be noted that for more difficult cases the Navier Stokes code may require more iterations (2,000 to 4,000) in the analysis mode to achieve similar convergence levels. However, the convergence characteristics described here are a function of the particular CFD solution procedure used as a basis for the design algorithm, and can be affected by a variety of parameters, including grid orthogonality, dissipation, and time-step size.

The calculated C_p values were next used as target pressures for the MGM2D code operated in the design mode. The baseline airfoil used for this case was an RAE2822 section. The computational grid for the starting configuration is shown in Figure 9. This airfoil has an aft-loaded camberline, and is significantly different in shape from the NACA 64A010 airfoil used to produce the target pressure distribution.

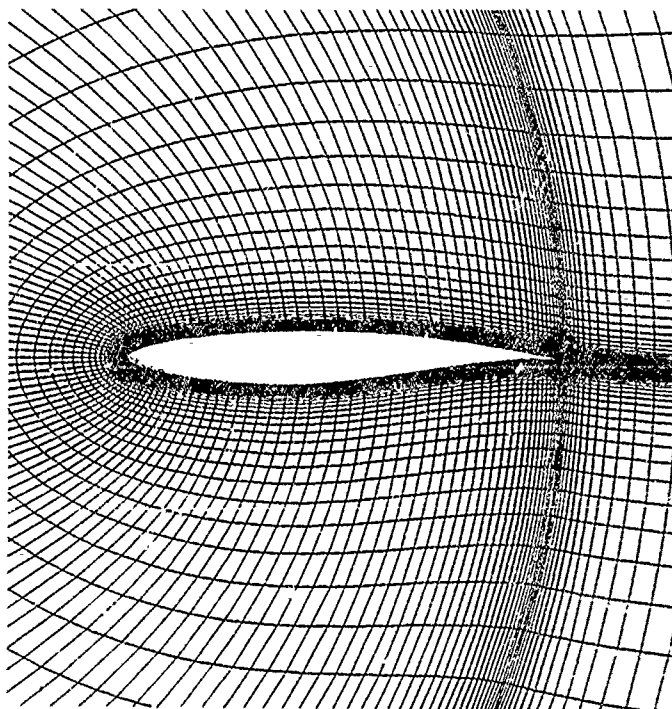


Figure 9. Baseline Airfoil Shape and Computational Grid for Case No. 1

The MGM2D code was run in the design mode for 4,000 iterations with uniform freestream conditions as the initial flowfield solution. That is, a converged flowfield solution for the baseline configuration was not needed to start the design process. The baseline served primarily to set the trailing edge thickness, which was held constant during the design iterations.

Equations 10 and 11 were evaluated by means of nonuniform physical coordinates for the finite-difference expressions (Design Option No.1). The values of the user-specified coefficients in these equations were fixed at $F_0 = F_1 = F_2 = 4.0$. This choice of coefficients had the effect of reducing the ΔY_i distribution to 25 percent of the values actually computed with Equation 9.

Figure 10 compares the final "designed" airfoil and the baseline configuration. To reach the final configuration, values of the maximum source term, Q_{max} , and the average value of the source term over the airfoil surface were both reduced more than two orders of magnitude.

Figure 11 compares the final and target pressure distributions, where the "final" pressures were obtained from an analysis run with the "designed" airfoil geometry. An analysis of the design configuration verifies that the computational procedure has produced a geometry that matches the target pressures within tolerances acceptable to the program user. For this example case, the final design configuration was achieved with not much more computational effort than would have been required to analyze a single airfoil geometry by a cut and try approach.



Figure 10. Comparison of Baseline and Design Airfoil Contours for Case No. 1

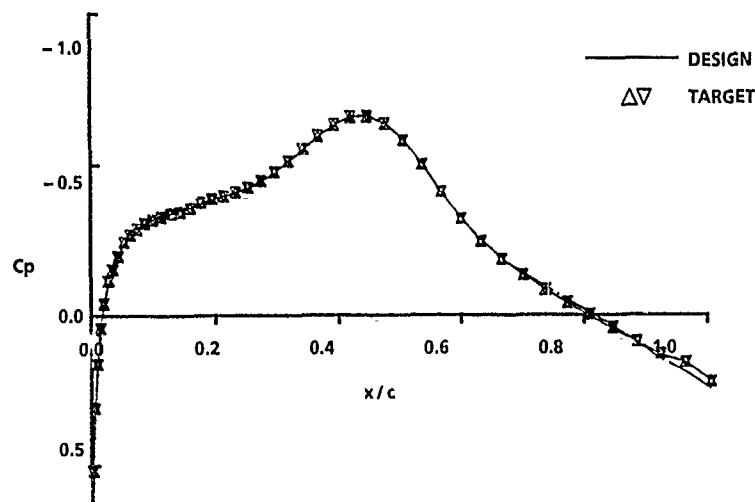


Figure 11. Comparison of Design and Target Pressure Distributions for Case No. 1

6.2 Design Case No. 2

The design goal for Case No. 2 was to demonstrate that the MGM2D code can produce airfoils whose pressure distributions required significant modifications to the baseline leading-edge geometry. As in Case No. 1, target pressures were first computed for a known baseline configuration, and then the MGM2D code was used to reproduce the target geometry.

For this example, the target pressures were computed for an NACA 0006 airfoil section at $M_\infty = 0.6$, $\alpha = 0.0^\circ$, and $Re = 1,000,000$. An NACA 0012 airfoil was used for a baseline configuration. A converged flowfield solution for the NACA 0012 airfoil was used to start the design process. Then four thousand iterations were performed in the design mode, using "Design Option No. 1." At this point, the design airfoil had achieved a reasonable match to the targets everywhere except near the leading-edge position, upstream of the 1.7-percent chord location. The second design option was then applied for 1,000 iterations, after this design cycle, the value of the maximum source term had dropped by an order of magnitude. For this final design run, the coefficients F_0 , F_1 , and F_2 were set to values of 100, 200, and 200, respectively.

Results for this sample problem are given in Figures 12 to 14. Figure 12 shows the leading-edge region of the NACA 0012 baseline airfoil, while Figure 13 illustrates the leading-edge region of the designed airfoil. Finally, Figure 14 compares the upper-surface pressure coefficient distributions for the target pressures, the design pressures after 4,000 iterations, and the final design pressures after an additional 1,000 iterations. Although Case No. 2 is a relatively simple design problem, it demonstrates that the present numerical procedure can produce successful airfoil designs even when large changes are required to a given baseline shape (100 percent t/c perturbation for this case). A design procedure with this type of characteristic frees the aerodynamics engineer from the need to know a starting, or baseline configuration that will be "close" (in camber or t/c) to the final design configuration ultimately produced.

6.3 Design Case No. 3

For Case No. 3, an airfoil was to be designed with a maximum thickness of approximately 11 percent of chord; a nose-up pitching moment coefficient of 0.0078 at a Mach number of 0.78, a Reynolds number of 4.2 million, and a drag divergence Mach number greater than 0.78 at a lift coefficient of 0.128. The ADAM system was used to find pressure distributions that would satisfy these requirements and yield low drag coefficients.

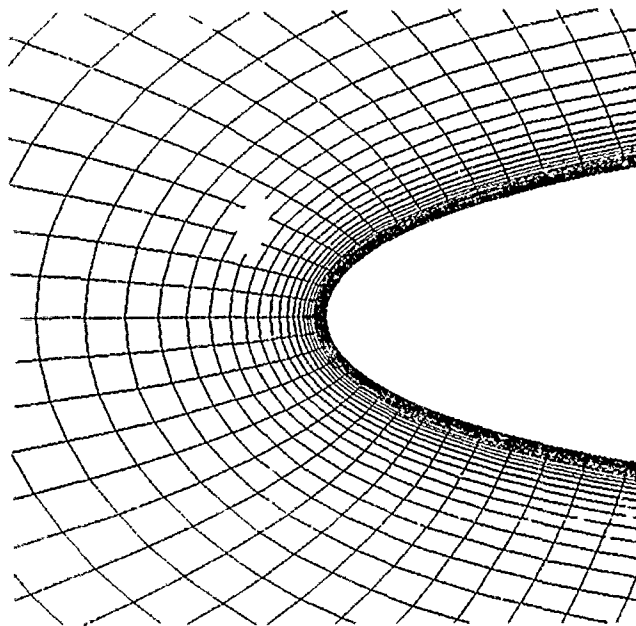


Figure 12. Airfoil Contour and Computational Grid at the Leading Edge of the Baseline Configuration for Case No. 2

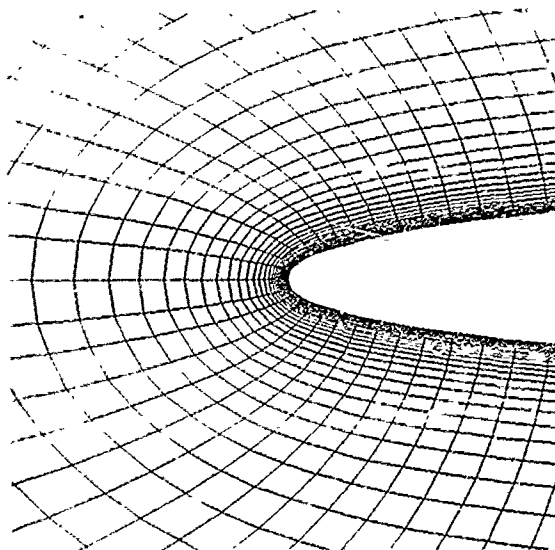


Figure 13. Airfoil Contour and Computational Grid at the Leading Edge of the Designed Configuration for Case No. 2

The problem posed by Case No. 3 represents a robust test of the MGM2D code for two reasons. First, the target pressure distribution incorporates a medium strength shock wave on the airfoil upper surface. In addition, the target pressures selected are flat "roof-top" type distributions ($\partial C_p / \partial x = 0$) over large portions of the upper and lower surfaces of the airfoil. This target C_p distribution is plotted in Figure 15 as upper (Δ) and lower (∇) surface symbols.

The starting configuration used for this problem was a symmetric NACA 64A010 airfoil section. As in Case No. 1, this design problem used an impulsive start from uniform freestream conditions. Also, Equations 10 and 11 were evaluated with non-uniform x coordinates throughout the design process.

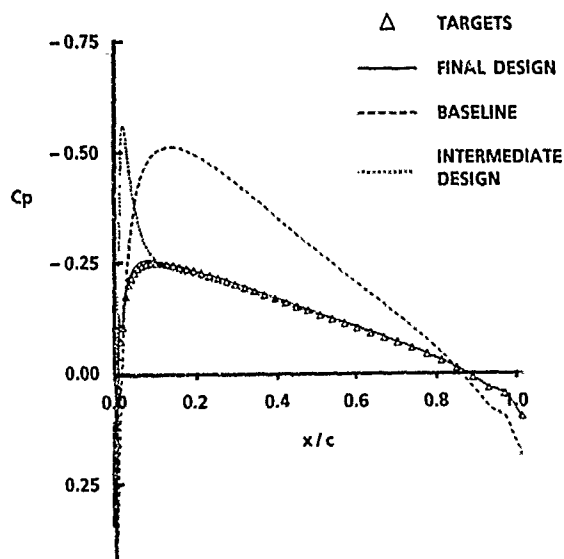


Figure 14. Comparison of Baseline, Target, and Design Pressures for Case No. 2

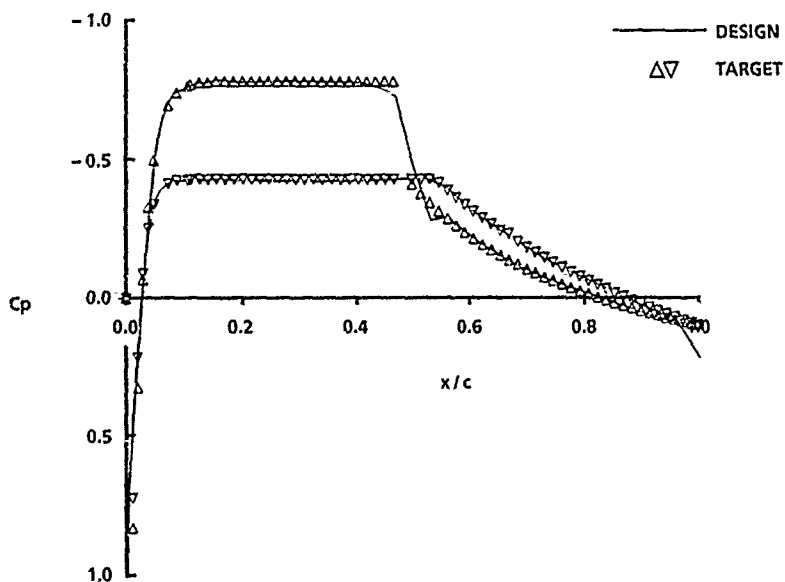


Figure 15. Comparison of Design and Target Pressure Distributions for Case No. 3

Approximately 12,000 iterations were used to produce an airfoil shape that gave a reasonably close match to the target pressure distribution. The design was generated with two different sets of coefficients F_0 , F_1 , and F_2 . For the initial 4,000 iterations, values of these coefficients were set at $F_0 = F_1 = F_2 = 4.0$. For the second 4,000 iterations, the design process was slowed down slightly by increasing the values of these coefficients to $F_0 = F_1 = F_2 = 10.0$. This has the effect of further reducing the amount of the correction, ΔY_i , applied to the airfoil surface. The final 4,000 iterations used values of $F_0 = F_1 = F_2 = 4.0$.

The airfoil pressures resulting from the final design geometry are also shown in Figure 15, while the design airfoil contour and computational grid are shown in Figure 16. Comparisons of the target and design airfoil lift and moment coefficients are given below:

Coefficient	Target	Design
C_L	0.1280	0.1200
C_M	0.0078	0.0070

These results reflect a six-percent difference in lift and a ten-percent difference in moment. An examination of Figure 15 shows that the region of greatest discrepancy between the target and design pressures occurs near the airfoil trailing edge. It is likely that a target pressure distribution with more pressure recovery at the trailing edge would produce a better airfoil design, as discussed in Section 5.6.

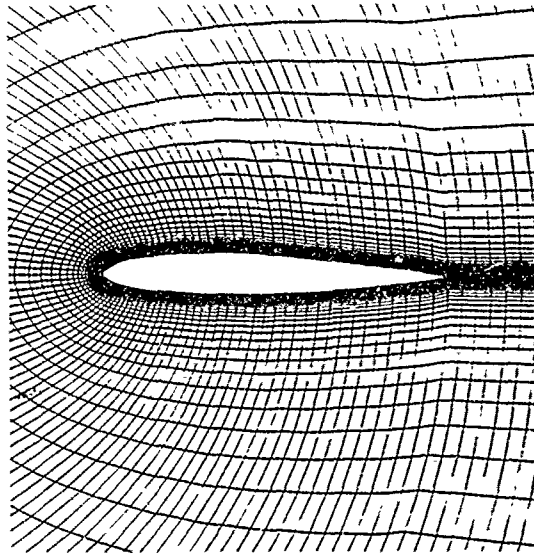


Figure 16. Design Airfoil Shape and Computational Grid for Case No. 3

7. CONCLUSIONS

The MGM design procedure has been incorporated into an existing Navier-Stokes code. The method is relatively efficient in that it does not significantly increase the computational effort required to obtain airfoil designs above that normally required to use the Navier-Stokes code in the analysis mode. Many design problems can be solved for the same computational effort as that required for a single Navier-Stokes analysis. Since the present design method is based on a Navier-Stokes formulation, it should be able to account for viscous flowfield phenomena that may not be detected by design methods based on FPE flow solvers.

8. REFERENCES

- 1 Sloof, J. W., "Computational Methods for Subsonic and Transonic Aerodynamic Design," AGARD Report No. 712, 1983.
- 2 Lores, M. E. and Smith, P. R., "Supercritical Wing Design Using Numerical Optimization and Comparisons with Experiment," AIAA Paper No. 79-0065, 1979.
- 3 Weed, R. A., Anderson, W. K., and Carlson, L. A., "A Direct-Inverse Three-Dimensional Transonic Wing Design Method for Vector Computers," AIAA Paper No. 84-2156, 1984.
- 4 Volpe, G. and Melnik, R. E., "A Method for Designing Closed Airfoils," AIAA Paper No. 85-5023, 1985.
- 5 Takanashi, S., "Iterative Three-Dimensional Transonic Wing Design Using Integral Equations," *Journal of Aircraft*, Vol. 22, No. 8, August 1985, pp. 655-660.
- 6 Mani, K.K., "Design Using Euler Equation," AIAA Paper No. 84-2166, 1984.
- 7 Giles, M. B. and Drela, M., "Two-Dimensional Transonic Aerodynamic Design Method," *AIAA Journal*, Vol. 25, No. 9, September 1987, pp. 1199-1205.

8. Risk, M. H., "Application of Single Cycle Optimization Approach to Aerodynamic Design," AIAA Paper No. 84-2165, 1984.
9. Hirose, N., Takanashi, S., and Kawai, N., "Transonic Airfoil Design Procedure Utilizing a Navier-Stokes Analysis Code," *AIAA Journal*, Vol. 25, No. 3, March 1987, pp. 353 - 359.
10. Garabedian, P. and McFadden, G., "Design of Supercritical-Swept Wings," *AIAA Journal*, Vol. 20, No. 3, March 1982, pp. 289 - 291.
11. Malone, J. B., Vadyak, J., and Sankar, L.N., "Inverse Aerodynamic Design Method for Aircraft Components," *Journal of Aircraft*, Vol. 24, No. 1, January 1987, pp. 8 and 9.
12. Hazarika, N., "An Efficient Inverse Method for the Design of Blended Wing-Body Configurations," Ph D. Thesis, Georgia Institute of Technology, June 1988.
13. Sankar, L. N. and Tang, W., "Numerical Solution of Unsteady Viscous Flow Past Rotor Sections," AIAA Paper No. 85-0129, January 1985.
14. Huff, D. L. and Sankar, L.N., "Analysis of Viscous Transonic Flow Over Airfoil Sections," AIAA Paper No. 87-0420, January 1987.
15. Pulliam, T. H., "Euler and Thin Layer Navier-Stokes Codes: ARC2D and ARC3D," Proceedings of the Computational Fluid Dynamics User's Workshop, University of Tennessee Space Institute, Tullahoma, Tennessee, March 1984.
16. Beam, R. M. and Warming, R. F., "An Implicit Factored Scheme for the Compressible Navier-Stokes Equations," *AIAA Journal*, Vol. 16, No. 4, April 1978, pp. 393 - 401.
17. Baldwin, B. and Lomax, H., "Thin-Layer Approximation and Algebraic Model for Separated Turbulent Flow," AIAA Paper No. 78-0257, 1978.
18. Davis, W.H., "Technique for Developing Design Tools from Analysis Methods of Computational Aerodynamics," AIAA Paper No. 79-1529, 1979.
19. Anderson, D. A., Tannehill, J. C., and Pletcher, R.H., *Computational Fluid Mechanics and Heat Transfer*, McGraw-Hill Book Company, 1984.
20. Vanderplaats, G. N., *CONMIN-A Fortran Program for Constrained Function Minimization - User's Manual*, NASA TMX-62282, August 1973.
21. Malone, J.B., "A Subsonic Panel Method for Iterative Design of Complex Aircraft Configurations," *Journal of Aircraft*, Vol. 19, No. 10, October 1981, pp. 820 - 825.
22. Narramore, J. C. and Yeary, R. D., "Airfoil Design and Analysis Using an Information Systems Approach," AIAA Paper No. 80-1444, 1980.
23. Yoshihara, H., "Transonic Viscous Interactions," AIAA Professional Study Series, Seminar Notebook, Snowmass, Colorado, July 1980.
24. Ames Research Staff, "Equations, Tables, and Charts for Compressible Flow," NASA Report 1135, 1953.
25. Wortmann F. X., "A Contribution to the Design of Laminar Profiles for Gliders and Helicopters," Ministry of Aviation Translations TIL/T4903, September 1960.
26. Walz, A., *Boundary Layers of Flow and Temperature*, edited and translated by Hans Joerg Oser, The M.I.T. Press, Cambridge, Massachusetts, 1969, pp 262 - 270.
27. Eppler, R., and Somers, D. M., "A Computer Program for the Design and Analysis of Low-Speed Airfoils," University of Stuttgart, NASA TM 80210, Langley Research Center, August 1980.

ACKNOWLEDGEMENT

The authors thank Cray Research, Inc. for providing computer resources used in developing and validating the computational design method described in this paper. They offer special thanks to John Ahnert, Victor Stack, and Hector Gonzalez of Cray Research, Inc., Dallas District.

AN ITERATIVE PROCEDURE FOR THE DESIGN OF PRESSURE-SPECIFIED
THREE-DIMENSIONAL CONFIGURATIONS AT SUBSONIC AND SUPERSONIC SPEEDS
BY MEANS OF A HIGHER-ORDER PANEL METHOD

L. Fornasier

Theoretical Aerodynamic Department FE 122
Military Aircraft Division
Messerschmitt-Bölkow-Blohm GmbH
Postfach 80 11 60
D-8000 München 80 - Federal Republic of Germany

S U M M A R Y

An advanced panel method employing singularity distributions of higher order and based on mixed boundary conditions of Dirichlet- and Neumann-type has been recently developed for the potential flow analysis of arbitrary airplane configurations at subsonic and supersonic speeds. Some work is in progress to provide this method with a design option capable of re lofting the surface of a given configuration from prescribed pressure distributions. The purpose of this paper is to present the mathematical background of the herein used inverse algorithm and to account on some examples of application.

I N T R O D U C T I O N

The numerical procedure presented in this paper belongs to the inverse methods in the sense that it is capable to define the geometrical corrections from a baseline configuration required to obtain a target pressure distribution. Such methods can be very useful during the aerodynamic design process since they allow the designer to specify directly the surface pressure rather than to find out by intuition or by trial-and-error procedures the particular geometry pertinent to the desired aerodynamic characteristics. Their applicability spectrum is very broad, ranging from the design of entire configuration components like wing surface or external stores (i.e. wing tip pods or underwing tanks) to the re lofting of local regions like - for example - for minimising the fuselage-induced interference effects on wing isobar patterns or mitigating the adverse pressure gradients causing drag penalty or boundary layer separation.

In contrast to the analysis case, the problem of determining the geometry corresponding to a given pressure distribution is nonlinear even within the potential flow assumption. However, the problem can be solved in an iterative way, starting from an initial geometry, linearising the relationship between geometry and pressure and approaching the final result by a succession of linearized cycles, which, in turn, consist of three steps. First the aerodynamic characteristics of the given configuration are computed (analysis step). The comparison of the actual pressure distribution with the target is used to define the goal function for the inverse step. Application of the inverse algorithm is then used to determine the value of the design variables which define the geometry corrections (inverse step). According to the values of the design variables, the new geometry is computed (re lofting step). This geometry is then analysed and if it does not fulfill the target the whole procedure must be repeated until a determined 'convergence' criterion is satisfied. It is to note here that 'convergence' must be considered in an engineering sense, since neither from a mathematical point of view the uniqueness of the solution can be guaranteed for any arbitrary pressure distribution nor any solution is physically meaningful (e.g. solutions with negative thickness).

Due their ability to efficiently handle complicate three-dimensional configurations, several investigators have used a panel method in the analysis step, although only a handful of the existing panel method codes incorporate a design option. Each of these methods features different choices as regarding to the type of inverse algorithm used, the degree of linearisation assumed and the definition of the design variables. Of course the particular choice for each of these parameters have a large impact on applicability, accuracy and computational efficiency of the methods.

Earlier methods - such those of Ref.s 1 to 3 - used various arrangements of vortex sheets located on the wing mean plane for yielding the additional velocity distribution required to match the prescribed pressure distribution. The change in the chordwise slopes are obtained from the normal velocity induced by this additional vorticity distribution. In principle, such methods are especially suited for the optimization of wing camber and twist. Wing section thickness and real fuselage interference effects can be taken into account by the methods of Ref.s 2 and 3, while the method of Ref. 1 is limited to presence of axisymmetrical bodies. Inclusion of source distribution within the design variable coupled with use of singularity distributions located on the actual surface of the configuration was instrumental in attaining the arbitrary three-dimensional capability of the methods of Ref.s 4 to 7. The normal velocity distribution is directly controlled in

these methods either by specification of the perturbation potential function - Ref. 4 - or by use of a surface-transpiration technique - Ref.s 5 and 7 - derived from the potential flow/boundary layer interaction modelling. The non-linear operator which relates the change of pressure to the geometry correction is approximated by using a Taylor expansion around the given geometry. In Ref. 6 the linear derivate of the potential function with respect to a displacement in z -direction is analitically taken into account, giving the method the ability to accurately analyze large changes to wing section geometry. All other methods retain only the constant terms of the Taylor serie, so that only smaller pressure changes may be achieved during one iteration step. Excepting the method of Ref. 5, all other methods require the calculation of different aerodynamic influence coefficients (AIC) during the analysis and the inverse step of each iteration cycle. Finally, design applications for supersonic speeds are only known for the method of Ref. 1, although the PANAIR design procedure - Ref.s 4 and 8 - should not be in principle restricted to subsonic flow conditions.

In the last years the advanced panel method HISSS has been developed by the author for the calculation of linearized potential flow about arbitrary three-dimensional configurations at subsonic and supersonic speeds. Since this code is capable to yield smooth pressure distributions at both subsonic and supersonic Mach numbers, it was assumed that it could be possible to develop a common inverse procedure for both speeds regimes using the HISSS code in the analysis steps. The purpose of this paper is to briefly present the numerical formulation followed in the definition of this inverse procedure and to report on some demonstrative applications of the so far developed algorithm. A brief description of the HISSS code is also given for completeness.

DIRECT ANALYSIS: THE HISSS PANEL CODE.

HISSS is a three dimensional panel method based on the use of surface singularity distributions of higher order for the calculation of linearized subsonic and supersonic potential flows. The configuration is modelled by networks of panels carrying linearly varying sources and quadratically varying doublets whose unitary induced perturbation velocity and potential are computed at a set of discrete points - control points - and assembled into the aerodynamic influence coefficients (AIC) matrices. Fulfillment of appropriate boundary conditions at the control points generates a linear system of equations for the unknown singularity strengths. Once this system has been solved, the perturbation velocity at each control point is computed. Surface pressures are derived from local velocities at control points. Integration of such pressures is then performed over the configuration surface in order to calculate aerodynamic forces and moments.

The HISSS program permits many different modeling options. Singularity distributions of source and/or doublet type must be defined for each non-wake network. Different types of boundary conditions are available for each set of network control points. These are of Neumann-type - i.e. normal mass flux or normal velocity - and of Dirichlet-type - i.e. potential of perturbation velocity, which can be specified on both sides of a panel, or as average and difference values of the above quantities at a control point. A more complete presentation of the mathematical formulation of the method is found in Ref. 9. Examples of application of the method to airplane and missile configurations can be found in Ref.s 10 to 12. More recently, the part of the code relevant to the calculation of the AIC matrices has been restructured for allowing efficient vectorisation on the Fujitsu/Siemens VP200 vector processor.

FORMULATION OF THE DESIGN PROCEDURE.

OBJECTIVES

The inverse algorithm presented herein was developed aiming at complying to the following requirements. First, the same basic procedure had to be applicable to any type of configuration components for subsonic or supersonic design purposes. Second, the selection of the algorithm had to consider - for computational efficiency - the possibility of utilizing the AIC matrices already available from the analysis step during a given cycle of the iterative process. Third, the algorithm had to be stable and exhibit good convergence characteristics. Fourth, a relifting procedure had to be incorporated within the design loop, enabling the analysis of the new geometry in a fully automatic way. Moreover, the new geometry had to be easily accessed from the computer-aided, interactive graphic application system used for defining the geometry data base of the configurations. Finally, high compatibility with the analysis method was desirable for minimizing the user's effort required for operating the design option.

DERIVATION OF THE INVERSE ALGORITHM

In its more general modelling option, the HISSS method employs a set of combined source-doublet networks to represent the solid surface of the given configuration. The individual strength of the source and doublet distribution must then be determined by specification of two different types of boundary conditions at the midpanel control points. According to Green's third identity, the proper combination of sources and doublets can be determined by setting to zero the total mass-flux through the impermeable surface and the perturbation potential on the internal side of the wetted surface. Inspection of local velocity/singularity relationships shows that the mass-flux condition determines directly the local strength of the source distribution, which is proportional to the normal component of the freestream velocity vector, i.e.

$$\sigma = -V_\infty \cdot n \quad (1),$$

where n is the unitary normal vector at the control point. On the other side, the incremental velocity on the external side - and hence the pressure - depends directly on the local gradient of the doublet strength. This can be easily explained by following considerations. A local orthogonal coordinate system ξ, η and ζ is constructed in the tangent plane with the origin in the control point, ζ being the unitary normal at the control point. Expressing the total velocity as sum of the freestream velocity V_∞ and of the perturbation velocity v_p components we can write

$$V_{tot} = (V_{\infty\xi} + v_{p\xi}, V_{\infty\eta} + v_{p\eta}, V_{\infty\zeta} + v_{p\zeta}) \quad (2)$$

for both the internal and the external side. Assuming that the zero perturbation potential on the inner side implies also zero perturbation velocity there, the total velocity at the external side can be expressed as

$$\{V_{tot}\}_e = V_\infty + \Delta v_p \quad (3),$$

where Δv_p indicates the variation of the perturbation velocity between the two side of the singularity distribution which is equal to

$$\Delta v_p = (\mu_\xi, \mu_\eta, \sigma) \quad (4).$$

Substituting (4) in (3) and making use of (1) we finally obtain

$$\{V_{tot}\}_e = (V_{\infty\xi} + \mu_\xi, V_{\infty\eta} + \mu_\eta, 0) \quad (5).$$

The relations (1) and (5) show clearly the complementary role played by the two singularity types in the analysis problem. The sources provide the geometrical information while the doublets drive the kinematic field. The consideration of these different contributions was used in the formulation of the present inverse algorithm. At each iteration cycle, the comparison of the actual pressure distribution vs. the target one can be converted into an incremental tangential velocity distribution which, following equation (5), determines directly the gradient of the incremental doublet distribution required to match the target pressure. On the sought geometry, a source distribution proportional to the still unknown local normal fulfills the internal potential boundary condition. Conversely, fulfillment of this boundary condition on the given geometry determines an additional distribution of sources whose local strength can be used for updating the geometry.

The advantages of this formulation are manifold. First, the same boundary condition - i.e. zero internal perturbation potential at midpanel control points - and the same AIC matrix are used in both the direct and the inverse loop. Second, the aerodynamic interference between different configuration components is automatically taken into account through the AIC matrix. Third, the method is equally suited for the design of the whole configuration as for the design of local regions. The partial design case can be regarded as a mixed direct/inverse problem, where the doublet distribution is pre-determined at the pressure-specified regions and the source strengths are known in the geometry-specified regions.

The three-dimensional application of this algorithm is explained next. At the beginning of the first cycle the given configuration is analysed by the HISSS code. After having obtained the solution for the direct case, the target pressure distribution is defined at the control points of the regions to be modified. The specification is done at a network level, so that during the inverse loop the total configuration consists of 'design network', i.e. networks for which a pressure target is defined, and - possibly - of 'analysis networks', whose geometry has to be kept fix. The first step is related to the determination of the gradient of the additional doublet distribution for the design networks. Direct differentiation of the surface pressure distribution was considered too expensive. Instead, in consideration of the small variation assumption within each iterative cycle, the following approximation is used. The magnitude of the additional velocity v_a is obtained from the difference between the target and the actual pressure coefficients. The direction of v_a is assumed to be parallel to the local flow round at the present iteration. Then the doublet distribution over the surface of the design network are determined by numerical evaluation of the integral

$$\mu = \int v_s \times ds + C \quad (6)$$

where s is a curvilinear coordinate along the integration path and C an arbitrary constant. In order to obtain the necessary accuracy, the distribution of v_s computed at the control points is interpolated using the quadratic spline functions already available from the doublet singularity distributions used in the analysis step. The numerical integration starts from the most upstream panel corner, where the constant C is first set to zero. When the values of μ are determined for all the control points of the pressure-specified regions, a linear system is set up, using the AIC matrices of the direct loop for imposing the zero internal perturbation condition on all the control points. The solution of this linear system determines the additional source distribution σ' on the design networks and the additional doublet distributions μ' on the analysis networks. The constant C must now be determined from closure considerations. The integral displacement

$$W = \int \sigma' ds \quad (7)$$

is computed for each design network. If the edges of the network are to be maintained, the quantity W must be zero. Due to linearity of the problem, the value of C satisfying this condition can be easily determined.

DERIVATION OF THE RELOFTING ALGORITHM.

The next task is to modify the geometry of the design networks so that the normal at each control point satisfy the relationship

$$V_n \times n' = \sigma + \sigma' \quad (8).$$

The displacement of the panel corner points has been selected as design variable. This choice allows to maintain geometrical continuity during the relofting process, a mandatory requirement for the supersonic case. Moreover, possible geometrical constraints can be easily incorporated. Each corner point is allowed to move along the local normal at the surface of a quantity λ . In the case that the points along two or more edges of the networks are to be maintained, the number of the design variables λ is smaller of the number of conditions (8) so that a least square approximation must be used. To this purpose, a goal function is defined as

$$R(\lambda_j) = \sum_i w_i (\tilde{n}_i - n'_i)^2 \quad (9)$$

$$\text{with } j = (1, 2, \dots, M), \quad i = (1, 2, \dots, N) \quad \text{und } M < N,$$

where M and N are respectively the total number of design variables and constraints conditions, \tilde{n} is the approximation of n , and w is a weight function. The solution of the least square method can be expressed in matrix form as

$$\{ \lambda \} = [\{ v \} \cdot \{ w \} \cdot \{ v \}^T]^{-1} \cdot \{ w \} \cdot \{ v \} \{ n' \} \quad (10)$$

where

$$\{ \lambda \} = \begin{pmatrix} \lambda_1 \\ \lambda_2 \\ \vdots \\ \lambda_N \end{pmatrix},$$

$$[v] = \begin{pmatrix} \partial \tilde{n}_1 / \partial \lambda_1 & \cdot & \cdot & \partial \tilde{n}_j / \partial \lambda_1 & \cdot & \cdot & \partial \tilde{n}_N / \partial \lambda_1 \\ \cdot & \cdot & \cdot & \cdot & \cdot & \cdot & \cdot \\ \partial \tilde{n}_1 / \partial \lambda_i & \cdot & \cdot & \partial \tilde{n}_j / \partial \lambda_i & \cdot & \cdot & \partial \tilde{n}_N / \partial \lambda_i \\ \cdot & \cdot & \cdot & \cdot & \cdot & \cdot & \cdot \\ \partial \tilde{n}_1 / \partial \lambda_N & \cdot & \cdot & \partial \tilde{n}_j / \partial \lambda_N & \cdot & \cdot & \partial \tilde{n}_N / \partial \lambda_N \end{pmatrix},$$

$$[w] = \begin{pmatrix} w_1 & 0 & \cdot & 0 & \cdot & 0 & 0 \\ 0 & w_2 & \cdot & 0 & \cdot & 0 & 0 \\ \cdot & \cdot & \cdot & \cdot & \cdot & \cdot & \cdot \\ 0 & 0 & \cdot & w_1 & \cdot & 0 & 0 \\ \cdot & \cdot & \cdot & \cdot & \cdot & \cdot & \cdot \\ 0 & 0 & \cdot & 0 & \cdot & w_{N-1} & 0 \\ 0 & 0 & \cdot & 0 & \cdot & 0 & w_N \end{pmatrix}$$

and

$$\begin{pmatrix} n'_1 \\ n'_2 \\ \vdots \\ n'_N \end{pmatrix} = | n'_i |$$

Since the functions $\tilde{n}_i(\lambda_j)$ are non linear, an iterative procedure must be used. The procedure employed is an adaptation of the Newton-Raphson method used in Ref. 13 for computing the geometry of the leading edge vortex sheet. In this method, at each iteration step the nonlinear functions are approximated by the corresponding linear terms of the Taylor series. For example, the zero values of a nonlinear function $F(x)$ are obtaining through a series of iterations of the form

$$(\partial F / \partial x)^{(t)} \Delta x^{(t)} = - F^{(t)} \quad (11),$$

where

$$x^{(t+1)} = x^{(t)} + \Delta x^{(t)}.$$

It can be seen that the solution x at the iteration $(t+1)$ depends only on the values of the function F and its derivative $\partial F / \partial x$, which are known from the previous iteration step (t) . This scheme can be applied for the solution of the system (10), provided that the vectors $\{\lambda\}$ and $\{n'\}$ be replaced by the following

$$\{\Delta \lambda^{(t)}\} = \begin{pmatrix} \lambda_1^{(t+1)} - \lambda_1^{(t)} \\ \lambda_2^{(t+1)} - \lambda_2^{(t)} \\ \vdots \\ \lambda_N^{(t+1)} - \lambda_N^{(t)} \end{pmatrix}$$

and

$$\{\Delta \tilde{n}^{(t)}\} = \begin{pmatrix} n'_1 - \tilde{n}_1^{(t)} \\ n'_2 - \tilde{n}_2^{(t)} \\ \vdots \\ n'_N - \tilde{n}_N^{(t)} \end{pmatrix}$$

and that the derivatives $\partial n_i / \partial \lambda_j$ be computed at the iteration level (t) .

The iterative process starts using the values computed for the given geometry, i.e. at the level $t=1$ is

$$\{\tilde{n}^{(1)}\} = \{n\}$$

and

$$\{\lambda^{(1)}\} = 0.$$

The derivatives in the matrix $[v]^{(1)}$ are also computed for the starting geometry. The solution of the system gives the first approximation of the geometrical corrections $\{\lambda^{(1)}\}$. For increasing the stability of the scheme, a relaxation parameter δ is introduced so that at each step the corrections effectively used are first reduced to

$$\{\lambda^{(t+1)}\} = \delta \{\Delta \lambda^{(t)}\} + \{\lambda^{(t)}\} \quad \text{mit } \delta < 1.$$

Now the new normals $\tilde{n}_i^{(t+1)}$ are computed for the perturbed geometry. The increment of the norm of the panel normals, defined as

$$N_{n1} = || \{\tilde{n}^{(t+1)}\} - \{\tilde{n}^{(t)}\} ||$$

is introduced to control the convergence of the process. Is this norm smaller of a given convergence parameter ϵ , the iterative process is stopped. If the norm is larger than ϵ , the quality of the solution is controlled by examination of the norm

$$N_1 = || \delta [w]^{(t)} \{\Delta \lambda^{(t)}\} ||$$

which represents the norm of the linear contribution to N_{n1} . To reduce the problem of overshoot in the classical Newton scheme, a halving process of the relaxation parameter δ is applied to limit at each iteration the norm N_{n1} by ensuring that

$$N_{n1} - N_1 \leq N_1.$$

APPLICATIONS

Before being able to incorporate the present design option into a program system as HISSS, a large array of testcases should be computed to acquire a sufficient knowledge and confidence on the algorithm performance. This was not entirely possible so far. Hitherto applications cover only simple tests chosen to explore some typical areas of applications so as to be able to determine where future additional work is required. For better evaluation of the algorithm capability, in the examples presented here the pressure distributions selected as target for the design procedure were obtained from the analysis of a known geometry, so that the convergence of the pressures and of the geometry can be judged at the same time. Three cases are presented here.

REDESIGN OF NLF1 AIRFOIL.

This testcase was computed using a two-dimensional implementation of the present design algorithm. A constant source/doublet panel method employing the Dirichlet formulation was used in the analysis of the wing sections. A NACA 0006 symmetric profile airfoil at zero angle of attack was chosen as initial geometry. The analysis of the NLF1 at zero angle of attack provided the target pressure for the design exercise, see figure 1. During the refoiling steps all the endpoints of the panels but those on the trailing edge were allowed to move principally along to the local normal. An underweighted movement along the tangential direction was also permitted for easing the refoiling task in the leading edge region. Figure 2 shows the convergence history of the profile contour during the Newton-Raphson procedure of the first iteration step. The comparison of the actual vs. the target pressure distribution at the end of the first iteration cycle is presented next, figure 3. After two further iterations a reasonable agreement with the specified was target for the pressure was produced, see figure 4. Further iteration cycles did not produce any substantial improvement, but proved the stability of the present scheme. The geometry produced at the tenth iteration was almost indistinguishable from that of the reference airfoil. The residual differences in the pressures are thought to be attributable to the excessive sensibility of the low-order panel method used for the analysis to local variations of panel lengths. Since it has been often demonstrated that the higher order formulation employed in the HISSS is by far more forgiving to irregularities in panel spacings, generation of irregular panel density was not considered as a drawback for the three dimensional applications of the design procedure.

SUBSONIC AND SUPERSONIC REDESIGN OF A THREE-DIMENSIONAL BODY.

A fully-three dimensional geometry was used for testing the pilot implementation of the design option into the HISSS code. The target body features an axisymmetrical ogive followed by an indented region consisting of circular sections. The axial distribution of the radii and the location of their origin are specified in such a way that the upper crown line describes a convex-concave-convex curve while the bottom line is straight, figures 5 and 9. The purpose of the test was to determine if the design option could reproduce this geometry starting from an ogive-cylindrical body, figures 6 and 10. The two configurations were panelled using one network for the ogive and one network for the aft part. In the design case the rear network was defined as design network while the geometry of the ogive had to remain unchanged. The pressure coefficients calculated at the panel control points of the target body were used as boundary conditions to determine the additional doublet distribution. Fulfillment of the zero perturbation potential condition on the inner inside of the ogive-cylinder configuration together with the use of the closure condition resulted in the determination of the additional source distribution. The geometry of the cylindrical surface was then refoiled allowing each panel corner point to move in the x constant plane along the local normal so that to minimize the function $R(\lambda)$. The exercise was carried out at subsonic and supersonic speeds.

At subsonic speeds, two iterations of this design procedure produced a pressure distribution almost identical to the original one, the difference between the first and the second iteration being relatively small, figure 7 and 8. This indicated that for engineering purposes one iteration cycle could be sufficient. The convergence of the geometry shows a good qualitative agreement. However the cross sections of the generated surface are not circular, indicating the necessity to allow the panel corner points to move also in a tangential direction.

At supersonic speeds, three iterations were necessary to obtain a good global agreement with the target pressures. Figures 11 and 12 show the results at the end of the first and the third iteration cycle. Local failure to complete match the target pressure distribution at both fore and aft ends of the design networks are attributable to the coarseness of the modelling. The decrease of the convergence rate in comparison with the subsonic is due to the more complicate pattern of the supersonic pressure distributions. Here again uncomplete convergence of the geometry indicates the necessity of moving the grid points in two directions.

CONCLUSIONS

An inverse design procedure capable of re lofting the geometry of a given configuration or of parts of it by specification of a target pressure distribution has been developed. As demonstrated by its application on simple testcases, the basic algorithm is very general and applicable to any kind of geometry at subsonic and supersonic flows. Fast convergence characteristics and good computational efficiency are achieved by the use of the same aerodynamic matrices in the direct and in the inverse loops. Some additional work is needed to further generalize the re lofting procedure before incorporating the present algorithm as fully-automated design procedure into the HISSS panel code.

REFERENCES

- [1] Woodward, F.A., Tinoco, E.N., and Larsen, J.W., 'Analysis and Design of Supersonic Wing-Body Combinations, Including Flow Properties in the Near Field', NASA CR-73106, Aug. 1967.
- [2] Fornasier, L., "Wing Design Process by Inverse Potential Flow Computer Programs", The Use of Computers as a Design Tool, AGARD CP280, 1979, pp14-1 to 14-14.
- [3] Pray, J.M.J., and Slooff, J.W., 'A Constrained Inverse Method for the Aerodynamic Design of Thick Wings with Given Pressure Distribution in Subsonic Flow', Subsonic/Transonic Configuration Aerodynamics, AGARD CP-285, 1980, pp.16-1 to 16-9.
- [4] Johnson, F.T., 'A General Panel Method for the Analysis and Design of Arbitrary Configurations in Incompressible Flows', NASA CR-3079, 1980.
- [5] Malone, J.B., 'A Subsonic Panel Method for Iterative Design of Complex Aircraft Configurations', J. of Aircraft, Vol. 19, No. 10, 1982, pp. 820-825.
- [6] Hawk, J.D., and Bristow, D.R., 'Subsonic Surface Panel Method for Airframe Analysis and Wing Design', AIAA Paper 83-341, 1983.
- [7] Kubrynski, K., 'A Subsonic Panel Method for Design of 3-Dimensional Complex Configurations with Specified Pressure Distribution', Panel Methods in Fluid Mechanics with Emphasis on Aerodynamic, Notes on Numerical Fluid Mechanics, Vol. 21, pp.137-146, Vieweg Verlag, 1987.
- [8] Magnus, A.E., 'PAN AIR - A Computer Program for Predicting Subsonic or Supersonic Linear Potential Flow about Arbitrary Configurations Using a Higher Order Panel Method', Vol. I and II, NASA CR-3251, 1980.
- [9] Fornasier, L., 'HISSS - A Higher-order Panel Method for Subsonic and Supersonic Flow about Arbitrary Configurations', Panel Methods in Fluid Mechanics with Emphasis on Aerodynamic, Notes on Numerical Fluid Mechanics, Vol. 21, pp. 52-70, Vieweg Verlag, 1987.
- [10] Fornasier, L., 'Linearized Potential Flow Analysis of Complex Aircraft Configurations by HISSS, a Higher-order Panel Method', AIAA Paper 85-281, 1985.
- [11] HeiB, S., and Fornasier, L., 'Analysis of a Fighter Type Aircraft Configuration with the HISSS Panel Method at Subsonic and Supersonic Speeds', Z. Flugwiss. und Weltraumforsch., Vol. 12, 1988, pp. 224-232.
- [12] Fornasier, L., and D'Espiney, P., 'Prediction of Stability Derivatives for Missiles Using the HISSS Panel Code', Stability and Control of Tactical Missile Systems, AGARD CP-451, 1988.
- [13] Brune, G.W., 'A Three-Dimensional Solution of Flows over Wings with Leading Edge Vortex Separation', NASA CR-132708, 1975.

ACKNOWLEDGMENT

This research work was sponsored by the German Ministry of Defence, under contract T/RP41/E0010/E14.

FIGURES

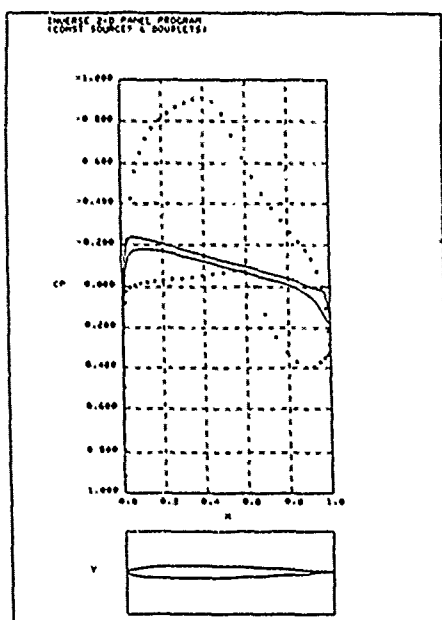


Figure 1 - Comparison of pressures of the the initial geometry - NACA 0006 - and the target - NLF1 wing section - .

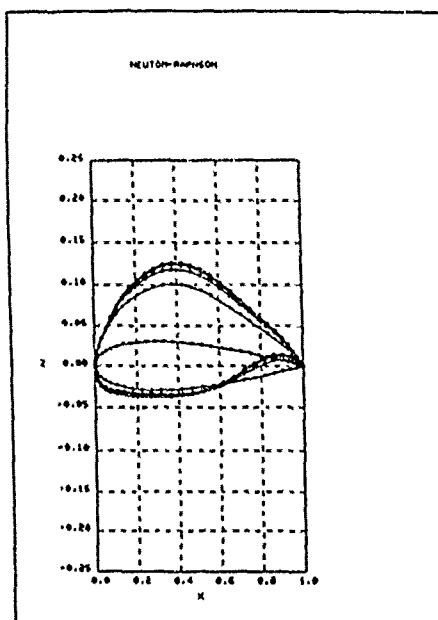


Figure 2 - First iteration cycle: redesign of the initial profile by Newton-Raphson inverse procedure.

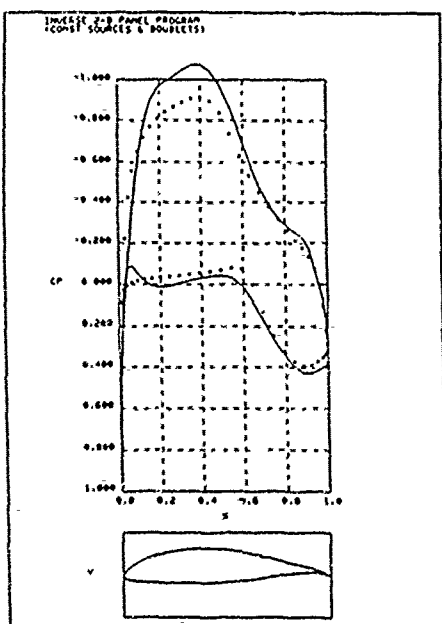


Figure 3 - Comparison of pressures of the redesigned profile - first cycle - and the target - NLF1 wing section - .

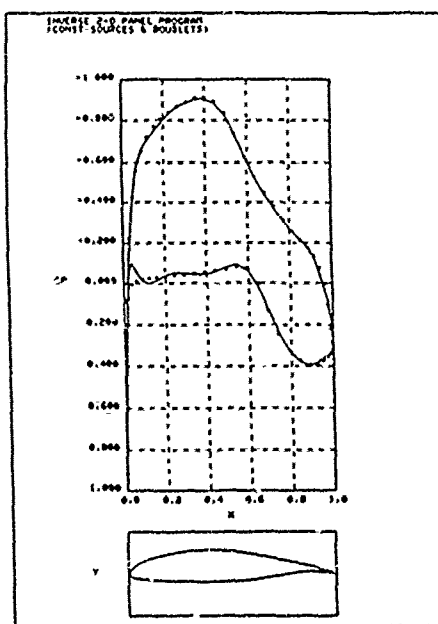
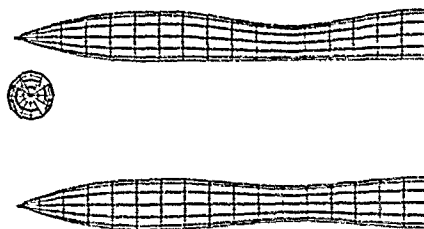


Figure 4 - Comparison of pressures of the redesigned profile - third cycle - and the target - NLF1 wing section - .

TESTCASE FOR WINGLESS - NON-AXISYMMETRICAL BODY - OGIVE-CYLINDER
DESIGN NETWORK ON REAR PART OF THE CONFIGURATION
SUBSONIC ITERATIVE DESIGN RUN OF THE TARGET GEOMETRY



TESTCASE FOR WINGLESS - NON-AXISYMMETRICAL BODY - OGIVE-CYLINDER
DESIGN NETWORK ON REAR PART - 1ST ITERATION CYCLE - ANALYSIS
SUBSONIC ITERATIVE DESIGN RUN FROM THE INITIAL CONFIGURATION

TESTCASE FOR WINGLESS - NON-AXISYMMETRICAL BODY - OGIVE-CYLINDER
DESIGN NETWORK ON REAR PART - 1ST ITERATION CYCLE - ANALYSIS
SUBSONIC ITERATIVE DESIGN RUN FROM THE INITIAL CONFIGURATION

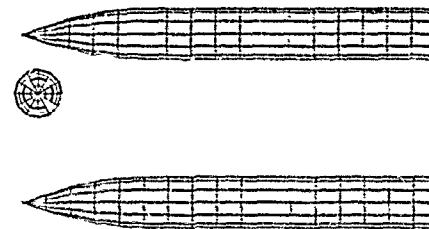
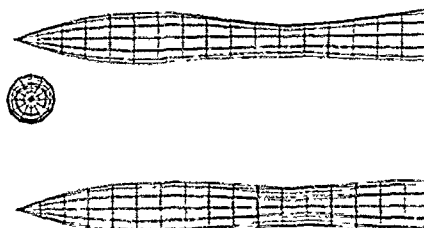


Figure 5 - Panelling of the target geometry and relevant longitudinal pressures for the case Mach 0.41, $\alpha = 0$. degree.

Figure 6 - Panelling of the initial geometry and relevant longitudinal pressures for the case Mach 0.41, $\alpha = 0$. degree.

TESTCASE FOR WINGLESS - NON-AXISYMMETRICAL BODY - OGIVE-CYLINDER
DESIGN NETWORK ON REAR PART - 2ND ITERATION CYCLE - ANALYSIS
SUBSONIC ITERATIVE DESIGN RUN FROM THE TARGET CONFIGURATION



TESTCASE FOR WINGLESS - NON-AXISYMMETRICAL BODY - OGIVE-CYLINDER
DESIGN NETWORK ON REAR PART - 2ND ITERATION CYCLE - ANALYSIS
SUBSONIC ITERATIVE DESIGN RUN FROM THE INITIAL CONFIGURATION

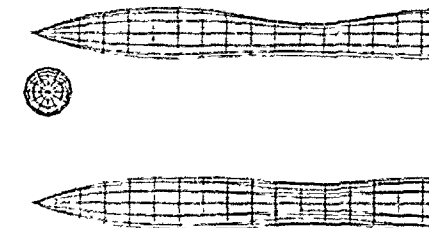


Figure 7 - Panelling of the redesigned geometry - first iteration cycle - and relevant longitudinal pressures for the case Mach 0.41, $\alpha = 0$. degree.

Figure 8 - Panelling of the redesigned geometry - second iteration cycle - and relevant longitudinal pressures for the case Mach 0.41, $\alpha = 0$. degree.

TESTCASE FOR HINCESS - NON-AXISYMMETRICAL BODY - CYCLES 1-200
DESIGN NETWORK ON NEAR PART OF THE CONFIGURATION
SUPERSONIC ITERATIVE DESIGN RUN FROM THE INITIAL CONFIGURATION

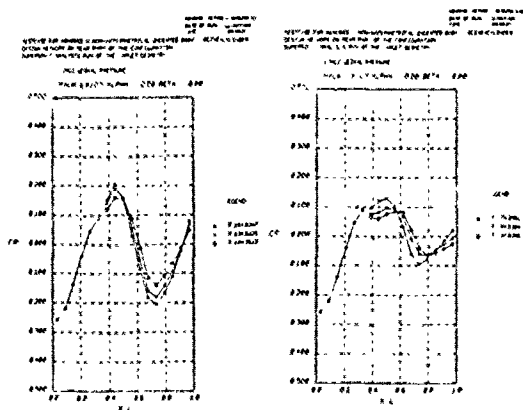
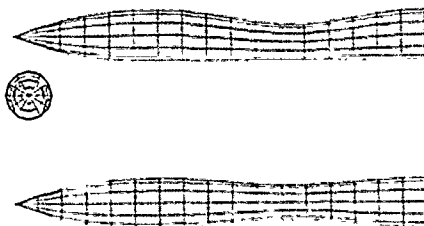


Figure 9 - Panelling of the target geometry and relevant longitudinal pressures for the case Mach 1.41, $\alpha = 0$ degree.

TESTCASE FOR HINCESS - NON-AXISYMMETRICAL BODY - CYCLES 1-200
DESIGN NETWORK ON NEAR PART - 1ST ITERATION CYCLE - ANALYSIS
SUPERSONIC ITERATIVE DESIGN RUN FROM THE INITIAL CONFIGURATION

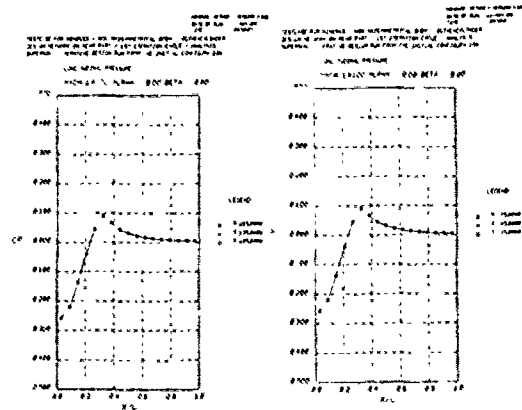
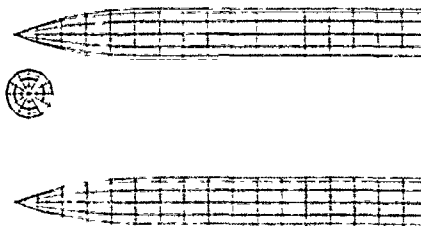


Figure 10 - Panelling of the initial geometry and relevant longitudinal pressures for the case Mach 1.41, $\alpha = 0$ degree.

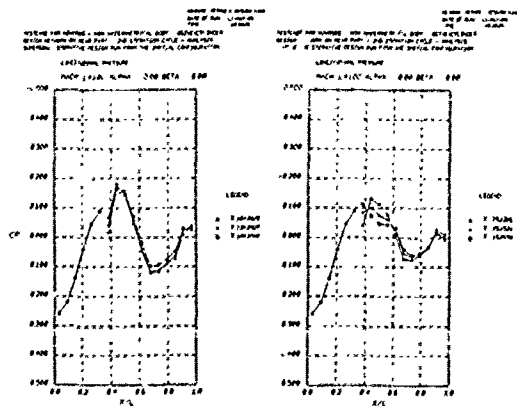
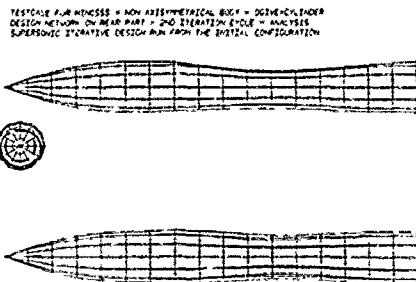


Figure 11 - Panelling of the redesigned geometry - first iteration cycle - and relevant longitudinal pressures for the case Mach 1.41, $\alpha = 0$ degree.

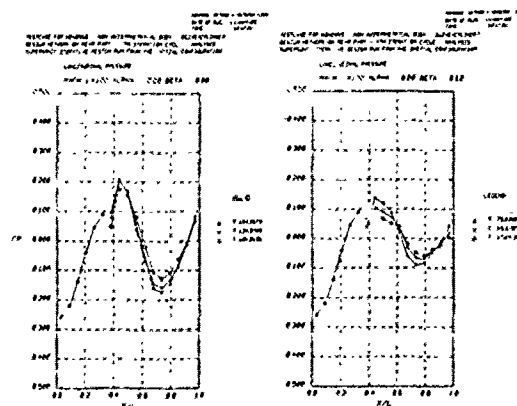
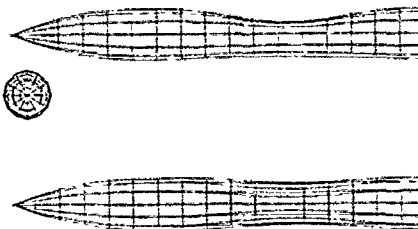


Figure 12 - Panelling of the redesigned geometry - third iteration cycle - and relevant longitudinal pressures for the case Mach 1.41, $\alpha = 0$ degree.

A SYSTEM FOR TRANSONIC WING DESIGN WITH GEOMETRIC CONSTRAINTS BASED ON AN INVERSE METHOD

by

F.J. Brandsma and J.M.J. Fray
National Aerospace Laboratory, NLR
P.O. Box 90502
1006 BM Amsterdam
The Netherlands

1. INTRODUCTION

A well known problem in the field of aerodynamic design is the inverse problem of finding the geometry of a wing which produces a given target pressure distribution (and hence has given aerodynamic characteristics) for prescribed free stream conditions. In this inverse problem, non-linear boundary conditions of a mixed type should be applied on the unknown wing surface from which its geometry should be calculated. The resulting non-linear equations may be solved by means of an iterative method. Existing iterative methods for solving the inverse aerodynamic problem can roughly be divided into two classes (see Ref.1).

In the first type of methods, each iteration starts with the calculation of a flow field which produces the prescribed target pressure distribution on the wing surface iterate, but in general will allow a non-zero mass flow through this surface. The geometry corrections are then derived in such a way that the transpiration mass flow will vanish.

In the second type of method, usually called residual correction methods, first the actual flow around the wing surface iterate is calculated (satisfying the zero mass flow condition at this surface), by means of an analysis code. An iteration is completed by applying some approximate inverse correction rule for the calculation of geometry corrections driving the pressure defect (the difference between the target- and the current pressure distribution) to zero.

At NLR, the development of inverse aerodynamic methods has been directed towards the second type of methods. The main reason for choosing a residual correction type of method is its simplicity. An existing flow solver (with the desired level of flow modelling) can be used without modifications for the analysis step. Only rather simple correction rules have to be developed and coupled to such a flow solver. If a converged solution is obtained, the required pressure distribution will indeed be produced by the designed geometry, within the accuracy limits of the flow solver used. Also the present design system is based on a residual correction method.

The flow solver used for the analysis is, at present, a transonic full potential code (XFL022), capable of calculating the inviscid flow about a wing/body combination. In the near future, this flow solver will be replaced by a transonic full potential code coupled to a boundary layer calculation method, in order to include viscous effects due to wing boundary layer and wake.

The applied approximate inverse calculation is based on two former developments at NLR. The basic correction rule consists of the 3D inverse subsonic panel method which is used in the subsonic wing design method, reported in reference 2, being available at NLR since 1974. The adaptation of the correction rule to transonic flows, is based on the supersonic geometry correction module applied in the 2D transonic airfoil design method INTRAFS (Ref.3), which was completed in 1984. This correction consists of the application of the supersonic wavy-wall formula in the way as suggested in reference 4, of which for the present method a 3D interpretation is used.

In this way, 3D transonic wing design can be performed. Just like in the former subsonic design method, mentioned above, the influence of a fixed body, to which the wing may be attached, can be taken into account.

In practical wing design, it is usually necessary to impose some constraints on the desired wing geometry. First of all, such geometric constraints may prove to be necessary in order to prevent the iteration process from converging to physically unrealistic geometries (e.g. local negative thickness), or even to obtain a converged solution at all. In this light it should be mentioned, that in case of 2D airfoil design, the well-posedness of the inverse problem can only be established when some auxiliary constraint relations for regularity and closure are satisfied. For the 3D inverse problem, however, the question of well-posedness seems still to be an open question, even for incompressible flow. In that case, the possibility of intervening in the iteration process and apply or change some geometric constraints may turn out to be an indispensable instrument to obtain a reasonably converged solution. In the second place, some geometric constraints may be necessary from the structural engineer's point of view, who in general will have some requirements with respect to the geometric properties of the wing to be designed (i.e. a lower bound for the thickness, prescribed trailing edge angle or leading edge radius). The present design system offers, just like its predecessors mentioned above, the possibility of imposing geometric constraints. The inverse correction procedure uses a weighted least square error approach for solving the over-determined system of equations resulting from the pressure defect corrections and the geometric constraints. Weight factors assigned to the residuals in pressure defects and in geometric constraints can be prescribed and adjusted during the iteration process. In this way a flexible control over the design procedure is realized, and the design goals can be reached in the best possible way, avoiding troubles arising from the possible ill-posedness of the inverse problem.

During the development of the present system for transonic wing design with geometric constraints, a modular set-up has been pursued (see Fig.1), which also provides a great flexibility. The PRE- and POSTPROCESSING subsystems perform tasks which are most conveniently handled in an interactive way. The flow solver included in the ANALYSIS subsystem as well as the correction procedure included in the INVERSE subsystem, are running in batch mode. All subsystems make use of a common database. The flexibility exists to replace a subsystem easily by another one (e.g. replace the flow solver by a more advanced one), or even to run the subsystems on different computers (e.g. at present arrangements are made to perform the flow solver calculations, the most time consuming part of the process, on NLR's NEC SX-2 supercomputer).

In the present system, no attention is paid to the subject of designing an aerodynamically attractive target pressure distribution on the wing. At NLR some computational tools are available to support this task. In case of complex configurations, the spanwise load distribution can be optimized (to produce minimum drag) by means of the system SAMID (Ref.6). Optimization of the sectional pressure distributions

is a task which can be performed with the help of the general optimization package CADOS (Ref.7).

In the subsequent sections the design procedure included in the transonic wing design system will be described in more detail. Emphasis will lie on the extensions which are made to the former residual correction methods mentioned above. For completeness sake, a short description of the 3D inverse subsonic panel method is included, in order to show the way in which geometrical constraints are taken into account. Finally, the practical applicability of the present transonic wing design system will be demonstrated by an example.

2. TRANSONIC WING DESIGN PROCEDURE

A functional breakdown of the transonic wing design procedure is depicted in Fig.2. It shows the relevant processes which are included in a single iteration. With the flow conditions, the body geometry and the iterate for the wing geometry as input, the current pressure distribution is calculated with the analysis code. The pressure defect (δC_p) is then calculated as the difference between the target- and the current pressure distribution. The inverse calculation, described in the next sections, translates the pressure defects into geometry corrections for thickness and camber (δz and δz_c). These geometry corrections are added to the iterate for the wing geometry, and a new wing geometry is obtained. The results of the present iteration can be inspected and intermediate results may be written to an output file. Depending on these results, the weight factors on pressure defect residuals and on geometric constraint residuals may be adjusted. Now, either a new iteration can be initiated with the input taken from the updated database, or the iteration process can be terminated in case of a suitably converged solution.

3. INVERSE CALCULATION PROCEDURE

The inverse calculation procedure is schematically represented in figure 3. Details of the most important steps involved, will be described below.

3.1 Defect pressure splitting

First the pressure defect is splitted into a subsonic- and a supersonic part, distinguishing between regions where the flow behaves subsonic and regions with supersonic behaviour of the flow. The split will be defined for the pressure distribution of a streamwise wing section, and is essentially the same as the split described in reference 3 for the airfoil case. In the present 3D method, however, a modification in the definition of the critical pressure coefficient is applied. The relevant formulas are derived from those applied in the transonic airfoil design method, by means of simple sweep theory. The transformation is exact for the inviscid flow around an infinite swept constant chord wing, and is in the present 3D method applied to the quantities of the equivalent 2D flow normal to the local geometric angle of sweep (Fig.4). The approximations introduced in this way, are based on the assumption that a high aspect ratio wing is considered with its taper near unity. The relevant "critical" pressure coefficient is derived as,

$$C_p^{**} = \frac{2}{\gamma M_\infty^2} \left\{ \left(\frac{2}{\gamma+1} + \frac{\gamma-1}{\gamma+1} M_\infty^2 \cos^2 \Lambda \right)^{\frac{\gamma}{\gamma-1}} - 1 \right\} \quad (1)$$

Under the assumption that subsonic theory should be applied in case both the actual- (C_p^n) and the target pressure coefficient (C_p^*) are subsonic (in the sense as described above), and pure supersonic theory if both coefficients are supersonic, the following split is applied (see Fig.5),

$$\begin{aligned} \delta_{sub} C_p &= \max(C_p^t, C_p^{**}) - \max(C_p^n, C_p^{**}) , \\ \delta_{sup} C_p &= \min(C_p^t, C_p^{**}) - \min(C_p^n, C_p^{**}) . \end{aligned} \quad (2)$$

3.2 Subsonic perturbation velocity defect

The subsonic part of the pressure defect is expressed in terms of a perturbation velocity defect distribution. The procedure followed is exactly the same as in the 3D inverse subsonic panel method of reference 2. The target and the actual calculated pressure (velocity) distributions are linearized into chordwise perturbation velocity distributions, in the same way as is done in the compressibility correction of the NLR panel method (Ref.8). This correction includes an inverse form of the Riegels'-type leading edge correction, which removes the singular behaviour at the leading edge of the usual thin wing theory. According to reference 2, this correction is essential for the convergence of the iteration process. The resulting perturbation velocities are used to calculate the chordwise subsonic perturbation velocity defects on the upper- and lower wing surface ($\delta_{sub} u_u$ and $\delta_{sub} u_l$).

3.3 Supersonic corrections

The supersonic pressure defect is first expressed in term of corrections for the slope of a streamwise wing section ($\delta z' = \partial z / \partial x$). For this purpose use is made of the supersonic wavy-wall formula in the way as suggested in reference 4. This concept was already successfully used in the 2D transonic airfoil design system (Ref.3). The supersonic wavy-wall formula was derived for 2D supersonic flows (Ref.9), and establishes a nonlinear relation between the pressure coefficient and the surface slope of an airfoil. In fact, the formula is only valid for small perturbations to a uniform supersonic flow. In reference 3, the formula is applied in a linearized form to the supersonic pressure defect resulting into an expression for the airfoil surface slope corrections. In the present context, the formulas derived in reference 3 are applied to the quantities of the 2D equivalent flow (Fig.4). The results are transformed back to the 3D flow, again using simple sweep theory, resulting into the following chordwise slope corrections on the wing surface,

$$\delta z' = \frac{1}{2} \sec \Lambda \left[\left(\frac{2}{\gamma-1} + M_\infty^2 \cos^2 \Lambda \right) / \left(1 + \frac{1}{2} \gamma M_\infty^2 C_{p_{loc}} \right)^{\frac{\gamma}{\gamma-1}} - \frac{\gamma+1}{\gamma-1} \right]^{\frac{1}{2}} \delta_{sup} C_p \quad (3)$$

where the "local" pressure coefficient $C_{p_{loc}}$ is given by,

$$C_{p_{loc}} = \frac{1}{2} \left[\min(C_p^t, C_p^{**}) + \min(C_p^n, C_p^{**}) + C_p^{**} \right]. \quad (4)$$

The supersonic slope corrections are calculated for the upper- and lower surface separately

$$(\delta z'_u \text{ and } \delta z'_l)$$

In order to proceed for the supersonic corrections in the same way as for the subsonic corrections, the surface slope corrections are not applied directly to correct the wing geometry. First, they will be expressed in terms of equivalent subsonic perturbation velocity defects. In that way care has been taken that the same representation for the subsonic- and supersonic corrections is used in the process of compromising between corrections based on the pressure defects and those based on the geometric constraints (see section 4). The equivalent perturbation velocity defects are derived by means of a linear thin airfoil analysis, just like in reference 3, but now corrected for the local angle of sweep (Fig. 4). The sectional slope corrections for thickness and camber are calculated,

$$\delta z'_t = \frac{1}{2} (\delta z'_u + \delta z'_l), \quad \delta z'_c = \frac{1}{2} (\delta z'_u - \delta z'_l), \quad (5)$$

after which the following equivalent perturbation velocity defects for thickness and camber are derived,

$$\begin{aligned} \delta_e u_t &= \frac{\cos \Lambda}{(1-M_\infty^2 \cos^2 \Lambda)^{\frac{1}{2}}} \int_0^c \frac{(\delta z'_t(\xi)) d\xi}{(x-\xi)^{\frac{1}{2}}}, \\ \delta_e u_c &= \frac{\cos \Lambda}{(1-M_\infty^2 \cos^2 \Lambda)^{\frac{1}{2}}} \left(\frac{c-x}{c} \right)^{\frac{1}{2}} \int_0^c \left(\frac{\xi}{c-\xi} \right)^{\frac{1}{2}} \frac{(\delta z'_c(\xi)) d\xi}{(x-\xi)^{\frac{1}{2}}}. \end{aligned} \quad (6)$$

in which c is the chordlength of the wing section. In fact, the expressions in (6) are obtained from the standard thin airfoil theory applied to the local equivalent 2D flow after which the results are transformed to the 3D flow.

It can be observed from the equations presented above, that the whole procedure of defect pressure splitting and translation of supersonic pressure defects into equivalent perturbation velocity defects, provides exactly the same formulas as has been used in reference 3, when the local angle of sweep is set equal to zero. As mentioned in reference 3, the supersonic correction procedure forms a rather poor approximation of the full potential flow. In addition to the deficiencies mentioned there, the deviation of the real flow from a quasi 2D flow, which has been the basis for the present formulation, makes the present approach still more approximate. However, for practical transonic design, the present supersonic corrections seem to drive the geometry corrections into the right direction, and in general a converged solution can be obtained in a reasonable number of iterations (see section 5).

4. SUMMARY OF THE 3D INVERSE PANEL METHOD

The subsonic- and the equivalent perturbation velocity defects are added, resulting into perturbation velocity defects for thickness and camber,

$$\begin{aligned} \delta u_t &= \frac{1}{2} \epsilon_t (\delta_{sub} u_u + \delta_{sub} u_l) + \epsilon \delta_e u_t, \\ \delta u_c &= \frac{1}{2} \epsilon_c (\delta_{sub} u_u - \delta_{sub} u_l) + \epsilon \delta_e u_c, \end{aligned} \quad (7)$$

where ϵ_t , ϵ_c and ϵ are relaxation parameters for the overall iteration process.

The translation of the perturbation velocity defects into geometry corrections is carried out by means of the 3D inverse subsonic panel method described in reference 2. Some crucial details of this method will be summarized below.

4.1. Singularity distributions

The small chordwise perturbation velocity defects are represented by singularity distributions over the wing mean plane and the body's surface. As described in reference 2, thickness effects are represented by a distributions of x-doublets (μ), which has the advantage that the condition of trailing edge closure is implicitly satisfied.

Camber effects are represented by a distribution of vorticity (γ), with the effects of trailing vorticity included in the influence functions. Finally, the induced normal velocity at the body's surface due to the above mentioned singularity distributions, is compensated by introducing a source distribution (σ) on the body's surface. For discretization purposes, the wing mean plane and the body's surface are divided into quadrilateral panels and the singularity distributions are assumed to be constant over each panel. The discrete system of equations can be represented by

$$Kd_x \underline{u} + Ks_x \underline{\sigma} = \underline{\delta u_t} \quad (\text{wing mean plane}) ,$$

$$\frac{1}{2} \underline{\gamma} = \underline{\delta u_c} \quad (\text{wing mean plane}) ,$$

$$Kd_n \underline{u} + Kv_n \underline{\gamma} + Ks_n \underline{\sigma} = 0 \quad (\text{body}) , \quad (8)$$

where the vectors \underline{u} , $\underline{\gamma}$, $\underline{\sigma}$, $\underline{\delta u_t}$ and $\underline{\delta u_c}$ represent the values of the corresponding quantities in the panel midpoints, and the aerodynamic influence coefficients are represented by the matrices Kd_x , Ks_x , Kd_n , Kv_n , Ks_n . The last equation may be used to express $\underline{\sigma}$ in terms of \underline{u} and $\underline{\gamma}$, which are the basic unknowns.

4.2. Geometry corrections

The geometry corrections associated with thickness and camber in the panel midpoints, are related to the singularity strengths by

$$\underline{\delta z_t} = \frac{1}{2} \underline{u} \quad (\text{panel midpoints}) ,$$

$$\frac{\partial}{\partial x} \{ \underline{\delta z_c} \} = -Kv_z \underline{\gamma} - Ks_z \underline{\sigma} \quad (\text{panel midpoints}) , \quad (9)$$

It is preferred, however, to obtain the corrections in the panel corner points. Averaging the doublet strengths of the panels with a common corner point leads to,

$$\underline{\delta z_t} = Zt_d \underline{u} \quad (\text{panel corners}) , \quad (10)$$

for the thickness corrections. Averaging and chordwise integration leads to,

$$\underline{\delta(\Delta z_c)} = Zc_v \underline{\gamma} + Zc_s \underline{\sigma} \quad (\text{panel corners}) , \quad (11)$$

for the camber difference in a streamwise section, with respect to a fixed reference point in that section.

The matrix elements of Zt_d , Zc_v and Zc_s can easily be derived.

4.3 Geometric constraints

In a presant transonic wing design system, two options for imposing geometric constraints are

place, the possibility exists for imposing a constraint on the thickness. Such a constraint is rational by specifying respectively:

- a point where the constraint should be applied;
- a target value for the thickness at that point (z_t^t) leading to a target value for the thickness correction in each iteration ($\delta z_t^t = z_t^t - z_t^n$);
- a nonnegative weight factor (w_t) to be assigned to this constraint.

Secondly, it is possible to impose a constraint on camber (difference) by specifying respectively:

- two points in a streamwise section between which the camber difference should be controlled;
- a target value for the difference in camber between those two points (Δz_c^t) from which in each iteration a target value for the associated correction is derived ($\delta(\Delta z_c^t) = \Delta z_c^t - \Delta z_c^n$);
- a nonnegative weight factor (w_c) to be assigned to this constraint.

4.4 Solution procedure

The resulting over-determined system of equations is solved in a least square error sense. A functional is drawn up by adding the squares of residuals associated with respectively the pressure defects on the upper surface, the pressure defects on the lower surface, the thickness constraints, and the camber constraints, each of them multiplied by their specified weight factors,

$$\begin{aligned}
F(\underline{u}, \underline{y}) = & \frac{1}{2} w_{cp}^2 (1+d_w) \left\| K d_x \underline{u} + \frac{1}{2} \underline{y} + K a_x \underline{\sigma} - \underline{\delta u}_1 \right\|^2 + \\
& + \frac{1}{2} w_{cp}^2 (1-d_w) \left\| K d_x \underline{u} - \frac{1}{2} \underline{y} + K a_x \underline{\sigma} - \underline{\delta u}_1 \right\|^2 + \\
& + \left\| w_t (z_t \underline{u} - \underline{\delta z}_t) \right\|^2 + \\
& + \left\| w_c (z_c \underline{y} + z_c \underline{\sigma} - \underline{\delta(z)_t}) \right\|^2. \quad (12)
\end{aligned}$$

The factor w_{cp} is used for the pressure defect corrections, while the difference in weights for the upper- and lower surface corrections is controlled by the constant d_w . The matrices W_t and W_c are diagonal matrices with their diagonal elements equal to the square-roots of the appropriate weight factors (w_t and w_c) for the points where constraints are operational, and equal to zero for the other points.

The system of equations to be solved is derived from,

$$(\partial F / \partial u_i) = 0, \quad (\partial F / \partial y_i) = 0, \quad (i=1, 2, \dots, N) \quad (13)$$

where it should be mentioned that although $\underline{\sigma}$ depends formally on \underline{u} and \underline{y} , the derivatives in (13) are calculated as if $\underline{\sigma}$ is a constant vector, after which $\underline{\sigma}$ is expressed in terms of \underline{u} and \underline{y} . The neglected terms are expected to be small because they represent only a second order correction to the influence of the sources on the body, which effect decays rapidly with increasing distance. The resulting system of equations is solved by a block iteration procedure. The geometry correction calculations are straight-forward, once \underline{u} and \underline{y} are known.

In this way the geometry corrections are calculated as a compromise between driving the pressure defects to zero and keeping some properties of the geometry fixed. To which extent each of these goals is reached, depends on the weight factors, which can be prescribed and adjusted during the iteration process.

5. EXAMPLE

The practical applicability of the present transonic wing design system is demonstrated by an reconstruction example. The wing geometry to be reconstructed is the well known DFVLR-F4 wing, for this purpose attached to an imaginary pencil shaped cylindrical body. The F4 wing is a supercritical wing with an aspect ratio of 9.5, a taper ratio of 0.3, and a kink in planform at 40% span. The leading edge sweep is 27.1° and the thickness chord ratio varies from 0.15 at the root to 0.122 at the tip. The wing planform is shown in Fig.6a where also an impression is given of the body to which the wing has been attached for the present example. A perspective view of the original wing geometry is given in Fig.6b. For the reconstruction example, the target pressure distribution (the dashed lines in Fig.7a) corresponds to the original F4/body geometry of Fig.6 as calculated by the flow solver used in the design system (XFLO22). The original geometry has been distorted to produce the initial pressure distribution (the lines marked with an a) in Fig.7a). Starting with this distorted geometry as the initial geometry, an attempt has been made to reconstruct the original F4 geometry using the present design system.

For the inverse calculations the wing planform has been panelled using 9 panels in spanwise direction and 30 in chordwise direction (see Fig.6a). The direct flow solver calculations with XFLO22 has been performed on a medium coarse mesh of 80 (chord) x 16 (span) x 14 (normal) points. After a few iterations it turned out to be necessary to freeze some parts of the current geometry. Small weights have been put on the leading edge thickness of the root- and tip sections, and also on the trailing edge angle at the kink section. The way in which these weights have been applied, is representative for a realistic design process.

The final result has been obtained after six iterations. As can be seen in Fig.7a, the target pressure distribution is very well reproduced near the tip. Near midspan, some deviations are still present towards the trailing edge and after the shock. The suction peak, however, is very well reproduced. Near the root section some more deviations can be observed which are concentrated in the leading edge region. Such problems were to be expected because the correction rules are in this regions rather poor approximations to the real 3D flow. Furthermore, the thick nose of the root section forms a severe test for the present design system. The overall agreement between final- and target pressure distribution, however, can still be called good.

The final geometry is compared with the original F4 geometry in Fig.7b. The original geometry is very well reconstructed near the tip, but also at the kink section the resemblance between target- and final geometry is remarkably good. At the root section, the thickness of the original geometry is not fully reached.

6. CONCLUSIONS

A new system has been described for transonic wing design with prescribed pressure distribution in the presence of a fixed body. The residual correction method, on which the design system is based, combines a "complex" direct flow solver with "simple" correction rules (inverse supersonic wavy-wall + inverse 3D panel method). It is possible to define geometric constraints for the wing to be designed, which is an essential part of the method. Weight factors on the pressure defect corrections and on the corrections associated with the geometric constraints can be adjusted during the iteration process, allowing a maximal control over the design procedure, in order to reach the design goals in the best possible way. The practical applicability of the transonic wing design system has been demonstrated by an example.

7. REFERENCES

1. Slooff, J.W.; "Computational methods for subsonic and transonic aerodynamic design", Chapter 3 of AGARD report No.712: Special course on subsonic/transonic aerodynamic interference for aircraft, 1983.
2. Fray, J.M.J., Slooff, J.W.; "A constrained inverse method for the aerodynamic design of thick wings with given pressure distribution in subsonic flow", 1980, AGARD CP-No.285, paper 16.
3. Fray, J.M.J., Slooff, J.W. Boerstoel, J.W., Kassies, A; "Design of transonic airfoils with given pressure subject to geometric constraints", 1984, NLR TR 84064 U.
4. Davis Jr., W.H.; "Technique for developing design tools from the analysis methods of computational aerodynamics", AIAA paper 79-1529, 1979.
5. Volpe, G., Melnik, R.E.; "The role of constraints in the inverse design problem for transonic airfoils", AIAA-81-1233, 1981.
6. Van den Dam, R.F.; "Constrained spanload optimization for minimum drag of multi-lifting surface configurations", paper to be presented at this AGARD meeting, May 1989.
7. Van Egmond, J.A.; "Numerical optimization of target pressure distributions for subsonic and transonic airfoil design", paper to be presented at this AGARD meeting, May 1989.
8. Labrujere, Th.E., Loeve, W., Slooff, J.W.; "An approximate method for the calculation of the pressure distribution on wing-body combinations at subcritical speeds", 1970, AGARD CP-No.71, paper 11.
9. Spreiter, J.R., Alkane, A.Y.; "Thin airfoil theory based on approximate solution of the transonic flow equation", 1958, NACA Rep.1359.

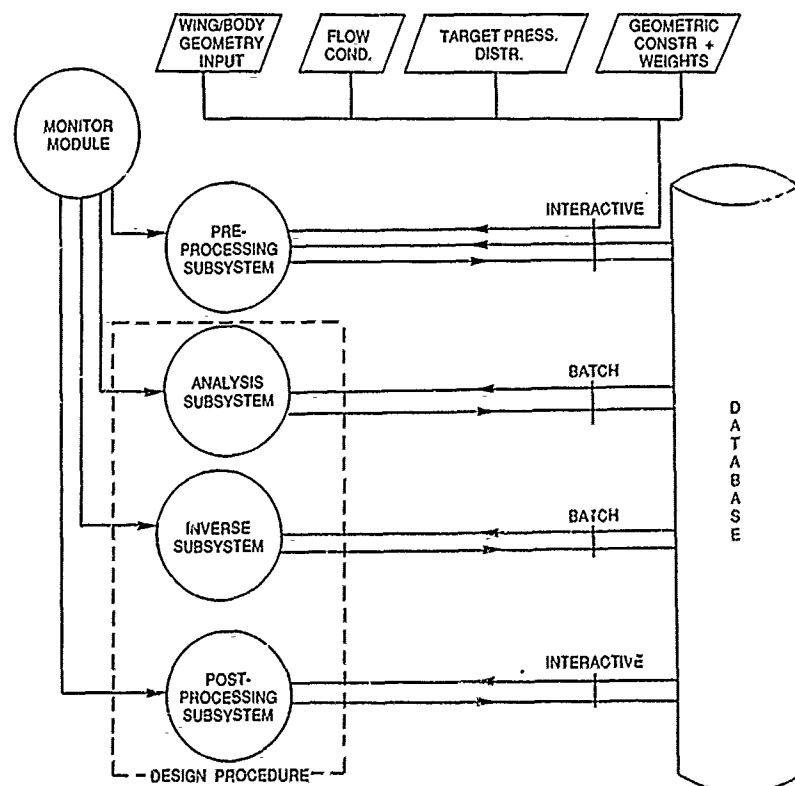


Fig. 1 Main functional processes and interfaces of present transonic design system

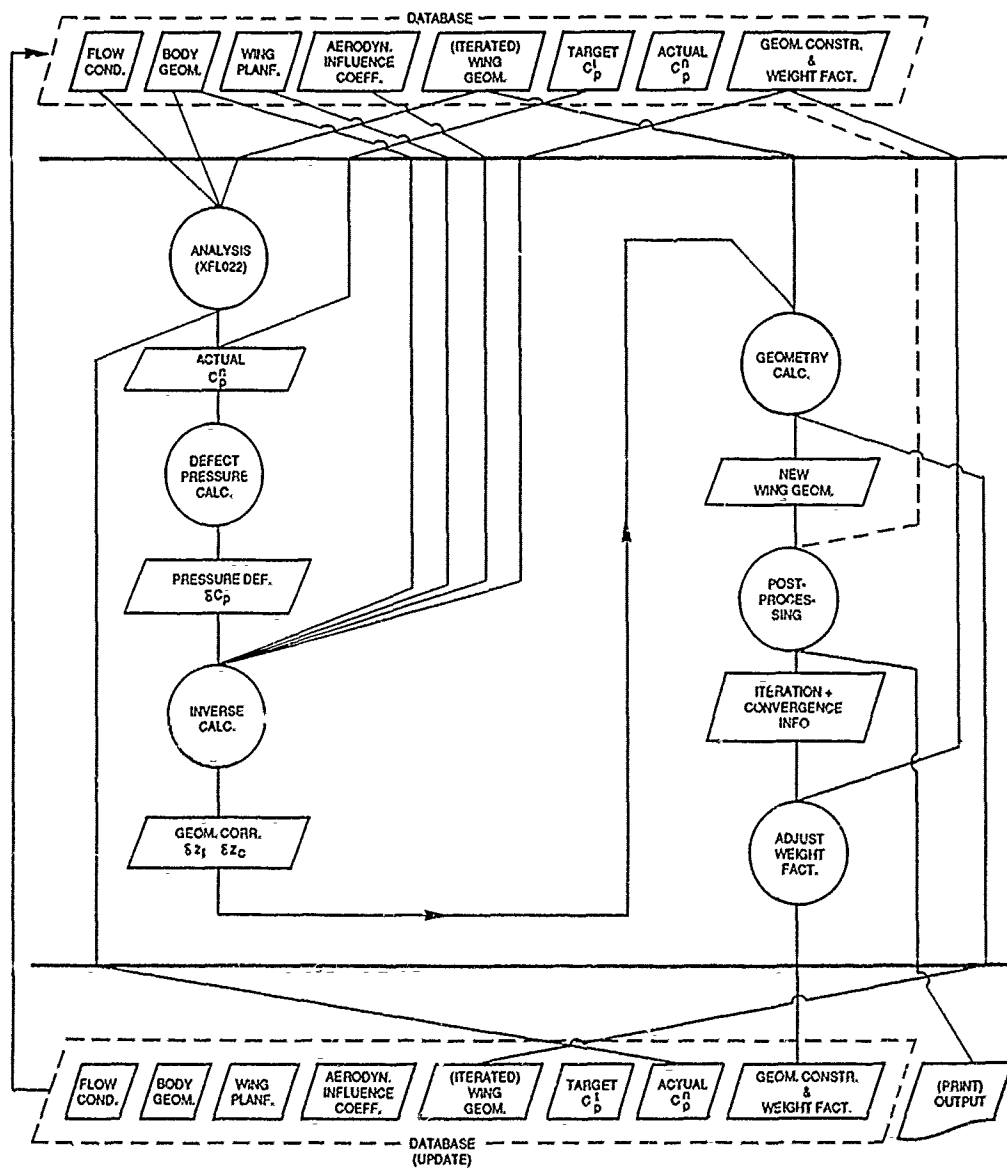


Fig. 2 Functional breakdown of the design procedure

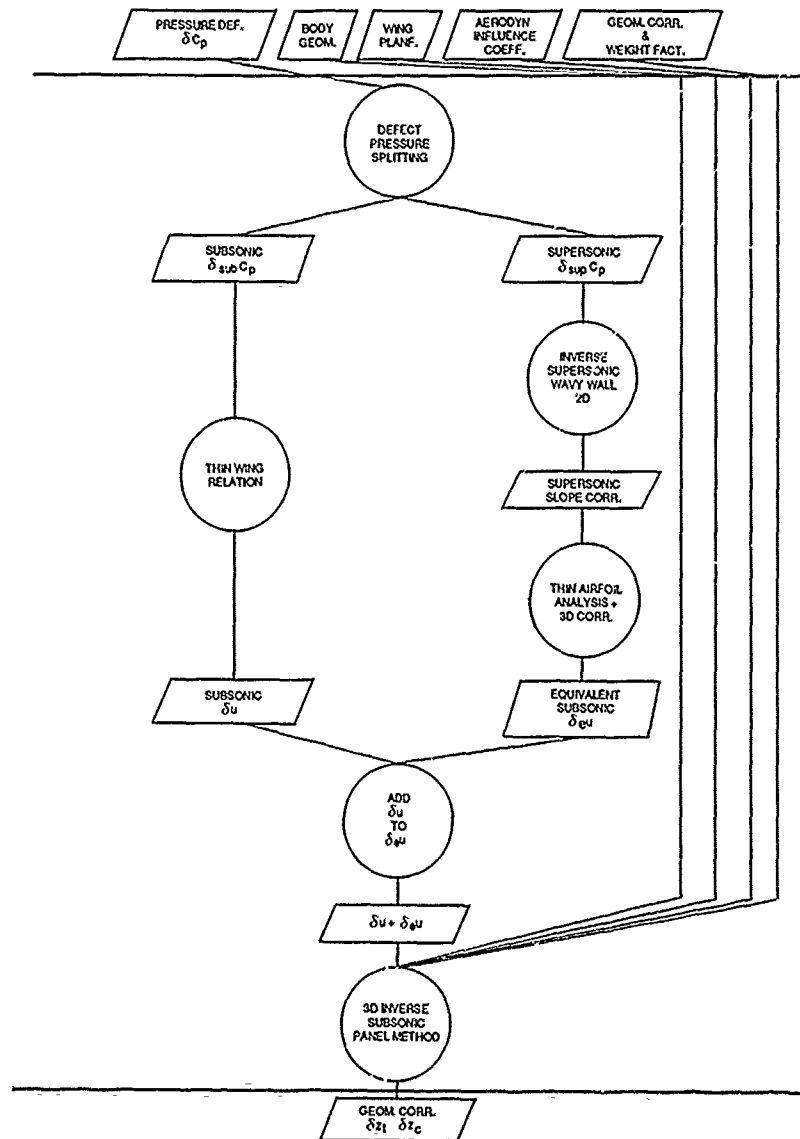
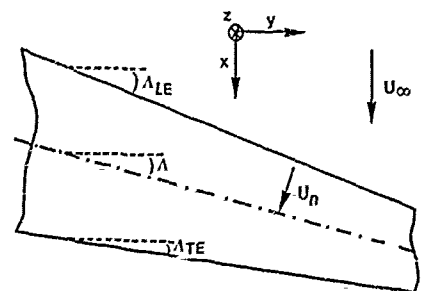


Fig. 3 Functional breakdown of the inverse calculation



λ : GEOMETRIC SWEEP ANGLE
 U_n : VELOCITY OF THE LOCAL EQUIVALENT 2D FLOW

Fig. 4 Local equivalent 2D flow

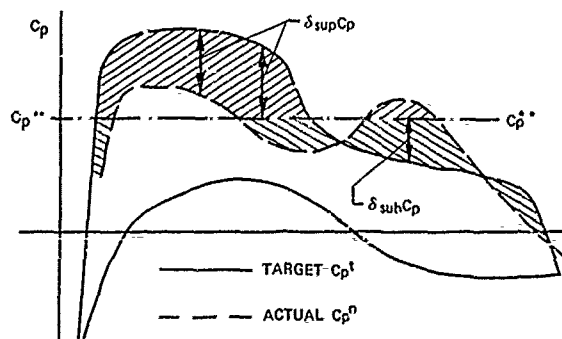


Fig. 5 Defect pressure split

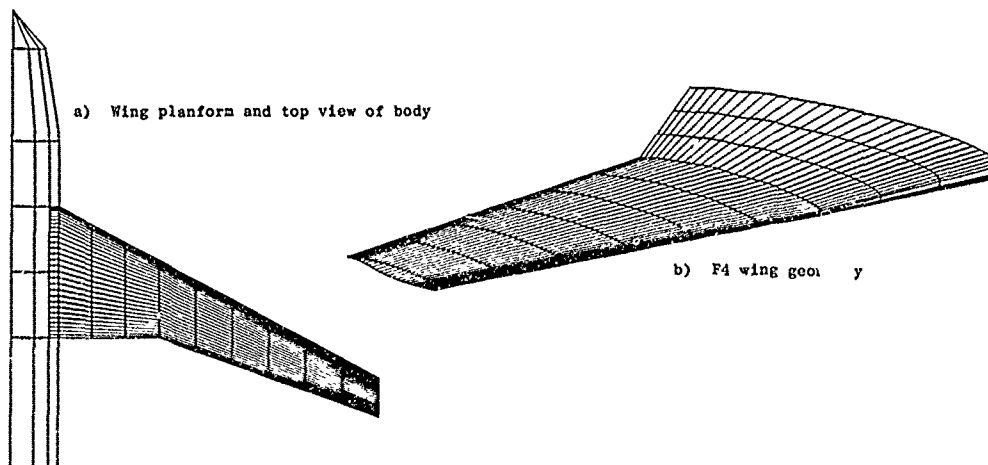
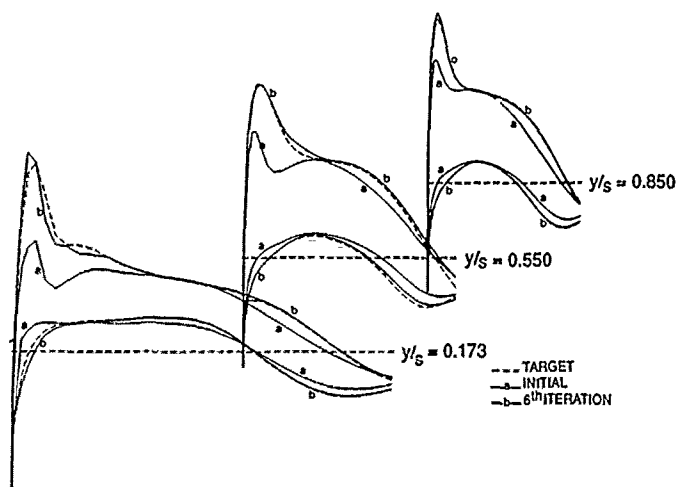
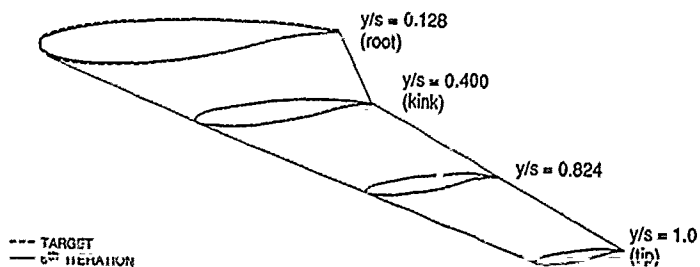


Fig. 6 F4 wing attached to pencil shaped body used as an example



a) Results for the pressure distribution at three spanwise stations (near root, near midspan, near tip)+



b) Results for the geometry at four spanwise stations

Fig. 7 Results of F4 wing reconstruction with influence of body for $M=0.75$ and $\alpha=0^\circ$ (the target corresponds to the original geometry of fig. 6)

A FAST COLLOCATION METHOD FOR TRANSONIC AIRFOIL DESIGN

by

Sergio De Ponte*, Maurizio Boffadossi† and Claudio Mantegazza**
 Politecnico di Milano — Dipartimento di Ingegneria Aerospaziale
 Via Golgi 40
 I-20133 Milano
 Italy

ABSTRACT

In the method of fictitious gas for transonic airfoil modification, it is attempted to introduce a fully elliptic calculation code by the use of compressibility sources.

This is done both with the idea of overcoming some of the finite-difference limitations and in order to reduce the computational time.

Taking as reference the standard Hess-Smith panel method in two dimensions, compressibility effects are taken into account by means of source panels into the flowfield. The panels form a grid which is limited in extension only where Mach number gradients are expected and much more limited compared to usual computational domains.

The system is fast and in general does not present convergence problems from the practical point of use, although large numbers of iterations may have some convergence problems.

The final result is always a very strong reduction in wave drag of the airfoil, as it is the aim of the method.

Notation

L	Chord length	∇	nabla operator
V	Velocity vector	ϕ	Velocity potential
u	x-component of velocity vector	ρ	Density
v	y-component of velocity vector		
x, y	geometrical coordinates		

INTRODUCTION

The "fictitious gas methods" are rather well known as a mean of inverse airfoil design (1).

Their advantages may be summarized as follows:

- they do not modify the airfoil nose,
- they allow a few number of free parameters,
- they do not produce shockless flow only near the contour and shock waves in the field.
- they tend to modify the airfoil so that the pressure distribution is similar to the subcritical one.

The first advantage means that it is possible to improve high speed performances without reducing the low speed capabilities. Other methods, like optimization, may introduce simple empirical correlations as upper surface coordinates, which are reliable only for rather thin airfoils.

The second is related to the simplicity of the parameter choice and the versatility of it. In fact, in many cases, simply one parameter is needed for the fictitious gas law.

The third is very significant, because there is no grant that a regular pressure distribution on the airfoil contour will mean a fully regular flowfield. Although it could avoid shock induced separation, it will not avoid large wave drags.

The last one is one of the most attracting: while there is no rationale proof of the fact, it is interesting to note that the tendency of reproducing similar pressure distributions allows an airfoil design based on boundary layer concepts.

This is true because the Mach number influence on boundary layer parameters is rather small so that an approximate but reliable procedure.

All considerations show an interest of the method in designing airfoils for rather high lift coefficients at rather low Mach numbers, as for transport airplanes, while, probably, inverse or actual state optimization methods, except the most complex, are more suitable for combat aircraft wings.

*Politecnico di Milano †winner of "Foresio" fellowship **Aermacchi

A brief summary of the "fictitious gas" concept is the following: It is assumed that the flowfield is represented by its correct equations in the subsonic part, while in the supersonic part the equations of motions belong to a fictitious gas and are elliptic. Fictitious gas has in fact any relationship between density and Mach number to produce elliptic equations. It is therefore possible to introduce one or more free parameters in the law, in order to allow some freedom. At this stage, a fictitious sonic line divides the flowfield into a correct and fictitious part. This sonic line is regular and the velocity field is continuous across it.

At this stage it is possible to attempt to solve the flowfield inside the fictitious part by correct equations, trying to define a new contour of the body, starting from the shape of the sonic line. If the attempt is successful, we have to exact parts of the flowfield, so that the all stream is represented by correct equations.

Of course, there is no theoretical proof that the procedure is successful, but with a good choice of the free parameters it is usually possible to find a quick solution.

The proposed method is new only in the solution of the elliptic equations, while all the rest of the procedure is quite similar to the usual one.

Taking into account that we need to solve an elliptic flowfield, it is attempted to solve it by means of a modified incompressible code, and the choice is a collocation method.

Compared to finite difference solution, it has some advantages. First of all, it is very fast because it does not require a change in the influence matrix, which could be inverted or factorized once for all. Second, it is possible to limit the computational domain, because the representing functions automatically represent the farfield, i.e. obey to asymptotic conditions: this avoids to approach infinity in some way. Third, they allow the usual form of displacement thickness corrections in the same standard ways as in incompressible flow.

The compressibility is therefore represented by sources in the near field, where Mach number gradients are significant, while the other farfield is constant density, therefore incompressible. Of course this limits only to subsonic onset flows, but this is practically also a limit of the fictitious gas method.

The problem is non linear in a full-potential formulation, and is solved by simple iteration.

In this way there is no limit either in angle of attack or in airfoil shape, as in usual incompressible collocation methods. In principle, there is no limitation to two-dimensional case.

1) THE SOURCE FIELD

Potential flow equations are written in their complete form for the two-dimensional field. The velocity divergence is non zero and may be written in the following form, where the right-hand side represents the non harmonic part:

$$\text{div } V = -u \partial \epsilon / \partial x - v \partial \epsilon / \partial y$$

and it is assumed at the n-th iteration that the Mach number distribution is known from the previous iteration. From the Mach number we obtain the density either for real or for the fictitious gas. We need therefore the first derivatives of the velocity vector and of the speed of sound, i.e. of the temperature as usual thermodynamic relationships. The velocity derivatives are different in harmonic and non harmonic potential flow and it is therefore impossible to represent the compressibility by discrete point sources. Any attempt to do so, will lead to the impossibility to connect the source field to the Mach number and therefore to iterate the procedure.

The key of the method is to represent the Mach number gradient by locally constant source distribution in a discrete number of points in the field. For seek of computational speed, the compressibility induced field on the body contour is afterwards computed by discrete sources collocated at the same points, with the same strength as used to compute the Mach number gradient.

In terms of potential, the previous equation may be rewritten in the form:

$$\text{div } V = \frac{u^2}{a^2} \frac{\partial^2 \phi}{\partial x^2} + \frac{v^2}{a^2} \frac{\partial^2 \phi}{\partial y^2} + 2 \frac{uv}{a^2} \left(\frac{\partial^2 \phi}{\partial x \partial y} \right)$$

which shows the non linear nature of the equation and the appearance of the second derivatives of the potential, i.e. the first derivatives of the velocity. Also the Mach number components u/a and v/a appear in the equation.

This divergence is represented by the sources and induces a velocity field on the airfoil collocation points. This field is added to the constant onset flow and treated in the same way, except for the point that it changes at each iteration. It is easy to see that at each iteration the only unknowns are the singularities on the airfoil and we need to solve a system of equations equal to the unknown. We use a standard Hess-Smith method where we have an unknown source for each collocation point and a single vortex distribution and a normal velocity condition for each collocation point plus the Kutta condition.

Only the right-hand side of the system of equations changes with iteration and therefore the system matrix remains unchanged. Also the influence coefficients of the field sources is dependent only upon the geometry and may be computed only once. The resultant computing code is therefore rather fast.

As starting flow condition, either incompressible flow or Prandtl-Glauert corrected flow may be used. Both were tested, and of course the latter leads to faster convergence. It should be noted that, in any case, for compressible subsonic flow fields, the simple compressibility source method is a fast and accurate computational code.

The source field has two many advantages with respect to differential equations: first, the system matrix is unchanged during the iteration process, so that it might be inverted or factorized once as for incompressible calculations.

The second advantage is that source strength is significant only in two conditions, i.e. where velocity gradients are large and Mach number is not low. This means that the sources might be distributed only in a limited flow part around the airfoil. Furthermore, the source influence on the airfoil is inversely proportional to their distance from the contour.

In general, the nose is the most critical part is around the former stagnation point, near the airfoil nose.

A second point is that source points must be closely placed where Mach number gradients are not small, otherwise their spacing might be larger.

According to the former considerations, it is useful to lay a panel mesh on the flowfield and put constant strength sources on each panel.

2) THE CHOICE OF THE GRID

As seen, the source field should be divided into elements defined by a grid. This grid has quite different requirements from a grid for finite-difference calculation, and is requiring features similar to the standard panel methods. Therefore its shape is different from usual computational grids.

We may summarize the main requirements.

a) The grid should be aligned to the airfoil contour.

b) The elements should not be stretched too much in one direction, otherwise "control" points may lay close to singular points.

c) Grid should be finer where larger density gradients are expected, i.e. near the leading edge.

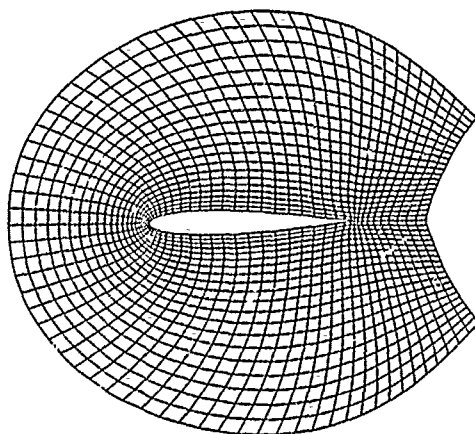
d) The grid should include only the significant part of the source distribution in a simple form. After that, there is no requirement for orthogonality of the grid.

After some tests, described in (2), the chosen grid is the following, called a "ballistic analogy". A first family of mesh lines is made by the trajectories of points "shot" in direction normal to the contour from panel nodes in a quadratic gravity field depending on three parameters. The quadratic form allows to bend forwards the lines in the nose region and afterwards in trailing edge region. The second family is made by lines connecting points positions at constant time intervals.

The final result is a "C" mesh around the airfoil matching the panel distribution of the Hess-Smith method. A further "homogenization" of the grid is necessary around the trailing edge: it cancels the effect of the trailing edge angle.

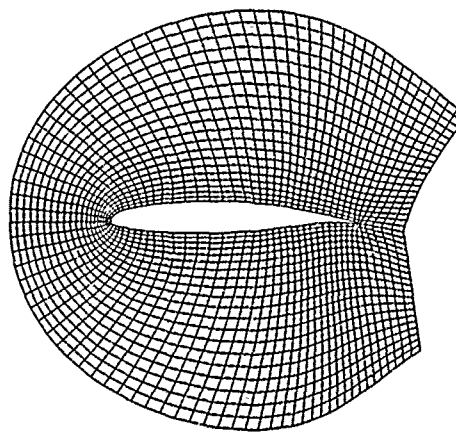
Figure 1 shows examples of grid

NACA0012



2000 2-4.00

GAW2



2000 2-4.35

2000 2-1.55

3) SOME PRELIMINARY RESULTS

After the simple test of fully subsonic flow, which gives fast converging and accurate results after 3-5 iterations (1 or 2 starting from Prandtl-Glauert correction), tests were made to compare final results. Of course, fictitious gas solution by itself cannot be compared to other analytical solutions because they are not correct, and only the final, modified airfoil contour could be compared in transonic regime. This is a disadvantage, because all the errors of the supersonic flow calculations are included in the comparison. In the actual case, simple straight segment method of characteristics and simple Euler integration of the contour gave not very accurate results.

But despite of those limits, a modified NACA 0012 airfoil was computed with a coarse mesh FLO-6 (3) code. The agreement was encouraging, although the FLO-6 gave a shock wave. Computed as an overall momentum defect, the wave drag was in all cases no more than one fourth of the one of the original airfoil, which is surely a good technical result.

In the figure the comparison is shown.

It became quite clear that the good results in subsonic regime and the less good in transonic could depend by a set of causes. One could be the parabolic nature of equations along the sonic line, while the method basis assumes elliptic equations, but the others could be related to the rough approximation of the supersonic region.

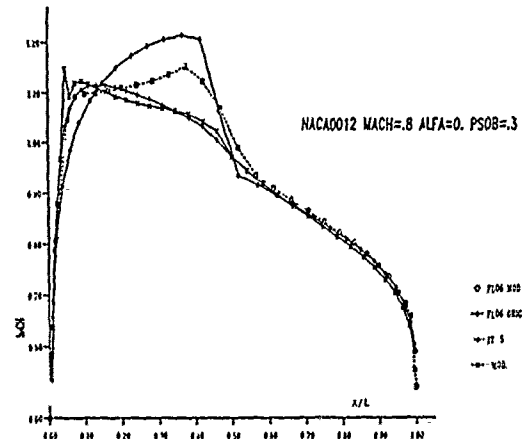
So a further investigation work regarded the three problems of smoothing the sonic line shape, improving the supersonic calculations by a quadratic approximation of the characteristics and introducing a second-order predictor-corrector scheme for the contour integration.

In order to avoid numerical accuracy embedded in the potential-flow code, an exact Joukowski airfoil and the Prandtl-Glauert corrections were used at this stage.

In this way it was possible to decouple the numerical errors of the supersonic flow calculations from the source field code.

The sonic line was smoothed by Fourier-series representation, filtering high order harmonics in a reasonable way. Good results were obtained retaining no more than 20 terms (4).

Of course, because the Prandtl-Glauert correction is not exact, this kind of results could not be compared to transonic code calculations, but the effect of a much smaller error in the closure of the contour at the last supersonic point was an indication of the increased accuracy.



4) PROBLEMS OF CONVERGENCE

Stating that the computational code was at a reasonable development stage, it was decided to investigate the convergence far beyond the 5-10 iterations used up to that point. A wide range of Mach numbers and lift coefficients was therefore investigated.

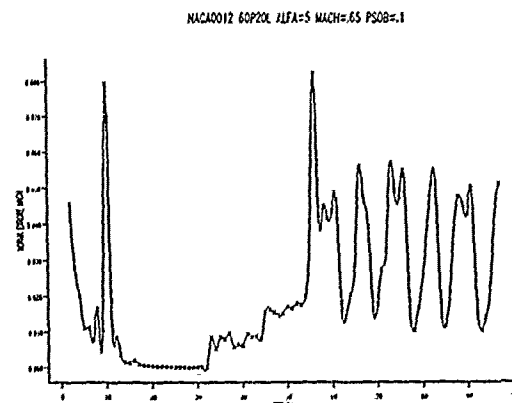
A typical "strange" convergence history is shown in the figure. It is not only strange in aspect, but also because it seems to be "FORTRAN compiler dependant", as with a change of the compiler all oscillations disappeared in some cases!

The convergence is very fast in the first steps, but at some point there is a sudden divergence followed by a further convergence, in some cycle-like behaviour.

In all tests no relaxation was attempted, to have an insight into the problem.

It might be supposed that a simple .5 relaxation parameter could avoid many problems, but the fact that oscillations in convergence appear only at a number of iterations probably larger than any required in a design procedure has suggested to fix simply the number of iterations required in the computation.

The figure shows one of the most critical convergence histories, while in many cases there is not any oscillation.



5) COMPARISONS AND RESULTS

After the first adjustment of the computational code, it was tried to modify systematically a set of airfoils for transonic operations.

First tests were made at low lift coefficients, in order to have a sonic line monotonically increasing in the X axis direction in its first part. On the other hand, at high lift peaks in the airfoil nose, the sonic line turns forward putting a lot of geometrical problems in the supersonic calculations. They are simply problems of code organization and not conceptual problems regarding the nature of the solution.

The convergence was fast and after no more than ten iterations it was attempted to modify the airfoil.

Of course, one does not know "a priori" the new airfoil contour, so that before the end of the computation it is impossible to know if the supersonic part of the flow, laying between the sonic line and the modified contour is effectively shockless.

In any case, there is a remarkable tendency to crossing of characteristics in the inner part of the airfoil, both close to the beginning and to the end of the sonic line. But in no case it was necessary to change the choice of the fictitious gas parameters, while using the laws suggested by Sobieczky (1). Only an attempt to use the fictitious gas of Nakamura (5) gave significant shocks. The reasons of that were not investigated and the laws of Nakamura were no more attempted.

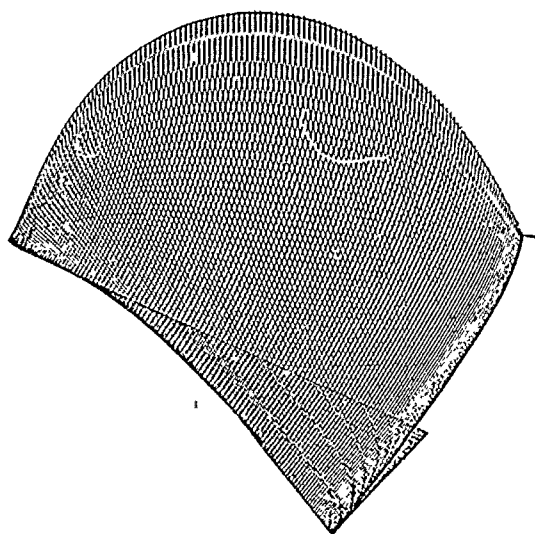
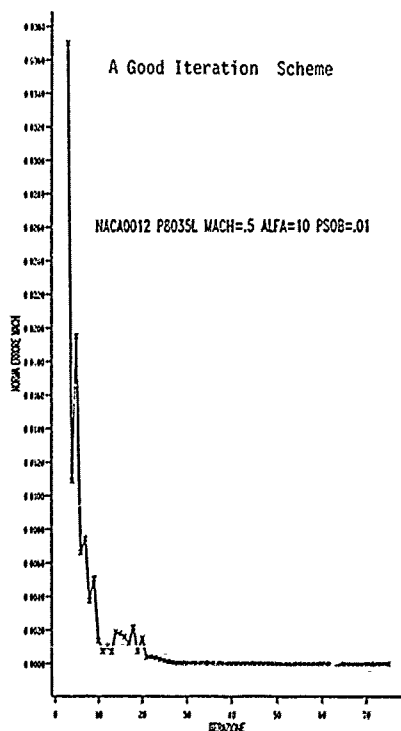
Comparisons with FLO-6 calculations gave again a shock-like behaviour, in the sense that around the end of supersonic regions there is, at least, a steeper pressure recovery as in the design calculations. An attempt to refine the FLO-6 mesh led to pressure oscillations, probably due to the insufficient experience in the use of this code by the authors, so that it is difficult to say whether the pressure gradient is a numerical error of the comparison code or not.

Further comparison with an Euler code calculation will be attempted but is not available up to now.

In any case, the comparison of computed original airfoil and the modified one by means of the same code gave a strongly reduced wave drag. From a technical point of view it is surely a success.

It is difficult to evaluate data for a computer time estimation for two reasons. The first is that the code is not optimized in the informatics sense of view, and the second is that, due to the lack of central memory of the virtual machine on which computations were performed, it was necessary to recompute the influence coefficients of the field sources at each iteration step, while with a more powerful machine they could be easily kept in the central memory. Of course, the effect on computational times is very large.

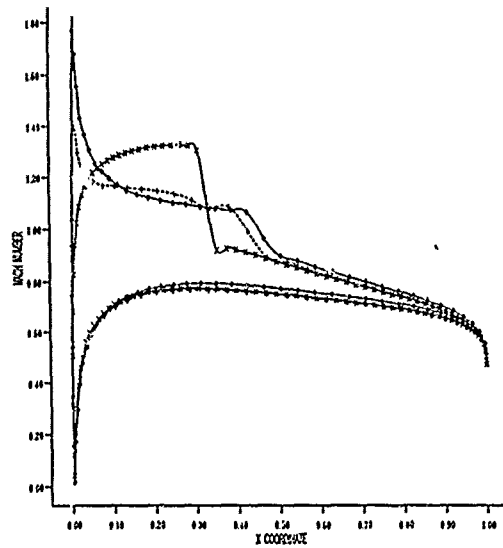
The following figures show some of the comparisons.



A Refined sonic line and its characteristic net

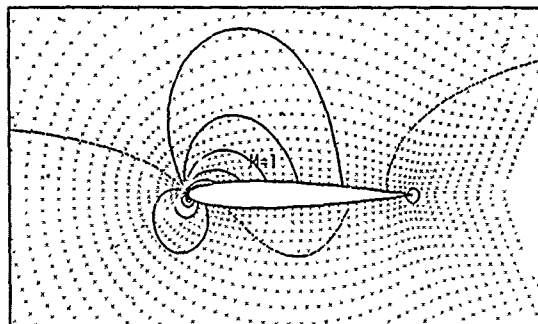
NO. 1000000 PAGE 1000000 PREPARED MAY 15, 1969 11:24

NACA0012 ALPHA=3. MACH=.7 PSOB=.0001 (MOD. CA)



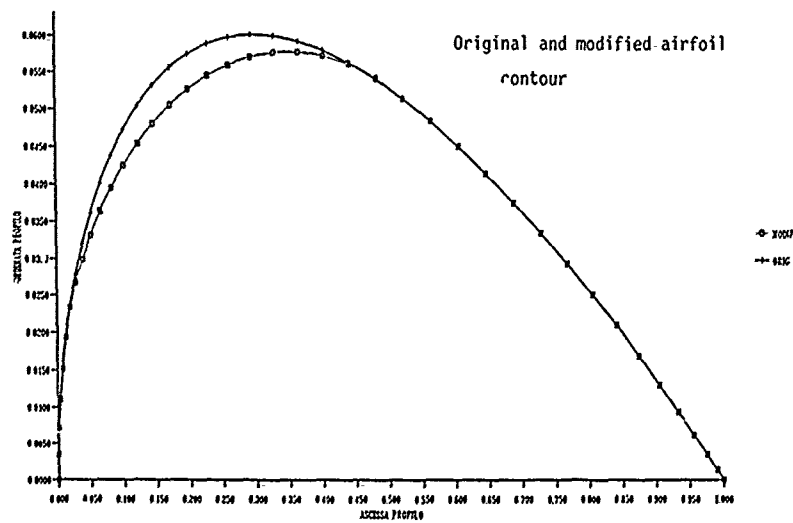
NACA0012 ALFA=3 M=.7

--- M = 0.70 STEP = 0.100



NO. 1000000 PAGE 1000000 PREPARED MAY 15, 1969 11:17

NACA0012 ALPHA=3 MACH=0.7 PSOB=.001 (MOD. B1)



6) STUDIES FOR A 3-D METHOD

Although the method was implemented for airfoil design only, a set of studies is starting for extending it either to axisymmetrical or fully three-dimensional cases.

An axisymmetrical code will require the evaluation of elliptic integrals for the calculation of the velocity derivatives, and was not attempted.

3-D models will require a difficult grid calculation, so that it was suggested to see if it would be possible to work in a rectangular frame.

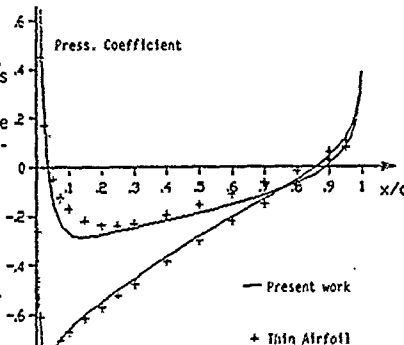
As first, it was seen if it could be possible to write a computational code in which panels are inside the contour and parallel to the chord (or X axis in some case) while the usual normal velocity condition is retained on the contour. The fact that the singular points at the end of panels are not coinciding increases the level of singularity. After a long work (6), it was shown that it is possible to find a solution and it is to represent the airfoil nose by matching it to a Rankine ogee and to include its source field in the onset flow. In this way panels mean only a small correction and the calculations are of the same accuracy as the usual panel methods.

The figure shows a typical result as compared to the Hess-Smith and thin airfoil results.

Keeping that in mind, it would be possible to extend the method to three-dimensional flows.

Of course, the method of characteristics is no more the best one, but the method proposed by Ziqiang and Sobieczky (7) seems to be promising.

This is the actual stage of the work and no further result is now available.



7) CONCLUDING REMARKS

The use of field sources instead of complex transonic code was successful in fictitious gas airfoil design and is a good alternate to finite-difference codes.

In principle, the following advantages might be seen:

- there is a less strict requirements for grids, both in geometrical properties and extension into the field, as compared to finite difference codes,
- there is only one, rather small size matrix to be solved and its behaviour is well known, as it is the Hess-Smith method matrix with all his troubles and its advantages,
- the method is fast converging towards a good technical approximation, with no "tricks", although large iteration numbers pose some convergence problems,
- we do not see any large difficulty to extend the method to wing design.

Of course, further investigation is needed, mainly from the point of view of an industrial use, but the main part of the research might be considered to be well-established in two dimensions.

REFERENCES

- 1) Sobieczky, H. "Design of Advanced Technology Transonic Airfoils and Wings" AGARD CP 285, 1980
- 2) De Ponte - Boffadossi - Mantegazza "Le sorgenti di comprimibilità nella continuazione ellittica di un campo transonico" IX Congr. AIDAA - Palermo, 1987
- 3) Jameson, A. "Transonic Flow Calculation" Numerical Methods in Fluid Dynamics - McGraw-hill, 1978
- 4) Preatoni, M. "Continuazione ellittica di correnti transoniche" Thesis, Milano, 1987
- 5) Nakamura, M. "A Method for Obtaining Shockless Transonic Flows Past Two-Dimensional Airfoils Whose Profiles are Partially Modified from a Given Arbitrary Profile." Japan Soc. Aero. Space Sci. Vol 23 No.62, 1981
- 6) Colombo - Fiecchi "Calcolo aerodinamico per collocazione con elementi paralleli agli assi coordinati" Thesis, Milano, 1988
- 7) Ziqiang Z - Sobieczky, H. "An Engineering Approach for Nearly Shock-free Wing Design" ICFM Beijing, 1987

* This research was partially supported by CNR (Italian research council)

SUBSONIC AND TRANSONIC BLADE DESIGN BY MEANS OF ANALYSIS CODES

R. A. Van den Braembussche, O. Léonard, L. Nekmouche
von Karman Institute
Rhode-Saint-Genèse, Belgium

ABSTRACT

An iterative procedure for cascade blade design, using a direct flow solver and a blade geometry modification algorithm is presented. The procedure starts with the analysis of a given cascade geometry using an existing flow solver. The difference between the calculated velocity distribution and the required one is used as an input for the modification algorithm. This procedure results in the definition of a new blade shape for which the calculated velocity distribution is closer to the desired one.

Examples for both subsonic and transonic flow are presented and show a rapid convergence to the geometry required for the desired velocity distribution. The main advantage of the proposed method is that existing analysis codes can be used, for the design and for the off-design analysis.

Some restrictions which have to be imposed on the required velocity distribution are also discussed.

LIST OF SYMBOLS

c	chord length	γ	strength of a vortex
H	coupling factor	Γ	circulation
M	Mach number	λ	blade stagger angle
n_x, n_y	local normal vector components	ρ	density
N	number of vortices on the contour	σ	solidity
P	total pressure	ξ, η	vortex coordinates
p	static pressure		
s	curvilinear coordinate	subscripts	
t	pitch of the cascade	n	component normal to the blade
T_o	total temperature	t	component tangential to the blade
W	velocity	1	cascade inlet
x, y	local coordinates of the blade contour	2	cascade outlet
greek symbols		superscript	
β	local slope of the blade contour	req	required
β_1	inlet flow angle (with resp. \vec{ox})		
β_2	outlet flow angle (with resp. \vec{ox})		

1. INTRODUCTION

In order to improve the performances of a compressor or a turbine, it is important to design aerodynamically efficient blade profiles. In the past, this was done iteratively by successive modifications of the blade geometry and experimental verification or by direct flow calculations. However, depending on the designer experience, such a process can be very time consuming and can result in increased design costs. Moreover it does not always lead to the expected results.

A more efficient approach is the use of inverse design methods. Starting from a given velocity or pressure distribution imposed on the two sides of the blade, the calculation results in the blade geometry. The classical boundary conditions of zero through-flow at the blade wall, used in direct solvers, are replaced by other boundary conditions which impose the required velocity or pressure distribution. The direction of the flow is an unknown and the velocity can have a component normal to the wall. The normal velocity component is then used to modify the blade shape. Depending on whether or not this normal component goes in or out the computational domain, the blade wall has to be treated just as a subsonic inlet or outlet, and complementary boundary conditions may be needed.

Alternatively, a direct calculation code can be used as the base of an inverse method, if it is coupled with a suitable blade modification algorithm. The modification algorithm proposed here is derived from the singularity theory and is based on the superposition principle. It is therefore correct only for incompressible potential flows, however, experience has shown that it can also be efficiently used for compressible flows. The way in which the blade geometry is calculated may be physically less accurate than that derived from the modified boundary conditions, it has however the great advantage of simplicity, allowing the use of accurate and efficient direct solvers which have been developed in the past and are well documented in the literature. Using the inviscid direct solver, the resulting geometry includes the blade and the boundary layer displacement thickness, while the use of a Navier-Stokes solver would result directly in the blade geometry.

Another advantage of the use of a direct solver is that, once the blade geometry has been determined, the off-design analysis can be carried out using the same flow solver.

2. BLADE DESIGN PROCEDURE

The method starts from an initial approximation of the blade geometry which is analysed by a direct solver. If the calculated velocity distribution is not close enough to the required one, the initial blade geometry must be modified.

This is done by distributing vortices on the blade contour, the strengths of which are defined in such a way as to adjust the local velocity to that required. The blade shape is then modified using an algorithm based on the transpiration method or by recomputing the position of the wall streamline. The new blade shape is not yet the final one since the required tangential velocity was imposed on the previous blade approximation.

Once the blade shape has been modified, a new velocity distribution is calculated by the flow solver. This procedure of modifying the blade geometry and calculating the velocity distribution is repeated until the difference between the required and the calculated velocities is small enough. The procedure is summarised in fig. 1.

3. BLADE MODIFICATION ALGORITHM

The blade modification algorithm consists of two parts :

- define a vortex distribution on the blade contour. This is done to modify the tangential velocity to adjust it to the required value; it allows the calculation of a normal velocity component;
- use the normal component of the velocity to define a new blade shape.

3.a. Calculation of the Normal Velocities

The actual modification algorithm makes use of the singularity theory to modify the tangential velocity at each point of the blade contour where it may be required.

The first effect of a vortex distribution is to create a difference between the tangential velocity at the outer and the inner part of the contour :

$$W_{to} - W_{ti} = \gamma \quad (1)$$

this difference being equal to the local vortex strength. Moreover, the flow field induced by the vortices must be defined in such a way as to obtain zero tangential velocity inside the contour as a kinematic condition. Therefore we have :

$$W_{to} = \gamma \quad (2)$$

If we want to increase or to decrease an already existing velocity locally at the outer side of the blade, a vortex can be added with its strength defined as :

$$\Delta W_t = \gamma \quad (3)$$

or

$$W_t - W_t^{req} = \gamma \quad (4)$$

A second effect of this vortex distribution is the creation of a velocity normal to the blade contour, which for a cascade is given by :

$$W_n = \frac{1}{2t} \oint \frac{\sinh X \cos \beta + \sin Y \sin \beta}{\cosh X - \cos Y} \gamma ds \quad (5)$$

with :

$$X = \frac{2\pi}{t}(x - \xi)$$

$$Y = \frac{2\pi}{t}(y - \eta) \quad (6)$$

where ξ, η are the vortex coordinates and x, y is the location where the value of W_n is calculated.

This normal velocity-flow field must be superimposed with the velocity field calculated by the solver.

The discretization of (5) for N intervals results in :

$$W_n(i) = \frac{1}{2t} \sum_{j=1}^N H(i, j) \gamma(j) \Delta s(j) \quad (7)$$

with

$$H(i, j) = \frac{\sinh X \cos \beta + \sin Y \sin \beta}{\cosh X - \cos Y} \quad (8)$$

Calculation of the normal velocities W_n at the N positions where the vortices are located results in the following linear system of N equations :

$$\begin{pmatrix} W_n(1) \\ W_n(2) \\ \vdots \\ W_n(N) \end{pmatrix} = \begin{pmatrix} 0 & H(1,2) & \dots & H(1,N) \\ H(2,1) & 0 & \dots & H(2,N) \\ \vdots & \vdots & \ddots & \vdots \\ H(N,1) & \dots & H(N,N-1) & 0 \end{pmatrix} \begin{pmatrix} \gamma'(1) \\ \gamma'(2) \\ \vdots \\ \gamma'(N) \end{pmatrix} \quad (9)$$

with

$$\gamma'(j) = \gamma(j) \Delta s(j) \quad (10)$$

Unfortunately the matrix H has a zero diagonal since a vortex has no contribution to the local normal velocity. This can give rise to a wavy velocity distribution since two adjacent vortices $\gamma(i-1)$ and $\gamma(i+1)$ of the same sign and equal strength induce zero normal velocity at the point i .

Since a vortex cannot create flow, the total mass flux induced by each vortex across the closed profile must be equal to zero. Therefore we have :

$$\oint W_n ds = 0 \quad \text{for each vortex} \quad (11)$$

or

$$\sum_{j=1}^N H(i,j) \gamma(j) \Delta s(j) = 0 \quad j=1 \dots N \quad (12)$$

In order to correct the numerical error introduced by the discretization, a normal velocity is calculated by (11) and added at each point to that calculated using (7).

3.b. Modification of the Blade

Two models can be used to define a new blade shape. The basic procedure is to calculate the new position of the wall streamline resulting from the superposition of the W_t flow field and the W_n flow field.

In the transpiration model, the old blade wall is considered as porous with a normal velocity going through it. The mass balance is applied in the cell defined by the points $(i)^{old}$, $(i-1)^{old}$, $(i)^{new}$ and $(i-1)^{new}$ as shown in fig. 2a. This results in :

$$d(\rho W_t \Delta n) = \rho W_n ds \quad (13)$$

or in discretized form :

$$\Delta n \rho W_t|_{i-1} + \Delta s \frac{\rho W_n|_i + \rho W_n|_{i-1}}{2} = \Delta n \rho W_t|_i \quad (14)$$

Expression (14) allows the calculation of the shift Δn_i if Δn_{i-1} is known.

The streamline model calculates the position of the new blade wall by setting this wall parallel to the local velocity $\vec{W} = \vec{W}_t + \vec{W}_n$ as illustrated in fig. 2b.

This results in :

$$\Delta n(s) = \int_0^s \frac{dn}{ds} ds = \int_0^s \frac{W_n}{W_t} ds \quad (15)$$

The discretized form of (15) is :

$$\begin{aligned} x_i^{new} - x_{i-1}^{new} &= x_i^{old} - x_{i-1}^{old} + \frac{\Delta s}{2} \left\{ \frac{dn}{ds}|_{i-1} + \frac{dn}{ds}|_i \right\} n_x \\ y_i^{new} - y_{i-1}^{new} &= y_i^{old} - y_{i-1}^{old} + \frac{\Delta s}{2} \left\{ \frac{dn}{ds}|_{i-1} + \frac{dn}{ds}|_i \right\} n_y \end{aligned} \quad (16)$$

4. RESTRICTIONS ON THE REQUIRED VELOCITY DISTRIBUTION

Blade designs in which the required velocity is obtained from the analysis of an existing cascade do not show any particular problem. The method rapidly converges to the correct blade shape.

However, solutions for blade designs to be derived from arbitrary suction and pressure side velocity distributions do not always converge. This is related to the problem of the existence of a solution. The required velocity distribution must be compatible with the free stream conditions upstream and downstream of the cascade and must result in a realistic blade profile (closed with a positive thickness). These constraints generate restrictions on the required velocity distribution, analytical expressions for which are available only for incompressible potential flows over isolated airfoils and cascades; see [1] and [2]. Expressions for the constraints cannot be derived for the compressible flow of a perfect gas, but their existence can be inferred from the fact that the incompressible flow case is a subcase of the more general compressible flow problem.

A solution can be obtained by introducing some freedom into the prescribed velocity distribution, expressed by some parameters relating the velocity distribution to the free stream flow conditions. These parameters are then modified until the prescribed velocity distribution corresponds to a physical solution [3].

Another way to obtain a solution is to modify some geometrical parameters of the blades and the cascade such as pitch, stagger and trailing edge thickness.

The method presented should not suffer from problems with contour intersection because the blade is defined by streamlines. Contour intersections have been observed occasionally for very thin blades during the first geometry correction, when the blade modification is important. These are due to numerical errors that result when integrating the streamlines and can easily be avoided by introducing an under-relaxation factor.

Experience has shown that some simple restrictions on the desired velocity distribution can be defined. The blockage created by the non zero blade thickness requires the average prescribed velocity at the leading and the trailing edge to be higher than the free stream velocity upstream and downstream of the cascade. Violation of this condition will prevent the method from converging.

Increasing or decreasing the average velocity at leading and trailing edges allows the local blade thickness to be increased or decreased. If an inviscid solver is used, the trailing edge thickness will also include the boundary layer displacement thickness. This boundary layer displacement thickness can be calculated in advance since the required velocity distribution is known.

Similar restrictions also apply to the velocity distribution between leading and trailing edges. These are more difficult to formulate because they depend on the local flow direction which is not a priori known.

Other problems arise from the fact that the outlet velocity is not known in advance and that the Time Marching Euler solvers require an outlet boundary condition (static pressure, velocity or Mach number) to be specified on the downstream boundary. However, these outlet conditions can be calculated from the required velocity distribution and the continuity equation before starting the inverse calculations.

The circulation around the blades is calculated from

$$\Gamma = \oint W_t^{req} ds \quad (17)$$

and is related to the inlet and outlet tangential velocities by

$$\Gamma = (W_2 \sin \beta_2 - W_1 \sin \beta_1) t \quad (18)$$

The upstream velocity and flow angle are given in the input data.

The downstream axial velocity component is derived from the continuity equation :

$$\rho_1 W_1 \cos \beta_1 = \rho_2 W_2 \cos \beta_2 \quad (19)$$

The density at the outlet is a function of the outlet static pressure and therefore is a function of the unknown outlet velocity W_2 . For this reason, an iterative procedure is used to solve equations (17) to (19).

The outlet velocity is needed to verify if the required velocity allows for a solution and, if a Time Marching solver is used, to calculate the static pressure imposed as the boundary condition downstream of the cascade.

The procedure just described is valid only for irrotational flows and is therefore not exact if shocks are present.

5. NUMERICAL EXAMPLES

Four examples are presented to demonstrate the method. Two examples show the results obtained when the incompressible potential flow method, described in [4], is used as a direct solver. The other two examples make use of the Time Marching Euler solver described in [5]. Each solver has been used to design a compressor and a turbine blade. One turbine blade, designed for an outlet Mach number of 1.2, has also been analysed for a lower outlet Mach number to demonstrate the change in performance at off-design.

The first example demonstrates the procedure in the design of a compressor blade for incompressible flow with the required velocity distribution shown in figure 3a. The calculations use as a first guess a NACA-65(18A₁₀)10 blade at zero stagger (fig. 3b). The ratio of local velocity over inlet velocity obtained from a first analysis at $\beta_1 = 30$ deg. and a pitch-chord ratio of 0.9, is shown in figure 3c. The velocity distribution is very different from the required one.

For the same inlet air angle and pitch-chord ratio a new blade shape, shown in figure 3d, is obtained after 40 iterations. With a blade definition of 40 points, the CPU time on a VAX 180 for this example is 55 sec.. This new geometry is very different from the first guess (fig. 3b). The stagger angle has increased from 0 to 4.6 deg. and the new blade is much thicker. This large trailing edge thickness results from the required velocity distribution and accounts for both the geometrical blade thickness and the boundary layer displacement thickness on the pressure and suction side.

The potential flow calculation method does not account for wakes and the blade contour is therefore closed by rounding-off at the trailing edge. The blade velocity distribution agrees very well with the required one as shown in figure 3.e. Discrepancies are observed only at the last two points on the pressure and suction side, at the trailing edge round-off. The local overshoot of the velocity is due to the flow acceleration around the thick circular trailing edge and cannot be avoided with potential flow calculations.

The second example demonstrates the procedure in the redesign of a turbine rotor hub section. The velocity distribution on the initial blade is compared to the desired one in figure 4a. The last one has a considerably larger loading than the initial blade and the pitch-chord ratio has been increased proportionally to obtain the same outlet flow conditions.

The new blade shape, obtained after only 10 modifications, is compared to the initial shape on figure 4b. Also shown are the initial and new cascade parameters. Figure 4c shows the comparison between the required velocity distribution and that corresponding to the final blade shape. Discrepancies are observed at the leading edge pressure side where the calculated velocity is higher than the required one. This is a result of the special conditions discussed in the previous chapter. In particular, the mean value of the required pressure and suction side velocity at the leading edge is lower than the inlet velocity. This would imply a negative blade thickness (negative blockage). The discrepancy does not disappear when the number of iterations is increased.

The second solver to be demonstrated is a Time Marching procedure that solves the Euler equations for transonic flows in axial machines. This uses a corrected viscosity scheme with a finite area discretization. The calculation is carried out for a section of constant radius and no provision is made for a variable streamtube thickness. A full theoretical description of this solver, the system of equations, the discretization of the physical domain and the description of the input data are given in reference [5].

The modification method coupled with this solver does not satisfy the Euler equations since singularities are used, and is therefore not exact. However it can be assumed that the correction of the blade shape is in the right direction, and a rapid convergence to the required blade shape is observed.

Using the flow solver [5], this method was first demonstrated with a required velocity distribution calculated from a classical NACA-65 (12A₂I₈)10 blade. The NACA-65 (12A₁₀)10 blade was used as a first guess. The geometries of both blades are compared in figure 5a. The velocity distribution on the initial blade and the required velocity distribution are shown on figure 5b.

The flow conditions are: $P_1 = 1.33$ bar, $T_{01} = 341.5$ K, $\beta_1 = 45$ deg, $p_2 = 1.173$ bar. The cascade geometry is defined by $\lambda = 31$ deg and $\sigma = 1$ for both blades.

Figures 5c and 5d show the convergence of the calculated velocity. Good agreement with the prescribed velocity distribution is evident in fig. 5d, except for the leading edge and the trailing edge regions. This can be due to the fact that the discretization with a H-type grid is not suited to describe accurately the flow field in these regions. The comparison between the final blade geometry and the NACA-65 (12A₂I₈)10 is shown in figure 5e. The calculations are made with 71 stations in the streamwise direction and 21 points in the pitchwise direction. The CPU time on a VAX 780 was about 5 hours for 12 modifications.

The second example demonstrates the procedure in the design of a turbine blade. The starting geometry is that of the workshop VKI-LS 82-05 [6]. The flow conditions are: $P_1 = 1$ bar, $T_{01} = 278$ K, $\beta_1 = 0$ deg, $M_2 = 1.2$. The cascade geometry is defined by $\lambda = -60$ deg and $\sigma = 1.25$.

Problems have been encountered modifying the suction and pressure surfaces at the same time, since there is a strong interaction between both surfaces. The expansion waves starting from the pressure side trailing edge interact with the suction side.

To work around this problem, only the pressure side velocity was imposed during the first modifications. This reduces the expansion in the trailing edge region. Figure 6a shows the starting velocity distribution and the required velocity distribution, while figure 6b shows the velocity distribution after 2 modifications.

Once the required velocity distribution has been obtained on the pressure side, a similar procedure has been applied on the suction side, in which we impose simultaneously the suction- and pressure side velocity distribution. Six modifications were needed to obtain the required suction side velocity distribution. Figure 6c shows the final velocity distribution while the comparison of the initial and the final blade geometry can be seen in figure 6d.

Using the same Time Marching solver, an off-design analysis has been made for this final blade. Results are shown on figures 7a for $M_2 = 1$ and 7b for $M_2 = 0.8$. One can see that a blade which has been optimized for one outlet Mach number does not necessarily give a good velocity distribution at other outlet Mach numbers.

6. CONCLUSIONS

An iterative design method based on both potential and Euler type solvers and a geometry modification algorithm has been developed. Good results have been obtained for both subsonic and transonic cases. The modification is fast due to its physical basis, so that a limited number of iterations have to be performed. This modification algorithm can be coupled with any direct solver.

REFERENCES

- [1] Lighthill, J.M.; "A new method of two-dimensional aerodynamic design", ARC R&M 2112, Apr. 1945.
- [2] Woods, L.C.; "The design of two-dimensional airfoils with mixed boundary conditions", Quarterly of Applied Mathematics, Vol. 13, 1955, pp. 139-146.
- [3] Volpe, G. and Melnik, R.E.; "Role of constraints in inverse design for transonic airfoils", AIAA Journal, Vol. 22, No 12, Dec. 1984, pp. 1776-1778.
- [4] Van den Braembussche, R.; "The application of the singularity method to blade-to-blade calculations", in "Thermodynamics and Fluid Mechanics of Turbomachinery", NATO Advanced Sciences Institutes Series, series E, Applied Sciences, No 97A, 1984, eds A.S. Ucer, P. Stow and Ch. Hirsch, pp. 167-191.
- [5] Arts, T. and Van Hove, W.; "Cascade flow calculation using a finite volume method", VKI TN 146, Oct. 1982.
- [6] Arts, T.; "Numerical methods for flow in turbomachine bladings", Workshop on 2D and 3D flow calculations in turbine bladings, VKI LS 1982-05.

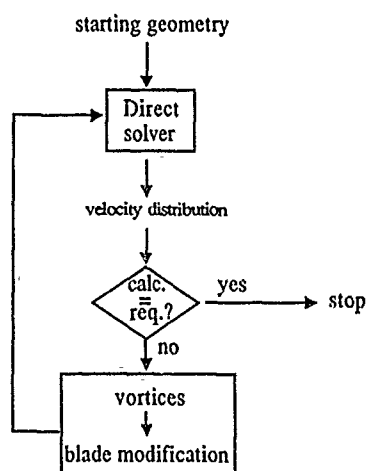


Fig. 1 Flow chart

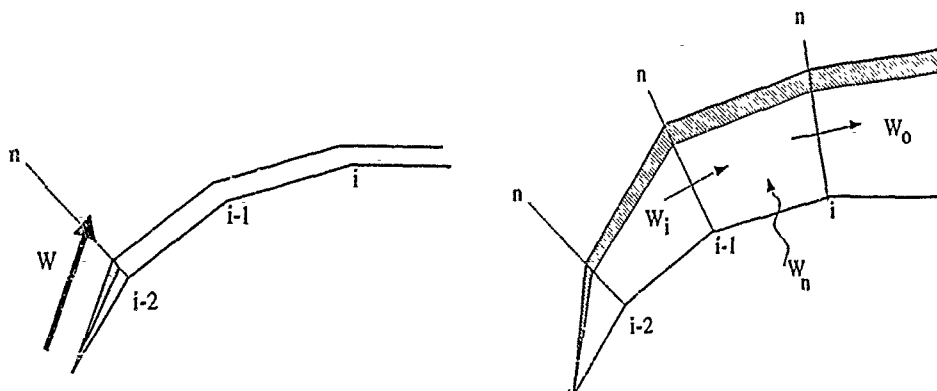


Fig. 2 Blade modification

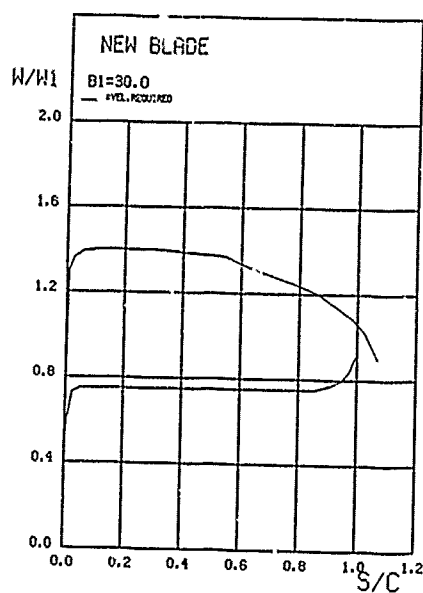


Fig. 3a Required velocity distribution

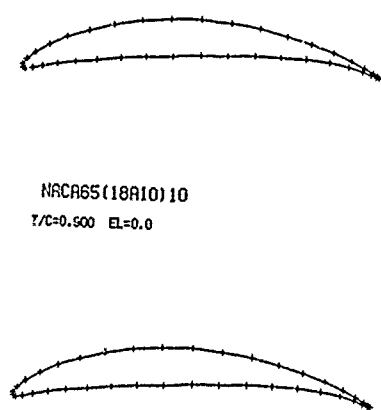


Fig. 3b Initial geometry

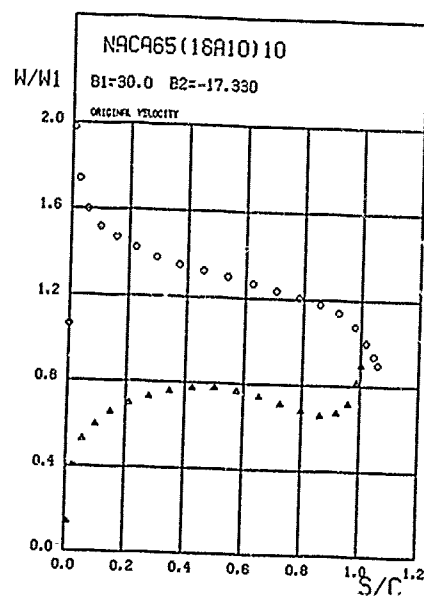


Fig. 3c Initial velocity distribution

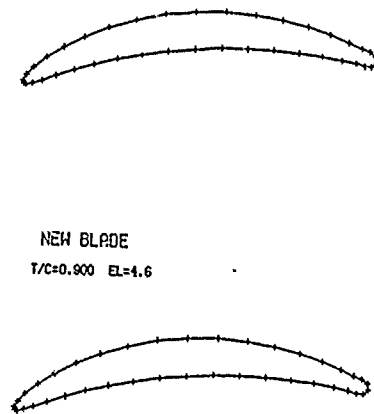


Fig. 3d Final blade geometry

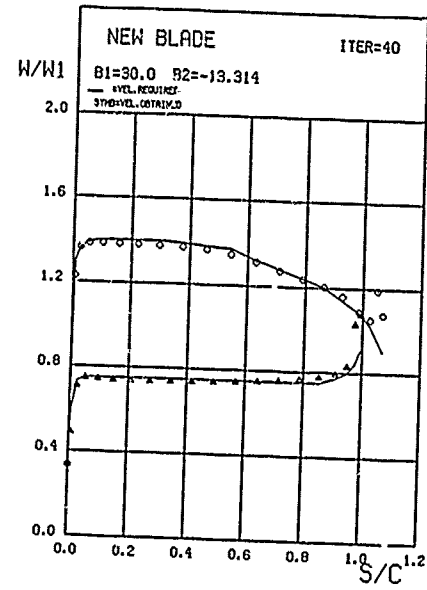


Fig. 3e Final velocity distribution

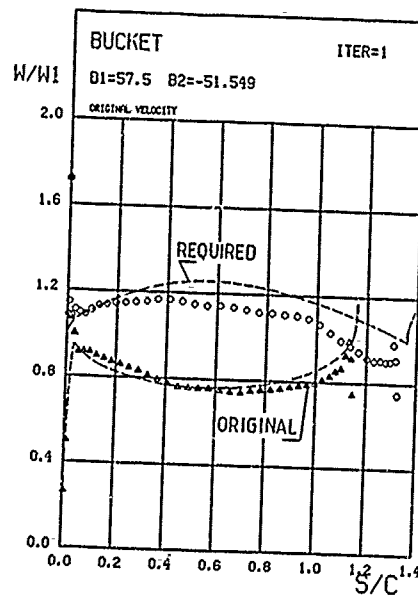


Fig. 4a Initial and required velocity distributions

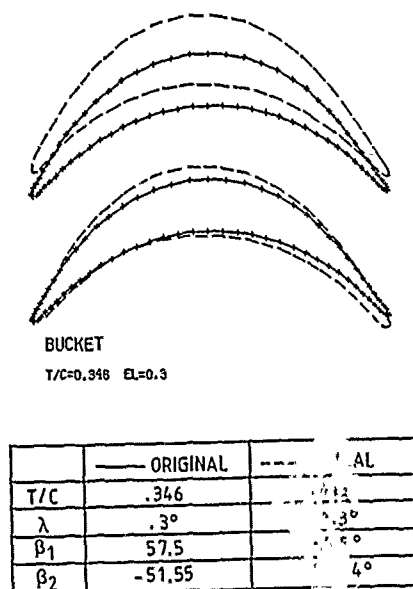


Fig. 4b Initial and final blade geometry

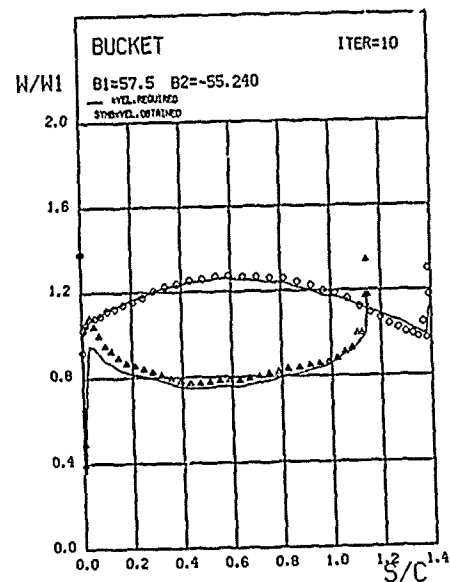
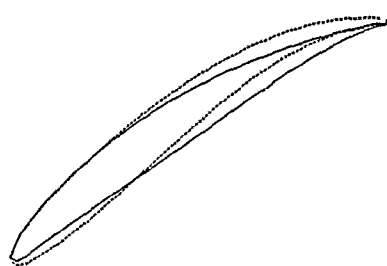
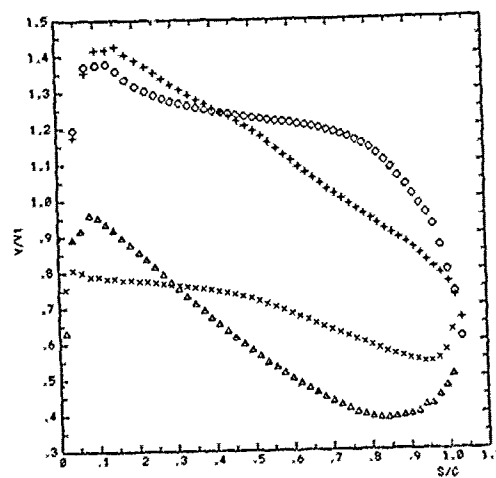


Fig. 4c Final velocity distribution

Fig. 5a NACA-65(12A₁₀)10 () and
NACA-65(12A₁₀)10 ()Fig. 5b Initial (+, x) and required (O, Δ)
velocity distributions

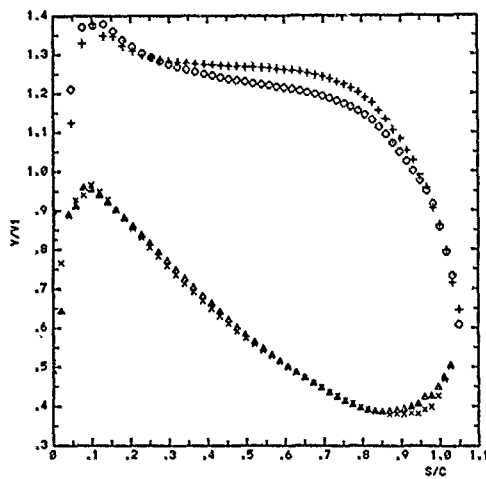


Fig. 5c Required velocity (O, Δ) versus velocity distribution obtained after 5 modifications (+, ×)

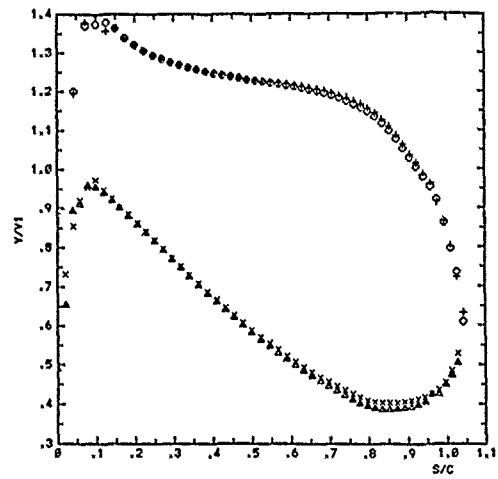


Fig. 5d Required velocity (O, Δ) versus velocity distribution obtained after 12 modifications (+, ×)

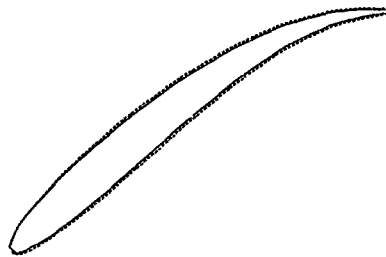


Fig. 5e Final blade shape (----) versus NACA-65(12A1J33)10 (—)

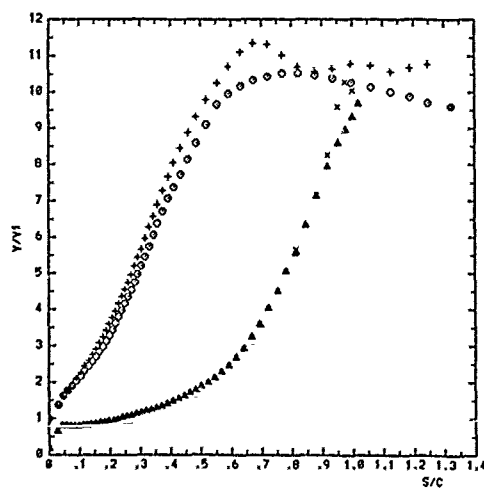


Fig. 6a Initial (+, ×) and required (O, Δ) velocity distributions

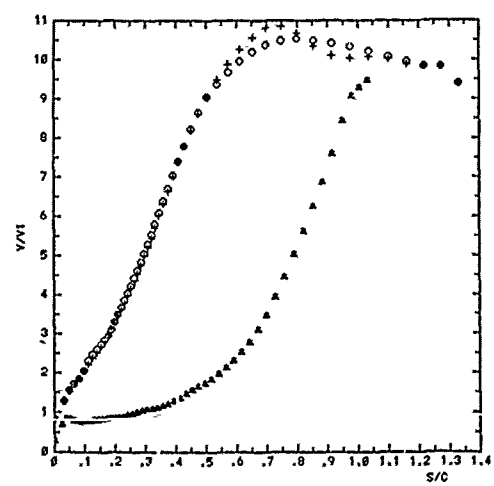


Fig. 6b Velocity distribution after 2 modifications of the pressure side only

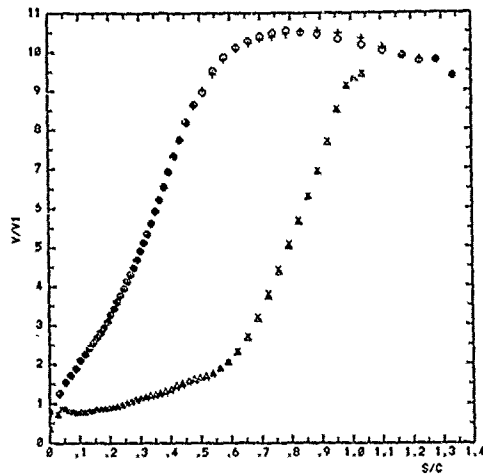


Fig. 6c Required velocity (O, Δ) versus velocity distribution obtained after 8 modifications (+, ×)

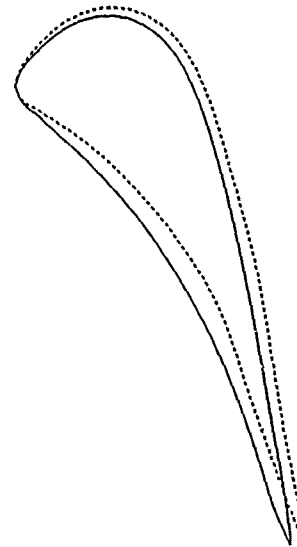


Fig. 6d Final blade shape (-----) versus initial blade shape (—)

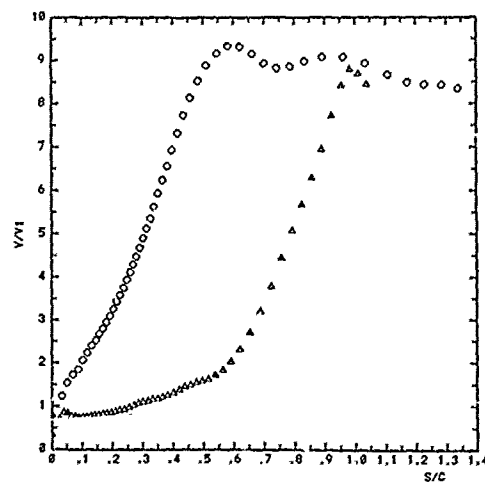


Fig. 7a Off-design velocity distribution ($M_2 = 1$)

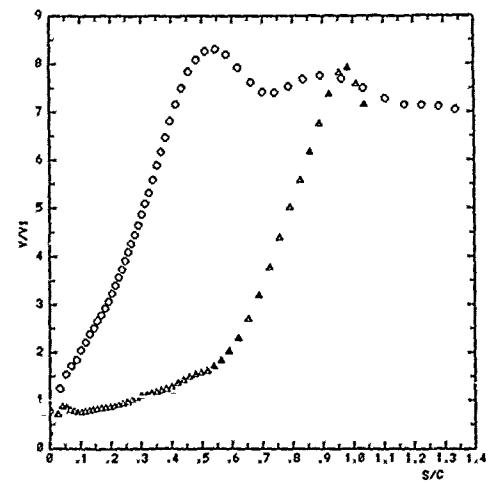


Fig. 7b Off-design velocity distribution ($M_2 = 0.8$)

A COMPUTATIONAL DESIGN METHOD FOR SHOCK FREE TRANSONIC CASCADES AND AIRFOILS

by
T.A. Cotinkaya
I.S. Akmandor
A.S. Ucer
Middle East Technical University
Ankara - Turkey

SUMMARY

A computational method has been formulated for efficient inverse design of blading. The surface pressure distribution is specified and, as a result, the geometric shape of an airfoil or cascade blade is obtained. A steady, two dimensional Euler code for transonic flow has been implemented. The code uses a finite volume technique on a computational grid which is based on assumed streamlines. The grid is being updated during the solution procedure. The blade contour, being a streamline, corresponds to a part of the solution domain boundary where the desired pressure distribution is given. Free parameters are introduced into the prescribed pressure distribution and this satisfies the closure constraints. Examples based on redesign of known shapes are presented.

LIST OF SYMBOLS

\vec{A}, \vec{B}	area vectors	α	angle of attack; inlet flow angle
A_n	area normal to velocity	Δn	displacement of current streamline node
C	axial chord	$\Delta \rho$	density change
C_1, C_2	multiplication factors of pressure distribution constraint	Φ	farfield velocity potential
C_L	lift force coefficient	γ	specific heat ratio
C_D	drag force coefficient	Γ	circulation
C_x	axial force coefficient	μ	artificial compressibility coefficient
C_y	pitchwise force coefficient	Π	pressure on streamline faces of a cell
f_1, f_2	cell geometry functions	ρ	density
g_1, g_2	cell geometry functions	Σ	source strength
F	arbitrary shape function	θ	angular polar coordinate
G	arbitrary shape function		
H	stagnation enthalpy		
I	unit tensor		
i	grid index along a streamtube		
j	grid index for streamlines		
\dot{m}	mass flow rate		
M	Mach number		
n_x, n_y	components of unit vector normal to current streamline		
P	pressure at inlet and outlet surfaces of a cell		
\mathcal{P}	prescribed surface pressure		
s	surface arc length		
S	pitch		
V	speed		
\vec{V}	velocity		
x	axial coordinate		
y	pitchwise coordinate		

INTRODUCTION

The aircraft and missile industries are in constant need of developing low drag -high lift -highly maneuverable, versatile transonic configurations with optimal design characteristics. The computational methods have been developed primarily to treat the direct problem of determining the load characteristic of a prescribed shape. Using these analysis methods, the shape has been modified by trial-and-error. More recently, analysis methods in combination with a numerical optimization to minimize an aerodynamic object function are appearing to be useful design tools [1,2,3] although they require excessive computational effort. Beside minimizing the difference between computed pressures and the target pressure distribution as a basic design approach, these methods can minimize other aerodynamic quantities such as drag.

The inverse problem is associated with the determination of the airfoil section shape that will produce a preassigned pressure loading or surface speed distribution. For incompressible flow, Lighthill [4] demonstrated that prescribed speed distribution can not be arbitrary and certain constraints must be imposed on this distribution. Similar constraints were expressed by Woods [5] for compressible, subsonic flow. Recently Volpe and Melnik [6]

emphasized on the necessity of the constraints on prescribed pressure distribution for transonic inverse design. Using this definition, the inverse design procedure finds an airfoil shape that produces a desired pressure as closely as possible.

Computational design procedures for transonic airfoils have been in use for many years. Hodograph design methods were developed by Nieuwland [7], Bauer, Garabedian and Korn [8], and Sobieczky [9]. In spite of their usefulness in development of shock-free airfoil sections, they require too many input parameters and have no direct control over geometry and aerodynamic quantities. Hodograph methods and fictitious gas methods [10,11] are oriented toward achieving shock-free designs, but don't address the problem of determining shapes which give prescribed pressure distributions. In this respect, they are categorized as indirect design methods. More recently an inverse design procedure [12] for subsonic airfoils, based on hodograph technique, has been developed to determine the shape that gives the prescribed pressure distribution.

Tranen [13] used the potential equation as a first attempt to solve two-dimensional transonic inverse airfoil problem. Similar approach by Volpe [14] in developing an inverse method for two-element airfoil systems. Carlson [15] used Cartesian coordinates in the physical plane instead of using a body forming mesh in the circle plane. However all these attempts are not well formulated because the issue of constraints are not addressed completely. Role of constraints are discussed by Volpe and Melnik [6] in a more recent potential flow approach.

Transonic inverse procedures for three-dimensional wings have been developed by Shankar, Malmuth and Cole [16] whose method is based on modified small disturbance theory, and by Gally and Carlson [17] whose method is based on a potential solver including a finite volume formulation.

This paper presents results obtained by a method similar to a design method developed by Giles and Drela [18]. In concept, it has similarities to both the streamline curvature analysis methods and the full potential inverse design methods. It is based on quasi-one-dimensional Euler solution of streamtubes. Using a solution domain as considered to be formed by a bunch of streamtubes, two-dimensional transonic cascade and isolated airfoil problems are handled. The finite volume techniques [19,20] are based on numerical discretization of conservation equations written in integral form. The flow domain is divided into several elemental control volumes (areas in 2-D case) which exchange mass, momentum and energy. In the present method, finite volume cells are fitted along the streamtubes. Therefore two of the faces of a cell correspond to streamlines and the flux will exist only on other two faces. The discretized Euler equations are linearized by a Newton-Raphson method and resulting system of linear equations is solved implicitly using a Gaussian elimination technique. The system of linear equations mainly corresponds to the streamwise momentum conservation on the cell basis and a condition of coupling of streamtubes by the pressure existing in their streamline interface. The unknown variables are both the density of fluid and the position of the streamlines. For inviscid flow, slip condition implies that the blade contour is a streamline. By imposing the target surface pressure distribution, on the streamlined grid boundary representing the blade, the code will find the blade geometry through the updating of streamline shapes together with the flow field.

FORMULATION AND DISCRETIZATION

Integral forms of mass, momentum and energy conservation laws are used for a steady, inviscid flow of a compressible, non-conducting fluid. These are :

$$\int_S \rho \tilde{V} \cdot d\tilde{s} = 0 \quad (1)$$

$$\int_S (\rho \tilde{V} \tilde{V} + P \tilde{I}) \cdot d\tilde{s} = 0 \quad (2)$$

$$\int_S (\rho \tilde{V} H) \cdot d\tilde{s} = 0 \quad (3)$$

where surface integral reduces to line integral along the closed curve bounding the flow area in the case of two-dimensional flow modelization. These integral equations are discretized by applying them on a conservation cell of the finite volume (area) method.

A part of initial grid and a conservation cell are shown in Fig. 1. A conservation cell is formed by connecting the mid-points of line segments between grid nodes. The geometry of the cell is completely known in terms of nodal coordinates of the grid at a solution step. If grid lines are labeled as j-constant lines and i-constant lines, where i and j are indexing parameters, j-constant lines are assumed to be streamlines. In the present method, one of the main task is to update the grid so that it would represent the actual streamlines when the algorithm converges to the solution.

The geometry of a conservation cell and the variables on its surfaces can be seen in Fig. 2. Since the upper and lower surfaces correspond to streamlines, there is no flux through them and the only contribution from these surfaces is the pressure force term in the momentum equation. The density ρ , pressure P , and speed V are defined to be uniform on inlet and outlet faces of the conservation cell. The direction of velocity is defined by taking the average direction of upper and lower streamline segments of the conservation cell. The discretization is possible if a different pressure variable Π is defined on the streamline faces to describe the pressure distribution in the pitchwise direction. For a consistent discretization of the pressure an additional constraint equation is necessary for each cell.

$$\Pi^+ + \Pi^- = P_1 + P_2 \quad (4)$$

This condition implies that the average of Π^+ and Π^- and the average of P_1 and P_2 are same and the average represent the pressure value for the cell center if it is to be located. In the case of infinitely small mesh size, pressure values on the sides of the conservation cell become almost the same. However for finite mesh size, these

four pressure variables have different values and should satisfy a consistent pressure distribution in the flow domain given by Eqn. 4.

By discretizing the mass conservation (Eqn. 1) on the conservation cell, an algebraic relation expressing that mass flow rate remains constant along a streamtube is obtained

$$\dot{m} = \rho_1 V_1 A_{n1} = \rho_2 V_2 A_{n2} \quad (5)$$

where A_n is the area (length in two-dimensional case) normal to velocity.

The discretized form of the momentum equation becomes

$$-\rho_1 V_1 A_{n1} \bar{V}_1 + \rho_2 V_2 A_{n2} \bar{V}_2 + P_1 \bar{A}_1 + P_2 \bar{A}_2 + \Pi^+ \bar{B}^+ + \Pi^- \bar{B}^- = 0 \quad (6)$$

where \bar{A} and \bar{B} are area vectors shown in Fig. 3.

Discretization of the energy conservation (Eqn. 3) gives the following algebraic equation:

$$H = \frac{\gamma}{\gamma-1} \frac{P_1}{\rho_1} + \frac{V_1^2}{2} = \frac{\gamma}{\gamma-1} \frac{P_2}{\rho_2} + \frac{V_2^2}{2} \quad (7)$$

As it is expected for an adiabatic steady flow, Eqn. 7 states that the stagnation enthalpy remains constant along a streamtube.

The momentum equation (Eqn. 6) is in vectorial form and can be expressed as two scalar equations: one in the streamwise direction which contains pressures P_1 and P_2 , the other in the normal direction which contains pressures Π^+ and Π^-

$$\dot{m} (V_1 f_1 - V_2 f_2) + P_1 - P_2 = 0 \quad (8)$$

$$\dot{m} (V_1 g_1 - V_2 g_2) + \Pi^- - \Pi^+ = 0 \quad (9)$$

where f_1 , f_2 , g_1 , and g_2 are functions of geometry.

At a solution step, all geometric and state variables are input as the initial solution. For a specified mass flow rate and stagnation enthalpy, new velocities are computed by using the continuity Eqn. 5 and new "P" pressures are obtained from the energy equation (Eqn. 7). Momentum equation in the normal direction (Eqn. 8) and the constraint relation of auxiliary pressure (Eqn. 4) are solved simultaneously to determine new values of Π^- and Π^+ . All variables (except the density and the geometric ones) are assigned to their new values. The computation of these variables in the existing iteration step is done by sweeping the conservation cells along each streamtube. While this procedure is applied to the next (adjacent) streamtubes, Π pressure values on the interfacing streamline has already been updated at the previous streamwise sweep. Different values for Π^-_j and Π^+_{j-1} are obtained of a nonconverged result and this violates the necessary condition

$$\Pi^-_j - \Pi^+_{j-1} = 0 \quad (10)$$

which states the compatibility of pressure at the common boundary of two adjacent streamtubes (j^{th} and $j-1^{\text{th}}$). The streamwise momentum equation (Eqn. 9) is the other equation which has remained unsatisfied at a nonconverged iteration step. The compatibility condition (Eqn. 10) and the streamwise momentum equation (Eqn. 9) give residuals which vanish as the algorithm converges. These equations are linearized by using Newton-Raphson method. In their linearized form, the perturbation (change) of the variables are given by $\Delta\rho$, Δv , ΔP , $\Delta\Pi$, ΔA_n etc... All change parameters can be expressed in terms of grid node displacement Δn and density change $\Delta\rho$ where the displacement describes the change of streamline position in the direction normal to current streamline. In this process, linearized forms of governing algebraic equations and geometrical relations are used. Therefore the resulting system of linear equations contains two equations with two unknowns ($\Delta\rho$ and Δn) for each computational cell. At the boundaries of solution domain, the boundary condition should replace Eqn. 10.

There are some additional constraints or conditions to be satisfied such as the closure constraints for inverse design calculation or Kutta condition for analysis calculation. The linearized forms of the constraint equations are additional linear equations to be solved for the additional unknowns that are the changes of variables such as the free parameters of specified pressure and the circulation around the airfoil. Once the system of linear equations is solved the unknown change parameters (perturbations) are found. Using Δn the new grid node coordinates are computed from

$$x_{\text{new}} = x + n_x \Delta n \quad (11a)$$

$$y_{\text{new}} = y + n_y \Delta n \quad (11b)$$

where n_x and n_y are directional cosines of the unit vector along which the node is allowed to move.

The new density is calculated from:

$$\rho_{\text{new}} = \rho + \Delta\rho \quad (12)$$

ARTIFICIAL COMPRESSIBILITY:

In the present method, steady Euler equations which are essentially elliptic are solved in the conservation form. In the supersonic regions, it is necessary to include some form of supersonic upstream dependence to change the character of the governing equations. Therefore, artificial compressibility is introduced. The concept of artificial compressibility was first introduced by Hafez et al. [21] for the solution of transonic full potential equation. A similar approach was used by Worman [22] for quasi-one-dimensional Euler equations. In principle, density is modified

in supersonic regions using a discretization in the upwind direction as

$$\rho_2 = \rho_2 - \mu (\rho_2 - \rho_1) \quad (13)$$

where μ is a function of local Mach number and has zero value in subsonic regions. This density modification is equivalent to the artificial viscosity implementation. Strength and location of shocks are calculated correctly without any special treatment such as shock fitting.

BOUNDARY CONDITIONS

CASCADE

A typical numerical domain for cascade flow is made up of one blade passage and extends approximately one chord upstream and downstream as shown in Fig. 4. Boundaries AB, EF, CD, and GH are assumed to be stagnation streamlines. A grid node on AB and the grid node on EF having same streamwise station index i acquire the same x coordinate while their y coordinates will differ by the pitch. Hence both grid points would have equal nodal displacement Δn in the same direction after a solution step always keeping the stagnation streamlines parallel. Also pressure P on these grid nodes are forced to be equal using Eqn. 10. Hence, periodicity of the flow on AB-EF and CD-GH is satisfied.

At the upstream boundary AE stagnation enthalpy and stagnation density are specified for each streamtube. Besides these flow variables the first segments of grid lines (streamlines) are constrained to be parallel to each other using the specified inlet flow angle (inlet slope). Similar parallelity condition is also applied to the last segments of the streamlines. At the downstream boundary, the common slope is a variable whose change ΔS_{out} is an unknown to be found in a solution step.

For inviscid flow, slip condition on the wall implies that the wall itself is a streamline. In the present method set of J -constant lines correspond to assumed streamlines. The grid locations and the solution domain are not fixed, they may move during the solution. In fact, grid points and therefore the shape of streamlines are computed at each iteration step. Therefore initially assumed blade contour as a streamline will change during the computation. Once the convergence is obtained the updated boundary streamline becomes the designed blade surface for which the target pressure distribution is specified. Hence the only boundary condition to be employed on the wall-shaped boundary (BC and FG) is to specify target surface pressure distribution. However this target pressure distribution is not arbitrary. It was shown by Lighthill [4] that the prescribed surface speed distribution for incompressible flow must satisfy three constraints. Volpe and Melnik [6] have pointed out the necessity and importance of similar constraints on surface pressure distribution in the inverse design of transonic airfoils. In the present method three constraints have been imposed at the grid nodes corresponding to leading and trailing edge stations on the suction and pressure surfaces. These constraints on node displacements are

$$\Delta n_{LE,SS} = 0 \quad (14)$$

$$\Delta n_{LE,PS} = 0 \quad (15)$$

$$\Delta n_{TE,PS} = \Delta n_{TE,SS} \quad (16)$$

as shown in the Fig. 5. The first constraint (Eqn. 14) prevents the rigid body motion of whole domain. The second keeps the specified pitch unchanged (or imposes the closure of leading edge). The third constraint (Eqn. 16) imposes the closure of trailing edge. The addition of the linearized forms of these constraints into the overall equation set, make it necessary to describe three unknowns (or free parameters to be updated.) One of them is the outlet slope S_{out} which describes the flow angle at the far downstream boundary. The other two free parameters appear in the target pressure distribution. The specified surface pressure distribution $P(s)$ is imposed to the solution in the following form.

$$\Pi(s) = P(s) + C_1 F(s) + C_2 G(s) \quad (17)$$

where C_1 and C_2 are two new free parameters (multiplication factors) and where $F(s)$ and $G(s)$ are arbitrary shape functions of relative arc length s . Linearization of the boundary condition (Eqn. 17) introduces the changes of free parameters ΔC_1 and ΔC_2 as unknowns. The exact distribution of the pressure imposed on the blade surface can be determined when the solution converges. The pressure distribution obtained at the convergence is referred as "output" pressure distribution in this study.

AIRFOIL

A typical numerical domain for an airfoil can be seen in Fig. 6. The flow domain for the airfoil consists of a bunch of streamtubes as in the case of cascades. To be able to make a distinction between the suction and pressure surface streamlines, the grid is generated such that there are two grid lines coincident along the stagnation streamline. These grid lines should be observed as separating from each other at the node corresponding to the leading edge, one of them follows the suction surface while the other is following pressure surface. Hence conditions on upstream and downstream stagnation lines are the same as the periodic boundary conditions of the cascade flow case. Therefore nodes $(i,1)$ and (i,j_{max}) shown on the Fig. 6 satisfy the following conditions:

$$\Pi_{i,1} = \Pi_{i,j_{max}} \quad (18.a)$$

$$x_{i,1} = x_{i,j_{max}} \quad (18.b)$$

$$y_{i,1} = y_{i,j_{max}} \quad (18.c)$$

On the airfoil surface pressure is specified through Eqn. 17 and the constraints (Equations 14, 15 and 16) are also valid. The circulation Γ around the airfoil is used as a free parameter and replaces the outlet slope of cascade case.

The farfield boundary conditions are based on the farfield potential Φ that is obtained by superimposing a free stream and a vortex flows as proposed by Ludford [23]. This procedure is also used by Giles and Drela [18] in which they discussed the effect of additional doublet flow on the solution. The velocity potential is taken as

$$\Phi = x + \frac{\Sigma}{2\pi} \log r - \frac{\Gamma}{2\pi} \theta \quad (19)$$

where r and θ are the polar coordinates of the grid measured from the moment center of the airfoil. Σ is the source strength which only exists for entropy generating flows. The velocity distribution at the farfield boundary can be found from this velocity potential. Using the resulting velocity distribution, the pressure Π is computed and specified as boundary condition at a grid node on the upper or lower boundary of the farfield. The upstream and downstream farfield boundary conditions are treated as in the case of cascade flows. However, the slopes of streamlines are computed from the farfield velocity potential and each streamline may have a different slope.

SOLUTION PROCEDURE

The initial solution (i.e. the approximated streamline grid and approximated flow field) is found to be important for the present inverse method. Solution domain for cascade inverse solution was constructed by assuming a blade contour. The stagnation streamlines were taken as straight lines and extended from the leading edge at the specified inlet flow angle and from the trailing edge as tangent to the camberline. Far-upstream and far-downstream boundary lines are then located one chord away from leading and trailing edges in the case of cascade flows and six chord away from leading and trailing edges for airfoil case. Using an elliptic grid generator method developed by Thompson [24], the initial grid with j -constant lines approximately corresponding to streamlines of incompressible flow is constructed. The remaining part of initial solution, i.e. the flow field, is approximated by assigning a constant pressure and density corresponding to a low-subsonic value and a coarse distribution of speed. This initial solution is good enough for the analysis of transonic flow and converged flow field can be obtained in 5 to 15 iterations. But starting the inverse design from this initial solution which has low-subsonic pressure caused excessive accelerations and generally ended up with a negative enthalpy near the solid surface. This was probably due to large difference between the specified transonic surface pressure and the low-subsonic pressure of neighboring nodes. Therefore before the design procedure was started, the coarse incompressible initial solution was improved by employing a few iterations in the analysis mode from which a flow field distribution for pressure at transonic or high-subsonic level was obtained. There was no need to continue the iterations to obtain a converged solution of the analysis mode.

The analysis mode of the code differs from design mode mainly in the boundary conditions of the blade contour, instead of target pressure specification by Eqn. 17, the rigid wall condition

$$\Delta n_{\text{wall}} = 0 \quad (20)$$

was applied.

The system of linear equations which are obtained after discretization and linearization includes governing equations, boundary conditions and constraints. Unknowns for cascade solution are density change $\Delta \rho_i$ at each state node, Δn_i at each grid node, and four additional unknowns ΔC_1 , ΔC_2 , ΔS_{out} , and ΔS_{in} which are the changes of first and second multiplication factors of the pressure distribution, the outlet slope and the inlet slope. Unknowns for airfoil solution are the same except ΔS_{in} and ΔS_{out} are replaced by $\Delta \alpha$ (angle of attack) and $\Delta \Gamma$ (circulation). This system of linear equations is solved by a direct method employing Gaussian elimination technique.

RESULTS AND DISCUSSION

For the purpose of illustrating the ability and accuracy of the present method three test cases were used. These were an airfoil test case NLR 7301 from Ref. [25] and two cascade configurations; Sanz supercritical propeller from Ref. [26] and Hobson-2 impulse turbine cascade from Ref. [25]. The blade geometries and analytical solutions of these test cases are available in the above mentioned references. These test cases are well known for testing transonic direct solutions. In the present investigation, these test cases are used for the inverse solution by redesigning the blades from the specified pressure distributions. Calculated geometries were then compared with the original (actual) ones, for the assessment of the accuracy.

HOBSON-2 Impulse Turbine Cascade Test Case:

Hobson-2 is an impulse turbine cascade for which accurate analytical solution is available in Ref. [25]. The geometry of this cascade was originally obtained by a hodograph solution to the transonic flow equation. Hobson-2 cascade blade has sharp leading and trailing edges. The cascade produces shockless flow at the design conditions of $M_1=0.575$, $\alpha_1=46.123^\circ$ and spacing $S/C=0.5259$.

Fig. 7 shows original, starting and designed blade geometries. As it is seen from the figure original and designed blade shapes are indistinguishable. A specified surface pressure distribution which is the "input" to the program usually differs slightly from the surface distribution resulted over the designed blade due to free parameters introduced in Eqn. 17. Since the specified pressure distribution is not an arbitrary one but corresponds to an actual cascade, in this test case free parameters should be zero in the converged solution. This can be seen in Fig. 8 in which the specified and the "output" pressure distributions are almost the same. Initial surface pressure distribution around the hand-drawn starting geometry is also depicted in the same figure from which the design procedure starts. The initial flow field was obtained by running the analysis program for a guessed blade geometry. Fig. 9 shows the starting surface Mach number distribution and the designed ("output") one to give an idea about the development of the new flow field in this design procedure. Axial and pitchwise force coefficients are computed as $C_x=0.2252$ and $C_y=1.042$ respectively.

SANZ Supercritical Propeller Cascade Test Case:

Sanz supercritical propeller blade is a transonic airfoil fit for a mid-span section of a modern propeller for which the accurate analytical solution is available in NASA TP-2676 [26]. The geometry of this cascade was originally obtained by a hodograph related method with boundary layer corrections. Therefore as a test case for inviscid solutions, the blade has to be treated with open trailing edge geometry. During the design procedure nodes corresponding to suction and pressure side trailing edge are displaced by the same amount as imposed by Eqn. 16. Hence the trailing edge opening was kept constant. Therefore the trailing edge opening in the starting geometry must be equal to the original opening. For this cascade design values of upstream Mach number, upstream flow angle and spacing are: $M_1=0.828$, $\alpha_1=25.72^\circ$ and $S/C=1.055$ respectively.

The original and the designed blade geometries together with the starting (initial) geometry are shown in Fig 10. Designed blade shape was found to be almost the same as the original blade shape. Fig. 11 depicts starting, input (specified), and output surface pressure distribution. The starting surface pressure distribution which was obtained by analyzing the starting geometry shows a shock-like suction pressure variation. The specified pressure has a shock free feature corresponding to original Sanz surface pressure distribution. The design code is therefore capable of removing the possible shocks by modifying the blade shape. Starting and output Mach number surface distributions are shown in Fig. 12. The input pressure distribution is not available in Ref. [26], therefore it was obtained by using the code in analysis mode. The Mach number distribution which is available in Ref. [26] was compared with the output distribution of Fig. 12 and they are found to be consistent. Axial and pitchwise force coefficients are calculated as $C_x = -0.152$ and $C_y = 0.390$ respectively.

NLR 7301 Airfoil Test Case:

The NLR 7301 airfoil section is a representative aft-loaded airfoil designed especially for wing tips at high subsonic speeds. The NLR 7301 section also provide a rather uniform pressure distribution over the forward 50% of the chord at low angles of attack and at high subsonic speeds. The ability to predict the design shape of this airfoil has been demonstrated in this research. Ref. [25] reports analytical and computational results about the characteristics of this airfoil. The input airfoil shape thickness was randomly chosen to be a thin section at $\alpha = -0.194^\circ$. The calculated pressure distribution shows a weak shock formation around $x/c=0.3$ from the leading edge (Fig.13). At the final pressure distribution, this is removed and the loading conforms with the designed target pressure distribution (Fig. 14 and 15). It should be noted that due to fewer calculation nodes in the normal direction, the upper boundary condition at the farfield was chosen to be close to the airfoil section. This, in turn, caused the upper surface pressure to be smaller than expected. The airfoil loading characteristics are calculated as $C_l = 0.524$ and $C_o = 0.0009$ at $M_\infty = 0.721$ and $\alpha = -0.194^\circ$.

The following table lists the convergence behavior of the code.

	MESH POINTS		NUMBER OF ITERATIONS	RESIDUALS	
	total	on blade		rms	max
HOBSON-2	78X15	56+56	9	4.07×10^{-8}	1.58×10^{-7}
SANZ	88X17	60+60	9	7.62×10^{-9}	1.45×10^{-7}
NLR	102x31	59+59	9	8.47×10^{-9}	1.87×10^{-7}

CONCLUSIONS

A design method has been described for the design of cascade blades and airfoils with given pressure distribution in transonic flow.

In the present method, steady Euler equations are discretized on a streamline grid using finite volume method. Finite volume cells are aligned with the streamlines with non-zero flux terms only in the streamwise direction. The method is suitable for specifying pressure distribution along streamline segments. Discretized nonlinear governing equations and boundary conditions are linearized by using Newton's method. The resulting linear equations are reduced to a system which mainly consists of two equations per cell. The unknowns in a solution step become the density change and the displacement (position change) at nodes.

The advantage of present approach is that it is conceptually straight forward and can be easily handled. Contrary to unsteady Euler codes, the convergence of the present method is not limited by relatively slow propagation of pressure waves throughout the flow domain. All boundary conditions are physical and easy to apply.

Application of the method to transonic cascade and airfoil designs showed that, if surface pressure distribution is not arbitrary but corresponds to actual blade, free parameters of the pressure specifying equation tend to zero as expected.

The method is capable of solving sharp and blunt leading edge shapes with either sharp or open trailing edge configurations.

REFERENCES

1. Vanderplaats, G.N., "An Efficient Algorithm for Numerical Airfoil Optimization," AIAA Paper 79-0079, Jan. 1979.
2. Hicks, R.M., Henne, P.A., "Wing Design by Numerical Optimization," AIAA Paper 77-1247, 1977

3. Davit, W.M., "Techniques for Developing Design Tools from the Analysis Methods of Computational Aerodynamics," AIAA Paper 79-1529, July 1979.
4. Lighthill, M.J., "A New Method of Two-Dimensional Aerodynamic Design," Aeronautical Research Council, R&M-2112, 1945.
5. Woods, L.C., "The Design of Two-Dimensional Aerofoils with Mixed Boundary Conditions," Quarterly of Applied Mathematics, Vol. 13, 1955, pp. 139-146.
6. Volpe, G. and Melnik, R.E., "Role of Constraints in Inverse Design for Transonic Airfoils," AIAA Journal, Vol. 22, No. 12, Dec. 1984.
7. Nieuwland, G.Y., "Transonic Potential Flow Around a Family of Quasi-Elliptical Aerofoil Sections," NLR-TR-T. 172, 1967.
8. Bauer, F., Garabedian, P. and Korn, D., "Supercritical Wing Sections," Springer Verlag, New York, 1972.
9. Sobieczky, H., "Related Analytical, Analog, and Numerical Methods in Transonic Airfoil Design," AIAA Paper 79-1556, July 1979.
10. Sobieczky, H., Yu, N.J., Fung, K.Y., and Seebass, R., "A New Method for Designing Shock-Free Transonic Configurations," AIAA Paper 78-1114, 1978.
11. Yu, N.J., "An Efficient Transonic Shock-Free Wing Redesign Procedure Using a Fictitious Gas Method," AIAA Paper 79-0075, 1979.
12. Hassan, A., Sobieczky, H., and Seebass, A.R., "Subsonic Airfoils with a Given Pressure Distribution," AIAA Journal, Vol. 22, No. 9, Sept. 1984.
13. Tranen, T.L., "A Rapid Computer Aided Transonic Airfoil Design Method," AIAA Paper 74-501, 1974.
14. Volpe, G., "Two-element Airfoil Systems Design: An Inverse Method," AIAA Paper 78-1226, 1978.
15. Carlson, L.A. "Transonic Airfoil Analysis and Design Using Cartesian Coordinates," J. Aircraft, Vol. 13 May 1976.
16. Shankar, V., Malmuth, N.D., and Cole J.D. "Computational Transonic Inverse Procedure for Wing Design," AIAA Journal Vol. 20, August 1982.
17. Gally, T.A. and Carlson L.A., "Transonic Wing Design Using Inverse Methods in Curvilinear Coordinates," J. Aircraft Vol. 25, November 1988.
18. Giles, M.B. and Drela, M., "Two-Dimensional Transonic Aerodynamic Design Method," AIAA Journal Vol. 25, September 1987.
19. McDonald, P.W., "The Computation of Transonic Flow Through Two-dimensional Gas-turbine Cascades," ASME paper 71-GT-89, 1971.
20. Denton, J.D. "A Time Marching Method for Two and Three Dimensional Blade to Blade Flow," Aeronautical Research Council, R&M 3775, 1974.
21. Hafez, M., South, J. and Murman, E. "Artificial Compressibility Methods for Numerical Solutions of Transonic Full Potential Equation," AIAA Journal Vol. 17 August 1979.
22. Wornom, S., "Application of Two-point Difference Schemes to the Conservative Euler Equations for One-Dimensional Flows," NASA TM-83262 1982.
23. Ludford, G.S.S. "The Behavior at Infinity of the Potential Function of a Two-dimensional Subsonic Compressible Flow," Journal of Mathematical Physics Vol. 30, 1951.
24. Thompson, G.F., Thames, F.C., Mastin, C.W., "Automatic Numerical Generation of Body Fitted Curvilinear Coordinate System for Field Containing Any Number of Arbitrary Two-dimensional Bodies," Journal of Computational Physics, Vol. 15, 1974.
25. AGARD Working Group 7, "Test Cases for Inviscid Flow Field Methods," AGARD Rept. AR-211, 1985.
26. Sanz, J.M. "Lewis Inverse Design Code (LINDES)," NASA TP-2676 March 1987.

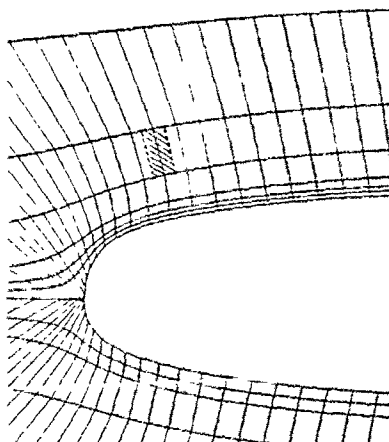


FIGURE 1. A Conservation Cell on the Grid

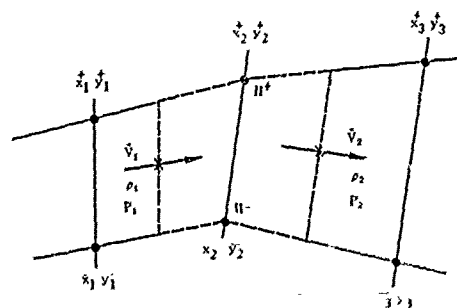


FIGURE 2. Grid Node Coordinates and State Variables

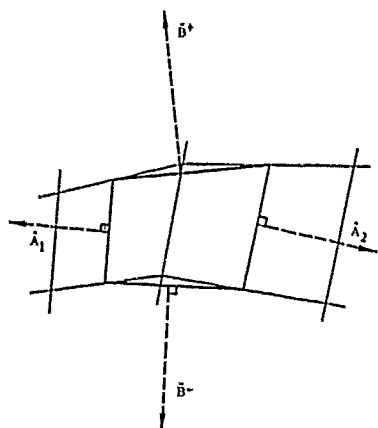


FIGURE 3. Area Vectors for a Conservation Cell

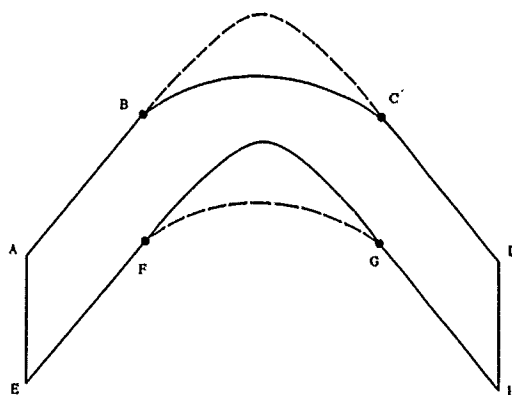


FIGURE 4. A Typical Cascade Flow Domain

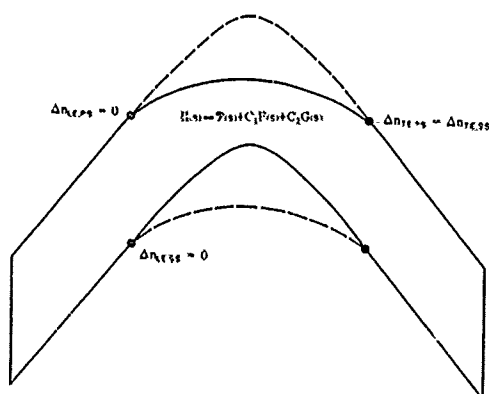


FIGURE 5. Inverse Design Boundary Condition and Constraints

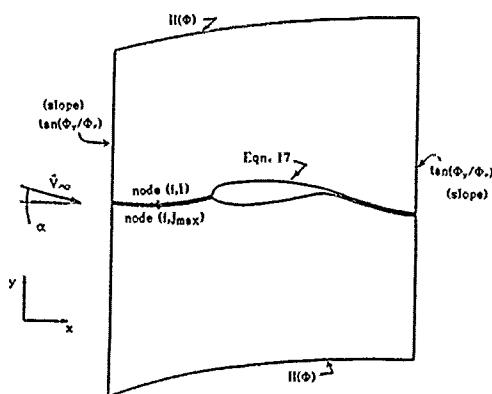
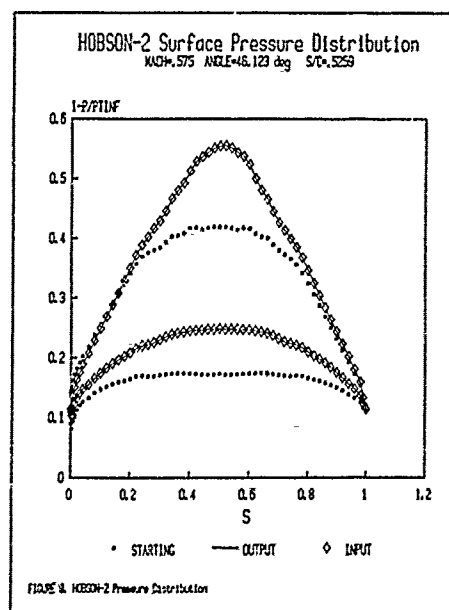
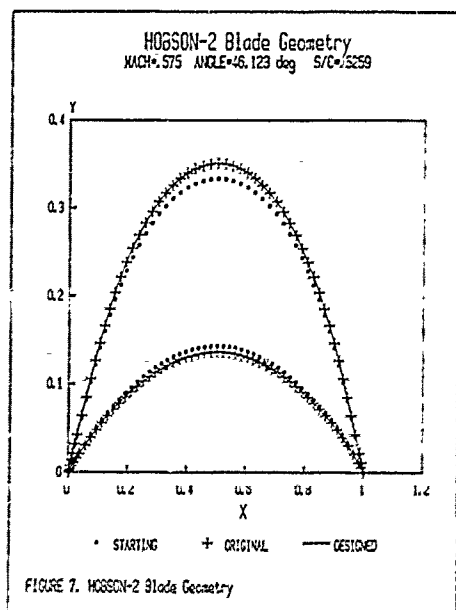
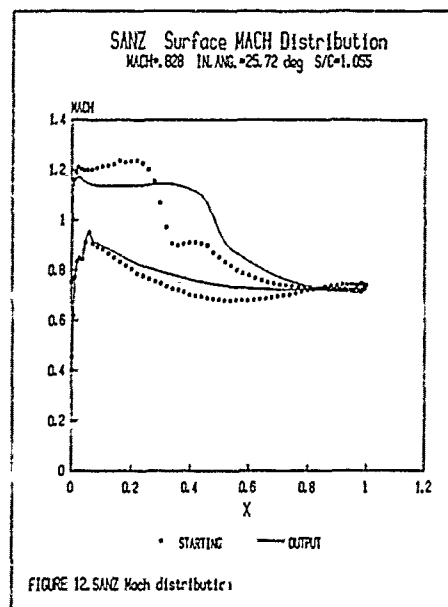
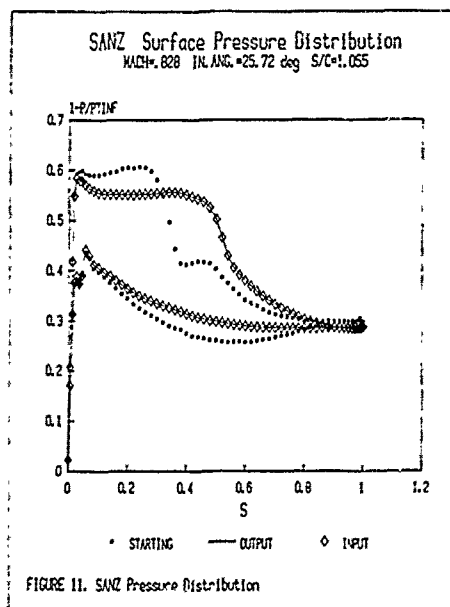
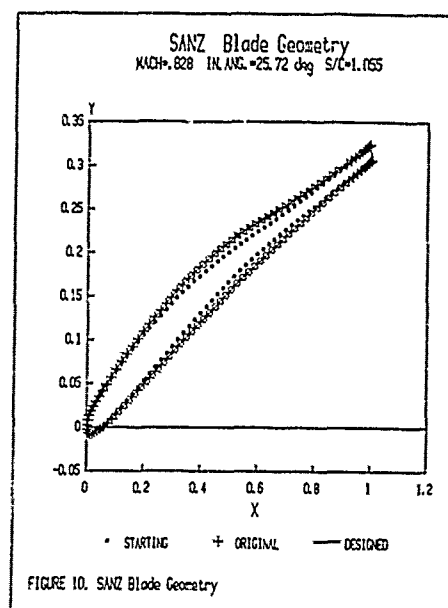
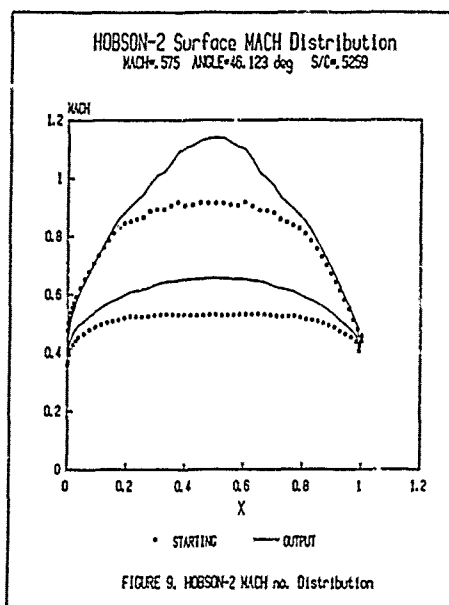
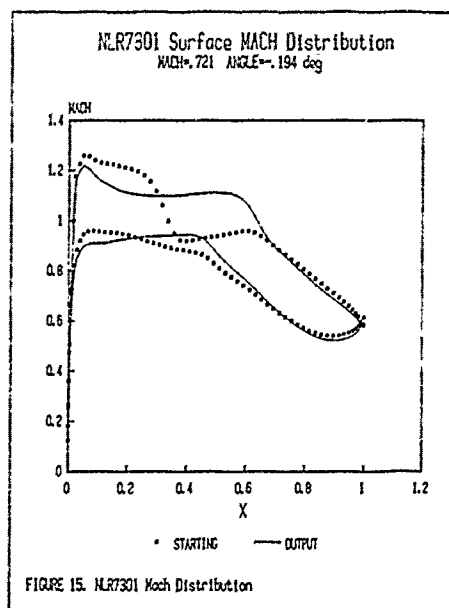
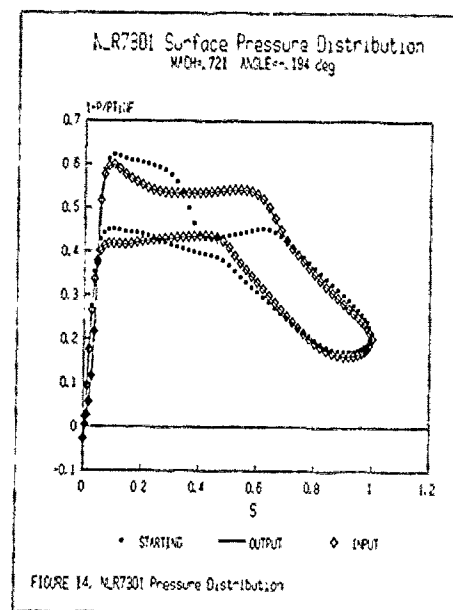
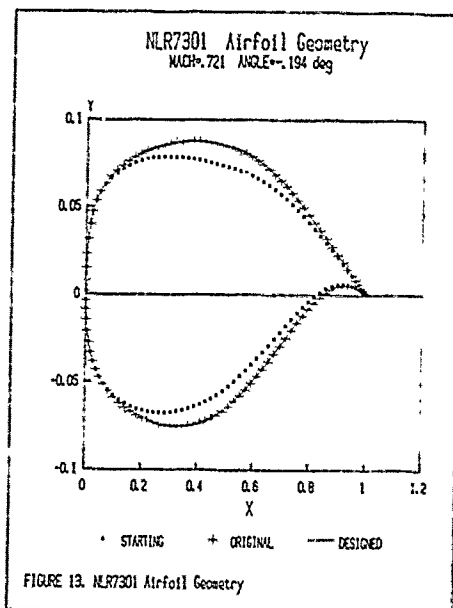


FIGURE 6. A Typical Airfoil Domain and Boundary Conditions







INVERSE COMPUTATION OF TRANSONIC INTERNAL FLOWS WITH APPLICATION FOR MULTI-POINT-DESIGN OF SUPERCRITICAL COMPRESSOR BLADES

E. Schmidt* and F. Klimetzek†

*Institut für Aero- und Gasdynamik
Universität Stuttgart
Pfaffenwaldring 21
D-7000 Stuttgart 80

†now: Daimler-Benz AG
Forschung und Technik FVT/TA
D-7000 Stuttgart 60

Summary

The method solves the inverse problem for supercritical blade-to-blade flow on stream surfaces of revolution with variable radius and variable stream surface thickness in a relative system. Some provisions for the treatment of the "ill-posed" design problem in local supersonic regions are discussed. A procedure for the design of cascades with improved off-design behaviour is described and compared with experimental results. Comparisons with other numerical methods and experimental results are also included.

Nomenclature

$C_1 \dots C_7$	coefficients of potential equation
d	profile thickness
h_1	metric factor
l	chord length
La	Laval number; velocity related to critical sonic velocity
m	meridional coordinate
R	radius
s	arc length along streamlines
t	stream surface thickness
T	pitch
W	velocity magnitude
z	axial coordinate
β	flow angle, measured against circumferential direction
Γ	circulation
δ	flow angle, measured against inlet direction
θ	polar angle
λ	angle of stream surface against axial direction
ρ	density
φ	coordinate function normal to streamlines
ψ	stream function
ω	angular velocity
Ω	axial velocity density ratio

Subscripts

1,2 upstream, downstream

Introduction

Blade design for turbomachines has the aspiration to obtain energy transfer as high as possible between the fluid and the blading with as little as possible manufacturing expenses at lowest flow losses. Manufacturing costs can only effectively be reduced by raising the flow velocity. The reinforcement of the velocity differences between blade suction- and pressure-side for increase of turning and the raising of the velocity level for growing mass flow lead to local supersonic regions on the blade suction sides (supercritical flow) which mostly return with a shock to subsonic velocity. As the pressure rise of the shock may cause boundary layer separation and with it increased losses, the formation of shocks should be prevented as far as possible.

In the regions with pressure rise, boundary layer separation can only be avoided by careful blade-profiling. Since in the transonic velocity domain shockfree solutions can be found with only poor chances by iterative contour variation, a convenient alternative is given by the inverse design: Starting from a prescribed shockfree velocity distribution the corresponding profile contour is calculated numerically. The prescribed distribution of the pressure

or velocity can be clearly influenced in the direction of a loss minimization or boundary layer optimization. If in this way a profile adapted to the referred blade section was found, the off-design range has to be verified by an analysis method which is connected with a loss determination based on a boundary layer calculation. The demand for low loss supercritical blade flow has to be performed not only in the design point at a high upstream Mach number, but also in an off-design range of the blading as extended as possible. But hitherto it is not possible to prescribe the extent of the off-design range in the cascade design. Likewise until now it is not possible to prescribe the position of the off-design range relatively to the design point in a desired mode, e.g. this way, that there exists a sufficient extended region with low loss for deviations of the incidence angle to positive and negative directions. That means for the compressor design that the design point can be obtained nearly exactly but that no exact specification can be made for the partial-load behaviour.

For the supercritical blade cascade design the combination of a design method and an analysis method is required. The published literature about cascade computation methods is governed by the analysis methods. In the transonic velocity range for higher accuracy only numerical methods come to the fore. They are based on relaxation, e.g. /1,2/, finite element /3,4/, or time-dependent solution processes /5,6/. Computations for comparison have shown that there are application problems especially in the local supersonic region.

The design methods, mostly suitable for blade-to-blade calculations can be divided into different groups:

The pure inverse methods deal with the classical problem to determine the complete detailed geometry for a prescribed velocity distribution along the arc length. Their advantage is given by the fact that one prescribes the physical quantity about the course of which one has the best knowledge for obtaining the target of low loss flow. One of the earliest formulations of the inverse problem for plane compressible potential flow originates in Stanitz /7/, on which the method of the author, developed for transonic and supercritical flows /8,9/, is based. Other inverse methods using the time-dependent solved 2D-Euler equations exist of Meauzé /10/ and Zanetti /11/.

In the semi-inverse or hybrid methods on parts of the contour the velocity, on other parts the geometry is prescribed, e.g. in /12/. In indirect methods like the hodograph method /13/ no direct control occurs by aerodynamic quantities (velocity or pressure distribution) or by the geometry. Direct methods start from a geometry prescription, for which the respective pressure or velocity distribution is calculated. Dependent on the result the geometry is varied in this way that the new results approach to a desired target distribution /14/.

Fundamental procedure

The following method, an extension of earlier developments in /9,15/, solves the inverse problem for supercritical blade-to-blade flow on stream surfaces of revolution with variable radius and variable stream surface thickness in a relative system /16/. Prandtl's concept of distinct potential flow- and boundary layer-calculation can be applied, since inverse design strives for low loss flow without shocks and boundary layer separation.

In Fig.1 the solution process of the method is sketched. The sensitive cross-section dependence of the transonic flow requires the treatment of a flow passage between two blades from far upstream to far downstream. The velocity distributions are prescribed along the arc length of the stagnation streamlines of the suction and pressure sides of the flow channel. Thus, velocity gradients can be prescribed which is important for the boundary layer development. Moreover, radius and thickness of the stream surface of revolution are prescribed along the axial coordinate. These boundary conditions are transformed by integration into the computation plane with stream function coordinates and their normals. The computation grid is rectangular in this plane and contour adapted in the physical plane. Therefore, no interpolations are necessary on the boundaries. The flow field is computed by the solution of the difference equation system applying relaxation combined with multi-grid. The gradients of the velocity field are used to determine the flow angle field, and finally, by integration, the field boundaries in the physical plane, i.e. the contour shapes, are computed.

Governing equations

For steady, compressible, isentropic flow the full potential equation, transformed into the potential-stream-function-plane is /17/:

$$\begin{aligned}
 & C_1 \cdot \frac{\partial^2 \ln W}{\partial \varphi^2} + C_2 \cdot \frac{\partial^2 \ln W}{\partial \psi^2} + C_3 \cdot \left(\frac{\partial \ln W}{\partial \varphi} \right)^2 + C_4 \cdot \left(\frac{\partial \ln W}{\partial \psi} \right)^2 \\
 & + C_5 \cdot \frac{\partial \ln W}{\partial \varphi} + C_6 \cdot \frac{\partial \ln W}{\partial \psi} + C_7 = 0 \\
 & C_i = f(W, R, t, h_1) \quad i = 1, \dots, 7
 \end{aligned} \quad (1)$$

with the metric factor

$$h_1(\psi) = h_{1u} \cdot \frac{W}{W_u} \cdot \exp \left[\int_{\psi_u}^{\psi} \frac{\omega \sin \lambda}{\rho t W^2} d\psi \right] \quad (2)$$

As $h_1 \cdot W$ is valid for the flows in an absolute system, it is used as the condition for the free integration constant h_{1u} , so that $h_{1u}(\psi=0) = W_u$.

For flows with constant stream surface thickness and constant radius the introduction of the logarithm in the differentials reduces the terms C_5 to C_7 to zero.

The type of this quasilinear partial differential equation of second order changes according to the sign of C_1 . It is elliptic for C_1 positive ($Ma < 1.0$), hyperbolic for C_1 negative ($Ma > 1.0$), and parabolic for $C_1 = 0$ ($Ma = 1.0$).

For the numerical solution of the potential equation (1) with finite differences the flow field is covered with a computational grid which is rectangular in the φ, ψ -plane. The adjustment to the different domains of dependence occurs by type-dependent switching between the respective difference stars. The solution of the difference equation is performed by successive line over-relaxation. The relaxation factors were optimized dependent on the computed local Mach number. An additional convergence acceleration has been obtained by the application of the multi-grid-method /18/. For the non-linear difference equation system of ISGAV suitably the "full approximation scheme" was applied.

Local grid refinement is provided for regions with steep gradients, since mesh sizes for sufficient resolution of these gradients are not acceptable for application in the whole flow field. The results of the coarse grid computation are used as presetting of the fine grid. For high accuracy, a feed-back calculation can be performed which uses the results of the fine grid for recalculation in the coarse grid in an iterative way with overlapping boundaries of both regions.

The flow field solution has to be transformed from the computation plane into the physical plane. From the computed velocity field, the flow angles can be calculated by integrating the continuity equation on normal lines and the equation of motion on streamlines.

$$\int_{\delta_u}^{\delta} d\delta = \int_{\psi_u}^{\psi} \left[\frac{-h_1}{\rho t W} \cdot \frac{\partial \ln(\rho R t W)}{\partial \varphi} \right] d\psi \quad (3)$$

$$\int_{\delta=\delta_i}^{\delta} d\delta = \int_{\varphi=\varphi_i}^{\varphi} \left[\frac{\rho t W}{h_1} \cdot \frac{\partial \ln(R W)}{\partial \psi} + \frac{2 \omega \sin \lambda}{W h_1} \right] d\varphi \quad (4)$$

To avoid numerical inaccuracies in determining the derivatives on normal lines at the boundary, equation (4) is used only to compute the flow angle of the mean streamline. From the mean streamline to the boundary the flow angle can be calculated by using equation (3).

Analogously the physical coordinates on streamlines can be calculated from:

$$\int_{\theta_1}^{\theta} R d\theta = \int_{\varphi=0}^{\varphi} \frac{\cos \delta}{h_1} d\varphi \quad \int_{m_1}^m dm = \int_{\varphi=0}^{\varphi} \frac{\sin \delta}{h_1} d\varphi \quad (5)$$

and on normal lines from:

$$\int_{\theta_1}^{\theta} R d\theta = \int_{\psi=0}^{\psi} \frac{-\sin \delta}{\rho t W} d\psi \quad \int_{m_1}^m dm = \int_{\psi=0}^{\psi} \frac{\cos \delta}{\rho t W} d\psi \quad (6)$$

Boundary conditions

In transonic flows with local supersonic regions, it is generally not possible to predict whether a certain prescribed profile velocity distribution would lead to a convergent solution as this represents an "ill-posed problem" and therefore a physical solution need not exist in this case. The non-elliptical type of the differential equation in the supersonic areas admits the flow computation only in the domain of dependence. By completely prescribing the boundary values along the profile contour, the interaction between the elliptic subsonic differential equation and the hyperbolic type in the supersonic field leads to an overdetermination of the equation system. For a "bad" prescription, the differential equation system cannot be solved, i.e. non-convergence of the numerical system appears or an unsteady shock is formed in the flow field (Fig.2). In such cases iterative modification of the boundary conditions is required:

If weak shocks are present, their location in the flow field - mostly easily recognized in the shape of the sonic line - is traced back to the flow field boundary (Fig.3). For this the local characteristic directions are plotted throughout the local supersonic region. Following these directions, the position of the producing boundary values is found. They have to be modified so that additional expansion waves are generated and remove the weak shock.

If strong oscillating shocks appear in the field, the prescription of a shock on the boundary with consideration of the Rankine-Hugoniot relation is the only alternative. Otherwise a total change of the velocity distribution with lower maximum velocity and different distribution of the circulation over the blade depth is needed.

The correct periodical velocity distribution on the upstream stagnation streamline has to be found iteratively by checking the complete covering of the upstream region with flow, i.e. the upstream suction and pressure side stagnation streamlines have to coincide.

Since the course of the deceleration in front of the leading edge depends on the blade nose shape and therefore on the prescribed velocity distribution over the blade contour, this laborious iterative process should be solved by the program: Interchanging computation of a standard upstream flow field and a transposed second field between the mean streamlines of two adjacent flow channels leads to the final upstream velocity distribution.

The transformation of the prescribed radius and stream surface thickness along the axis of rotation z has to be performed iteratively, since the function of the axial coordinate $z = f(\varphi, \psi)$ is a result of the computation itself.

A further iteration occurs for the rotor calculation in the relative system. The transformation of the prescribed velocity distribution into the computation plane is carried out by integration of the prescribed velocity distribution to determine the normal function φ . The suction side values can be integrated directly, whereas the metric factor h_1 of the pressure side streamline has to be determined iteratively.

Iterative adjustment of cascade parameters

A prescribed velocity distribution does not necessarily result in a profile with desired parameters such as turning angle, pitch-chord ratio or profile thickness.

For obtaining these target quantities the prescribed velocity distribution - due to the non-linearity of the problem - has to be varied iteratively.

Necessary but not sufficient condition for the prescribed turning is the correct adjustment of the circulation quantity over the blade to the value from up- and downstream flow parameters. In the rotor case an additional integral term results from the rotation of the flow field, thus the complete circulation is given by

$$\Gamma = - \oint_D \omega R \cdot ds - \int_D W_2 ds + \int_K W_1 ds \quad (7)$$

For sufficient fulfilment of the conditions for the validity of this equation the arc lengths on the flow channel boundaries have to be prescribed correctly. Moreover, the periodicity conditions have to be observed on the up- and downstream streamlines. Therefore, since the geometry is unknown at the beginning, an iterative procedure is necessary. The kind of correction depends on the monitoring of the pitch-chord ratio which is acting simultaneously.

After adjusting turning and pitch-chord ratio, the thickness distribution of the computed profile is investigated. The variation of the velocity distribution for a desired profile thickness distribution is accomplished this way that not only negative profile thickness can be avoided but also a maximum thickness can be obtained in a specified region. Thus, the thickness distribution can be adjusted successively to prescribed values in the whole profile range.

At the beginning of the thickness iteration the existing velocity distribution has to be varied so that after the subsequent field solution the desired thickness will be obtained.

The modification needed on the boundary of the computation field is obtained by transformation of the profile velocity distribution with application of trigonometrical functions. Depending on the profile region, where the maximum modification is necessary, different functions of transformation are applied.

For greater thickness modifications unfavourable distributions can arise. This will be recognized in the program and be solved in this way, that the maximum modification in the profile region will be shifted to points where such difficulties cannot appear, i.e., either to the profile trailing edge or to the point of maximum velocity (Fig.4). As the point of maximum velocity modification on the profile has to be identical with the point of thickness modification to calculate, a certain thickness modification in the new point is assumed dependent on the desired value in the former point (centre of Fig.4). Since the resulting inaccuracies cause deviations from the desired thickness distribution, the prescribed values are obtained only after some iterations.

If one of the considered cross-sections is placed in the supersonic region of the profile, an additional difficulty appears by the reversing of the mass flow density behaviour and the condition of constant circulation. In this case the mass flow density requires an opposing velocity modification, i.e. for obtaining a greater profile thickness a lowering of the velocity in the supersonic region and a lifting in the subsonic flow. Therefore, it would be necessary to widen the distribution around the maximum in order to maintain the circulation constant. Numerically this would be an aggravation, since the necessary widening should be introduced into the equation system, so that an analytical solution would be impossible.

Furthermore, some cascade designs have shown that the influence of the field distribution leads to stronger deviations from the linear one-dimensional assumptions so that opposite thickness modifications may arise. By widening the supersonic part of the velocity distribution the local supersonic field may spread to such an extent, that a reversing of the thickness dependence may appear.

The cascade, Fig.5, yielded the following course of iteration for a desired thickness of 3.5 % in the trailing edge region:

start	minimum thickness	1.85 % (D/L)
1. iteration	"	3.72 % (D/L)
2. iteration	"	3.47 % (D/L)

The relative error of 0.8 % is less than the prescribed error limit of 1 %. In the prescription of the error limit it is to be considered that not the profile thickness but the channel cross-section is the result of the design. In this example the tolerance of 1 % means an accuracy of 0.02 % for the channel geometry. In this range the accuracy of some computers (e.g. IBM, VAX) is not too far away.

The inverse design method computes the isentropic potential flow boundaries. For consideration of friction effects the results have to be corrected by boundary layer calculations. Against analysis methods the inverse method needs no iterative procedure. The calculated boundary layer displacement thickness can be subtracted directly from the potential flow boundaries. By this step the metal or fabrication contour is obtained. (The thickness distribution iteration also works with these contour values if desired.)

Cascade design for extended off-design range

For the design of cascades with extended off-design range the following procedure is applied (Fig.6):

Starting from experimental velocity distributions or results of analysis methods for off-design conditions - e.g. positive and negative incidence against design upstream flow direction - new velocity distributions for these conditions are designed which may be expected to produce a more favourable boundary layer behaviour, but retain the characteristic off-design behaviour. For these new distributions the cascade contours are inversely designed. Hence, for these cascades the velocity distributions for the original design point are computed by an analysis method. Of course, they are differently shaped. Therefore, from both distributions a new distribution is developed with the aid of boundary layer calculations. This new distribution produces the new cascade by application of the inverse method. Analysis computations for this new cascade in the off-design have to demonstrate, whether additional changes are necessary /19/.

Starting point for the design of a cascade for extended off-design range was the off-design behaviour of the cascade SKG 2.2 at incidence angles of -3 and +3 degrees (data in Fig.8). Based on the measurements for these conditions new distributions with less critical boundary layer behaviour were developed, and by application of an analysis method /20/ the velocity distributions for the design angle of the original cascade ($\beta_1 = 142$ degrees) were computed.

The comparison with the design distribution of the original cascade SKG 2.2 in Fig.7 demonstrates that the off-design effect was underestimated: The design of the negative incidence point (N) produces already a front peak on the suction side distribution at original design point upstream flow conditions and the design of the positive incidence point (P) a front bay in the velocity distribution relevant to design condition. Consequently, the suction side velocity gradients in the nose regions have to be reduced, whereas the pressure side gradients near the nose have to be raised. Since the circulation is reduced by these variations the suction side velocity distribution has to be raised in the rear part of the profile.

For comparison purposes with the new design results, in Fig.8 the design and computed off-design distributions of the SKG 2.2 are given. In Fig.9 in the centre the new design velocity distribution is shown together with the negative incidence (left) and positive incidence distribution (right). The velocity peaks of the suction side front at positive incidence and of the pressure side front at negative incidence are clearly reduced, but not the peak of the suction side centre at negative incidence.

The shape of the complete cascade SKG 3.3 and the respective flow field, given by constant velocity lines, is shown in Fig.10. For high resolution of the steep gradients in the leading edge region local grid refinements have been introduced (Fig.11).

After modifications in the inverse design method by introducing the stream surface thickness into the governing equations, for the purpose of comparison analysis computations at the design point were made by a flux finite element method (FFEM) /20/ shown in Fig.12. Except for some differences in the leading

edge region of the pressure side and in the local supersonic region there is very good agreement.

The experimental velocity distributions (Fig.13) from the DFVLR, Cologne, /20/ show satisfactory agreement with the design distribution. The total pressure losses (Fig.14) in the design point and in the range of ± 2 degrees of incidence have the same favourable behaviour as the cascade SKG 2.2. The velocity modifications on the profile suction side lead to distinctly lower total pressure losses in the range of positive incidence. The increase of the losses in the range of negative incidence is probably to be explained by the shifting of the maximum velocity on the suction side towards the trailing edge.

Cascade design on stream surfaces with increasing radius

A cascade has been designed for high subsonic flow with $La_1 = 0.786$ and a turning angle of 33 degrees. The mean divergence angle of the 1^{st} stream surface is $\lambda_1 = 30$ degrees, and the side wall contraction with sinusoidal slope through the cascade amounts 33 percent. In Fig.15 the prescribed velocity distribution is given by the solid line. The computed profile contour on the bottom has been transformed to an equivalent cylindrical stream surface.

For comparison, analysis computation with a time dependent finite volume method originating from P.W. McDonald /21/ has been performed. The result is given by the symbols in Fig.15. Almost excellent agreement is obtained.

Conclusions

Inverse design methods receive growing interest, since in this way progress can be achieved for low loss turbomachinery bladings, especially in the transonic flow region.

The present extended inverse design method seems to be an effective procedure to design highly loaded axial compressor cascades on stream surfaces of revolution. It produces accurate results compared with measurements and computations from other methods. It was applied to cascade and multi-section compressor blade design. Lower losses were obtained compared with conventional blading.

Acknowledgements

This research was considerably supported by the "Deutsche Forschungsgemeinschaft" (DFG) and by the "Forschungsvereinigung Verbrennungskraftmaschinen" (FVV).

References

- /1/ Ives, D.C. Second Order Accurate Calculation of Transonic Flow
Liutermoza, D.S. over Turbomachinery Cascades.
AIAA-J. 17, Aug. 1979, pp. 870-876,
- /2/ Dulikravich, D.S. Numerical Calculation of Transonic Axial Turbo-
machinery Flows.
NASA TM-81544, 1980
- /3/ Deconinck, H. Subsonic and Transonic Computation of Cascade
Hirsch, C. Flows.
Proc.IV Int.Symp.Comp.Math.Appl.Sci.
Eng., IRIA, Dec. 1979
- /4/ Lucci, C.W. Developments of Flux Finite Element Method in
Two-Dimensional Potential Flow Problems.
AIAA-Paper 78-55, 1978
- /5/ Denton, J.D. A Time Marching Method for Two- and Three-
Dimensional Blade-to-Blade Flows.
Aeronautical Research Council,
R&M No. 3775, London, Oct. 1974
- /6/ McDonald, P.W. The Computation of Transonic Flow through Two-
Dimensional Gas Turbine Cascades.
ASME-Paper 71-GT-89, 1971

- /7/ Stanitz, J.D. Design of Two-Dimensional Channels with Prescribed Velocity Distributions along the Channel Walls.
NACA TR 1115, 1953
- /8/ Schmidt, E. Transsonische Gitterströmungsberechnung mit der Relaxationsmethode.
9. DGLR-Jahrestagung, München,
Sept. 1976, DGLR 76-186
- /9/ Schmidt, E. Computation of Supercritical Compressor and Turbine Cascades with a Design Method for Transonic Flows.
Trans. ASME, J. Eng. Power, Vol. 102,
Jan. 1980, pp. 68-74
- /10/ Meauzé, G. An Inverse Time Marching Method for the Definition of Cascade Geometry.
Trans. ASME, J. Eng. Power; Vol.104, July 1982
- /11/ Zannetti, L. Time-Dependent Computation of the Euler-Equations for Designing 2D Cascades, Including the Case of Transonic Shock-Free Design.
83-TOKYO-IGTC-54, Oct. 1983
- /12/ Meauzé, G. On the Use of Inverse Modes of Calculation in 2D Cascades and Ducts.
ICIDES Conf. Proc., Oct. 1984,
Univ. of Texas, Austin, pp.327-341
- /13/ Sanz, J.M. Design of Supercritical Cascades with High Solidity.
AIAA-Journ. Vol. 21, No. 9,
Sept. 1983, pp. 1289-1293
- /14/ Thompkins, W.T. Inverse or Design Calculations for Nonpotential Flows in Turbomachinery Blade Passages.
Siu Shing Tong
Trans. ASME, J. Eng. Power, Vol. 104,
Apr. 1982, pp. 281-285
- /15/ Schmidt, E. Inverse Design of Supercritical Nozzles and Cascades.
Berger, P.
Int. J. Num. Meth. Eng., Vol. 22
Feb. 1986, pp.417-432
- /16/ Klimetzek, F. Inverse Profilauslegung auf rotationssymmetrischen Stromflächen für Leit- und Laufräder von Turbomaschinen.
Dissertation, Universität Stuttgart 1989
- /17/ Schmidt, E. Inverse Methods for Blade Design, Controlled Diffusion Blading for Supercritical Compressor Flow.
VKI-LS 1988-03 Transonic Compressors
- /18/ Brandt, A. Multigrid-Techniques: 1984 Guide with Application to Fluid Dynamics.
GMD-Studien Nr. 85, St.Augustin, 1984
- /19/ Schmidt, E. Erweiterung des Anwendungsbereichs der Berechnungsverfahren für verlustarme superkritische Schaufelgitter.
Klimetzek, F.
Abschlußbericht Teil I, FVV-Vorhaben Nr. 325, 1987
- /20/ Faden, M. Erweiterung des Anwendungsbereichs der Berechnungsverfahren für verlustarme superkritische Schaufelgitter.
Starken, H.
Weber, A.
Abschlußbericht Teil II, FVV-Vorhaben Nr. 325, 1987
- /21/ Happel, H.W. Anwendung neuer Entwurfskonzepte auf Profile für axiale Turbomaschinen.
MTU Techn. Bericht 78/54 A,
München 1978

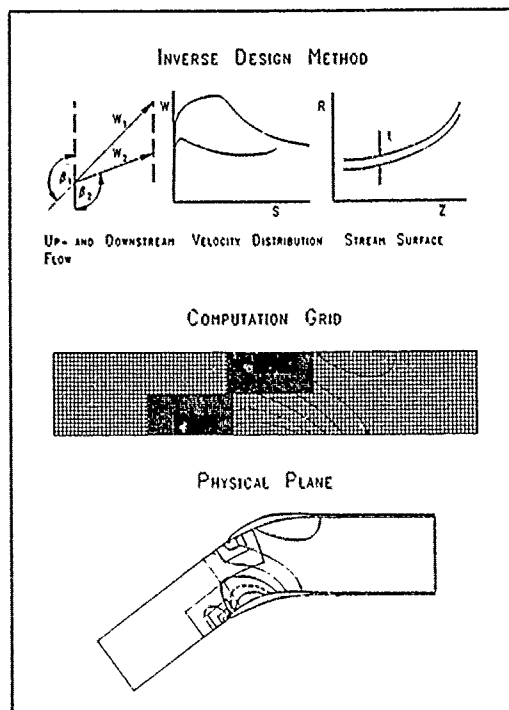


Fig. 1: Solution process of the inverse design method.

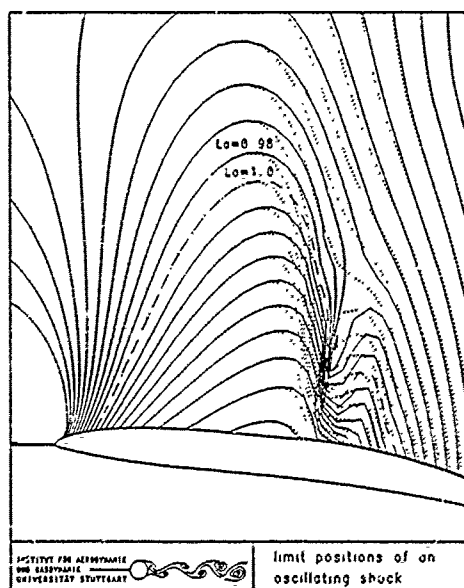


Fig. 2: Velocity fields and profile contours for the limit position of an oscillating shock.

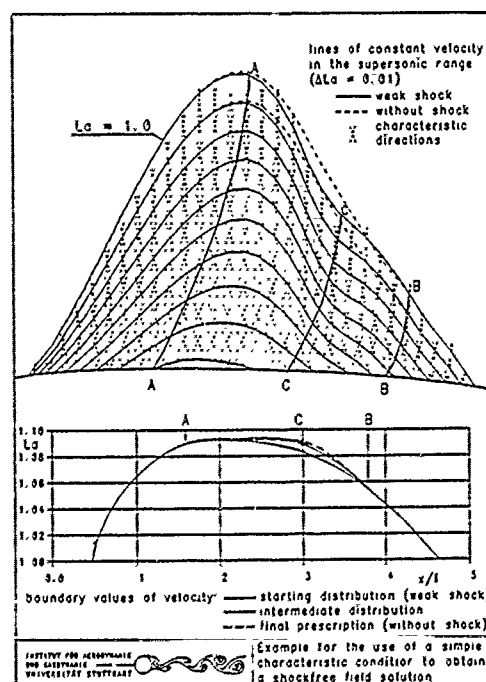


Fig. 3: Procedure for shockfree design.

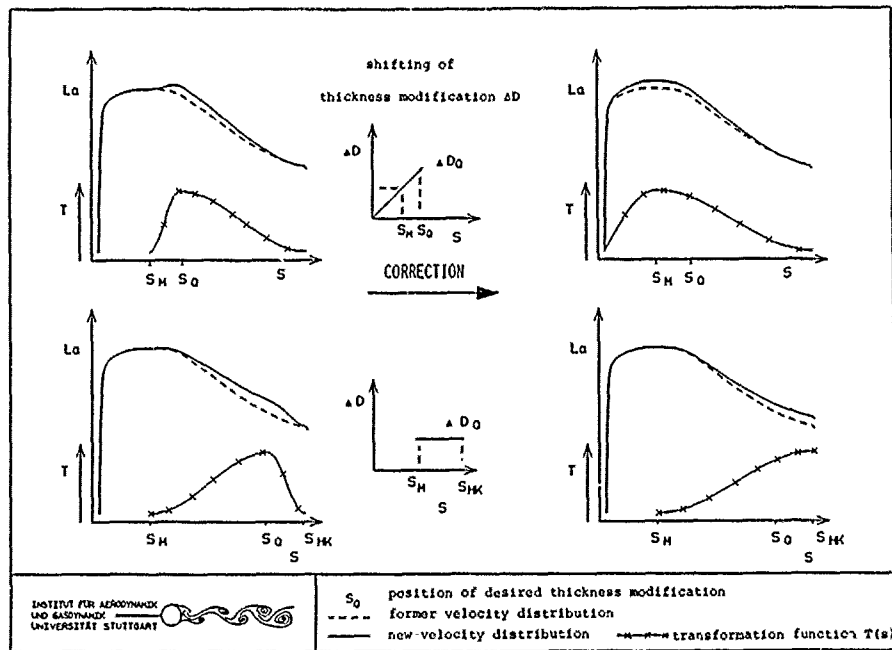


Fig. 4: Transformation of velocity distributions for the profile thickness iteration with shifting corrections.

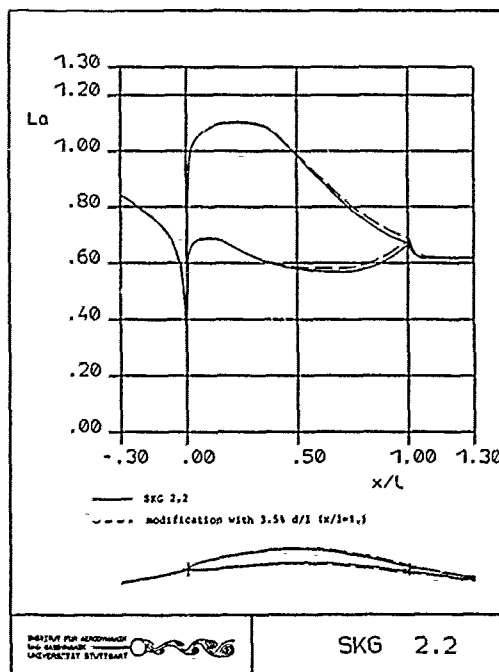


Fig. 5: Thickening of the profile trailing edge.

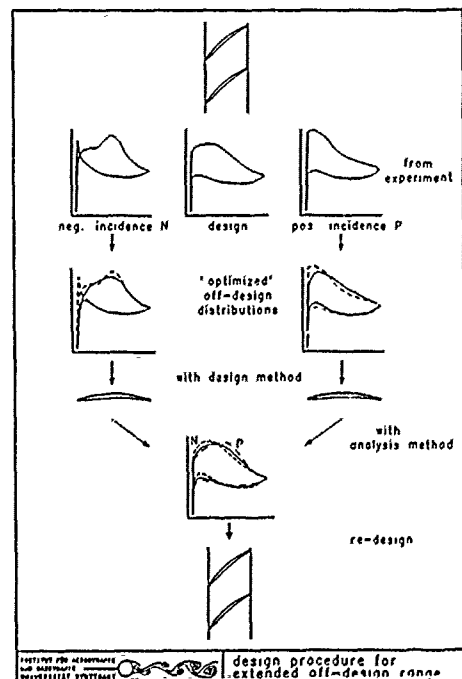


Fig. 6: Design procedure for extended off-design range.

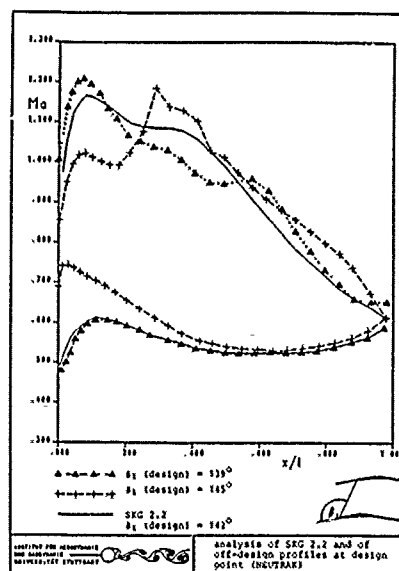


Fig. 7: Comparison of design-point distributions of the original and of the new off-design optimized profiles.

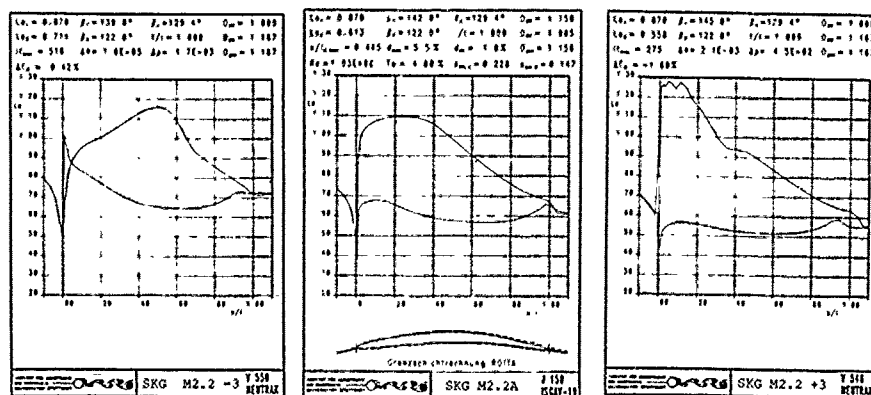


Fig. 8: Design point (centre) and off-design (± 3 degrees) velocity distributions of the original cascade.

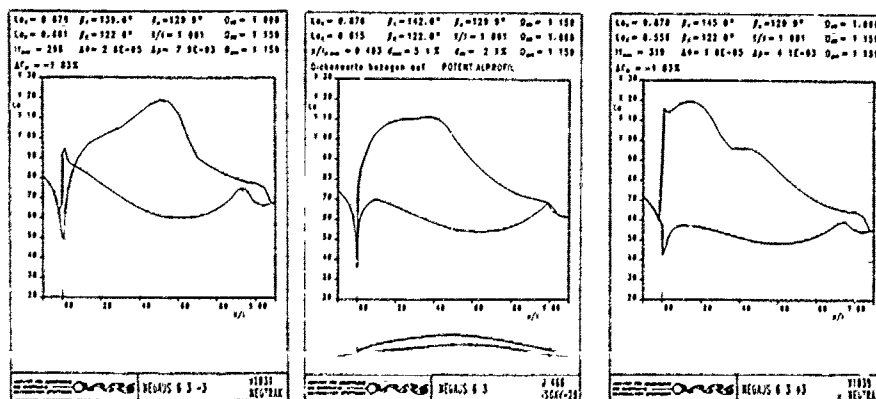


Fig. 9: Design point (centre) and off-design velocity distributions of the off-design optimized cascade.

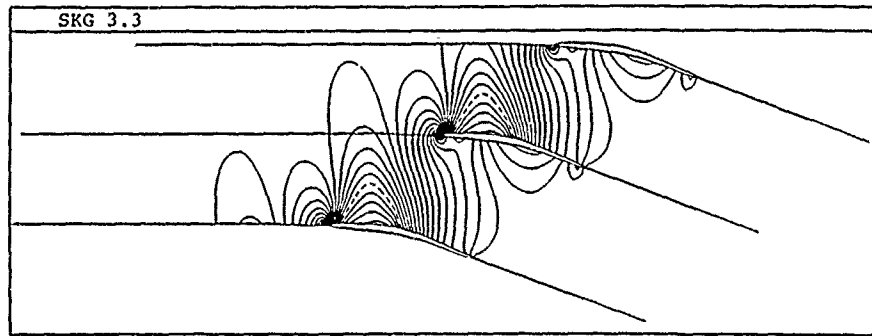


Fig. 10: Contour shape and velocity field of the off-design optimized cascade.

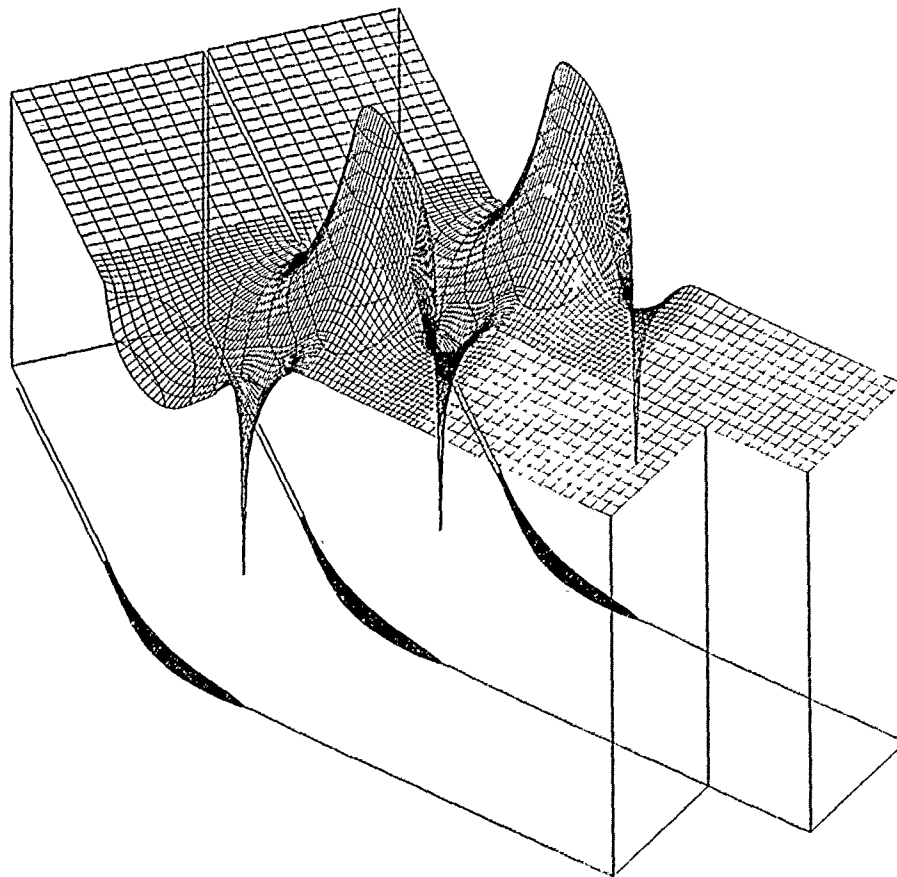


Fig. 11: Computation grid in the flow plane with velocity as height coordinate.

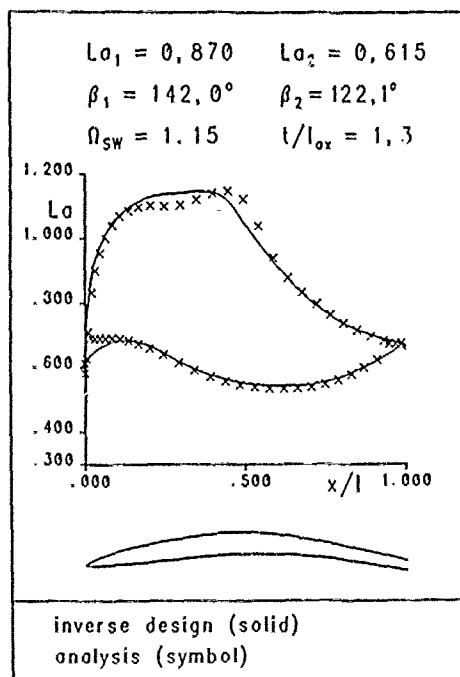


Fig. 12: Comparison of inverse design and analysis computation of the off-design optimized cascade.

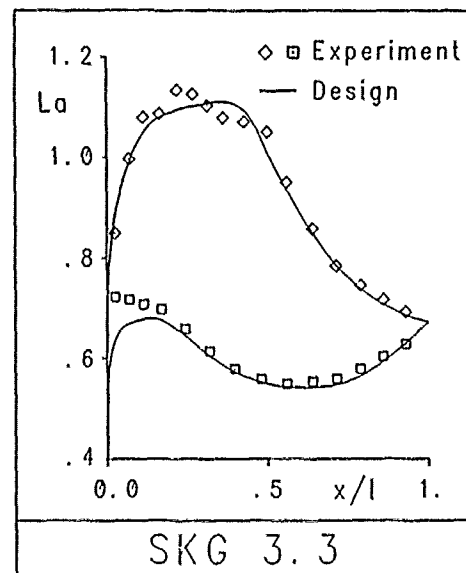


Fig. 13: Comparison of design computation and of experiment.

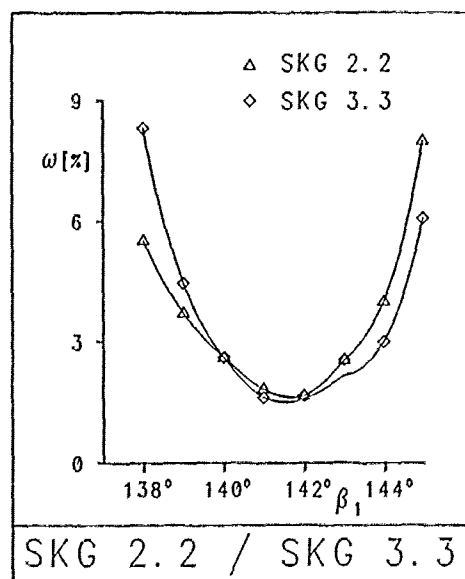


Fig. 14: Comparison of losses of original and off-design optimized cascade /20/.

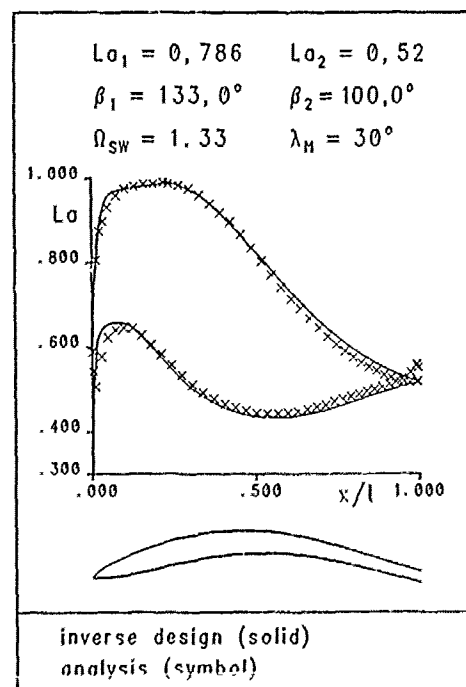


Fig. 15: Comparison of inverse design and analysis computation of a cascade with increasing radius of stream surface.

UNE METHODE INVERSE POUR LA DETERMINATION D'AUBES DE TURBOMACHINES

Olivier-Pierre JACQUOTTE

Office National d'Etudes et de Recherches Aérospatiales
Direction de l'Aérodynamique
92322 CHATILLON-FRANCE

RESUME

Cet article décrit une méthode inverse de détermination de profils de grilles d'aubes de turbomachines, applicable en écoulement transsonique. La méthode développée est relative à l'écoulement quasi-tridimensionnel autour d'une grille d'aubes et est basée sur la résolution en mode inverse de l'équation du potentiel scalaire associé à la vitesse absolue dans un repère relatif lié à l'aube. La définition mathématique correcte de la formulation inverse pour les grilles d'aubes en compressible est examinée. Le profil désiré est obtenu après une série d'itérations résultant de l'ajustement de paramètres autorisant la convergence du procédé. La résolution numérique emploie la méthode des éléments finis. Des résultats sont ensuite présentés. Ils concernent tout d'abord les validations préliminaires de la méthode et montrent la possibilité qu'a celle-ci de restituer un profil connu à partir d'initialisations grossières. Certains cas tests traités sont enfin montrés.

INTRODUCTION

Les performances (charge aérodynamique, rendement) d'un profil dans une grille d'aubes en écoulement subsonique ou transsonique non bloqué sont essentiellement déterminées par la vitesse à l'extrados et à l'intrados du profil. Cette distribution influe en effet directement sur le comportement des couches limites qui se développent sur le profil. Ceci justifie l'étude d'une méthode permettant de définir un profil conduisant à une répartition de vitesse imposée sur celui-ci. Deux approches peuvent être adoptées pour obtenir des profils d'aubes qui possèdent les caractéristiques requises. Les méthodes "directes" d'une part qui consistent à analyser l'écoulement autour d'un profil donné, puis à en modifier la forme si la vitesse sur celui-ci n'est pas satisfaisante; les méthodes "inverses" d'autre part, dans lesquelles une distribution de vitesse ou de pression est choisie et le profil directement déterminé à partir de cette distribution. Alors que la première approche nécessite en général une certaine expérience de l'utilisateur et conduit à un grand nombre d'itérations ou nécessite le couplage avec une méthode d'optimisation numérique, la seconde apparaît mieux adaptée car elle permet d'utiliser directement la distribution de vitesse idéale du point de vue de la couche limite. Naturellement le profil obtenu ne satisfait pas nécessairement les contraintes géométriques ou de structure qui pourraient par ailleurs être imposées. Nous nous proposons de présenter ici une telle méthode inverse appliquée à la détermination de profils d'aubes de turbomachines dans l'approximation d'écoulement potentiel quasi-tridimensionnel (ou approximation 2,5D).

Pour une revue complète des deux classes de méthodes, nous renvoyons à Sloof [7]; nous tenons cependant à mentionner ici certains auteurs qui ont développé des méthodes qui nous ont apporté des idées importantes. Dans [8], Volpe et Melnik ont insisté sur l'importance de contraintes mises en évidence par Lighthill [5], et ont construit un algorithme permettant de déterminer des profils isolés satisfaisant ces contraintes. Cependant leurs choix ne peuvent être appliqués pour la détermination de profils non isolés d'aubes et il a été nécessaire de trouver les bons paramètres permettant de satisfaire ces contraintes. Dans [2], Cedar et Stow ont proposé une méthode d'analyse et de détermination de grilles d'aubes basée sur une discrétisation de type éléments finis. Cette méthode permet d'obtenir un profil par modifications successives en utilisant un modèle de transpiration, cependant, elle ne garantit ni l'existence d'un profil, ni la convergence du processus de modification.

Certains problèmes théoriques sont liés à l'existence de solutions au problème inverse et seront tout d'abord évoqués. En particulier, nous précisons les paramètres qui doivent être laissés libres afin de garantir l'existence d'une solution et la convergence de l'algorithme de détermination de forme. Les équations régissant le modèle potentiel quasi-tridimensionnel sont ensuite rappelées. Elles permettent de prendre en compte les effets de l'épaisseur et de la conicité de la nappe de courant, ainsi que ceux de la rotation de la roue, pour un écoulement de fluide parfait irrotationnel. Pour une distribution de vitesse donnée, nous montrons comment résoudre ces équations de manière à pouvoir modifier un profil

quelconque et en obtenir un nouveau autour duquel l'écoulement correspond à la distribution donnée. L'algorithme numérique utilise une discrétisation par éléments finis qui inclut deux champs d'inconnues: le potentiel dans le domaine et le déplacement normal de la courbe représentant le profil. Nous montrons enfin certains exemples qui ont été traités afin de tester la méthode; en particulier nous montrons un cas de non-unicité qui a été obtenu quand le nombre de paramètres laissés libres n'est pas correct. Quand cette difficulté est correctement prise en compte, la méthode permet, à partir d'initialisations quelconques, d'une part de retrouver un profil connu et d'autre part de déterminer le profil autour duquel l'écoulement correspond à une distribution de vitesse quelconque.

EXISTENCE D'UNE SOLUTION POUR LE PROBLEME INVERSE

Les contraintes de Lighthill

Depuis plusieurs dizaines d'années, le problème inverse en théorie des profils a été étudié et de nombreuses méthodes de construction de profils ont été formulées pour des écoulements incompressibles ou compressibles, subsoniques ou transsoniques, avec ou sans choc. Il a été en particulier démontré par Lighthill [1] que pour un écoulement incompressible autour d'un profil isolé, la solution du problème inverse n'existe pas, à moins que la répartition de vitesse prescrite W_0 ne vérifie certaines contraintes intégrales. Ces relations peuvent s'écrire:

$$\int_{\text{Profil}} \log \left| \frac{W_0(\omega)}{W_\infty} \right| d\omega = 0 \quad (1)$$

$$\int_{\text{Profil}} \log \left| \frac{W_0(\omega)}{W_\infty} \right| \cos \omega d\omega = 0 \quad (2)$$

$$\int_{\text{Profil}} \log \left| \frac{W_0(\omega)}{W_\infty} \right| \sin \omega d\omega = 0 \quad (3)$$

où W_∞ est la vitesse à l'infini, et ω est l'angle polaire dans le plan défini par transformation conforme du profil en cercle. La première contrainte est une conséquence de la conservation de la masse ou, de manière équivalente, elle exprime une nécessaire compatibilité entre la vitesse à l'infini et la vitesse prescrite sur le profil. Les deux dernières contraintes sont liées à la fermeture du profil; si celles-ci ne sont pas satisfaites, un profil peut être obtenu, mais il ne sera pas nécessairement fermé.

Plus tard, Woods [12] a généralisé les résultats de Lighthill au problème inverse mixte où la distribution de vitesse est prescrite sur une partie du profil, la forme étant fixée sur une autre. Certaines autres généralisations ont été obtenues pour l'écoulement incompressible autour de grilles d'aubes (Rosenblat et Woods [6]) ou pour certaines approximations de gaz compressibles: approximation de Karman-Tsien (Woods [11]) ou loi de Chaplyguine (Karadimas [4]). Cependant, aucune relation explicite n'est actuellement connue pour les écoulements transsoniques de gaz parfaits, et aucune étude ne semble avoir été engagée pour les écoulements quasi-tridimensionnels qui sont l'objet de cet article. Il est néanmoins raisonnable de penser que ces relations existent dans le cas général par passage à la limite d'un écoulement incompressible lorsque le nombre de Mach tend vers zéro. Ceci se traduit par le fait que, pour une répartition arbitrairement donnée, il n'existe pas de profil sur lequel la vitesse tangentielle soit égale à la répartition donnée. Afin d'assurer l'existence d'un tel profil, quelques ajustements doivent être autorisés dans la donnée de la vitesse sur le profil pour que trois contraintes soient satisfaites. Ceci peut être accompli en laissant trois paramètres libres dans la répartition donnée.

Récemment, Volpe et Melnik [8, 10] ont proposé quelques choix possibles de paramètres. Ils ont choisi comme premier paramètre la vitesse W_∞ , afin de satisfaire à l'équivalent en incompressible de la première contrainte de Lighthill. Ainsi, en s'imposant une distribution de vitesse donnée en fonction d'une abscisse réduite

$$\xi_{red} = \frac{s}{s_{total}} \quad (4)$$

variant de 0 à 1 sur le profil, ils ont mis au point une méthode permettant d'obtenir un profil, non-fermé, dont la vitesse égale la vitesse donnée à un facteur multiplicatif près [9]. Utilisant cette méthode initiale, ils ont obtenu empiriquement certaines fonctions de modification qui, ajoutées à la distribution initiale,

permettent de contrôler l'épaisseur de l'ouverture du bord de fuite. Ainsi leur méthode permet d'obtenir un profil fermé dont la réponse W_e (vitesse tangentielle) est voisine de celle imposée W_0 , et de la forme:

$$\frac{W_e}{W_\infty} = \frac{a_0}{W_\infty} W_0 + a_1 q_1 + a_2 q_2 \quad (5)$$

où a_0 (respectivement a_1 et a_2) est voisin de 1 (resp. voisins de 0) et q_1 , q_2 sont les fonctions de modification.

Renforcement des contraintes pour les grilles d'aubes

Le cas du calcul inverse est sensiblement différent pour les grilles d'aubes. Tout d'abord, il est apparu que pour les utilisations futures de la méthode, la vitesse à l'infini W_∞ ne peut être modifiée, et ceci interdit l'utilisation de cette quantité comme un paramètre ajustable. D'autre part, le constructeur n'est pas intéressé par l'obtention d'un profil à partir d'une distribution donnée sur tout le profil à l'aide d'une abscisse réduite unique: cette donnée fixe (dans le cas purement bidimensionnel) les longueurs relatives de l'extrados et de l'intrados du profil et donc la position du point d'arrêt. Au contraire, la répartition de vitesse est plus avantageusement utilisable si celle-ci est prescrite indépendamment sur l'extrados et l'intrados du profil, et donc donnée par deux fonctions définies à l'aide de deux abscisses curvilignes réduites, $s_{ext.}$ et $s_{int.}$. La position relative du point d'arrêt sur le profil peut alors être laissée libre, et constituer le premier degré de liberté nécessaire à satisfaire une contrainte.

Il est d'autre part possible de considérer le pas inter-aube comme le second paramètre nécessaire. En effet, dans l'étude menée par Lighthill, le profil recherché est isolé, ce qui revient à fixer le pas ($h \rightarrow \infty$). De même, dans les travaux de Woods, le pas relatif (pas rapporté à la corde du profil) est fixé. Il est d'autre part apparu que pour le constructeur, il est nécessaire dans certains cas de fixer le pas en laissant la corde libre en particulier pour obtenir un nombre entier d'aubes par roue. Ce paramètre est donc choisi pour satisfaire une deuxième contrainte.

Tout comme Volpe et Melnik, le troisième paramètre laissé libre est l'ouverture angulaire au bord de fuite ϵ .

LE MODELE POTENTIEL QUASI-TRIDIMENSIONNEL

Les équations du modèle

L'étude aérodynamique d'une roue de turbomachine axiale peut être abordée avec une certaine approximation en décomposant l'écoulement tridimensionnel en:

- un écoulement moyen dont la caractéristique principale est d'admettre des surfaces de courant de révolution autour d'un axe Oz ,
- un écoulement de grille d'aubes sur chacune des surfaces de révolution constituant une nappe de courant.

Nous supposons que le résultat du calcul de l'écoulement moyen est connu et en particulier que la forme des nappes de courant est donnée par une fonction $r(z)$. On tient compte de la conicité de la veine dans l'écriture de l'équation de continuité en introduisant l'épaisseur $b(z)$ entre deux nappes de courant. Le calcul se fait alors sur une nappe en prenant comme variables indépendantes m et θ où m est l'abscisse curviligne de la méridienne et θ est l'angle repérant une telle méridienne (fig.1). Ces hypothèses constituent l'approximation "2,5D".

Les hypothèses aérodynamiques sont celles d'un écoulement irrotationnel de fluide parfait:

$$\text{rot } \mathbf{V} = 0 \quad (6)$$

où \mathbf{V} est la vitesse absolue du fluide. En tenant compte de la rotation ω de la roue, cette vitesse peut être décomposée en une vitesse relative \mathbf{W} dans un repère lié à l'aube et une vitesse d'entraînement $\omega \mathbf{k} \times \mathbf{r}$:

$$\mathbf{V} = \mathbf{W} + \omega \mathbf{k} \times \mathbf{r} \quad (7)$$

où \mathbf{k} est le vecteur unitaire de l'axe Oz et \mathbf{r} est le vecteur radial repérant le point considéré par rapport à l'axe Oz . D'après (6), il est possible de déduire l'existence d'une fonction potentiel ϕ telle que:

$$\mathbf{V} = \text{grad } \phi \quad (8)$$

et donc:

$$W_m = \frac{\partial \phi}{\partial m} \text{ et } W_\theta = \frac{\partial \phi}{r \partial \theta} - \omega r \quad (9)$$

où W_θ et W_m sont les projections de W sur les axes définis sur la nappe de courant. L'équation de continuité pour l'écoulement supposé stationnaire dans le repère relatif:

$$\operatorname{div}(\rho b r W) = 0 \quad (10)$$

s'écrit alors:

$$\frac{1}{r} \frac{\partial}{\partial \theta} (\rho b r (\frac{\partial \phi}{r \partial \theta} - \omega r)) + \frac{\partial}{\partial m} (\rho b r \frac{\partial \phi}{\partial m}) = 0 \quad (11)$$

La masse volumique s'obtient à l'aide de l'équation de Bernoulli dans le repère relatif:

$$I = \frac{\gamma}{\gamma-1} \frac{p}{\rho} + \frac{1}{2} (W^2 - \omega^2 r^2) = \text{Constante} \quad (12)$$

où la pression p est donnée par:

$$p = p_1 \left(\frac{\rho}{\rho_1} \right)^\gamma \quad (13)$$

Dans la suite, les indices 1 et 2 feront référence aux quantités à l'amont et à l'aval. La masse volumique apparaît donc comme une fonction du potentiel:

$$\rho = \rho_1 \left[1 + \frac{\gamma-1}{2} \frac{M_1^2}{W_1^2} (W_1^2 - W^2 - \omega^2 (r_1^2 - r^2)) \right]^{1/(\gamma-1)} \quad (14)$$

avec:

$$W^2 = \left(\frac{\partial \phi}{\partial m} \right)^2 + \left(\frac{\partial \phi}{r \partial \theta} - \omega r \right)^2 \quad (15)$$

Le système d'équations (11, 14), complété par des conditions aux limites, peut être résolu numériquement par les méthodes classiques, notamment par la méthode des éléments finis qui sera détaillée plus loin. Ces équations sont valables dans le cas où l'écoulement du fluide est transsonique sans choc ou avec des chocs d'intensité faible, c'est à dire pour des nombres de Mach ne dépassant pas 1,4 avant le choc.

Les conditions appliquées aux limites du domaine de calcul et plus particulièrement sur le profil déterminent le mode de résolution: calcul direct ou calcul inverse.

Conditions aux limites en dehors du profil

Supposons tout d'abord que le domaine de calcul soit constitué d'un canal s'appuyant sur deux aubes consécutives (fig.2a). Cette topologie sera dénotée par la lettre II en référence au maillage qui sera aussi construit. Une autre topologie (C) sera aussi considérée (fig.2b); dans celle-ci, le domaine entour l'aube et est limité par deux lignes successives tracées au milieu d'un canal inter-aube.

Nous désignons par h le pas angulaire inter-aube (à l'amont) et nous n'excluons pas la possibilité d'avoir un profil "ouvert" au bord de fuite: celui-ci est alors prolongé par un pseudo-sillage, sans portance, de même épaisseur angulaire ϵ que l'obstruction du bord de fuite. Toutefois dans le cas de l'étude quasi-tridimensionnelle, il n'est pas possible de donner d'interprétation physique au cas où l'obstruction présenterait un décalage en m . Nous limiterons donc l'étude aux seuls cas où les bords de fuite intrados et extrados ont même abscisse m_{BF} . Le canal inter-aube a donc une largeur h en amont et $h-\epsilon$ en aval.

La résolution de (11, 14) nécessite alors la donnée de certaines quantités relatives à l'écoulement en amont et en aval. Le choix fait par le constructeur consiste en la donnée des conditions génératrices amont, nombre de Mach M_1 et direction de l'écoulement α_1 , ainsi que la direction de l'écoulement à l'aval α_2 . Dans le cas où il y a rotation des aubes, outre la valeur ω de la vitesse de rotation, une autre quantité (température ou pression) doit être donnée afin de fixer le paramètre $\omega r_1 / W_1$. Les quantités données à l'amont permettent de calculer celles relatives à l'aval (vitesse W_2 et masse volumique ρ_2), en utilisant la conservation du débit qui peut s'écrire:

$$h b_1 r_1 \rho_1 W_1 \cos \alpha_1 = (h - \epsilon) b_2 r_2 \rho_2 W_2 \cos \alpha_2 \quad (16)$$

Alors, sur la frontière AB et GH du domaine (fig.2a), on peut appliquer une condition de débit (condition de Neumann):

$$\rho b \frac{\partial \phi}{\partial n} = \rho_1 b_1 W_1 \cos \alpha_1 \quad \text{sur AB} \quad (17.a)$$

$$\rho b \frac{\partial \phi}{\partial n} = \rho_2 b_2 W_2 \cos \alpha_2 \quad \text{sur GH} \quad (17.b)$$

En ce qui concerne la topologie en C (fig.2b), ces conditions sont appliquées sur les côtés AB d'une part, et CD \cup EF d'autre part.

La périodicité des aubes fournit un autre type de condition aux limites du domaine; en effet, si la vitesse est la même entre deux points quelconques séparés d'un pas angulaire h , il est clair que la différence de potentiel en ces deux points est une constante. En effet, si on a:

$$W_m(m, \theta+h) = W_m(m, \theta) \quad \text{et} \quad W_\theta(m, \theta+h) = W_\theta(m, \theta) \quad (18)$$

on a nécessairement:

$$\phi(m, \theta+h) = \phi(m, \theta) + C \quad (19)$$

En particulier pour les parties AC et BD d'une part, et EG et FH d'autre part, une condition de périodicité est imposée:

$$\phi_{BD} = \phi_{AC} + C_1 \quad (20.a)$$

$$\phi_{FH} = \phi_{EG} + C_2 \quad (20.b)$$

où les constantes C_1 et C_2 sont calculées à l'amont et à l'aval où l'écoulement est supposé uniforme:

$$C_1 = h r_1 (W_1 \sin \alpha_1 + \omega r_1) \quad (21.a)$$

$$C_2 = (h - e) r_2 (W_2 \sin \alpha_2 + \omega r_2) \quad (21.b)$$

Dans le cas de la topologie C, les conditions de périodicité s'écrivent:

$$\phi_{BF} = \phi_{AC} + C_1 \quad (22.a)$$

$$\phi_{HE} = \phi_{GD} + C_3 \quad (22.b)$$

avec

$$C_3 = C_1 - C_2 \quad (23)$$

PRINCIPE DE LA DÉTERMINATION INVERSE

Conditions sur le profil

Les conditions manquantes sur le profil (côtés CE et DF dans la topologie H et GH dans la topologie C) dépendent du problème traité. Pour un calcul direct, des conditions de paroi de type Neumann (vitesse relative normale au profil nulle) sont appliquées. Il est alors nécessaire de fixer le potentiel en un point du domaine afin d'assurer l'unicité de celui-ci.

En mode inverse, une condition de type Dirichlet est imposée sur le profil: supposons que l'on se donne sur le profil une répartition de vitesse relative W_0 ; on peut alors définir une fonction ϕ_0 par intégration de W_0 le long du profil donné par une représentation $(m, \theta(m))$. Cette fonction doit vérifier:

$$W_0(s)^2 = \left(\frac{\partial \phi_0}{\partial m} \right)^2 + \left(\frac{\partial \phi_0}{r \partial \theta} - \omega r \right)^2 \quad (24)$$

où s représente l'abscisse curviligne le long du profil:

$$ds^2 = dm^2 + r^2 d\theta^2 \quad (25)$$

La fonction ϕ_0 peut donc être obtenue par intégration de:

$$\frac{d\phi_0}{ds} = W_0 + \omega r^2 \frac{d\theta}{ds} \quad (26)$$

La résolution de l'équation du potentiel avec prescription de ϕ_0 sur le profil est appelée résolution inverse et est à la base de la méthode de détermination de profil proposée dans cet article.

Modification du profil

La détermination inverse consiste à trouver un profil qui satisfait à la fois:

a) Vitesse Normale = 0
et b) Vitesse tangentielle = W_0 donnée
sur le profil. La solution du problème direct (condition de Neumann sur le profil) satisfait a) mais pas b). La solution d'un problème inverse (condition de Dirichlet issue de l'intégration d'une donnée W_0) satisfait b) mais une vitesse normale au profil non nulle est obtenue si le profil n'est pas celui recherché. Cette vitesse normale résiduelle W_n peut alors être utilisée pour modifier le profil; l'équation régissant cette modification peut être déduite d'un modèle de transpiration dans lequel on considère une injection fictive de fluide à travers la surface du profil associée à la vitesse normale et de débit $\rho b W_n$. Le nouveau profil recherché doit constituer alors une surface de courant. Le déplacement normal à la paroi ξ à effectuer pour passer d'un profil à l'autre peut être obtenu en écrivant la conservation de la masse entre deux surfaces (figure 3):

$$\rho b W_n ds = \rho b W_0 \xi|_{r+d} - \rho b W_0 \xi|_r \quad (27)$$

d'où l'équation pour ξ :

$$\frac{d}{ds} (\rho b W_0 \xi) = \rho b W_n \quad (28)$$

Principe de la méthode

La méthode inverse consiste donc en une succession d'itérations comportant les trois étapes suivantes:

- 1) calcul de la condition de Dirichlet par intégration de (26);
- 2) résolution du problème inverse avec condition de Dirichlet sur le profil;
- 3) modification du profil par résolution de (28).

Les étapes 1 et 3 sont des intégrations unidimensionnelles. L'étape 2 est la résolution d'une équation aux dérivées partielles bidimensionnelles, non linéaire, du second ordre que l'on choisit de résoudre en utilisant une méthode dérivée de celle mise au point pour les écoulements dans les tuyères et autour de profils isolés [1] et décrite plus loin. Remarquons d'une part que cette méthode détermine les valeurs du potentiel aux noeuds d'un maillage et donc la valeur de la vitesse et de la masse volumique au barycentre des mailles; la dérivée curviligne dans le membre de gauche dans (28) ne peut donc être définie que dans un sens faible. D'autre part, la vitesse normale est difficilement évaluée à partir de valeurs du potentiel aux noeuds mais peut, elle aussi, être définie dans un sens faible. Ces remarques mettent en évidence la nécessité d'introduire une formulation correcte de (28) compatible avec la méthode utilisée pour calculer le potentiel.

RESOLUTION NUMERIQUE DU PROBLEME INVERSE

Formulation variationnelle continue du problème inverse

La méthode inverse décrite introduit à chaque itération deux champs d'inconnues: le potentiel ϕ défini dans le domaine et sur le profil, ainsi que le déplacement normal ξ défini sur le profil à chaque modification. Une méthode d'éléments finis a été choisie pour la résolution numérique des équations du modèle; celle-ci repose sur une formulation variationnelle qui est obtenue par multiplication des équations (11, 26, 28) par des fonctions test ψ (admissible) et ζ définies respectivement dans Ω et sur le profil. Par "admissible" nous signifions que les fonctions test ψ satisfont la condition de périodicité. Après intégration par parties, on obtient une formulation qui couple les deux champs d'inconnues:

Trouver ϕ défini dans Ω et ξ défini sur le profil tels que:

$$\int_{\Omega} \rho b \left[\frac{\partial \phi}{\partial m} \frac{\partial \psi}{\partial m} + \left(\frac{\partial \phi}{r \partial \theta} - \omega r \right) \frac{\partial \psi}{r \partial \theta} \right] r dm d\theta - \int_{\Gamma_{rofil}} \psi d(\rho b W_0 \xi) = \int_{\Gamma_{\infty}} g \psi dV \quad (29.a)$$

$$\int_{\Gamma_{rofil}} \rho b W_0 \zeta (d\phi - \omega r^2 d\theta) = \int_{\Gamma_{rofil}} \rho b W_0^2 \zeta ds \quad (29.b)$$

pour tout ψ admissible défini dans Ω et ζ défini sur le profil.

La formulation mixte (29) présente plusieurs attraits. Tout d'abord, elle est symétrique par rapport aux deux couples de champs (ϕ, ξ) et (ψ, ζ) (quand la masse volumique est supposée constante), ce qui est satisfaisant mathématiquement: en effet les théorèmes d'existence, d'unicité et de convergence de solutions pour de tels problèmes mixtes ne peuvent être établis que pour des systèmes symétriques. D'autre part, c'est cette formulation qui permettra, une fois discrétisée, d'intégrer l'équation de modification de manière consistante avec la méthode des éléments utilisée pour calculer le potentiel.

Les formulations variationnelles correspondant à chacune des trois étapes du calcul inverse sont donc:

- *Intégration de la vitesse sur le profil:* on résout (29.b) ce qui permet de calculer ϕ_0 sur le profil:

Trouver ϕ_0 défini sur le profil tel que:

$$\int_{\text{Profil}} \rho b W_0 \zeta (d\phi_0 - \omega r^2 d\theta) = \int_{\text{Profil}} \rho b W_0^2 \zeta ds \quad (30)$$

pour tout ζ défini sur le profil.

Cette formulation variationnelle est en fait équivalente à la formule d'intégration (26).

- *Calcul du potentiel avec condition de Dirichlet sur le Profil:* on se limite dans (29.a) aux fonctions tests ψ nulle sur le profil:

Trouver ϕ défini dans Ω tel que $\phi = \phi_0$ sur le profil et

$$\int_{\Omega} \rho b \left[\frac{\partial \phi}{\partial m} \frac{\partial \psi}{\partial m} + \left(\frac{\partial \phi}{r \partial \theta} - \omega r \right) \frac{\partial \psi}{r \partial \theta} \right] r dm d\theta = \int_{\Gamma_{\infty}} g \psi d\Gamma \quad (31)$$

pour tout ψ défini dans Ω et nul sur le profil.

- *Modification du Profil:* ϕ étant connu dans tout le domaine, on résout (29.a) en se limitant aux restrictions des fonctions ψ sur le profil:

Trouver ξ défini sur le profil tel que:

$$\int_{\text{Profil}} \psi d(\rho b W_0 \xi) = \int_{\Omega} \rho b \left[\frac{\partial \phi}{\partial m} \frac{\partial \psi}{\partial m} + \left(\frac{\partial \phi}{r \partial \theta} - \omega r \right) \frac{\partial \psi}{r \partial \theta} \right] r dm d\theta \quad (32)'$$

pour tout ψ défini sur le profil.

Le second membre de (32) constitue une représentation faible du flux normal $\rho b W_n$ à travers le profil.

Discrétisation par éléments finis

La première étape de la discrétisation consiste à construire dans les domaines considérés (topologie II ou C) un maillage. Pour les calculs, il est utile de profiter des simplifications qu'apporte une structure "i,j" de ce maillage: construction facile du maillage, programmation et vectorisation aisées. On choisit donc une discrétisation utilisant des éléments finis quadrilatéraux Q_1 . Une contrainte imposée aux maillages est dictée par les conditions aux limites de type périodique: afin de pouvoir facilement les prescrire, on impose que les noeuds situés sur les lignes BD et FH du domaine (topologie en II) se déduisent par translation d'un pas des noeuds sur AC et EG. En ce qui concerne la topologie en C, on suppose qu'il en est de même pour la ligne de maillage BF par rapport à AC, ainsi que HE par rapport à CD (translation de ϵ). Un exemple de chacun des types de maillages qu'il est possible de construire est montré sur la figure 4; ils permettent de disposer d'une partition du domaine Ω :

$$\Omega = \bigcup_e \Omega_e \quad (33)$$

où les Ω_e dénotent les éléments du maillage. On définit tout d'abord un espace de dimension finie V^h , espace d'approximations des fonctions admissibles, défini par:

$$V^h = \{ \phi^h \text{ admissible et continue ; } \phi^h|_{\Omega_e} \in Q_1(\Omega_e) \} \quad (34)$$

où Q_1 est l'ensemble des polynômes bilinéaires sur \mathbb{R}^2 :

$$Q_1 = \{ a + bx + cy + dxy; (a, b, c, d) \in \mathbb{R}^4 \} \quad (35)$$

Une base de V^h est constituée des fonctions ϕ_{ij} valant 1 au noeud (i,j) du maillage et 0 en tous les autres et qui respectent les conditions de périodicité.

Un espace d'approximation pour les fonctions de modification doit aussi être choisi. Remarquons tout d'abord que cet espace peut inclure des fonctions discontinues. L'intégrale du membre de gauche de (32) est alors définie au sens des distributions et peut s'exprimer en terme de saut:

$$\int_{\text{profil}} \psi_i d(\rho b W_0 \xi) = \rho b W_0 \xi |_i^+ - \rho b W_0 \xi |_i^- \quad (36)$$

où ψ_i est une fonction de base de V^h valant 1 sur un noeud i du profil, et + et - désignent les valeurs de quantités à droite et à gauche de ce noeud sur le profil.

Conformément à ce qui est d'habitude choisi pour ce genre de problème mixte afin d'assurer l'unicité de la solution, il est raisonnable de prendre l'espace d'approximation des fonctions ζ dans un espace de polynômes de degré moindre que celui des fonctions ψ . L'espace choisi est donc:

$$Q^h = \{ \zeta^h / \zeta^h |_{\Gamma_e} \text{ constant sur } \Gamma_e \} \quad (37)$$

où Γ_e désigne un élément sur le profil:

$$\Gamma_e = \Omega_e \cap \text{Profil} \quad (38)$$

La formulation discrète du problème variationnel (29) s'obtient en remplaçant les fonctions continues par leurs approximations. Dès lors, la résolution de (30) est immédiate, elle correspond à l'intégration de la vitesse W_0 donnée et permet d'obtenir les valeurs du potentiel aux noeuds situés sur le profil par:

$$\phi^{i+1/2} = \phi^i + W_0^{i+1/2} \Delta s^{i+1/2} + \omega r^{i+1/2} \Delta \theta^{i+1/2} \quad (39)$$

où l'indice $i+1/2$ désigne la valeur des quantités correspondantes entre les noeuds i et $i+1$. Conformément aux choix imposés pour l'existence d'une solution de la méthode inverse, cette intégration est effectuée séparément sur l'extrados et l'intrados du profil à partir du point d'arrêt où le potentiel peut être choisi égal à 0. Ceci permet de calculer la différence de potentiel $\Delta \phi$ au bord de fuite entre l'intrados et l'extrados, puis la valeur du pas inter-aube et des conditions à l'aval: en effet, ces quantités doivent satisfaire:

• l'équation de circulation:

$$\Delta \phi = r_2 (h - e) (W_2 \sin \alpha_2 + \omega r_2) - r_1 h (W_1 \sin \alpha_1 + \omega r_1) \quad (40)$$

• l'équation de conservation du débit:

$$\rho_1 b_1 r_1 h W_1 \cos \alpha_1 = \rho_2 b_2 r_2 (h - e) W_2 \cos \alpha_2 \quad (41)$$

avec

$$\rho_2 = \rho_1 \left[1 + \frac{\gamma-1}{2} \frac{M_1^2}{W_1^2} (W_1^2 - W_2^2 - \omega^2 (r_1^2 - r_2^2))^{1/(\gamma-1)} \right] \quad (42)$$

Ces trois équations sont résolues simultanément de manière itérative et permettent de calculer h , ρ_2 et W_2 .

Le problème variationnel (31) conduit à la formulation faible discrète d'un problème de Dirichlet. En prenant successivement comme fonctions tests toutes les fonctions de bases de V^h nulles sur le profil, on obtient un système d'équations non-linéaires de la forme:

$$A(\Phi) \cdot \Phi = B \quad (43)$$

où Φ dénote le vecteur formé des valeurs de ϕ aux noeuds du maillage et où A est une matrice qui dépend de Φ du fait de la dépendance de ρ en ϕ . La non-linéarité de ce système est traitée par un algorithme mixte combinant un algorithme de point fixe dans les régions supersoniques et un algorithme de Newton dans les régions subsoniques. D'autre part, afin d'assurer l'unicité d'une solution physique, une viscosité artificielle est introduite dans les régions supersoniques par le biais d'un décentrement de la masse volumique effectué conformément aux résultats satisfaisants obtenus pour les profils isolés [1]. Il consiste à considérer une combinaison de la masse volumique dans l'élément et dans l'élément amont:

$$\bar{\rho}_i = \rho_i - \nu_i (\rho_i - \rho_{i-1}) \quad (44)$$

où ν_i est une fonction du nombre de Mach local:

$$\nu_i = \max(0, 1 - \frac{1}{0.3 M_{i-1}^2 + 0.7 M_i^2}) \quad (45)$$

Les systèmes linéaires obtenus à la suite de cette linéarisation sont résolus par un algorithme de gradient conjugué avec préconditionnement incomplet de Choleski [1].

Finalement, la résolution de (32) peut être effectuée en considérant les fonctions ψ_i de la base de V^h égales à 1 au noeud i du profil et 0 à tous les autres. Le déplacement ξ n'étant pas nécessairement continu, les intégrales dans (32) sont prises au sens des distributions et conduisent au saut de la quantité $\rho b W_0 \xi$.

$$\rho b W_0 \xi|_i^+ - \rho b W_0 \xi|_i^- = \rho b W_n|_i \quad (46)$$

où la quantité au second membre représente le flux de masse à travers le noeud i qui est calculé par:

$$\rho b W_n|_i = \int_{\Omega} \rho b \left[\frac{\partial \phi}{\partial m} \frac{\partial \psi_i}{\partial m} + \left(\frac{\partial \phi}{r \partial \theta} - \omega r \right) \frac{\partial \psi_i}{r \partial \theta} \right] r \, dm \, d\theta \quad (47)$$

Le déplacement normal ξ de chaque facette est donc intégré à partir du point d'arrêt vers le bord de fuite. Une moyenne en chaque noeud est ensuite effectuée pour obtenir le nouveau profil. D'autre part, afin d'éviter des oscillations et d'accélérer la convergence des profils, un coefficient de sous-relaxation ($\delta = 0.5$) a été introduit dans l'équation de modification, ainsi (46) est remplacée par:

$$\rho b W_0 \xi|_i^+ - \rho b W_0 \xi|_i^- = \delta \rho b W_n|_i \quad (48)$$

RESULTATS NUMERIQUES

Dans cette partie nous montrons et commentons les résultats que la méthode a permis d'obtenir. Ils concernent les premiers essais qui ont été faits afin de vérifier la possibilité qu'a la méthode de retrouver des profils connus à partir d'initialisations arbitraires dans le cas purement bidimensionnel ($\omega=0, r=b=1$), nous comparons ensuite les résultats obtenus en utilisant les deux types de maillage. Un exemple quasi-tridimensionnel à caractère plus industriel est enfin présenté.

Grille Hobson

Afin de tester la méthode inverse, il est tout d'abord apparu intéressant de vérifier si celle-ci était capable de retrouver un profil connu à partir d'initialisations relativement éloignées de la solution. Le profil choisi est le profil Hobson (fig.5a) [3], dont la distribution de vitesse exacte est montrée sur la figure 5b. Les grandeurs caractéristiques sont les suivantes:

$$\begin{aligned} M_1 &= 0.575 \\ \alpha_1 &= +0.805 \text{ rad} \\ \alpha_2 &= -0.805 \text{ rad} \\ h &= 0.5259 \end{aligned}$$

Différentes initialisations de plus en plus lointaines du profil Hobson recherché ont été essayées, en particulier:

- une initialisation symétrique constituée d'un autre profil de type Hobson plus épais (fig.6a),
- une initialisation non-symétrique et fermée constituée du profil recherché ayant subi une rotation de 5 degrés (fig.6b),
- un profil ouvert constitué de l'extrados du profil recherché ayant subi une rotation de 5 degrés, et d'un intrados tel que $y = 0$: ce profil est ouvert au bord de fuite (fig.6c).

Pour ces trois initialisations, le profil a été retrouvé respectivement après 5, 8 et 12 modifications. Pour 10 modifications d'un profil défini par 121 points dans un maillage de 1936 noeuds, le temps cpu nécessaire est de 8 s. sur CRAY XMP-18.

Nous avons aussi essayé de relâcher la contrainte $\Delta m = 0$ au bord de fuite. Conformément à l'étude théorique qui prévoit la non-unicité du profil, plusieurs profils peuvent être trouvés selon l'initialisation. Nous montrons sur la figure 7a les modifications successives du profil à partir de la troisième initialisation précédemment décrite. Le maillage autour du profil convergé ainsi que les lignes iso-nombre de Mach sont aussi montrées (fig.7b et c): la distribution pariétale obtenue est bien celle imposée.

Détermination d'un Profil de Redresseur

Pour cet exemple, la distribution de vitesse représentée sur la figure 8 a été fournie. Les deux versions (II et C) du code ont été testées avec les initialisations suivantes:

- Maillage en II: profil d'épaisseur nulle d'équation $y = 0$,

- Maillage en C: profil NACA12 ayant subi une rotation de 5 degrés.

Les figures 9a et b montrent les modifications successives des profils à partir de l'initialisation. Les maillages autour des profils convergés sont ceux ayant servi d'illustration précédemment (fig. 4a et b).

Les formes des profils obtenus sont voisines (fig. 10); cependant le profil obtenu avec la version en H (fig. 10a) reste pointu alors que le profil obtenu avec le maillage en C (fig. 10b) est arrondi. Les résultats d'un calcul direct autour de ces profils montrent le meilleur respect de la distribution de la vitesse imposée par le profil obtenu par le code avec maillage en C. Le pas relatif (rapporté à la corde du profil) est également calculé par le code; les valeurs obtenues sont voisines: 0.6908 pour le code avec maillage en C et 0.6787 pour le code avec maillage en H. La valeur plus petite calculée avec le code avec maillage en H s'explique par le bord d'attaque pointu du profil qui allonge le profil et donc diminue la valeur de h .

Résultat d'un calcul inverse quasi-tridimensionnel

Le problème consiste à retrouver un profil à partir des résultats obtenus par un calcul direct par une méthode de différences finies. Les données sont les suivantes:

- donnée de la nappes sous la forme d'une série de points (z_i, r_i, b_i) reportés sur la figure 11a,
- donnée d'une distribution du nombre de Mach en fonction de l'abscisse réduite sur l'extrados et l'intrados (figure 11b),
- vitesse de rotation de la roue: $\omega = -9551 \text{ tours/minute}$,
- conditions génératrices: $M_1 = 0.691$, $\alpha_1 = 35.41^\circ$, $\alpha_2 = -11.88^\circ$,
- température totale en repère fixe: $T_0 = 288^\circ \text{K}$.

Les résultats obtenus sur ce cas test sont montrés sur la figure 12. Ils montrent les modifications successives à partir d'un profil initial (NACA12 ayant subi une rotation de 20 degrés) vers un profil à bord d'attaque arrondi. Ce calcul permet d'autre part de calculer le pas: on obtient $h = 0.1897$ ce qui correspond à 33-aubes.

REMERCIEMENTS

Cette étude a été effectuée avec le soutien financier de la S.N.E.C.M.A. (Société Nationale d'Etude et de Construction de Moteurs d'Avions) sous contrat SNECMA/ONERA N° 265 883 DY.

REFERENCES

- [1] M. BREDIF, "A Fast Finite Element Method for Transonic Potential Flow Calculations", AIAA Paper N° 83-0507, AIAA 21st Aerospace Sciences Meeting, Reno, NEV, U.S.A., 1983.
- [2] R.D. CEDAR and P. STOW, "A Compatible Mixed Design and Analysis Finite Element Method for the Design of Turbomachinery Blades", Int. J. Num. Meth. in Fluids, Vol. 5, pp. 331-345, 1985.
- [3] D.E. HOBSON, "Shock-Free Transonic Flow in Turbomachinery Cascade", Cambridge Univ. Eng. Dept., CUED/A Turbo/TR65, 1974.
- [4] G. KARADIMAS, "Calcul Analytique des Grilles d'Aubes", Septième Colloque d'Aéronautique Appliquée organisé par l'A.F.T.A.E., 4-6 Déc. 1970.
- [5] M.J. LIGHTHILL, "A New Method of Two-Dimensional Aerodynamical Design", R. & M. N° 2112, Aeronautical Research Council, London, 1945.
- [6] S. ROSENBLAT et L.C. WOODS, "A Method of Cascade Design for Two-Dimensional Incompressible Flow", Report N° ACA-58, Australian Aeronautical Research Committee, 1956.
- [7] J.W. SLOOF, "A Survey of Computational Methods for Subsonic and Transonic Aerodynamic Design", Proceedings of the International Conference on Inverse Concepts in Engineering, Austin, TX, U.S.A., 1984.
- [8] G. VOLPE et R.E. MELNIK, "The Role of Constraints in the Inverse-Design Problem for Transonic Airfoils", AIAA Paper N° 81-1233, AIAA 14th Fluid and Plasma Conf., 1981.
- [9] G. VOLPE et R.E. MELNIK, "The Inverse Design of Closed Airfoils in Transonic Flows", AIAA Paper N° 83-0504, AIAA 21st Aerospace Sciences Meeting, Reno, NEV, U.S.A., 1983.
- [10] G. VOLPE et R.E. MELNIK, "The Design of Transonic Airfoils by a Well-Posed Inverse Method", Proceedings of the International Conference on Inverse Concepts in Engineering, Austin, TX, U.S.A., 1984.
- [11] L.C. WOODS, "Airfoil Design in Two-Dimensional Subsonic Compressible Flow", R. & M. N° 2845, Aeronautical Research Council, London, 1952.
- [12] L.C. WOODS, "The Design of Two-Dimensional Airfoils with Mixed-Boundary Conditions", Quart. Appl. Math., Vol. 13, pp. 139-145, 1955.

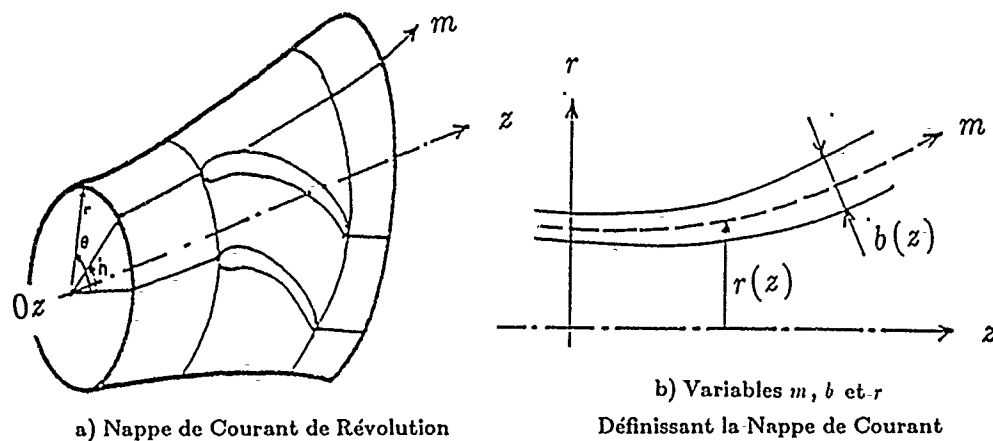


Figure 1: Définition de la Géométrie Quasi-Tridimensionnelle

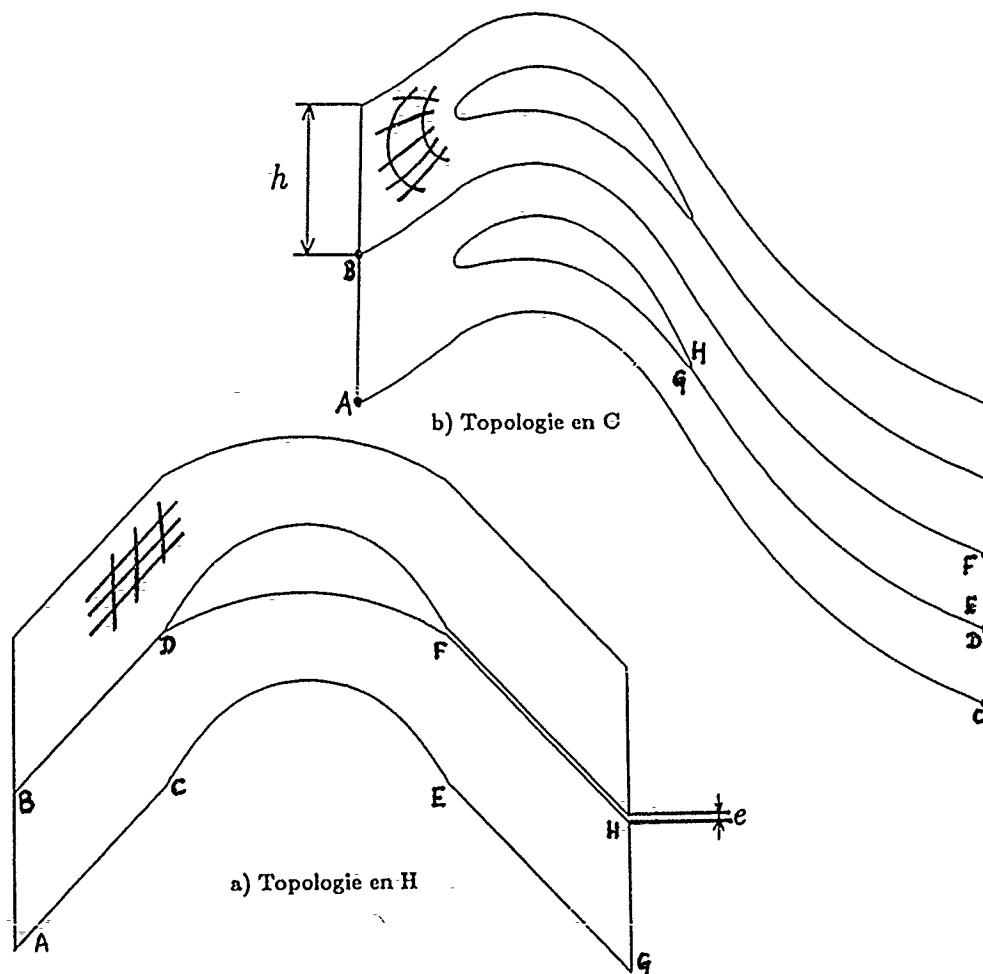


Figure 2: Topologies du Domaine de Calcul

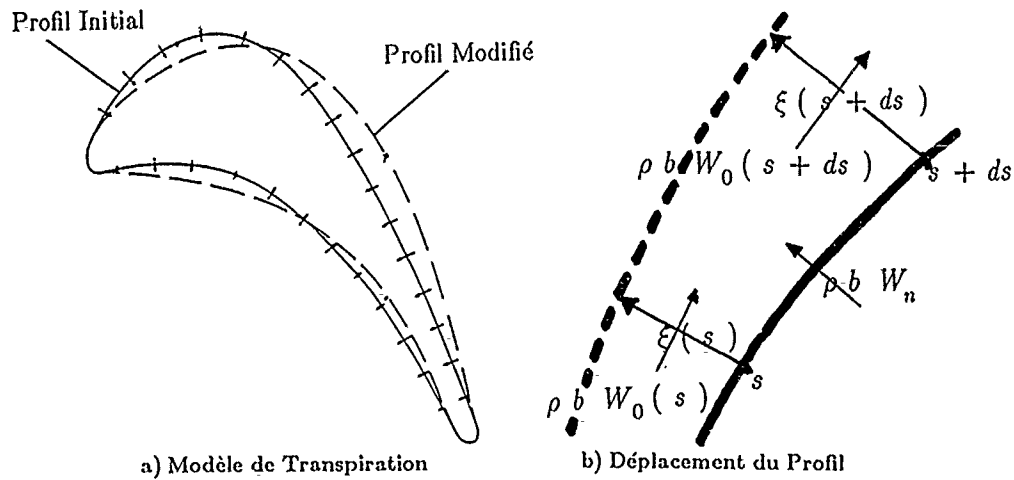


Figure 3: Déplacement Normal du Profil

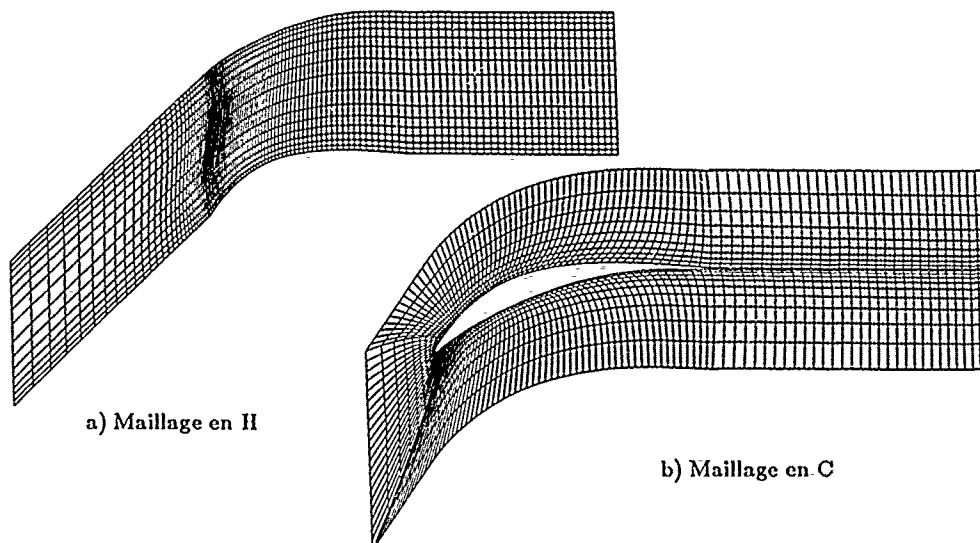


Figure 4: Exemples de Maillages

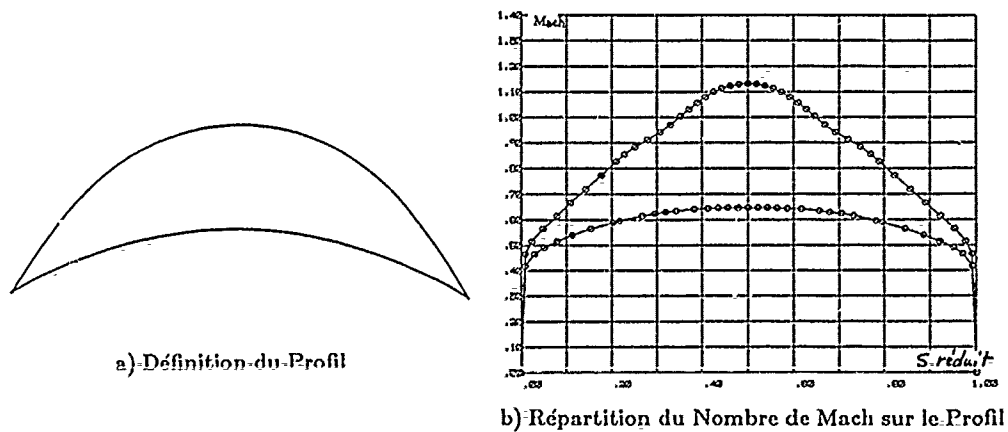
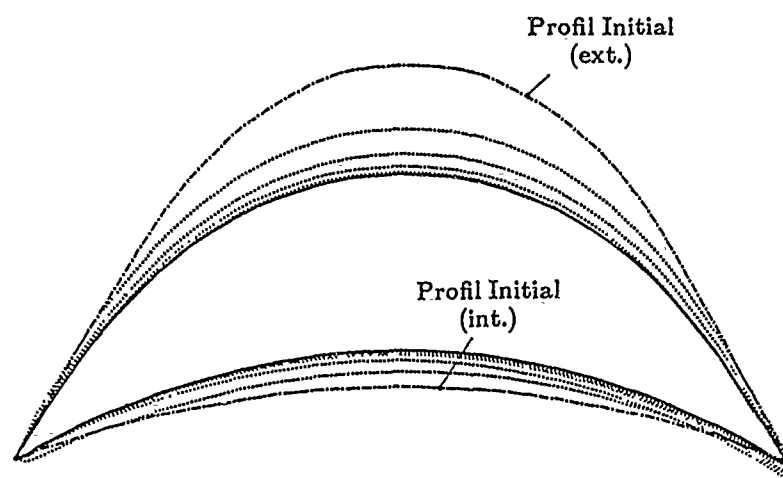
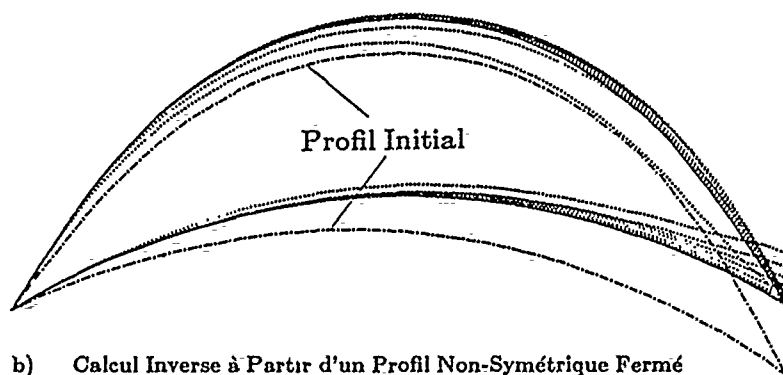


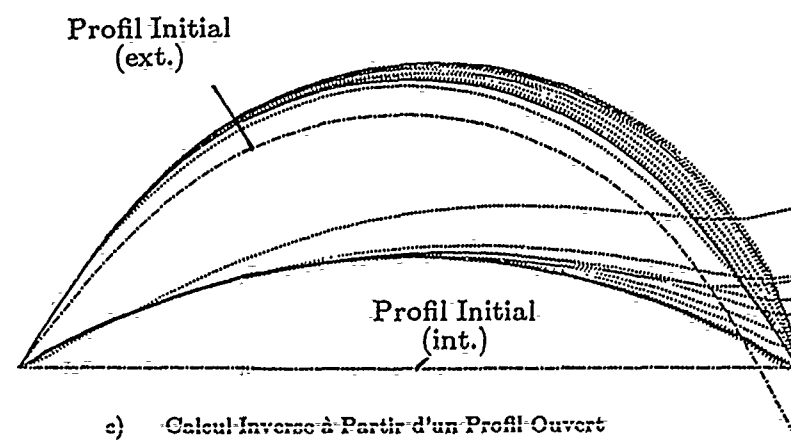
Figure 5: Profil Hobson



a) Calcul Inverse à Partir d'un Profil Symétrique

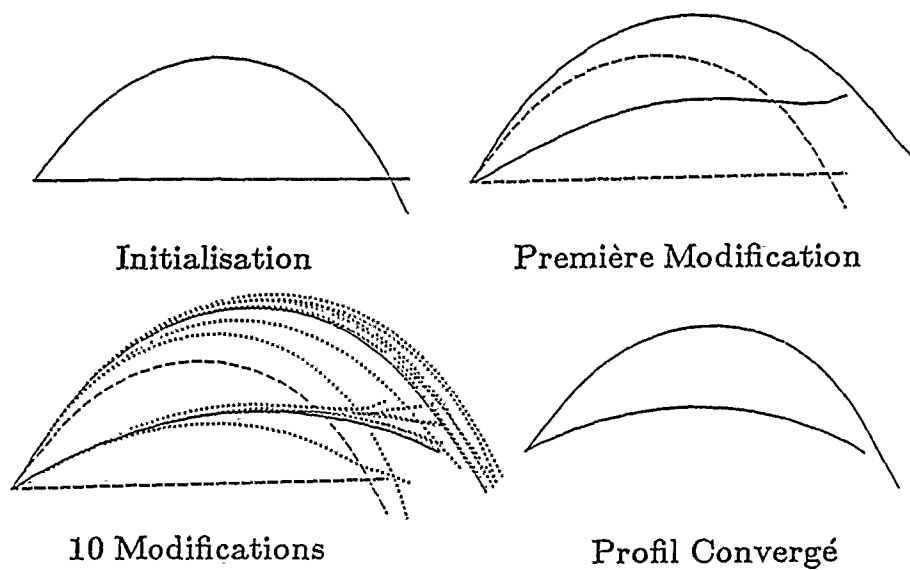


b) Calcul Inverse à Partir d'un Profil Non-Symétrique Fermé



c) Calcul Inverse à Partir d'un Profil Ouvert

Figure 6: Calcul Inverse: Modification Successives du Profil



a) Dix Premières Modifications et Profil Convergé

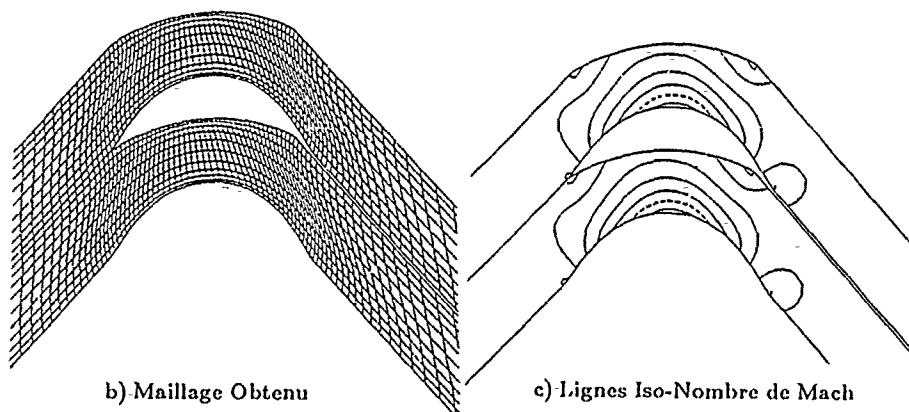


Figure 7: Non-Unicité de la Solution du Calcul Inverse

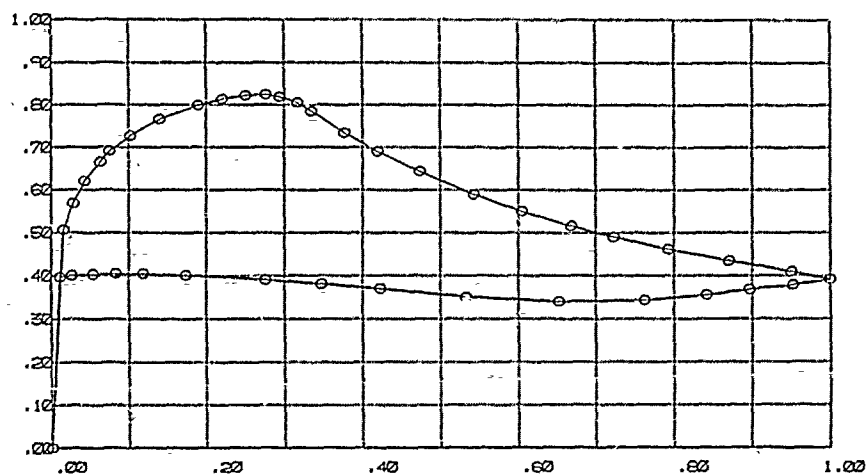
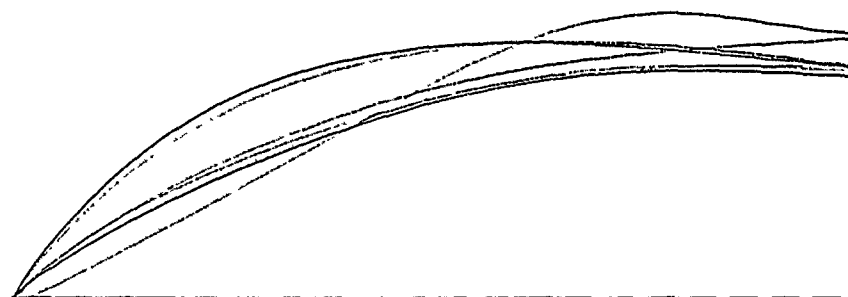
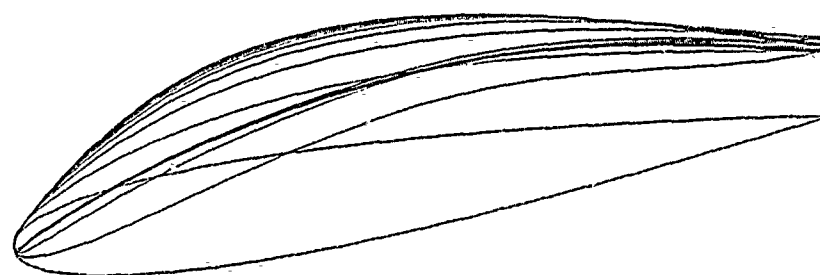


Figure 8: Distribution du Nombre de Mach pour le Calcul du Redresseur

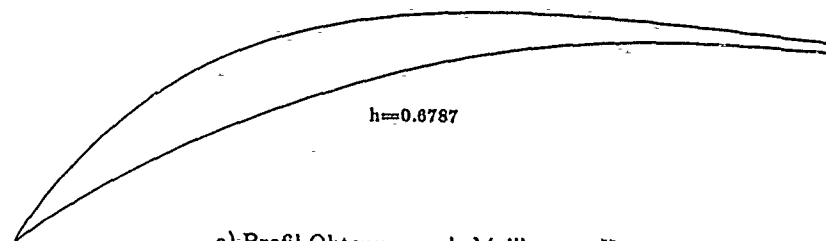


a) Modifications Successives du Profil (Version en H)

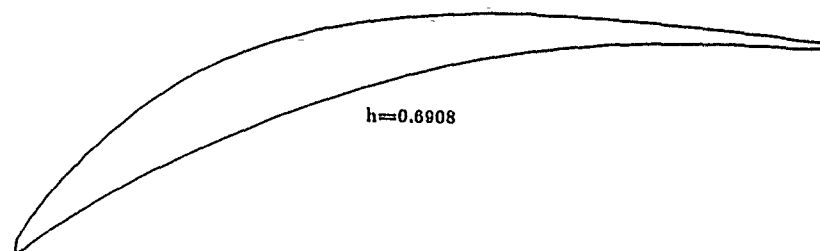


b) Modifications Successives du Profil (Version en C)

Figure 9: Modifications du Profil pour le Calcul Inverse du Redresseur

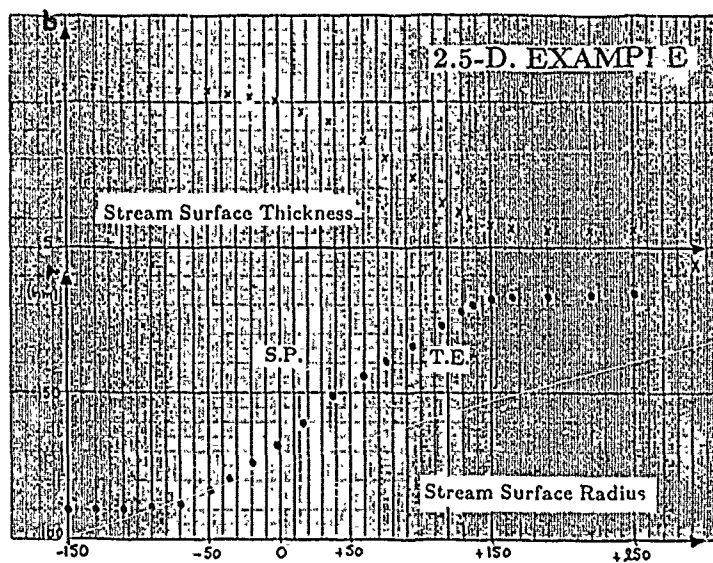
 $h=0.6787$

a) Profil Obtenu avec le Maillage en H

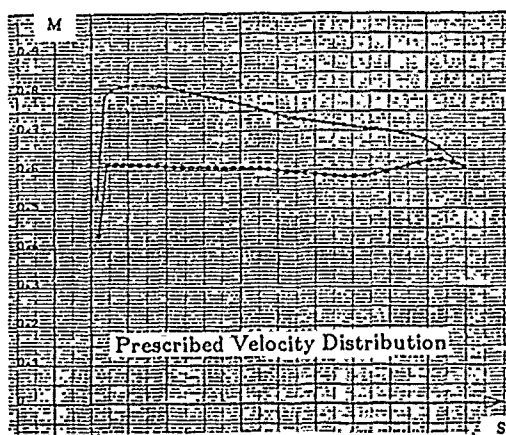
 $h=0.6908$

b) Profil Obtenu avec le Maillage en C

Figure 10: Comparaison entre les Profils Obtenus



a) Epaisseur de la Nappe et Rayon de la Méridienne



b) Répartition de Nombre de Mach Imposée

Figure 11: Données nécessaires au Calcul Quasi-Tridimensionnel

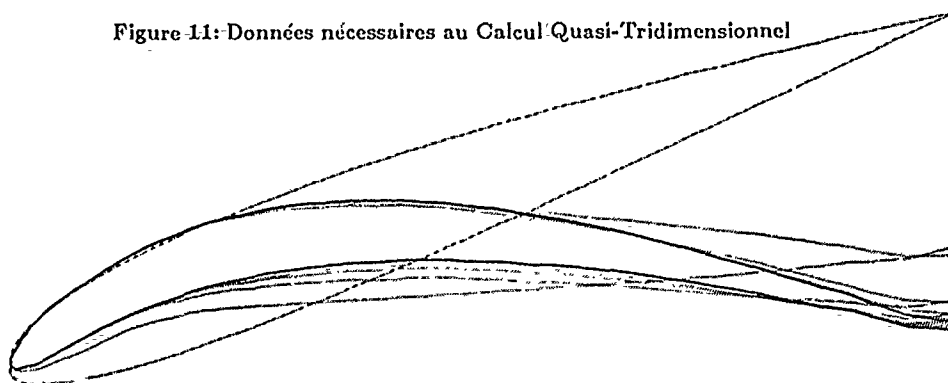


Figure 12: Calcul Inverse-Quasi-Tridimensionnel: Modifications Successives du Profil

Application of an Inverse Method to the Design of a Radial Inflow Turbine

João Eduardo Borges

Instituto Superior Técnico,
Mechanical Engineering Department
Av. Rovisco Pais
1096 Lisboa Codex
PORTUGAL

Summary

A truly three-dimensional inverse method is described and applied to the design of the rotor of a radial inflow turbine with a specific speed equal to 0.6. The described indirect method uses a mean swirl (i. e. radius times mean tangential velocity) specification and applies to inviscid and incompressible fluid. In addition, it is assumed that the inlet flow is uniform and that the blades are infinitely thin. The action of the blades is modelled by surface vorticity, using the Clebsch formulation for the calculation of the velocity field. The blade shape is evaluated by requiring it to be aligned with the local velocity vectors throughout its entire length. Since the vorticity depends on the blade shape, the problem must be solved iteratively. As the mean swirl specification is not a familiar input design, its physical significance is discussed and some advice is given on the best way of choosing it. Finally, the results of some experimental tests are briefly discussed. In these tests the performance of a rotor designed using the present indirect method was compared with that achieved by an impeller designed using conventional techniques. It is shown that the rotor designed using the inverse method is more efficient than the conventional impeller.

Notation

B	number of blades	θ	angular coordinate
C_p	pressure coefficient (see (33))	ξ	coordinate in the transformed domain
D	rotor tip diameter	ρ	density
f	angular coordinate of blade surface (wrap angle) in radians	σ_k	Lanczos's smoothing factors
k	integer	Φ	potential
m	along a streamline	Ψ	streamfunction
n	normal to a boundary	ω	rotational speed
N	number of harmonics used	Ω	vorticity
N_s	specific speed (non-dimensional - see (31))		
p	static pressure		
p_0	stagnation pressure		
Q	volume flow		
r	radius		
$r\bar{V}_\theta$	mean swirl (radius times mean tangential velocity)		
S	saw-tooth function		
U	blade speed		
u	periodic absolute velocity at the blade (see (28))		
\underline{V}	absolute velocity		
\bar{V}_θ	mean tangential velocity		
\underline{W}	relative velocity		
z	axial coordinate		
α	auxiliary coordinate (see (4))		
Γ	circulation		
δ_p	periodic delta function		
η	coordinate in the transformed domain		

Subscripts

bl	referring to blade
$downstream$	referring to the downstream boundary
k	kth harmonic
o	mean value
r	in the radial direction
ref	reference value
tip	tip of impeller
$upstream$	referring to the upstream boundary
z	in the axial direction
θ	in the tangential direction
1	turbine inlet
3	turbine exit

Superscripts

c	cosine harmonic
s	sine harmonic
$+$	suction surface
$-$	pressure surface

1. Introduction and Literature Survey.

When designing a radial inflow turbine for a particular application, the first step to be taken is the choice of overall dimensions and parameters suitable for the case in study. This preliminary

design is done using one-dimensional calculations based on simple models and past experience, correlated in terms of non-dimensional similarity parameters.

A classical example of this sort of approach is provided by Rohlik [1]. In this work optimum design parameters, such as ratio of overall dimensions, angles and blade-jet speed ratio, were calculated using a simple one-dimensional model. The unidimensional loss model used took into account the stator and rotor boundary layers, rotor blade tip clearance, disc windage and kinetic energy loss at exit. The optimum design parameters were determined so as to maximize the overall efficiency and were correlated as functions of the specific speed. The theoretical results thus obtained are in agreement with the experimental results described in Kofskey and Wasserbauer [2] and Kofskey and Nusbaum [3].

The information presented in reports like these ones permits the choice of the overall dimensions and rotational speed of the turbine, given the desired nominal conditions (mass flow and power). However, at the end of this preliminary design, the blade geometry is not defined in great detail, this detailed definition of the turbine geometry being the object of the next stage in the design process. A study of the published literature and of the present state-of-art shows that usually the detailed definition of the turbine geometry is done by using iteratively direct or analysis codes. This process consists in guessing a blade geometry, and then analysing the flow field produced by it using direct codes. If adequate flow field conditions are not achieved, than a new blade geometry is guessed and the whole process is repeated, until the desired results are obtained, eventually.

The task of guessing a blade geometry has been done in a great variety of ways. For example, it is common to use straight lines and circular arcs, or in general conic sections (such as ellipse arcs), both in the definition of the meridional geometry and of the camber surface (see Moore [4]). Another different form of doing this is presented in Raines et al. [5] who used Lamé ovals for the definition of the geometry of mixed flow turbines.

Techniques used for the definition of the rotor geometry of centrifugal compressors can also be used for the case of radial inflow turbines, since the problems to be solved are quite similar. So, three-dimensional analytic surfaces defined with the help of the interpolation formulae of Coons could be used for this purpose, as was done by Smith and Merryweather [6] and Came [7], or alternatively, Bernstein-Bézier surfaces could be used, an example being the work of Casey [8].

A slightly different way of generating the blade geometry is that applied by Smith et al. [9] to the design of two radial inflow turbines and described in more detail in Platt [10]. In this instance, the blade is generated by a series of straight-line generatrices which are defined either by joining the camberlines specified along the shroud and hub or by giving the three-dimensional orientation of the generatrices and the camberline on the shroud. These camberlines are determined using a specified blade camber angle distribution or estimated by imposing a desired aerodynamic loading.

Once the meridional and blade geometry are defined in detail using any one of the above methods, an analysis or direct code is run to check if the flow field conforms with the conditions the designer wishes to obtain. There are a great number of analysis programs that can be used for this task, either hub-to-shroud, quasi-three-dimensional or completely three-dimensional. In fact, most of the papers mentioned above also describe analysis codes directly connected to the geometry generating programs. Other possible alternatives include the throughflow program published by Katsanis and McNally [11], which is based on a finite-difference stream function solution, the quasi-three-dimensional method presented in Katsanis [12] which uses the streamline curvature technique both in the hub-to-shroud and blade-to-blade planes or the three-dimensional time-marching method described in Denton [13], but this list is by no means exhaustive.

This method of designing radial inflow turbines through the iterative use of analysis programs, which is typical of the present state-of-the-art, is recognized to be an inefficient process which may lead to a geometry far from the optimal configuration. Ideally, the blade geometry should be defined using inverse codes, by which it is meant programs that automatically calculate the blade shape required for obtaining certain flow field conditions specified as input to the process. Nevertheless, as far as the author is aware, this is seldom the case when designing this sort of machines. In part, this state of affairs is due to the fact that the flow inside the rotor of a radial inflow turbine is highly three-dimensional. Therefore, for an inverse method to stand a chance of being successful, it must take into account three-dimensional effects. However, there are only a handful of published indirect methods that are truly three-dimensional, the overwhelming majority of indirect methods being two-dimensional (mostly blade-to-blade and a few hub-to-shroud). Instances of three-dimensional inverse methods can be found in the work of Falcão [14] who used the concept of lifting surface and in Tan et al. [15] who developed a method using as input specification, a

distribution of mean swirl (radius times mean tangential absolute velocity, $r\bar{V}_\theta$) and determine the velocity by using the Clebsch formulation. Another example is provided by Zhao et al. [16], who use a Taylor series expansion in the circumferential direction and uses as design specification an imposition of the value of rV_θ (radius times tangential velocity) at the mean stream surface. Nevertheless, none of these three-dimensional inverse methods have been applied to radial inflow turbines, the examples of application presented in these reports being either linear cascades or axial turbomachines.

In the present report, the application of a truly three-dimensional inverse method to the rotor design of a radial inflow turbine is described. The design technique used is an extension of the method proposed in [15], to radial turbomachinery. This extension entails the use of more general boundary conditions in the partial differential equations ([15] only considered mean swirl distributions which were functions of axial distance z , a fact that leads to considerable simplification in the boundary conditions), and a different form of solution of the resultant partial differential equations - instead of using spectral methods as was done in [15], the partial differential equations are solved using finite difference techniques. Due to these modifications the present method is able to cope with the more general geometries typical of radial inflow turbines (and in general, radial turbomachinery) and is not restricted to simple annular ducts with constant hub and tip radius which were the only cases considered in [15]. However and similarly to what is done in [15] it is assumed that the blades are infinitely thin and that the fluid is inviscid and incompressible. In addition, only blade rows that accept an uniform inlet flow and do constant work along the span are considered.

2. Description of the Design Method.

The inverse method to be presented uses as design specification a mean swirl ($r\bar{V}_\theta$) distribution instead of imposing, for example, the velocity distribution on both blade surfaces. Although it may seem a rather odd specification at first sight, it is ideally suited to a three-dimensional situation because it can be specified without unduly inflexible restrictions. In fact, it is not necessary to impose restrictions on this sort of input, like those that are needed if the velocity along the whole blade surface was to be imposed, restrictions that are difficult to satisfy (they involve the calculations of integrals). In conjunction with this point, note that in a three-dimensional situation these restrictions would be even more complicated and severe than the corresponding conditions for a two-dimensional case, since the velocity level in the shroud stream surface depends on the velocity level on the hub stream surface and the curvature of the machine in the meridional plane.

In addition, the quantity $r\bar{V}_\theta$ plays an important physical role, since it is the mean angular momentum per unit mass and so is related to the way work is imparted to the fluid as it moves through the machine. As the mean angular momentum can only be changed by a tangential force, the way it varies along a streamline gives us an idea of the variation of this tangential force, or in other words, gives an idea of the blade pressure loading.

Another physical interpretation for the quantity $r\bar{V}_\theta$ consists in saying that it is directly proportional to the circulation Γ , a relation that can be easily justified making use of the definitions of Γ and $r\bar{V}_\theta$. In fact, the circulation at a given point can be calculated, as usual by the integral:

$$\Gamma = r \int_0^{2\pi} V_\theta d\theta \quad (1)$$

where θ is the angular coordinate, r is the radius (here and in the following, a right-handed cylindrical polar coordinate system defined by (r, θ, z) will be used) and V_θ is the local value of the absolute tangential velocity. On the other hand, the definition of mean absolute tangential velocity is given similarly to the definition of mean of any other quantity, by:

$$\bar{V}_\theta = \frac{B}{2\pi} \int_0^{2\pi} V_\theta d\theta \quad (2)$$

where \bar{V}_θ is the mean value and V_θ the local value of the absolute tangential velocity (mean values will be denoted with an overbar in this report) and B is the number of blades of the cascade being designed. Comparing Eqs.(1) and (2) it is seen that the relation between the circulation Γ and $r\bar{V}_\theta$ is quite simply:

$$\Gamma = 2\pi r \bar{V}_\theta \quad (3)$$

The interpretation of $r\bar{V}_\theta$ as being linked to the circulation Γ is useful when considering what happens downstream of a blade row. If the circulation Γ is not constant at the trailing edge then there will be necessarily, trailing vortices issuing from the trailing edge of the blade row. These vortices will have some kinetic energy associated with them, so that the exit flow will possess a kinetic energy greater than the minimum possible. Therefore, if one wants to minimize the exit kinetic energy loss, in order to obtain as good a total-to-static efficiency as possible, it is essential to reduce these trailing vortices to a minimum (or to zero if that is feasible). Perhaps this argument is best understood if a parallel with external aerodynamics is made. In fact, it is a well known fact that for a finite wing the

circulation can not be constant along the span, and that fact is linked with the existence of a surface of vortices issuing from the wing trailing edge. It is also known that there is a distribution (more precisely, an elliptic distribution of circulation) that minimizes the kinetic energy associated with the trailing surface of vortices leading to the best design for the wing. Returning to the internal aerodynamics case, the circulation distribution that minimizes the exit kinetic energy loss, is a constant circulation along the trailing edge, for which case, there are no additional trailing vortices being introduced in the flow. In other words, if the total-to-static efficiency of a blade row is to be

maximized than that blade row should be designed so that $r\bar{V}_\theta$ at the trailing edge is constant, implying constant work along the span if the inlet flow is uniform. For these conditions (irrotational inlet flow of an inviscid fluid and constant circulation), there is no trailing vorticity issuing from the blades and so the flow must remain everywhere irrotational according to Kelvin's theorem. So, if there is any vorticity at all, it must be bound to the blade surfaces, and indeed, the action of the blades (supposed to have zero thickness) is modelled by sheets of vorticity whose strength can be known.

Before going on discussing the value of vorticity, it is convenient to have a simple way of defining the blade geometry. In the present work this is done introducing an auxiliary coordinate α defined by:

$$\alpha = \theta - f(r, z) \quad (4)$$

where $f(r, z)$ is the angular coordinate of a point on the blade surface (f will be called wrap angle in the following). This variable α can be interpreted as a sort of helical angular coordinate, that takes a constant value along each blade. More precisely, the blade surfaces are obtained when:

$$\alpha = \frac{2k}{B}\pi, \quad k = \dots, -1, 0, 1, 2, \dots \quad (5)$$

Now that the blades are easily defined in terms of α , let us return to the discussion of the value of vorticity. Since the velocity field is solenoidal (i.e., $\nabla \cdot \Omega = 0$), it can be written as the cross product of two gradients of scalar functions. It is convenient to choose one of the factors of this cross product as $\nabla \alpha$ because it is already known that the vorticity is lying on the blade surfaces and so it must be normal to the vector $\nabla \alpha$ (recall that $\nabla \alpha$ is perpendicular to surfaces $\alpha = \text{const.}$ and that the cross product is perpendicular to any of its factors). If this choice is made, it turns out that the other factor is $\nabla r\bar{V}_\theta$ as is shown in more detail in Borges [17]. Therefore, the final form for the vorticity vector is:

$$\Omega = [\nabla r\bar{V}_\theta \times \nabla \alpha] \delta_p(\alpha) \quad (6)$$

where $\delta_p(\alpha)$ is the periodic delta function and gives the dependence of the vorticity vector on the angular coordinate - the vorticity is zero throughout, except at the blades where it takes the infinite value responsible for the velocity jump occurring there. The Fourier expansion of the periodic delta function is:

$$\delta_p(\alpha) = 1 + \sum_{k=1}^{\infty} 2 \cos(kB\alpha) \quad (7)$$

The knowledge of all the vorticity existing in the flow field enables us to evaluate the complete velocity field, a task done in our case, using the Clebsch formulation. After the velocity is determined, the blade shape is calculated requiring it to be parallel to the local velocity vector, throughout its length. Since the vorticity depends on the blade shape through the variable α , the problem must be solved iteratively. This is, in brief, the basic idea of the method being described, and which will be explained in more detail in the following two subsections.

2.1 Velocity Field

As already discussed, the velocity field will be calculated from the knowledge of the vorticity, using the Clebsch formulation. In this formulation, the velocity is written in such a way that its curl gives identically the vorticity existing in the flow-field. The adopted expression must depend on an unknown scalar function which is then evaluated by satisfying the continuity equation. Putting this idea into practice, the velocity will be written as:

$$\underline{V} = \nabla \phi(r, \theta, z) + r\bar{V}_\theta \nabla \alpha - S(\alpha) \nabla r\bar{V}_\theta \quad (8a)$$

inside the blade passage and as:

$$\underline{V} = \nabla \Phi(r, \theta, z) \quad (8b)$$

outside it. In these equations, Φ is a potential, so that $\nabla \Phi$ accounts for the irrotational part of the velocity (its curl is zero), while the other two terms are rotational. The function $S(\alpha)$ is to be determined in such a way that the curl of Eq.(8) is equal to the expression giving the vorticity and presented in Eq.(6). So, taking the curl of (8), we arrive at:

$$\underline{\Omega} = [\nabla \times \underline{V}] = [S'(\alpha) + 1] \nabla r \nabla_\theta \times \nabla \alpha \quad (9)$$

which, when compared with Eq.(6), shows that $S(\alpha)$ must be a function defined by:

$$S'(\alpha) = \delta_p(\alpha) - 1 \quad (10)$$

This shows that $S(\alpha)$ is the integral of $(\delta_p(\alpha)-1)$, or, in other words, it is the periodic sawtooth function with zero mean value. Its Fourier expansion is:

$$S(\alpha) = \sum_{k=1}^{\infty} \frac{2}{kB} \sin(kB\alpha) = \sum_{k=1}^{\infty} \frac{2 \cos(kBf)}{kb} \sin(kB\theta) - \sum_{k=1}^{\infty} \frac{2 \sin(kBf)}{kb} \cos(kB\theta) \quad (11)$$

Now that the unknown function $S(\alpha)$ has been determined using one of the conditions that Eq.(8) must satisfy, namely the value of vorticity, it is necessary now to evaluate the unknown scalar function $\Phi(r, \theta, z)$. This unknown will be calculated forcing the velocity field defined by Eq.(8) to satisfy the continuity equation. For incompressible flow, the continuity equation takes the form:

$$\nabla \cdot \underline{V} = 0 \quad (12)$$

Substituting here the value of the velocity \underline{V} given by Eq.(8), the following equation is obtained:

$$\nabla^2 \Phi = -r \nabla_\theta \nabla^2 \alpha + [S'(\alpha) + 1] \nabla \alpha \cdot \nabla r \nabla_\theta + S(\alpha) \nabla^2 r \nabla_\theta \quad (13a)$$

inside the blade region and:

$$\nabla^2 \Phi = 0 \quad (13b)$$

outside it.

For the solution of this equation in Φ , and since the flow variables are periodic in the tangential direction, both Φ and the remaining terms appearing in Eq.(13) are going to be expanded in a Fourier series in the tangential direction. For example, Φ will be written as:

$$\Phi = \Phi_0(r, z) + \sum_{k=1}^{\infty} \Phi_k^c(r, z) \cos(kB\theta) + \sum_{k=1}^{\infty} \Phi_k^s(r, z) \sin(kB\theta) \quad (14)$$

Then, by equating the values of all the harmonics a second-order differential equation is obtained for each of the harmonics of Φ . For example, the mean value of Φ , $\Phi_0(r, z)$, is calculated by solving the following Poisson equation:

$$\frac{\partial^2 \Phi_0}{\partial r^2} + \frac{1}{r} \frac{\partial \Phi_0}{\partial r} + \frac{\partial^2 \Phi_0}{\partial z^2} = \frac{1}{r} \frac{\partial}{\partial r} \left[r^2 \nabla_\theta \frac{\partial f}{\partial r} \right] + \frac{\partial}{\partial z} \left[r \nabla_\theta \frac{\partial f}{\partial z} \right] \quad (15a)$$

inside the blade passage and

$$\frac{\partial^2 \Phi_0}{\partial r^2} + \frac{1}{r} \frac{\partial \Phi_0}{\partial r} + \frac{\partial^2 \Phi_0}{\partial z^2} = 0 \quad (15b)$$

upstream and downstream of the blade row.

For the k th cosine harmonic of Φ , represented by $\Phi_k^c(r, z)$, the equation to solve is:

$$\frac{\partial^2 \Phi_k^c}{\partial r^2} + \frac{1}{r} \frac{\partial \Phi_k^c}{\partial r} + \frac{\partial^2 \Phi_k^c}{\partial z^2} - \frac{k^2 B^2}{r^2} \Phi_k^c = - \left[\nabla^2 r \nabla_\theta \right] \frac{2 \sin(kBf)}{kB} + \left[\nabla \alpha \cdot \nabla r \nabla_\theta \right] 2 \cos(kBf) \quad (16a)$$

in the bladed region and

$$\frac{\partial^2 \Phi_k^c}{\partial r^2} + \frac{1}{r} \frac{\partial \Phi_k^c}{\partial r} + \frac{\partial^2 \Phi_k^c}{\partial z^2} - \frac{k^2 B^2}{r^2} \Phi_k^c = 0 \quad (16b)$$

outside the bladed region. Similarly, the k th sine harmonic of Φ , represented by $\Phi_k^s(r, z)$, satisfies the

following equation:

$$\frac{\partial^2 \Phi_k^i}{\partial r^2} + \frac{1}{r} \frac{\partial \Phi_k^i}{\partial r} + \frac{\partial^2 \Phi_k^i}{\partial z^2} - \frac{k^2 B^2}{r^2} \Phi_k^i = [\nabla^2 r \bar{V}_\theta] \frac{2 \cos(kBf)}{kB} + [\nabla \alpha \cdot \nabla r \bar{V}_\theta] 2 \sin(kBf) \quad (17a)$$

inside the blade passage and

$$\frac{\partial^2 \Phi_k^i}{\partial r^2} + \frac{1}{r} \frac{\partial \Phi_k^i}{\partial r} + \frac{\partial^2 \Phi_k^i}{\partial z^2} - \frac{k^2 B^2}{r^2} \Phi_k^i = 0 \quad (17b)$$

outside the blade passage. Equations (16) and (17) are partial differential equations of the Helmholtz type.

The determination of Φ requires the solution, in the meridional section of the turbomachine, of Eq.(15) and one pair of Eqs.(16), (17) for each harmonic considered in the Fourier expansion. This can be done provide appropriate boundary conditions are imposed at the endwalls and at the far-upstream and far-downstream boundaries.

The boundary condition to be imposed at the endwalls (hub and shroud) states that there is no flow through these solid surfaces, a fact that can be expressed mathematically as:

$$\underline{V} \cdot \underline{n} = 0 \quad (18)$$

where \underline{n} is the normal vector to the endwalls. Using the expression (8) for the velocity, and considering the expansion of Φ in a Fourier series, it is seen that Φ_0 , Φ_k^c and Φ_k^s must satisfy the following boundary conditions at the endwalls, respectively:

$$\frac{\partial \Phi_0}{\partial n} = r \bar{V}_\theta \frac{\partial f}{\partial n} \quad (19a)$$

$$\frac{\partial \Phi_k^c}{\partial n} = -\frac{2 \sin(kLf)}{kB} \frac{\partial r \bar{V}_\theta}{\partial n} \quad (19b)$$

$$\frac{\partial \Phi_k^s}{\partial n} = \frac{2 \cos(kBf)}{kB} \frac{\partial r \bar{V}_\theta}{\partial n} \quad (19c)$$

inside the blade region and:

$$\frac{\partial \Phi_0}{\partial n} = \frac{\partial \Phi_k^c}{\partial n} = \frac{\partial \Phi_k^s}{\partial n} = 0 \quad (20)$$

outside the blade region. The partial derivatives appearing in these boundary conditions are taken in the direction normal to the endwalls.

At the far-upstream the flow is uniform according to an assumption already made. At the far-downstream boundary a similar condition applies since the flow is irrotational and there is no trailing vorticity being introduced in the flow. This implies that the boundary condition for the mean value of the potential, Φ_0 , is :

$$\nabla \Phi_0 = \underline{V}_{\text{upstream}} = \text{Const.} \quad (21a)$$

at the upstream boundary and at the downstream boundary is:

$$\nabla \Phi_0 = \underline{V}_{\text{downstream}} = \text{Const.} \quad (21b)$$

where $\underline{V}_{\text{upstream}}$ and $\underline{V}_{\text{downstream}}$ are respectively the uniform velocity at the far-upstream boundary and at the far-downstream boundary. As they are supposed to be constant values, they can be evaluated from the specified flow-rate and the passage area of the corresponding boundaries.

For the remaining harmonics of Φ , the boundary conditions to be imposed are:

$$\Phi_k^c = 0 \quad (22a)$$

$$\Phi_k^s = 0 \quad (22b)$$

taking the same form both at the far-upstream and far-downstream boundaries. This condition can be justified bearing in mind that, since the flow is uniform at the far-upstream and far-downstream boundaries, the higher order harmonics must contribute a zero value to the velocity (the periodic velocity must be zero). This can only be the case for the θ component of the velocity, if conditions (22) are satisfied, according to Eqs.(8) and (14).

The mean flow field can be calculated using a partial differential equation different from Eq.(15). This other way of solving the mean flow field uses the streamfunction concept, Ψ , and it can be shown (see [17]) that the equation to be solved in this case is:

$$\frac{\partial^2 \Psi}{\partial r^2} - \frac{1}{r} \frac{\partial \Psi}{\partial r} + \frac{\partial^2 \Psi}{\partial z^2} = -r \left[\frac{\partial f}{\partial z} \frac{\partial r \bar{V}_\theta}{\partial r} - \frac{\partial f}{\partial r} \frac{\partial r \bar{V}_\theta}{\partial z} \right] \quad (23)$$

inside the blade passage and outside it, the right-hand side of (23) is equal to zero. These two approaches are equivalent since they satisfy the same conditions, namely the continuity equation for incompressible flow and the condition stating that the curl of the mean velocity is equal to the mean value of the vorticity (mean value of expression (6) - see [17]). However this last equation based on the streamfunction has boundary conditions more easily imposed - for example, at the endwalls, the boundary conditions are of the Dirichlet type, since at the endwalls the streamfunction is a constant. For this reason, in the Fortran program written to implement the present inverse method, the mean flow was calculated using Eq.(23).

There is one last condition that the velocity field calculations must satisfy which is the Kutta-Joukowski condition, requiring zero pressure loading at the trailing edge. In order to impose this condition, an expression for the blade pressure loading is needed. In [17] it is shown that this pressure loading is given by:

$$p^+ - p^- = \frac{2\pi}{B} \rho \underline{W}_{bl} \cdot \nabla r \bar{V}_\theta \quad (24)$$

where ρ is the density of the fluid and p^+ and p^- are respectively the static pressures on the suction and pressure surfaces of the blade and the term \underline{W}_{bl} represents the relative velocity calculated at the blade sheet (for example, for $\alpha=0$). Making use of Eq.(24), it is seen that the Kutta-Joukowski requires that:

$$\underline{W}_{bl} \cdot \nabla r \bar{V}_\theta = 0 \quad (25)$$

In the present method, this condition is satisfied by specifying an $r \bar{V}_\theta$ distribution that is constant along the trailing edge and which has zero derivative perpendicularly to it. In this way condition (25)

is automatically satisfied, because $\nabla r \bar{V}_\theta = 0$ at the trailing edge. A similar condition is also imposed at the leading edge which corresponds to designing a blade row that is exactly aligned with the local velocity vector at the leading edge, so that the pressure loading there is zero.

2.2 Calculation of Blade Camber.

In the previous subsection, the method for the calculation of the flow field was discussed, but the blade shape was supposed to be known. However, the determination of the blade shape is the principal aim of this inverse method, so that an equation for its calculation must be provided. This will be done by requiring that the blade be aligned with the local relative velocity vector, \underline{W}_{bl} . This condition can be expressed mathematically as:

$$\underline{W}_{bl} \cdot \nabla \alpha = 0 \quad (26)$$

noting again that $\nabla \alpha$ is a vector normal to the blade camber surface. This equation can be expanded in the form:

$$\left[\bar{V}_z + \underline{v}_{bl} \right] \frac{\partial f}{\partial z} + \left[\bar{V}_r + \underline{v}_{bl} \right] \frac{\partial f}{\partial r} = \frac{r \bar{V}_\theta}{r^2} + \frac{\underline{v}_{bl}}{r} - \omega \quad (27)$$

where f is the angular coordinate of the blade camber surface, or wrap angle, and ω is the rotational speed of the blade row. $\bar{V}_r, \bar{V}_\theta$ and \bar{V}_z are the three components of the mean absolute velocity and \underline{v}_{bl} , \underline{v}_{bl} and \underline{v}_{bl} are the three components of the periodic absolute velocity evaluated at the blade ($\alpha = 0$). This periodic component of velocity at the blade is the summation of the contribution of all the periodic harmonics and is calculated by:

$$\underline{v}_{bl} = \sum_{k=1}^{\infty} \frac{\partial \Phi_k^r(r, z)}{\partial r} \cos(kBf) + \sum_{k=1}^{\infty} \frac{\partial \Phi_k^t(r, z)}{\partial r} \sin(kBf) \quad (28a)$$

$$\underline{v}_{bl} = - \sum_{k=1}^{\infty} \frac{kB}{r} \Phi_k^r(r, z) \sin(kBf) + \sum_{k=1}^{\infty} \frac{kB}{r} \Phi_k^t(r, z) \cos(kBf) \quad (28b)$$

$$\underline{v}_{bl} = \sum_{k=1}^{\infty} \frac{\partial \Phi_k^r(r, z)}{\partial z} \cos(kBf) + \sum_{k=1}^{\infty} \frac{\partial \Phi_k^t(r, z)}{\partial z} \sin(kBf) \quad (28c)$$

Equation (27) will be referred to as the blade boundary condition in the following and its solution will give us the desired blade shape, provided the velocity at the blade is known. The values of the blade velocity are known from the previous iteration, being calculated with the help of the equations described in subsection 2.1 and using Eqs.(28). The blade boundary condition is a first-

order partial differential equation with characteristic lines coincident with the meridional projection of the blade streamlines. In order to integrate this differential equation, some initial data (values of f) must be specified along a line roughly perpendicular to these characteristic lines and extending from hub to shroud. This initial data on f will be called the stacking condition of the blade. In our method this stacking condition is implemented by giving as input, the values of blade wrap angle, f , along a quasi-orthogonal, for example, at the leading edge.

If in the calculations described so far, the periodic value of the velocity (Eqs.(28)) is neglected, a simpler version of the inverse method is obtained which is simply a hub-to-shroud method and not a truly three-dimensional technique. This axisymmetric solution requires much less computing power than the three-dimensional solution since one only needs to solve two differential partial equations, Eq.(23) (or alternatively, Eq.(15)) for the mean flow and the blade boundary condition, Eq.(27). This simpler inverse technique is designated an actuator duct solution in [15] and that name will be adopted here.

2.3 Numerical Techniques Used.

The calculation of the velocity field and blade shape requires the solution of partial differential equations on the meridional section of the turbomachine. This meridional section has, in general, a complicated geometry with curved endwalls, especially in the case of radial turbomachinery (see Fig. 1 as an example). In order to avoid numerical difficulties with the implementation of the boundary conditions at the curved endwalls, and the possible loss of accuracy, it was decided to use a transformation of coordinates from (r, z) to a body-fitted curvilinear coordinate system (ξ, η) with the points equally distributed along quasi-orthogonals, extending from hub-to-shroud, obtaining a grid like the one shown in Fig. 1. A more complete discussion of this technique and some examples of its practical application to the solution of partial differential equations can be found in Thompson et al. [18]. The form taken by equations (15), (16), (17) and (27) in the transformed numerical plane is given in [17].

The equations for the calculation of the velocity field in the transformed numerical plane are solved using finite difference techniques. It is used throughout second-order accurate, central difference formulae and a nine-point numerical molecule (see [17]). The resulting finite difference equations are solved by relaxation, the particular method used in our case being the Gauss-Seidel relaxation scheme. In our program this was implemented in conjunction with a multi-grid technique in order to accelerate the convergence rate of the solution. A good description and discussion of multi-grid methods can be found in Hackbusch and Trottenberg [19], together with several instances of its practical implementation.

Finite difference techniques are also used for the solution of the blade boundary condition in the transformed numerical plane. However, this time it is not possible to use a relaxation scheme similar to the one used for the velocity calculation because Eq.(27) is a first-order differential equation which must be solved by respecting the direction of the characteristic lines. Due to this fact, the blade boundary condition is solved using an Euler's modified method (see Roache [20]). This is an implicit numerical scheme that has a truncation error of second order in $\Delta\eta$ and $\Delta\xi$ and is consistent and stable. In order to start this method the values of wrap angle, f , must be known along an initial quasi-orthogonal. This information is provided by the stacking condition.

It is obvious that there is a need to truncate the Fourier series for the velocity profile in the tangential direction after a certain, finite, number of harmonics. Since the velocity profile is discontinuous across the blade, it is then inevitable that the Gibbs phenomenon will appear. This phenomenon is present no matter how many harmonics are taken in the truncated series, seriously affecting the accuracy of the flow calculation near the blade. In order to counteract this influence, it was decided to use the "Lanczos' smoothing factors" (see Lanczos [21]), which is a sort of numerical filter. This procedure consists in multiplying each harmonic by a factor σ_k depending on the maximum number of harmonics used, N . These factors are defined by:

$$\sigma_k = \frac{\sin\left(\frac{k\pi}{N+1}\right)}{\frac{k\pi}{N+1}} \quad (29)$$

For an assessment of the influence of the truncation of the Fourier series into the accuracy of the method, a comparison was made between a test case with 15 harmonics and another with 30 harmonics. The case considered was the rotor redesign to be discussed later, the maximum difference found in wrap angle, f , between the two runs being 0.0028 rad (0.16°). This is a value smaller than the unavoidable manufacturing errors, and so can be considered acceptable.

If trying to solve the equations in the form just presented, it is found that the velocity shows a logarithmic singular behaviour at the intersection of the blades with the endwalls, leading to a divergence of the method. In order to better understand this sort of behaviour let us recall that, when using a Clebsch formulation in the form:

$$\mathbf{Y} = \nabla\Phi + \mu\nabla\nu \quad (30)$$

the vortex lines lie at the intersection of the surfaces $\mu = \text{const.}$ and $\nu = \text{const.}$. In our case, this means that the vortex lines lie at the intersection of the blades ($\alpha = \text{const.}$) and surfaces where $r\bar{V}_\theta = \text{const.}$ (Fig. 3 gives the intersection of surfaces $r\bar{V}_\theta = \text{const.}$ with the meridional plane, for the particular application discussed later in this paper). Since, in general, neither the blade camber surface nor the surfaces of constant swirl ($r\bar{V}_\theta = \text{const.}$) intersect the endwalls perpendicularly it follows that, in general, the vortex lines intersect the solid endwalls at an angle different from 90° (in fact, in cases

where $\frac{\partial r\bar{V}_\theta}{\partial n} = 0$, the numerical results show that $\frac{\partial f}{\partial n} \neq 0$). If one tries to model the solid wall by placing behind the wall the reflexion of the original vortex line, a line vortex with a kink situated at the solid wall will be obtained. However, it is a well known fact that this geometry leads to a logarithmic singularity - see Brebner and Wyatt [22] who discuss theoretically this behaviour and Küchemann [23] who presents this effect in connection with the simulation of swept aircraft wings. This last reference also describes some of the physical consequences of this vortex geometry, giving the name of kink effect to the phenomenon originated in this way. Similar problems also arise when modelling cascades of swept blades as was shown in [14].

Ideally this singular behaviour should be handled in an analytical way in order to obtain exact results. Unfortunately the problem is very complicated and non-linear, and an analytic solution is not known. Therefore our only hope of tackling the problem is by making some numerical approximations. So, it was decided to follow the suggestion made in [14] in the present study. This consists in extrapolating towards the endwalls the results obtained a short distance from them. In our case, this entails two approximations. In the first place, the term containing the velocity component along the quasi-orthogonals is neglected in a small region near the endwalls, when solving the blade boundary condition (i. e., the equation obtained from Eq.(27) after the transformation of coordinates is done). This velocity is exactly equal to zero at the endwalls and it should have small values in the regions where it is being neglected. The second approximation involves the boundary conditions for the periodic velocity, Eqs.(19b) and (19c), and consists in substituting the right-hand side of these

equations by zero (i.e., it is assumed that $\frac{\partial r\bar{V}_\theta}{\partial n} = 0$). A more detailed discussion of the approximations made can be found in [17], together with some numerical tests that showed that these approximations do not introduce appreciable errors in the main part of the flow field (its influence is restricted to the small region near the endwalls where the approximations were introduced).

Finally, it should be noted that the equations must be solved iteratively, since the vorticity depends on the blade shape which is not known at the start of the method. Each iteration is started by the calculation of the velocity field using the equations presented in subsection 2.1, and then the blade shape is updated using the blade boundary condition, Eq.(27). Further information on the numerical procedure can be found in [17].

3. Application to the design of a radial inflow turbine.

As an example of application of the three-dimensional inverse method just outlined, the redesign of the rotor of a radial inflow turbine will be discussed. This will be a stringent test since this is a machine with important three-dimensional flows. The rotor that was redesigned belonged to a low-speed model of a radial inflow turbine. Therefore, the flow can be considered incompressible and the inverse method described can be applied.

The specific speed of this turbine, defined by:

$$N_s = \frac{\omega\sqrt{Q}}{\left[\frac{(p_{01} - p_{03})}{\rho}\right]^{3/4}} \quad (31)$$

has the value 0.6. This value was chosen because it is for values near this one that one can expect the best level of total-to-static efficiency for radial inflow turbines.

Both rotors (the original or conventional impeller and the new rotor, as they will be called, for short) have the same tip diameter of 310 mm and 17 blades. The meridional geometry is also the same for both rotors and is indicated in Fig. 1. The conventional rotor was designed using methods typical of the current know-how, i.e., was designed by an iterative use of direct methods and has radial blades. It was tested in order to obtain a set of data typical of what can be achieved with the present technology.

The grid used in the inverse design calculations was formed by 145 quasi-orthogonals and 49 quasi-streamlines - every other line of the grid used is shown in Fig. 1. The number of harmonics considered in the circumferential direction was 15 (each harmonic has two components, the cosine and sine one). Notice that the present grid has a region both upstream and downstream of the impeller, with 81 quasi-orthogonals placed inside the bladed region.

An important input to the present inverse method is the specification of mean swirl, $r\bar{V}_\theta$, on the meridional section of the blade row to be designed. As discussed in [17], this sort of input is chosen bearing in mind two main requirements:

- the pressure distribution on the blade surfaces should show a smooth evolution with the loading distributed along the blades as evenly as possible;
- the variation in wrap angle, f , along the blade should not be excessive, in order to avoid a highly twisted blade that would be very difficult to manufacture and could present high stress levels for the rotational speeds usually used.

Both points can be controlled through an appropriate specification of mean swirl. In fact, Eq.(24) shows that there is a close relationship between the derivatives of $r\bar{V}_\theta$ and the pressure loading across the blades. As a consequence, if a smooth variation of pressure loading is desired, it is essential to specify the mean swirl, $r\bar{V}_\theta$, so that its derivatives do not change abruptly. On the other hand, the blade boundary equation (Eq.(27)) can be written along a streamline, in the form:

$$f_a - f_b = \int_a^b \frac{(\bar{V}_m + \bar{V}_{mb}) - \omega r}{r(\bar{V}_m + \bar{V}_{mb})} dm \quad (32)$$

where a and b are two arbitrary points along the same streamline, $(\bar{V}_m + \bar{V}_{mb})$ is the blade velocity component in the meridional plane and m is distance along the meridional projection of the streamline. If it is desired to keep down the total variation of wrap angle between the leading and trailing edges, it is convenient that the expression under the integral sign in Eq.(32) should present small values. This can be achieved if one specifies the value of $r\bar{V}_\theta$ so that the value of \bar{V}_θ closely follows the local value of the transport velocity, ωr . This is the more important, the lower is the value of radius, r , or the meridional velocity, $(\bar{V}_m + \bar{V}_{mb})$. So, this means that at the hub, where the radius is small and the meridional velocity usually takes the smallest values, it is highly recommended to specify an $r\bar{V}_\theta$ distribution following the local value of ωr^2 (see [17] for a more detailed discussion of this point).

The specified $r\bar{V}_\theta$ for the present application was chosen along these general guide-lines. The imposed variation of mean swirl, $r\bar{V}_\theta$, along hub and shroud is plotted in Fig. 2, and in Fig. 3 are shown contours of the input $r\bar{V}_\theta$ in the meridional plane (in these two plots the linear dimensions were made non-dimensional dividing them by the tip radius of the rotor and the velocities were non-dimensionalised using the blade tip speed). As can be seen, the imposed variation is smooth everywhere, although at hub the variation is clearly more irregular than at shroud. This is so because in this particular case, the $r\bar{V}_\theta$ along the hub was chosen trying to minimize the total variation of wrap angle. On the contrary, at the shroud, most consideration was given trying to obtain a smooth variation of the pressure distribution on the blade surfaces. This compromise resulted in a blade which is heavily loaded at the hub inlet while, at the shroud, most of the load is concentrated near the trailing edge.

The blade geometry obtained as output using the input just discussed, is described in the next two figures. Fig. 4 is a plot of wrap angle, f , along some typical quasi-streamlines, as a function of meridional distance. The quasi-streamlines considered are hub, 1/4 of the span, mid-span, 3/4 span and shroud. This plot shows that the maximum variation of wrap angle is not excessive, taking a value around 0.75 rad (this variation is of the order of 2 blade pitches for a rotor with 17 blades, as is the case). The next figure, Fig. 5, is a plot of contours of the wrap angle, f , on the meridional section of the rotor. It should be noted that the resultant blade shape has double curvature (it could not be generate by a straight line). Therefore, it would be very difficult, if not impossible, for a designer to guess such a blade shape, and so, it is highly unlikely that this design could ever be reached by an iterative use of analysis programs. This illustrates one of the big advantages of inverse design techniques.

Another important output of the present inverse method is the pressure distribution on the blade surfaces. This result is presented in the next plot, Fig. 6, which gives the pressure coefficient on hub and shroud as a function of percent meridional distance. The value of the pressure coefficient C_p , used in this plot, is defined as:

$$C_p = \left[\frac{W}{W_{ref}} \right]^2 - 1 \quad (33)$$

where W_{ref} is the relative velocity at the intersection of the leading edge with hub. For the present case, $W_{ref} = 0.278 \omega r_{tip}$. The pressure distribution has a smooth variation throughout except at the shroud where it has a small dip, located towards the trailing edge at around 80% of the meridional distance. This dip is caused by a sudden change in the radius of curvature of the shroud profile in the meridional plane (check with the next figure - the point A marked there corresponds to the intersection of an arc of circle with a straight line and is coincident with the place where the dip occurs). This suggests that the definition of the meridional section using only arcs of circle and straight lines is not the best choice. However, this meridional geometry was not changed since, for comparison purposes, it was advisable to maintain the meridional geometry the same for both rotors.

Contours of pressure coefficient, C_p , on the suction surface of the rotor blades are presented in the next figure, Fig. 7, and Fig. 8 is the equivalent plot for the pressure surface. These plots show that the pressure distribution vary smoothly for the most part of both blade surfaces. The more marked exceptions are the region near the trailing edge where there is a rapid variation of C_p which is a consequence of the rapid unloading imposed to the blades, and, to a less extent, the region near the leading edge where again the pressure varies quickly, this time because of the rapid loading of the blades.

It is instructive to compare this fully three-dimensional solution with the axisymmetric solution or actuator duct solution as was called above. As in this solution only the mean flow is computed, its representation of reality is less accurate than the completely three-dimensional solution, the flow being modelled only in an average sense. This can be seen, comparing the next two plots, Fig. 9 which gives the wrap angle along some typical quasi-streamlines and Fig. 10 which presents contours of the wrap angle with the corresponding figures for the three-dimensional solution, Fig. 4 and Fig. 5. The differences are obvious, the actuator duct solution giving a less twisted blade than the three-dimensional solution. This is in agreement with what one would expect, since in the three-dimensional case the flow always turns less than the value of the blade angle. Therefore, in order to obtain in the three-dimensional case the same mean swirl and mean quantities, it is necessary to use a more curved blade.

Using the results of the actuator duct solution it is possible to estimate the blade velocities and pressure distribution on the blade surfaces, by assuming a linear tangential variation for the velocity profile, between the suction and pressure surfaces. A plot of the pressure coefficient, C_p , calculated in this way, is shown on the next figure, for the hub and shroud streamlines (see Fig. 11). Comparing this plot with the corresponding results for the three-dimensional solution (Fig. 6) it is seen that there are some differences between the two results, as one would expect. Nevertheless, notice that the pressure distribution predicted by the actuator duct solution gives a pretty good idea of the overall shape of the pressure distribution. The same can be stated about the blade geometry since the actuator duct solution gives a blade shape which is similar to the three-dimensional solution, presenting the same sort of value for the total amount of blade twist (i.e. total variation in wrap angle). This is an important asset because, as already mentioned, the actuator duct solution requires much less computing time than the three-dimensional solution (typically, the computing time required is two orders of magnitude less). So, the above similarities can be explored with advantage to scan quickly and inexpensively several inputs to the design program (in particular, different mean swirl schedules). In fact, this was the process followed for the final choice of mean swirl distribution used in the present design, among several other distributions that followed the guide-lines regarding the control of pressure loading and total amount of blade twist, discussed above.

The rotor redesigned using an earlier version of the inverse program just described was actually built and tested. Its experimental performance was compared with that obtained with the impeller typical of the present know-how. The tests involved the measurement of overall quantities such as variation of efficiencies with volume flow together with some detailed traverses, using a three-hole probe, made both upstream and downstream of the rotor.

A detailed description of the experimental results obtained from these tests can be found in [17]. Here, the only results that will be presented are the variation of total-to-total and total-to-static efficiencies as a function of non-dimensional volume flow (this non-dimensional volume flow is defined as $Q/\omega D^3$ - see Fig. 12). For the calculation of these efficiencies, use was made of the mass averaged values of the downstream stagnation and static pressures (these values were obtained from the detailed traverses made).

First of all, notice that the peak value for the total-to-static efficiency of the conventional impeller is around 88.3% which compares favourably with the present state-of-the-art. In fact Rohlik [1] predicted a maximum value for the total-to-static efficiency of 0.87 for a specific speed around 0.6, the value of specific speed of the present turbine. Some experimental results described in [2] and [3] also corroborate this conclusion. For example, a maximum value of the total-to-static efficiency equal to 0.87 was reported in [2] for a turbine with specific speed of 0.67 and Kofskey and Nusbaum [3] obtained a value of 0.880 for a specific speed of 0.59. More recently, Ribaud and Mischel [24]

measured a maximum value of 0.883 for the total-to-static efficiency of a radial inflow turbine of specific speed equal to 0.58. All these results indicate that the efficiency levels achieved by the conventional rotor are representative of the current know-how and so the conventional rotor is a good standard against which to compare the performance of the new impeller.

Comparing the peak values of efficiency for both rotors, it is seen that the new impeller gives better results than the conventional built, both in a total-to-total and total-to-static sense. Indeed, the difference between the peak values of the total-to-static efficiency is 1.7% and between the total-to-total efficiencies a difference of around 1.6% is found. These differences are significant, implying that the redesign changed the blade geometry in the right direction.

Finally notice that the improvements in the total-to-static efficiency are more marked than the corresponding improvements in the total-to-total efficiency, and extend to all the volume flows investigated. This indicates lower exit kinetic energy losses for the new impeller due to more orderly exit flows and suggests that it is possible to improve the total-to-static efficiency by avoiding the introduction in the flow field of unnecessary trailing vortices. In order to achieve this the blade rows must be designed so that they execute constant work along the span, as already mentioned.

In spite of the fact that the present inverse method leads to blades more difficult to manufacture and is less familiar to turbine designers than present techniques, it should find application in situations where efficiency is of paramount importance. More research should be done on the extension of this method to compressible flow, on the inclusion of thickness effects and a more careful investigation should be carried out on the best way of specifying the $r\bar{V}_0$ distribution.

4. Summary and Conclusions.

A review of the available literature showed that the usual way of designing radial inflow turbines consists in the iterative use of analysis or direct methods. As described, this is a process whereby a blade geometry is guessed, followed by a calculation of the flow field produced by it to check whether it has desirable characteristics. This is recognized as being inefficient and time consuming so that it would seem appropriate to design this kind of machines using inverse methods. However, this only makes sense if a truly three-dimensional inverse method is used because these turbomachines have significant three-dimensional effects. This need for a three-dimensional inverse method was the motivation behind the present work. In fact, a completely three-dimensional indirect method was developed and applied to the redesign of an impeller of a radial inflow turbine.

This inverse method uses as input a prescribed mean swirl distribution specified throughout the meridional section of the turbomachine. It can be applied to the design of rotating or stationary blade rows with any amount of blade turning and any meridional section (either radial or axial). However, in the present implementation it is supposed that the fluid passing through the turbomachine is inviscid and incompressible. In addition, it is assumed that the flow far upstream of the blade row is uniform (irrotational) and the blades are considered to have zero thickness.

By applying this method to a concrete and difficult case - the rotor of a radial inflow turbine - it was shown that it is possible to obtain a design with a reasonable pressure distribution on the blade surfaces, keeping at the same time, the total amount of blade twist under acceptable limits. This was achieved by means of a convenient choice of the mean swirl distribution. Based on the experience obtained with this design, some guide-lines for the choice of the mean swirl were advanced which permitted a first approximation to the $r\bar{V}_0$ schedule to be used. For the final selection of this input, it was found helpful to use an axisymmetric (actuator duct) solution since it requires much less computing effort than the complete three-dimensional solution giving, however, a good idea of the blade pressure distribution and total amount of blade twist. So the actuator duct

solution can be used to scan quickly and inexpensively several different $r\bar{V}_0$ distributions.

All these theoretical considerations were put into practice and experimentally verified by actually testing an impeller designed using an earlier version of this inverse method and comparing its performance with that achieved by a rotor designed with conventional techniques. The results for the new impeller showed an improvement in the peak values of the total-to-total and total-to-static efficiencies over the corresponding values of the conventional rotor. As the performance of the conventional wheel could be considered typical of the present day technology, it can be concluded that this application of an inverse method was successful and constitutes an advance over what can be done nowadays. Therefore, it is recommended that radial inflow turbines be designed using a truly three-dimensional inverse method.

References

- [1] Rohlik, H. E.: *Analytical Determination of Radial Inflow Turbine Design Geometry for Maximum*

- Efficiency*, NASA TN D-4384, 1968.
- [2] Kofskey, M. G. and Wasserbauer, C. A.: *'Experimental Performance Evaluation of a Radial-Inflow Turbine over a Range of Specific Speeds'*, NASA TN D-3742, 1966.
 - [3] Kofskey, M. G. and Nusbaum, W. J.: *'Effects of Specific Speed on Experimental Performance of a Radial-Inflow Turbine'*, NASA TN D-6605, 1972.
 - [4] Moore, J.: *'Eckardt's Impeller - A Ghost from Ages Past'*, CUED Turbo Report, TR 83, Cambridge, England, 1976.
 - [5] Baines, N. C. ; Wallace, F. J. and Whitfield, A.: *'Computer Aided Design of Mixed-Flow Turbines for Turbochargers'*, ASME Paper 78-GT-191, 1978.
 - [6] Smith, D. J. L. and Merryweather, H.: *'Representation of the Geometry of Centrifugal Impeller Vanes by Analytic Surfaces'*, N.G.T.E. Rep. R322, and Intl. Jnl. for Numerical Methods in Engineering, Vol. 7, pp. 137-154, 1973.
 - [7] Came, P. M.: *'The Development, Application and Experimental Evaluation of a Design Procedure for Centrifugal Compressors'*, Proc. Inst. Mech. Eng., Vol. 192, n° 5, pp. 49-67, 1978.
 - [8] Casey, M. V.: *'A Computational Geometry for the Blades and Internal Flow Channels of Centrifugal Compressors'*, Trans ASME, J. Engineering for Power, Vol. 105, n° 2, pp. 288-295, 1983.
 - [9] Smith, G. E., Holland, J. E. and Jansen, W.: *'The Design of Two Radial Inflow Turbines'*, ASME Paper 84-GT-236, 1984.
 - [10] Platt, M.: *'Computerized Compressor Design - The Future of Centrifugal Compressor Design: Better Engineered Designs in Less Time at Lower Cost'*, Turbomachinery International, May-June 1981.
 - [11] Katsanis, T. and McNally, W. D.: *'Revised Fortran Program for Calculating Velocities and Streamlines on the Hub-Shroud Midchannel Stream Surface of an Axial-, Radial-, or Mixed-Flow Turbomachine or Annular Duct. 1 - User's Manual'*, NASA TN D-8430, 1977.
 - [12] Katsanis, T.: *'Fortran Program for Quasi-Three Dimensional Calculation of Surface Velocities and Chocking Flow for Turbomachine Blade Rows'*, NASA TN D-6177, 1971.
 - [13] Denton, J. D.: *'Solutions of the Euler Equations for Turbomachinery Flows, Part 2 - Three Dimensional Flows'*, in *Thermodynamics and Fluid Mechanics of Turbomachinery*, A. S. Üçer, P. Stow and Ch. Hirsch, eds., NATO ASI Series, Martinus Nijhoff Publishers, pp. 313-347, 1985.
 - [14] Falcão, A. F. de O.: *'Lifting-Surface Theory of Straight Cascades of Swept Blades'*, Intl. Mechanical Science, Vol. 18, pp. 313-320, 1976.
 - [15] Tan, C. S.; Hawthorne, W. R.; McCune, J. E. and Wang, C.: *'Theory of Blade Design for Large Deflections: Part II - Annular Cascades'*, Trans. ASME, J. of Eng. for Gas Turbines and Power, Vol. 106, N° 2, pp.354-365, and GT & PDL N° 168, MIT, 1983.
 - [16] Zhao, K. L.; Sun, C. L. and Wu, C. H.: *'A Simple Method for Solving Three-Dimensional Inverse Problems of Turbomachine Flow and the Annular Constraint Condition'*, ASME Paper 84-GT-198, 1984.
 - [17] Borges, J. E.: *'Three- Dimensional Design of Turbomachinery'*, Ph D Thesis, Cambridge University, Cambridge, England, 1986.
 - [18] Thompson, J. F.; Warsi, Z. U. A. and Mastin, C. W.: *'Numerical Grid Generation - Foundations and Applications'*, North-Holland, New York, 1985.
 - [19] Hackbusch, W. and Trottenberg, U.: *'Multigrid Methods - Proceedings'*, Proceedings, Köln-Porz, Lecture Notes in Mathematics, Springer-Verlag, New York, 1981.
 - [20] Roache, P. J.: *'Computational Fluid Dynamics'*, Herimosa Publishers, Albuquerque, N. M., U.S.A., pp.84-85, 1982.
 - [21] Lanczos, C.: *'Discourse on-Fourier Series'*, Oliver & Boyd, Edinburgh and London, 1966.

- [22] Brebner, G. G. and Wyatt, L. A.: 'The velocities induced by distributions of infinite kinked source and vortex lines representing wings with sweep and dihedral, in incompressible flow', Royal Aircraft Establishment TR 70077, 1970.
- [23] Küchemann, D.: 'The Aerodynamic Design of Aircraft', Pergamon Press, Oxford, pp. 136-137, 1985.
- [24] Ribaud, Y. and Mischel, C.: 'Study and Experiments of a Small Radial Turbine for Auxiliary Power Units', ASME Paper 86-GT-23, 1986.

Acknowledgements

This work was supervised by Professor Sir W. R. Hawthorne and done while the author was at Whittle Laboratory. The help of the staff of this laboratory is gratefully acknowledged. The author is also grateful to Holset Engineering Co. Ltd. (England), Churchill College (Cambridge, England), and Junta Nacional de Investigação Científica e Tecnológica - INVOTAN (Portugal) for the financial support they gave to this project.

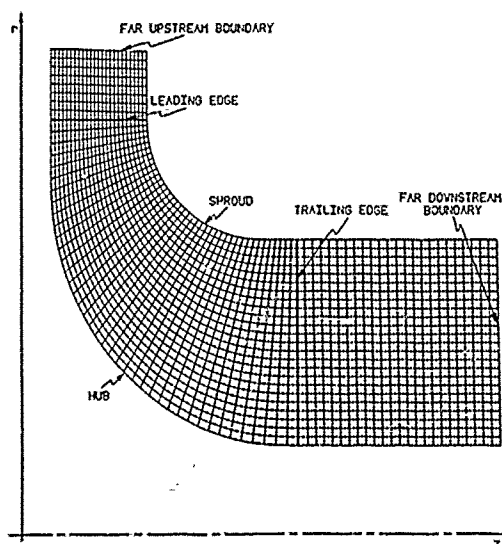


Fig. 1 Grid used in the Meridional-Plane.

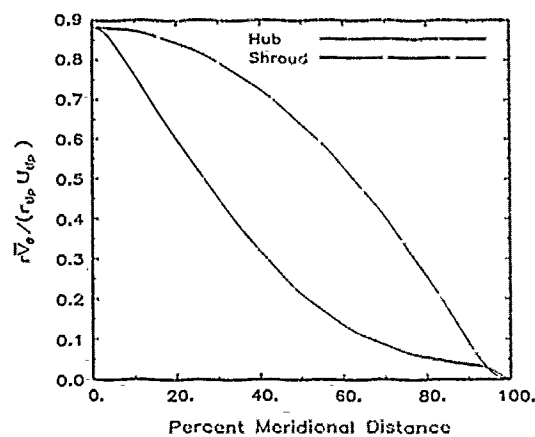


Fig. 2 Input Mean Swirl Distribution on the Hub and Shroud Stream Surfaces.

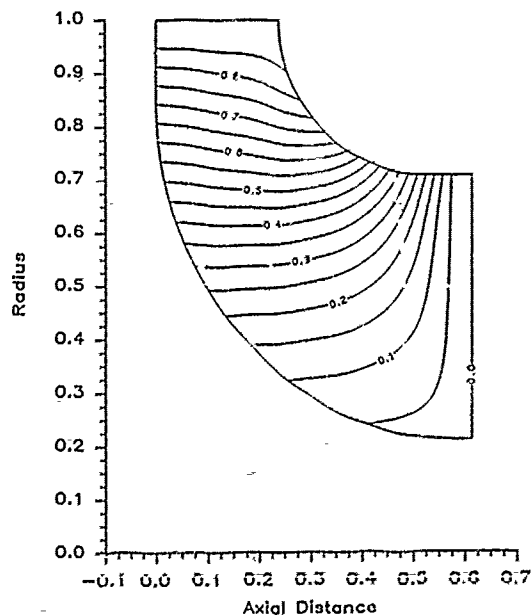


Fig. 3 Contours of the Input Mean Swirl Distribution (defined as $rV_{\theta}/(r_{tip} U_{tip})$).

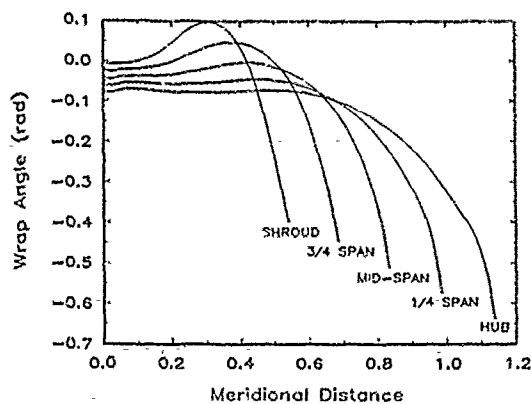


Fig. 4 Wrap Angle Distribution along Quasi-Streamlines (the Meridional Distance is made non-dimensional using r_{tip}).

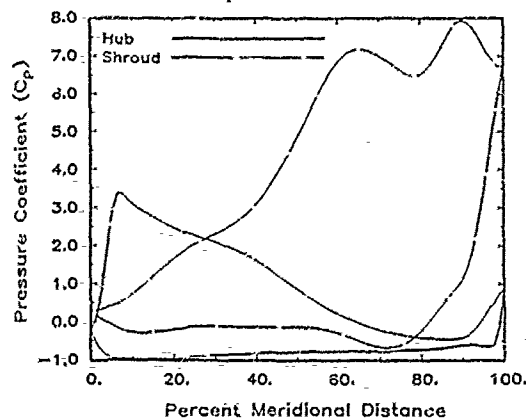


Fig. 6 Pressure Distribution on the Hub and Shroud Stream Surfaces.

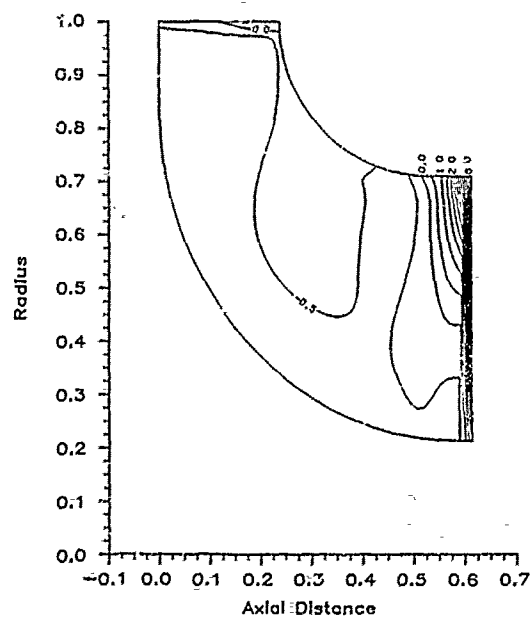


Fig. 8 Contours of Pressure Coefficient, C_p , on Pressure Surface.

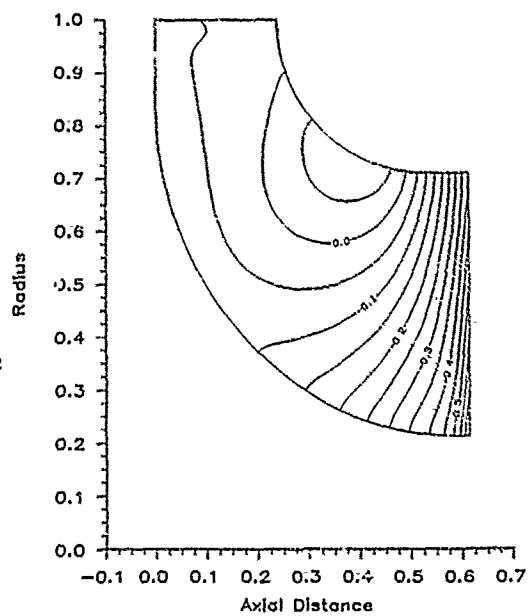


Fig. 5 Contours of Wrap Angle, f (in radians).

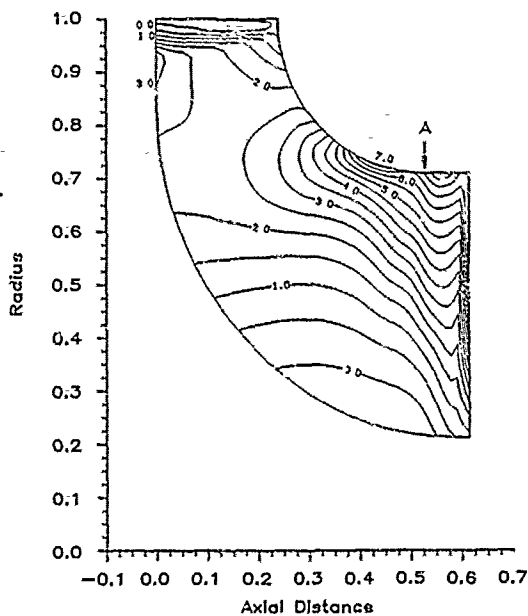


Fig. 7 Contours of Pressure Coefficient, C_p , on Suction Surface.

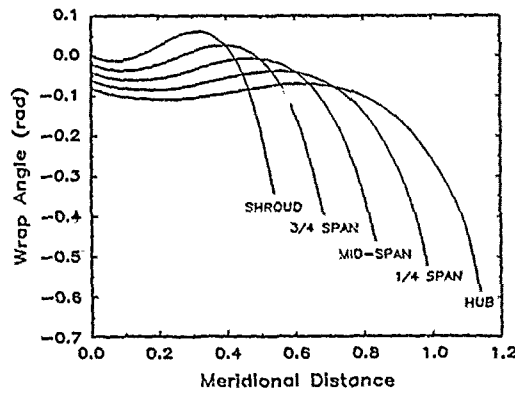


Fig. 9 Wrap Angle Distribution along Quasi-Streamlines for the Actuator Duct Solution.

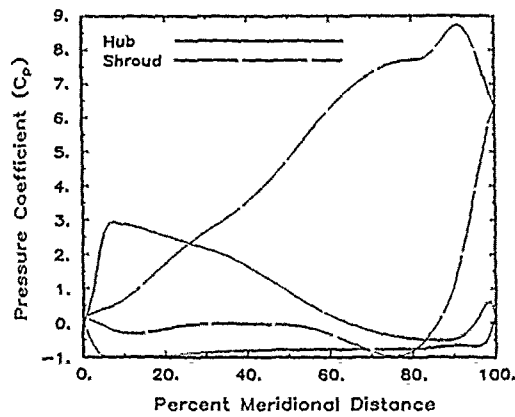


Fig. 11 Pressure Distribution on the Hub and Shroud Stream Surfaces for the Actuator Duct Solution.

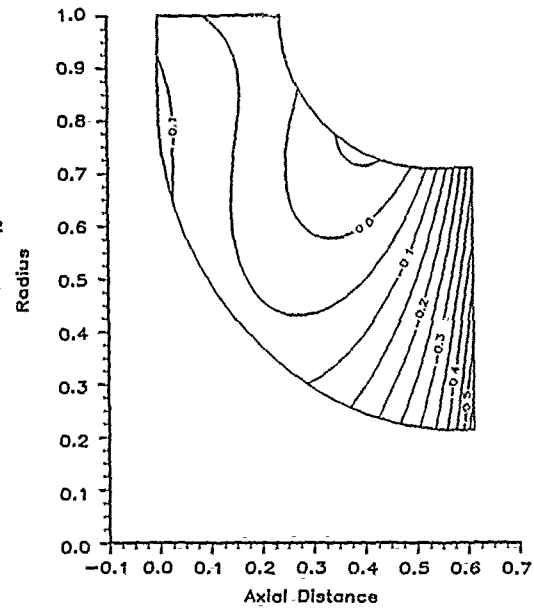


Fig. 10 Contours of Wrap Angle, f , for the Actuator Duct Solution (in radians).

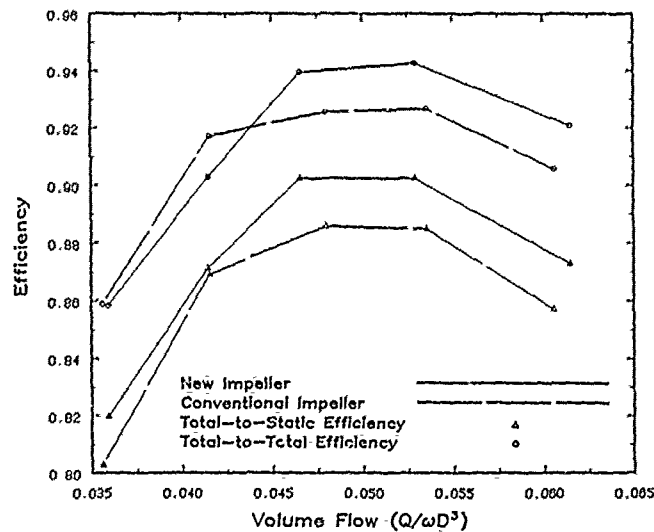


Fig. 12 Comparison of Efficiencies (Total-to-Total and Total-to-Static).

NUMERICAL METHOD FOR DESIGNING 3D TURBOMACHINERY BLADE ROWS

by

L. Zannetti, Politecnico di Torino, Italy
 E. Larocca, FIAT Aviazione, Torino, Italy
 R. Marsilio, Politecnico di Torino, C. so duca degli Abruzzi 24
 10129 Torino
 Italy

1 Introduction

In order to improve the performance of modern highly loaded turbomachinery components, attention must be paid in aerodynamic blade profiles design. The viscous effect and shock intensities, for example, can be reduced by designing blade geometries which give a proper velocity (or pressure) distribution.

A possible approach for designing blade rows consists on carrying out successive modification of blade shape and direct flow field calculations in an iterative way. However the procedure can be quite time consuming and does not provide always the expected results. A very interesting approach to design blade is given by inverse method. That is the designer prescribes some design data satisfying some criteria, as for instance minimizing viscous effects, and look for the shape that the walls of the blades have to assume in order to satisfy the prescribed flow properties.

The time-dependent technique has been shown quite effective on solving numerically inverse problems under the assumption of inviscid rotational flow fields, governed by Euler equations.

Following the early formulations given in Ref. [1], the basic idea is to consider bodies with deformable walls along which velocity or pressure distributions are given together with suitable conditions at infinity; an initial configuration of the flow field and an initial shape of the deformable walls are guessed; the evolution in time of both flow field and walls shape are described numerically by integrating in time the time-dependent Euler equations by means of a finite difference method; when the steady state is reached the deformable walls assume the shape that solves the inverse problem.

Since Ref. [1] was published, several improvements have been done. Upwind numerical schemes have been adopted to attain consistency with the wave propagation phenomena described by the Euler equations, as a consequence the computation at the boundaries has been improved; the extension to 3D problems has been shown feasible; different formulations have been attempted. The path of the evolution we followed runs from Ref. [1] to Ref. [5]. Similar ideas have been pursued by other authors, see for instance Ref. [6,7].

The aim of the present work is the presentation of a newly improved method to solve inverse problems for inviscid, compressible, rotational flows in 3D ducts or 3D rows of blades. The basic idea is the same as in Ref. [1]: a finite-difference time-dependent computation is performed in a channel whose walls are deformable and that adjust themselves to the design data. In the present 3D formulation we follow the ideas outlined in Ref. [8], we use a mathematical model based on the contravariant components of the flow velocity and a second-order accurate finite-difference scheme. A new procedure is used at the boundaries, which is simpler and more rigorous than the previous one [4].

2 The mathematical model

Let us denote by y^n , ($n = 1, \dots, 4$), the cartesian coordinate in the Euclidean space-time four-dimensional space, E^4 , reserving the apex 4 to denote time. Let us denote

by x^n , ($n = 1, \dots, 4$), a curvilinear frame of reference in E^4 , whose transformation from the Cartesian coordinates has the form:

$$\begin{aligned} x^\alpha &= x^\alpha(y^n) \quad (\alpha = 1, \dots, 3) \quad (n = 1, \dots, 4) \\ x^4 &= y^4 \end{aligned} \quad (1)$$

The mapping 1 is sufficiently general to define the curvilinear, time-dependent, body-fitted grid we use to discretize the physical domain in our inverse method. Moreover, we define a vector Q in E^4 , whose (contravariant) components Q^α ($\alpha = 1, \dots, 3$) coincide with the components of the flow velocity q and whose time component is constant and equal to one, $Q^4 = 1$. With such assumptions, the Euler equations can be written in a form invariant for transformations with the form 1. According to tensor notations, the 3D time-dependent Euler equations can be written as:

$$\begin{aligned} Q^n a_{,n} + \delta a Q_{,\alpha}^\alpha &= 0 \\ Q^n Q_{,n}^\alpha + a \left(\frac{a_{,\beta}}{\delta} - \kappa s_{,\beta} \right) g^{\alpha\beta} &= 0 \\ Q_{,n}^\alpha s_{,\alpha} &= 0 \end{aligned} \quad (2)$$

where latin indexes run from 1 to 4, greek indexes run from 1 to 3, " , " denotes tensor derivative. a is the speed of sound, $\delta = 2/(\gamma - 1)$, $\kappa = a/(2\gamma\delta)$, γ is the specific heats ratio and $g^{\alpha\beta}$ is the metric tensor and all the variables are normalized with respect to suitable reference values.

Following Ref. [8], eqs. 2 can be rearranged in a form suitable for upwind discretization by decomposing the 3D unsteady motion as due to waves fronts parallel to the coordinate surfaces; the resulting set of equations prompt an upwind discretization that preserves the 3D nature of the actual flow and that is particularly convenient from the point of view of the treatment of the boundaries, as shown in section 3:

$$\begin{aligned} a_{,4} &= \frac{\delta}{2} [\xi_d + \xi_e + \eta_d + \eta_e + \zeta_d + \zeta_e] + \delta \kappa s_{,4} \\ Q_{,4}^1 &= \frac{1}{2} \left\{ \sqrt{g^{22}} \left[2\eta_b + \frac{g^{21}}{g^{22}} (\eta_e - \eta_d) \right] + \right. \\ &\quad \left. \sqrt{g^{11}} [\xi_e - \xi_d] + \sqrt{g^{33}} \left[2\zeta_b + \frac{g^{23}}{g^{33}} (\zeta_e - \zeta_d) \right] \right\} \\ Q_{,4}^2 &= \frac{1}{2} \left\{ \sqrt{g^{11}} \left[2\xi_b + \frac{g^{12}}{g^{11}} (\xi_e - \xi_d) \right] + \right. \\ &\quad \left. \sqrt{g^{22}} [\eta_e - \eta_d] + \sqrt{g^{33}} \left[2\zeta_e + \frac{g^{31}}{g^{33}} (\zeta_e - \zeta_d) \right] \right\} \\ Q_{,4}^3 &= \frac{1}{2} \left\{ \sqrt{g^{11}} \left[2\xi_e + \frac{g^{13}}{g^{11}} (\xi_e - \xi_d) \right] + \right. \\ &\quad \left. \sqrt{g^{22}} \left[2\eta_e + \frac{g^{23}}{g^{22}} (\eta_e - \eta_d) \right] + \sqrt{g^{33}} [\zeta_e - \zeta_d] \right\} \\ s_{,4} &= \xi_a + \eta_a + \zeta_a \end{aligned} \quad (3)$$

The terms ξ_s, η_s, ζ_s in eqs. 3 are relative to waves fronts parallel to $x^1 = \text{const.}$,

$x^2 = \text{const.}$, $x^3 = \text{const.}$ surfaces, propagating with speeds λ_s , Φ_s , μ_s , respectively:

$$\begin{aligned}
 \xi_a &= -\lambda_a s_{,1} & \lambda_a &= Q^1 \\
 \xi_b &= -\lambda_b \left(\frac{Q^1_{,1}}{\sqrt{g^{11}}} - \frac{g^{12}}{g^{11}} \frac{Q^1_{,2}}{\sqrt{g^{11}}} \right) & \lambda_b &= Q^1 \\
 \xi_c &= -\lambda_c \left(\frac{Q^1_{,1}}{\sqrt{g^{11}}} - \frac{g^{13}}{g^{11}} \frac{Q^1_{,3}}{\sqrt{g^{11}}} \right) & \lambda_c &= Q^1 \\
 \xi_d &= -\lambda_d \left(\frac{a_1}{\delta} - \kappa s_{,1} + \frac{Q^1_{,1}}{\sqrt{g^{11}}} \right) & \lambda_d &= Q^1 + a\sqrt{g^{11}} \\
 \xi_e &= -\lambda_e \left(\frac{a_1}{\delta} - \kappa s_{,1} - \frac{Q^1_{,1}}{\sqrt{g^{11}}} \right) & \lambda_e &= Q^1 - a\sqrt{g^{11}} \\
 \eta_a &= -\Phi_a s_{,2} & \Phi_a &= Q^2 \\
 \eta_b &= -\Phi_b \left(\frac{Q^2_{,2}}{\sqrt{g^{22}}} - \frac{g^{12}}{g^{22}} \frac{Q^2_{,1}}{\sqrt{g^{22}}} \right) & \Phi_b &= Q^2 \\
 \eta_c &= -\Phi_c \left(\frac{Q^2_{,2}}{\sqrt{g^{22}}} - \frac{g^{23}}{g^{22}} \frac{Q^2_{,3}}{\sqrt{g^{22}}} \right) & \Phi_c &= Q^2 \\
 \eta_d &= -\Phi_d \left(\frac{a_2}{\delta} - \kappa s_{,2} + \frac{Q^2_{,2}}{\sqrt{g^{22}}} \right) & \Phi_d &= Q^2 + a\sqrt{g^{22}} \\
 \eta_e &= -\Phi_e \left(\frac{a_2}{\delta} - \kappa s_{,2} - \frac{Q^2_{,2}}{\sqrt{g^{22}}} \right) & \Phi_e &= Q^2 - a\sqrt{g^{22}} \\
 \zeta_a &= -\mu_a s_{,3} & \mu_a &= Q^3 \\
 \zeta_b &= -\mu_b \left(\frac{Q^3_{,3}}{\sqrt{g^{33}}} - \frac{g^{13}}{g^{33}} \frac{Q^3_{,1}}{\sqrt{g^{33}}} \right) & \mu_b &= Q^3 \\
 \zeta_c &= -\mu_c \left(\frac{Q^3_{,3}}{\sqrt{g^{33}}} - \frac{g^{23}}{g^{33}} \frac{Q^3_{,2}}{\sqrt{g^{33}}} \right) & \mu_c &= Q^3 \\
 \zeta_d &= -\mu_d \left(\frac{a_3}{\delta} - \kappa s_{,3} + \frac{Q^3_{,3}}{\sqrt{g^{33}}} \right) & \mu_d &= Q^3 + a\sqrt{g^{33}} \\
 \zeta_e &= -\mu_e \left(\frac{a_3}{\delta} - \kappa s_{,3} - \frac{Q^3_{,3}}{\sqrt{g^{33}}} \right) & \mu_e &= Q^3 - a\sqrt{g^{33}}
 \end{aligned} \tag{4}$$

The terms ξ_s, η_s, ζ_s express quantities carried by the waves in the unsteady motion, in a numerical process they have to be approximated by an upwind numerical scheme to preserve correctly the domain of dependence of the compute points. The numerical scheme we use is explicit, second order accurate in time and space, it is a variation of the λ -scheme described in Ref. [9].

In order to simplify the computation and to improve the accuracy, we prefer to avoid explicit evaluation of Christoffel symbols when computing the tensor derivatives of the vector Q . In fact, a tensor derivative has the general form:

$$Q^k_{,n} = \frac{\partial Q^k}{\partial x^n} + Q^n \Gamma^k_{nm} \tag{5}$$

The balancing in 5 of the partial derivative, approximated by one-sided differences, and the Christoffel symbol Γ^k_{nm} , evaluated on nodes, is quite delicate. We prefer to base our approximation on the formula:

$$Q^k_{,n} = \frac{\partial U^j}{\partial x^n} \frac{\partial x^k}{\partial y^j} \tag{6}$$

where U^j are the Cartesian components of Q .

It is also convenient to integrate in time the Cartesian components of Q , getting their derivatives in time from eqs. 3 and the formula:

$$\frac{\partial U^k}{\partial x^4} = Q_{,4}^j \frac{\partial y^k}{\partial x^j} \quad (7)$$

avoiding again the evaluation of Christoffel symbols.

3 The formulation of the inverse problem

The numerical process that we follow to solve 3D inverse problems is based on physical models that are straight forward extension of the 2D model of Ref. [2]. We use as physical frame of reference the cylindrical coordinates instead of the Cartesian coordinates, therefore the equations of section 2 have now to be read considering y^1 as radius, y^2 as tangential angle and y^3 as axial coordinate. As a consequence some equations have to be modified. For instance eq. 6 is replaced by:

$$Q_{,m}^k = \left(\frac{\partial U^j}{\partial x^m} + U^n \Gamma_{mn}^j \frac{\partial y^i}{\partial x^m} \right) \frac{\partial x^k}{\partial y^j} \quad (8)$$

where U^j are the cylindrical contravariant components of the vector Q and Γ_{mn}^j are the Christoffel symbols in the cylindrical frame of reference.

We take into consideration a channel whose walls GLTQ and CFPM are impermeable and deformable, with DEON and HISR representing the suction and pressure sides of the blades, respectively. The surfaces GCFL and QMPT are the annulus solids walls, the surface GCMQ is the inlet surface and LEPT is the outlet surface. Fig. 1) shows a typical initial configuration and Fig. 2) the shape of the channel solving a given inverse problem.

The inlet and the exit surfaces are $y^3 = \text{const.}$ plane surfaces, the equations of the solid surfaces are:

$$GCFL: \quad y^1 = b(y^3) \quad (9)$$

$$QMPT: \quad y^1 = c(y^3)$$

The equations defining the flexible walls are:

$$CMPF: \quad y^2 = d(y^1, y^3, y^4) \quad (10)$$

$$GQTL: \quad y^2 = e(y^1, y^3, y^4)$$

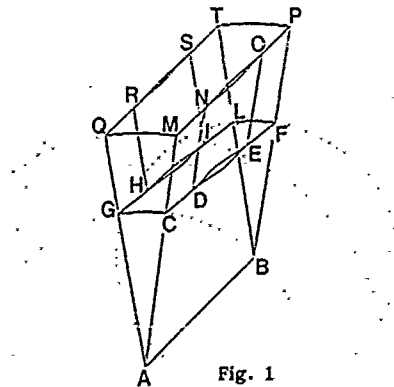


Fig. 1

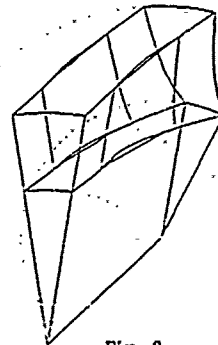


Fig. 2

The coordinate transformation:

$$\begin{aligned}x^1 &= \frac{(y^1 - b)}{(c - b)} \\x^2 &= \frac{(y^2 - d)}{(e - d)} \\x^3 &= y^3 \\x^4 &= y^4\end{aligned}\tag{11}$$

is used to define a time-dependent grid that fits the walls and adapts itself to the motion of the flexible walls.

Inverse-problems for blade to blade flows are constrained by the periodicity or by the requirement, identical from the geometrical viewpoint, that the blade profiles must be closed: in fact, the pitch is a geometrical parameter that is known a priori as function of the radius and that must be satisfied by the solution of an inverse problem. The 3D inverse problem is formulated following [2]: we prescribe a design pressure jump between pressure and suction sides Δp and design thickness t as function of radial and axial coordinates

$$\Delta p = f(y^1, y^3) \quad , \quad t = g(y^1, y^3)\tag{12}$$

and look for the blade camber geometry.

The whole flexible surfaces CFPM and GLTQ are computed satisfying eqs. 12: in the CDNM, EFPO, GHRQ and ILTS surfaces in front and behind the blades eqs. 12 reduce to:

$$\Delta p = 0, \quad t = 0\tag{13}$$

Total temperature, entropy and flow direction are prescribed at inlet surface, static pressure is prescribed at exit surface in case of subsonic flow; the vanishing of the normal component of the flow velocity is imposed on solid walls. With such boundary conditions a time dependent computation is performed over the x^j grid 11 according to the numerical scheme described on the previous section. Fig. 2), for instance, shows the shape that the channel has at the end of the transient, solving the inverse problem for the prescribed pressure distributions over the flexible walls.

The enforcement of the boundary conditions is the most delicate operation of the numerical process, depending the solution primarily on the boundary conditions. We use the same general idea of Refs. [8,10]: at each boundary a certain number of ξ , or η , or ζ , express the propagation of signals coming inward from the boundary, such terms depend on the boundary conditions and are independent of the inner flow field. In the numerical process, they cannot be computed according to eqs. 3, but they must be computed enforcing some boundary conditions. The number of boundary conditions needed by the finite difference equations (FDE) does not necessarily match the number of boundary conditions needed by the partial differential equations (PDE); if the boundary conditions needed by the FDE outnumber the boundary conditions needed by the PDE some additional numerical boundary conditions must be enforced. It is quite obvious that an algorithm that asks always for the FDE the same boundary conditions as for the PDE is optimal, this is the case of the numerical scheme applied to eqs. 3. Details on this matter can be found in Ref. [8].

Let us consider, for instance the GCFL surface of Figs. 1), 2). At this boundary, the ξ , referring to positive speeds of propagation, $\lambda_i > 0$, have to be computed enforcing the boundary conditions. The GCFL surface is a solid wall, the physical boundary condition is the vanishing of the normal component of the flow velocity, that is:

$$Q^1 = 0\tag{14}$$

There is one positive speed of propagation in x^1 direction: λ_d , as a consequence there is one term, ξ_d , to be evaluated enforcing eq. 14. We rewrite eq. 14 as:

$$\left(U^j + \frac{\partial U^j}{\partial x^4} \frac{\Delta x^4}{2} \right) \frac{\partial x^1}{\partial y^j} = 0 \quad (15)$$

By substituting eqs. 7 and 3 in eq. 15 we obtain one algebraic equation in one unknown, ξ_d , which satisfies eq. 14 in both predictor and corrector steps of the integration scheme. Any boundary can be computed following the same idea. For the moving walls, for example, the boundary conditions prescribe that the pressure jump and the pitch have to be preserved in time. The enforcement of the eqs 12 and 13 yield:

$$\left\{ p + \frac{a}{\gamma} \left(\frac{a_{s,4}}{\delta} - \kappa s_{s,4} \right) \frac{\Delta x^4}{2} \right\}_P - \left\{ p + \frac{a}{\gamma} \left(\frac{a_{s,4}}{\delta} - \kappa s_{s,4} \right) \frac{\Delta x^4}{2} \right\}_S = \Delta p \quad (16)$$

$$d_{y^4} = e_{y^4}$$

with "P" and "S" denoting pressure and suction sides, respectively, and d, e are defined by eqs. 10. The second of eqs. 16 can be written as:

$$\left\{ U^2 - U^n \frac{\partial d}{\partial x^\alpha} \frac{\partial x^\alpha}{\partial y^n} + \left(\frac{\partial U^2}{\partial x^4} - \frac{\partial U^n}{\partial x^4} \frac{\partial d}{\partial x^\alpha} \frac{\partial x^\alpha}{\partial y^n} \right) \frac{\Delta x^4}{2} \right\}_P = \left\{ U^2 - U^n \frac{\partial e}{\partial x^\alpha} \frac{\partial x^\alpha}{\partial y^n} + \left(\frac{\partial U^2}{\partial x^4} - \frac{\partial U^n}{\partial x^4} \frac{\partial e}{\partial x^\alpha} \frac{\partial x^\alpha}{\partial y^n} \right) \frac{\Delta x^4}{2} \right\}_S \quad (17)$$

with $\alpha = 1, 2, 3$; $n = 1, 3$ and $\partial d/\partial x^\alpha$, $\partial e/\partial x^\alpha$ approximated by finite difference. The first of eqs. 16 and eq. 17, combined with eqs. 3, allow η_d , unknown at the pressure side boundary, and η_s , unknown at the suction side boundary, be valued satisfying the boundary conditions 12.

The geometry of the pressure and suction sides, given in general form by eqs. 11, are updated at each time step by means of the eqs. :

$$d \left(y^1, y^3, y^4 + \frac{\Delta y^4}{2} \right) = d(y^1, y^3, y^4) + d_{y^4} \frac{\Delta y^4}{2} \quad (18)$$

where the derivatives $d_{y^4} = e_{y^4}$ are expressed by the condition of impermeability of the wall: the contravariant component Q^2 of the vector Q has to be zero, that is:

$$d_{y^4} = U^2 - U^n \frac{\partial d}{\partial x^\alpha} \frac{\partial x^\alpha}{\partial y^n} \quad (n = 1, 3) \quad (\alpha = 1, 2, 3) \quad (19)$$

In computing eq. 19, $\partial d/\partial x^\alpha$ are approximated by finite differences.

The other solid or moveable walls are computed in the same way, once the proper unknown terms ξ_s or η_s are detected.

4 Numerical examples

The proposed method has been tested first of all by replicating the same numerical examples of Refs. [1,2,4]. One new example is here presented: it refers to the design of the blades of a 3D rotational subsonic stator.

Figs. 3), 4), show the initial and final 3D view, respectively. The tip and hub solid annulus walls are cylindrical:

$$y_c^1 = r_t ; \quad y_b^1 = r_h$$

with $r_t/r_h = 1.5$.

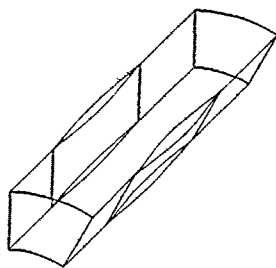


Fig. 3

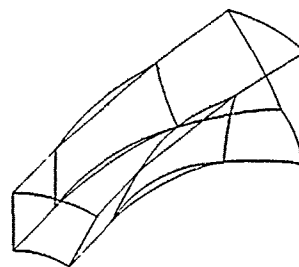


Fig. 4

The design thickness is:

$$t = .07 \sin \left[\pi \frac{y^3 - y_l^3}{y_t^3 - y_l^3} \right]$$

with $y_t^3 - y_l^3$ = axial chord.

The design loading is:

$$\Delta p = .08 \sin \left[\pi \frac{y^3 - y_l^3}{y_t^3 - y_l^3} \right]$$

Since Euler equations can transport vorticity, in order to have the development of passage vortices a viscous velocity profile is simulated at inlet by imposing total temperature constant $T^0 = 1$, and a parabolic distribution of total pressure with smallest value at hub:

$$p^0 = g\sqrt{y^1} + h$$

with $g = .1/(\sqrt{r_t} - \sqrt{r_h})$, $h = 1 - g\sqrt{r_t}$.

At the exit we prescribe the static pressure: at the hub radius we prescribe $p_h = .7$, at greater radius the static pressure is computed according to the radial equilibrium.

Figs. 5), 6) show the isoMach lines of the initial and final configurations of blade to blade sections at the hub-radius, respectively. Figs. 7)-10) represent the final configurations of intermediate and tip sections.

The constant entropy surfaces coincide with stream surfaces; as it has been pointed out in Ref. [4], looking at Figs. 11a) and 11b) one would expect to see the typical rotation of such surfaces as consequence of the secondary flows generated in 3D rotational flow. Actually, an axial component of the vorticity is correctly generated, it does not reveal itself as a rotation of the streamtubes, but rather as a peculiar twisting of the blades: the loading is prescribed as design data and it cannot be decreased as a consequence of secondary flows, but the lower is the total pressure (and density) the higher the deflection to provide such loading.

Finally, two integral checks have been done on the continuity and angular momentum of the computed flow field: Fig. 12) shows the mass flow computed on cross sections along the blade to blade channel; Fig. 13) compares the angular momentum evaluated on cross sections along the channel with the corresponding torque due to the design loading.

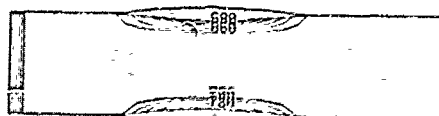


Fig. 5

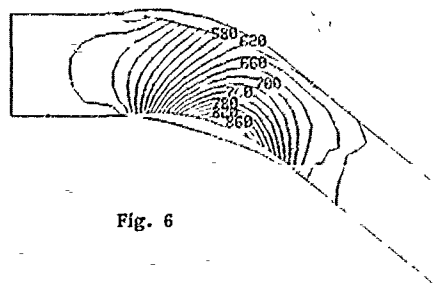


Fig. 6

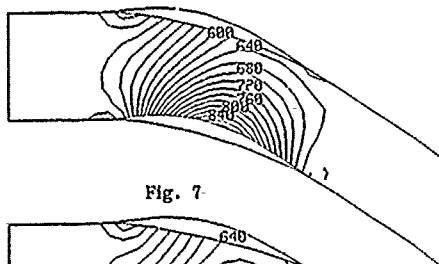


Fig. 7

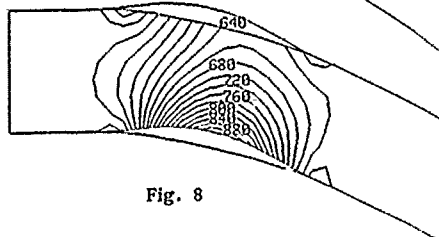


Fig. 8

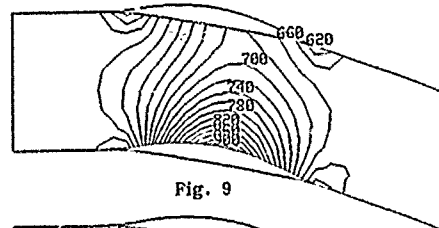


Fig. 9

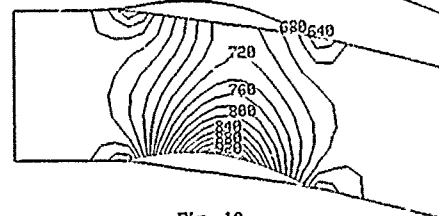


Fig. 10

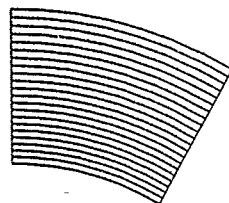


Fig. 11a



Fig. 11b

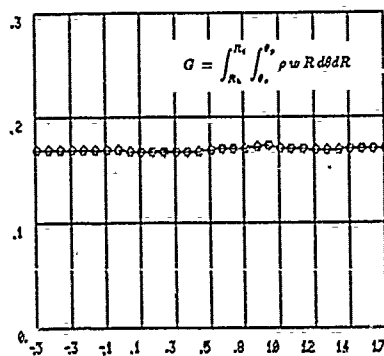


Fig. 12

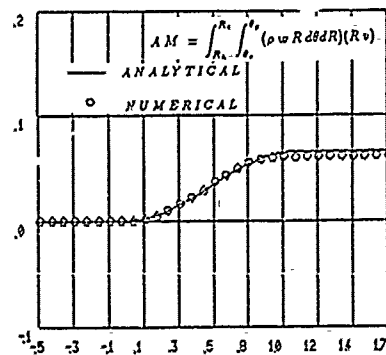


Fig. 13

References

- [1] L. Zannetti, *Time Dependent Method to Solve Inverse Problems for Internal Flows*, AIAA J., 18 July 1980, pp. 754-758.
- [2] L. Zannetti, M. Pandolfi, *Inverse Designe Techinque for Cascades*. NASA CR 3836, Nov. 1984.
- [3] L. Zannetti, *A Natural Formulation for the Solution of 2D or Axisymmetric Inverse Problems*, Int. J. Num. Meth. in Eng., Vol. 22, Feb. 1986, pp. 451-463.
- [4] L. Zannetti, T. T. Ayele, *Time Dependent computation of the Euler Equations for Designing Fully 3D Turbomachinery Blade Rows, Including the Case of Transonic Shock Free Design*, AIAA 25th Aerospace Sciences Meeting, Reno, Nevada, Jan. 1987, AIAA-87-0007.
- [5] L. Zannetti, F. Larocca, *Time Dependent Solution of Multidimensional Inverse Problems*, 2nd Int. Conf. on Inverse Designe Concept Optimization in Engineering Sciences, University Park, Pen. Oct. 1988.
- [6] G. Meauze, *An Inverse Time Marching Method for the Definition of Cascade Geometry*, ASME Paper 81-GT-167.
- [7] W. T. Thompkins, Sia Shing Tong, *Inverse Design Calculation for non Potential Flow in Turbomachinery Blade Passages*, J. Eng. for Power, 104, pp. 281-285.
- [8] L. Zannetti, B. Favini, *About the Numerical Modelling of Multidimensional Unsteady Compressible flows*, Symposium on Physical Aspects of Numerical Gas Dynamics, Polytecnic University New York, Aug. 1987, to Appear in Computer & Fluids.
- [9] G. Moretti, *An Improved λ -Scheme for One-Dimensional Flows*, NASA CR 3712, 1983.
- [10] G. Moretti, L. Zannetti, *A New Improved Computational Technique for 2D Unsteady Flow*, AIAA J., Vol. 22, June 1984, pp. 852-856.
- [11] L. Zannetti, *Time Dependent Computation of the Euler Equations for Designing 2D Cascades, including the Case of Transonic Shock Free Design*, Tokio Int. Gas Turbine Congress, Oct. 1983, Tokio, IGTC-54.

AERODYNAMIC OPTIMIZATION BY SIMULTANEOUSLY UPDATING FLOW VARIABLES AND DESIGN PARAMETERS*

by

M. H. Rizk

Sverdrup Technology, Inc.

P.O. Box 1935

Eglin Air Force Base, Florida 32542-5000

U.S.A.

SUMMARY

The application of conventional optimization schemes to aerodynamic design problems leads to inner-outer iterative procedures that are very costly. In this paper, an alternative approach is presented based on the idea of updating the flow variable iterative solutions and the design parameter iterative solutions simultaneously. Two schemes based on this idea are applied to problems of correcting wind tunnel wall interference and optimizing advanced propeller designs. The first of these schemes is applicable to a limited class of two-design-parameter problems with an equality constraint. It requires the computation of a single flow solution. The second scheme is suitable for application to general aerodynamic problems. It requires the computation of several flow solutions in parallel. In both schemes, the design parameters are updated as the iterative flow solutions evolve. Computations are performed to test the schemes' efficiency, accuracy, and sensitivity to variations in the computational parameters.

SYMBOLS

c_1	incrementing factor for optimization scheme [see Equation (9)]
c_2	decrementing factor for optimization scheme [see Equation (9)]
C	positive constant for chord method [see Equation (7)]
C_p	power coefficient; also pressure coefficient
C_{po}	desired power coefficient
D	propeller diameter
\hat{e}_l	unit vector along the P_l axis
E	objective function
f	constraint function
\bar{g}	solution of the flow governing equations
\bar{G}_l	l^{th} component of ∇f relative to rotated coordinate system
h	tunnel height
\hat{i}_l	unit vector along the E_l axis with components defined relative to the unrotated design parameter coordinate system
$\hat{\bar{i}}_l$	unit vector along the E_l axis with components defined relative to the rotated design parameter coordinate system
L	number of design parameters
L_c	measured model lift coefficient
L_F	computed lift coefficient for model in free air
L_T	computed lift coefficient for model in wind tunnel
M	Mach number
N	number of problems solved in parallel by the optimization scheme
n_a	number of iterations required for the convergence of the analysis problem's solution
n_c	number of iterations required for the convergence of the optimization problem's solution
\bar{P}	vector of design parameters
\bar{P}	vector of design parameters relative to rotated coordinate system
P_l	l^{th} component of design parameter vector
E_l	l^{th} component of design parameter vector relative to rotated coordinate system
r	radial coordinate
R	blade tip radius
R_E	residual Euclidean norm
R_{max}	maximum residual
α	angle of attack
$\beta_{3/4}$	3/4 blade angle at 75% blade span
β_o	unperturbed blade angle distribution
$\beta_{o3/4}$	$\beta_{3/4}$ which corresponds to the power coefficient C_{po}
ΔM	Mach number correction
$\Delta \alpha$	angle of attack correction
β^l	blade angle distribution perturbation
$\delta \bar{P}$	incremental vector used to update the vector of design parameters
δP_{max}	maximum incremental value allowed in updating the design parameters
ΔN	number of iterative steps at which \bar{P} is periodically updated

* This work was supported by NASA-Lewis Research Center under Contract NAS3-24855 and NASA-Ames Research Center under Contract NAS2-12157. It was completed while the author was at Flow Research Co., Kent, Washington.

ϵ	small positive incremental value used to perturb the design parameters
η	efficiency
λ	$= N/L$
μ	parameter determining the allowable region in design parameter space for searching for the optimum solution [see Equation (22)]
ν	$= \lambda\sigma$
σ	$= n_c^o / n_c^q$
ψ	flow iterative solution

Superscripts

n	iteration number
$*$	optimum value

Subscripts

e	measured tunnel condition
F	computed free-air condition
f	corrected condition
M	coordinate system rotated by the modified scheme
S	body surface
T'	computed tunnel condition
∞	free-stream condition
$-$	rotated coordinate system

1. INTRODUCTION

Solutions of constrained optimization problems minimize an objective function, E , subject to given constraints. In aerodynamic applications, the objective function and the constraint functions, f_i , $i = 1, 2, \dots$, depend on the flow field solution, \vec{g} . The optimization schemes presented here are applicable to situations in which the flow governing equations are nonlinear equations that are solved iteratively.

Conventional optimization methods (e.g., the steepest descent method and the conjugate gradient method) are iterative procedures that require the evaluation of the objective function many times before the converged optimum solution is determined. Since E and f_i are dependent on the flow solution, \vec{g} , in addition to the vector of design parameters, \vec{P} , the flow governing equation must be solved each time E and f_i are evaluated. Therefore, the application of conventional optimization schemes to aerodynamic design problems (References 1-5) leads to two-cycle (inner-outer) iterative procedures. The inner iterative cycle solves the analysis problem for \vec{g} iteratively, while the outer cycle determines the optimum \vec{P} iteratively. An alternative to the costly conventional optimization approach is the approach based on the idea of updating the flow variable iterative solutions and the design parameter iterative solutions simultaneously. Two schemes based on this idea are presented here. The first is applicable to a limited class of problems, while the second is a general scheme applicable to general aerodynamic optimization problems. The results of applying the schemes to two different problems are presented. In the first problem wind tunnel wall interference corrections are determined and in the second problem advanced propeller designs are optimized. Computations are performed to test the efficiency, accuracy and sensitivity of the schemes to variations in the computational parameters.

2. APPROACH

In the optimization problems considered here, the optimum design parameter vector, \vec{P}^* , is determined such that

$$E(\vec{P}^*; \vec{g}) = \min_{\vec{P}} E(\vec{P}; \vec{g}) \quad (1)$$

subject to the constraint

$$f(\vec{P}; \vec{g}) = 0 \quad (2)$$

with the flow variable vector \vec{g} satisfying the flow governing equation

$$\vec{D}(\vec{g}) = 0 \quad (3)$$

subject to the boundary condition

$$\vec{B}(\vec{g}; \vec{P}) = 0 \quad (4)$$

Two optimization schemes are presented here. The first, scheme I, is applicable to a limited class of two-design-parameter problems with an equality constraint. The objective function is assumed to be of special form and the constraint line is assumed to be normal to the P_1 axis in design parameter space. The second, scheme II, is applicable to multi-design-parameter problems with a single equality constraint. Extensions for solving multi-constraint problems and problems with inequality constraints are also presented. Although scheme I is a special scheme, which may be applied only to a limited class of problems, including it here serves two purposes. It provides a second example of a scheme which updates the design parameters and the flow variables simultaneously. Moreover, results obtained from applying scheme I to optimization problems provide an additional set of data for determining the effects of updating the design parameters while the flow solution is developing.

The goal of the optimization schemes is to determine the values of the design parameters that minimize the objective function, E , subject to an equality constraint. A search must therefore be conducted in the design parameter space \bar{P} for the optimum solution, \bar{P}^* . This optimization problem is most conveniently solved in the rotated design parameter space \bar{P}_l with the P_1 coordinate normal to the constraint surface and the P_l coordinates, where $l = 2, 3, \dots, L$, parallel to the constraint surface. In the case of scheme I a rotation of the coordinate system is not required, since both design parameter spaces \bar{P} and \bar{P}_l are equivalent. For fixed values of the components of \bar{P}_l , let

$$\bar{g}^{n+1} = \bar{\psi}(\bar{g}^n; \bar{P}), \quad n = 0, 1, 2, \dots \quad (5)$$

be the iterative solution for the analysis problem, where $\bar{\psi}$ denotes the solution obtained by applying the iterative scheme for solving the flow governing equations once using \bar{g}^n as an initial guess. As for the analysis solution, obtaining the optimization solution requires the repeated application of Equation (5) to update the flow field. While \bar{P} is held fixed in the former case, it is allowed to vary in the latter.

The vector of design parameters \bar{P} is updated every ΔN iterations. Therefore,

$$\bar{P}^{n+1} = \bar{P}^n + \delta \bar{P}^{n+1} \quad (6)$$

where

$$\delta \bar{P}^{n+1} = 0, \quad (n+1)/\Delta N \neq 1, 2, 3, \dots$$

In the iterative steps that satisfy the relation $(n+1)/\Delta N = 1, 2, 3, \dots$, the incremental values for the design parameters are given by

$$\delta P_1^{n+1} = -\frac{f^n}{|f^n|} [\min(|f^n|, \delta P_{max})] \quad (7)$$

$$\delta P_l^{n+1} = \min\left(1, \frac{\delta P_{max}}{|\Delta P_l^{n+1}|}\right) \Delta P_l^{n+1}, \quad l = 2, 3, \dots, L \quad (8)$$

where

$$f^n = f(\bar{P}^n; \bar{g}^n)$$

$$\Delta P_l^{n+1} = \frac{1}{2} [c_1(\tau_l^{n+1} + 1) + c_2(\tau_l^{n+1} - 1)] \delta P_l^{n+1-\Delta N} \quad (9)$$

$$\tau_l^{n+1} = -\frac{\Delta E_l^n \delta P_l^{n+1-\Delta N}}{|\Delta E_l^n \delta P_l^{n+1-\Delta N}|} \quad (10)$$

The purpose of ΔE_l^n appearing in Equation (10) is to determine the sign of $\partial E / \partial P_l^n$, which in turn determines the sign of the new incremental step along the P_l^n direction. The main difference between schemes I and II is in the definition of ΔE_l^n .

The incremental displacement in the design parameter space introduced so that the constraint may be satisfied is taken in the direction normal to the constraint surface and is determined by the chord method in Equation (7). The constant δP_{max} sets an upper limit on the magnitude of this incremental displacement. The incremental displacements given by Equation (8) are introduced along the coordinate axes, which are parallel to the constraint surface with the purpose of reducing the value of the objective function. The sign of the incremental correction δP_l^{n+1} , where δP_l^{n+1} is the l^{th} component of the vector $\delta \bar{P}^{n+1}$, is chosen to be opposite to that of $\partial E / \partial P_l^n$. The magnitude of the increment δP_l^{n+1} is given by

$$|\delta P_l^{n+1}| = c |\delta P_l^{n+1-\Delta N}|$$

with an upper limit given by δP_{max} , where $c > 0$. If the signs of $\delta \bar{P}_l^{n+1}$ and $\delta \bar{P}_l^{n+1-\Delta N}$ are in agreement, then the last two iterative solutions \bar{P}_l^n and $\bar{P}_l^{n-\Delta N}$ fall to one side of the point along the \bar{P}_l direction at which E is a minimum. In this case, c is set equal to the constant c_1 , which is greater than 1. Increasing the magnitude of the step size in this manner accelerates the approach toward the point along the \bar{P}_l direction at which E is a minimum. On the other hand, if the signs of $\delta \bar{P}_l^{n+1}$ and $\delta \bar{P}_l^{n+1-\Delta N}$ are not in agreement, then \bar{P}_l^n and $\bar{P}_l^{n-\Delta N}$ fall on opposite sides of the point along the \bar{P}_l direction at which E is a minimum. In this case, c is set equal to the constant c_2 , which is less than 1. Decreasing the magnitude of the step size in this manner is necessary for convergence to the point along the \bar{P}_l direction at which E is a minimum.

The updated components of the design parameter vector \bar{P}^{n+1} are used to calculate the new flow iterative solution, \bar{g}^{n+1} , given by

$$\bar{g}^{n+1} = \bar{\psi}(\bar{g}^n; \bar{P}^{n+1}) \quad (11)$$

2.1 Scheme I

This scheme was developed for application to a particular problem arising from a transonic wind tunnel wall interference correction procedure. In this procedure the free air flowfield around the model is computed. The design parameters are the model angle of attack α_F and the free-air Mach number $M_{\infty F}$, so that $\bar{P} = (\alpha_F, M_{\infty F})$. Their optimum values are determined so that Equation (1) is satisfied with

$$E = \frac{\int (M_{FS} - M_{TS})^2 ds}{\int M_{TS}^2 ds} \quad (12)$$

subject to the constraint

$$f = L_F - L_e = 0 \quad (13)$$

where M_{FS} is the computed Mach number distribution on the model surface in free-air and M_{TS} is the corresponding Mach number distribution in the wind tunnel. This is obtained from a wind tunnel flow computation which is performed prior to the free-air computation. The integrals in Equation (12) are taken over the model surface.

In scheme I a single solution given by Equation (11) is computed. To determine the sign of $\partial E^n / \partial \bar{P}_l^n$ it is therefore necessary to use values of E at different iterative steps. In this scheme $\Delta N = 1$ and ΔE_2^n is defined by

$$\Delta E_2^n = (E^n - E^{n-1})(e^n - e^{n-1})$$

where

$$E^n = E(\bar{P}^n; \bar{g}^n)$$

$$e^n = e(\bar{P}^n; \bar{g}^n)$$

$$e = \frac{\int (M_{FS} - M_{TS}) ds}{\int M_{TS} ds}$$

Because ΔE_1^n is evaluated at two different time steps the sign of ΔE_1^n may not always agree with that of $\partial E^n / \partial \bar{P}_1^n$. As long as the frequency at which this disagreement occurs is below a certain limit the scheme converges to the correct solution. The coordinate system in design parameter space is not rotated. Therefore, the search for the minimum objective function is conducted along constant \bar{P}_1 lines. In general, this will not lead to accurate determination of the optimum solution, however, in the particular problem considered here the constant \bar{P}_1 lines are nearly parallel to the constraint curve. The resulting error is therefore negligible.

2.2 Scheme II

This scheme is a general scheme, which does not have the limitations of scheme I. In addition to the main solution given by Equation (11), this scheme computes the perturbed solutions \bar{g}_l^{n+1} , $l = 1, 2, \dots, L$, given by

$$\bar{g}_l^{n+1} = \bar{\psi}(\bar{g}_l^n; \bar{P}^{n+1} + \epsilon \bar{i}_l^{n+1}) \quad (14)$$

where ϵ is a small positive constant and \bar{i}_l^{n+1} , $l = 1, 2, \dots, L$, are the set of orthogonal unit vectors along the axes of the rotated coordinate system $\bar{P}_1^{n+1}, \bar{P}_2^{n+1}, \dots, \bar{P}_L^{n+1}$. In Equation (10) ΔE_1^n is given by

$$\Delta E_1^n = E(\bar{P}^n + \epsilon \bar{i}_1^n; \bar{g}_1^n) - E(\bar{P}^n; \bar{g}^n)$$

While the optimization procedure is most suitably conducted in terms of the transformed parameters P_l , $l = 1, 2, \dots, L$, the flow solution is computed in terms of the physical design parameters P_l , $l = 1, 2, \dots, L$. To express the transformed design parameters in Equations (11) and (14) in terms of the original design parameters, it is necessary to use the transformation equation, which relates these two sets of parameters. This equation is

$$\bar{P}^{n+1} = T^{n+1} \bar{P}^{n+1}$$

where the orthogonal transformation matrix T^{n+1} is given by

$$T^{n+1} = [\bar{i}_1^{n+1} \bar{i}_2^{n+1} \dots \bar{i}_L^{n+1}]$$

The unit vector \bar{i}_1^{n+1} is normal to the constraint surface at $\bar{P} = \bar{P}^n$ and is given by

$$\bar{i}_1^{n+1} = \nabla f(\bar{P}^n; \bar{g}^n) / |\nabla f(\bar{P}^n; \bar{g}^n)| \quad (15)$$

where an estimate for \bar{Q}_1^n , the i^{th} component of ∇f , is given by

$$\bar{Q}_1^n = [f(\bar{P}^n + \epsilon \bar{i}_1^n; \bar{g}^n) - f(\bar{P}^n; \bar{g}^n)] / \epsilon \quad (16)$$

The Gram-Schmidt orthogonalization process, which uses a set of L linearly independent vectors to construct a set of L orthonormal vectors, is used to construct the unit vectors \bar{i}_l^{n+1} , $l = 2, 3, \dots, L$, along the rotated axes \bar{P}_l^{n+1} , $l = 2, 3, \dots, L$. The following equation is used for this purpose:

$$\bar{i}_l^{n+1} = \frac{\bar{j}_l^{n+1}}{|\bar{j}_l^{n+1}|}, \quad l = 2, 3, \dots, L$$

where

$$\bar{j}_l^{n+1} = \bar{i}_l^n - \sum_{k=1}^{l-1} (\bar{i}_l^n \cdot \bar{i}_k^{n+1}) \bar{i}_k^{n+1} \quad (17)$$

In the initial iterative step, the vectors \bar{i}_l are given by $\bar{i}_l^1 = \bar{e}_l$, $l = 1, 2, \dots, L$, where \bar{e}_l , $l = 1, 2, \dots, L$, are the set of orthogonal unit vectors along the axes of the coordinate system P_1, P_2, \dots, P_L . While the flow variable vector \bar{g} is updated each iterative step, the coordinate system in the design parameter space is rotated every ΔN iterations. The unit vectors \bar{i}_l , like the vector of design parameters \bar{P} , are updated only in the iterative steps that satisfy the relation $(n+1)/\Delta N = 1, 2, 3, \dots$

The optimization scheme described above requires that $L + 1$ iterative problems be solved in parallel. In addition to the main solution, L perturbed solutions are computed in which each of the design parameters in the transformed space P_1, P_2, \dots, P_L is perturbed. The computational costs and the computer memory requirements are therefore proportional to $L + 1$. A modification to this scheme, which requires that only L iterative solutions be obtained, is now introduced. In the modified procedure, the perturbation solution associated with the perturbed design parameter in the direction of the P_1 axis, normal to the constraint surface, is not computed. This solution was used in Equation (16) to compute \bar{Q}_1^n , which is required for the calculation of the vector \bar{i}_1^{n+1} , which determines the direction normal to the constraint surface in Equation (15). In the absence of this solution, a new procedure for rotating the design parameter space must be defined. The procedure is first explained for the case of a two-design-parameter problem, and then it is extended to the general multi-design-parameter problem.

Figure 1 shows the design parameter space for a two-design-parameter problem. In the figure, the constraint function values f_0^n , f_1^n , f_2^n are defined as follows:

$$\begin{aligned} f_0^n &= f(\bar{P}^n; \bar{g}^n) \\ f_1^n &= f(\bar{P}^n + \epsilon \bar{i}_1^n; \bar{g}^n) \\ f_2^n &= f(\bar{P}^n + \epsilon \bar{i}_2^n; \bar{g}^n) \end{aligned}$$

In the modified procedure, the chord method, used in Equation (7) to satisfy the constraint condition, is used to rotate the design parameter space. The rotation angle $\delta\theta_M^{n+1}$ given by

$$\delta\theta_M^{n+1} = \tan^{-1} \left(\frac{C(f_2^n - f_0^n)}{\epsilon} \right) \quad (18)$$

is used to rotate the coordinate system, where the subscript M indicates that the modified scheme is used. The angle $\delta\theta_M^{n+1}$ is now compared to the corresponding rotation angle $\delta\theta^{n+1}$ used in the original scheme and given by

$$\delta\theta^{n+1} = \tan^{-1} \left(\frac{f_2^n - f_0^n}{f_1^n - f_0^n} \frac{\epsilon}{f_1^n - f_0^n} \right) \quad (19)$$

This comparison shows that the term $f_1^n - f_0^n$ in the original scheme is replaced by ϵ/C in the modified scheme. Therefore, the modified scheme may be viewed as the original scheme with the exception that the exact value for \bar{i}_1 is replaced by an approximate estimate in which the gradient of f in the direction of the \bar{P}_1 axis, \bar{G}_1 , is not calculated but is estimated using the same proportionality constant used in the chord method of Equation (7). Thus,

$$\bar{G}_1 = \frac{1}{C} \quad (20)$$

This is applicable for both the two-design-parameter problem and the general multi-design-parameter problem.

In the optimization scheme developed here, corrective increments are applied to the design parameter solutions every few iterations of updating the flow solutions. For convergence to occur, the signs of the increments must be chosen correctly to allow the iterative solution to approach the desired solution. The magnitudes of the increments are dependent on the computational constants c_1 , c_2 , and C . Because the design parameters are updated frequently during the iterative process, we are not concerned with determining the incremental step sizes that lead to the highest short-term convergence rate. In fact, this may be difficult to define, since the flow variable solutions are continuously changing during the iterative process. Our aim is to achieve design parameter convergence over a long term defined by the number of iterations required for the flow solution convergence. A wide range of incremental step sizes should produce the desired convergence properties over many iterations, even though convergence properties over a few iterations may differ. These comments apply to both of the schemes described above for determining the design parameter space rotation. The direct procedure for determining the design parameter space rotation in the original scheme is replaced by an iterative procedure in the modified scheme. Since this rotation is updated frequently during the iterative process, this replacement should have no substantial effect on the overall convergence of the solution.

A potential problem exists when the modified scheme is used for rotating the design parameter axes. This problem is now discussed, then suggestions for overcoming it are presented.

In the first $\Delta N - 1$ iterative steps of solving the problem, the coordinate system in the design parameter space coincides with the original unrotated design parameter space P_1, P_2, \dots, P_L . At the ΔN^{th} iterative step, a new rotated coordinate system is determined. When Equation (16) for determining $\bar{G}_1^{\Delta N-1}$ is used, we are guaranteed that the vector $\bar{i}_1^{\Delta N}$ points in the direction in which the constraint function increases. Consequently, the use of Equation (7) will cause the iterative solution to approach the constraint surface. When Equation (16) is replaced by Equation (20) for determining $\bar{G}_1^{\Delta N-1}$, there is a possibility that the computed vector $\bar{i}_1^{\Delta N}$ will point in the direction in which the constraint function decreases. In this case, the assumption that C is positive is wrong, and using it will cause the solution to diverge. This occurs if the vector \bar{z}_1 is nearly in the direction of $-\nabla f^{\Delta N-1}$.

That is, if the quantity

$$-\frac{\nabla f^{\Delta N-1}}{|\nabla f^{\Delta N-1}|} \cdot \bar{z}_1$$

is close to unity. The probability of this occurring is approximately 1:4 in a two-design-parameter problem and is reduced further as the number of design parameters increases. There are two suggested approaches for overcoming this problem. In the first approach, the initial few iterations are performed using the original scheme for determining \bar{G}_1^n by Equation (16) in order to determine the correct initial directions for the P_1 axis. This may then be updated using the modified scheme, Equation (20), in the rest of the computation. Realizing that the probability for the potential problem to occur is small, the second approach uses the modified scheme from the beginning of the computation. If divergence does occur, then the constraint function is redefined to be equal to the negative of the original constraint function, and the problem is solved again.

2.3 Extension of Scheme II

Scheme II is applicable to optimization problems with a single equality constraint. However, this scheme may be extended to more general problems such as multiple constraint problems and problems with inequality constraints. These extensions are now briefly presented.

In the case of multiple constraints, the set of equations,

$$f_k(\bar{P}; \bar{q}) = 0, \quad k = 1, 2, \dots, K$$

replaces Equation (2), where K is the number of constraints. For this problem, Equation (7) is replaced by

$$\delta \bar{P}_l^{n+1} = - \frac{f_l^n}{|\bar{P}_l^n|} [\min (C|f_l^n|, \delta P_{max})], \quad l = 1, 2, \dots, K$$

Equation (8) is applied for values of l given by $l = K+1, K+2, \dots, L$ and the unit vectors \bar{r}_l^{n+1} are given by

$$\bar{r}_l^{n+1} = \begin{cases} \nabla f_l(\bar{P}^n; \bar{g}^n) / |\nabla f_l(\bar{P}^n; \bar{g}^n)|, & l = 1 \\ \bar{Q}_l^{n+1} / |\bar{Q}_l^{n+1}|, & l = 2, 3, \dots, K \\ \bar{r}_l^{n+1} / |\bar{r}_l^{n+1}|, & l = K+1, K+2, \dots, L \end{cases}$$

where

$$\bar{Q}_l^{n+1} = \bar{N}_l^{n+1} - \sum_{r=1}^{l-1} (\bar{N}_l^{n+1} \cdot \bar{r}_r^{n+1}) \bar{r}_r^{n+1}, \quad l = 2, 3, \dots, K$$

$$\bar{N}_l^{n+1} = \nabla f_l(\bar{P}^n; \bar{g}^n)$$

and \bar{r}_l^{n+1} was defined in Equation (17).

In the case of an unconstrained problem, the problem is solved in the original, unrotated design parameter space. In this case Equation (7) is not used and Equation (8) is applied for l values given by $l = 1, 2, \dots, L$.

In the case of a problem with inequality constraints, the solution procedure at a given iterative step is equivalent to that of an unconstrained problem, if none of the constraints are effective, and it is equivalent to that of a problem with K_e equality constraints, if K_e of the constraints are effective. For the problem with inequality constraints, Equation (2) is replaced by

$$f_k(\bar{P}; \bar{g}) \leq 0, \quad k = 1, 2, \dots, K$$

At the iterative step $n+1$, the k^{th} constraint is effective if either of the following conditions is satisfied:

$$f_k(\bar{P}^n; \bar{g}^n) \geq \delta$$

where δ is a small positive number, or

$$f_k(\bar{P}^n; \bar{g}^n) < \delta, \quad \frac{\partial E(\bar{P}^n; \bar{g}^n)}{\partial \bar{P}_k^n} < 0$$

Otherwise it is not effective.

3.0 RESULTS

The optimization procedures described above were applied to wind tunnel wall interference problems and to propeller design problems. The computations were performed on the Cray X-MP computer. The results of these computations are presented below.

3.1 Wind Tunnel Wall Interference Corrections

References 6 and 7 present a wall interference correction procedure which is divided into two main steps. In the first step the flow is computed around the model in the wind tunnel subject to measured boundary conditions at the tunnel walls. The model angle of attack, α_T , that causes the computed model lift, L_T , to match the measured lift, L_e , is determined by the chord method. The Mach number distribution on the model surface, M_{TS} , is also determined in this step. In the second step, which is formulated as an optimization problem, the flow is computed around the model in free air. The design parameters P_1 and P_2 are the model angle of attack, α_F , and the free stream Mach number, $M_{\infty F}$, respectively. They are determined such that the objective function given by Equation (12) is minimized subject to the constraint given by Equation (13). The Mach number correction, ΔM , and the angle of attack correction, $\Delta \alpha$, are given by

$$\Delta M = M_{\infty F} - M_{\infty e}; \quad \Delta \alpha = \alpha_F - \alpha_T$$

and the corrected Mach number and angle of attack are then found from the relations

$$M_{\infty f} = M_{\infty e} + \Delta M; \quad \alpha_f = \alpha_e + \Delta \alpha$$

The flow was assumed to be governed by the Euler equations. The flow solver used was based on a finite volume discretization. A multigrid strategy together with a multistage time-stepping scheme were used to advance the flow solution to a steady state as rapidly as possible. Details of the dissipative terms, the multistage scheme and the multigrid method are given in References 8-10. Some results of applying the optimization procedures to the wall interference problem in References 6 and 7 are presented below.

The correction procedure was applied to a wing/body combination consisting of an ONERA M6 wing, with a wing span and maximum chord of 2.4 and 0.6737 unit lengths, respectively, mounted on a cylindrical body of a 0.2-unit-length radius. The model was assumed to be tested in an open jet with zero pressure perturbations along its boundaries. The tunnel height and width considered were 2.0 and 4.0 unit lengths, respectively. The computational domain consisted of half the flow field by including the plane of symmetry as one of its boundaries. The computational parameters δP_2^0 , c_1 , c_2 , C , and δP_{max} were assigned the values 0.005, 1.2, 0.6, 0.3, and 0.2 respectively. The initial guess for the flow solution was set equal to free-stream conditions. A $72 \times 24 \times 12$ mesh was used for the tunnel computation, while a $72 \times 32 \times 12$ mesh was used for the free-air computation. The free-air mesh and the tunnel mesh were identical in a region bounded by the upper and lower tunnel walls and the wing tip. Beyond the wing tip, the meshes did not coincide. The experimental conditions were given by $M_{\infty e} = 0.84$ and $L_e = 0.20$.

In the first step of the correction procedure, the tunnel flow is computed and the angle of attack, α_T , is determined. It was found to be given by $\alpha_T = 2.777^\circ$. In the second step of the correction procedure, the free-air flow is computed and the parameters P_1 and P_2 are determined by using scheme I, where

$$P_1 = \alpha_F \text{ and } P_2 = M_{\infty F}.$$

Their values were found to be given by $\alpha_F = 2.468^\circ$ and $M_{\infty F} = 0.833$. The angle-of-attack and Mach number corrections are, therefore, given by $\Delta\alpha = -0.309^\circ$ and $\Delta M = -0.007$. Figure 2 shows the iterative histories for α_F and L_F , while the iterative history for $M_{\infty F}$ is shown in Figure 3. Figure 4 compares R_{max} for the second step in the correction procedure, in which \bar{g} is updated in addition to α_F and $M_{\infty F}$, to R_{max} for the regular analysis solution, in which only \bar{g} is updated while α_F and $M_{\infty F}$ are held fixed. The figure indicates that the convergence rates for the analysis and the correction schemes are comparable. The high-frequency oscillations apparent in the curve associated with the correction procedure are due to the introduction of perturbations in the flow field as $M_{\infty F}$ is updated. The computational requirements for the free-air correction scheme and the analysis scheme are essentially the same. The first of these computations required 153 cpu seconds, while the second required 150 cpu seconds. For the uncorrected free-air flow ($M_{\infty F} = 0.84$, $\alpha_F = 2.777^\circ$), the values of L_F and E are given by $L_F = 0.235$, $E = 5.2 \times 10^{-6}$. For the corrected free-air flow ($M_{\infty F} = 0.833$, $\alpha_F = 2.468^\circ$), these values are given by $L_F = 0.200$, $E = 6.92 \times 10^{-7}$. The corrections therefore achieved the goal of satisfying the lift constraint and of reducing the value of the objective function.

Scheme I was applied to different three-dimensional configurations with success. However, problems developed when applying it to two-dimensional configurations, as the supersonic bubble size increased beyond a certain limit. To demonstrate this problem the procedure is now applied to a NACA 0012 airfoil tested in an open jet of height $h = 3.6$. The airfoil is assumed to have a chord of unit length and to be located in the middle between the upper and lower boundaries. A 72×64 mesh is used for the tunnel simulation and a 72×96 mesh is used for the free-air simulation. The airfoil lift coefficient and the tunnel Mach number are given by $L_e = 0.35$ and $M_{\infty e} = 0.7$.

In the first step of the correction procedure, the wind tunnel flow is computed and the angle of attack α_T is determined. In the second step of the correction procedure, the free-air flow is computed and the parameters α_F and $M_{\infty F}$ are determined. The initial iterative values of α_F and $M_{\infty F}$ are chosen to be equal to α_T and $M_{\infty e}$, respectively. The initial flow field solution is set equal to free-stream conditions. The parameters δP_2^0 , c_1 , c_2 , C , δP_{max} , ΔN , and ϵ are given, respectively, by 0.005, 1.2, 0.6, 0.3, 0.2, 4, and 10^{-5} .

The iterative history of $M_{\infty F}$ resulting from using scheme I is shown in Figure 5a. An initial stage of about 60 iterative steps of rapid variations is observed in this figure. The solution beyond this point seems to be essentially converged. However, at approximately the 80th and the 230th iterative steps, a rapid departure from the apparently converged solution takes place. Within about 25 iterative steps in both cases, an essentially converged solution is observed again. We have conducted many computations, using scheme I, for different test conditions. The appearance of local spike-shaped deviations is a common feature among these solutions. However, the size of these spikes and the frequency of their occurrence depend on the particular problem being solved. The iterative history of $M_{\infty F}$ resulting from using scheme II is shown in Figure 5b. In this figure, an initial stage of about 150 iterative steps is identified in which relatively rapid variations in the value of $M_{\infty F}$ take place. At the end of this stage, the value of $M_{\infty F}$ is essentially converged. Only minor variations are observed in the value of $M_{\infty F}$ beyond the initial stage. In scheme II, the incremental value δP_2 is determined by comparing two objective functions at the same time step. In scheme I, this value is determined by comparing two objective functions at different time steps. Scheme I functions properly as long as the dependence of the objective function on the parameter $M_{\infty F}$ is stronger than its dependence on time. As its dependence on time becomes comparable or stronger than its dependence on $M_{\infty F}$, the computed δP_2 values no longer lead to convergence to the optimum solution. The local divergence shown in Figure 5a is due to the solution's weak dependence on $M_{\infty F}$ as the values of δP_2 become small. As the local divergence occurs, the value of δP_2 increases, causing a stronger dependence on $M_{\infty F}$ and causing reconvergence. In other words, the process that takes place at the spikes is self-stabilizing. It is, therefore, possible to use scheme I to determine a solution by simply ignoring the local solutions at the spikes. However, as the supersonic region increases in size, the size of the spikes also increases. Eventually, it becomes no longer possible to use scheme I for determining valid solutions. Figure 5c shows the iterative history of $M_{\infty F}$ resulting from using scheme I in the same problem solved above, but with a value of $M_{\infty e}$ of 0.75 rather than 0.7. It is apparent that a converged solution in this figure is no longer identifiable. Therefore, scheme I is no longer useful in determining a solution

Figure 6 shows the history for the maximum residual, R_{max} , for the three cases corresponding to Figure 5. While the effect of the spikes is seen to be local and limited to a few time steps in Figure 5a, the recovery to the prespike level is seen to take a relatively longer time interval in the case of the maximum residual, as indicated in Figure 6a, which shows that, beyond 300 time steps, the maximum residual oscillates about a fixed value. We have continued the computation to 800 time steps, and the oscillatory behavior was found to continue. This behavior is due to the same process that leads to the local divergence observed above. As indicated above, at certain stages of the computation, the signs and values of δP_2 are no longer chosen in a manner that causes $M_{\infty F}$ to approach its optimum value. If conditions are such that the sign of δP_2 remains unchanged for a large number of steps, then the local divergence observed above will occur. On the other hand, if the positive and negative signs of δP_2 are reasonably well balanced, then the oscillatory behavior observed in Figure 6a occurs. It should be noted that, even though the maximum residual may no longer converge, the level at which this occurs in Figure 6a does indicate that, for practical purposes, the solution is converged. The uncertainty caused by scheme I in this particular problem should be of no practical concern.

Table 1 compares the accuracy of the schemes I and II. The exact solution was obtained by solving a series of problems with different values of $M_{\infty F}$. In each problem the value of α_F , which satisfies the lift constraint, was determined by the chord method. In each of these problems, the objective function was computed. The exact solution is the solution that results in the minimum value for the objective function. It does appear from the table that the results obtained by each of the two schemes are accurate and the errors are within acceptable levels.

Table 1. A Comparison of the Accuracy of the Optimization Schemes

	exact	scheme I	scheme II
$\Delta\alpha$	-1.6000°	-1.5981°	-1.5999°
ΔM	-0.0062	-0.0065	-0.0062
error in $\Delta\alpha$	0.0 %	0.1 %	0.0 %
error in ΔM	0.0 %	- 4.8 %	0.0 %
E	8.97×10^{-4}	8.98×10^{-4}	8.97×10^{-4}

To compare the efficiency and relative costs of the two schemes, it is necessary to set a convergence criterion. The convergence criterion used here assumes that convergence is attained when $R_{max} = 10^{-4}$. At this value of the maximum residual, it is found that the values of $\Delta\alpha$, ΔM , and E are all essentially converged. Based on this convergence criterion, Table 2 compares the number of iterations and the computational time required for convergence for the different schemes and for a regular analysis solution. It is clear from the table that updating the angle of attack and the Mach number in addition to the flow variables results in reduced convergence rates relative to that of an analysis problem in which only the flow variables are updated. The table also indicates that the computational time per iteration required for scheme II is double that of scheme I. This is due to the requirement of computing two solutions in parallel when scheme II is used. While scheme I updates α_F and $M_{\infty F}$ each iterative step, scheme II, through the parameter ΔN , allows the user to specify the frequency of updating these parameters. In the present computations, these parameters were updated every four iterative steps. We did not attempt to determine the value of ΔN that maximizes the rate of convergence. Therefore, there is a good possibility that the efficiency of scheme II can be improved over that indicated.

Table 2. A Comparison of the Efficiency of the Optimization Schemes

	analysis	scheme I	scheme II
Number of Iterations	92	174	268
CPU Seconds	23	44	137

The above computations were performed for a case in which scheme I functions properly to allow comparison between that scheme and scheme II in the range in which it is valid. Scheme II was applied successfully to cases at high-Mach numbers (Reference 6) in the range where scheme I cannot be used. An example of these cases is defined by the test conditions $h = 4.5$, $M_{\infty F} = 0.8$ and $L_e = 0.35$. A 72×80 mesh was used for the tunnel simulation and a 72×112 mesh was used for the free-air simulation. The first step of the correction procedure determined an α_T value of 2.8296° . Figure 7 shows the iterative histories for $M_{\infty F}$, α_F , L_F and R_{max} in the second step of the correction procedure. This step determined an α_F value of 1.6488° and an $M_{\infty F}$ value of 0.7871 . A comparison between the solution obtained in the second step and a regular analysis solution indicates that 246 iterations and 143 cpu seconds are required for the present solution to achieve convergence, while 66 iterations and 19 cpu seconds are required for the analysis solution to achieve convergence. The correction results are given by

$$\Delta\alpha = -1.1808^\circ, \Delta M = -0.0129, E_M = 3.54 \times 10^{-4}$$

These values are identical to the exact solution. Figure 8 presents a comparison between the pressure on the airfoil surface for the wind-tunnel flow ($M_{\infty T} = 0.8$, $\alpha_T = 2.8296^\circ$), the free-air flow at the uncorrected conditions ($M_{\infty F} = 0.8$, $\alpha_F = 2.8296^\circ$) and the free-air flow at the corrected conditions ($M_{\infty F} = 0.7871$, $\alpha_F = 1.6488^\circ$). As indicated from the figure, the correction procedure does accomplish the goal of determining the free-air corrected conditions (α_F , $M_{\infty F}$) with aerodynamic properties nearly matching the corresponding properties for the tunnel conditions (α_T , $M_{\infty T}$). The value of E is reduced from 384.36×10^{-4} for the free-air flow at the uncorrected conditions to 3.54×10^{-4} for the free-air flow at the corrected conditions.

Scheme I was applied in References 11 and 12 to the problem of wall interference correction. There, however, the transonic small disturbance equation was assumed to be the flow governing equation and the solution was obtained by successive line overrelaxation.

3.2 Propeller Design

The optimization procedure II described above, combined with the Euler analysis code developed by Yamamoto et al. (Reference 13), was used to find the twist distribution for the blades of the eight-bladed SR-3 propeller with the objective of maximizing its efficiency under the constraint of a desired power coefficient given by $C_{po} = 1.7$. The computations were performed for a free-stream Mach number of 0.8 and an advance ratio of 3.06. We let $\beta_{0.75}$ be the blade angle at the 75% blade span corresponding to the desired power coefficient, and we took the blade angle distribution, $\beta_o(r)$, corresponding to this propeller as our base configuration. A perturbation, $\beta'(r)$, to the blade twist distribution, $\beta_o(r)$, was computed so that the propeller efficiency is maximized subject to the power constraint. The perturbation twist distribution is given by

$$\beta'(r) = P_1 + P_2 \left(\frac{r - R/2}{R/2} \right) + 2P_3 \left\{ \left(\frac{r - R/2}{R/2} \right)^2 - \frac{1}{2} \right\} \quad (21)$$

where P_1 , P_2 , and P_3 are the components of the vector of design parameters \vec{P} and R is the propeller radius. Experimentation with the propeller analysis code indicated that the flow iterative solution diverges when the blade tip angle exceeds a certain limit. To exclude the region leading to the divergence from our search in the design parameter space, the following redefinition of the objective function was introduced:

$$E = -\eta + \max \left\{ 0.0, 0.1 \left(\sqrt{P_2^2 + P_3^2} - \mu \right) \right\} \quad (22)$$

where μ determines the allowable search region. As the value of μ increases, the allowable search region also increases. The value of μ was taken to be equal to 5.0 unless otherwise specified.

The mesh used in the following computations consists of 45 points in the axial direction, 21 points in the radial direction, and 11 points between adjacent blades in the circumferential direction. Computations are initialized by the SR-3 flow solution, which corresponds to a $\beta_{0.75}$ angle of 54.9° , the value of C_p was 1.1. This initial solution was intentionally chosen not to be a close approximation of the desired solution. In all the following computations, the modified coordinate rotation scheme, which determines \mathcal{Q}_1 by Equation (20) instead of Equation (16), is used unless otherwise specified. Also, unless otherwise specified, the initial iterative guesses for the design parameters are set equal to zero and the computational parameters c_1 , c_2 , C , δP_2^0 , δP_3^0 , δP_{max} , ϵ , and ΔN are given, respectively, by 1.2, 0.6, 3.0, 0.5, 0.5, 1.0, 0.0001, and 40.

The optimization procedure was applied to two-design-parameter problems and to three-design-parameter problems. For the two-design-parameter computations, the values of P_3 in Equations (21) and (22) are set equal to zero. Results for the two-design-parameter problem are presented, followed by those for the three-design-parameter problem. For the initial flow solution, which corresponds to a $\beta_{0.75}$ value of 54.9° , the value of C_p was 1.1. Also the value of $\beta_{0.75}$ was determined to be 58.067° . The design parameters predicted by the optimization scheme are given by $P_1^* = -2.83^\circ$, $P_2^* = 5.51^\circ$. The predicted solution does satisfy the power constraint. The value of C_p corresponding to this solution is 1.6999. The objective function, E , was reduced from the value -0.839 in the case of the original design, with $P_1 = P_2 = 0.0$, to the value -0.908 in the case of the optimized design. The value of the efficiency was increased from 0.839 for the original design to 0.910 for the optimized design.

The computed value of efficiency, which corresponds to the optimized design, is approximately 5% higher than expected. Towards the end of this study it was discovered that an approximate formulation used in the analysis code to integrate the aerodynamic forces near the blade base was the cause of this overprediction. The main portion of the results presented here was obtained using the approximate formulation for computing the performance. These results are presented first. They are then followed by results obtained by using an accurate formulation for computing the performance. While there may be no interest in the first set of solutions for the purpose of improving the propeller design, these results are valid for the purpose of testing the optimization scheme. In this case, $-\eta$ is viewed as an objective function without attaching a physical meaning to it. In the second set of results it was necessary to use an accurate formulation for computing the performance in order to show the required blade shape modification for improved performance and the corresponding increase in performance obtained by optimization.

The iterative histories of the design parameters are shown in Figure 9, while the iterative histories of the power and efficiency are shown in Figure 10. From these figures two distinct stages in the convergence process of the solution may be identified. In the first stage, relatively rapid changes in the values of \vec{P} , C_p and η occur as they approach the converged values of the solutions. At the end of this stage, these parameters are close to their final values. In the second stage, minor adjustments take place as the parameter solutions converge to their final values.

The residual, R_E , is a measure of the convergence of the flow field solution. Figure 11 compares the residual history for the design problem, in which \vec{P} is updated in addition to \vec{f} , to the residual history for the regular analysis problem, in which \vec{f} only is updated while \vec{P} is held fixed. The figure indicates that modifying the propeller geometry in the design problem as the iterative solutions for the flow variables are updated does not negatively affect the rate of convergence of the flow field solution in comparison to the analysis problem. In fact, the following results of our computations show that the convergence of the flow field solution is accelerated when the design parameters are updated to satisfy the power constraint or to satisfy the conditions of the optimization problem. For a regular analysis problem with \vec{P} set equal to \vec{P}^* , the number of iterations required for convergence was 4710. Hereafter, convergence is assumed to be achieved when the magnitude of the residual, R_E , is reduced to the value of 10^{-7} . For a constrained solution in which the second component of the design parameter vector, P_2 ,

was set equal to the value P_2^* , while the first component was updated throughout the iterative process so that the constraint $C_p = C_{p0}$ would be satisfied, convergence was attained after 4040 iterative steps, indicating an increased convergence rate relative to the regular analysis problem. For the design problem in which both P_1 and P_2 were updated in a manner that allows the constraint $C_p = C_{p0}$ to be satisfied and the objective function E to be minimized, the number of iterative steps required for convergence was further reduced to 3250.

On the average, 0.972 cpu second was required for the iterative step in the design problem, while 0.403 cpu second was required for the iterative step in the analysis problem. Therefore, the average design iterative step required slightly more than double the cpu requirements for the analysis iterative step. In the design problem, two analysis problems are solved in parallel. The additional cpu requirement for the design problem is mainly due to generating a new computational mesh whenever the design parameters are updated.

For a regular analysis problem, the computational mesh is generated only one time at the beginning of the computation. For a design problem, however, it is necessary to regenerate the computational mesh whenever the design parameters are updated. In the present computations, this was done once every 40 iterative steps. The cost of mesh generation relative to the cost of solving the flow equations was acceptably low. As the value of ΔN decreases, however, a point may be reached at which the cost of generating the mesh becomes excessively high, and it may represent a substantial fraction of the total computational cost. In this case, a possible alternative to regenerating new meshes, whenever the design parameters are updated, is the use of approximate meshes that are generated by linearly combining $L+1$ reference meshes. The reference meshes may be updated every $J \Delta N$ iterative steps, where $J > 1$. The need for making this approximation does not arise here, as the propeller analysis code used here has relatively slow convergence properties and, therefore, the appropriate ΔN value is relatively large. However, the use of accelerating schemes, such as the multigrid scheme, would allow the ΔN value to be sufficiently low to require the use of the mesh approximation discussed above.

We have performed a single computation using the exact formulation for calculating \bar{i}_1 , as given by Equation (15), with G_1 computed by Equation (16). This formulation requires solving $L+1$ problems in parallel instead of L problems, in the case of the approximate formulation given by Equation (20). The average iterative step for this computation required 1.474 cpu second. The number of iterations required for convergence was 3425. Comparing these values to the corresponding values for the approximate formulation indicates that there is a strong advantage in using the approximate formulation over the exact formulation.

To verify that the computed solution is indeed the optimum solution, solutions were computed that were slightly perturbed from the optimum predicted solutions but that satisfied the power constraint. Table 3 compares the values of the objective function for the solution predicted by the optimization scheme, shown in the first row, to those for the perturbed solutions, shown in the second and third rows. It is apparent from the table that perturbing the design parameters causes the value of the objective function to increase. Therefore, the design parameters predicted by the optimization scheme do indeed minimize the value of the objective function.

Table 3. The Objective Function at the Optimum Solution and Perturbed Solutions for the Two-Design-Parameter Problem

P_1	P_2	E
-2.83	5.51	-0.90773
-2.73	5.31	-0.90730
-2.93	5.71	-0.90728

The sensitivity of the scheme's convergence to the initial iterative guesses of the solution and to the computational parameters was tested by recomputing the problem defined above with perturbed initial conditions and computational parameters. Table 4 shows the number of iterative steps, n_c^0 , required for convergence when different values are used for the initial iterative solutions and the computational parameters. It is clear from the table that the convergence properties of the scheme are weakly sensitive to the values of the initial conditions and the computational parameters. Needless to say, there is an optimum set of values for these parameters that maximizes the convergence rate of the scheme for a given problem. However, within a relatively wide range of these parameter values, good convergence is achieved. This is due to the frequent updating of the design parameters in the course of solving the problem. The cpu requirement for the average iterative step is approximately the same for all the cases solved, except for the case in which $\Delta N = 25$. The cpu requirement for the average iterative step in this case is given by 1.078 seconds, in comparison to approximately 0.972 second for the other cases. This is due to the increased frequency of generating the computational mesh in the case with $\Delta N = 25$. Figures 12 through 14 show the iterative histories for P_1 , P_2 , η , C_p and R_F for the case in which the initial iterative guesses for the design parameters, P_1^0 and P_2^0 , were perturbed. Among all the perturbed computations, the rate of convergence for this case was affected the most.

Table 4. Effect of Perturbing the Initial Conditions and the Computational Parameters on the Scheme's Convergence for the Two-Design Parameter Problem

P_1^0	P_2^0	ΔN	C	c_1	c_2	n_c^0
0.0	0.0	40	3.0	1.2	0.6	3250
3.0	-5.0	40	3.0	1.2	0.6	3690
0.0	0.0	25	3.0	1.2	0.6	3376
0.0	0.0	40	4.5	1.2	0.6	3252
0.0	0.0	40	6.0	1.2	0.6	3250
0.0	0.0	40	3.0	1.5	0.6	3333
0.0	0.0	40	3.0	1.2	0.4	3120
0.0	0.0	40	3.0	1.5	0.4	3281

The computations performed above for the two-design-parameter problem were performed with a value of 5.0 for μ . To perform computations that allow both parabolic and linear modifications to the blade angle distributions, it was necessary to reduce the value of μ to 4.0. The three-design-parameter optimization computations were solved using this value for μ . The main two-design-parameter computation was also repeated using this value for μ to allow a comparison between the two-design-parameter and the three-design-parameter results. The optimum values of the design parameters for the two-design-parameter problem with $\mu = 4.0$ were found to be given by $P_1^* = -2.35^\circ$ and $P_2^* = 4.56^\circ$. The value of C_p corresponding to this solution is 1.6999. The objective function E was reduced from the value -0.839 in the case of the original design, with $P_1 - P_2 = 0.0$, to the value -0.897 in the case of the optimized design. The value of η was increased from 0.839 for the original design to 0.900 for the optimized design. As expected, the magnitudes of both E and η determined with $\mu = 4.0$ are less than those determined with $\mu = 5.0$. As the value of μ decreases, the restriction on the allowable search region in the design parameter space increases. In the two-design-parameter problem, 3235 iterative steps were required for convergence. The cpu requirement per iterative step was 9.972 second. The optimum values of the design parameters for the three-design-parameter problem with $\mu = 4.0$ were found to be $P_1^* = -2.77^\circ$, $P_2^* = 4.50^\circ$, and $P_3^* = -1.20^\circ$. The corresponding values of C_p , E , and η are given by 1.6999, -0.900, and 0.905, respectively, indicating a superior design to that achieved by using only two design parameters. The number of iterative steps required for convergence was 3228, while the cpu requirement per iterative step was 1.459 seconds. The iterative histories for P_1 , P_2 , P_3 , η , C_p and R_E are shown in Figures 15 through 17.

To verify the accuracy of the computed solution, several solutions were computed that were slightly perturbed from the optimum-predicted solution but that satisfied the power constraint. Table 5 compares the values of the objective function for the solution predicted by the optimization scheme, shown in the first row, to those for the perturbed solutions shown in the following rows. It is apparent from the table that perturbing the design parameters causes the value of the objective function to increase. Therefore, the design parameters predicted by the optimization scheme do indeed minimize the value of the objective function.

Table 5. The Objective Function at the Optimum Solution and Perturbed Solutions for the Three-Design-Parameter Problem

P_1	P_2	P_3	E
-2.77	4.50	-1.20	-0.90026
-2.87	4.50	-1.45	-0.90311
-2.87	4.69	-1.20	-0.89986
-2.67	4.50	-0.93	-0.90012
-2.67	4.30	-1.20	-0.89933

Computations were performed using the accurate formulation for computing the propeller performance. In these computations it was found that η responds to changes in the design parameters at an iteratively much slower rate than that associated with the first set of computations. For that reason it was necessary to reduce the value of c_1 to 0.98. All other computational parameters were set equal to their same values used in the first set of computations. In this set of computations, it was determined that $\beta_{0.3/4} = 57.648^\circ$. The value of C_p for the initial flow solution, which corresponds to a $\beta_{3/4}$ value of 54.9° , was 1.2. By optimizing the blade shape for the two-design-parameter problem, the value of the efficiency was increased from 0.8229 for the original design to 0.8233 for the optimized design. For a regular analysis problem with P set equal to \bar{P}^* the number of iterations required for convergence was 4320. A comparison of this number with the number of iterations required to solve the optimization problem, 3260, shows that the cost of solving the optimization problem is approximately twice the cost of solving a regular analysis problem.

In the computations presented above, the effect of varying the linear term of Equation (21) on the propeller efficiency was investigated. To investigate the effect of varying the quadratic term in Equation (21) on the propeller efficiency, a computation was performed in which P_3 was allowed to vary while P_2 was set equal to zero. In this case, the design parameters predicted by the optimization scheme were given by $P_1^* = -0.79^\circ$, $P_3^* = -2.07^\circ$. The value of C_p corresponding to this solution was 1.7000, and the value of η was 0.82549. The number of iterations required for convergence was 3550. A comparison of the values of η for the two cases in which (P_1^*, P_2^*) and (P_1^*, P_3^*) were the design parameters shows that the introduction of a quadratic perturbation to the twist distribution is more effective in increasing the efficiency than the introduction of a linear perturbation.

Finally, the optimum values of the design parameters for the three-design-parameter problem were found to be $P_1^* = -3.34^\circ$, $P_2^* = 3.92^\circ$, and $P_3^* = -3.23^\circ$. The corresponding values of C_p and η are given by 1.7000 and 0.83291, respectively. It is apparent that using a combination of linear and quadratic perturbations in the blade angle distribution is much more effective for improving the efficiency than using only one of these distributions. Relative to the original SR-3 design, using both perturbed distributions increased the propeller efficiency by 0.0100. This is compared to a value of 0.0026 for the quadratic distribution alone and a value of 0.0004 for the linear distribution alone. The number of iterative steps required for convergence was 4380 in comparison to 4460 for the regular analysis problem.

The iterative histories for \bar{P} , η , C_p , and R_E in the second set of computations, not presented here, are similar to those of the first set of computations (Figures 9 through 17), and may be found in Reference 14.

Figure 18 compares the optimum blade angle perturbations from the SR-3 baseline design predicted for the cases of linear, quadratic, and combined linear and quadratic shape functions. Curve C, which gives the blade angle perturbation distribution for maximum improvement in efficiency, shows that the efficiency of the SR-3 propeller can be improved by reducing the blade angle distribution both at the hub and at the tip. This explains the observed weak sensitivity of the propeller efficiency to linear variations in the blade angle distribution. The use of a linear shape function allows an increase in the blade angle at either the tip or the hub positions and a decrease in the blade angle at the other position. Therefore, the positive effect on efficiency resulting from the perturbed blade angle distribution at one of these positions tends to cancel the negative effect resulting from the perturbed blade angle distribution at the other position leading to the apparent insensitivity of the efficiency to linear variations in the blade angle distribution. The maximum improvement in efficiency obtained here resulted from the use of linear and quadratic shape functions. Further improvement may be obtained by using other shape functions.

3.3 Efficiency of Optimization Schemes

Schemes I and II were applied in this paper and in References 11 and 12 to wall interference correction problems (WIC) and to propeller design problems (PD). In these applications both the transonic small disturbance (TSD) equation and the Euler equations were assumed to be the flow governing equations. The TSD equation was solved by successive line overrelaxation (SLOR), while the Euler equations were solved by either method A, which is described in References 8-10 or by method B which is described in Reference 13. One-, two-, and three-design-parameter problems were solved.

To compare the efficiency of different optimization schemes it is convenient to define the parameter ν , where

$$\nu = \lambda \sigma, \quad \lambda = \frac{N}{L}$$

and

$$\sigma = \frac{n_c^o}{n_c^a}$$

Here N is the number of problems solved in parallel, n_c^o is the number of iterations required for convergence, when solving the optimization problem, and n_c^a is the corresponding number of iterations required for convergence, when solving the analysis problem. In the definition of λ the number of problems, N , is normalized by the number of design parameters, L . The parameter σ is a measure of the effect of perturbing the design parameters, as the iterative flow solution evolves, on the convergence of the flow solution. The following table compares the parameters ν , and σ for the different problems solved in this paper and in References 11 and 12. The first row gives results of unconstrained single-design-parameter problems from Reference 11, and the second row presents results from Reference 12.

Table 6. Efficiency of Solving Optimization Problems

Problem	Governing Equations	Method of Solution	Scheme	L	N	σ	ν
WIC	TSD	SLOR	I	1	1	0.9-1.1	0.9-1.1
WIC	TSD	SLOR	I	2	1	0.9	0.5
WIC	Euler	A	I	2	1	1.0-1.9	0.5-1.0
WIC	Euler	A	II	2	2	2.9-3.7	2.9-3.7
PD	Euler	B	II	2	2	0.7-0.8	0.7-0.8
PD	Euler	B	II	2	3	0.7	1.1
PD	Euler	B	II	3	3	0.7-1.0	0.7-1.0

4.0 CONCLUSIONS

In this paper, an approach based on updating the flow variables and the design parameters simultaneously was presented. This approach is applicable to aerodynamic optimization problems in which the flow governing equations are nonlinear equations that are solved iteratively. Two schemes based on this approach were presented. The first, scheme I, is a special scheme, which may be applied only to a limited class of problems. Under those conditions for which scheme I is applicable, it has advantages of higher efficiency and less memory requirements in comparison to the second scheme, II.

Scheme II is a general scheme. It was applied to two- and three-design-parameter problems with a single equality constraint. However, extensions of this scheme applicable to optimization problems with multiple equality and inequality constraints were presented. The results show that the scheme is highly accurate in determining the solution of constrained optimization problems. The cost of solving the optimization problems presented here was within the range $(0.7L - 3.7L)$ times the cost of solving a regular analysis problem, where L is the number of design parameters. This wide range is a reflection of the different problems solved, the different procedures used in solving the flow governing equation, and the different degrees of accuracy to which the design parameters were determined. Tests performed on scheme II indicate that the convergence rate of the solution is weakly sensitive to variations in the computational parameters and the initial iterative guesses for the design parameters.

The two schemes presented here are only examples of schemes which update the flow variables and the design parameters simultaneously. Other schemes based on this approach may be developed. The results of the preliminary tests conducted indicate that the approach of updating the flow variables and the design parameters simultaneously is an attractive alternative to the costly inner-outer iterative procedure associated with the use of conventional optimization schemes. Further tests, however, are required to better evaluate this approach. Direct comparisons between the results of this approach to the results of conventional schemes are necessary. Applying this approach to problems with a larger number of design parameters than used here and investigating its performance in this case is also necessary for a better evaluation of this approach.

REFERENCES

1. Hicks, R. M., Murman, E. M., and Vanderplaats, G. N., "An Assessment of Airfoil Design by Numerical Optimization," NASA TM X-3092, July 1974.
2. Haney, H. P., Johnson, R. R., and Hicks, R. M., "Computational Optimization and Wind Tunnel Test of Transonic Wing Designs," *Journal of Aircraft*, Vol. 17, July 1980, pp. 457-463.
3. Hicks, R. M., "Transonic Wing Design Using Potential-Flow Codes - Successes and Failures," SAE Paper 810565, April 1981.
4. Cosentino, G. B., and Holst, T. L., "Numerical Optimization Design of Advanced Transonic Wing Configurations," AIAA Paper 85-0424, January 1985.
5. Davis, W., "TRO-2D: A Code for Rational Transonic Aero Optimization," AIAA Paper 85-0425, January 1985.
6. Rizk, M. H., Lovell, D. R., and Baker, T. J., "Euler Procedure for Correcting Two-Dimensional Transonic Wind-Tunnel Wall Interference," *AIAA Journal*, Vol. 26, December 1988, pp. 1457-1466.
7. Rizk, M. H., Lovell, D. R., and Baker, T. J., "Euler Procedure for Three-Dimensional Transonic Wall Interference," *Journal of Aircraft*, Vol. 26, January 1989, pp. 48-55.
8. Jameson, A., and Baker, T. J., "Solution of the Euler Equations for Complex Configurations," AIAA Paper 83-1929, July 1983.
9. Jameson, A., and Baker, T. J., "Multigrid Solution of the Euler Equations for Aircraft Configurations," AIAA Paper 84-0093, January 1984.
10. Jameson, A., Schmidt, W., and Turkel, E., "Numerical Solutions of the Euler Equations by Finite Volume Methods Using Runge-Kutta Time-Stepping Schemes," AIAA Paper 81-1259, June 1981.
11. Rizk, M. H., "A New Approach to Optimization for Aerodynamic Applications," *Journal of Aircraft*, Vol. 20, January 1983, pp. 94-96.
12. Rizk, M. H., and Murman, E. M., "Wind Tunnel Wall Interference Corrections for Aircraft Models in the Transonic Regime," *Journal of Aircraft*, Vol. 21, January 1984, pp. 54-61.
13. Yamamoto, O., Barton, J. M., and Bober, L. J., "Improved Euler Analysis of Advanced Turboprop Propeller Flows," AIAA Paper 86-1521, June 1986.
14. Rizk, M. H., "Aerodynamic Optimization by Simultaneously Updating Flow Variables and Design Parameters With Application to Advanced Propeller Designs," NASA CR-182181, July 1988.

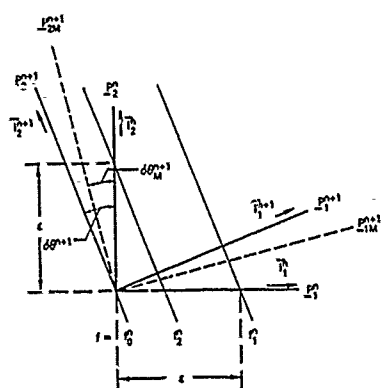


Figure 1. Two-Dimensional Design Parameter Space

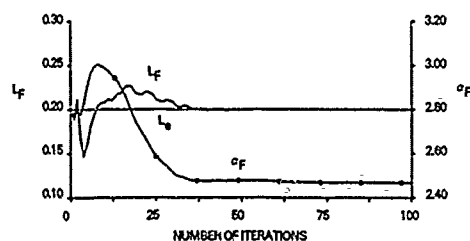


Figure 2. Iterative Histories for the Free-Air Solutions (Scheme I)

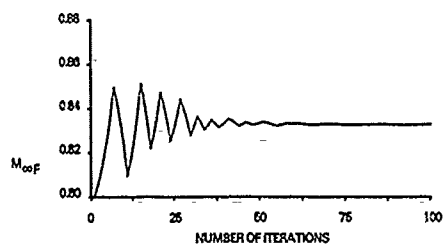
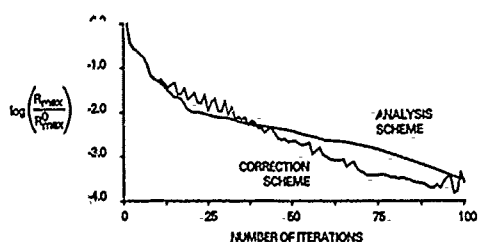
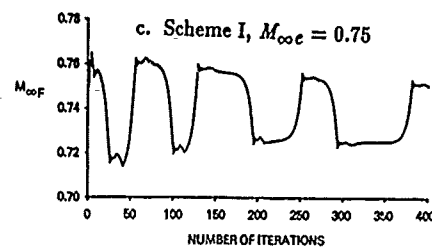
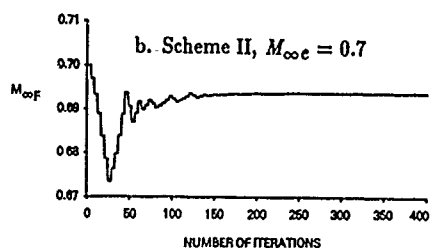
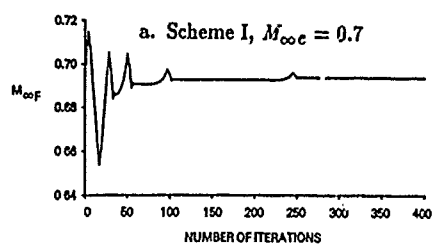
Figure 3. Iterative History for $M_{\infty F}$ (Scheme I)

Figure 4. Residual Evolution Histories for the Correction Problem and the Analysis Problem in Free Air (Scheme I)

Figure 5. Iterative History for $M_{\infty F}$ ($h = 3.6$, $L_c = 0.35$)

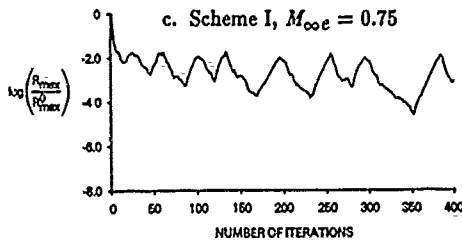
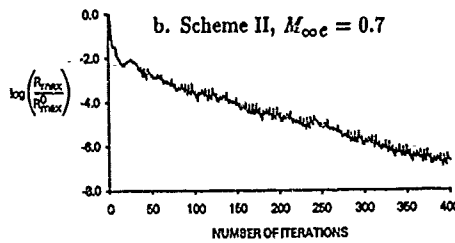
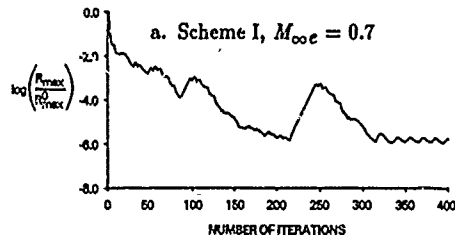


Figure 6. Maximum Residual Evolution History
($h = 3.6$, $L_e = 0.35$)

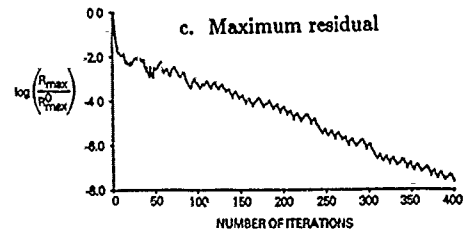
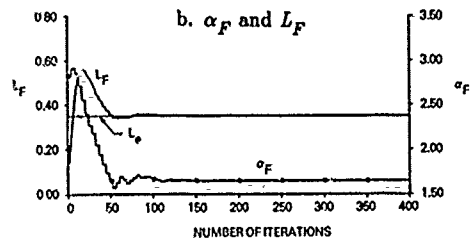
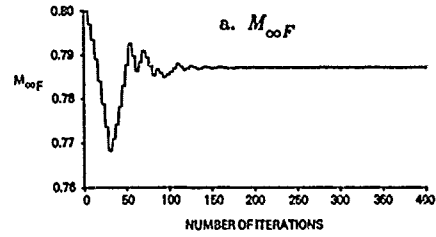


Figure 7. Iterative Histories for the Free-Air
Solutions Using Scheme II ($h = 4.6$, $M_{\infty e} = 0.8$,
 $L_e = 0.35$)

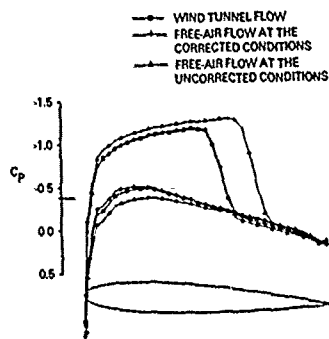


Figure 8. Pressure Distribution on the Airfoil Surface ($\lambda = 4.6$, $M_{\infty} = 0.8$, $L_c = 0.35$)

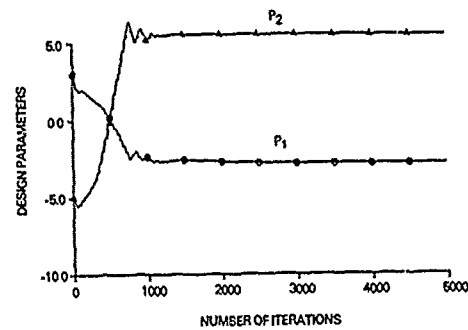


Figure 12. Design Parameter Iterative Histories for the Two-Design-Parameter Problem with Perturbed Initial Conditions

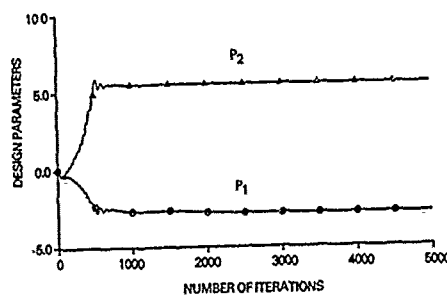


Figure 9. Design Parameter Iterative Histories for the Two-Design-Parameter Problem

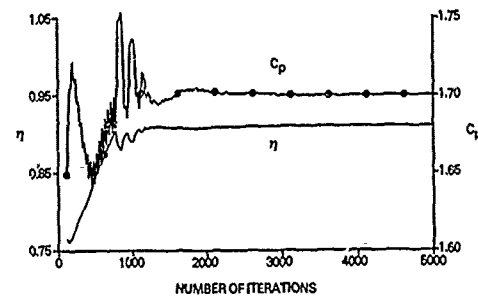


Figure 13. Power and Efficiency Iterative Histories for the Two-Design-Parameter Problem with Perturbed Initial Conditions

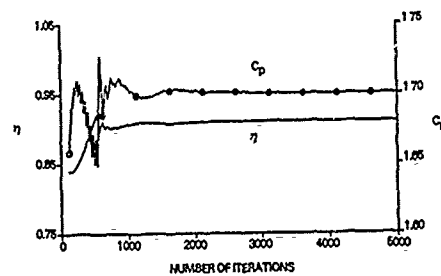


Figure 10. Power and Efficiency Iterative Histories for the Two-Design-Parameter Problem

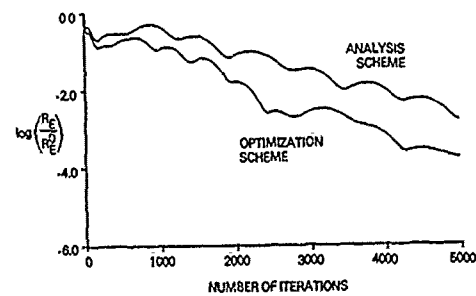


Figure 14. Residual Iterative Histories for the Analysis Problem and the Two-Design-Parameter Optimization Problem with Perturbed Initial Conditions

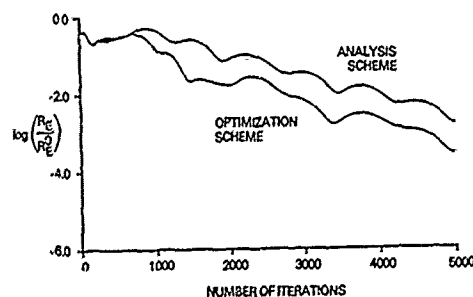


Figure 11. Residual Iterative Histories for the Analysis Problem and the Two-Design-Parameter Optimization Problem

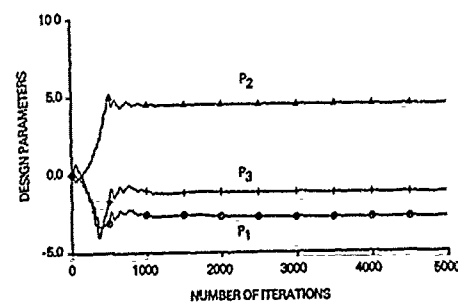


Figure 15. Design Parameter Iterative Histories for the Three-Design-Parameter Problem

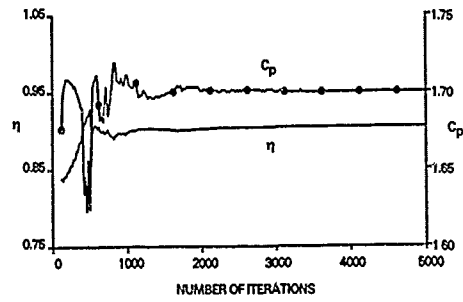


Figure 16. Power and Efficiency Iterative Histories for the Three-Design-Parameter Problem

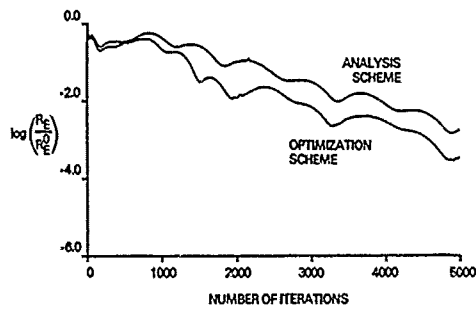


Figure 17. Residual Iterative Histories for the Analysis Problem and the Three-Design-Parameter Optimization Problem

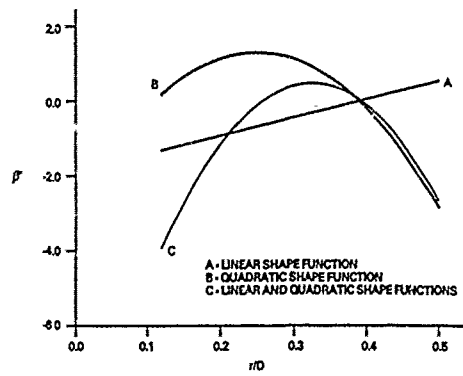


Figure 18. Optimum Blade Angle Perturbations

CONSTRAINED SPANLOAD OPTIMIZATION FOR MINIMUM DRAG OF MULTI-LIFTING-SURFACE CONFIGURATIONS*

R.F. van den Dam
National Aerospace Laboratory NLR
P.O. Box 90502 Amsterdam The Netherlands

SUMMARY

An interactive computer program system has been developed that can be used in aircraft drag minimization studies. It comprises algorithms for choosing the spanwise distributions of lift, pitching moment, chord and thickness-to-chord ratio of lifting elements. The choices are optimal in that they minimize induced plus viscous drag while satisfying constraints of aerodynamic, flight-mechanical and structural nature. The configurations that can be dealt with, may consist of a number of segments representing, for instance, wings or parts of wings, horizontal tails or canards, winglets, flap-rail-fairings, etc. Also the interaction between propellers and lifting elements may be included in the procedure.

The induced drag is computed using the Trefftz-plane integral (farfield analysis), while the viscous drag follows from form factor methods. Novel mathematical formulations of the constrained optimization problems are used, that are based on the calculus of variations. The method has been integrated in an infrastructure that allows the capabilities of the method to be efficiently exploited in a multidisciplinary environment. This paper presents the theoretical models and methods underlying the analysis and optimization capability, comparisons with other theories, information aspects, and some examples of applications.

1 INTRODUCTION

The success of an aircraft design depends largely upon finding an optimal balance between the contributions of the disciplines involved. Moreover, many of the benefits from emerging technologies can only be fully exploited through their interactions with other disciplines. Good examples of these are the technologies of active control and composites which make it possible to design aircraft with forward swept wings and relaxed static stability. In order to find an optimal balance between the contributions of the disciplines and to take maximum advantage of technology advances, the interactions should be identified and quantified before the main decisions concerning the overall configuration design are made. This implies the necessity of developing the analysis and design capability to a suitable breadth and depth for earlier application in the design process. Increased breadth means the inclusion of the appropriate spectrum of disciplines and new technologies early in the design. Increased depth in the early design stage is required to assure that the interactions are correctly quantified before the main decisions are made. An example of developing methods of this nature is the interactive program system for drag minimization studies described in the paper.

Minimization of (aerodynamic) drag is an important goal in aircraft configuration design studies as it helps to improve upon fuel efficiency. In these studies, it has been common practice to decompose the aircraft drag in components that are to a large extent independent. Computational Fluid Dynamics have created possibilities for drag breakdown that is based on physical principles (Sect. 2.3 of Ref. 1). In such a breakdown it is convenient to distinguish between viscous (boundary layer) drag, induced (or vortex) drag and wave drag.

With respect to the choice of independent variables in drag minimization problems one may distinguish different approaches. One is to use parameters defining the geometry as the independent variables (direct numerical optimization). While this approach is feasible in two dimensions (see e.g. Ref. 2) it is hardly so, at present, in the case of three-dimensional configurations because of the lack of accuracy in the available three-dimensional codes in combination with the limited computer power available (Ref. 3).

At NLR, an alternative approach is adopted, namely the use of aerodynamic (load and pressure distributions) rather than geometric shape functions as independent variables (Ref. 4). This approach, called inverse numerical optimization (see Fig. 1), involves the successive determination of optimal target spanloads (using methods as described in the paper), target pressure distributions (optimal with respect to the specified drag characteristics and providing the prescribed spanloads), and corresponding lifting-surface geometries (using an inverse code). This process is repeated until a geometry is obtained having acceptable performances for all flight conditions.

This paper concerns the first step in the inverse numerical optimization approach: the determination of optimal spanloads. In literature, various theoretical methods can be found for determining spanloads for minimum drag. Almost all of them consider induced drag only in determining optimal spanloads (see e.g. Ref. 5, 6, 7). Inclusion of other drag components in the optimization procedure can produce substantially different minimum drag spanloads compared with induced-drag-only results.

* The work described here was performed under contract with the Netherlands Agency for Aerospace Programs (NIVR)

Methods that extend the induced drag minimization theory to include other components as well, and can be used in preliminary aircraft design, are the subcritical design code of Kuhlman (Ref. 8) and the transonic optimization scheme of Mason (Ref. 9).

The method described in this paper provides capabilities for choosing the spanwise distributions of lift, pitching moment, chord and thickness-to-chord ratio of lifting elements of an aircraft configuration. The choices are optimal in the sense that they minimize induced plus viscous drag, or induced drag only, while satisfying constraints on, for example, pitching moment and section lift coefficients. Determining minimum drag spanloads, also the interaction between propellers and lifting elements may be included in the procedure. With an optimal spanload, the wing can restore much of the (rotational) energy loss associated with propeller swirl (Ref. 10, 11). The method may provide direct input for more detailed aerodynamic design (e.g. the inverse numerical optimization procedure), but may also be used for parametric airplane configuration design studies. In these parametric design studies, the method is used to quickly assess the consequences of changes in the configuration of (complex) aircraft.

In the following sections, an outline of the analysis and minimization technique developed is presented. Informatics aspects of the interactive system in which the method has been implemented and of its environment, will also be described. Comparison with other theories are given. Finally, the capabilities of the system will be illustrated by some examples of application.

2 FORMULATION OF THE PROBLEM

It is assumed that the projection of the aircraft configuration onto a plane perpendicular to the flight direction can be approximated by a number of straight line segments, representing the various elements of the configuration. An example is shown in figure 2(a). The geometry description can include wings (or parts of wings), tailsurfaces, pylons, winglets, etc. The planform geometries of the configuration lifting elements can be described by the spanwise distributions of chord-length, together with the coordinates of the 1/4-chord point locations, defining the planform sweeps (see Fig. 2(b)). The vortex sheets aft of the configuration are assumed to remain undistorted. The latter can be argued to be a reasonable approximation in the case of planar optimal spanloads. It is assumed that this also holds for optimal spanloads of non-planar configurations. The airplane lift and drag are thought of as being composed of wing, tail and/or canard, fuselage and nacelle contributions, as illustrated in figure 2(c). The lift of the fuselage is modelled using the principle of lift carry-over from the wing, resulting in a constant distribution of bound circulation of the fuselage width.

If the interaction between propellers and lifting elements has to be considered as well, each propeller is assumed to shed a helical vortex sheet that is not influenced by the presence of the wing (Ref. 2), and that is confined inside a cylindrical "stream" tube parallel to the flight direction. The velocity distribution inside the slipstream has to be known for a specified propeller and required thrust.

The following problems are to be addressed:

- determination of optimal spanwise lift-distributions plus, if applicable, spanwise pitching moment distributions that result in either minimum induced drag or minimum induced plus viscous drag. In this procedure, constraints may be imposed on total pitching moment (trimmed aircraft), section liftcoefficients (feasible airfoils), rolling moment and, if applicable, bending moment. A part of the total spanwise lift-distribution may be specified in advance. In that case, the induced (plus viscous) drag is to be minimized by adjusting the remaining part of the lift-distribution.
- computation of the induced (plus viscous) drag for given (non-optimal) spanwise lift distributions. For instance, to quickly quantify the penalties that arise from the use of non-optimal loadings, to determine the performance under off-design conditions, or to estimate the induced drag associated with flap deflection.

3 DETERMINATION OF DRAG AND LIFT

The aircraft is assumed to fly with a constant velocity in a uniform, inviscid and irrotational medium. An expression for the induced drag in the Trefftz-plane can be derived by applying the momentum theorem to a control surface enveloping the aircraft (Ref. 4, 13). Consider a control surface S of the type as indicated in figure 3. Several subsurfaces of S can be distinguished: the Trefftz plane (S_u), a similar plane far upstream (S_∞), the top and bottom plane (S_B), the body surface (S_b), the shockwave surface (S_s), the vortex sheet surface (S_v), the propeller surface (S_p) and the slipstream surface (S_{sl}). Application of the conservation laws of momentum leads to the integral expression:

$$\oint_S (p n_x + \rho u q_n) dS = 0, \quad (1)$$

where $S = S_u + S_\infty + S_B + S_p + S_v + S_{sl} + S_s$.

p is the (local) static pressure, \vec{q} is the total velocity vector, ρ is the density, \vec{n} is the unit outward-normal to the control surface, and u is the component in the free-stream (x -)direction of \vec{q} .

Splitting-off the body pressure integral and realizing that $q_n = 0$ on S_B leads to the following expression for the total pressure drag of the aircraft:

$$D = \oint_{S_B} p n_x dS = - \int_{S-S_B} (p n_x + \rho u q_n) dS. \quad (2)$$

Working out this expression and splitting-off the wave drag integral the following Trefftz-plane integral for the induced drag can be derived (see Ref. 14):

$$D_i = \int_{S_T} \left\{ (p - p_\infty) + \rho(u - u_\infty)u - \rho \frac{(H - H_\infty)u}{u_\infty} \right\} dS - \sum_{i=1}^N \frac{1}{J_i} \left(\frac{Q}{D} \right)_i \quad (3)$$

H represents the stagnation enthalpy. D is the slipstream diameter, J is the propeller advance ratio ($= u_\infty/\omega D$, where ω is the propeller angular velocity), Q is the propeller torque and n_p is the number of propellers.

Assuming small perturbations in the Trefftz-plane, the flow being isentropic, and using the law of Biot-Savart, equation (3) may be worked out further to obtain (see again Ref. 14):

$$D_i/\rho_\infty = \frac{1}{2} \int_{S_V \cap S_T} \Gamma(n) v_n(n) dn + \int_{S_V \cap (S_{TII} + S_{TIII})} \Gamma(n) (\vec{v}_p \cdot \vec{n}) dn + \frac{1}{2} C^* S_{ref} u_\infty^2 \quad (4)$$

where

$$C^* = \frac{2}{S_{ref} u_\infty^2} \left\{ \frac{1}{2} \int_{S_T} \vec{v}_p \cdot \vec{v}_p dS - \sum_{i=1}^N \frac{1}{J_i} \left(\frac{Q}{D} \right)_i \right\}.$$

Γ is the bound circulation, v is the velocity induced in the Trefftz-plane normal to the vortex sheet segment, and $\vec{v}_p = (u, v, w)^n$ is the (fixed) perturbation velocity in the slipstream of an isolated propeller. n denotes the distance (spanwise parameter) along $S_V \cap S_T$. The last term in equation (4) represents the magnitude of the "swirl loss" of the propeller. In the first right-hand term of equation (4) the integration is performed over all lifting elements, in the second term the integration is performed over the lifting elements in the slipstream only. The local trailing vortex sheet strength is equal to the derivative of the bound circulation at that spanwise position; so, using the law of Biot-Savart, the following expression for v_n can be derived:

$$v_n(n) = \frac{1}{2\pi} \int \frac{d\Gamma(\tau)}{d\tau} \cdot \frac{\vec{n}(n) \cdot (\vec{r}(\tau, n) \times \vec{e}_x)}{|\vec{r}(\tau, n)|^2} d\tau \quad (5)$$

Again, the line integral is taken over the projections of all lifting configuration elements onto the Trefftz-plane. $\vec{n}(n)$ is the unit vector normal to the position n , and \vec{e}_x is the (downstream directed) unit vector along the x -axis. The vector $\vec{r}(\tau, n)$ denotes the vector from the spanwise position τ to the spanwise position n . Integrating by parts with respect to τ , equation (5) can be rewritten into:

$$v_n(n) = S_{ref} u_\infty^2 \int f(\tau, n) \Gamma(\tau) d\tau \quad (6)$$

where

$$f(\tau, n) = - \frac{1}{2\pi S_{ref} u_\infty^2} \frac{\partial}{\partial \tau} \left(\frac{\vec{n}(n) \cdot (\vec{r}(\tau, n) \times \vec{e}_x)}{|\vec{r}(\tau, n)|^2} \right) \quad (7)$$

The other term at the right side of (6) has disappeared since $\Gamma = 0$ at the free end of a lifting element. Substitution of (6) in (4) yields:

$$C_{D_i} = \iint f(\tau, n) \Gamma(\tau) \Gamma(n) d\tau dn + \frac{2}{S_{ref} u_\infty^2} \int \Gamma(n) (\vec{v}_p \cdot \vec{n}(n)) dn + C^* \quad (8)$$

Thus, the optimal circulation distribution may be computed with the propeller and wing located both far upstream, eliminating the 3D computation of velocities induced by the wing on the propeller and by the propeller bound vorticity on the wing. In fact, this expression underlines the correctness of the postulation of reference 10 concerning the generalisation of the stagger theorem of Munk. The generalized version of the stagger theorem allows the farfield computation as it states that also for propeller-wing combinations the "net force in the streamwise direction is independent of the streamwise position of lifting surfaces with a given circulation distribution".

Viscous drag

The viscous drag is derived for given airfoil characteristics. These airfoil characteristics define the viscous drag at each spanwise station as a function of the local section lift coefficient. An expression for the viscous drag can be derived using the (2D, incompressible) DATCOM/Hoerner formulae:

$$C_{d_{visc}} = C_F \left\{ 1 + k(t/c) + 100 (t/c)^4 \right\} \cdot \frac{S_{wet}}{S_{ref}} \quad (9)$$

C_F denotes the flat plate friction coefficient (depends on location of transition point and local Reynolds number, see Ref. 14) and k is the thickness location factor (depends on location of maximum thickness). t/c represents the thickness-to-chord ratio. For common airfoils, the wetted surface S_{wet} is about twice the reference surface S_{ref} .

Applying thin airfoil theory and considering the velocity distribution and the drag contribution of both the upper surface and lower surface individually (hereby assuming the same class of pressure distributions, see Fig. 4), expression (9) can be written in the form:

$$C_{d_{visc}} = C_{F_{up}} \left\{ 1 + k_{up}(\bar{u}_t + \bar{u}_l) + 100 (\bar{u}_t + \bar{u}_l)^4 \right\} + \\ + C_{F_{lo}} \left\{ 1 + k_{lo}(\bar{u}_t - \bar{u}_l) + 100 (\bar{u}_t - \bar{u}_l)^4 \right\} \quad (10)$$

\bar{u}_t and \bar{u}_l represent average perturbation velocities as a result of airfoil thickness and lift, respectively:

$$\bar{u}_l = \frac{1}{4} C_z \quad \text{and} \quad \bar{u}_t = \frac{(t/c) \cos \Lambda}{\beta_n} \quad (11)$$

$$\text{where } \beta_n = \sqrt{1 - M_\infty^2 \cos^2 \Lambda} \quad (12)$$

Λ denotes the sweepback and M_∞ denotes the (3D) undisturbed Mach number. C_z denotes the (3D-) lift coefficient that is linked, according to the Kutta-Joukowski theorem, to the bound circulation (see eq. 15). Substitution of (11) in (10) leads to an expression for the viscous drag as function of C_z and t/c . It is plausible to assume, on the basis of DATCOM's formulae, that k varies continuously with the position of the pressure recovery starting point x_R (see Fig. 4):

$$k = 2 \frac{x_R/c}{0.3} - 8.26 \left(\frac{x_R}{c} - 0.3 \right) \sim 2.5 - 1.6 \frac{x_R}{c}$$

Using this formula, $k = 2$ for $x_R/c = 0.3$ and $k = 1.2$ for $x_R/c = 0.8$, which corresponds with DATCOM's formulae.

In the C_z -range of interest, the viscous drag function (10) is approximated by a polar of the form

$$C_{d_{visc}}(C_z(\Gamma(n))) = C_{vis}^* + K^*(C_z - C_z^*)^2, \quad (13)$$

where the factors C_{vis}^* , K^* and C_z^* follow from a least square fit to the function. Integration results in the total viscous profile drag:

$$C_{D_{visc}} = \int \frac{C_{d_{visc}}(\Gamma(n), \eta) c(n)}{S_{ref}} d\eta. \quad (14)$$

Expressions for lift and moments

An expression for the local lift follows from the Kutta-Joukowski theorem applied in the lift direction:

$$C_z(n) = g_1^*(n) \Gamma(n) \quad \text{where} \quad g_1^*(n) = \frac{2 \cos(\varphi(n))}{u(n)c(n)} \quad (15)$$

$u(n)$ is the local upstream velocity for a lifting element at the position η . If (a part of) the lifting element is situated in the slipstream, $u(n)$ differs from the undisturbed velocity. $\varphi(n)$ denotes the dihedral angle. The total lift of the configuration follows from integration:

$$C_L = \int g_1(n) \Gamma(n) d\eta \quad \text{where} \quad g_1(n) = \frac{2 \cos(\varphi(n)) u(n)}{S_{ref} u_\infty^2} \quad (16)$$

If the section pitching moment distribution is not given, it can be deduced from the pressure recovery point locations. For the class of pressure distributions given in figure 4, the next expression for the section pitching moment C_m w.r.t. the quarter chord point $x_{1/4}$ can be derived:

$$C_m(C_L) = C_m^* - A^* C_L \quad (17a)$$

where

$$C_m^* = m_1 \left(\frac{4 (t/c) \cos \Lambda}{\sqrt{1 - M_\infty^2 \cos^2 \Lambda}} + .4 \right) \left(\frac{a_1 a_4 - a_2 a_3}{a_1 + a_2} \right) \quad (17b)$$

$$A^* = m_2 \left(\frac{a_3 + a_4}{a_1 + a_2} \right) \quad (17c)$$

and

$$\begin{aligned} a_1 &= \frac{1}{2} + \frac{1}{2} x_{R_u}, & a_3 &= \frac{1}{24} + \frac{1}{24} x_{R_u} + \frac{1}{6} x_{R_u}^2, \\ a_2 &= \frac{1}{2} + \frac{1}{2} x_{R_L}, & a_4 &= \frac{1}{24} + \frac{1}{24} x_{R_L} + \frac{1}{6} x_{R_L}^2. \end{aligned}$$

C_L follows from (15). m_1 and m_2 are known constants. With the section pitching moment defined with respect to the quarter-chord point, the total contribution of the lifting elements to the aircraft pitching moment w.r.t. the centre of gravity then follows from:

$$C_M = \int g_2(n) \Gamma(n) dn + \frac{1}{S_{ref} c_{ref} u_\infty^2} \int C_m^*(n) c^2(n) u^2(n) dn \quad (18a)$$

where

$$g_2(n) = \frac{2 u(n)}{S_{ref} c_{ref} u_\infty^2} (x_{c.g.} - x_{1/4}(n) - A^*(n) c(n)) \cos(\varphi(n)) \quad (18b)$$

c_{ref} denotes the length of the reference chord, and $x_{c.g.}$ is the longitudinal coordinate of the configuration centre-of-gravity.

If the aircraft configuration is asymmetrical, (e.g. a configuration with propellers all rotating in the same direction), a rolling moment constraint C_R w.r.t. the point $\eta = 0$ (in the plane of symmetry) may be imposed:

$$C_R = \int g_3(n) \Gamma(n) dn \quad (19a)$$

where

$$g_3(n) = \frac{2 u(n)}{S_{ref} b_{ref} u_\infty^2} \left[\{y(n) - y(0)\} \cos(\varphi(n)) + \{z(n) - z(0)\} \sin(\varphi(n)) \right] \quad (19b)$$

b_{ref} is the reference span. Note that the rolling moment coefficient C_R equals 0 if the aircraft configuration is symmetrical.

Limitation in design c_L , t/c , c_m and M

In order to ensure that the computer program works with feasible airfoil characteristics, a relation defining feasible combinations of (design) lift coefficient, (design) Mach number, wing thickness-to-chord ratio and pitching moment coefficient may be formulated. For supercritical airfoils, a graphical representation of such a relation between t/c , c_L and M is given in figure 5 for $c_m = -.110$. Data for other c_m -levels follow from the relation $\delta(t/c)/\delta c_m = -.6$. The relation can be considered to represent a "condensed" section characteristics data base for a feasible class of supercritical airfoils. This class is described by a relation between allowable combinations of design c_L , M , t/c , c_m . The data base holds for 2D-airfoils. If a sweep angle Λ is applied, the 3D-values have to be calculated from the 2D-values using the relations:

$$\begin{aligned} C_L(3D) &= C_L(2D) \cos \Lambda, & C_m(3D) &= C_m(2D) \cos^2 \Lambda, \\ \frac{t}{c}(3D) &= \frac{t}{c}(2D) \cos \Lambda, & M(3D) &= M(2D) / \cos \Lambda. \end{aligned}$$

The data base is used when imposing (local) lift coefficient constraints in drag minimization procedures. In the case that the user provides pitching moment coefficient distributions, the combination of t/c , M and c_m directly leads to the upper limit of the allowed range for the (design) lift coefficient. If the pitching moment coefficients are not directly specified, the combination of t/c and M only results in a feasible c_m - c_L area. In that case, the pitching moment coefficient

distribution may be defined by relation (17), which further restricts the possible combinations of c_m and c_x in this feasible area. Both c_m and c_x are then found as part of the solution.

It is emphasized that the "data base" of feasible characteristics is representative for a certain class of airfoils. The user should check whether this data base is compatible with his own experience. If required, the relation may be modified to his own experience.

4 DRAG MINIMIZATION

General

The numerical optimization of drag is based on an approach, in which the evaluation of double integrals (see eq. 8) is avoided. This is realized by first deriving analytically the necessary optimality equations before doing any discretization. Discretization of the bound-circulation distribution in the (single) integrals is performed starting from these analytical necessary optimality equations.

Analytical necessary optimality equations

The drag minimization problem can be stated as follows: determine the function $\Gamma(n)$ that minimizes the functional $C_{D_i} + C_{D_{visc}}$ subject to constraints imposed on C_L , C_M and, if required, on C_R :

$$\begin{aligned} G_1 &= C_L - C_{L_{des}} = 0 \\ G_2 &= C_M - C_{M_{des}} = 0 \\ G_3 &= C_R - C_Q = 0 \end{aligned} \quad (20)$$

Also $C_x(n)$ may be constrained:

$$G_4(n) = C_x(n) - C_{x_{des}}(n) \leq 0, \quad \forall n. \quad (21)$$

$C_{L_{des}}$, $C_{M_{des}}$ and the (dimensionalized) propeller torque C_Q are prescribed values for C_L (eq. 16), C_M (eq. 18) and C_R (eq. 19). $C_{x_{des}}(n)$ follows from the relation between c_x , t/c , c_m and M as described in the preceding section. Expression (8) and (14) specify the induced drag C_{D_i} and viscous drag $C_{D_{visc}}$, respectively.

The problem may be solved through the introduction of Lagrange multipliers. That is, the augmented integral

$$I = C_{D_i} + C_{D_{visc}} + \sum_{i=1}^3 \lambda_i G_i + \int \mu(n) G_4(n) dn$$

is formed, where the Lagrange multipliers λ_i ($i = 1, 3$) and $\mu(n)$ are to be determined. The next step towards the solution of the optimization problem is to write $\Gamma(n) = \Gamma(n) + \delta\Gamma(n)$, and to form the first variation δI of I with respect to variations of $\Gamma(n)$,

$$\begin{aligned} \delta I = & \int_{S_{ref}} \left[2 \int E(\tau, n) \tilde{\Gamma}(\tau) d\tau + \frac{2}{S_{ref} U_\infty^2} (\vec{v}_p(n) \cdot \vec{n}(n)) + \right. \\ & \left. + 2 K^*(n) g_1^{*2}(n) \tilde{\Gamma}(n) - 2 K^*(n) g_1^*(n) C_x^*(n) + \sum_{i=1}^3 \lambda_i g_i^*(n) + \mu(n) g_1^*(n) \right] \delta\Gamma(n) dn \end{aligned} \quad (22)$$

In this variation, the parameters v_p , K^* and C_x^* , and all geometry-related parameters, have fixed values.

The necessary condition for the minimization of I is that the first variation vanishes. This condition holds for any arbitrary function $\delta\Gamma(n)$, hence the term between brackets in (22) must vanish at all spanwise positions. In fact, this necessary condition for the minimization of I is nothing else but the Euler-Lagrange equations of variational calculus. Upon substitution of the expression (6) for $f(\tau, n)$, the condition can also be written in the form:

$$\frac{2}{S_{ref} U_\infty^2} \left(\vec{v}_n(n) + \vec{v}_p(n) \cdot \vec{n}(n) \right) + 2K^*(n) g_1^{*2}(n) \Gamma(n) - 2K^*(n) g_1^*(n) C_x^*(n) + \sum_{i=1}^3 \lambda_i g_i^*(n) + \mu(n) g_1^*(n) = 0 \quad (23)$$

that must hold for all n . In combination with the constraint relations (20) for C_L , C_M and C_R , and the constraint for $C_x(n)$ written in the form

$$\left. \begin{aligned} v(n)(C_L(n) - C_{L_{des}}(n)) &= 0 \\ v(n) &\geq 0, \end{aligned} \right\} v_n \quad (24)$$

the optimal bound circulation is determined.

It may be noted that, if only the induced drag is minimized ($K = 0$) in a flow without propeller slipstreams ($\bar{v} = 0$) and imposing the total lift constraint only, the necessary condition reduces to Munk's criterion for minimum induced drag (Ref.15)

$$\frac{2}{s_{ref} u_\infty} v_n(n) + \lambda_1 (C_L - C_{L_{des}}) = 0, \quad \forall n.$$

In words, "the induced drag will be a minimum when the component of the induced velocity normal to the lifting element at each point is proportional to the cosine of the dihedral angle of the lifting element at that point ($v_n = w_0 \cos \psi$)".

Numerical approach

The necessary optimality conditions (23) for the drag minimization includes an integral expression for v_n . Direct integration can be done analytically only for the most simple bound circulation distributions. Thus, to solve the integral equation (23) by approximation, it is necessary to assume a priori a convenient shape of the bound-circulation distribution function $\Gamma(n)$. The discretization model adopted here is the same as that utilized by Kuhlman (Ref.7) viz. a piecewise quadratically varying bound circulation:

$$\frac{d\Gamma_i(\rho)}{d\rho} = \gamma_{i-1} + \frac{\rho + h_i}{2h_i} (\gamma_i - \gamma_{i-1}), \quad -h_i \leq \rho \leq h_i \quad (25)$$

where h_i is the half-width of the panel i . ρ is the panel coordinate: $\rho = 0$ coincides with the panel midpoint, while ρ is positive if located outboard of this point. γ_i and γ_{i-1} denote the trailing vortex sheet strength at the panel ends. Using this discretization model and a suitable panel-spacing technique, sufficiently accurate solutions can be obtained with a relatively small number of panels.

The integral expression (5) for the normal velocity v_n can be written as a summation of panel integrals. Upon substitution of the discretization model, the following expression for v_n induced at panel j and at a distance τ from its midpoint can be derived from (5) and (25):

$$v_{nj}(\tau) = \frac{1}{2\pi} \sum_{i=1}^{2k} \left\{ \frac{\gamma_i + \gamma_{i-1}}{2} \int_{-h_i}^{+h_i} A(\rho, \tau) d\rho + \frac{\gamma_i - \gamma_{i-1}}{2h_i} \int_{-h_i}^{+h_i} \rho A(\rho, \tau) d\rho \right\} \quad (26)$$

where

$$A(\rho, \tau) = \frac{\vec{n}(\tau) \cdot (\vec{r}(\rho, \tau) \times \vec{e}_x)}{|\vec{r}(\rho, \tau)|^2} \quad \text{and} \quad \tau = [-h_j, h_j]$$

The summation is performed over all $(2k)$ panels at both sides of the (xz) -plane of symmetry. The integrals in equation (26) over each individual panel are evaluated analytically.

From equation (25) follows

$$\Gamma(\tau) = \Gamma(h_i) - \frac{\gamma_{i-1} + 3\gamma_i}{4} h_i + \frac{\gamma_i + \gamma_{i-1}}{2} \tau + \frac{\gamma_i - \gamma_{i-1}}{4h_i} \tau^2 \quad (-h_i \leq \tau \leq h_i) \quad (27)$$

where

$$\Gamma(h_i) = - \sum_m (\gamma_{m-1} + \gamma_m) h_m.$$

The summation is performed over all panels located outboard panel i .

Application of the necessary condition (23) at all panel midpoints, using expressions (26) and (27) for v_n and Γ respectively, then results in $2k$ relations for the unknown trailing vortex sheet strength values γ_i and Lagrange multipliers λ_i and μ_i :

$$\sum_{i=1}^{2k} B_{ij} \gamma_i + \sum_{i=1}^3 g_{ij} \lambda_i + \mu_j g_{ij}^* = b_j, \quad j = 1, 2k \quad (28)$$

where the index j indicates the panel at the midpoint of which the necessary condition is imposed.

Substituting the discrete bound-circulation model (25) in the equations (16), (18), (19) and (15) for C_L , C_D , C_R and $C_L(n)$, respectively, these equations can be integrated analytically and can be expressed in terms of the trailing vortex-sheet strength values γ_i . Together with the $2k$ -relations (28) and the constraints (20) and (24) they form a system of linear equations for the unknown trailing vortex-sheet strengths and Lagrange multipliers. This system determines the optimal spanwise bound-circulation distribution that results in minimum drag.

The method developed automatically takes care of satisfying Helmholtz' theorem at configuration element intersections, which is manifested by jumps in the bound circulation distribution. If a symmetrical aircraft configuration is considered (no propellers, or a counterrotating pair of propellers) this results in k unknown vortex sheet strengths γ_j , and the range of j in equation (78) reduces to $j = 1, k$. In addition, the rolling moment constraint may be deleted.

In order to avoid rather complicated and computationally expensive integrals the drag components are calculated using a numerical integration rule, instead of integrating analytically. Two options are provided: the midpoint rule and the Simpson rule. Using a panel arrangement method with properly increased panel density in regions with comparatively large Γ_v -variations, use of the midpoint rule already results in a sufficiently accurate approximation with a relatively small number of panels.

Knowing the spanwise bound-circulations also other quantities of interest can be determined. Examples are trimdrag, bending moment distribution, and the overall forces acting on the aircraft components.

5 INFORMATICS ASPECTS

The drag analysis and minimization has been integrated in the NLR software infrastructure for computer aided engineering. The integration is required to apply the system for parametric configuration design studies (interaction with other disciplines) alternately with existing detailed aerodynamic analysis and design methods (iterative adjustment of aerodynamic design choices). The existing infrastructure reflects the industrial infrastructure for computer aided design in order to facilitate the transfer of information systems to industry.

The integration as described above requires

- methods for the generation of the information;
- means for the management of information;
- means for the management of methods

At NLR, solutions for these requirements have been found in developing an architecture in which a data base and a data manager, and a method base and a method manager, form the key elements (Ref. 16). The data manager enables storage and searching of data in terms familiar to the user. It is used as a means for conservation of data produced in the information system, or transfer of information between subsequent phases, between steps in each phase (iteration), and between the disciplines involved (interaction).

The method manager enables structured storage and searching of methods which extensive descriptions of their functions and their implementations. The methods themselves are stored in a method base. The method manager supports the composition of existing methods to a new method, and consistency checking of the implementations in such a composition of methods. Through the use of a method manager the method development can be controlled, the methods can be maintained during a long period of time and can be re-used in several applications.

An executive supports the execution of methods on a network of computers. It takes care of the file transfers over the network, and of job execution. Whereas the method manager checks the correctness of a composition of methods, the executive checks the compatibility of the methods and the input information.

The architecture of which the system for constrained spanload optimization is a part is given in figure 6.

6 EXAMPLES OF APPLICATIONS

In this section, a number of typical examples is presented that demonstrate some of the capabilities of the method developed. The examples do not represent actual design studies.

Induced drag only

Obviously, the accuracy of numerical induced drag methods is affected by the discretization model of the bound circulation distribution. It has been shown for a planar wing (Ref. 7), that methods using piecewise quadratically varying bound circulations, are approximately four to five times as accurate in computing the induced drag as a vortex-lattice method with the same equal-sized panel arrangements. In figure 7, the present method is compared, for a planar wing, with the method of Kuhlman (Ref. 7), in which also quadratically varying bound circulations are used. Although the present method is less time-consuming than Kuhlman's method, it can be seen that the differences in accuracy and convergence are very small; both methods approach the exact value of the induced drag rapidly at the number of panels increases. Using 10 wake panels per semi-span, the minimum induced drag of the planar wing is computed with an accuracy of about 0.2 percent.

For a non-planar configuration, the present method is compared with a result obtained by Lundry using a conformal-mapping technique (Ref. 17). In figure 8, the optimal bound circulations are compared for a wing configuration with vertical endplates (or winglets). As can be seen, the results of both methods agree well.

In figure 9, some of the system capabilities with respect to trimmed induced drag minimization are demonstrated for a transport-aircraft type configuration, a sketch of which is given. The minimum induced drag as function of the centre-of-gravity location for three different vertical positions of the horizontal tail is shown in figure 9a. The spanwise C_p -distribution was specified ($C_p(\eta) = -0.106$ | $0 \leq \eta \leq b/2$) and for the body pitching moment coefficient, $C_{m,0} = +0.007$ was adopted. This figure shows that for (conventional) cases of negative tail loads, the minimum induced drag increases with increasing height of the horizontal tail. Note that the lowest values of minimum induced drag are obtained for high-tail configurations with positive tail loads. This suggests that, from the point of view of induced drag, there might be a preference for high-tail positions for configurations combining relaxed static stability with active control technology.

In figure 9b, the influence of the tail-to-wing span ratio and the vertical position of the horizontal tail on the minimum induced drag is displayed for two different positions of the centre-of-gravity. It can be seen that, for a fixed height of the horizontal tail, the minimum induced drag increases with decreasing tail-to-wing span ratio.

The inclusion of $C_p(\eta)$ -constraints in the optimization procedure is realized using a relation between $c_p(\text{des})$, $c_p(\text{des})$, M and t/c (see section 4). As an example, the same configuration of figure 9 is considered for $M = 0.735$. The limitations in design c_p , t/c , c and M of figure 5 (supercritical airfoils) are used. Instead of giving a specified spanwise C_p -distribution, now the pressure recovery point locations have been given ($x_{p,u}(\eta) = .5$ | $0 \leq \eta \leq b/2$). With this, a relation between C_p and C_m is specified (see eq.(17)), ($t/c(\eta) = 15.5\%$ | $0 \leq \eta \leq b/2$). In figure 10, the optimal C_p -distribution is compared with those of the "no wing-thickness constraint" option ($x_{p,u}$ at 30% MAC). The figure shows that, in this particular example, the C_p -distribution has changed 60% constant C_p over a portion of the wing. The inclusion of wing-thickness constraints results in an induced-drag increase of about 2%.

Induced drag minimization including propeller slipstreams

In order to examine the effects of the propeller slipstream on the aircraft induced drag, the axial and tangential velocities in the propeller slipstream have to be given. For a particular example design condition, the distribution of propeller induced velocities of figure 11 has been used (advance ratio of $J = 0.13$ and a thrust coefficient of $C_T = 0.12$).

For a wing configuration with two "up-inboard" rotating propellers, located at 25% of the semispan with a diameter-to-span ratio of 13%, the optimal spanwise bound circulation distribution is shown in figure 12. This distribution greatly differs from the optimal "clean wing" distribution that is also shown in figure 12. With this distribution, the wing is capable of restoring much of the loss associated with slipstream swirl.

In figure 13, the effects of the horizontal propeller position for different rotating concepts of the propellers on the minimum induced drag coefficient have been plotted. As can be seen clearly from this figure, two up-inboard rotating propellers lead to a most favourable configuration with respect to the minimum induced drag. If the location of the propeller-centre is moved outboard, induced drag will decrease for two up-inboard rotating propellers and will be a minimum when the propellers are located at the wing tips (see also Ref. 11).

It is apparent from the results above that favourable lifting-element/propeller interference resulting in lower induced drag or, equivalently, induced thrust, may be produced by appropriate wing design. The required C_p -distribution may be realized by, for instance, adjusting twist, thickness, camber and chord distributions. The results obtained agree with those of Kroo (Ref. 10), who showed that in some cases all of the swirl loss can be recovered.

Also proper design of the engine nacelle/pylon may possibly contribute to swirl loss recovery. Figure 14 presents the optimum span loads for two configurations (with up-inboard rotating propellers) one utilizing passive (streamline) shaping of the pylon and the other having an active loading on the pylon. In this particular example, a 9% reduction of the minimum induced drag is realized. Of course, this is not an actual design case and the benefit can be realized only at the cost of a more complicated detailed design, but it may be interesting to investigate the possibilities of a more active role of the nacelle/pylon.

Induced + viscous drag minimization

The importance of including the viscous drag component in the minimization procedure is illustrated by the next example. This example concerns a wing-canard configuration. In this example, the pressure recovery point locations have been given ($(x/c)_{p,u} = .5$; $(x/c)_{p,l} = .4$), while for the thickness-to-chord ratio (t/c) a constant value of 12% has been adopted.

In figure 15, the drag as function of the centre-of-gravity location is displayed. The upper set of drag curves represent the sum of induced + viscous drag (only the viscous drag of wing and canard is considered), while the lower curves are for the induced drag alone. By optimizing the sum of the induced and viscous drag, the total drag is less than it would have been if only the induced drag was minimized and the viscous drag added afterwards. Of course, the induced drag alone is greater when the sum of the drags is minimized than when induced drag alone is optimized. In addition, the total drag minimum is located about 10% $b/2$ ahead of the minimum induced drag alone position, stressing the importance to include (estimation of) viscous drag in configurational design studies.

In figure 16, the section C_d 's for both minimum induced-drag and minimum induced plus viscous drag are given for the minimum (induced + viscous) drag c.g.-position. As can be seen, the inclusion of profile drag results in a reduction of peak section C_d and an inboard shift of the spanloading for the main wing.

The results agree with those of Mason (Ref. 9), who showed that a drag reduction of about 5% could be achieved by including the profile drag in the optimization procedure.

Configuration design studies

The method developed can also be used for parametric preliminary design studies, for instance, to assess the effect of changes in size, location, dihedral and sweepback of wing, tail or canard, winglets, etc. The configuration may be of the conventional type (tail-aft) or nonconventional type (canard, three-surface configuration, forward swept wing, etc.).

A typical example of a nonconventional aircraft configuration is the three-surface aircraft (canard, wing and aft tail) given in figure 17. For the canard-wing and wing-tail configuration, the specification of the centre-of-gravity position (static margin) and the trim condition are most decisive to fix the balance of lift between the wing and control surface, but for the canard-wing-tail configuration the lift distribution among the surfaces can be chosen to reduce the total induced drag while retaining trimmed conditions at a specified static margin. The three-surface circulation distributions of figure 17 are only presented to illustrate the capabilities of the system and are not meant to represent an actual configuration design study.

In the past couple of years, there has also been a renewed interest in aircraft configurations with forward swept wings (FSW). According to reference 18, the application of forward swept wings may result in, among others, lower induced drag and higher maximum lift coefficient as compared with an aft swept wing (ASW). The problem of aero-elastic problems for forward swept wings may nowadays be solved by using an aero-elastically tailored wing using composite materials. Figure 18 shows that in the case of forward swept wings, the tendency of spanwise loading for minimum trimmed induced drag is to move inboard.

Configuration design studies may concern the composition of the total aircraft lay-out as well as local alterations of the aircraft configuration as is the case, for instance, when the effectiveness of winglets is investigated.

7 CONCLUSIONS

An induced (plus viscous) drag analysis and minimization method has been developed that provides a low cost and useful tool, that can be used both for preliminary aircraft design purposes, and for providing direct input to detailed aerodynamic design procedures. In the latter function, the method provides bound-circulation distributions that may be used in specifying target pressure distributions for inverse aerodynamic design codes.

Complementary to the determination of optimal spanloads, the method can also be used to support selection of spanwise distributions of pitching moment, chord and thickness-to-chord ratio. In the procedure, the interaction between propellers and lifting elements may be included. Compared to other methods in this spirit, the present method is less time-consuming than near field methods and more accurate than vortex-lattice methods. Comparisons with known solutions of other theoretical methods have proven excellent agreement.

The examples shown in this paper illustrate the importance of considering, early in the design, all aspects that may influence the drag characteristics. The inclusion of, for instance, viscous drag and/or propeller slipstream may lead to other choices for the spanwise distributions of lift, pitching moment, chord, and thickness-to-chord ratio than when only the induced drag without propeller-slipstream is considered.

The method has been incorporated in a CAD-type program system with alpha-numeric and graphic display capability and may be used as a stand alone system. The system is fast and easy to use, and therefore very suitable for interactive design purposes in which rapid configuration trade-offs have to be made. The system has a wide field of application. It may be especially useful to support the assessment of unconventional design concepts in which lack of experience precludes good design decisions. Examples of unconventional concepts are three-surface configurations, relaxed static stability, "active" nacelle/pylons, forward swept wings, etc.

The capabilities of the system are exploited more efficiently when used in a multidisciplinary design environment. The existing infrastructure in which data management and method management are key elements, meets this requirement. The application of data and method management supports the composition of existing methods, control of method development, incorporation of improved versions and re-use of software. In addition, it supports the transfer of the information system from the development environment to the design environment in industry. This is important as return-on-investment is realized only by application of the system in the design process in industry.

8 REFERENCES

1. Holst, T.L., Slooff, J.W., Yoshihara, H., Ballhaus, W.F., Applied computational transonic aerodynamics. AGARD-AG-266, 1982.
2. Vanderplaats, G.N., Approximation concepts for numerical airfoil optimization. NASA TP-1370, 1979.
3. Hicks, R.M., Transonic wing design using potential flow codes - successes and failures. SAE-paper 810565, 1981.
4. Slooff, J.W., Computational Drag analysis and Minimization; Mission Impossible? AGARD-R-723, 1985.
5. Feifel, W.M., Optimization and design of three-dimensional aerodynamic configurations of arbitrary shape by a vortex lattice method. NASA SP 405, 1976.
6. Lamar, J.E., A vortex-lattice method for the mean camber shapes of trimmed non-planar planforms with minimum induced drag. NASA TN D-8090, 1976.
7. Kuhlman, J.M., Higher order farfield drag minimization for a subcritical wing design code. J. of Aircraft, Vol.17, No.9, 1980.
8. Kuhlman, J.M., Iterative optimal subcritical aerodynamic design code including profile drag, AIAA-83-0012, 1983.
9. Mason, W.M., Wing-canard aerodynamics at transonic speeds. Fundamental considerations on minimum drag spanloads. AIAA-82-0097, 1982.
10. Kroo, I., Propeller-wing integration for minimum induced loss. J. of Aircraft, Vol.23, No.7, July 1986.
11. Loth, J.L., Loth, F., Induced drag reduction with wing tip mounted propellers, AIAA-84-2149, 1984.
12. Prabhu, R.K., Tiwari, S.N., Studies on the interference of wings and propeller slipstreams, Report Old Dominion University, Ph.D. Thesis, 1984.
13. Vooren, J. v.d., Slooff, J.W., XFLO22 NLR, a modified version of FLO22, NLR IW-80-004 C, 1980.
14. Dam, R.F. van den, SAMID, an interactive system for aircraft drag minimization studies, NLR TR 88071, 1988.
15. Munk, M.M., The minimum induced drag of airfoils. NACA Report 121, 1921.
16. Loeve, W., Integrated automation for support of research and development. NLR MP 88063 U, 1988.
17. Lundry, J.L., A numerical solution for the minimum induced drag, and the corresponding loading, of nonplanar wings. NACA CR-1218, 1968.
18. Sweiger, J., Schneider, G., Sensberg, O., Löbert, G., Design of a forward swept wing fighter aircraft. ICAS-paper 84-09, 1984.

(c) SIDEVIEW

Figure 1 is a graph showing the relationship between the LUST COEFFICIENT - C_m DEC (Y-axis) and the ratio of the LUST COEFFICIENT to the C_m DEC, $\frac{\Delta(t/c)}{\Delta C_m} \approx -0.5$ (X-axis). The Y-axis ranges from 0 to 1.0, and the X-axis ranges from 0 to 1.0. Data points are plotted for various samples, with some points labeled with sample numbers (8, 9, 10, 11, 12, 13, 14, 15, 16, 17) and others with 'SYM. DEC.'. A dashed line labeled $C_m M = 11$ is shown, and a solid line labeled $\frac{\Delta(t/c)}{\Delta C_m} \approx -0.5$ is also present.

```

graph LR
    USER((USER)) --> UI[USER INTERFACE]
    UI --> MM[METHOD MANAGER]
    UI --> EX[EXECUTIVE]
    MM --> MB[METHOD BASE]
    EX --> DMS1[DATA MANAGEMENT SYSTEM]
    subgraph DMS1 [DATA MANAGEMENT SYSTEM]
        TO1[TRANSLATION OPTIMIZATION]
        TO2[TRANSLATION OPTIMIZATION]
        VD[VESSEL DESIGN]
        OP[OPTIMIZATION PROGRAMS]
    end
    DMS1 --> DMS2[DATA MANAGEMENT SYSTEM]
    subgraph DMS2 [DATA MANAGEMENT SYSTEM]
        GD[GEOMETRIC DATA]
        MD[MESH DISTRIBUTION]
        LD[LIFT DISTRIBUTION]
        AC[AERODYNAMIC CHARACTERISTIC DATA]
    end
    DMS2 --> DB[DATA BASE]
  
```

Fig. 6 Conceptual design of aerodynamic design system

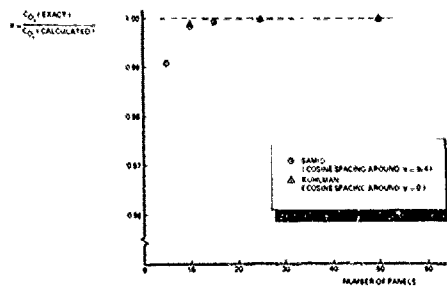


Fig 7 Accuracy of the method for a planar wing

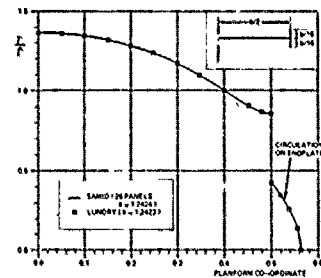


Fig 3 Bound-circulation distribution of a wing with end plates

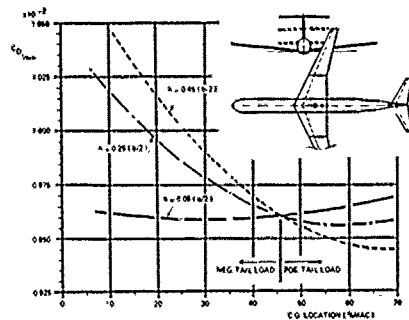
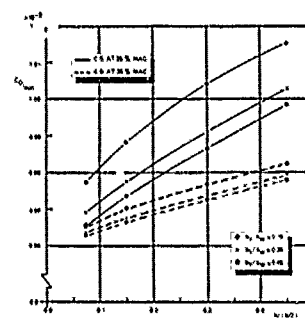
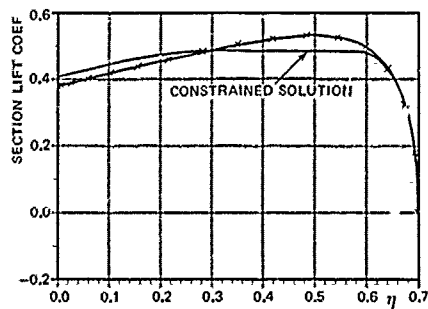
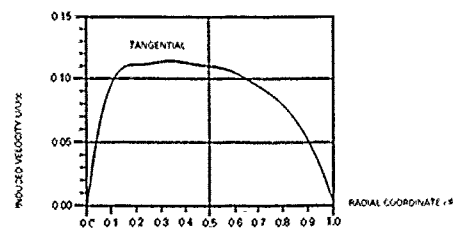
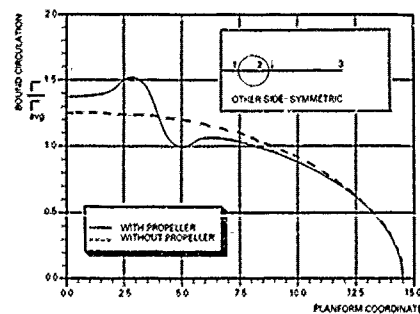
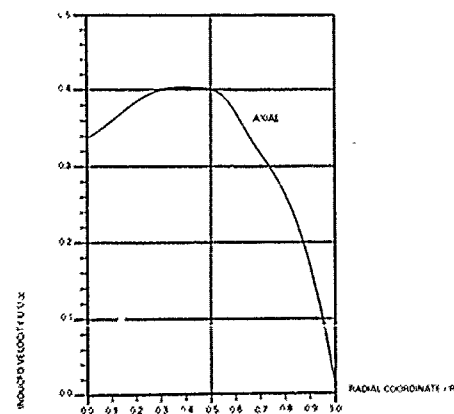
(a) Effects on the location of center of gravity and the tail height relative to the wing on the minimum trimmed induced-drag ($C_{M/W/B} = -0.09$)(b) Effects of the tail height and the tail-to-wing span ratio on the minimum trimmed induced-drag ($C_{M/W/B} = -0.09$)

Fig. 9 Examples of trimmed induced drag minimization studies

Fig. 10 The influence of C_L -constraints (for given x_R -distribution)

(a) propeller-induced tangential velocity

Fig. 12 Optimal bound circulation distribution γ for a wing with two up-inboard rotating propellers

(b) propeller-induced axial velocity

Fig. 11 Propeller-induced velocities

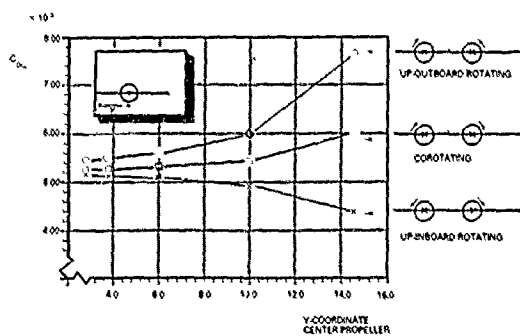


Fig. 13 Effects of the horizontal propeller location on the minimum induced drag

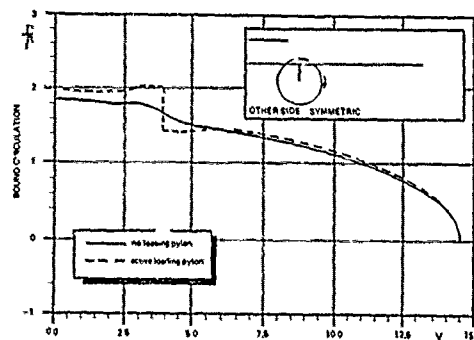


Fig. 14 Optimal bound distributions for configurations with "up-inboard" rotating propellers, with passive shaping and with "active" shaping of the pylon respectively

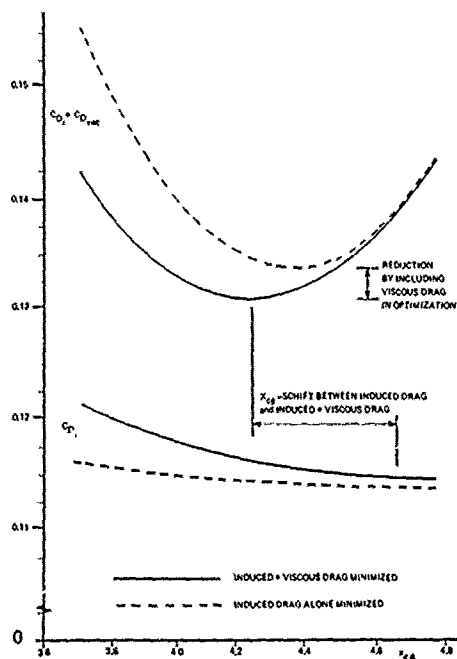


Fig. 15 "Induced" drag minimization versus "induced + viscous" drag minimization

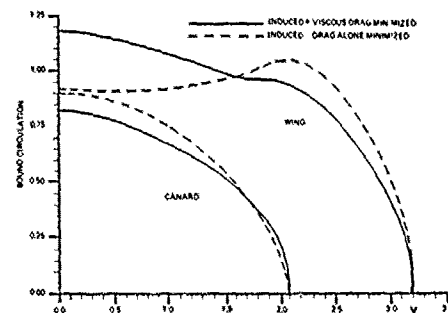


Fig. 16 Optimal C_D distributions for minimum "induced" drag and minimum "induced + viscous" drag, respectively (x/b at minimum "induced + viscous" drag position)

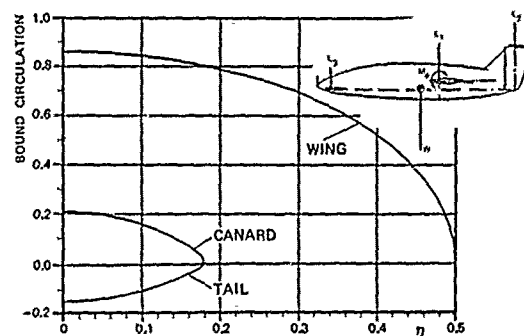


Fig. 17 Spanloads for minimum trimmed induced drag (three-surface aircraft)

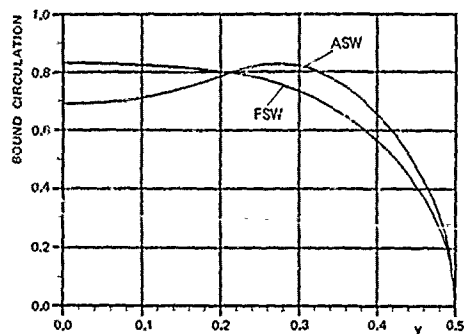
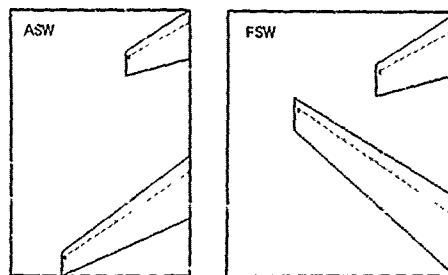


Fig. 18 Spanloads of forward and aft swept wing configurations



NUMERICAL OPTIMIZATION OF TARGET PRESSURE DISTRIBUTIONS FOR SUBSONIC AND TRANSONIC AIRFOIL DESIGN

J.A. van Egmond
National Aerospace Laboratory NLR
P.O. Box 90502
1006 BM AMSTERDAM; The Netherlands

Summary

Inverse aerodynamic design, calculating the geometry from prescribed pressure distributions, leaves the designer with the problem to define proper target pressure distributions. Numerical optimization techniques are employed to support the aerodynamic designer in the definition of target pressure distributions for subsonic and transonic airfoil design.

A general parametric representation of airfoil pressure distributions is given, taking into account the physical characteristics of the airfoil flow. This parametric representation enables the designer to define "optimum" target pressure distributions through numerical optimization techniques.

Worked out examples show that a large class of airfoils can be described by the proposed procedure. The nature of the aerodynamic design problem appears to be such that best results are obtained with a simple line search method. In general, a large number of iterations is needed to arrive at the final (optimal) solution. However the requirement of a large number of iterations is not a serious drawback of the approach described in this paper.

Finally, it is concluded that application of numerical optimization techniques is not (yet) to be considered as a routine job but considerable possibilities are offered to improve design results.

1. Introduction

Aerodynamic design by means of solving the inverse aerodynamic problem is common practice nowadays. The main problem the designer is faced with concerns the definition of the velocity - or pressure distributions that have to be realized. Figure 1 presents a typical flow chart for the aerodynamic design process. For a transport type wing design, the "man-in-the-loop" defines, apart from many other things, wing loading and load distribution along the span. Constrained induced drag optimization, as performed by SAMID (ref. 1), is found to be a valuable tool to select proper spanload distributions. Subsequently the chordwise load distributions have to be chosen in order to arrive at the starting condition necessary for the geometry calculations by means of, for instance, the wing design procedure, INSYST (ref. 2). The present paper deals with the development of a system to support the man-in-the-loop in defining chordwise pressure distributions. For a high aspect ratio transport wing this means the definition of equivalent two-dimensional target pressure distributions.

So far, the definition of target pressure distributions relied to a large extent on the knowledge and experience of the aerodynamic designer. However, it was felt that application of numerical optimization techniques could improve efficiency of the process and the quality of the process. So, NLR started a program to incorporate known numerical optimization techniques in the airfoil design procedure. Although it has to be kept in mind that the term optimization might be somewhat misleading and should be read as "design improvement" otherwise, according to Vanderplaats (ref. 3), -"Expectations of achieving the absolute best design invariably lead to maximum disappointment"-.

Application of numerical optimization techniques in airfoil design in itself is not new and a brief review will be presented in chapter 3. So far, the known applications operate directly on the airfoil geometry while the present approach deals with the pressure distribution only.

Experience so far indicates that the number of iterations during the optimization increases rapidly with the number of independent design variables. The latter approach requires only an evaluation of the boundary layer for each iteration instead of a complete flow field calculation. So, a large number of iterations is less of a problem. This allows a larger number of design variables and thus probably a larger design domain.

In order to perform the study an interactive optimization system designated CADOS (Computer Aided Design by Optimization System) was developed (ref. 4). It is a general modular system to handle all kinds of constrained optimization problems and will be briefly described in chapter 2.

The main body of the present study deals with the problem definition and parametrization of 2.D target pressure distributions (chapter 4). A few examples will be presented in chapter 5.

2. CADOS

The general design problem is characterized by:

- a number of independent design variables x_i $\{i=1,n\}$
- a function to be minimized (or maximized) $Fobj(x_i)$
- a number of constraints prescribed for the design variables and/or for some so-called constraint functions $g_j(x_i)$ $\{j=1,m\}$

Then the mathematical formulation reads:

$$\begin{array}{ll} \text{minimize} & Fobj(x_i) \\ \text{subject to} & \left. \begin{array}{l} x_1 \leq x_i \leq x_u \\ g_1 \leq g_j \leq g_u \end{array} \right\} \quad \begin{array}{l} i=1,n \\ j=1,m \end{array} \end{array}$$

where indices i and j stand for lower- resp. upper value to be prescribed by the designer.

The constrained minimization problem is often transformed in an unconstrained problem by redefining the constraint functions as so-called penalty functions. Then the problem formulation could be:

$$\text{minimize } Fobj(x_i) + \alpha_1 \Delta_1 + \alpha_2 \Delta_2 + \dots$$

Here $\Delta_1, \Delta_2, \dots$ are the constraint violations (penalty functions) and $\alpha_1, \alpha_2, \dots$ are some kind of multipliers used for a proper scaling of the penalty functions.

At present a large number of algorithms is available to solve the above problem (see e.g. refs 3, 5 and 6). Each of these methods has its own specific strong and weak points. Without detailed knowledge of the characteristics of the (design) problem to be solved it is not possible to select the best method. Nevertheless it should be kept in mind that the following characteristics apply to most of the available methods.

- A minimum found might be a local minimum and there is no straight forward way to find out whether the minimum is a local- or a global one.
- Optimization becomes increasingly difficult with the non-linearity of the problem.
- Continuous first- and second order derivatives are often assumed.

Note: Optimization convention is to minimize functions. However, it will be clear that a maximum is found by minimizing the function with reversed sign.

Now, CADOS stands for an interactive design system that controls the data flow between- and running of a number of user's specified (sub)routines in an optimization procedure (see figure 2). The user selects his routines from the available library and/or supplies additional routines. The user always supplies the routine ANALYSE (figure 2), in which design variables are defined, and functions determined. During the design session, the user interactively chooses the variables and functions to be active or non-active, and which of the "active" functions is to be object function and which are constraint functions (constraints may be adjusted). As a result a flexible system has been realized which enables the user to control the course of the optimization procedure to a large extent.

At present the following standard optimization routines have been implemented:

- POWELL (For non linear problems, includes a quadratic approximation of the Lagrangean function and a linear approximation of the constraint functions)
- SIMPLEX (a sequential search technique)
- NAG 0 (a sequential augmented Lagrangean method including a quasi Newtonian method)
- NAG 1 (a sequential quadratic programming algorithm)

For more details, see ref. 5.

3. Review of existing methods

Several authors have reported on the use of optimization techniques for the airfoil design problem (e.g. ref. 7, 8, 9, 10). All these applications have in common that, in some way or another the airfoil geometry (or a part of the airfoil geometry) is represented by general shape functions. Then, geometry perturbations are used to arrive at a better airfoil. The following typical methods can be distinguished

- A. Represent a (part of the) geometry by means of some general function, see fig. 3a (polynomial: Hicks/Vanderplaats, ref. 7; cubic splines: Misegades, ref. 8).
Because every geometry perturbation requires a complete flow field evaluation, the number of free variables is limited, for economic reasons. This restricts the design domain. Nevertheless, several successful airfoil improvements have been obtained (decreased transonic airfoil drag).
- B. Represent an airfoil by a linear combination of known airfoils, see fig. 3b (Vanderplaats ref. 9). A possible way to increase the design domain still for a limited number of design variables.
- C. Represent an airfoil by a basic shape plus a (linear) combination of typical geometry perturbations, see fig. 4 (Aidala/Davis/Mason ref. 10). Aidala et.al. define a limited number of so called aerofunction geometry perturbations each of which results from a typical pressure distribution modification. Aerofunction shapes are calculated from prescribed pressure distribution modifications for a known basic airfoil. It is claimed that a set of 6 aeroshape functions represents a sufficient large design domain.

From the data published by Aidala et.al. it can be seen that relatively simple pressure distribution perturbations require complicated geometry variations. Indicating the difficulty to realise a general geometry-shape function with only a limited number of independent variables. So, it seems a logical step to parametrize the pressure distribution and try to optimize the target pressure distribution directly. This approach offers the following advantages

- It matches the design philosophy as described in the introduction.
 - Only boundary layer calculations are needed during the iterative optimization procedure. So, a large number of iterations is less a problem, allowing a larger number of design variables.
- Of course there are some disadvantages too e.g.
- Care is needed to stay within feasible pressure distributions.
 - Curvature effects on the boundary layer development are taken into account for the starting geometry only and might be different for the new design.

Nevertheless, from a practical point of view, optimization of the (target) pressure distribution is promising and the present study investigates some of the possibilities.

4. Problem definition and parametrization

In order to make the definition of 2D target pressure distributions accessible for numerical optimization techniques, the pressure distribution has to be described by a limited number of characteristic parameters. The problem faced is; define a large class of possible pressure distribution shapes by means of as few as possible design parameters. Once the pressure distribution defined, only boundary layer calculations are needed to judge the quality of it (drag, transition location, etc.). There are some design problems best solved by defining a specific function for (a part of) the pressure distribution (an example will be shown in paragraph 5.5). However the main body of the present study concerns the description of a 2D pressure distribution in general terms by means of so-called aerodynamic shape functions.

It will be clear that in actual design practice a number of possible object- and constraint functions can be defined. However, a description of them all is beyond the scope of the present report. Some of them will be mentioned at the presentation of a few examples in chapter 5. Here, only the parametrization of the pressure distribution will be dealt with in more detail.

Roughly speaking, the velocity distribution on the airfoil upper- and lower surface can be characterized by three specific regions:

- (I) Stagnation point, immediately followed by a rapid acceleration.
- (II) A region with slightly accelerating, slightly decelerating or constant velocity, for transonic conditions often ended by a shock wave.

(III) The pressure recovery region where the velocities decrease to the trailing edge value. For the lower surface of rear loaded airfoils completed by a small region with accelerated flow. Figure 5 presents a characteristic pressure distribution defined by eight points and linear interpolation between these points. Without shock, points 2 and 2' coincide. With shock, the jump between 2 and 2' is determined by the local mach number at 2. For a given free stream mach number the points 4 (stagnation pressure) and 1 and 8 (trailing edge pressures) are considered to be known and fixed. This leaves level and position of the points 2, 3, 5, 6 and 7 (ten design variables) free to represent a large class of (simplified) pressure distributions. Refinement of this model would be possible by increasing the number of "characteristic" points. However, soon large number of points will be needed to represent more realistic shapes, resulting in a prohibitive large number of design variables. Other ways for refinement are, e.g. non-linear interpolation between the points; adding wave functions with amplitudes as design variables to a starting pressure distribution etc. Several of these options have been investigated during the present study. So far, best results have been obtained by a set of "interpolation rules", taking into account the characteristic behaviour of the specific part of the pressure distribution to be represented. Each of these so-called aerodynamic shape functions has been derived from well known aerodynamic theory. It is beyond the scope of the present report to describe the derivation of these functions in detail. It has to be sufficient to present the relations and to note that for certain combinations of the design variables (coefficients and exponents), approximations are possible of the typical classical flow characteristics. The following functions have been defined, with reference to figure 5.

A. Stagnation flow region (3-4-5)

Rather than suggested in figure 5, the stagnation point (4) will usually not occur exactly at the airfoil nose but somewhat downstream on the lower surface. In order to maintain physically realistic pressure distributions in this region, a stagnation flow shape function has been defined, approximating the potential flow velocity distribution for elliptic cylinders (for small x/c and small incidence):

$$\frac{u}{u_{\infty}} = \frac{(1+K_{a1}) \sqrt{K_{a3} \cdot \frac{x}{c}} \pm (K_{a2} + K_{a3} \cdot K_{a4} \cdot \frac{x}{c}) \sqrt{1-K_{a3} \cdot \frac{x}{c}}}{\sqrt{K_{a3} \frac{x}{c} + \frac{1}{4} K_{a1}^2}}$$

(N.B. + sign for upper surface; - sign for lower surface)

Here $K_{a1} - K_{a4}$ represent the design variables to be adjusted by the optimization procedure. Referring to the elliptic cylinder nose radius and (local) incidence at the nose may be estimated from.

$$\left(\frac{R}{c}\right)_{\text{nose}} = \frac{0.5}{K_{a3}} \cdot K_{a1}^2 (1-M_{\infty}^2) \quad \theta = K_{a2} \sqrt{1-M_{\infty}^2} \text{ [Radians]}$$

B. "High velocity" regions (from 3 to 2 and from 5 to 6, fig. 5)

These regions often exhibit small pressure gradients at design conditions. So, a relatively simple representation can be chosen. In order to be able to represent also laminar flow conditions the following function has been chosen.

$$\frac{u}{u_{\infty}} = K_{b1} + K_{b2} \left\{ \frac{x}{c} - \left(\frac{x}{c}\right)_{b0} \right\}^{1+K_{b3}}$$

which, for $(K_{b1}$ and $\left(\frac{x}{c}\right)_{b0}$ approaching zero, approximates the well known Falkner-skan solution for similar laminar boundary layers (index $b0$ refers to the start of the region). $K_{b1} - K_{b3}$ are the design variables to be adjusted by the optimization procedure.

C. Turbulent pressure recovery region (from 2 (2') to 1 and from 6 to 7)

The family of functions for this region should resemble concave and convex shapes, including the Stratford solution for turbulent zero skin friction pressure recovery (ref. 11). The Stratford solution exhibits two branches. The main branch, transformed from Stratford's canonical pressure coefficient to the ordinary C_p definition, can be generalized as follows:

$$C_p = C_{p_{c0}} + K_{c1} \left[\left(1 + \frac{\frac{x}{c} - \left(\frac{x}{c}\right)_{c0}}{K_{c2}} \right)^{1/5} - 1 \right] K_{c3}$$

Index $c0$ indicates the start of the recovery region and K_{c1} to K_{c3} are the design variables. This function represents a wide class of shapes, including an approximation of Stratford's pressure recovery solution.

D. Rear loading region (from 7 to 8)

For so called rear loaded airfoils, the lower surface velocity usually accelerates from the end of the pressure recovery region to the trailing edge. For this region, a simple polynomial was defined reading:

$$C_p = K_{d1} \left\{ \frac{x}{c} - \left(\frac{x}{c}\right)_{d0} \right\}^2 + K_{d2} \left\{ \frac{x}{c} - \left(\frac{x}{c}\right)_{d0} \right\} + C_{p_{d0}}$$

Again index $d0$ indicates conditions at the start of the region and K_{d1} and K_{d2} are design variables.

E. Shock relations (possibly at points 2 and/or 6)

Good transonic design conditions usually incorporate weak shocks at upper and/or lower surface. So, a

proper shock description is needed. In viscous airfoil flow, the pressure jump measured at the foot of the shock is less than the Rankine Hugoniot pressure jump. Besides, the shock will be "smeared out" in the boundary layer. So, in order to describe shocks directly in the pressure distribution some empirical relations are needed. From a compilation of experimental data (see fig. 6, taken from ref. 12) it is seen that the following modification of the Rankine Hugoniot relation is a reasonable approximation for weak 2 dimensional shocks ($M_1 < 1.3$):

$$\frac{P_{ds}}{P_{us}} = 0.7 \left[\frac{7M_{us}^2 - 1}{6} \right] + 0.3 \quad C_{p_{ds}} = C_{p_{us}} + 0.7 \left\{ C_{p_{us}} + \frac{1}{0.7 M_{us}^2} \right\} \left(\frac{7(M_{us}^2 - 1)}{6} \right)$$

(us and ds for upstream and downstream of shock).

An empirical rule for the shock thickness is presented by Delery (ref. 13) for weak 2 dimensional shocks:

$$\frac{\Delta x}{\delta_{us}^*} \sim 70 (H_1 - 1) \quad [M_{us} \leq 1.3]$$

Here δ_{us}^* and H_1 represent displacement thickness and kinematic boundary layer shape parameter respectively, just in front of the shock. The shock representation becomes active only if M_{local} exceeds 1.1 at point 2 and/or point 6.

Characteristic points and functions presented above represent a rather large class of airfoil design pressure distributions. Note that not all of the design variables indicated above are independent. Some of them are directly determined by the requirement of a continuous pressure distribution. With properly selected basic airfoil geometry and design requirements, a boundary layer calculation method and an optimizer as driver for defining the pressure distribution almost all ingredients are available for a system for designing airfoil target pressure distributions. However for transonic conditions with shock waves boundary layer calculations only do not account for the momentum loss through the shock. So, the evaluation of the pressure distribution has to be completed with an evaluation of the wave drag. A convenient relation to estimate the magnitude of the wave drag has been proposed by Lock (ref. 14):

$$C_{dw} = 0.243 \frac{R_s}{c} \left[\frac{1+0.2 M_\infty^2}{M_1} \right]^3 \left[\frac{(2-M_1)(M_1-1)^4}{M_1(1+0.2 M_1^2)} \right]$$

Where R_s is the radius of curvature of the airfoil geometry at the shock position. Lock found an accuracy between -10% and +30% of the wave drag for weak shocks ($1.1 < M_1 < 1.5$), which seems sufficient for the present application.

Finally some remarks concerning the parametrization described above:

- It becomes obvious that the aerodynamic design problem is strongly non linear and it is likely that non-continuous derivatives will occur as well as for object function(s) as for constraint functions.
- Sometimes a step by step approach is possible by splitting the design problem in several optimization problems of reduced size, e.g. deal with upper- and lower surface separately.

5. Examples

5.1. General

Unless otherwise stated the examples to be shown have been calculated for the parametrization as presented in chapter 4. Drag and boundary layer characteristics have been computed with an integral method (ref. 15).

This method comprises:

- Laminar boundary layer according to Thwaites
- Prediction of transition location according to Granville
- A fast integral method (lag entrainment) for the turbulent boundary layer
- Drag calculation according to Squire & Young formula

For every application, some care is needed in the exact formulation of the design problem. This is illustrated in fig. 7. Given the basic distribution (a) and define the following design problem:

- $M_\infty = 0.50$ $Re_c = 10 \cdot 10^6$
- . maximize : C_l
 - . subject to : $C_{p_{min}} \geq -2.0$
(x/c)_{sep} ≥ 0.95
 - . change only upper surface distribution ($C_{p_{te}}$ fixed)

This formulation will result in the unrealistic distribution (b), in itself a perfect solution of the defined problem. The following, slightly different formulation for the same free stream conditions will do far better:

- . maximize : C_l
- . subject to : $C_{p_{min}} \geq -2.0$
($C_{p_{te}} - C_{p_{sep}} \leq 0.2$)
- . change only upper surface distribution ($C_{p_{te}}$ fixed)

Then result (c) will be obtained. Although, it might be necessary to adjust a few times the constraint on ($C_{p_{te}} - C_{p_{sep}}$) in order to drive the separation position closely to 95% of the chord. The main features of the present design procedure will be discussed on the basis of some typical examples, presented below.

5.2. Medium speed natural laminar flow condition

The intention is to investigate possible lengths of laminar flow trajectories for a thick (18%) medium speed ($M_\infty = 0.65$) airfoil. To start with, the geometrical requirement of $t/c = 18\%$ has to be translated in a constraint function for the pressure distribution. A first order estimation of the max.

airfoil thickness is obtained by:

$$t/c \approx -0.5 \bar{C}_p \sqrt{1-M_\infty^2} \text{ where } \bar{C}_p = \int_0^1 \frac{C_{p_u} + C_{p_l}}{2} dx$$

Large laminar flow regions imply low airfoil drag. Then, together with the additional constraint to maintain subsonic flow in the design condition the following problem is formulated:

free stream conditions: $M_\infty = 0.65$, $Re_c = 15.10^6$

minimize : C_d

subject to : $C_l \geq 0.50$

$$C_{p_{min}} > -\frac{1.01}{0.5 \bar{C}_p \sqrt{1-M_\infty^2}} = 0.18$$

no separation

(transition free)

Fig. 8 presents the solution for this problem. A quick, first order solution was obtained with a simple representation of the pressure distribution (broken line); a linear interpolation between "free" points for the front part and a quadratic interpolation for the rear part of the airfoil. Then the representation was refined, using the aerodynamic shape functions discussed above, resulting in the full line.

This case study showed that:

- .. The design domain contains several local minima and some different start C_p -distributions were needed to arrive at the final solution.
- .. Approaching low drag values, the cost function C_d becomes "flat" and so sensitive to numerical irregularities. Numerical irregularities are easily introduced because the pressure distribution is discretized as input for the boundary layer calculations.

5.3. Low speed high lift condition

The design of single element, high lift airfoils by R.H. Liebeck is well known (see e.g. refs 16, 17). A.M.O. Smith (ref. 17) published some of Liebeck's results for the so-called turbulent roof-top. The airfoils meet the additional constraints for the flow to remain attached (and subsonic) everywhere on the airfoil. Then the following design problem is formulated:

free stream condition: $M_\infty = 0.10$, $Re_c = 5.10^6$

transition : upper surface $x/c \geq 1\%$

(lower surface: $x/c \geq 0.51$)

maximize : C_l

subject to : no separation

This problem has been solved by changing only the upper surface pressure distribution for a fixed, arbitrarily chosen, lower surface distribution. Two solutions have been generated, both depicted in fig. 9.

- a. With a fixed, approximated Stratford type pressure recovery the flat rooftop solution is found (full line). This compares reasonably well with Liebeck's optimal solution presented in ref. 17, indicating max. lift for $C_{p_{min}} \approx -2.6$ and pressure recovery point at $x/c \approx 0.30$.
- b. With the upper surface entirely free, the broken line is found, representing a slightly better solution than the roof top solution.

Airfoil geometries, inversely calculated, for these two solutions have also been given in fig. 9. The geometries have been computed with the method described in ref. 18.

Note: keeping in mind the approximations made for the present representation (for example, only one branch of the Stratford solution is considered), the above results are not considered to prove that Liebeck's flat roof top solution can be improved. However, it may be concluded that, from a practical point of view, both solutions exhibit comparable high lift capabilities, while solution b has the advantage of a somewhat less "exotic" geometry.

From this example it is concluded that the aerodynamic shape functions are applicable for low speed high lift design.

5.4. Transonic low drag solution

A typical transonic pressure distribution is shown in fig. 10 (full line). In order to find out to what extent this pressure distribution can be represented by the aerodynamic shape functions CADOS was used. With ΔC_p being the difference between the real and the shape function distribution, the functional $\int \Delta C_p dx$ was minimized. The result, designated best fit, is shown in fig. 10 as broken line.

Apparently, the shape functions lack refinement around the shock and in the nose region. To find out how serious a problem this is, for the practical design situation. A design study has been performed to improve the drag coefficient at the design lift coefficient. With the best fit as starting point the following optimization problem was defined.

free stream condition : $M_\infty = 0.77$ $Re_c = 10.10^6$

transition fixed at : $(x/c)_{us} = 0.05$ $(x/c)_{ls} = 0.10$

minimize : C_d

subject to : $C_l \geq 0.60$

$$C_m \geq -0.125$$

thickness $(= -0.5 C_p / (1-M_\infty^2)) \approx 0.10$, being the same value as for the best fit (actual starting airfoil $t/c = 0.11$)

The optimized pressure distribution is shown in fig. 11, together with the start ("best fit") indicating a drag improvement of 5 counts.

Then two possible ways are open to continue the design study.

1. Define a new target pressure distribution by adding the differences between best fit and optimized distribution to the actual airfoil pressure distribution.
 2. Define the optimized pressure distribution directly as the target for a new geometry design.
- Here, the latter approach was followed. In order to find out whether a less refined target will result in an acceptable airfoil design. Using the inverse airfoil design system INTRAFS (ref. 19), a new geometry has been generated. The new geometry differs only slightly from the original one. Analyses of both airfoils with the VGG program (ref. 20) indeed shows an improved drag coefficient for the new airfoil (see fig. 12). Although the drag reduction is less than expected from the CADOS calculations depicted in fig. 11;

three counts versus 5 counts, maybe due to the relative poor representation of the original pressure distribution. Nevertheless this example illustrates the ability of the present approach to improve transonic airfoil design.

5.5. Stable laminar flow

The last example to be discussed here is of a more fundamental character and differs from the design studies presented so far. It is an illustration of a special application of target pressure distribution optimization. The problem concerns the definition of the max. lift contribution that can be obtained with stable laminar flow over the first 60% of an airfoil. Stable with respect to the instability criterium for Tollmien Schlichting waves; instability occurs if $\frac{Re\theta}{Re\theta_1} > 1$. With the requirement of just sonic conditions at $s/c = 0.60$ for $M_\infty = 0.65$ and $Re_c = 15 \cdot 10^6$. Then the problem definition reads: find the C_p -distribution between $s/c = 0$; $M_{loc} = 0$ and $s/c = 0.60$; $M_{loc} = 1.0$ such that $\int_0^{0.6} C_p ds/c$ is maximum while everywhere $\frac{Re\theta}{Re\theta_1}$ approaches 1.0 as close as possible; or minimize $\int_0^{0.6} C_p ds/c + \int_0^{0.6} \max(0, \frac{Re\theta}{Re\theta_1} - 1) ds/c$. After a few attempts with different relations for $C_p = f(s/c)$ it was observed that reasonable results could be obtained with the following relation for the pressure gradient:

$$\frac{dC_p}{ds} = \frac{A}{s+c} + B\left(\frac{s}{c} + \epsilon\right)^N, \text{ where } \epsilon \text{ is a small value, to prevent the singularity at } \frac{s}{c} = 0.$$

Then, by integration:

$$C_p = C_{p_{st}} + A \ln\left(\frac{s+c}{c}\right) + B\left\{\left(\frac{s}{c} + \epsilon\right)^N - \epsilon^N\right\}$$

Where A , B , ϵ (> 0) and N are design variables and $C_{p_{st}}$ is pressure coefficient at stagnation point. Three of the design variables are independent, the fourth follows from the requirement of sonic flow at $s/c = 0.60$. Fig. 13 shows the results of the above problem. The C_p distribution for stable laminar flow over the whole region is depicted in fig. 13a, while fig. 13b shows that indeed $Re\theta$ and $Re\theta_1$ nearly coincide over the largest part of the region. These results were relatively easily obtained.

6. Concluding remarks

The application of constrained numerical optimization techniques in the inverse airfoil design procedure has been investigated. Taking into account physical flow characteristics, a set of aerodynamic shape functions has been formulated. It is shown that with these shape functions a wide class of airfoil flows is represented. Parametrization of the pressure distribution in combination with numerical optimization techniques enable the designer to define or improve 2D target pressure distributions.

With respect to the course of the optimization process, the following experiences have been obtained.

- The aerodynamic design problem is strongly non-linear and exhibits discontinuous derivatives for object as well as constraint functions. In general, a large number of local minima occur. So, a straight forward application of numerical optimization techniques which rely on first and second order derivatives is highly questionable. So far, best results have been obtained with a simple line search method (SIMPLEX).
- It is more efficient to define a combined object- and penalty function, rather than to bound the object function by constraints.
- Optimization for minimum drag is hampered by the "flat" shape of the drag function in the design space, in combination with numerical irregularities.
- In general a large number of iterations will be needed (several hundreds)

Despite the fact that a large number of iterations is not a serious drawback for the present approach, the procedure is still far from "stand alone" applications on routine basis.

The method, reviewed in the present paper, already has proven to be of significant value for the airfoil design practice at NLR. It is worth to consider improvements by paying attention to the following items.

- Smoothing options, to prevent problems with numerical irregularities.
- Splitting of the optimization problem in a number of problems of smaller scale (multi-level optimization).
- Looking for more efficient routines, taking into account the specific character of the aerodynamic design problem.
- Scaling of the independent design variables (The existing version of CADOS offers the user the possibilities to adjust the step for each variable, but in practice it is hardly possible to overview the consequences).

Acknowledgement

Important contributions to the present study have been provided by J.W. Boerstoele and A. Kassies by the definition and development of interactive system CADOS and by J.W. Slooff, who supplied ideas and suggestions for the definition of the aerodynamic shape functions.

7. References

1. van den Dam, R.F. Constrained spanload optimization for minimum drag of Multi-lifting-surface configurations
Paper presented at this conference, may 1989
2. Brandsma, F.J.
Fray, J.M.J. Insyst: A System for Transonic Wing Design with Geometric Constraints Based on an Inverse Method
Paper presented at this conference, may 1989
3. Vanderplaats, G.N. Numerical optimization techniques for engineering design: With applications
Mc. Graw-Hill Book Company, 1984
4. Kassies, A. User's Guide of CADOS, Version 1 NLR Memorandum IN-84-034 U
5. Fletcher, R. Practical Methods of Optimization, Wiley Chichester, 1981
6. Pierre, D.A. Optimization Theory with applications, John Wiley & Sons, 1969
7. Hicks, R.M. Airfoil Section Drag Reduction at Transonic Speeds by Numerical Optimization,
Vanderplaats, G.N. SAE Paper 760477, 1976
8. Misegades, K.P. Airfoil Optimization
AIAA Paper 84-0053, 1984
9. Vanderplaats, G.N. Approximation Concepts for Numerical Airfoil Optimization
NASA TP-1370, March, 1979
10. Aidala, P.V.
Davis, W.H.
Mason, W.H. Smart Aerodynamic Optimization
AIAA Paper 83-1863, 1983
11. Stratford, B.S. The Prediction of Separation of the Turbulent Boundary Layer
J. Fluid Mech. Vol 5, 1959
12. Tijdeman, H. Investigations of the transonic flow around oscillating airfoils. Dissertation
Technical University Delft, the Netherlands, 1977
13. Delery, J. L'Interaction onde de choc-couche limite turbulente et son controle,
AGARD-CP-365 Paper 21, 1984
14. Lock, R.C. Prediction of the drag of wings at subsonic speeds by viscous/inviscid
interaction techniques
AGARD-R-723, 1985
15. Green, J.E.
Weels, D.J.
Brooman, J.W.P. Prediction of turbulent boundary layers and wakes in compressible flow by a
lag-entrainment method
ARC R and M No. 3791, 1973
16. Liebeck, R.H. On the design of subsonic airfoils for high lift.
AIAA Paper No. 76-406, 1976
17. Smith, A.M.O. High lift Aerodynamics
AIAA Paper No. 74-939, 1974
18. Labrujère MAD, a system for computer aided analysis and design of multi-element airfoils
NLR TR 83136 L, 1983
19. Fray, J.M.J.
Slooff, J.W.
Boerstool, J.W.
Kassies, A. Design of transonic airfoils with given pressure, subject to geometric
constraints,
NLR TR 84064 U, 1984
20. Lock, R.C. The prediction of viscous effects on aerofoils in transonic flow
RAE TM Aero 1780, 1978

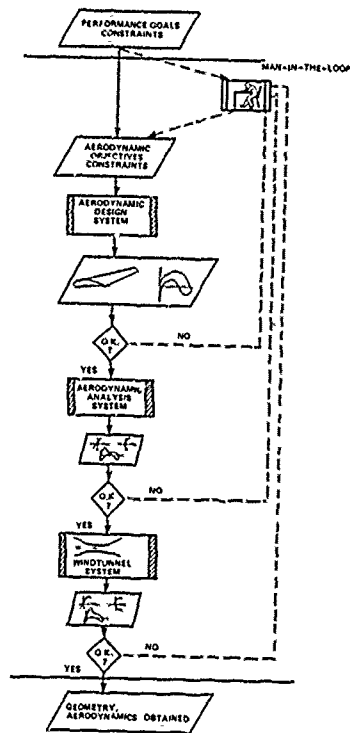


Fig. 1 Typical flow chart for aerodynamic design process

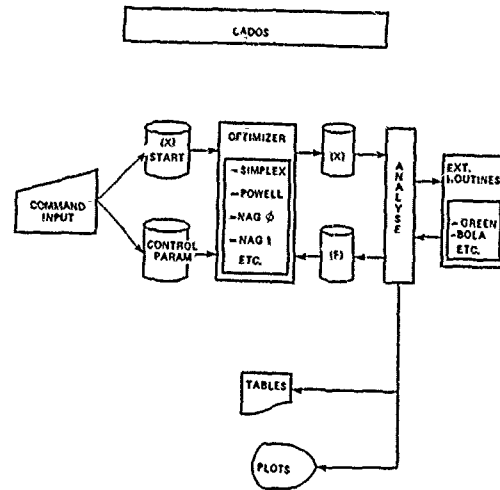


Fig. 2 Scheme of CADOS

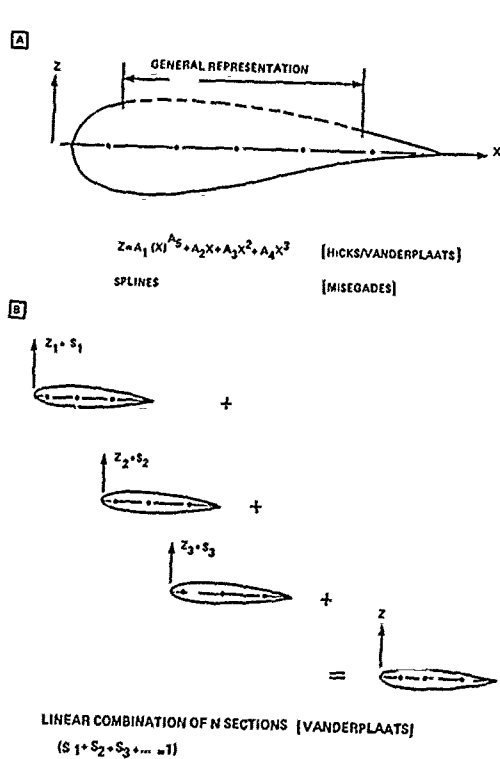


Fig. 3 Examples of "direct" design procedures

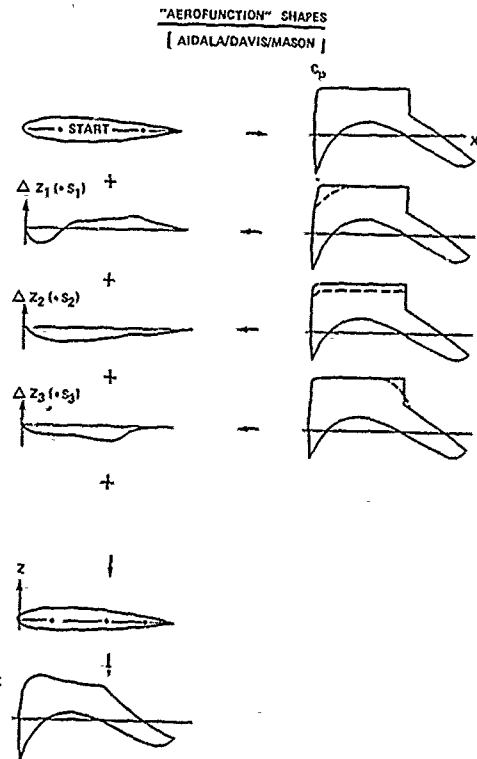
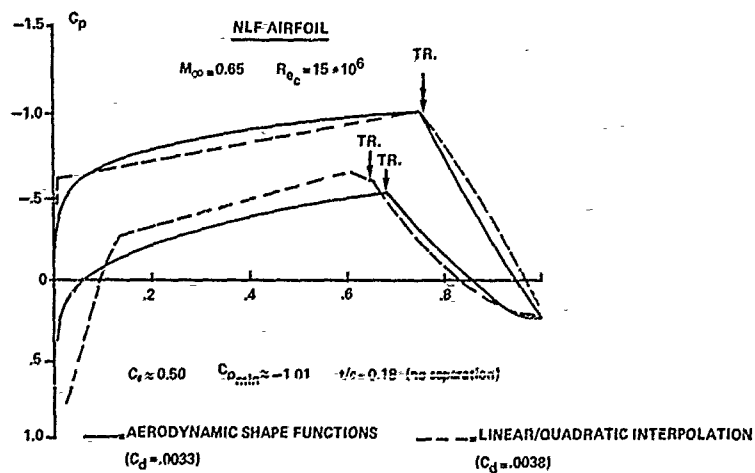
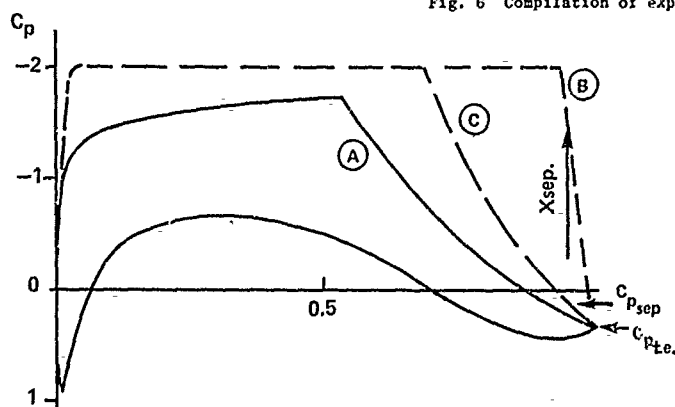
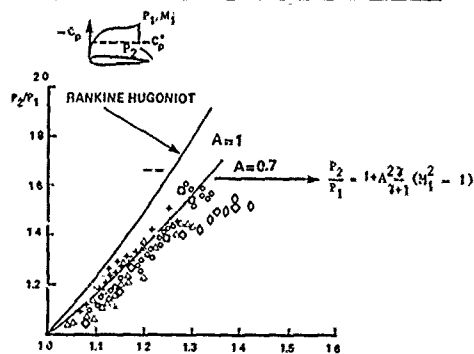
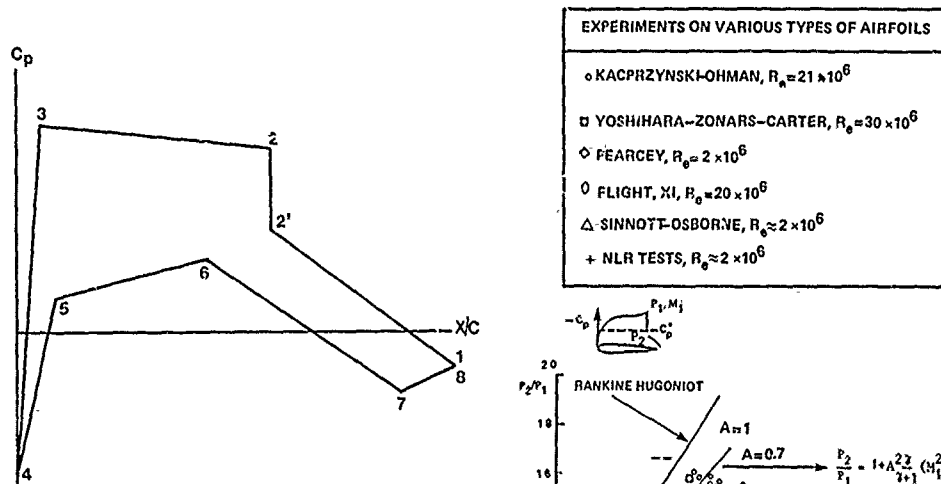


Fig. 4 Schematic representation of method from ref. 10



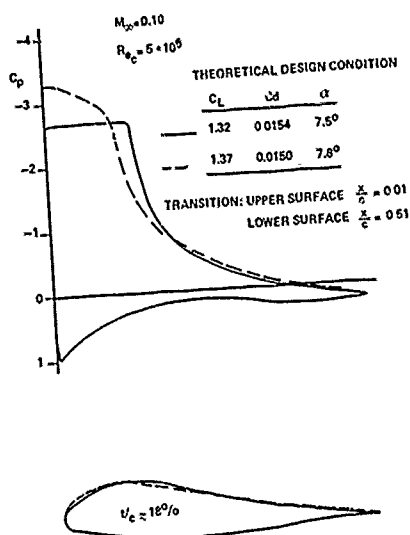


Fig. 9 High lift solutions

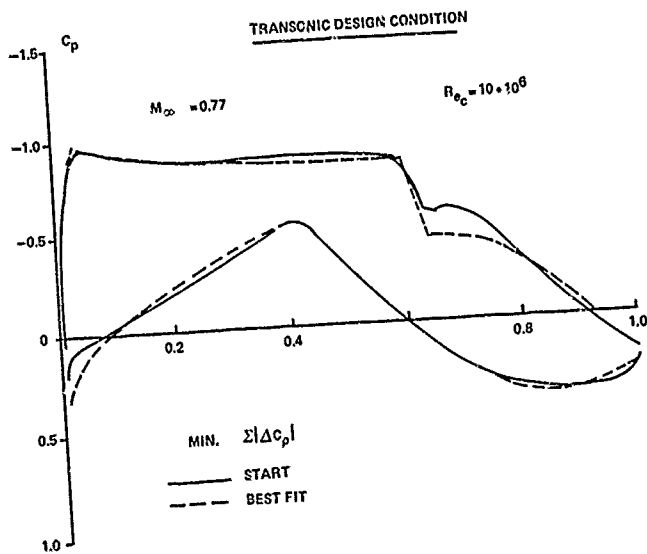


Fig. 10 Start condition

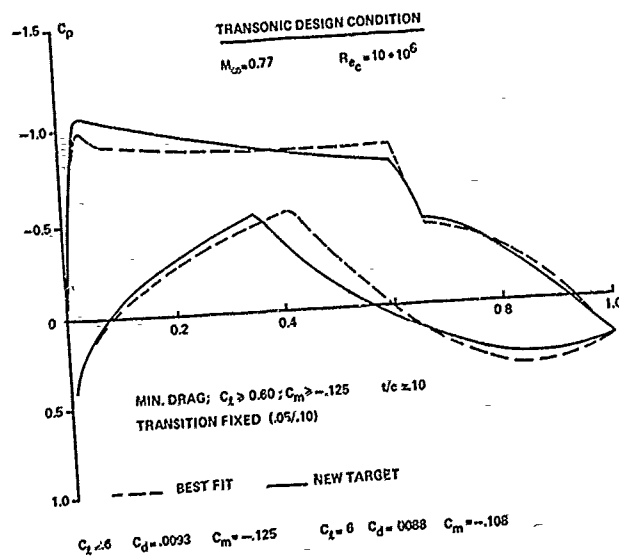


Fig. 11 Optimized target compared with start (aerodynamic shape functions)

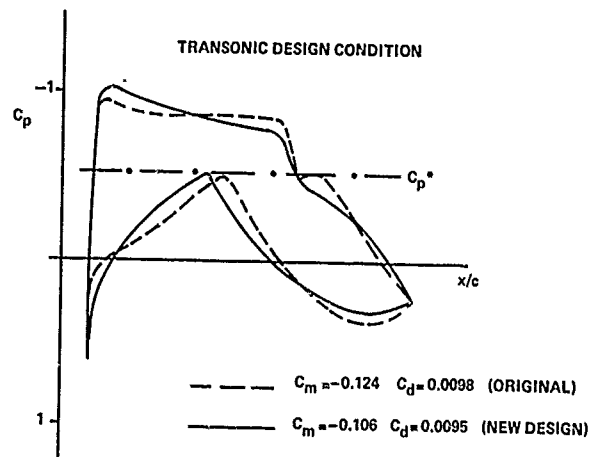


Fig. 12 VGK-analysis ($M_\infty=0.77$, $C_L=0.6$, $Re_c=10 \cdot 10^6$)

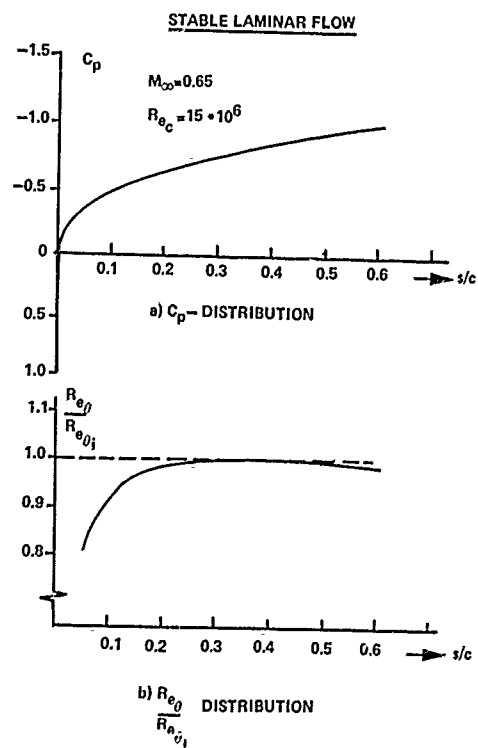


Fig. 13 Solution for stable laminar flow

A TOOL FOR AUTOMATIC DESIGN OF AIRFOILS IN DIFFERENT OPERATING CONDITIONS

by

L. Ghislini
Aerodynamics Engineer
Advanced Studies Department, Aermacchi S.p.A.
21100 Varese, Italy

and

R. Marazzi
Aerodynamics Engineer, Consultant
AEOLUS s.r.l.
Castronno (VA), Italy

A. Baron
Professor of Applied Fluid Dynamics
Aerospace Department, Politecnico di Milano
Via Golgi 40
20133 Milano, Italy

SUMMARY

An optimization procedure is described which applies to the design of airfoils able to satisfy requirements essentially set for transonic flight.

Suitable airfoils are obtained through radical changes of the starting geometry with little time consumption.

One of the main features of the design methodology is an extensive use of constraints; it proved to be very efficient both to obtain a good quality of the design and to reduce the time needed.

Another feature is the use of effective shape functions, which are not aerofunctions obtained through inverse methods.

The results show airfoils designed to satisfy both a maneuver and a dash performance requirement.

A comparison of different design approaches is also presented; this is made possible by the short times required for the design, which includes the optimized deflections of the L.E. and T.E. flaps.

Suggestions are given for further developments of a "smart" system for airfoil design.

1. INTRODUCTION

The results obtained through the adoption of optimization techniques for the design of wings and airfoils justify their use in the industry even if the success of an automatic design method is not secure a priori and these methods normally require great expertise /1/, /2/, /3/.

The reason for this is that an automatic design procedure must compound a large amount of knowledge to obtain a physically acceptable final solution which meets the actual operating requirements.

The aerodynamic optimization problem must not be considered as a routine exercise with a mathematical procedure; it must in fact manage checks able to produce an actually usable final result, also on the basis of comparisons with already obtained solutions.

Several authors have focused their attention on the development of effective modification functions: these are the shapes that, when added to the basic airfoil, permit its iterative modification. When these functions have a well defined effect on an aerodynamic characteristic, they are called aerofunctions and are often obtained through inverse methods.

Occasionally, the adoption of this type of modification functions permits the optimization methods and the inverse ones, that are usually considered mutually exclusive design tools /4/, /5/, /6/, to be conciliated.

Other techniques have been proposed which pursue the reduction of the number of airfoils to evaluate during the optimization process /7/. One of them suggests the adoption of second order approximations of the aerodynamic coefficients /8/.

This work describes an effective tool which modifies an arbitrary starting geometry to satisfy design requirements typical of the transonic range. The methodology emphasizes the use of the constraint functions, different from what has been used by many authors. An effective use of constraints is advantageous both in terms of design quality and of less time consumed is described in detail herein.

The shape functions used in this investigation are not obtained through inverse methods, but have a foreseen aerodynamic effect and retain their effectiveness when applied to a wide range of problems.

When showing the results, emphasis was placed on the comparison of the different design approaches made possible by the use of an optimization procedure.

2. THE COMPONENTS OF THE DESIGN PROCEDURE

The optimization problem consists of the definition of the values to assign to the vector of the design variables \bar{X} so as to minimize the objective function $F(\bar{X})$ (OBJ), while obtaining that the possible constraint functions $G_i(\bar{X})$ are ≤ 0 . The mathematical formulation of these functions is a responsibility of the designer, who also has to choose the design variables that govern the geometry. Elements of these functions are the aerodynamic coefficients, which are obtained through the coupling with an analysis code.

The selected optimization routine was algorithm CONMIN (CONstrained MINimization) /9/. This routine is widely used in the structural optimization field, and is used by several authors for aerodynamic design.

Since the routine permits constraint functions to be used, it sets no limitations on the inclusion of design controls which can be essential to obtain an actually usable final geometry. The routine solves the constrained minimization problem by following the steps described hereafter.

At each iteration "i" of the minimization process, the variable vector (\bar{X}) is updated according to the formula $\bar{X}_i = \bar{X}_{i-1} + w\bar{S}_i$, where \bar{S}_i is a unit vector representing a direction in a space having as many dimensions as the design variables, and w defines the displacement in direction \bar{S}_i .

Three methods for the search of direction \bar{S}_i are implemented in CONMIN. If the variables lay at a point in the space of the design variables where the constraints are not violated (that is all functions $G_i(\bar{X}) < 0$), two methods are employed that use information on gradients: They are the "steepest descent" (point A in fig. 1) and the "conjugate direction method" (point B of figure 1); the latter method also makes use of information from the previous iteration /1/. If one or more constraints are active ($G_i(\bar{X}) = 0$) or violated ($G_i(\bar{X}) > 0$), Zoutendijk's "feasible direction method" is used /1/: \bar{S}_i is chosen also based on the gradients of the active and violated constraints. In Fig. 1, one constraint is active at point C and one constraint is violated at point H.

The coupling of the optimization routine with an aerodynamic code requires approximation techniques. The aerodynamic coefficients in fact depend in a non-linear way on the design variables that are the perturbations to which geometry is subjected during the modification. These coefficients can be approximated by using the TAYLOR series:

$$F(\bar{X}) = F(\bar{X}_0) + \nabla F(\bar{X}_0) \delta \bar{X} + \frac{1}{2} \delta \bar{X}^T H(\bar{X}_0) \delta \bar{X} + \dots$$

where $F(\bar{X}_0)$ is the objective function or a constraint function, $\nabla F(\bar{X}_0)$ is the gradient and $H(\bar{X}_0)$ is the Hessian; $\delta \bar{X} = \bar{X} - \bar{X}_0$ is the perturbation vector.

The design problem is solved by modifying the geometry iteratively. The aerodynamic coefficients are linearized and the derivatives with respect to the design variables are updated at each iteration (sequential linear programming) /1/.

A scheme of a linearized problem is shown in figure 2. The maximum change of the value of the variables at each iteration is limited by the use of "side constraints".

This procedure is used for two reasons: not to impair the validity of the linear approximation and to face cases in which the objective function of the linearized problem is not constrained, contrary to what happens in the non linear problem (Fig. 2).

The aerodynamic analysis code plays an important role because it gives the values of the derivatives of the coefficients with respect to the design variables. Based on these derivatives, the optimization routine chooses the most suitable modification direction. The more reliable the aerodynamic code is, the more credible is the design. However, the design management, namely the interface between aerodynamic code and CONMIN, is fully independent of the aerodynamic code adopted and represents the true "heart" of the procedure.

The analysis code solves the full potential equation in subsonic and transonic range making use of a finite difference technique developed by A. Jameson. This code was made more complete with the inclusion of the computation of wave drag as a loss of momentum, across the shock wave, and of a viscous correction (AELFOIL code) /11/.

This code may obviously be replaced by a more sophisticated one (e.g. EULER SOLVER) /6/. In the automatic procedure, the design requirements must be "translated" in terms of constraint and objective functions.

A simple expression for the objective function includes the linear combination of aerodynamic coefficients (CD, CM, CL, Local Mach) at one or more operating conditions of the airfoil (n). In general, the coefficients must be weighted through multiplication coefficients.

For instance:

$$OBJ = \sum_{i=1}^n [K_{1i} CL(\alpha_i, M_i) + K_{2i} C_l(\alpha_i, M_i) + K_{3i} CM(\alpha_i, M_i) + K_{4i} Mach_{u.s.}(\alpha_i, M_i) + K_{5i} Mach_{l.s.}(\alpha_i, M_i)]$$

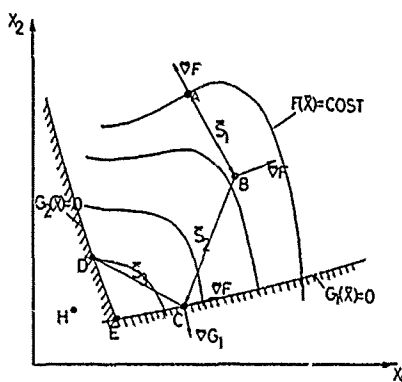


FIG. 1 MINIMIZATION OF THE OBJECTIVE FUNCTION IN PRESENCE OF CONSTRAINTS, USING THE METHOD OF GRADIENTS

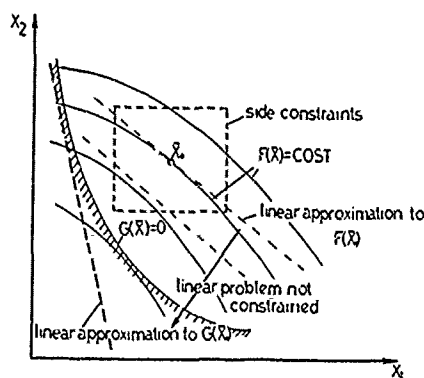


FIG. 2 "SIDE CONSTRAINTS" TO FACE SHORTCOMINGS OF THE SEQUENTIAL LINEARIZATION OF THE PROBLEM

where the index i defines the operating condition in which the coefficient is used. Geometric constraints are utilized, some of which serve to control aerodynamic characteristics in first approximation. For instance leading edge separation stall or loss of leading edge suction are connected with the value of the ordinates at the airfoil nose.

The aerodynamic constraints are used to control the values of the design coefficients (typically CL or CM).

The expression used for the constraints is as follows:

$$G = K \cdot (V - \bar{V})$$

where V is an aerodynamic coefficient or a geometrical parameter, \bar{V} is a limit imposed on it, and K is a multiplication factor.

In our exercises a constraint is active if $-0.01 < G(\bar{X}) < 0.001$, satisfied when $G(\bar{X}) < -0.01$, and violated when $G(\bar{X}) > 0.001$.

The multiplication factor K is used to "scale" the just specified values to constraints set on coefficients and parameters of different nature (aerodynamic rather than geometric), and which, in general, have different orders of magnitude.

3. EFFECTIVE USE OF THE AUTOMATIC DESIGN PROCEDURE

Our experience tells us that an objective function easy to manage contains only the aerodynamic coefficients which must be minimized. A real design problem can be fully formulated only by resorting to the constraint functions.

Some of these constraints, typically the geometric ones, govern the shape: it is often required that a dimension (ordinate, angle, etc), when modified, does not exceed a limit value suggested by experience, or is forced to attain a pre-set limit.

In the latter case, the constraint is initially violated and, as such, has a large weight in the assignment of the values to the modification variables. This is true to the extent that directly controlled aerodynamic requirements (controlled through the objective function) may be overlooked. To prevent this, we thus assign the right importance to the geometrical control, constraints are set on the aerodynamic coefficients even if they appear in the objective function; in this case, the initial solution deliberately violates the constraints.

Other aerodynamic constraints are used if there exist specific design values from which it is not desired to depart. A typical case is the one of the CL s controlled through the constraints instead of through the inclusion of terms of the $K(CL - \bar{CL})^2$ type in the objective function (\bar{CL} is the design value).

The use of constraints is here preferred to avoid a dynamic assignment of the weights (K) to the different terms included in the objective function. If this were not done in fact, the terms would be numerically different from one another, thus they would not have the same "importance".

Moreover, if terms are added, there is no guarantee that the value of all terms appearing in the objective function decreases during the optimization procedure.

The described example emphasizes that the role of the constraints is not only to discipline the modification, but also to complete the objective function. Besides, the careful choice of suitable values for the expressions of the constraints permits the

number of subsequent linear approximations of the problem to be reduced. Therefore, the refinement of this work makes use of geometrical and aerodynamic constraints that may be violated in the initial phase of the procedure.

As already said, the value of each of these expressions can be "adjusted" by use of a multiplication coefficient. For an effective management of the problem, it is convenient to choose the value of the coefficients so that the expressions of the violated constraints have values of different orders of magnitude. In this respect it is essential to ensure that, during optimization, the value of the violated constraints decreases progressively, so that the risk that different constraints may reach equal violation values also is avoided. It should also be remembered that the weight of a constraint is larger the more it is violated.

A concrete example permits the above qualitative discussions to be quantified (this description reports beforehand some of the results detailed in para 4).

The purpose of the design exercise is to decrease wave drag ($CDW(0.0020)$) in a transonic maneuver condition at high CL ($M=.745$ and $CL=.855$) and in a dash condition ($M=.845$ and $CL=.065$) for an airfoil having maximum thickness $t=5\%c$.

The initial geometry is a symmetric four-digit NACA 4 modified airfoil. A variant of this airfoil is searched by optimizing the thickness distribution and the ordinates of the camberline.

In the objective function:

$$CDW(\alpha_1, M_1) + CDW(\alpha_2, M_2)$$

the minimization of CDW is activated in the two design conditions.

The activated constraint functions are several; they are described in detail hereafter.

- Aerodynamic constraints on CL

An upper and a lower constraints are set for each value of CL . To obtain $CL = .855$ (maneuver), the limits are .8525 and .8575; to obtain $CL = .065$ (dash), the limits are .06 and .07.

The initial geometry is chosen at angles of attack at which these constraints are initially violated; for instance at $M=.745$ (maneuver) and $\alpha_1 = 2.4^\circ$, the airfoil gives $CL=.45$, and at $M=.845$ and $\alpha_2 = -1.3^\circ$, it gives $CL=-.35$. This choice was made on purpose to exploit the design variables to the fullest, as will be discussed later.

- Geometrical constraints

Several constraints are used to control the aerodynamic characteristics in first approximation.

A control is set on the minimum value of the ordinate of the airfoil upper surface at $x=1.25\%c$ ($Y(1.25)$) to improve performance in terms of leading edge suction recovery at subsonic Mach numbers. In the initial geometry $Y(1.25)$ is equal to .00753, and the lower limit set during optimization is .0080.

A second constraint function is activated to restrict the value of the angle at the trailing edge: it is thus possible to ensure satisfactory margins between the drag rise and buffet onset boundaries. The initial airfoil has an angle of 8.86° and the imposed upper limit is 9° .

The thickness of the trailing edge is controlled through another constraint, which imposes that this thickness remains lower than .0080 in order not to incur in an unacceptable base drag.

- Other aerodynamic constraints

In spite of the presence of a CD wave in the objective function, constraints are activated on this coefficient to avoid that the geometrical coefficients are the only violated ones, thus excessively affecting the modification.

All the constraints just described are weighted in the following order:

- aerodynamic constraints on CL
- aerodynamic constraints on other coefficients (CDW in the present case)
- geometric constraints

as indicated in the summary table I.

The wide range of values of weighting factor K should be noted.

The choice of the order of magnitude of the constraint functions makes the modification very effective since some variables, the most effective ones, are increased, at each iteration, by a value very close to that permitted by the side constraints.

Fig. 3 shows the significant modification evolution over four iterations only: at the fourth iteration the modification variables have nearly exhausted their geometry shaping action.

If the constraints on CL had been originally satisfied rather than violated, as much as forty iterations would have been required to reach a solution similar to the one shown.

From the physical point of view this happens because, with violated constraints on C_L , the major modification is that of camber while α doesn't change much during the optimization. On the other end, with satisfied constraints on C_L , α changes much from the value required by a symmetric airfoil to the one required by a cambered geometry.

$$G = K * (V - \bar{V})$$

$$\bar{V} = \text{DESIGN VALUE}$$

CONSTRAINT	G	K	V	\bar{V}	Order of magnitude of violated constraints
HIGH CL Lower limit	.402	1	.45	.8525	10^{-1}
HIGH CL Upper limit	-.407	1	.45	.8575	
LOW CL Lower limit	.406	1	-.346	.06	10^{-1}
LOW CL Upper limit	-.416	1	-.346	.07	
CDW Maneuver	.031	20	.0030	.0014	10^{-2}
CDW Dash	.0176	20	.0023	.0014	10^{-2}
Y (1.25)	.0233	50	.00753	.0080	10^{-2}
T.E. angle	-.068	.5	8.86	9	
T.E. thickness	-.07	10	.0010	.0080	

TABLE I: INITIAL CONDITIONS

A fast increase in camber is thus slowed down because the change of alpha and the increase in camber must concurrently satisfy the initial design CL. This way of using the constraints makes it natural to control the value of the constraint expressions during the modification; this action is extremely useful to ensure the soundness of the final results in terms of design richness. If some constraints are noted to become more stringent than envisaged, it is always possible to modify the weighting coefficients of the expressions. The procedure is not required to solve the design exercise without checks; it is in fact preferred that the designer retains the possibility of taking action to remove unforeseen obstacles during the design development (for instance, a geometric constraint that can be relaxed). The problem is therefore formulated with a good degree of design completeness, while man-in-the-loop actions permit this completeness to be maintained throughout the procedure.

The direct action of the designer may, however, be reduced by resorting to an expert system for the design of airfoils, as reported in the conclusions. For instance, after the fourth modification iteration, the values of the expressions of the constraint functions have been updated, as shown in table II.

It is apparent that the modification progresses as expected. At the beginning, there were five constraint expressions > 0 (violated), two of which had an order of magnitude equal to 10^{-1} (see table I); at this point, only the two CDWs are violated, the order of magnitude being now 10^{-2} . In the following iterations, the modification direction will be affected mostly by the control of these two coefficients.

As envisaged, the CLs have rapidly reached the design values, even if the dash CL is still a little lower than required.

As far as the constraint expressions related to geometrical parameters are concerned, the one of the ordinate on the airfoil upper surface at $X/C = 1.25\%$ has easily changed from positive values (10^{-1}) to negative values (the requirement is thus met), while the two other parameters have changed very little.

In this exercise, the control on geometrical dimensions did not require the updating of the value of coefficients K during the modification development. If the constraint on Y(1.25) had been more difficult to satisfy than it was, action could have been taken by giving K a value < 50 (or a value > 20 to K of the CDWs); this would have prevented the geometrical requirements from resulting in an excessive penalization of the aerodynamic behavior at the transonic design points.

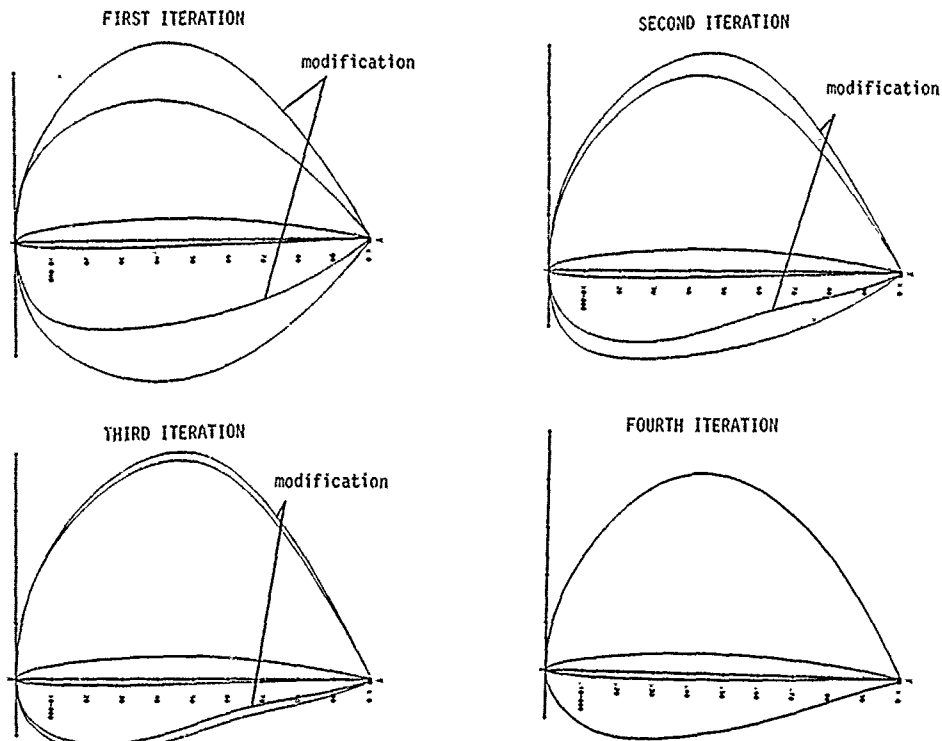


FIG. 3 AN EXAMPLE OF DESIGN PERFORMED THROUGH A RADICAL CHANGE OF GEOMETRY IN ONLY 4 OPTIMIZATION ITERATIONS. THE DESIGN VARIABLES MODIFY THE THICKNESS DISTRIBUTION, THE CAMBER LINE AND THE ANGLE OF ATTACK

$$G = K * (V - \bar{V})$$

\bar{V} = DESIGN VALUE

CONSTRAINT	G	K	V	\bar{V}	Order of magnitude of violated constraints
HIGH CL Lower limit	-.047	1	.855	.8525	
HIGH CL Upper limit	-.022	1	.855	.8575	
LOW CL Lower limit	.0007	1	.059	.06	
LOW CL Upper limit	-.010	1	.059	.07	
CDW Maneuver	.020	20	.0024	.0014	10^{-2}
CDW Dash	.018	20	.0023	.0014	10^{-2}
Y (1.25)	-.028	50	.00856	.0080	
T.E. angle	-.074	.5	8.85	9	
T.E. thickness	-.0704	10	.00098	.0080	

TABLE II: AFTER FOUR ITERATIONS

4. THE SHAPE FUNCTIONS

The final result of the modification is strongly influenced by the choice of the design variables.

Some geometrical shapes derived from the analysis of existing airfoils having specific aerodynamic features, cannot be obtained without suitable shape functions.

The shape functions can be classed in two main groups. The first includes the so-called aerofunctions /4/, /5/, that is the geometrical functions to which there is associated a well defined aerodynamic effect.

They are very effective, and a few of them are sufficient to modify the geometry; their use permits the number of aerodynamic analyses during optimization to be reduced.

These functions, however, are generally obtained through an inverse method; they are, therefore, tied to a given operating condition and depend heavily on the initial geometry.

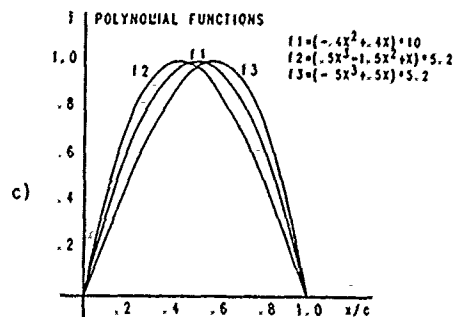
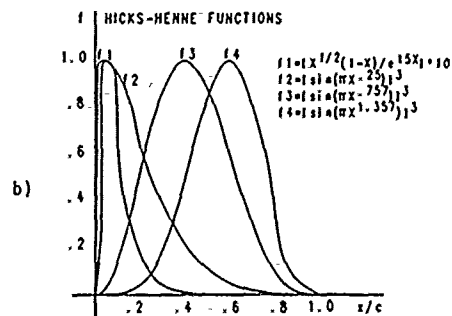
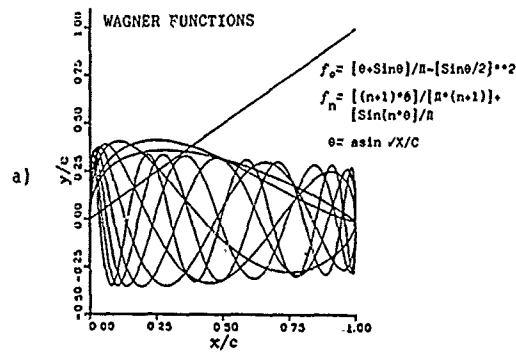


FIG. 4 EXAMPLES OF SHAPE FUNCTIONS FOR THE AIRFOIL DESIGN

It seems therefore that the effectiveness of these functions cannot be easily generalized.

The search for effective shape functions suggested that already existing airfoils be used /8/, whose behavior was close to the design specification in some respects.

Possible shape functions could be the differences between the ordinates of these airfoils and the ones of the initial airfoil (or of any of the intermediate airfoils).

This solution is interesting, but it requires that suitable airfoils be available. A database of geometries integrated in an expert system would permit the automatic selection of the adequate airfoils; this leads to a possible reduction of the aerodynamic analyses required for the optimization, and to a good quality of the final solution.

A second category of shape functions, such as those which we studied and used for this work, are less effective, but their adoption is more widespread.

These latter functions are chosen either because they ensure a broad variety of modifications or because they may lead to shapes that reflect existing airfoils from a qualitative viewpoint.

The form of the functions is selected to address the modification qualitatively as desired, while quantification is a task of the optimization; these functions are added linearly to the starting geometry.

Wagner functions were thence used (Fig. 4a), which permit a fairly large variation as far as the shape of the airfoil upper and lower surfaces are concerned. However, they cannot be used at the highest harmonics ($n > 7$) because they can cause waves in the geometry (changes in the sign of the slope over a small part of the chord). These functions are unsuitable to modify the camberline significantly (starting, for instance, from a symmetrical airfoil).

The Hicks-Henne (H.H.) functions (Fig. 4b) and the polynomial functions (Fig. 4c) have a simpler form, which makes

them particularly suited for even substantial changes of the camberline; hence they are mainly used for this purpose. They are characterized by different curvature towards the

trailing edge: H.H. functions are concave, polynomial functions are convex. The use of these functions during the optimization permits, in general, the attainment of the desired behavior in the upper surface portion just forward of the trailing edge: both concave and convex geometries are thus obtained, according to the requirements.

Other functions have been derived from the need to reproduce other geometrical behaviors typical of the transonic design: such as lower surface cusp for rear loading, and deflection of leading edge and trailing edge flaps.

Other design variables that have been used are the free parameters of the analytical expressions for symmetrical thickness distribution. In particular, in the case of the NACA 4 series modified family, the leading edge radius and the location of maximum thickness proved to most effectively control the solution.

All mentioned functions could be used concurrently in the modification of the airfoil, but this would give rise to some problems.

A first advice contrary to such a use comes from the expansion of the computation time. In the design of an airfoil required to operate at high CL, starting for instance from a symmetrical profile, functions for the refinement of the thickness distribution should be used only when the geometry has already been cambered enough.

Moreover, a modification using all variables at the same time, "masks" the impact that each type of function has on the geometry.

To have a knowledge of such an impact is on the other hand important because it may suggest the introduction of new, complementary functions.

The only shortcoming associated to the sequential use of sets of functions is, this being a non-linear problem, that the sequence in which these functions are used influences the final result.

Once again, design experience must give indications on the most adequate sequence.

5. DESIGN EXAMPLES

Attempting the study of a case which meets actual flight requirements is an extremely stimulating condition for the development and refinement of a system for automatic generation of new airfoils. The terms of comparison adopted to evaluate the effectiveness of the tool were the requirements applicable to a new high-performance military trainer. One of these requirements concerned sustained transonic maneuver under high g, and the other sea level dash performance (the formulation of this exercise is detailed in para 3).

These requirements also represent a very suitable ground for the application of an optimization procedure because they are in conflict with each other and need a compromise solution that cannot be obtained with inverse methods.

The design method uses solving techniques that are fully general and can, therefore, be used not only for the present examples, but also for many other design exercises involving maximum thickness and requirements different from those dealt with herein.

Two thin airfoils with maximum thickness $t/c = 5.5\%$ were designed.

The initial geometry, a symmetric airfoil in both exercises, was radically changed through the shape functions operating on thickness distribution and camberline.

Design was made with the aim of obtaining drag rise boundaries which include the design points ($M = .745$ and $CL = .855$, $M = .846$ and $CL = .06$), applying the criterion not to exceed 20 drag counts of wave drag ($CDW = .0020$). Shock waves are present on the airfoil during the design process; the aim is to keep their strength as low as possible. The exercises were made by using a grid which is sufficiently refined for the engineering requirements (128 circumferential divisions \times 32 radial divisions), and calculating drag as a variation of momentum through the shocks.

Inviscid computations have always been used in the design, while resort to the viscous correction was made only during the verification, because the Reynolds numbers of interest were fairly high ($>10^6$). This permitted the computation time to be kept low. The viscous correction demonstrated, in general, that the impact of viscosity on drag rise is small.

The buffet onset behavior is in first approximation controlled through the value of the trailing edge angle; a viscous analysis included in the optimization procedure would in fact require a significant increase in the computation time.

Geometrical constraints for the control of the geometry in the leading edge area have been used mainly to avoid convergence problems of the potential calculation, that are to be ascribed essentially to the high curvature of the airfoil in this area.

The relatively short time taken to obtain an airfoil capable of meeting the requirements favored a series of experiments aimed to compare different design approaches. The TRANSOL 5.5 airfoil (thickness 5.5%) was designed to concurrently meet the maneuver and dash requirements. This geometry (Fig. 5) gives the pressure distributions at the design points (Fig. 6) and the drag rise boundaries (Fig. 7). The latter can be expanded by using leading edge and trailing edge flaps, the deflection of which is obtained automatically through the optimization procedure.

An alternative approach, considers the flaps already in the phase in which the design points are chosen; it envisages that the flaps are used to attain the basic airfoil performance in one of the design conditions.

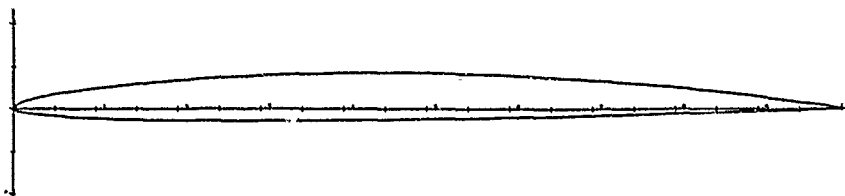


FIG. 5 TRANSOI 5.5: AIRFOIL DESIGNED BY OPTIMIZING A SYMMETRIC GEOMETRY, AND THAT CONCURRENTLY SATISFIES MANEUVER AND DASH REQUIREMENTS

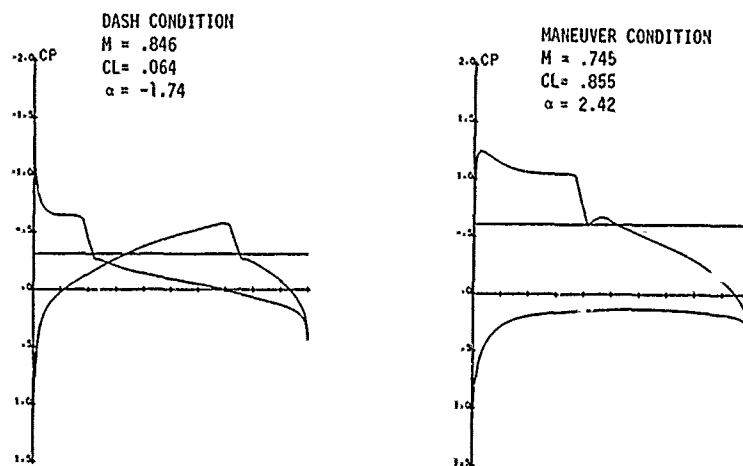


FIG. 6 TRANSOI 5.5: PRESSURE DISTRIBUTIONS AT OPTIMIZATION CONDITIONS

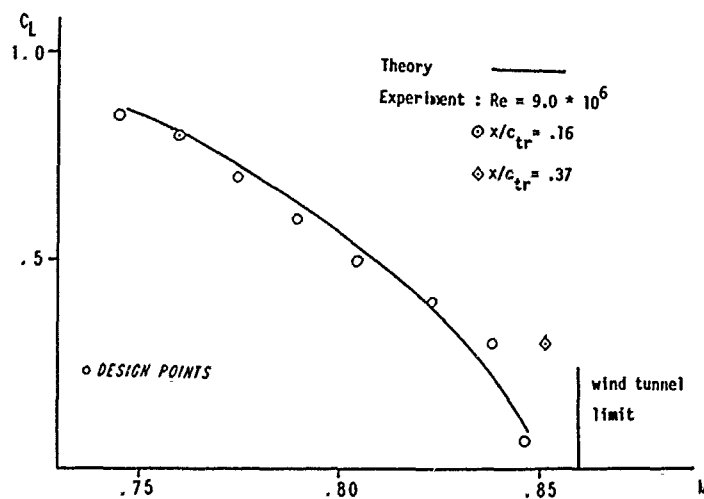


FIG. 7 TRANSOI 5.5: DRAG RISE BOUNDARIES

Basing on this consideration, another airfoil having thickness 5.5% c, TRANSO2 5.5, was generated by simply pushing performance at high C_L to the extreme. The aim of the latter design was to compare its drag rise boundaries with those of TRANSO1 5.5 that satisfied both the maneuver and dash performance requirement without flaps. TRANSO2 5.5 is shown in Fig.8; it gives the pressure distribution at the design point and the drag rise boundaries depicted in Fig.9

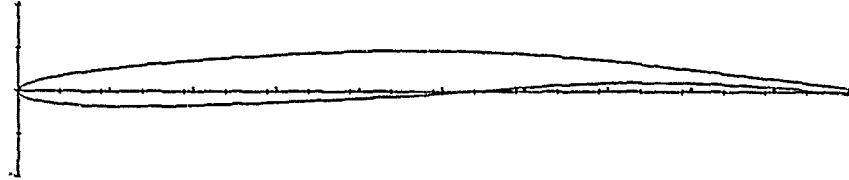


FIG. 8 TRANSO2 5.5: AIRFOIL DESIGN BY OPTIMIZING THE SYMMETRIC GEOMETRY, AND WHICH LARGELY SATISFIES THE MANEUVER DESIGN CONDITION

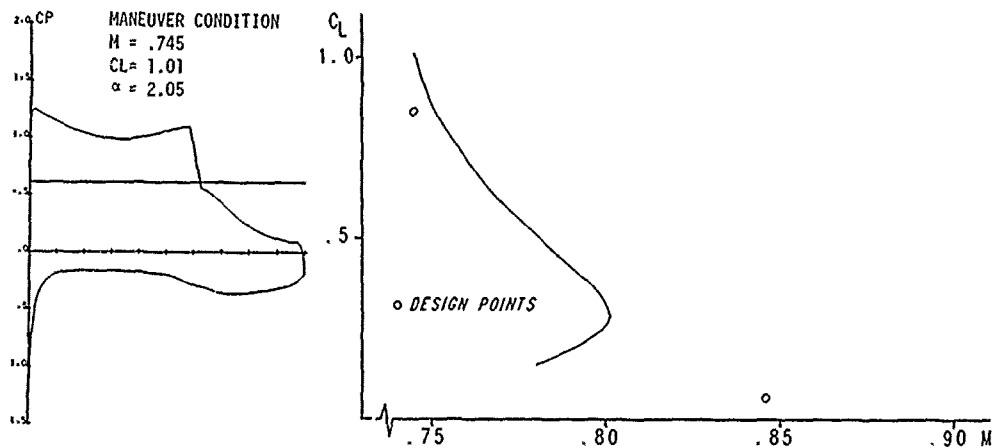


FIG. 9 TRANSO2 5.5: PRESSURE DISTRIBUTION AT OPTIMIZATION CONDITION AND DRAG RISE BOUNDARIES

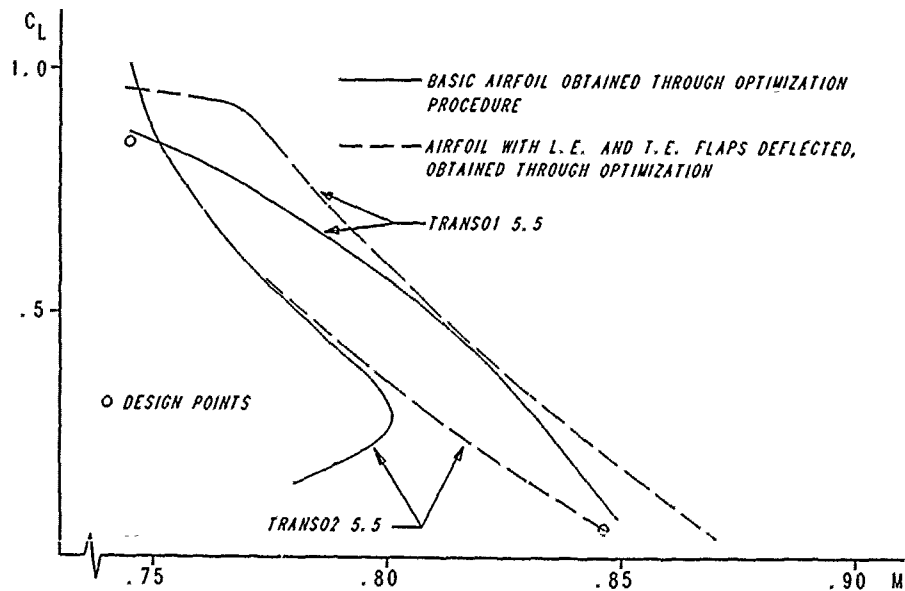


FIG. 10 COMPARISON OF DIFFERENT DESIGN APPROACHES MADE POSSIBLE BY THE USE OF AN OPTIMIZATION PROCEDURE

The concavity of the upper surface towards the trailing edge makes the installation of the flap deflection mechanism fairly difficult. The computed performance of airfoils TRANSO1 5.5 and TRANSO2 5.5 is compared in Fig. 10. With deflected flaps, the former shows better margins of approx .02 Mach in the entire CL range, except for the highest values, for which the second geometry was specifically generated. The method adopted permits the drag rise boundaries with deflected flaps to be determined, and design times are short: approximately one hour for a full design on Sperry UNIVAC 1100/90 machines. For these reasons it is possible to perform a comparison of different design solutions, which would be difficult and extremely burdensome with non-automatic techniques.

The behavior of the polar of TRANSO2 5.5 at high CL is as shown in Fig. 11, which reveals a marked oscillation of the wave drag value. This behavior becomes even more marked if the airfoil nose is rounded, as demonstrated by an investigation in which the constraints were ad-hoc values of the differences of the upper and lower surface ordinates at the leading edge. This investigation was made preserving the performance at design condition ($CDW \leq .0020$ at $CL > 1.0$). The design tool is therefore suitable to study effects of this type, should they emerge during the design or the verification.

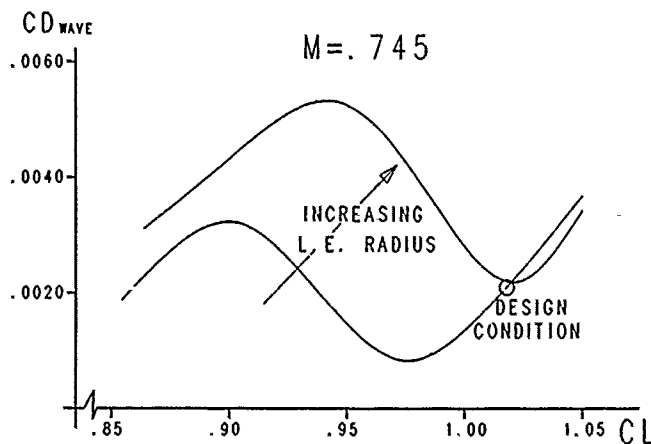


FIG. 11 AN EXAMPLE OF INVESTIGATION USING THE OPTIMIZATION PROCEDURE

6. CONCLUSIONS AND FUTURE DEVELOPMENTS

The considered examples covering the design in two operating conditions prove that the procedure is capable of matching the actual design requirements for airfoils. Some of them are to be investigated in the transonic wind tunnel. An adequate use of the constraints also permits the required computation times to be kept reasonably short.

It would conversely be pretentious to say that the procedure is complete as far as design is concerned, and that it does not need a refinement. In reality, an automatic design system is valid if it is managed dynamically, that is if its contents are updated with information drawn from design experiences made by others or from the solution of application exercises carried out using the same procedure.

An optimization procedure may conversely be considered the nucleus around which a system managing the design information is built.

This information required in the airfoil design process is:

- correlation of the 3D design points with the 2D ones: the airfoil design is normally the first step towards the design of the wing;
- control of the aerodynamic behavior through geometric design criteria (in the regimes non directly controlled through aerodynamic analyses during the optimization)
- choice of the most suited design approach (for instance, considering the flaps);
- choice of the initial airfoil, possibly searching for it in a database;
- choice of the most suited code to use, amongst the available ones, and setting of the computation parameters;
- effective use of the design method: the attempt was made in the previous pages to show how an optimization method can be used effectively;
- analysis of the intermediate results of the design process and updating of the parameters used during the modification;
- management of the verification, in particular if unforecast behavior of the airfoil is noted;
- comparison between the theoretical performance and the experimental performance of similar airfoils. Investigation to assess whether there can be scale effects.

The conventional implementation techniques (FORTRAN language) are unsuited to implement a system for the management of information of this type, which is to be constantly enriched and updated.

Procedural programming in fact requires that the system be analyzed before modifications are included; an evolving system is frequently subjected to changes, and the time required to make them operating would be too long.

The system updating time is conversely much reduced if resort is made to a declarative implementation: rules containing information may be added, removed, modified without worrying that this action may impair the validity of the other information in the system /12/.

Expert system development techniques permit the system to be built just as described. In this environment an "inferential engine" is implemented that permits automated reasoning based on the information included in the rules. The rules, in turn, represent the knowledge base and must be implemented by the specialist who develops the system. Moreover, resorting to extensive use of a 2D optimization procedure, possibly integrated in an expert system, is a good way to cut down the number of analyses required for a 3D optimization.

7. REFERENCES

1. R. HICKS, P.A. HENNE: WING DESIGN BY NUMERICAL OPTIMIZATION, JOURNAL OF AIRCRAFT VOL. 15 N.7, PAG. 407 - 412, 1978
2. H.P. HANEY: A-7 TRANSONIC WING DESIGN, TRANSONIC AERODYNAMICS - P. NIXON, VOL.81, PAG. 431 - 450, 1982
3. M.L. HINSON: A SERIES OF AIRFOILS DESIGNED BY TRANSONIC DRAG OPTIMIZATION FOR GATES LEARJET AIRCRAFT, TRANSONIC AERODYNAMICS - P.NIXON, VOL.81, PAG. 489 - 509, 1982
4. P.V. AIDALA, W.H. DAVIS JR., W.H. MASON: SMART AERODYNAMIC OPTIMIZATION, AIAA APPLIED AERODYNAMIC CONFERENCE, 83-1863, PAG. 1 - 12, 1983
5. W. DAVIS: TRO-2D: A CODE FOR RATIONAL TRANSONIC AERO OPTIMIZATION, AIAA 23RD AEROSPACE SCIENCES MEETING85-0425, PAG. 1 - 8, 1985
6. R. MARAZZI, L. GHIEMI: A PLAN FOR AN AUTOMATED DESIGN METHODS OF AIRFOILS, L'AEROTECNICA - MISSILI E SPAZIO, VOL.66, PART 1, PAG. 18 - 26, 1987
7. R.A. KENNELLY: IMPROVED METHOD FOR TRANSONIC DESIGN BY OPTIMIZATION, NASA CR-166497, 1983
8. G.N. VANDERPLAATS: APPROXIMATION CONCEPTS FOR NUMERICAL AIRFOIL OPTIMIZATION, NASA TP - 1370, 1979
9. G.N. VANDERPLAATS: CONMIN: A FORTRAN PROGRAM FOR CONSTRAINED FUNCTION MINIMIZATION, 1978
10. G.N. VANDERPLAATS: NUMERICAL OPTIMIZATION TECHNIQUES FOR ENGINEERING DESIGN (WITH APPLICATIONS), MC GRAW-HILL - INC., 1984
11. P. MAZZZI: PROGRAM AELFOIL, 1987
12. A. MAZZETTI: APPLICAZIONI DEI SISTEMI ESPERTI, 1' EDIZIONE, ITALY, F. MUZIO ED. PAG. 5 - 118, 1987

DEFINITIONS DE PROFILS ET DE PALES D'HELICOPTERE PAR OPTIMISATION NUMERIQUE

(The Use of Numerical Optimization
for Helicopter Airfoil and Blade Design)

par
J. RENEAUX

Office National d'Etudes et de Recherches Aérospatiales
Boîte Postale N° 72 - 92322 Chatillon CEDEX
FRANCE

et

M. ALLONGUE

AEROSPATIALE - Division Hélicoptère
Etablissement de Marignane - 13725 Marignane CEDEX
FRANCE

RESUME

Les techniques d'optimisation numérique ont été utilisées avec succès à l'ONERA pour la définition de profils et à l'Aéropatiale pour la définition de pales d'hélicoptère. La méthode de minimisation sous contraintes utilisée est celle développée par Vanderplaats. Pour l'optimisation des profils d'hélicoptère, la méthode de minimisation a été associée à un programme de calcul direct de l'écoulement transsonique visqueux. La définition de deux profils de pales d'hélicoptère de 12% et de 9% d'épaisseur relative a été effectuée en deux points d'adaptation représentant les conditions de fonctionnement en pale avançante et en pale reculante d'un cas de vol d'avancement. Les caractéristiques aérodynamiques déterminées expérimentalement en écoulement bidimensionnel dans la soufflerie S3MA de l'ONERA confirment les gains importants prévus par le calcul. La définition de pales d'hélicoptère est effectuée en associant la méthode de minimisation à une méthode de calcul des performances du rotor basée sur la théorie de l'élément de pale. L'optimisation de la position en envergure de profils de différentes épaisseurs relatives a été réalisée en considérant soit un point d'adaptation, soit deux points correspondant à des cas de vol différents. Les résultats sont présentés pour un rotor d'hélicoptère de 8-10 tonnes. Ces deux applications mettent en évidence l'intérêt du concept d'optimisation numérique pour la définition des rotors d'hélicoptère compte tenu des compromis à réaliser entre les différents cas de vol et du nombre important de paramètres et de contraintes qui doivent être considérés.

ABSTRACT

The numerical optimization methods have been successfully applied to airfoil design at ONERA, and to helicopter blade design at the Aerospatiale Helicopter Department. The constrained minimization method chosen is the one developed by Vanderplaats. For the design of helicopter airfoils, the minimization algorithm and a transonic viscous flow analysis method are linked together. The design of a 12% thick airfoil and a 9% thick airfoil for helicopter blades has been carried out with two design points, one corresponding to the advancing blade conditions and the other to the retreating blade conditions in forward flight. 2 D tests performed in the ONERA S3MA wind tunnel confirmed the theoretical predicted gains. The design of helicopter blades is achieved through the association of the minimization method and a rotor performance analysis method using the blade element theory. The optimization of the spanwise locations of the airfoils of different thickness-to-chord ratios has been carried out with one or two design points corresponding to different flight conditions. The method has been applied to the rotor design for a helicopter of the 8-10 tons gross weight class. The applications discussed in this paper show the interest of the numerical optimization techniques for the helicopter rotor design particularly when several flight conditions and many parameters and constraints have to be taken into account.

1 - INTRODUCTION

Les méthodes d'optimisation numérique s'avèrent particulièrement intéressantes dans le domaine aéronautique [1], lorsque plusieurs conditions de fonctionnement sont considérées, et elles permettent une réduction du temps de conception des divers éléments étudiés. Ces techniques ont été appliquées à l'ONERA et à l'AEROSPATIALE Division Hélicoptère pour la définition de profils et de pales d'hélicoptère en prenant en compte les nombreuses contraintes à considérer pour l'optimisation des rotors. Les méthodes d'optimisation numérique associent une méthode de calcul directe des performances d'une configuration donnée à une méthode de minimisation sous contraintes. Elles permettent de définir ou de modifier des formes aérodynamiques en se fixant un objectif aérodynamique et en respectant des contraintes aérodynamiques et géométriques.

L'optimisation de profils de pale d'hélicoptère a été effectuée en associant à la méthode de minimisation une méthode de calcul de l'écoulement transsonique visqueux et en considérant deux points d'adaptation représentant les conditions de fonctionnement en pale avançante et reculante d'un rotor en vol d'avancement.

Les caractéristiques aérodynamiques de ces nouveaux profils étant connues, l'optimisation de la position en envergure de profils de différentes épaisseurs relatives a été réalisée en utilisant une méthode de calcul des performances d'un rotor en vol stationnaire et en vol d'avancement, et en prenant en compte deux cas de vols différents.

Pour les applications présentées, le choix des fonctions objectif et contraintes est précisé ainsi que les variables de décision retenues pour effectuer l'optimisation. Les résultats obtenus mettent en évidence une amélioration significative des performances des pales d'hélicoptère ainsi optimisées.

2 - MINIMISATION SOUS CONTRAINTES

D'une manière générale, le processus d'optimisation consiste à déterminer les variables de décision $\bar{X} = (X_1, \dots, X_n)$ qui minimisent une fonction objectif $OBJ(\bar{X})$ et qui respectent les contraintes imposées écrites sous la forme :

$$\begin{aligned} G_j(\bar{X}) &\leq 0 & j = 1, \dots, m \text{ contraintes d'inégalité} \\ L_i &\leq X_i \leq U_i & i = 1, \dots, n \text{ contraintes latérales sur les variables de décision} \end{aligned}$$

La méthode de minimisation sous contraintes, qui a été retenue pour l'optimisation des profils et des pales d'hélicoptère, est celle développée par Vanderplaats [2]. Elle est itérative et s'appuie sur la formule de récurrence suivante :

$$\bar{X}_q = \bar{X}_{q-1} + \alpha^* \bar{S}_q$$

Pour l'itération q considérée, deux étapes peuvent être distinguées. La première est la recherche de la direction de descente \bar{S}_q dans l'espace de dimension n . La seconde est la détermination du scalaire α^* , module du déplacement à effectuer dans cette direction. La détermination de la direction de descente \bar{S}_q s'effectue à partir des gradients des fonctions $OBJ(\bar{X})$ et $G_j(\bar{X})$ calculés par différences finies, en utilisant différentes méthodes suivant l'état des contraintes. La contrainte $G_j(\bar{X})$ étant considérée :

- non active si $G_j(\bar{X}) < -a$;
- active si $-a < G_j(\bar{X}) < b$ $a, b > 0$;
- violée si $b < G_j(\bar{X})$.

Lorsqu'aucune contrainte n'est active ou violée la méthode employée dans CONMIN est la méthode des gradients conjugués de Fletcher et Reeves ($\bar{S}_q = -\nabla OBJ(\bar{X}_q) + \frac{|\nabla OBJ(\bar{X}_q)|^2 \bar{S}_{q-1}}{|\nabla OBJ(\bar{X}_{q-1})|^2}$)

réinitialisée toutes les $n+1$ itérations par la méthode de la plus grande pente ($\bar{S}_q = -\nabla OBJ(\bar{X}_q)$). Les méthodes de minimisation quasi newtoniennes DFP et BFGS qui ont été introduites dans la méthode constituent une alternative intéressante [3], et sont utilisées dans la plupart des optimisations effectuées. Dans ce cas, $\bar{S}_q = -H \nabla OBJ(\bar{X}_q)$, où H est une approximation de l'inverse de la matrice des dérivées partielles d'ordre deux de la fonction objectif par rapport aux variables de décision. Lorsqu'une ou plusieurs contraintes sont actives, la méthode des directions réalisables de Zoutendijk est utilisée. La recherche d'une direction \bar{S}_q adaptée au cas où une ou plusieurs contraintes sont violées, est également incluse dans la méthode.

Le déplacement optimal α^* dans la direction de descente \bar{S}_q est déterminé par une approximation polynomiale. Il peut correspondre à un minimum de la fonction objectif dans cette direction ou à une limitation imposée par les contraintes. Dans la plupart des cas, trois déplacements sont effectués dans la direction \bar{S}_q .

Le processus d'optimisation nécessite donc environ $1 + q(n+3)$ évaluations des fonctions objectif et contraintes. Le programme aérodynamique associé à la méthode de minimisation doit être robuste et rapide compte tenu du grand nombre de calculs à effectuer.

3 - DEFINITION DE PROFILS POUR ROTOR D'HELICOPTERE

L'augmentation des vitesses de croisière des hélicoptères a nécessité un développement de profils pour rotor principal dans les années 75-80 [4] [5] [6] et leur utilisation a été facilitée par l'introduction des matériaux composites pour la réalisation des pales. Ces profils définis par méthodes directe ou inverse ont pu être plus récemment améliorés avec l'utilisation des méthodes de définition de profils par optimisation numérique.

3.1 - Processus d'optimisation

3.1.1 - Programme aérodynamique

L'optimisation des profils étant effectuée sur les caractéristiques aérodynamiques globales et notamment la traînée, il est nécessaire de prendre en compte l'influence des effets visqueux dans le calcul de l'écoulement. La méthode d'optimisation bidimensionnelle développée à l'ONERA [7] associée au programme de minimisation, décrit au paragraphe 2, la méthode de calcul directe de l'écoulement transsonique visqueux [8]. Elle résout l'équation complète du potentiel écrite sous forme non conservative par la méthode de Garabedian et Korn pour le fluide parfait et détermine les couches limites laminares et turbulentes par la méthode intégrale de Michel. Les effets visqueux sont pris en compte par une technique de couplage faible, ce qui exclut tout calcul précis sur une configuration présentant des décollements importants. Les calculs sont effectués en transition naturelle en utilisant le critère de Granville, modifié pour prendre en compte l'influence du taux de turbulence extérieure. Pour un maillage comprenant 5000 points, le temps de calcul sur CRAY XMP 18 est compris entre 15s et 25s.

3.1.2 - Variables de décision

La modification géométrique du profil peut être effectuée soit de manière globale avec l'utilisation d'une bibliothèque de formes [9], soit localement en considérant des fonctions de modification analytiques ou des aéronctions [10].

L'utilisation d'une bibliothèque de profils permet de réduire le nombre de variables de décision à considérer pour l'optimisation et de retenir les fonctions de modification les mieux adaptées au problème posé. Dans ce cas, pour les variables de décision $\bar{X} = (X_1, \dots, X_n)$, les coordonnées du profil sont définies par $\bar{Y} = \bar{Y}_0 + X_1 (\bar{Y}_1 - \bar{Y}_0) + \dots + X_n (\bar{Y}_n - \bar{Y}_0)$ où \bar{Y}_0 est la géométrie du profil initial. Dans cette

formulation chaque profil de la bibliothèque ($\bar{V}_1, \dots, \bar{V}_n$) appartient à l'espace de recherche de la solution.

L'emploi de fonctions de modification analytiques ou d'aérofuctions permet d'affiner localement la géométrie obtenue avec l'approche précédente. La géométrie des profils est représentée en additionnant linéairement les fonctions de modification au profil initial. Les aérofuctions, fonctions définies à l'aide d'un programme inverse pour obtenir un changement de répartition de pression donné, peuvent être plus facilement adaptées aux optimisations à effectuer compte tenu de leur origine aérodynamique.

Les optimisations présentées ont été effectuées en considérant entre 5 et 10 profils de base ou fonctions de modification. Le programme d'optimisation numérique bidimensionnelle, qui a été utilisé avec succès pour la définition de profils d'avion de transport, d'hélice et d'hélicoptère [11], offre un avantage important sur les méthodes inverses de définition lorsque plusieurs points de fonctionnement doivent être considérés, ce qui correspond notamment aux conditions de définition des profils de pale d'hélicoptère.

3.2 - Définition des profils OA312 et OA309

Bien que les conditions de fonctionnement des pales de rotor d'hélicoptère soient instationnaires en vol d'avancement, le cahier des charges est exprimé en fonction des caractéristiques stationnaires des profils compte tenu des méthodes de définition disponibles. L'analyse de l'écoulement sur un rotor dans différentes configurations de vol a permis d'établir des objectifs pour la définition de profils destinés à équiper les sections internes et externes des pales de rotor principal. Les spécifications retenues sont les suivantes :

- nombre de Mach de divergence de trainée (M_{dx}) élevé à portance nulle pour caractériser le comportement en pale avançante d'un cas de vol d'avancement ;
- très faible coefficient de moment ($|C_m| < 0,01$) pour minimiser les efforts de commande de pas et la torsion de la pale ;
- coefficient de portance maximale élevé pour un nombre de Mach compris entre 0,3 et 0,5 et décrochage progressif pour caractériser le comportement en pale reculante ;
- finesse élevée à un nombre de Mach de 0,60 et un coefficient de portance $C_z \approx 0,60$ pour les conditions de vol stationnaire.

La méthode d'optimisation numérique a été utilisée pour améliorer les performances des profils OA213 et OA209 (définis par méthode directe ou inverse), dans les conditions de vol d'avancement compte tenu de l'augmentation de la vitesse de croisière des nouveaux projets d'hélicoptère actuellement à l'étude. Le problème d'optimisation a été formulé en utilisant pour fonctions objectif et contraintes les caractéristiques globales des profils C_x , C_z , C_m et les répartitions de pression. Le coefficient de portance maximale ne pouvant pas être déterminé directement avec une méthode de couplage faible, celui-ci est estimé à partir de la survitesse à l'extrados ou du nombre de Mach avant le choc. Pour les conditions de pale avançante, l'optimisation a été effectuée pour un nombre de Mach proche du nombre de Mach de divergence de trainée du profil initial pour diminuer le niveau de trainée et augmenter le M_{dx} à $C_z = 0$.

Le profil OA312, de 12% d'épaisseur relative destiné à équiper les sections internes des pales d'hélicoptère, a été défini pour les deux conditions de fonctionnement $M = 0,77$ et $C_z = 0$ (premier point représentant les conditions de pale avançante) et $M = 0,40$ et $C_z = 1,5$ (deuxième point représentant les conditions de pale reculante). Les fonctions objectif et contraintes retenues sont les suivantes :

OBJ = C_{x1}
 contraintes
 $|C_{m1}| < 0,01$
 $K_{p=ini2} > -a \quad a > 0$
 $e/c > 12\%$

Dans le processus d'optimisation, la solution obtenue dépend des fonctions de modification utilisées et peut en outre représenter un minimum relatif et non pas la solution optimale recherchée. Aussi la probabilité d'obtenir la meilleure solution possible est augmentée en effectuant plusieurs optimisations et en utilisant différentes fonctions de modification. La définition du profil OA312 a été effectuée en considérant deux étapes. La première optimisation est réalisée avec une bibliothèque de profils de base, profils d'hélicoptère dont la loi d'épaisseur a été modifiée par affinité pour obtenir l'épaisseur relative de 12%. Les caractéristiques du profil ainsi obtenu sont ensuite améliorées dans une deuxième phase en optimisant séparément l'intrados et l'extrados avec des fonctions de modification locales.

La figure 1 compare les caractéristiques aérodynamiques calculées du profil OA312 optimisé à celles du profil initial OA213 dans les conditions de pale avançante. Au nombre de Mach de 0,77, le profil OA312 présente un choc extrados de plus faible intensité et une survitesse intrados réduite de $\Delta M = -0,15$. L'évolution du coefficient de trainée à portance nulle en fonction du nombre de Mach pour la loi de Reynolds $Re = 8 \times M \times 10^6$ montre une amélioration importante du nombre de Mach de divergence de trainée ($\Delta M_{dx} = +0,03$). De plus le coefficient de moment est réduit et reste inférieur à 0,01 en valeur absolue jusqu'à environ $M = 0,77$. Les répartitions de pression des profils OA213 et OA312 calculées dans les conditions de pale reculante $M = 0,40$, $C_z = 1,50$ et $Re = 3,2 \times 10^6$ sont présentées figure 2. Les survitesses des deux profils sont situées respectivement à 7% de la corde pour le profil OA213 et au bord d'attaque pour le profil OA312. Le coefficient de portance maximale évalué à partir de l'évolution de la survitesse extrados en fonction du C_z est voisin de 1,50 pour les deux profils. Ces calculs montrent que le profil OA312 obtenu réalise un très bon compromis entre les conditions de pale reculante et de pale avançante. En effet, il présente aux basses vitesses des performances voisines de celles du profil OA213 et en transsonique un nombre de Mach de divergence de trainée augmenté de 0,03.

La définition du profil OA309, de 9% d'épaisseur relative destiné à équiper les sections externes des pales d'hélicoptère, a été effectuée avec le même processus d'optimisation. Dans ce cas les deux points

de fonctionnement retenus sont $M = 0,82$ et $C_z = 0$ pour le premier point représentatif des conditions de pale avançante et $M = 0,40$ et $C_z = 1,1$ pour le second point représentatif des conditions de pale reculante. Les fonctions objectif et contraintes considérées sont les suivantes :

$$\begin{aligned} \text{OBJ} &= C_x \\ \text{contraintes} & \\ |C_{x1}| &\leq 0,01 \\ K_{pmin12} &\geq -b \quad b > 0 \\ e/c &\geq 9\% \end{aligned}$$

Les caractéristiques du profil OA209 initial et du profil OA309 optimisé sont présentées figure 3 pour les conditions de pale avançante. L'évolution du coefficient de traînée à portance nulle en fonction du nombre de Mach pour $Re = 8 \times M \times 10^6$ montre que les deux profils ont des nombres de Mach de divergence de traînée identiques mais que le profil OA309 possède un coefficient de traînée nettement plus faible. La survitesse intrados du profil OA209 a été diminuée de $\Delta M = -0,19$ et la réaccélération conduisant à la formation d'un deuxième choc intrados à Mach élevé a été évitée sur le profil OA309. L'intensité du choc extrados a également été réduite et sa position est plus amont. La réduction de la traînée calculée à $M = 0,82$ et $C_z = 0$ est de 20%. La figure 4 présente les répartitions de pression des deux profils pour les conditions de pale reculante, au voisinage du C_z max. La survitesse extrados du profil OA309 est inférieure à celle du profil OA209, ce qui correspond à une augmentation du coefficient de portance maximale estimée à 0,05. Le profil OA309 présente donc à portance nulle un coefficient de traînée calculé inférieur à celui du profil OA209 pour un même nombre de Mach de divergence de traînée et un coefficient de portance maximale supérieur aux basses vitesses.

3.3 - Vérification expérimentale

Les essais des profils OA312 et OA309 ont été réalisés en écoulement bidimensionnel dans la soufflerie S3MA de l'ONERA en respectant la même loi de Reynolds $Re = 8 \times M \times 10^6$, déjà utilisée lors des essais des profils OA213 et OA209. De plus, tous ces essais ont été effectués sur des maquettes de cordes identiques, ce qui autorise des comparaisons au niveau des résultats bruts, non corrigés des effets de parois de soufflerie.

La figure 5 compare les caractéristiques aérodynamiques, non corrigées des effets de parois, des profils OA213 et OA312. Les gains les plus importants apportés par le profil OA312 apparaissent dans les conditions de pale avançante. Ils se traduisent par une augmentation du nombre de Mach de divergence de traînée de 0,75 à 0,78, par une diminution du niveau de traînée avant divergence et par une réduction du coefficient de moment en valeur absolue. Dans les conditions de pale reculante, les coefficients de portance maximale mesurés à $M = 0,4$ et $Re = 3,2 \times 10^6$ sont respectivement 1,50 et 1,54 pour les profils OA312 et OA213. Cependant le C_z max du profil OA312 est moins sensible au nombre de Mach et est supérieur à celui du profil OA213 pour $M = 0,3$, $M = 0,5$ et $M = 0,55$.

Ces résultats expérimentaux montrent que le profil OA312 présente de meilleures caractéristiques aérodynamiques dans les conditions de pale avançante et de pale reculante. Les améliorations des performances prévues par le calcul sont confirmées par l'expérience notamment en ce qui concerne la prévision de la divergence de traînée et du coefficient de portance maximale. L'évaluation de la traînée est effectuée avec moins de précision mais les tendances sont toujours retrouvées.

La comparaison des caractéristiques aérodynamiques des profils OA209 et OA309 mesurées à $M = 0,82$ est présentée figure 6. Les évolutions du coefficient de traînée à portance nulle montrent que le profil OA309 possède un coefficient de traînée nettement inférieur à celui du profil OA209 jusqu'à $M = 0,8$, bien que les nombres de Mach de divergence de traînée des profils OA309 et OA209 soient relativement proches, respectivement 0,845 et 0,85. Pour les conditions correspondant à la pale reculante, les coefficients de portance maximale du profil OA309 sont supérieurs à ceux du profil OA209 pour les nombres de Mach de 0,3, 0,4 et 0,50 : l'augmentation du C_z max est d'environ 5%.

Les gains de performances calculées, apportés par le profil OA309, sont confirmés par l'expérience. On retrouve notamment la réduction du coefficient de traînée à portance nulle de 20% à $M = 0,82$ et une augmentation du coefficient de portance maximale à $M = 0,4$ (+ 0,07 dans l'expérience et + 0,05 prévu par le calcul). Par contre l'évolution du coefficient de traînée au-delà du nombre de Mach de divergence de traînée n'est pas accessible avec la méthode de couplage faible utilisée dans le processus d'optimisation.

La figure 7 montre le compromis obtenu pour les profils OA2xx et OA3xx entre les comportements en pale reculante et en pale avançante, en considérant le coefficient de portance maximale à $M = 0,4$ et le nombre de Mach de divergence de traînée à portance nulle. Les iso-coefficients de traînée ($C_x = 0,01$ et $C_x = 0,02$) sont tracés dans le plan (C_z, M) figure 8 pour les profils OA213 et OA312. Les zones sombres mettent en évidence les gains qui ont été obtenus pour toutes les conditions de fonctionnement, pale reculante, pale avançante et vol stationnaire. La figure 9 présente les iso-coefficients de traînée pour les profils d'extrémité OA209 et OA309. Les régions sombres mettent en évidence les gains qui ont été obtenus avec le profil OA309 au voisinage des points d'optimisation. Pour les conditions de fonctionnement en vol stationnaire $M = 0,60$ et $C_z = 0,60$, les performances du profil OA309 sont toutefois légèrement inférieures à celles du profil OA209 tout en restant dans les limites imposées par le cahier des charges.

3.4 - Perspectives

L'évaluation des fonctions objectif et contraintes est effectuée par un programme aérodynamique indépendant, ce qui permet d'envisager des optimisations de profils avec une méthode de couplage fort ou une méthode instationnaire.

L'utilisation d'un programme de calcul de l'écoulement autour de profils prenant en compte les effets visqueux par une technique de forte interaction devrait conduire à des calculs plus précis sur des configurations présentant des décollements importants. Une telle méthode devrait permettre d'améliorer la qualité de l'optimisation compte tenu du cahier des charges imposé pour la définition des profils de pale d'hélicoptère (C_z max, M_{dx}). La figure 10 présente la comparaison entre les résultats d'essais et un calcul effectué avec la méthode [12] sur la géométrie réelle du profil dans la section médiane de la maquette, pour des conditions d'essai (M , α , Re) corrigées des effets de parois. Le fluide parfait est dans ce cas obtenu par résolution de l'équation du potentiel complet sous forme conservative. La méthode de couplage fort prenant en compte le sillage permet de prévoir correctement la répartition de pression au voisinage du bord de fuite aussi bien à $M \sim 0,40$ à C_z élevé que dans les conditions de pale avançante $M \sim 0,77$ et $C_z \sim 0$. En transsonique, cette méthode permet d'obtenir une position de choc et un saut de pression en bon accord avec l'expérience.

D'autre part, des améliorations importantes pourraient sans doute être réalisées en prenant en compte, au stade de la définition, les performances instationnaires des profils. Les progrès récents effectués dans la résolution des équations du potentiel complet et des équations d'Euler instationnaires permettent actuellement d'effectuer des calculs bidimensionnels dans les conditions de fonctionnement proches de celles des pales d'hélicoptère avec superposition des oscillations de tamis et d'incidence. La figure 11 présente les résultats obtenus sur le profil OA312 avec la méthode de fluide parfait [13] et les lois, $M = 0,67 + 0,18 \sin \phi$ et $\alpha = 2,22 - 3,25 \sin \phi$, reproduisant les conditions de vol que l'on peut rencontrer sur un hélicoptère. Les répartitions de pression sont comparées, pour les azimuts $\phi = 60^\circ$ et $\phi = 120^\circ$, à la solution stationnaire obtenue avec la même méthode pour les conditions de nombre de Mach et d'incidence correspondantes ($M = 0,827$ et $\alpha = -0,59^\circ$). Cette figure met en évidence l'effet instationnaire en pale avançante qui se caractérise par un retard à l'apparition du choc intrados et se traduit par un décalage du minimum de portance ($\phi = 90^\circ$ en quasi stationnaire et $\phi \sim 105^\circ$ en instationnaire).

L'utilisation de méthodes de couplage fort ou de méthodes instationnaires dans un processus d'optimisation numérique est cependant actuellement difficile compte tenu des temps de calculs importants qui en résultent.

4 - DEFINITION DE PALES D'HELICOPTERE

La définition de pales d'hélicoptère est effectuée en tenant compte des performances aérodynamiques du rotor dans tout le domaine de vol de l'appareil considéré. Les paramètres de définition à optimiser sont principalement :

- le rayon du rotor ;
- la loi de corde ;
- le vrillage ;
- le choix des profils ;
- la position des profils en envergure.

Les progrès technologiques effectués grâce aux matériaux composites permettent une grande liberté pour les géométries de la pale, avec la possibilité d'utiliser des profils, des formes en plan et des vrillages évolutifs en envergure. L'approche conventionnelle pour l'optimisation de ces différents paramètres consiste à examiner séparément l'influence de chacun d'entre eux sur les performances d'un rotor, soit à l'aide de méthodes de calculs, soit à l'aide d'essais en soufflerie et en vol.

En ce qui concerne le calcul, la prise en compte de l'ensemble de ces paramètres nécessite un grand nombre d'itérations de conception qui peuvent être minimisées en utilisant les méthodes d'optimisation numérique. Les hélicoptéristes ont montré récemment l'intérêt de cette approche [14], [15], [16]. A l'Aérospatiale Division Hélicoptère, les méthodes d'optimisation du rotor ont été développées en associant des méthodes de calculs de performances au programme de minimisation sous contraintes décrit paragraphe 2.

L'optimisation de la position des profils le long de la pale, présentée dans cet article, illustre les possibilités et les avantages de ce concept. Le choix des profils et leurs répartitions le long de la pale représentent des paramètres importants pour la conception d'un rotor : trois profils différents ont par exemple été utilisés pour la définition du rotor du Dauphin 365 N (figure 12).

4.1 - Processus d'optimisation

4.1.1 - Méthode de calcul de performances d'un rotor

Les évaluations des performances du rotor sont effectuées en stationnaire et en vol d'avancement en utilisant des méthodes basées sur la théorie de l'élément de pale. Pour le vol stationnaire, le champ des vitesses induites par le rotor est calculé à partir d'une méthode des anneaux [17]. En vol d'avancement deux modèles peuvent être utilisés ; le modèle de Moijer-Drees et un modèle plus élaboré basé sur une méthode tourbillonnaire à sillage figé. Les applications présentées ont été réalisées en considérant les cas de vol d'avancement et en utilisant le modèle simplifié de Moijer-Drees.

Les performances sont évaluées en imposant soit la traction et la portance sur le rotor, soit les lois de commande de pas. Le rotor est supposé isolé et la pale rigide. Les mouvements de battement, de trainée et de pas sont pris en compte et les équations de la mécanique régissent l'équilibre des pales en battement et en trainée. La méthode de résolution correspondant à l'organigramme présenté figure 13 est la suivante

- détermination des vitesses et des accélérations en tous les points de la pale ;
- calcul des efforts aérodynamiques et inertiels appliqués sur la pale ;
- transfert de ces efforts aux articulations de battement et de trainée.

Les trois étapes sont effectuées pour chaque azimut et les moments aux articulations de battement et de traînée sont décomposés en série de Fourier. L'annulation de ces coefficients de Fourier, pour la mise en équilibre du rotor, permet d'obtenir un système d'équations non linéaires. Le mouvement de la pale étant supposé périodique, les inconnues du problème sont les coefficients de la décomposition en série de Fourier des angles de battements et de traînée. La résolution est effectuée par itérations successives. Pour l'évaluation des efforts aérodynamiques, les coefficients C_z , C_x , C_m sont ceux mesurés en écoulement bidimensionnel stationnaire en soufflerie.

La figure 14 présente la comparaison calcul-expérience obtenue avec les mesures effectuées sur un rotor isolé dans la soufflerie S1 de Modane, en considérant les coefficients réduits de puissance et de portance, \bar{C} et \bar{Z}

$$\bar{C} = \frac{100 P}{\frac{1}{2} \rho b^2 c R U^3}$$

$$\bar{Z} = \frac{100 F_z}{\frac{1}{2} \rho b^2 c R U^2}$$

avec P Puissance totale
Fz Portance rotor
 ρ Masse volumique
b Nombre de pale
c Corde moyenne
U Vitesse périphérique
R Rayon du rotor

Un bon accord est mis en évidence pour les puissances et les portances modérées, et des écarts sensibles mais acceptables sont constatés pour les configurations plus chargées. Cette méthode permet de déterminer de manière fidèle les performances d'un rotor en vol d'avancement et son faible temps de calcul (de l'ordre d'une seconde sur CRAY XMP 18) facilite son intégration dans un processus d'optimisation.

4.1.2 - Variables de décision

Pour l'optimisation de la position des profils en envergure, les variables de décision sont les rayons limitant les parties de pale à profil constant. Le rayon de début de la partie profilée de la pale et le rayon du rotor étant imposés à ce stade de la définition du rotor, le problème d'optimisation comprend $2n-2$ variables à optimiser pour une base de n profils. La figure 15 présente les différentes parties de la pale à profil constant et à profil évolutif. La définition des variables de décision et les spécifications technologiques imposent sur les rayons de début et de fin, notés (R_{di} , $i = 1, n$) et (R_{fi} , $i = 1, n$), les contraintes suivantes :

$$\begin{array}{ll} R_{di} < R_{fi} & n \text{ contraintes} \\ R_{di+1} - R_{fi} < a R & n-1 \text{ contraintes} \end{array}$$

avec a constante permettant de contrôler l'étendue minimale des parties de pale à profil évolutif.

Dans le cas particulier d'une pale définie avec deux profils, le problème d'optimisation comprend deux variables de décision et trois contraintes (quatre variables de décision et cinq contraintes pour une base de trois profils).

L'optimisation de la position des profils en envergure est effectuée en conservant le vrillage aérodynamique de la pale pour limiter dans l'optimisation la modification de la loi de circulation. Le vrillage géométrique est modifié au cours des itérations pour tenir compte des incidences de portance nulle des différents profils.

4.2 - Optimisation en un point

Les résultats présentés concernent l'optimisation du rotor d'un hélicoptère de 8 à 10 tonnes : le rotor possède un rayon $R = 8$ m et comprend quatre pales rectangulaires de 0,6 m de corde. Les profils OA312 et OA309 présentés précédemment ont été retenus pour équiper ce rotor et les positions de ces profils en envergure ont été définies par optimisation numérique : les deux variables considérées étant le rayon de fin du profil OA312 ($R1/R$) et le rayon de début du profil OA309 ($R2/R$). La répartition initiale, déterminée à partir de l'expérience acquise sur les rotors existants, est $R1/R = 0,8$ et $R2/R = 0,9$. Dans une première étape, l'optimisation peut être effectuée pour une seule configuration pour établir des gains potentiels par rapport à la répartition initiale. Plusieurs cas de vol peuvent être distingués :

- vol stationnaire ;
- vol d'avancement ;
- vol en facteur de charge (virage ou ressource stabilisée) ;
- vol de montée.

L'objectif à minimiser est la puissance nécessaire au rotor principal ; pour les cas de vol en virage ou en ressource la maximisation du facteur de charge pourrait être considérée. A titre d'exemple, l'optimisation de la position en envergure des profils a été effectuée pour un cas de vol d'avancement à l'altitude $H = 0$ m, une traînée de fuselage $S_{Cx} = 2,1 \text{ m}^2$ et une vitesse de rotation du rotor $\omega = 259 \text{ tr/mn}$. La constante " a " a été choisie égale à 0 pour ne pas limiter l'étendue des parties de pale à profil évolutif dans cette étude paramétrique, effectuée en fonction de la masse de l'appareil et de la vitesse d'avancement.

La figure 16 met en évidence l'évolution de la répartition optimale des profils OA312 et OA309 en fonction de la masse de l'appareil pour une vitesse d'avancement de 275 km/h. L'augmentation de la portance du rotor nécessite l'utilisation du profil de 12% d'épaisseur relative sur une plus grande partie de la pale, compte tenu des meilleures caractéristiques de ce profil à C_z élevé.

L'évolution de la répartition optimale en fonction de la vitesse d'avancement est présentée figure 17 pour une masse d'appareil de 3 tonnes. Dans ce cas, les variations sont plus faibles : les avantages

apportés par le profil OA309 en pale avançante pouvant être compensés par de moins bonnes caractéristiques en pale reculante.

La réduction de la puissance obtenue avec l'optimisation en un point est tracée figure 18 en fonction de la masse de l'hélicoptère et de la vitesse d'avancement. Par rapport au rotor initial ($R1/R = 0,8$, $R2/R = 0,9$), les gains les plus importants correspondent à la configuration faible masse et vitesse élevée : la position optimale des profils étant dans ce cas $R1/R = 0,41$, $R2/R = 0,43$.

4.3 - Optimisation en deux points

Les conditions de fonctionnement étant très différentes en fonction des cas de vol considérés, le rotor optimisé peut présenter des caractéristiques aérodynamiques peu intéressantes en dehors des conditions d'optimisation. Afin de ne pas privilégier une seule configuration, la fonction objectif peut prendre en compte les performances du rotor, correspondant à deux cas de vols différents, de la manière suivante :

$$OBJ = (1 - n) P1 + n P2$$

avec P1 Puissance nécessaire au rotor pour le cas de vol n° 1
 P2 Puissance nécessaire au rotor pour le cas de vol n° 2
 n Variable de pondération comprise entre 0 et 1

Lorsque n est égal à 0 ou 1, l'optimisation est effectuée respectivement pour les configurations 1 et 2. Pour n compris entre 0 et 1, le rotor est optimisé en tenant compte des deux cas de vol avec la possibilité d'affecter un poids plus important sur l'un ou l'autre. Cette optimisation en deux points a été mise en oeuvre en considérant les deux cas de vol suivants :

- Point 1

- Point 2

M = 8t, H = 0 m, V = 250 km/h.

M = 8t, H = 3000 m, V = 360 km/h.

Ces configurations, rotor peu chargé à vitesse modérée et rotor chargé à vitesse élevée, imposent des répartitions différentes de profils en envergure : ($R1/R = 0,43$, $R2/R = 0,48$) pour le premier point et ($R1/R = 0,66$, $R2/R = 0,67$) pour le second.

La figure 19 montre les réductions de puissance obtenues après optimisation pour les deux points de fonctionnement considérés en fonction du coefficient de pondération n. La réduction de la puissance pour le premier cas de vol évolue de -3,9% à -3% pour respectivement n = 0 et n = 1. La réduction de la puissance pour le second cas de vol est comprise entre -3,3% et -5% avec une variation importante des gains pour des coefficients de pondération inférieurs à 0,4. Le meilleur compromis entre les réductions de puissance obtenues pour les deux cas de vol, semble correspondre à l'optimisation n = 0,4.

La figure 20 montre l'évolution des répartitions optimales des profils en envergure en fonction du coefficient de pondération n. La répartition optimale correspondant à l'optimisation n = 0,4 est la suivante :

- profil OA312 jusqu'à $0,56 R$;
- profil évolutif de $0,56 R$ à $0,66 R$;
- profil OA309 de $0,66 R$ jusqu'à l'extrémité.

Les performances du rotor optimisé sont comparées à celles du rotor initial figure 21. La modification de la position des profils en envergure modifie principalement la puissance due aux profils qui représente environ 30 à 40% de la puissance totale. Cette réduction est de -8% aux basses vitesses et de -13,5% aux grandes vitesses pour les deux altitudes considérées. En tenant compte des autres termes de puissance, puissance induite de mise en mouvement du fluide à travers le rotor et puissance de fuselage, la réduction de la puissance totale à fournir au rotor est respectivement -3,4% et -4,8%. Il apparaît ainsi que le choix des profils et de leurs positions en envergure constituent des paramètres importants pour l'optimisation des rotors.

Dans la conception générale des hélicoptères actuels, les cas de vol en facteur de charge constituent également des conditions de fonctionnement qui peuvent imposer des répartitions différentes de profils (utilisation du profil de 12% d'épaisseur relative jusqu'à $0,75 R$ ou $0,80 R$). Le cas de vol avec maximisation de la portance devra donc être intégré au processus d'optimisation.

4.4 - Perspectives

Dans les applications précédentes, l'utilisation des méthodes d'optimisation numérique permet d'éviter un grand nombre d'itérations de conception pour le choix de la répartition des profils en envergure avec la possibilité de prendre en compte deux cas de vols différents. L'optimisation de la loi de corde et du vrillage sont dès à présent possibles avec la méthode présentée. Les paramètres de définition de la pale peuvent être optimisés simultanément ce qui devrait permettre d'obtenir à moyen terme des gains significatifs par rapport aux rotors actuels. A plus long terme, l'optimisation des extrémités de pale pourrait être effectuée par optimisation numérique en utilisant les méthodes tridimensionnelles transsoniques [18].

5 - CONCLUSIONS

L'utilisation des méthodes d'optimisation numérique s'est avérée particulièrement intéressante pour les définitions de profils et de pales d'hélicoptère dans la mesure où ces méthodes permettent d'éviter un grand nombre d'itérations de conception, tout en prenant en compte plusieurs conditions de fonctionnement.

La méthode d'optimisation de profils associe une méthode de minimisation sous contraintes à un programme de calcul direct de l'écoulement transsonique visqueux. Elle a permis de définir deux profils de pale d'hélicoptère de 12% et 9% d'épaisseur relative en considérant deux points d'adaptation représentant les conditions de fonctionnement en pale avançante et reculante d'un cas de vol d'avancement. Les vérifications expérimentales effectuées dans la soufflerie S3MA de l'ONERA confirment les gains importants prévus par le calcul.

L'optimisation des pales d'hélicoptère est réalisée en associant la méthode de minimisation sous contraintes à une méthode de calcul des performances du rotor basée sur la théorie de l'élément de pale. L'optimisation présentée de la position des profils OA312 et OA309 le long de la pale illustre les possibilités et les avantages des méthodes d'optimisation numérique pour réaliser un bon compromis entre les différents cas de vol.

Les perspectives de développement envisagées concernent d'une part l'optimisation de profils de pale de rotor principal en couplage fort ou en écoulement instationnaire et d'autre part l'optimisation des rotors d'hélicoptère en considérant l'ensemble des paramètres de définition de la pale (rayon du rotor, loi de corde, vrillage, position des profils en envergure).

REFERENCES

- [1] ASHLEY H. On Making Things the Best-Aeronautical Uses of Optimization. AIAA 81-1738, 1981.
- [2] VANDERPLAATS G.N. CONMIN-A Fortran Program for Constrained Function Minimization. NASA TMX 62,282, 1973.
- [3] VANDERPLAATS G.N. Numerical Optimization Techniques for Engineering Design : With Applications. Mc GRAW-HILL Series in Mechanical Engineering, 1984.
- [4] THIBERT J.J., GALLOT J. A New Airfoil Family for Rotor Blades. Third European Rotorcraft and Powered Lift Aircraft Forum, 1977. TP ONERA 1977-113.
- [5] THIBERT J.J. and POURADIER J.M. Design and Test of an Helicopter Rotor Blade with Evolutive Profile. 12 th Congress of the International Council of the Aeronautical Sciences, 1980. TP ONERA 1980-125.
- [6] THIBERT J.J., GALLOT J. Advanced Research on Helicopter Blade Airfoils. Vertica, Vol 5, p. 279-300, 1981.
- [7] RENEAUX J. Numerical Optimization Method for Airfoil Design. La Recherche Aérospatiale, 1984 N° 5.
- [8] BOUSQUET J. Calculs bidimensionnels transsoniques avec couche limite. AAAF, 11e Colloque d'Aérodynamique Appliquée, 1977.
- [9] VANDERPLAATS G.N. and HICKS R. Numerical Airfoil Optimization Using a Reduced Number of Design Coordinates. NASA-TMX 73,151, 1976.
- [10] AIDALA P.V., DAVIS W.H., MASON W.H. Smart Aerodynamic Optimization. AIAA, 831863, 1983.
- [11] RENEAUX J., THIBERT J.J. The Use of Numerical Optimization for Airfoil Design. AIAA 85-5026, Colorado Springs, 1985. T.P. ONERA 1985-135.
- [12] LE BALLEUR J.C. Strong Matching Method for Computing Transonic Viscous Flows Including Wakes and Separations. Lifting Airfoils. La Recherche Aérospatiale, 1983 N° 3.
- [13] COSTES M., JONES H.E. Computation of Transonic Potential Flow on Helicopter Rotor Blades. 13 th European Rotorcraft Forum, Arles, Septembre 1987.
- [14] BENNETT R.L. Application of Optimization Methods to Rotor Design Problems. Vertica, Vol 7, N° 3, p. 201-208, 1983.
- [15] WALSH J.L., BINGHAM G.J., RILEY M.F. Optimization Methods Applied to the Aerodynamic Design of Helicopter Rotor Blades. AIAA 85-0644, 1985.
- [16] KUMAR S., BASSETT D. Rotor Performance Optimization for Future Light Helicopters. 43 rd Annual AHS Forum, Mai 1987.
- [17] FAVIER-D., VUILLET A. Etude du champ aérodynamique d'un rotor d'hélicoptère en vol stationnaire. Comparaison théorie-expérience. 23ème Colloque d'Aérodynamique Appliquée, 1986.
- [18] TAUBER M.E., LANGHI R.G. Transonic Rotor Tip Design Using Numerical Optimization. NASA TM 86771, 1985.

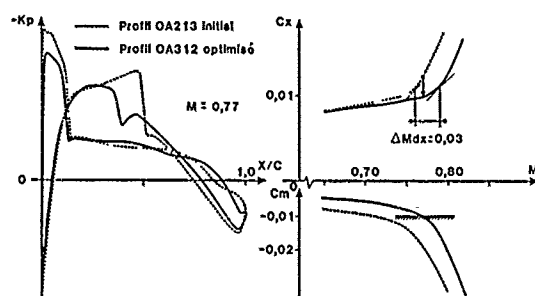


Fig 1 - Caractéristiques aérodynamiques calculées des profils OA213 et OA312 dans les conditions de pale avançante. $C_z=0$, $Re=8 \times 10^6$.

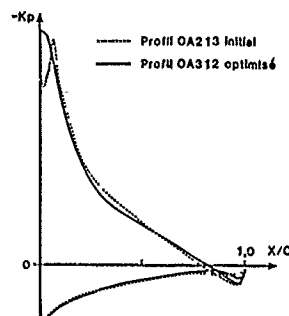


Fig 2 - Caractéristiques aérodynamiques calculées des profils OA213 et OA312 dans les conditions de pale reculante. $M=0,40$, $C_z=1,50$, $Re=3,2 \times 10^6$.

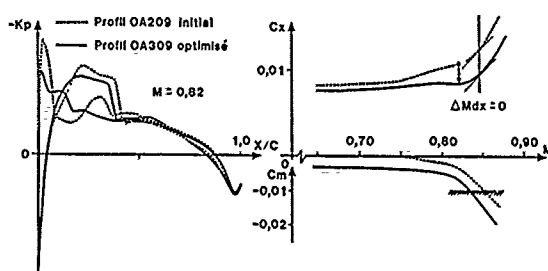


Fig 3 - Caractéristiques aérodynamiques calculées des profils OA209 et OA309 dans les conditions de pale avançante. $C_z=0$, $Re=8 \times 10^6$.

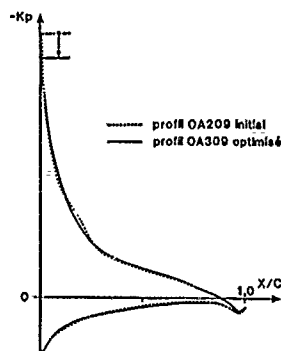


Fig 4 - Caractéristiques aérodynamiques calculées des profils OA209 et OA309 dans les conditions de pale reculante. $M=0,40$, $C_z=1,10$, $Re=3,2 \times 10^6$.

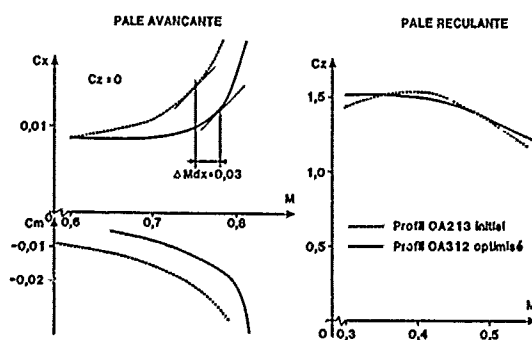


Fig 5 - Caractéristiques aérodynamiques mesurées à S3MA des profils OA213 et OA312. $Re=5 \times 10^6$.

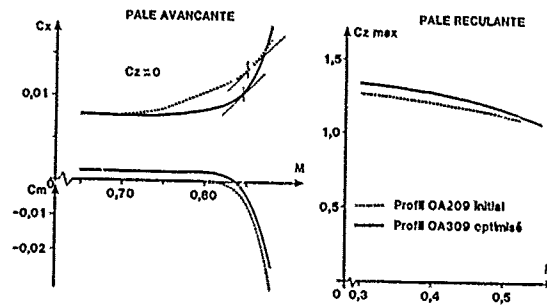


Fig.6 - Caractéristiques aérodynamiques mesurées à S3MA des profils OA209 et OA309. $Re=8 \times 10^6$.

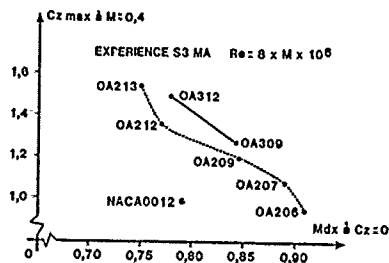


Fig.7 - Performances comparées des différents profils de pale d'hélicoptère.

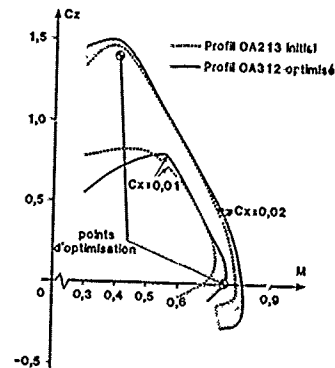


Fig.8 - Caractéristiques aérodynamiques mesurées à S3MA des profils OA213 et OA312. $Re=8 \times 10^6$.

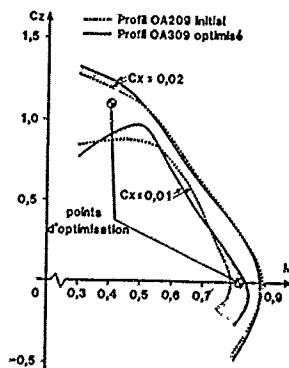


Fig.9 - Caractéristiques aérodynamiques mesurées à S3MA des profils OA209 et OA309. $Re=8 \times 10^6$.

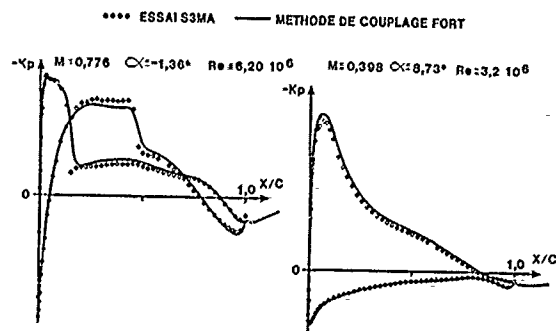


Fig.10 - Répartitions de pression mesurées et calculées par une méthode de couplage fort sur le profil OA312. Conditions de pale avançante et de pale reculante.

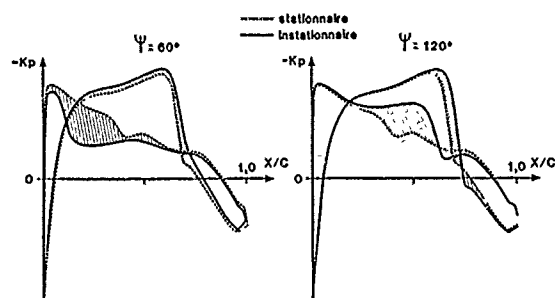


Fig.11 - Comparaison des répartitions de pression calculées sur le profil OA312 en écoulement stationnaire et instationnaire.

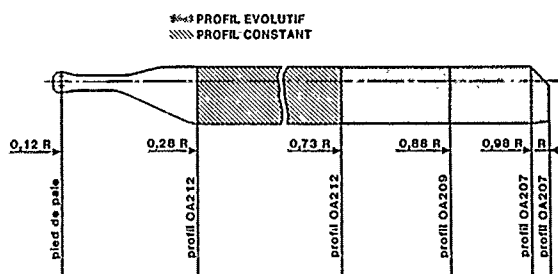


Fig.12 - Définition de la pale de l'hélicoptère Dauphin 365N.

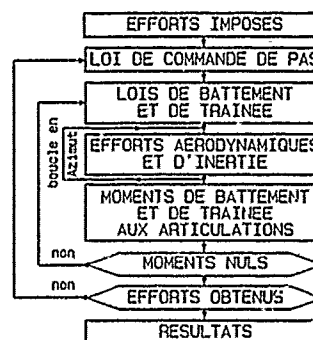


Fig.13 - Organigramme du programme de calcul des performances en vol d'avancement.

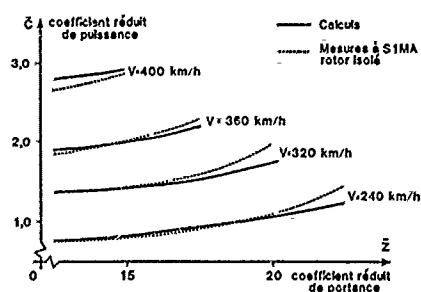


Fig.14 - Performances calculées et mesurées à S1MA d'un rotor d'hélicoptère.

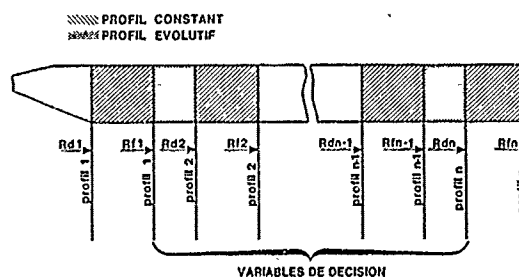


Fig.15 - Optimisation de la position des profils en «enveloppe» - Définition des paramètres à optimiser.

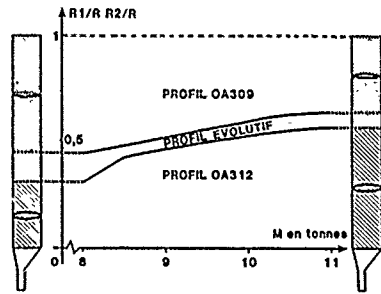


Fig.16 - Evolution de la position optimale des profils en fonction de la masse de l'hélicoptère pour une vitesse de 275 km/h.

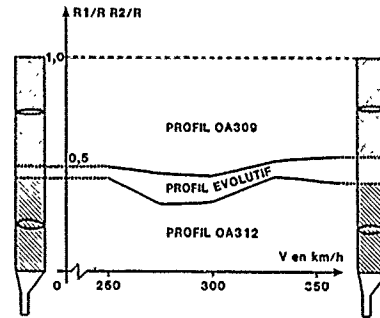


Fig.17 - Evolution de la position optimale des profils en fonction de la vitesse de l'hélicoptère pour une masse de 8 tonnes.

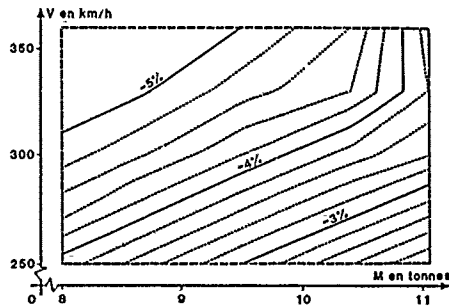


Fig.18 - Réduction de la puissance obtenue avec l'optimisation en un point en fonction de la masse de l'hélicoptère et de la vitesse.

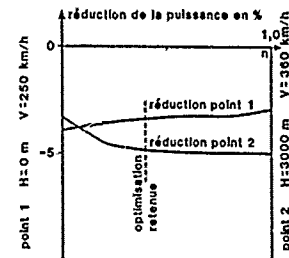


Fig.19 - Optimisation en deux points. Réductions des puissances obtenues en fonction du coefficient de pondération n .

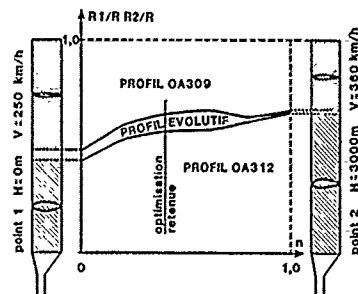


Fig.20 - Optimisation en deux points. Position optimale des profils en fonction du coefficient de pondération n .

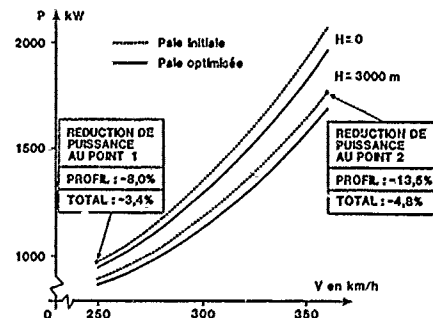


Fig.21 - Comparaison des performances de la pale initiale et de la pale optimisée.

AERODYNAMIC DESIGN BY OPTIMIZATION

by

K.-W. Bock
 Dornier Luftfahrt GmbH
 BF 20
 Postfach 1420
 7990 Friedrichshafen
 Federal Republic of Germany

ABSTRACT

This paper describes the experience gained when coupling different aerodynamic analysis codes and optimization procedures. First a simple problem is considered (airfoil of minimum wave drag, analysis by shock expansion theory) in order to compare the usability of a random search procedure to that of a gradient method (COPEs by G.N. Vanderplaats). The second one shows a superior performance. Then three aerodynamic programs are coupled with COPEs and tested: 1. Euler space-marching program for bodies of revolution at supersonic, 2. transonic airfoil redesign method (fictitious gas concept) and 3. multiple airfoil analysis code for flap position optimization. It can be demonstrated that COPEs is a very universal optimization tool which can be easily combined even with complex aerodynamic codes. Its convergence is good even under constraints. This is important because the number of analysis calculations is most important for typical aerodynamic problems of high numerical expense.

I. INTRODUCTION

To solve aerodynamic design problems two principally different procedures might be followed. 1) In some cases special design methods are available to determine the configuration (e.g. shape of an airfoil) satisfying the given design objective (e.g. a desirable pressure distribution). Such a design method might be created by integrating a variation function into an analysis method, and inserting an iteration procedure to minimize the design objective function following the steepest descend. A. Jameson⁽²⁰⁾ illustrates this "design via control theory" by three applications in aerodynamic design. 2) More often the only possibility is to solve the analysis problem (theoretically or by experiment) many times for more or less systematic variations of a starting configuration and thus approach the optimum design iteratively. This is necessary especially for those problems which are too complex for inverting the analysis code into a design code or which depend on too many design parameters and have to fulfil too many constraints. As long as the theoretical methods used for this purpose lack validity and accuracy, the experience of the designer is necessary to control this iteration process by skilful variation. But if a closed and reliable analysis code is available, it is obviously useful to combine it with an optimization method in order to find the best design automatically.

The aerodynamic design by optimization usually shows the following features:

- high number of design variables (e.g. if a surface to be optimized is described by a parameter function),
- high number of constraints (e.g. thickness, minimum pressure, stability margin), often of nonlinear character,
- well-defined design objective (e.g. maximum lift or lift to drag ratio, minimum drag, least square approximation of pressure distribution), nearly always of nonlinear character,
- existing theoretical or empirical computer codes for the aerodynamic analysis,
- computation time (and cost) of analysis often considerably high.

So the main requirements for an appropriate optimization are:

- simple integration of analysis code into optimization code,
- optimization of nonlinear design objective for nonlinear constraints,
- as few analysis calculations as possible.

II. COMPARISON OF TWO OPTIMIZATION METHODS

In literature many different optimization methods and computer codes can be found. The fundamentals of the main categories are described by G.N. Vanderplaats⁽¹⁾. In the aerodynamic design the application of optimization procedures becomes more and more important as several papers presented at the ICIDES-II⁽²⁾ demonstrate. For the design departments of an aero-space company it is necessary to make use of a well-tested and reliable optimization code which does not need complicate modification of the analysis code. Here two of such methods are examined and compared with special regard to aerodynamic problems:

- a random search method (based on evolution theory),
- a gradient method.

Both methods are used to solve an optimization problem which generally can be formulated by:

$F(\bar{X})$ is a design objective function which has to be minimized,

\bar{X} is the vector (X_1, X_2, \dots, X_n) of design variables which completely determine the design,

$G_j(\bar{X})$ are $j = 1, 2, \dots, m$ constraint functions which have to obey the condition $G_j(\bar{X}) \leq 0$ (this includes constraints of design variables).

II.1 Random Search

The random search method under consideration is based on the evolution theory which sometimes is considered to be an alternative to mathematically derived methods. More or less it is a simulation of the evolutionary progress in biology. The computer code GRUP was developed by H.P. Schwefel⁽³⁾. Figure 1 presents different levels of this method.

In figure 1A the simplest level, the 2-level evolution theory, is illustrated. At the beginning there is a single individual with a set of variables (design variables)

$$\vec{X} = (X_1, X_2, \dots, X_n) \quad (1)$$

which completely determine its quality

$$F(\vec{X}) = fkt(\vec{X}) \quad (2)$$

(design objective function). $F(\vec{X})$ is to be minimized by variation of the design variables. For that purpose this "parent individual" is duplicated and mutated. By this mutation the variables and thus the quality of the "child individual" are changed. Together with the parent individual it is put into a selection box from which the better one is selected to become the parent individual of the next optimization step. One important element of the evolution is the mutation i.e. the random variation of the design variables. GRUP uses the following procedure: At the beginning the input gives maximum step widths S_i which determine, how much each variable X_i is allowed to be changed. These maximum step widths are multiplied by a Gauss distribution random number r_i of the interval $(-1, +1)$. So the mutation is described by:

$$X_{c,i} = X_{p,i} + S_i \cdot r_i \quad (3)$$

Here c describes the child individual and p the parent individual. In order to improve the convergence, the maximum step widths S_i are adapted during the optimization progress. In the 2-level evolution theory of figure 1A the S_i are selected so that, at the average, one of a given number of mutations leads to an improvement of the design objective.

The simplest extension of the 2-level evolution theory is the multilevel theory of figure 1B: Instead of only one now more (e.g. 6 in figure 1B) child individuals are created by duplication and then independently mutated. These are put into the selection box together with the parent individual.

In the theory shown in figure 1C the parent individual itself is not put into the selection box. This corresponds to the situation in biology where each individual has a limited life time and normally is not mixed with the next generation.

Figure 1D illustrates a further improvement towards the simulation of biological evolution: Here of each generation not only the best individual does survive. Additionally a certain number of the next best individuals is selected for duplication. In the example of figure 1D from 3 parents 9 child individuals are created by random selection. These are mutated and put into the selection box from which the 3 best are selected to become the parents of the next optimization step.

The multi-level evolution theory code GRUP makes use of an improved mutation width adaption derived from the biological evolution and which is more successful concerning the convergence: The design variables $\vec{X} = (X_1, X_2, \dots, X_n)$ determine the objective function $F(\vec{X})$ to be optimized. So they shall be called "objective variables". In addition to them the step widths S_i of the mutation leading to each individual are introduced as further "strategy variables":

$$\vec{S} = (S_1, S_2, \dots, S_n) \quad (4)$$

When duplicating and mutating parent individuals these variables are duplicated and mutated in an appropriate manner (see H.P. Schwefel⁽³⁾). Thus the mutation width itself becomes an object of the optimization by evolution.

The constraints

$$G_j(\vec{X}) \leq 0; \quad j = 1, 2, \dots, m \quad (5)$$

are taken into consideration as follows: all duplications and mutations which violate one or more of the constraints are removed and repeated until all constraints are satisfied.

For a better simulation of the biological evolution I. Rechenberg⁽⁴⁾ developed further higher order theories, where sexual reproduction (mixture of two or even more parents) as well as the comparison, selection, and mixture of whole populations is taken into consideration. These strategies require a large number of mutations and validations or in other words analysis calculations. As the analysis in aerodynamics normally needs long computation times they are of no practical interest in aerodynamic optimization.

Example

To test the applicability of the GRUP-code for aerodynamic optimization a problem was selected where the analysis, in contradiction to normal cases, is very simple: Minimize the wave drag of a symmetrical sharp edged profile obeying different constraints at supersonic flow without angle of attack. By complete linearization the pressure coefficient at the contour is

$$C_p(x) = \frac{p(x) - p_\infty}{q_\infty} = \frac{2}{\sqrt{M_\infty^2 - 1}} \cdot \frac{dz}{dx} \quad (6)$$

and the drag coefficient is

$$C_D = \frac{D}{q_\infty \Delta y l} = 2 \int_0^1 C_p(x) \frac{dz}{dx} d\frac{x}{c} = \frac{4}{\sqrt{M_\infty^2 - 1}} \int_0^1 \left(\frac{dz}{dx}\right)^2 d\frac{x}{c}, \quad (7)$$

where $z(x)$ describes the contour, c is the chord length and Δy is the width in spanwise direction. For this eq. (7) exact solutions of minimum drag profiles are known (comp. A. Miele⁽⁵⁾ or D.R. Chapman⁽⁶⁾). E.g. for a required least thickness this is a double wedge profile with its maximum thickness in the middle of the chord. If the following pressure relation from the shock-expansion theory is used:

$$C_p(x) = \frac{\gamma+1}{2} m^2 \sin^2 \tau + \frac{2m \sin \tau}{M_\infty} \sqrt{1 + \left(\frac{\gamma+1}{2}\right)^2 m^2 M_\infty^2 \sin^2 \tau} \quad (8)$$

($m = M_\infty / \sqrt{M_\infty^2 - 1}$; γ = ratio of specific heats, $\tan \tau = dz/dx$), no analytical solutions can be given. The minimum drag profile is no longer symmetric to $x = c/2$. This problem was solved numerically by H.N.V. Dutt and A.K. Srekanth⁽⁷⁾ by use of the gradient method CONMIN of G.N. Vanderplaats⁽⁸⁾ and now shall be used as test case for the evolution theory code GRUP.

In order to convert the problem into one of variable optimization, the profile contour is approximated by the following superposition

$$\zeta = a_0 + a_1 P_1(\xi) + \dots + a_5 P_5(\xi) + a_6 Q(a_7, \xi) \quad (9)$$

with the nondimensional coordinates

$$\xi = \frac{x}{c/2} - 1 \quad \text{and} \quad \zeta = \frac{z}{c/2}. \quad (10)$$

As, according to G.N. Vanderplaats et al⁽⁹⁾, orthogonal polynomials are to be preferred, Legendre polynomials were chosen for the functions $P_i(\xi)$. $Q(\xi)$ is a linear triangle function with its maximum value $Q = 1$ at $\xi = a_7$. Using the conditions $\zeta(\xi = \pm 1) = 0$ (pointed leading and trailing edge) the coefficients a_0 and a_6 can be derived from the others by $a_0 = -a_1 - a_3 - a_5$ and $a_6 = -a_1 - a_3$. So in eq. (9) only six coefficients are free design variables.

Figure 2 shows the optimization progress of the minimum wave drag profile at the free stream Mach number $M_\infty = \sqrt{3}$ for the constraint

$$d/l \geq 0.1.$$

The starting profile contour is given by a parabola of second order ($a_1 = a_3 = a_5 = a_7 = 0$; $a_2 = -2/3 \cdot 0.1$). Its thickness $d/l = 0.1$ is at the minimum allowed value. The corresponding wave drag coefficient is $C_D = 0.0380$. According to D.R. Chapman⁽⁶⁾, the optimum profile is a double wedge. For $M_\infty = \sqrt{3}$ its maximum thickness is at $x/l = 0.5641$ and the minimum wave drag is $C_D = 0.0279$.

The best strategy found was a (2,20)-level evolution theory (comp. figure 1D). Figure 2B shows the drag coefficient over the number of analysis calculations which is of more importance than the number of iteration steps (change from one generation to the next). At the beginning there is a wide dispersion of drag values. It needs 33 analysis calculations until C_D is lower than the starting value for the first time and 178 calculations until the best result is reached. But still it is considerably higher than the minimum and the contour differs from the optimum double wedge. The adaption of the mutation width leads to the convergence but on the other hand may be the reason for not catching the optimum. As the number of analysis calculations is the main criterion for the numerical time consumption, it is important to know that in figure 2B only those steps are shown which obey the constraint. In addition to the 200 calculations with constraints fulfilled there were 100 calculations carried out with constraints violated.

Other examples with different constraints (e.g. the area between upper and lower contour) show a similar convergence of the GRUP-code. In general the optimization is faster if the optimum is approached from the unconstrained design area and not along the boundary of the constrained region as in figure 2.

II.2 Gradient Method

G.N. Vanderplaats developed a universal computer code for the variable optimization of constrained functions. It is known under the name COPES (Control Program for Engineering Synthesis). G.N. Vanderplaats gives a short review in ⁽¹⁰⁾ while the details of the fundamental theories can be found in his book ⁽¹¹⁾. Here only the most important features shall be described.

COPES includes the optimization code CONMIN⁽⁸⁾ (Constrained Function Minimization), the strategy of which shall be explained for the two-variable case by use of figure 3.

At the starting point \bar{X}^0 each component of the design variable vector \bar{X} is subsequently varied to find the gradient $\nabla F(\bar{X}^0)$. This comes to be the search direction \bar{S}^1 in which for two further design vectors \bar{X} the function value $F(\bar{X})$ is calculated (compare figure 3A). By interpolation the vector \bar{X}^1 is found where F approximately is a minimum in this search direction. Now this procedure might be repeated until the optimum is found. Unfortunately this leads to convergence problems for nonlinear functions $F(\bar{X})$. To overcome these difficulties, now, instead of searching in the gradient direction, the search vector \bar{S} is calculated after R. Fletcher and C.M. Reeves⁽¹¹⁾ from the gradient and the last search direction by

$$\bar{S}^q = -\nabla F^q + |\nabla F^q| / |\nabla F^{q-1}| \cdot \bar{S}^{q-1}. \quad (11)$$

This "method of conjugate directions" guarantees convergence towards the optimum of a quadratic function to occur in at least n iterations (n = number of design variables).

When the design reaches the vicinity of the constrained region (comp. figure 3B), the search direction is calculated from the gradient ∇F of the objective function and from the gradient ∇G_j of the active constraint. In order to avoid a slow "zig-zagging" along the boundary a "push off factor" (influenced by input) is used to orientate the search vector in the overlap of the feasible sector (allowed directions) and the usable sector (direction improving the objective function). If the starting or another preliminary design is in the constrained area there is a procedure to find the unconstrained region with best improvement or at least minimum worsening of the objective function.

Each iteration step of this procedure needs $n + 3$ analysis calculations (one for initial point, n to find the gradient, two in search direction). For typical aerodynamic problems, where the analysis might be extremely time-consuming, it is obviously not reasonable to forget all the gradient information gained during the preceding steps. For that reason the program COPES uses a more economical procedure:

For the initial design variables \bar{X}^q the objective function F and the constraint functions G_j are approximated by a second order Taylor series:

$$F(\bar{X}) = F^q + \Delta \bar{X}^T \nabla F^q + \frac{1}{2} \Delta \bar{X}^T H^q \Delta \bar{X}, \quad (12)$$

$$G_j(\bar{X}) = G_j^q + \Delta \bar{X}^T \nabla G_j^q + \frac{1}{2} \Delta \bar{X}^T H_j^q \Delta \bar{X}. \quad (13)$$

Using these Taylor approximations instead of the correct analysis calculation, an improved design is found by the optimization procedure described above. Thereby the step width has to be limited in order not to move too far away from the centre of the Taylor series. Finally now the correct analysis has to be done for this approximately improved design. These exact objective and constraint function values together with the preceding ones are used to determine the Taylor approximation at the new initial design. By this procedure only one exact calculation is necessary per optimization step and the approximation gets better and better. Only the "starting procedure" at the very beginning of the optimization needs more calculations because the complete 2nd order Taylor series requires $1 + n + n(n+1)/2$ points of support. The COPES code uses a starting procedure which improves the design already during building up the initial Taylor series. The starting procedure can be influenced by prescribing the starting design variable sets. It can be drastically shortened by the input of already known results, e.g. from an interrupted optimization or from similar optimizations with different constraints.

Example

To test the applicability of the COPES code for aerodynamic optimization and to compare it with the evolution theory code GRUP the example of figure 1 (comp. chapter II.1) has been repeated:

Find minimum wave drag sharp edged profile at $M_\infty = \sqrt{3}$ for thickness $d/l \geq 0.1$.

The pressure distribution is approximated by eq. (8) and the contour is represented by eq. (9) where the coefficients $a_1, a_2, a_3, a_4, a_5, a_6$ are the design variables. Figure 1B shows that, compared to GRUP, the COPES code needs much less analysis calculations N to improve the design. It should be noted that COPES not only uses the designs in the unconstrained area ("+"-Symbols in figure 1B) but also those in the constrained region ("x"-Symbols) for the Taylor series and thus for the optimization progress. Already at $N = 40$ a result is gained for which GRUP needs more than 100 analysis calculations (plus about 60 in the constrained area). The optimum drag value practically is reached at $N = 50$ while GRUP does not converge to that result. As the drag near the optimum is only slightly sensitive to the backward position of the maximum thickness the best COPES profile still differs a little bit from the optimum double wedge.

While the evolution theory code obviously is of no practical use for typical aerodynamic problems, the universal gradient method COPES seems to be a useful optimization tool even in combination with complex and time-consuming analysis programs.

III. APPLICATION OF GRADIENT METHOD TO AERODYNAMIC DESIGN PROBLEMS

The following examples present the combination of typical complex and time-consuming aerodynamic analysis codes with the optimization code COPES of G.N. Vanderplaats⁽¹⁰⁾. The main objective of these investigations was not to present optimized aerodynamic shapes of common interest. Instead, it was intended to gain experience in

- what is necessary to integrate analysis codes into COPES,
- what are the possibilities and limitations of COPES in aerodynamic optimization,
- how often is the analysis calculation necessary depending on the number of design variables and constraints?

III.1 Bodies of Revolution in Supersonic Flow

The optimization code COPES was combined with an Euler space-marching method by H. Rieger⁽¹²⁾ for the analysis of 2D- and 3D-bodies at supersonic flow. The fundamental equations to be solved are the conservation laws in integral form. By restriction to purely supersonic flows the problem becomes hyperbolic. So, by use of the balance of flux values across the surfaces of finite volumes, all flux values of one finite volume layer normal to the stream direction can be deduced from the values of the preceding layers. This allows to apply a Runge-Kutta integration method to the flux values in downstream direction.

Although the present method can be used for more general 3D-bodies, here only bodies of revolution shall be considered. These are of special interest because A. Miele⁽⁵⁾ presents some optimized shapes derived under special assumptions (linearized potential equation, slender body simplification). To convert the

contour optimization into a parameter optimization problem the superposition of eqs. (9 - 10) is used, where the coordinate z now has to be replaced by the radius r . Using the conditions $\zeta(\xi = -1) = 0$ (pointed nose) and $\zeta(\xi = +1) = \zeta_B$ (finite base radius) the coefficients a_0 and a_1 can be expressed by $a_0 = \zeta_B/2 - a_2 - a_4$ and $a_1 = \zeta_B/2 - a_3 - a_5$. So ζ_B and six coefficients of eq. (9) are free design variables. The triangle function $F(\xi)$ with its maximum at a , was introduced because minimum wave drag bodies for given least thickness might have a kinked contour (compare A. Miele⁽⁵⁾). The optimization code may use:

design variables: 6 coefficients of superposition eq. (9) and base radius,

design objective and constraints: C_L , C_D , C_m , r_{\max}/c , A/c^2 (area of body projection into r - x plane) and V/c^3 (body volume).

Example:

To demonstrate the efficiency of the combined code, the following optimization problem was examined:

design objectives: Find closed and pointed body of revolution with minimum wave drag coefficients C_D (referred to actual cross section area).

constraint: Least volume $V/c^3 \geq 0.005$.

design variables: Under special simplifications the optimum is the Sears-Haack-body without a contour kink. So the contour is described by eq. (9) without the triangle function ($a_1 = a_2 = 0$), and the coefficients a_3 to a_6 are the design variables.

constant value: $M = 3.0$.

starting design: The starting contour is a parabola with the thickness $2 r_{\max}/c = 0.1$ and the volume $V/c^3 = 0.00419$ ($a_1 = a_2 = a_3 = 0$, $a_4 = -2/3 \cdot 0.1$) shown in figure 4 (above right).

For this starting design the computational grid was selected fine enough to give reasonable accuracy concerning the wave drag. The corresponding pressure distribution is shown on the left side. The integrated wave drag is $C_D = 0.07289$.

Figure 5 presents the optimization progress of the design objective C_D and the constraint V/c^3 . In order to save computation time, at the beginning the analysis code was run with a coarser grid and later continued with the fine grid to find the best design. This is the reason for the jump of C_D from design $N = 29$ to design $N = 30$.

The steps $N = 1$ to 9 are small variations prescribed by input to establish the gradients at the beginning. From $N = 10$ the COPEs code is free to find its way to the optimum. Increasing the body volume, which is too small at the beginning, leads to a growing wave drag. From about $N = 23$ the volume is in the feasible area and the drag is decreasing again. The last coarse grid design is already near the real optimum so that the final fine grid optimization is slow.

In figure 6 this optimum body is compared to the Sears-Haack-body which is the optimum under the assumption of a linearized potential equation and slender body simplifications. For $M = 3.0$ there are some differences. For $M = 1.5$ the above mentioned assumptions are violated less and so the present method optimum is much nearer to the Sears-Haack body.

As the Sears-Haack body has a vertical tangent and therefore a small subsonic flow area at the leading end trailing edge, it cannot be calculated by the present Euler space-marching method. At $M = 3.0$ some modifications were possible to get the drag value nevertheless. It is considerably higher (3,6 %) than for the best design found even with the restrictions implied in the superposition formula.

III.2 Airfoils in Transonic Speed

Formally the simplest way to design an optimum transonic airfoil is to combine an optimization code with a reliable analysis program. Thus, indirectly a transonic design code is created. There have been many successful investigations of this kind (e.g. by R.M. Hicks, G.N. Vanderplaats⁽¹³⁾). Furthermore this procedure has also been applied to 3D-wing design with good results (e.g. by R.M. Hicks, P.A. Henne⁽¹⁴⁾ or G.B. Cossentino, T.L. Holst⁽¹⁵⁾). Here another way shall be examined: There is a "redesign theory" available which, by use of the fictitious gas concept, modifies existing airfoils in such a way that the result automatically is shockless. Some of the input parameters of this method can be used as design variables to find a profile which is not only shockless but also an optimum with respect to a certain objective and fulfils given constraints.

The details of the fictitious gas method are described e.g. by H. Sobieczky⁽¹⁶⁾. So here only a short review shall be given. For an existing reliable analysis algorithm for isentropic irrotational gas flow the density-velocity relation $\rho(V)$ is modified in such a way that the resulting basic partial differential equation to be solved becomes elliptic in the entire velocity range. The isentropic flow relation

$$\left(\frac{\rho}{\rho^*}\right)_{\text{isentr.}} = \left[\frac{\gamma+1}{2} - \frac{\gamma-1}{2} \left(\frac{V}{a^*}\right)^2\right]^{1/(\gamma-1)} \quad (14)$$

(*: critical condition) ensures an elliptic type only up to the critical speed, $V < a^*$, while for $V > a^*$ the equation becomes hyperbolic. The elliptic type can be gained also in the supersonic range if, in contradiction to the physical reality, the isentropic flow relation is changed as follows:

$$\left(\frac{\rho}{\rho^*}\right)_{\text{fictit.}} = \begin{cases} (\rho/\rho^*)_{\text{isentr.}} & ; V \leq a^* \\ (V/a^*)^{-P}, 0 < P < 1; V \geq a^*. \end{cases} \quad (15)$$

$P = 1$ means $\rho V = \text{const.}$ which leads to parabolic type while $P > 1$ still gives hyperbolic type equations.

The fictitious gas according to eq. (15) leads to a purely elliptical flow around the airfoil where the transition from sub- to supersonic (if there is a supersonic region at all) takes place without a shock. The result of this calculation is an exact one in the subsonic flow region. Inside the supersonic region a fictitious supersonic flow problem is solved which ensures conservation of mass and momentum globally. This is important for the subsequent calculation of the real supersonic domain, as it ensures that:

- taking the flow values at the sonic line as boundary condition, the supersonic flow region can be designed by use of the correct isentropic relation, provided there are no limit lines,
- there is a streamline in this supersonic region connecting the on- and the offset point of the sonic line,
- slope and curvature are continuous between this streamline and the adjacent original contour.

If the contour in the supersonic region is replaced by this special streamline, the result is a modified shock-free airfoil. The mass flux across the sonic line is the same for the fictitious and the physical flow. On the other hand the density for the physical gas is lower than for the fictitious one (figure 7); so the physical supersonic region is larger than the fictitious one. This means that the modified contour must be below (on the average) the original one.

The computer code by H. Sobieczky which is used here, uses the code FL06 of A. Jameson for the solution of the fully potential equation. The modifications necessary for the fictitious gas are done by H. Sobieczky. The supersonic region is designed (beginning at the sonic line) by use of characteristics in a rheograph plane (method by H. Sobieczky). For the valuation of the resulting airfoil a boundary layer calculation and a final analysis (now physical gas in whole flow field) of the modified profile plus displacement layer has to follow. In the analysis mode the program uses the original code FL06 by A. Jameson and a boundary layer calculation by M. Maudanan (method by J.C. Kotta with shock-boundary layer interaction by G.R. Inger).

The optimization procedure uses a special strategy which always gives shock-free airfoils and therefore needs no shock-boundary interaction code. By use of figure 9 it can be described as follows:

- starting contour is an existing airfoil to be optimized,
- the displacement thickness is estimated and added to get the "displacement contour",
- the "displacement contour" is varied by a modification function depending on the design variables,
- the fictitious gas redesign calculation is performed to get a new shock-free "displacement contour",
- a boundary layer computation follows to find the final contour of optimization step,
- all design objectives and constraints are calculated,
- new design variables are found by optimization code.

The optimization code may use:

design variables: up to 55 parameters for contour variation, the fictitious gas exponent P of eq. (15), the angle of attack,

design objective and constraints: C_L , C_D , C_m , C_L/C_D , t_{max}/c (max. thickness), t_{TE}/c (trailing edge thickness), $C_{p,min}$.

Example

Figure 10 shows an example of the starting design and the best design found by the present optimization using the fictitious gas method. The specifications are:

design objective: C_L/C_D shall become a maximum.

constraints: Maximum thickness $t_{max}/c \geq 0.144$, trailing edge thickness $0.001 \leq t_{TE}/c \leq 0.005$.

design variables: Six parameters of the upper contour modification function (test constant).

constant values: $M = 0.76$, $Re_c = 19 \cdot 10^6$, $\alpha = 0.5^\circ$. starting design: DOA7-airfoil with a special set of initial design variables.

The left side of figure 10 shows the contour (displacement and wall), the characteristics in the supersonic region, and the pressure distribution of the redesigned (already shock-free) airfoil at the first optimization step. As figure 11 illustrates (N = number of analysis calculations), the initial C_L/C_D -ratio is 39.7 and the constraints are fulfilled.

The steps $N = 1$ to 13 are small variations prescribed by input to establish the gradients at the beginning. The effects are too small to be seen in this figure. From $N = 14$ the optimization code is free to find its way to the optimum. It is beginning with good improvements of the objective allowing the constraints to be violated. Then the constraints are directed into the feasible region again with some disadvantages to the objective. The final design after $N = 72$ steps shows an improvement of 12 % from $C_L/C_D = 39.7$ to 44.5. The right side of figure 10 illustrates that the improvement results from the increased lift while the drag remained constant.

As a large number of additional test calculations shows, the present program is a powerful tool for the design of transonic airfoils for different purposes. It is very easy to redesign existing profiles with respect to new objectives and constraints (e.g. new lift, Mach-number or Reynolds number). It can be extended to include the off-design behaviour and be applied to 3D-redesign methods.

III.3 Multi-Element Airfoils

The optimization of multi-element airfoils is a very complex problem because not only the contour of the elements but also their relative position has to be varied. Furthermore such a variable geometry airfoil

has to be designed for different flow conditions. There are some successful efforts of multi-element airfoil optimization (e.g. by H. Schwarten⁽¹⁷⁾), but the number of analysis calculations is always high. So there was the idea to solve the problem by an alternate optimization concerning the relative position parameters and the contour. This paper only deals with the optimization by variation of the position parameters.

For that purpose the COPES-code was coupled with the subsonic multi-element airfoil analysis code PSM by K. Jacob^{(18),(19)}. As the main interest of this paper concerns the optimization procedure, only a rough survey of the PSM shall be given here. Three different flowfield elements are used: the inviscid outer flow, boundary layers, and dead-air regions with the fluid almost at rest. The solution is found by iteration. First the potential outer flow is calculated for estimated boundary layers and dead-air regions (simple shape, pressure constant in three control points), followed by a boundary layer calculation. Then the estimated separation points of all airfoil elements are moved from the trailing edge forward, until they are consistent with the boundary layer result. Compressibility is taken into account by a simple rule modifying the pressure distribution.

The optimization program (combination of PSM and COPES) may use:

design variables: Three position parameters for each flap (x , y -coordinates and deflection angle η).

design objective and constraints: C_L , C_D , C_m , C_L/C_D , s_k/c (width of each slot k), d_k/c (overlap at each slot k), $C_{p,min,i}$ (minimum pressure coeff. of each element i), some other constraints to prevent variations in regions where the analysis gets wrong.

Example

Figure 12 shows the starting design and the best design of a flap position optimization. The contour geometry of the two-element airfoil DOA5 is kept constant. The specifications are:

design objective: C_L should become a maximum.

design variables: x , y -coordinates of a flap fixed point in main coordinate system.

constraint: slot width $s/c \geq 0.01$.

constant values: $M = 0.1$, $Re_c = 5 \cdot 10^6$, $\alpha = 10^\circ$, flap deflection $\eta = -40^\circ$.

As the design objective C_L in this case depends on only two design variables, the optimization procedure can be graphically illustrated. Figure 13 shows the lift coefficient C_L in the area of interest for the flap fixed reference point. It can be seen that the reference point has to move from the starting position (starting design of figure 12) to the constraint line $s/c = 0.01$ nearer to the main element.

The same situation is shown again in figure 14 but now in form of iso-lift lines. The optimization path found by the COPES-code is also indicated. After the first 3 analysis calculations (to find the initial gradient) COPES was free to find its way to the optimum which was reached after totally 30 analysis calculations (plotting the iso-lift lines of course needed much more). The lift coefficient was improved from $C_L = 2.5$ to 3.6 (45 %).

Other examples of flap position optimization (transition and deflection angle) for three element airfoils were similarly successful to find the optimum provided by the PSM analysis code. As it turned out that PSM loses accuracy when the slot width becomes smaller, it was decided first to deal with that problem. Nevertheless COPES has proved to be a very good tool for this problem.

IV. CONCLUSIONS

Using different complex aerodynamic analysis codes it has been demonstrated that the universal optimization program COPES (gradient method) of G.N. Vanderplaats is suitable for typical constrained aerodynamic problems. As it takes care of reducing the necessary number of analysis calculations in a particular manner, it meets the demands of often numerically time-consuming aerodynamic programs. Due to the slower convergence random search routines, like the one examined here, should be restricted to problems where the analysis is easy to get.

The presented examples provided useful tools for body shape optimization at supersonic speed and for transonic airfoil design. It was possible to find optimum flap positions of multi-element airfoils, limited only by the accuracy of the analysis program. The experience gained by these examinations is encouraging to use the COPES-code whenever aerodynamic optimization is demanded and a reliable analysis program with continuous solutions in the design area is available.

V. LITERATURE

- (1) G.N. Vanderplaats:
Numerical Optimization Techniques for Engineering Design: with Applications.
McGraw-Hill, Inc. 1984.
- (2) ICIDES-II:
Second International Conference on Inverse Design Concepts and Optimization in Engineering Sciences,
Proceedings.
Penn State University, University Park, Pennsylvania, USA, Oct. 26 - 28, 1987.
- (3) H.P. Schwefel:
Numerische Optimierung von Computermodellen mittels der Evolutionsstrategie.
Birkhäuser-Verlag, Basel/Stuttgart, 1977.

- (4) I. Rechenberg:
Evolutionstrategien.
in: "Medizinische Informatik und Statistik (series), Simulationsmethoden in der Medizin und Biologie (volume)",
Springer-Verlag, Berlin/Heidelberg/New York, 1978.
- (5) A. Miele (editor):
Theory of Optimum Aerodynamic Shapes; External Problems in Aerodynamics of Supersonic, Hypersonic and Free-Molecular Flows.
Academic Press, New York/London, 1965.
- (6) D.R. Chapman:
Airfoil Profiles for Minimum Pressure Drag at Supersonic Velocities - General Analysis with Application to Linearized Supersonic Flow.
NACA-Report 1063 (1952).
- (7) H.N.V. Dutt, A.K. Skreekanth:
Design of Supersonic Airfoils by Numerical Optimization.
Computer Methods in Applied Mechanics and Engineering 19 (1979), pp. 417 - 427.
- (8) G.N. Vanderplaats:
CONMIN - FORTRAN Program for Constrained Function Minimization.
NASA TMX-62.282 (1973).
- (9) G.N. Vanderplaats, R.M. Hicks, E.M. Murman:
Application of Numerical Optimization Techniques to Airfoil Design.
NASA SP-347, Part 2 (1975).
- (10) G.N. Vanderplaats:
Approximation Concepts for Numerical Airfoil Optimization.
NASA TP-1370 (1979).
- (11) R. Fletcher, C.M. Reeves:
Function Minimization by Conjugate Directions. Brit. Computer Jour., vol. 2, no. 2, 1964,
pp. 149 - 154.
- (12) H. Rieger:
Aerodynamics of Hypersonic Lifting Vehicles.
AGARD CP-428 (1988).
- (13) R.H. Hicks, G.N. Vanderplaats:
Application of Numerical Optimization to the Design of Supercritical Airfoils without Drag-Creep.
SAE Paper 770440, Business Aircraft Meeting, 1977.
- (14) R.H. Hicks, P.A. Henne:
Wing Design by Numerical Optimization.
AIAA Paper 77-1247, Seattle, Washington, Aug. 1977.
- (15) G.B. Cosentino, T.L. Holst:
Numerical Optimization Design of Advanced Transonic Wing Configurations.
AIAA Paper 85-0424, Reno, Nevada, Jan. 1985.
- (16) H. Sobieczky:
Design of Advanced Technology Transonic Airfoils and Wings.
AGARD FDP Symposium "Subsonic/Transonic Configuration Aerodynamics" at Neubiberg, Germany, May 5 - 7, 1980.
- (17) H. Schwarten:
Ein inverses, subsonisches 2D-Panelverfahren nach der Methode der kleinsten Quadrate zum Entwurf und zur Modifikation von Mehrelementprofilen.
in "Jahrbuch der DGLR", 1987.
- (18) K. Jacob:
Berechnung der abgelösten inkompressiblen Strömung um Tragflügelprofile und Bestimmung des maximalen Auftriebes.
Z. Flugwiss. 17 (1969), pp. 221 - 230.
- (19) K. Jacob:
Weiterentwicklung eines Verfahrens zur Berechnung der abgelösten Profilströmung mit besonderer Berücksichtigung des Profilwiderstandes.
DLR-FB 76-36 (1976).
- (20) A. Jameson:
Aerodynamic Design via Control Theory.
12th IMACS World Congress on Scientific Computation, Paris, July 1986.

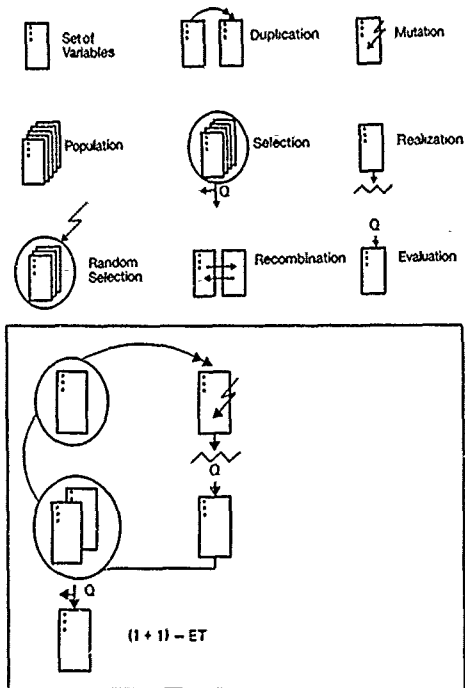


Fig. 1A: (1+1)-Level Evolution Theory

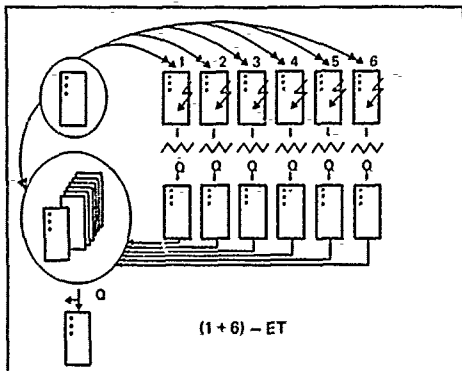


Fig. 1B: (1+6)-Level Evolution Theory

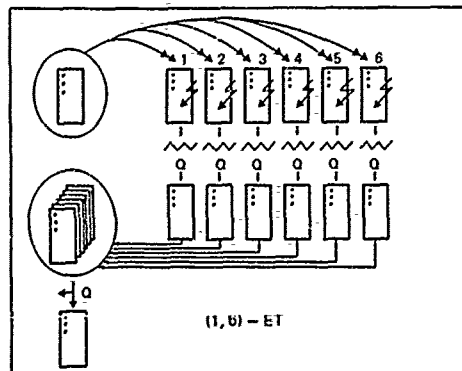


Fig. 1C: (1,6)-Level Evolution Theory

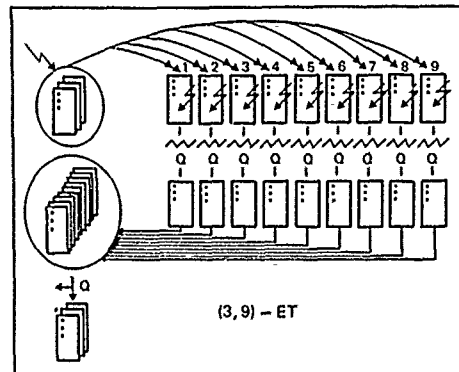


Fig. 1D: (3,9)-Level Evolution Theory

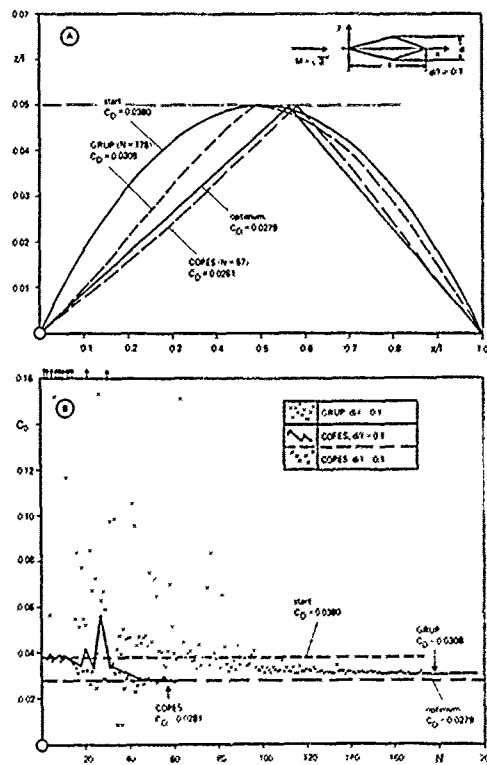


Fig. 2: Optimization of Minimum Wave Drag Profile for Least Thickness Constraint

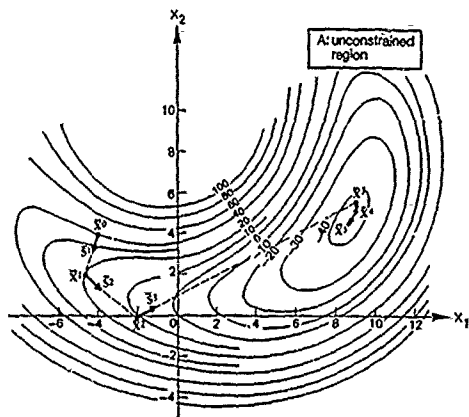


Fig. 3: Optimization Process of COPES
(from G.H. Vanderplaats)

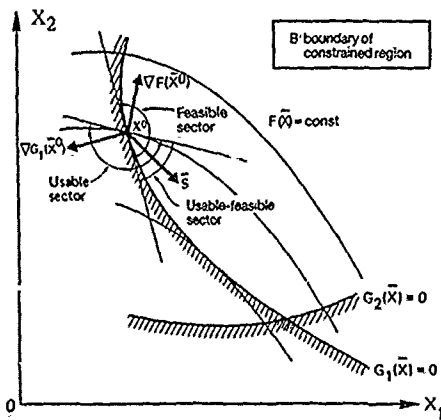


Fig. 4: Starting and Best Design of Minimum Wave Drag Body of Revolution

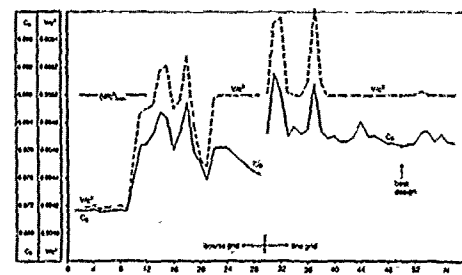


Fig. 5: Optimization Progress of Minimum Wave Drag Body of Revolution

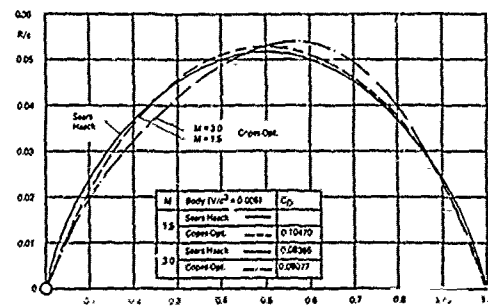


Fig. 6: Minimum Wave Drag Bodies Compared to Sears-Haack-Body

$$(\rho/\rho^*)_{\text{fictit}} = \begin{cases} (\rho/\rho^*)_{\text{isentr.}} & ; V \leq a^* \\ (V/a^*)^P, 0 < P < 1 & ; V \geq a^* \end{cases}$$

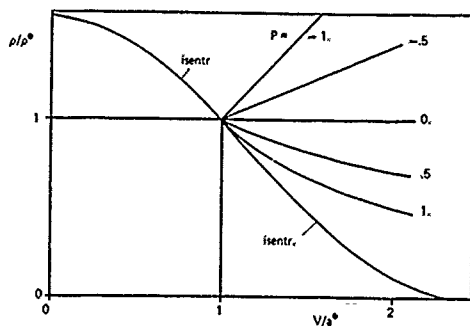


Fig. 7: Isentropic and Fictitious Density – Velocity Relations

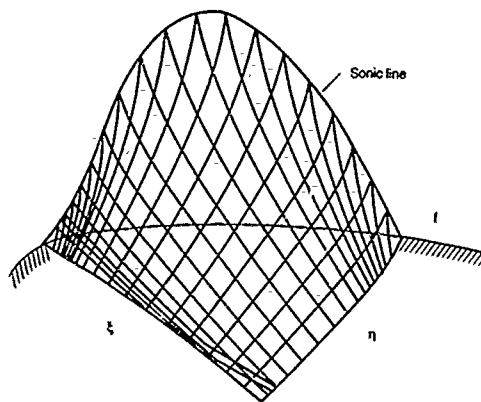


Fig. 8: Local Supersonic Shock-Free Flow Field

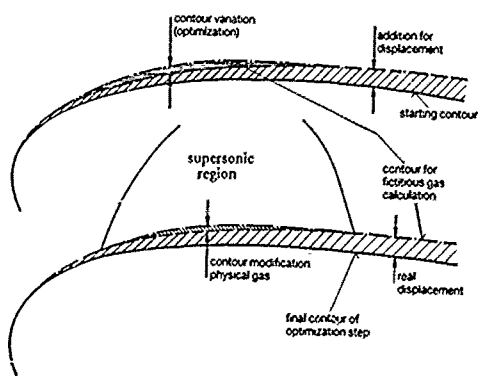


Fig.9: Contour Variation During Optimization by Use of Fictitious Gas Method

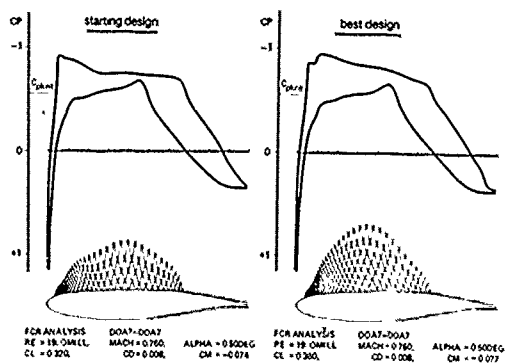


Fig. 10: Starting and Best Design of Transonic Airfoil Optimization

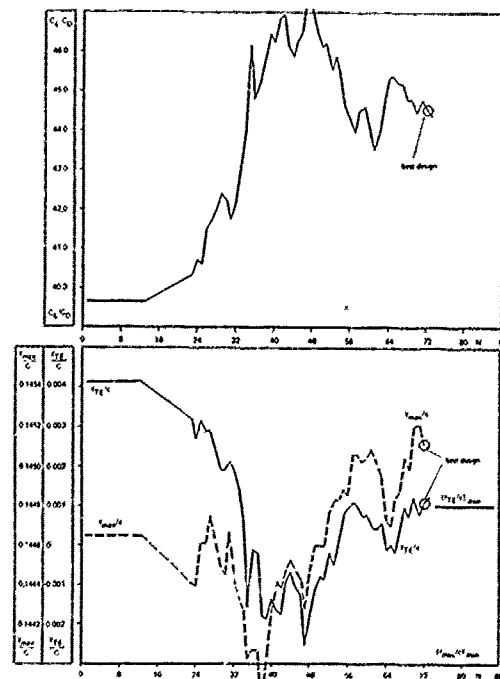


Fig. 11: Optimization Progress of Transonic Airfoil Optimization

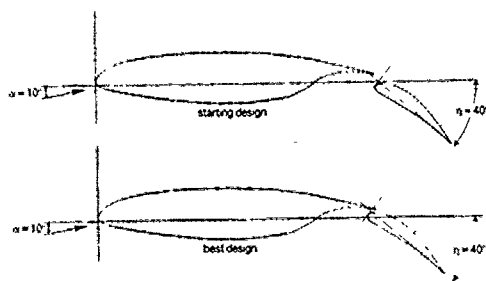


Fig. 12: Starting and Best Design of Flap Position Optimization

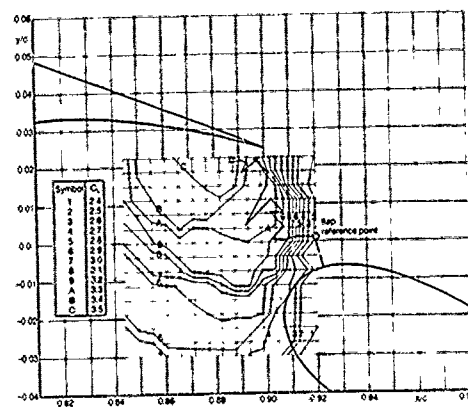


Fig. 14: Optimization Progress of Flap Position Optimization

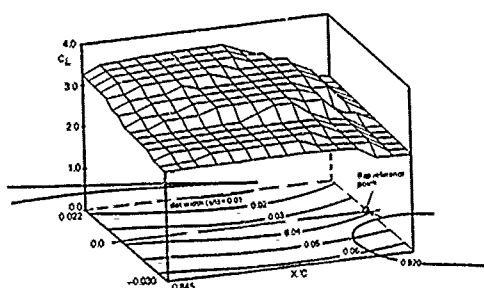


Fig. 13: Lift and Slot Width Depending on Flap Transition

OPTIMISATION NUMERIQUE DE VOILURES
EN REGIME TRANSSONIQUE
(Numerical Optimization of Wings in Transonic Flow)

par

D. DESTARAC - J. RENEUX

Office National d'Etudes et de Recherches Aéronautiques (ONERA)
B.P. N° 72 - 92322 Chatillon CEDEX (France)

et

D. GISQUET

AEROSPATIALE Division Avions

316 Rte de Bayonne 31060 Toulouse CEDEX 03 (France)

RESUME

La méthode d'optimisation d'ailes en transsonique présentée résulte de l'association d'un programme de minimisation sous contraintes, d'un code aérodynamique direct performant, et d'une technique de modification de forme. Les possibilités d'optimisation par rapport aux coefficients aérodynamiques globaux d'une aile sont présentées. Une méthode d'estimation du coefficient de traînée en fluide parfait est recommandée. Deux applications de la méthode d'optimisation en mode quasi-inverse, en visant une répartition de pression donnée, sont décrites. L'une est l'adaptation de la partie interne d'une aile d'avion de transport, problème pour lequel l'optimisation est une approche bien appropriée en raison du caractère fortement tridimensionnel des phénomènes transsoniques, et de la nécessité de respecter des contraintes d'avionnabilité. Un autre exemple, la modification d'une voilure de quadriréacteur pour réduire les perturbations causées par l'installation motrice, montre que les problèmes d'interaction entre l'aile et les autres composants de l'avion peuvent aussi être abordés par optimisation numérique.

ABSTRACT

The numerical optimization method for wings in transonic flow presented in this paper associates a constrained minimization program, a fast direct aerodynamic code, and a shape modification technique. Possibilities of optimization with regard to the total aerodynamic coefficients of a wing are shown. A method for estimating inviscid drag is recommended. Two application cases of the optimization method in the quasi inverse mode, by aiming at a given pressure distribution, are described. One is the adaptation of the inner part of a transport aircraft wing, a problem to which optimization is a well suited approach, considering the highly three-dimensional phenomena involved, and the necessity of respecting constraints related to the aircraft design. Another example, the modification of a four-engined jet aircraft in order to reduce perturbations created by the propulsive system, shows that interference problems between the wing and other components of the aircraft can also be approached by numerical optimization.

1. INTRODUCTION

Le développement de méthodes de définition tridimensionnelles adaptées à la conception de voilures s'avère particulièrement nécessaire en transsonique, compte tenu de la complexité des phénomènes tridimensionnels non linéaires qui doivent être pris en compte.

Les méthodes d'optimisation numérique [1] [2] présentent, sur les approches indirecte et inverse, l'avantage d'assurer un contrôle de la géométrie. Dans ces méthodes, l'association d'un code de calcul direct de l'écoulement et d'un programme de minimisation sous contraintes permet de modifier une voilure donnée en se fixant un objectif aérodynamique et en respectant des contraintes aérodynamiques et géométriques.

La méthode d'optimisation numérique tridimensionnelle développée à l'ONERA en collaboration avec l'Aérospatiale fait appel à deux programmes de minimisation sous contraintes différents. Les fonctions objectif et contraintes aérodynamiques sont évaluées par un code performant de calcul de l'écoulement transsonique autour d'ailes. La modification de la géométrie est effectuée à partir d'un système industriel de conception de formes.

Trois applications sont présentées. La première est le cas d'une aile rectangulaire de grand allongement définie à partir d'un profil unique, ce qui permet d'effectuer des comparaisons avec une méthode d'optimisation de profil. Le deuxième cas est l'optimisation de la partie interne d'une aile d'avion de transport, c'est-à-dire un problème fortement tridimensionnel pour lequel les méthodes bidimensionnelles ne peuvent pas être utilisées. La troisième application présentée est la modification d'une voilure pour atténuer la perturbation aérodynamique qui résulte de l'installation motrice.

2. METHODE D'OPTIMISATION

2.1. Programme de minimisation sous contraintes

Le code d'optimisation numérique tridimensionnelle transsonique offre la possibilité de faire appel, selon le choix de l'utilisateur, à deux programmes de minimisation sous contraintes, l'un COMMIN développé par Vanderplaats [3], l'autre issu de la Bibliothèque MAG, EO4VAF. Cette double possibilité est intéressante dans les cas d'optimisation difficiles présentant des minima relatifs. Elle permet aussi de comparer les performances des deux programmes.

Le programme COMMIN permet de minimiser une fonction objectif $OBJ(\bar{X})$ fonction de n variables de décision ($X_i, i = 1, \dots, n$) tout en respectant les m conditions : $G_j(\bar{X}) \leq 0 \quad j = 1, \dots, m$. Les variables de décision X_i qui forment le vecteur \bar{X} peuvent être bornées ($L_i \leq X_i \leq U_i$).

Le processus d'optimisation est itératif et s'appuie sur la formule de récurrence suivante :

$$\bar{x}_q = \bar{x}_{q-1} + \alpha^* \bar{s}_q$$

A l'itération q , deux étapes peuvent être distinguées. La première est la recherche de la direction de descente \bar{s}_q qui s'effectue à partir de la connaissance des gradients des fonctions objectif et contraintes, en utilisant différentes méthodes suivant l'état des contraintes (non-actives, actives, violées). La seconde étape est la détermination, par une approximation polynomiale du scalaire α^* , module du déplacement à effectuer dans la direction de descente \bar{s}_q choisie.

Le second programme de minimisation sous contraintes EO4VAF, issu de la bibliothèque NAG, permet de minimiser une fonction $OBJ(\bar{x})$ de n variables soumises aux contraintes :

$$Li \leq Xi \leq Ui \quad i = 1, \dots, n$$

$$G1j(\bar{x}) \geq 0 \quad j = 1, \dots, m1$$

$$G1k \leq G2k(\bar{x}) \leq Guk \quad k = 1, \dots, n2$$

$$G3l(\bar{x}) = 0 \quad l = 1, \dots, m3$$

Dans ce cas, de nouvelles variables sont introduites pour ramener les contraintes d'inégalité à des contraintes d'égalité Ci et une fonction Lagrangienne augmentée est ensuite formée avec les multiplica-

teurs de Lagrange λ_i et le paramètre ρ tel que $OBJ' = OBJ + \sum_{i=1}^M \lambda_i Ci + \rho |Ci|^2$

Cette fonction est minimisée par une méthode quasi-newtonienne en considérant également la formule de récurrence $\bar{x}_q = \bar{x}_{q-1} + \alpha^* \bar{s}_q$

Pour les deux programmes, les gradients des fonctions objectif et contraintes sont évalués par différences finies. Leurs performances sont sensiblement équivalentes dans les cas de minimisation sans contrainte. L'utilisation du programme EO4VAF s'avère plus délicate dans les cas de minimisation sous contraintes compte tenu de l'importance du choix du paramètre ρ sur le résultat de l'optimisation.

2.2. Programme de calcul aérodynamique

Une optimisation requiert un grand nombre de calculs aérodynamiques directs ; ceux-ci doivent donc être rapides. Mais par ailleurs, il est primordial pour l'optimisation que les calculs aérodynamiques soient parfaitement convergés pour assurer une bonne évaluation des fonctions objectif et contraintes et surtout de leurs gradients. La méthode de calcul d'écoulements transsoniques autour d'ailes développée par M. Brédif [4] satisfait à ces deux exigences grâce, notamment, à un algorithme de gradient conjugué avec un préconditionnement efficace.

Cette méthode résout l'équation complète du potentiel sous forme conservative, dans une discrétisation par éléments finis hexaédriques. La densité est moyennée sur les éléments, images du cube de référence par des transformations isoparamétriques, et les intégrales sont évaluées par la formule d'intégration de Gauss à 8 points. Le potentiel approché est recherché dans l'espace des fonctions continues sur le domaine et trilineaires par rapport aux coordonnées du cube de référence sur chaque élément. En supersonique, la densité est décentrée pour stabiliser le schéma. L'algorithme de résolution comporte une boucle externe non linéaire traitée soit par une méthode de point fixe, soit par une méthode de Newton, et une boucle interne de gradient conjugué avec préconditionnement par la factorisée incomplète de Cholesky. Une condition de glissement est imposée sur l'obstacle. La nappe tourbillonnaire est une surface de maillage où est imposé un saut de potentiel constant sur une ligne $y = cte$, égal à la circulation dans la section considérée. Le maillage est généré par une méthode d'interpolation transfinie, suivant une topologie en H-H.

Avec une méthode aérodynamique donnée, la précision des calculs dépend principalement de la finesse du maillage et du degré de convergence. Mais une convergence poussée sur un maillage fin est coûteuse. Pour l'optimisation il faut privilégier la convergence par rapport à la finesse du maillage, afin que l'estimation des gradients des fonctions objectif et contraintes soit correcte. Avec la présente méthode, des temps de calcul de l'ordre d'une minute CPU CRAY-XMP18 permettent d'obtenir des résultats parfaitement convergés sur des maillages d'environ 13000 points. Il est évident que la précision des solutions obtenues sur de tels maillages ne peut être excellente. L'intensité des ondes de choc, en particulier, y est sous-estimée. Cependant une bonne estimation de la valeur absolue des résultats n'est pas indispensable pour l'optimisation : il suffit que la méthode rende correctement compte des différences entre deux solutions, ce qui est possible même sur des maillages très grossiers.

2.3. Méthode de modification de forme d'une voilure

Les modifications apportées à une aile au cours d'une optimisation sont des combinaisons linéaires de fonctions de modification de base définies a priori. Les coefficients multiplicatifs de ces fonctions de modification sont des variables de décision du processus d'optimisation. Les modifications de formes sont effectuées à partir du système de conception et de gestion de formes MICA2 de l'Aérospatiale, dans lequel une aile est définie comme une surface biparamétrée. Cette surface est un ensemble cartésien de pavés dont les limites sont des lignes isoparamétriques. Pour un ensemble de $m \times n$ pavés, si $(U_i)_{i=1,m+1}$ et $(V_j)_{j=1,n+1}$ sont les valeurs limites des paramètres sur ces pavés, $d_{1,1,k}$ et $d_{2,1,k}$ les degrés respectivement en u et en v de la composante k sur le pavé (i, j) , les coordonnées d'un point de ce pavé sont définies par des polynômes de la forme :

$$x_k = \sum_{i=0}^{d_{1,i,k}} \sum_{j=0}^{d_{2,j,k}} a_{i,j,i,j,k} u^i v^j, \quad k=1,3$$

Les fonctions de modification sont des expressions polynômiales de la coordonnée z définies sur le paramétrage de l'aile à modifier :

$$\delta z_{ij}(u, v) = \sum_{k=0}^{d_{i,j}} \sum_{l=0}^{d_{i,j}} a_{k,l,i,j} u^k v^l$$

Elles excluent donc des modifications de la forme en plan. Le paramètre u évolue le long des profils générateurs, v le long de l'envergure. Les polynômes sont factorisés en $\delta z_{i,j}(u, v) = \delta z_i(u) \cdot \delta z_j(v)$, de telle sorte que $\delta z_i(u)$ détermine la modification d'un profil dans une section $v = \text{cte}$, et $\delta z_j(v)$ règle l'extension de cette modification en envergure.

3. OPTIMISATION D'UNE AILE RECTANGULAIRE

3.1. Définition du problème et cas bidimensionnel associé

Le premier problème d'optimisation tridimensionnelle abordé est défini de manière à être transposable en bidimensionnel à des fins de vérification par une méthode 2D éprouvée [5]. Il s'agit d'une aile de forme en plan rectangulaire, sans vrillage, de grand allongement, à génération cylindrique à partir d'un seul profil. C'est un profil représentatif de ceux utilisés par la première génération d'avions de transport transsoniques. Les modifications de forme affectent le profil générateur unique, et sont assurées par une base de quatre ailes de même forme en plan définies chacune par un profil, soit *peaky*, soit *supercritique*. Les ailes sont représentées sur la figure 1. Au cours du processus d'optimisation, les modifications appliquées à l'aile initiale sont des combinaisons linéaires des écarts entre chacune des ailes de base et l'aile initiale : chaque forme de la base appartient à l'espace de recherche de la solution. Le problème peut être transposé en bidimensionnel : il consiste en l'optimisation du profil de l'aile initiale à l'aide d'une bibliothèque composée des quatre profils générateurs des ailes de la base.

La fonction objectif à minimiser dans le cas bidimensionnel de référence est la traînée de pression. Une contrainte impose une borne inférieure au coefficient de portance. Le vecteur des variables de décision est composé des quatre variables associées aux modifications de forme, et de l'incidence. La figure 2 présente les répartitions de pression sur le profil initial et sur le profil optimisé, et l'évolution de l'objectif au cours du processus d'optimisation. L'optimisation permet d'obtenir logiquement un profil sans choc, la traînée de pression correspondant, en bidimensionnel et en fluide parfait, à la traînée de choc. L'historique de la convergence montre que la réduction de la traînée de pression du profil initial atteint plus de 90% de la réduction finale dès la troisième itération.

3.2. Minimisation de la traînée

En fluide parfait, la traînée d'une aile obtenue par intégration du coefficient de pression à la surface est théoriquement la somme de la traînée de choc et de la traînée induite. Le terme induit, absent dans le cas d'un profil, dépend essentiellement de la portance et de sa répartition le long de l'envergure, et ne doit donc jouer aucun rôle dans le cas tridimensionnel considéré. D'autre part, l'allongement de cette aile sans flèche est suffisant pour que les effets tridimensionnels soient limités. L'optimisation de l'aile par minimisation du coefficient de traînée de pression avec une contrainte sur la portance devrait donc donner un résultat comparable à celui de l'optimisation bidimensionnelle de référence. La figure 3 montre que ce n'est pas le cas. Les répartitions de pression représentées sur cette figure sont calculées dans la section de contrôle la plus proche du plan de symétrie. La répartition sur l'aile initiale a bien la même allure que sur le profil initial dans le cas bidimensionnel. Le choc est plus étalé, non pas par un effet tridimensionnel, mais à cause du maillage nécessairement beaucoup plus grossier du code aérodynamique tridimensionnel. Par contre, la solution obtenue par l'optimisation est très différente de la solution de l'optimisation bidimensionnelle. Le processus d'optimisation est interrompu par la divergence d'un calcul aérodynamique dans le cas d'une aile présentant un rayon de courbure de bord d'attaque anormalement faible. Malgré la diminution de la traînée de pression au cours de l'optimisation, la solution finale n'est pas une solution sans choc.

Des calculs directs du profil initial, du profil optimisé en bidimensionnel, du profil de l'aile optimisée en tridimensionnel, et des trois ailes définies par ces profils, effectués à l'aide des méthodes aérodynamiques utilisées pour l'optimisation 2D et 3D montrent que cette anomalie n'est pas liée à un phénomène de minimum relatif. Le problème réside donc dans l'estimation de l'objectif, c'est-à-dire l'évaluation de la traînée. Des calculs 3D et 2D montrent encore que ce problème n'est pas spécifiquement tridimensionnel, mais qu'il provient de l'utilisation de maillages trop grossiers pour l'optimisation 3D. Le maillage utilisé par le code d'optimisation bidimensionnelle comporte 4991 points, alors que celui de la méthode aérodynamique pour l'optimisation 3D en comporte 12844 dans 13 sections soit seulement 988 par section. Ce n'est qu'au delà de 4000 points, pour un profil, que cette méthode donne le classement correct des trois profils par rapport à la traînée de pression. Un tel maillage conduirait à plus de 50000 points en tridimensionnel, soit un temps de calcul d'environ 4 minutes CRAY XMP18, inacceptable pour des optimisations qui nécessitent plusieurs dizaines, voire centaines de calculs directs.

La traînée estimée par intégration du coefficient de pression ne peut donc pas constituer un objectif fiable pour l'optimisation, sur les maillages grossiers auxquels il faut se limiter pour des problèmes de temps de calcul. Une autre méthode pour calculer le coefficient de traînée consiste à le décomposer en fluide parfait, en un terme de traînée de choc et un terme de traînée induite, évalués séparément par des bilans de quantité de mouvement dans le champ. Dans le cas présent, la traînée induite ne doit jouer aucun rôle dans l'optimisation. La figure 4 montre les résultats du cas d'optimisation précédent traité cette fois en substituant comme objectif la traînée de choc évaluée par un bilan de quantité de mouvement dans un domaine entourant le choc. La traînée de pression calculée par intégration du coefficient de pression à la surface de l'aile. La solution obtenue est cette fois bien une solution sans choc. Le profil de l'aile optimisée en tridimensionnel n'est pas identique au profil optimisé en bidimensionnel (figure 2). Des calculs par plusieurs méthodes aérodynamiques montrent que la différence de coefficient de traînée, aussi bien de choc que de pression, entre ces deux profils est inférieure à 10^{-4} , en faveur du résultat tridimensionnel. L'estimation de la traînée de choc par un bilan de quantité de mouvement semble donc assez fiable, même en maillage grossier, pour constituer une fonction objectif d'optimisation correcte.

La difficulté d'utiliser le coefficient de traînée de pression comme objectif est mentionnée par Cosentino et Holst [6]. Bien que le code aérodynamique TWING utilisé par ces auteurs fournisse, au moins dans les conditions d'utilisation imposées par l'optimisation (maillage grossier), des valeurs absolues erronées [7], les erreurs sont des erreurs de troncature qui n'affectent pas la justesse relative des résultats les uns par rapport aux autres [8]. C'est pourquoi, ces auteurs ont pu utiliser avec succès la traînée de pression comme objectif d'optimisation. Il faut cependant noter que Cosentino et Holst utilisent un maillage de 40 000 points, au lieu de 13 000 avec la présente méthode, et une topologie en C-H mieux adaptée aux calculs autour d'ailes que la topologie en H-H. Les résultats ci-dessus montrent que, pour un maillage donné, des bilans de quantité de mouvement donnent une estimation plus fiable de la traînée que l'intégration du coefficient de pression sur l'aile, et confirment la recommandation de Lock [7] d'utiliser de préférence la première méthode pour l'optimisation.

3.3. Optimisation visant une répartition de pression prescrite

Les méthodes inverses permettent de définir une forme à partir d'une répartition de pression prescrite. Leur usage est rendu délicat par l'impossibilité de contrôle de la géométrie et le risque d'obtenir des solutions irréalistes, ou de ne pas obtenir de solution puisqu'il n'est pas sûr que, dans le cas d'une aile en transsonique, le problème soit bien posé. Il peut donc être intéressant d'utiliser une méthode d'optimisation numérique en mode quasi-inverse, en visant une répartition de pression imposée. Cela est possible en adoptant comme fonction objectif une mesure de l'écart entre le champ de pression sur l'aile et le champ de pression prescrit.

Le calcul d'optimisation présenté sur la figure 5 vise une répartition de pression extrados dans la section de contrôle de l'aile la plus proche de l'emplanture. Cette répartition est celle de l'aile définie par le profil optimisé en bidimensionnel (paragraphe 3.1), ce qui assure qu'il existe dans l'espace des fonctions de modification une solution permettant d'annuler la fonction objectif. Celle-ci est définie par l'aire comprise entre les courbes $Kp(x/c)$ imposée et courante, à l'extrados de la section de contrôle considérée. Contrairement aux cas d'optimisation précédents, il n'est pas nécessaire d'imposer de contrainte, la répartition visée assurant un coefficient de portance acceptable. Comme le montre la figure 5, la solution obtenue en six itérations est très proche de la solution visée. La valeur de la fonction objectif est divisée par 50. La convergence du processus d'optimisation est très rapide : la figure 6 indique que l'essentiel des modifications est assuré en deux itérations seulement.

Tous les calculs d'optimisation présentés jusqu'ici ont été effectués à l'aide du programme de minimisation CONMIN. Dans le cas considéré ici, la figure 7 compare les résultats obtenus avec les programmes CONMIN et NAG-E04VAF. La convergence des deux calculs est très comparable : une vingtaine de calculs aérodynamiques suffit pour diviser la valeur de l'objectif par 10. Après 50 calculs aérodynamiques, la solution obtenue avec le code E04VAF est légèrement plus proche de la solution visée. Le cas présenté ici est un cas d'optimisation sans contrainte. Dans les cas comportant des contraintes le choix de certains paramètres du programme E04VAF peut influencer considérablement le résultat de l'optimisation et rend donc l'utilisation de la méthode plus délicate.

4. OPTIMISATION DE LA PARTIE INTERNE D'UNE VOILURE D'AVION DE TRANSPORT

4.1. Problème d'optimisation

Sur un avion de transport transsonique, la partie externe de la voilure est équipée d'un profil de base défini par des méthodes bidimensionnelles. Dans la partie interne les phénomènes tridimensionnels, particulièrement importants en régime transsonique, et les contraintes d'avionnabilité rendent le problème de conception plus complexe. Pour le traiter, une méthode d'optimisation tridimensionnelle est bien adaptée.

Le cas considéré, illustré sur la figure 8, est celui de l'optimisation d'une voilure supercritique à $M = 0,82$ et $C_z = 0,47$. Le réseau de lignes iso-nombre de Mach extrados représenté sur cette figure est calculé par une méthode aérodynamique servant ici de référence [9] (maillage de 200 000 points environ).

L'écoulement sur l'aile interne comporte, au droit de la cassure un choc supersonique-supersonique qui devrait pouvoir être supprimé. Pour compenser la perte de portance qui résulterait de cette modification, la section d'emplanture pourrait supporter un écoulement extrados plus accéléré.

Le problème d'optimisation est abordé en mode quasi-inverse, en visant deux répartitions de pression $Kp(x/c)$ dans deux sections de contrôle différentes situées à l'emplanture et à 20% de l'envergure. Les sections de contrôle et les régions modifiées dans l'optimisation sont représentées sur la figure 8. Les répartitions de pression visées sont tracées figure 9 : les répartitions de pression de l'aile initiale qui leur sont superposées sont calculées par la méthode aérodynamique intégrée au code d'optimisation. Contrairement au cas précédent, le problème est pleinement tridimensionnel ; l'optimisation vise des objectifs non seulement différents, mais à certains égards opposés dans les deux régions considérées. Dans la section 1, l'objectif est d'augmenter la portance par une modification du niveau de vitesse à l'extrados. Le but visé dans la section 2 est de diminuer la survitesse à l'extrados qui induit la formation d'un choc de forte intensité aux portances élevées.

4.2. Calculs d'optimisation

Les fonctions de modifications locales retenues sont définies pour modifier la géométrie dans les deux régions entourant les sections de contrôle. Chacune d'elles assure une modification particulière des répartitions de pression à l'extrados et leur amplitude est maximale au droit des sections de contrôle. Le respect de la loi d'épaisseur relative de la voilure est obtenu en effectuant pour chaque fonction une homothétie sur l'intrados : cette technique permet de ne pas considérer de contrainte dans le processus d'optimisation.

Le problème peut être abordé globalement en considérant comme objectif à minimiser la somme des écarts entre les répartitions de pression courantes et visées dans les deux sections de contrôle considérées, et en utilisant les fonctions de modification affectant la région 1 et la région 2. Mais dans ces conditions, il s'avère impossible d'aboutir à une optimisation satisfaisante, avec le programme CONMIN comme

avec MAG-EQ4VAF. La difficulté provient du caractère contradictoire des modifications visées dans les deux sections, et de ce que ces sections sont trop voisines pour que les effets des fonctions de modification, centrées sur celles-ci, soient découplés.

Le problème est résolu en décomposant le calcul en deux étapes successives relatives aux sections 1 et 2. La première optimisation est effectuée en considérant trois aérofonctions relatives à la section 2 et en retenant la répartition de pression extrados visée dans cette même section comme objectif. L'optimisation à l'aide du programme de minimisation CONMIN est effectuée en cinq itérations. La solution optimisée est présentée figure 10. La diminution de la survitesse dans la section 2 a bien été obtenue ; de faibles écarts subsistent avec la répartition de pression visée au-delà de 50% de la corde. La répercussion de la modification sur la section d'emplanture reste faible.

La deuxième étape de l'optimisation est effectuée avec comme voilure initiale celle définie dans la première étape, c'est-à-dire modifiée dans la section 2. Trois aérofonctions relatives à la section 1 sont considérées et l'objectif retenu est la répartition de pression visée dans la même section. Les répartitions de pression de la solution finale, obtenue après cinq itérations, sont présentées figure 11. Le bénéfice de la première optimisation relative à la section 2, c'est-à-dire la réduction de la survitesse, n'est pas remis en cause par l'optimisation de la section 1, qui consiste au contraire en une augmentation du niveau de vitesse. S'il n'en était pas ainsi, le processus pourrait être poursuivi par une nouvelle optimisation de la section 2.

4.3. Comparaison des caractéristiques aérodynamiques de la voilure initiale et de la voilure optimisée

Les calculs aérodynamiques effectués dans la procédure d'optimisation utilisent des maillages très grossiers. Il est donc nécessaire d'effectuer après optimisation des calculs directs de la voilure initiale et de la voilure optimisée avec la méthode mentionnée au paragraphe 4.1 afin de vérifier que le but a été atteint.

La figure 12 présente la comparaison des deux voilures sous la forme de réseaux d'iso-nombre de Mach pour le même coefficient de portance à $M = 0,82$. Dans toute la région comprise entre 15% et 45% de l'envergure, la diminution du niveau de survitesse atténue très sensiblement l'intensité de l'onde de choc. Des calculs ont également été effectués pour évaluer l'amélioration de la solution à un coefficient de portance plus élevé que le C_z d'optimisation et ils confirment l'amélioration des caractéristiques aérodynamiques de la voilure optimisée dans la région de la cassure de l'aile.

5. OPTIMISATION D'UNE VOILURE DE QUADRIRÉACTEUR TENANT COMPTE DE L'EFFET DE L'INSTALLATION MOTRICE

5.1. Problème et méthodologie

L'installation motrice, mâts et nacelles, induit sur l'aile une perturbation aérodynamique qui en dégrade les performances. Le but visé ici est de prévenir ce phénomène en modifiant la géométrie de la voilure de telle sorte que la voilure optimisée permette d'obtenir en présence de l'installation motrice les caractéristiques aérodynamiques (ou du moins des caractéristiques aussi proches que possible) de la voilure initiale en configuration lisse.

Les méthodes de calcul aérodynamique d'une aile motorisée en transsonique sont encore trop coûteuses pour être intégrées à une méthode d'optimisation. Le problème peut cependant être abordé à l'aide d'une méthode aérodynamique de calcul d'une aile lisse, en considérant dans la définition de l'objectif à minimiser une estimation de l'effet de l'installation motrice, effectuée a priori.

Dans le cas présent, cette estimation est fournie par des résultats expérimentaux obtenus en soufflerie. Il s'agit d'un quadriréacteur sur lequel les nacelles sont supportées par des mâts symétriques. La perturbation déterminée en soufflerie de part et d'autre de chaque installation motrice est représentée sur la figure 13. L'optimisation en mode quasi-inverse videra donc, pour l'aile lisse, des modifications du champ de pression opposées à celles qui sont représentées sur la figure. L'effet le plus important et le plus défavorable de l'installation motrice sur l'aile est l'accélération de l'écoulement du côté interne de chaque mât à l'intrados, qui provoque un choc à environ 20% de la corde. Pour s'opposer à ce phénomène, il faut diminuer les niveaux et les gradients de vitesse dans ces régions. Du côté externe de chaque mât, à l'intrados la perturbation est plus faible et plus localisée. À l'extrados, c'est surtout du côté externe de l'installation externe que la motorisation perturbe l'écoulement. L'optimisation doit viser une accélération dans cette région.

Les objectifs sont donc définis par des répartitions de pression dans les quatre sections où l'effet de la motorisation est maximal. L'extension de cet effet suivant l'envergure n'entre pas dans la définition des objectifs mais dans celle des zones à modifier par l'optimisation, comme le montre la figure 14. Les résultats expérimentaux disponibles ne donnent pas d'indications sur cette extension : elle est estimée par des calculs des configurations lisse et motorisée par une méthode de singularités.

La figure 14 montre que l'effet de l'installation interne et celui de l'installation externe sont découplés : les zones d'influence ne se recouvrent pas. L'adaptation de l'aile autour de chaque installation peut faire l'objet de calculs d'optimisation séparés et indépendants.

De part et d'autre d'un mât, la perturbation est très différente et parfois opposée ; les objectifs visés le seront de même. Or la méthode aérodynamique, limitée au calcul d'une aile lisse, ne peut respecter la discontinuité du phénomène. Il faut donc décomposer l'optimisation autour de chaque installation en deux calculs, l'un visant l'objectif défini du côté interne, l'autre l'objectif défini du côté externe : il y a au total quatre calculs d'optimisation à effectuer.

5.2. Calculs d'optimisation

L'effet de l'installation motrice est beaucoup plus important et plus complexe à l'intrados qu'à l'extrados. Les fonctions de modification utilisées dans les calculs d'optimisation sont au nombre de huit pour l'intrados, trois pour l'extrados, plus une fonction de modification du vrillage local. Toutes ne sont

pas utilisées pour traiter chacun des quatre problèmes d'optimisation. A titre d'exemple, la figure 15 montre la définition des huit fonctions de modification intrados. Ce sont des aérofonctions définies à l'aide de calculs bidimensionnels inverses de manière à agir de façon bien définie chacune sur une zone limitée de l'intrados, depuis la détente au bord d'attaque (modification 5) jusqu'à la charge arrière (modification 8). La fonction de modification 6 est une homothétie, utile pour les cas où une contrainte est imposée sur l'épaisseur relative. On remarque que les modifications aérodynamiques localisées sont obtenues par des modifications géométriques qui s'étendent presque toutes du bord d'attaque au bord de fuite.

La première optimisation effectuée est celle relative à l'installation motrice interne, côté interne. Compte tenu des perturbations aérodynamiques mesurées en soufflerie, il apparaît que le but principal dans cette section est d'éviter la formation d'un choc situé à environ 20% de la corde, sur la voilure motorisée. Pour l'optimisation, l'objectif retenu de type répartition de pression est présenté figure 16. Cette répartition visée est définie pour compenser l'effet de l'installation motrice, c'est-à-dire, de façon à diminuer le niveau de vitesse à 20% de la corde et à accélérer l'écoulement entre 40% et 70% de la corde à l'intrados.

L'optimisation a été effectuée en considérant l'épaisseur au droit du longeron avant pour tenir compte des contraintes structurales. La contrainte géométrique est écrite pour limiter la diminution de l'épaisseur à 20% de la corde, notée δ , en deçà d'une borne donnée. Plusieurs calculs d'optimisation avec une contrainte géométrique plus ou moins sévère ont été effectués : $\delta \leq 0$, c'est-à-dire sans amincissement au droit du longeron, $\delta \leq 5\%$, $\delta \leq 10\%$, et enfin un calcul sans contrainte géométrique. Six fonctions de modification intrados ont été utilisées. La figure 16 présente l'historique des convergences et les résultats pour les différentes contraintes considérées. Les solutions sont proches de l'objectif visé dans la région du bord d'attaque et au-delà de 40% de la corde. Par contre à $X/C = 20\%$, le niveau de pression obtenu n'est proche de la répartition de pression objectif que pour l'optimisation sans contrainte géométrique : les solutions intermédiaires correspondent aux différentes contraintes imposées. Les modifications géométriques résultantes au droit du mât interne à 20% de la corde provoquent une variation de l'épaisseur de respectivement + 1,8%, - 3,3%, - 8,0% et - 17,6%.

Une adaptation significative n'est donc obtenue qu'en l'absence de contrainte géométrique. C'est pourquoi à titre de démonstration du concept d'adaptation de la voilure, les optimisations relatives aux autres sections ont été effectuées sans contrainte géométrique.

L'optimisation relative à l'installation motrice interne, côté externe, a été effectuée en considérant un objectif de type répartition de pression, visant à neutraliser l'effet de l'installation motrice. On cherche comme le montre la figure 17, à retarder la détente de bord d'attaque, puis à accélérer l'écoulement de part et d'autre du maximum de vitesse à l'intrados. La même base de six fonctions de modification est utilisée. La solution obtenue après 14 itérations, présentée figure 17, ne s'écarte de l'objectif que sur une zone très réduite.

Alors que le mât interne ne s'étend que jusqu'à environ 60% de la corde, le mât externe occupe toute la corde de l'aile. Aux six fonctions de modification intrados utilisées pour l'installation interne, il faut donc adjoindre les fonctions 7 et 8 de la figure 15 pour optimiser l'aile autour de l'installation externe.

L'optimisation du côté interne de celle-ci est présentée sur la figure 18. Dans une première étape, le problème est abordé comme pour l'installation interne, en visant une répartition de pression intrados sans contrôle de l'extrados. La répartition objectif ne peut pas être rigoureusement atteinte sur les vingt premiers pour cent de la corde : le but visé est de réduire autant que possible le niveau de vitesse dans cette zone afin de prévenir la formation du choc visible sur la figure 13. Dans cette première étape, la modification de l'intrados a une répercussion aérodynamique à l'extrados, où le niveau de vitesse est diminué sur toute la corde, ce qui peut induire une perte de portance peu souhaitable sur la voilure optimisée.

La deuxième étape vise à rétablir la répartition de pression extrados de l'aile initiale. Une base très simple constituée par deux fonctions de modification de l'extrados suffit, comme le montre la figure 18, à résoudre ce problème. La modification aérodynamique de l'intrados à la première étape n'est pas remise en cause dans la deuxième étape.

Compte tenu des effets de l'installation motrice externe côté externe présentés figure 13, l'adaptation de la voilure a été réalisée avec une optimisation simultanée des répartitions de pression extrados et intrados. La répartition objectif est présentée figure 19. A l'extrados, le but visé est d'augmenter le niveau de vitesse dans la région supersonique jusqu'à 40% de la corde et de reculer légèrement la position du choc. A l'intrados, il s'agit principalement de prévenir le développement du pic de survitesse et de diminuer la charge arrière : cette modification de la charge arrière est déduite des calculs en l'absence de résultats expérimentaux disponibles dans cette région.

Cette optimisation est effectuée avec douze fonctions de modification : les huit fonctions de modification intrados présentées figure 15, trois fonctions de modification extrados et une fonction de modification relative au vrillage local. La solution obtenue après quatorze itérations, présentée sur la figure 19, est très proche de la répartition de pression visée, dont elle ne s'écarte guère qu'au voisinage du bord de fuite. Une modification manuelle d'une variable de décision a dû être effectuée à l'itération 9 pour éviter un minimum relatif.

5.3. Comparaison de l'aile initiale et de l'aile optimisée

Les quatre modifications définies par les calculs d'optimisation sans contrainte présentés précédemment sont appliquées simultanément à la voilure initiale et raccordées sur l'épaisseur du mât. A l'intrados, les raccords sont donc en grande partie noyés dans l'intersection avec les mâts. Les modifications relatives à l'installation motrice externe s'avèrent moins pénalisantes par rapport aux contraintes de structures que celles imposées par l'installation motrice interne ; la modification simultanée de l'extrados et de l'intrados y contribue. Les modifications de l'épaisseur relative de part et d'autre de l'installa-

tion motrice externe à des abscisses (20% et 60% de la corde) proches de l'emplacement des longerons sont respectivement - 8,5% et + 15,9% du côté interne et + 4,9% et + 8,1% du côté externe.

La vérification la plus rigoureuse de l'optimisation consisterait en un essai en soufflerie de la voilure modifiée équipée de l'installation motrice. La vérification présentée ici n'est qu'approximative car elle est effectuée à l'aide d'une méthode numérique de singularités, dont les hypothèses ne prennent pas en compte les effets visqueux ni les ondes de choc. Les effets de la compressibilité sont introduits par une correction de Goethert.

Les écarts entre le champ de pression sur l'aile initiale motorisée ainsi que sur l'aile optimisée motorisée, et le champ de pression sur l'aile initiale lisse, calculés par cette méthode, sont présentés sur les figures 20 et 21 pour l'intrados et l'extrados de la voilure.

A l'intrados, où l'optimisation vise essentiellement à prévenir la formation d'un choc à 20% de la corde du côté interne, le but visé a été atteint. La perturbation de l'installation motrice interne côté interne est bien annulée dans cette région. Elle a été partiellement déplacée vers l'amont et vers l'aval, ce qui ne devrait pas provoquer de problème particulier compte tenu de l'effet de l'installation déterminé en soufflerie et présenté figure 13. L'adaptation effectuée autour de l'installation externe annule presque entièrement la perturbation sur l'aile optimisée.

A l'extrados, seule l'aile au droit de l'installation motrice externe a été optimisée : ce qui apparaît sur la figure 21. La diminution de la perturbation de l'installation motrice externe confirme l'intérêt de contrôler la répartition de pression extrados et de modifier à la fois les deux faces de l'aile.

L'application présentée met en évidence l'intérêt de modifier la voilure pour tenir compte de l'effet de l'installation motrice. Mais les résultats de calculs montrent clairement que dans une application industrielle la totalité de cet effet ne pourrait pas être annulée par une modification de la voilure seule.

6. CONCLUSION

Une méthode d'optimisation de voilures peut donner lieu à deux types d'applications : l'optimisation par rapport aux coefficients aérodynamiques globaux, par exemple la minimisation de la traînée pour une portance donnée, et l'optimisation en mode quasi-inverse, qui vise une répartition de pression donnée.

Dans le premier type d'optimisation, la difficulté consiste à obtenir une estimation fiable des coefficients globaux à l'aide d'une méthode aérodynamique qui doit être peu coûteuse. Il est indispensable que la convergence des calculs aérodynamiques soit très poussée pour que le calcul des fonctions objectif et contraintes et de leurs gradients soit correct. Ceci conduit, pour des considérations de coût, à utiliser des maillages grossiers, sur lesquels l'estimation du coefficient de traînée est délicate : la méthode usuelle d'estimation de la traînée en fluide parfait par intégration de la pression à la surface de l'aile doit être remplacée par une technique de bilans de quantité de mouvement dans le champ, dont la précision reste acceptable en maillage grossier.

Les applications de la méthode d'optimisation en mode quasi-inverse sont nombreuses. L'adaptation de la partie interne d'une voilure dans un écoulement transsonique en est un exemple. Etant donné le caractère fortement tridimensionnel des phénomènes et la nécessité de respecter des contraintes d'avionnabilité, une approche par optimisation en mode quasi-inverse est bien appropriée au traitement de ce problème.

L'approche quasi-inverse est également intéressante pour optimiser les phénomènes d'interaction entre l'aile et les autres composants de l'avion. Même si le code aérodynamique intégré à la méthode d'optimisation n'est pas capable de modéliser les phénomènes complexes d'interaction, ceux-ci peuvent être évalués par ailleurs et pris en compte dans la définition de l'objectif ou des contraintes. L'exemple de l'adaptation d'une voilure de quadricopteur montre qu'il est ainsi possible de réduire considérablement les perturbations causées par l'installation motrice en modifiant l'aile par optimisation numérique.

REFERENCES

- [1] HICKS R., HENNE P.A. Wing Design by Numerical Optimization. AIAA 77 - 1247, Seattle 1977.
- [2] HANEY H.P., JOHNSON R.R., HICKS R. Computational Optimization and Wind-Tunnel Test of Transonic Wing Designs. AIAA 79 - 0080, New Orleans 1979.
- [3] VANDERPLAATS G.N. CONMIN, A Fortran Program for Constrained Function Minimization. NASA TM X-62, 282-1973.
- [4] BREDIF M. Finite Element Calculation of Potential Flow around Wings. 9ème Congrès International sur les Méthodes Numériques en Mécanique des Fluides. Saclay, juin 1984. Lecture Notes in Physics, Vol. 218, Springer Verlag 1985.
- [5] RENEUX J., THIBERT J.J. The Use of Numerical Optimization for Airfoil Design. AIAA 85-5026, Colorado Springs, October 1985.
- [6] CONSENTINO G.B., HOLST T.L. Numerical Optimization Design of Advanced Transonic Wing Configurations. Journal of Aircraft, Vol. 23 n° 3, March 1986, pp. 192-199.
- [7] LOCK R.C. Comment on "Numerical Optimization Design of Advanced Transonic Wing Configurations". Journal of Aircraft, Vol. 24 n° 8, August 1987, p. 575.
- [8] CONSENTINO G.B., HOLST T.L. Reply by Authors to R.C. Lock. Journal of Aircraft, Vol. 24 n° 8, August 1987, pp. 575-576.
- [9] CHATTOT J.J., COULOMBIEUX C., DA SILVA TOME C. Calculs d'écoulements transsoniques autour d'ailes. La Recherche Aérospatiale, n° 1978-4, p. 143-159, 1978.

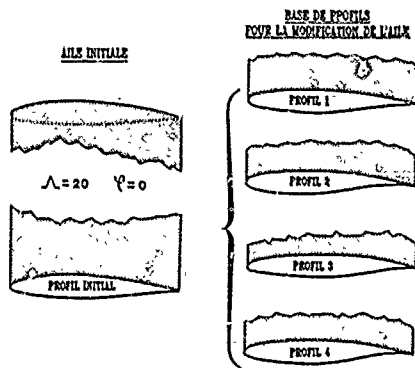


Fig.1 : Optimisation d'une aile rectangulaire de grand allongement définie par un profil unique.

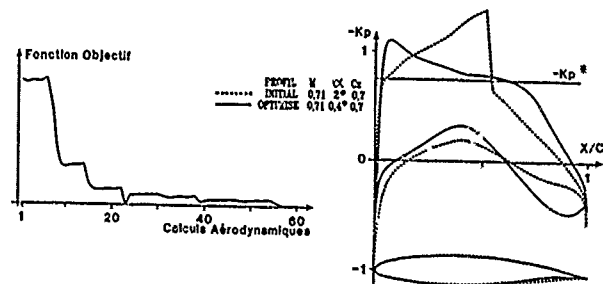


Fig.2 : Optimisation bidimensionnelle de référence. Minimisation de la traînée de pression C_{xp} . Contrainte : $C_z > C_{z0}$.

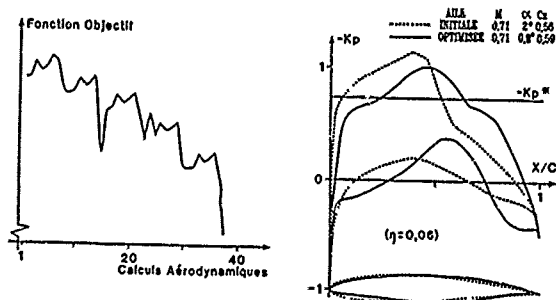


Fig.3 : Optimisation d'une aile rectangulaire. Minimisation de la traînée de pression C_{xp} . Contrainte : $C_z > C_{z0}$.

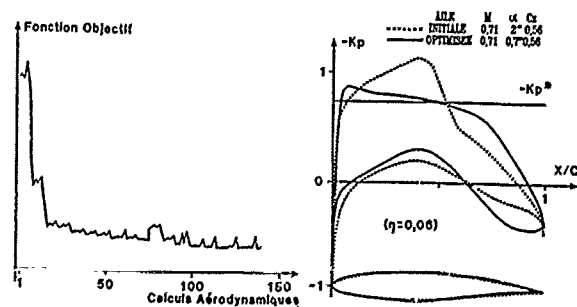


Fig.4 : Optimisation d'une aile rectangulaire. Minimisation de la traînée de choc C_{xchoc} . Contrainte : $C_z > C_{z0}$.

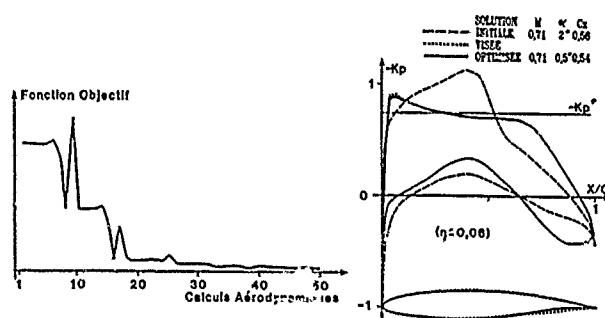


Fig 5 : Optimisation d'une aile rectangulaire. Répartition de pression extrados en objectif. Pas de contrainte.

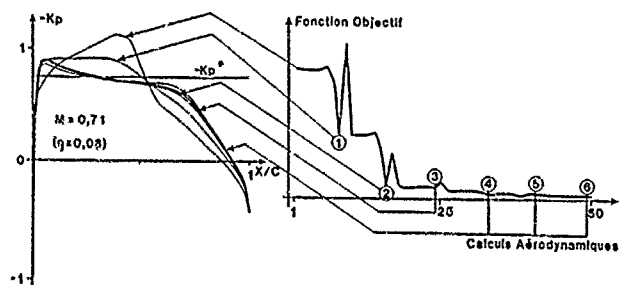


Fig 6 : Evolution de la solution au cours de l'optimisation. Aile rectangulaire. Répartition de pression extrados en objectif. Pas de contrainte.

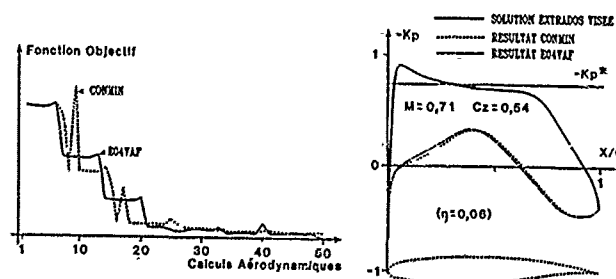


Fig 7 : Comparaison des programmes de minimisation CONMIN et EO4VAF. Aile rectangulaire. Répartition de pression extrados en objectif. Pas de contrainte.

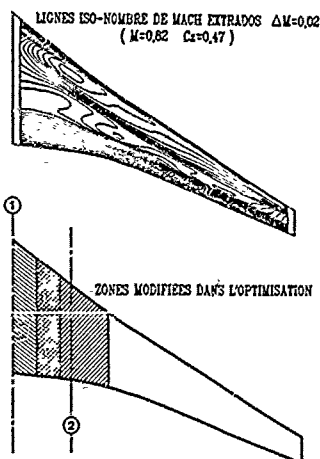


Fig 8 : Optimisation de la partie interne d'une aile d'action de transport.

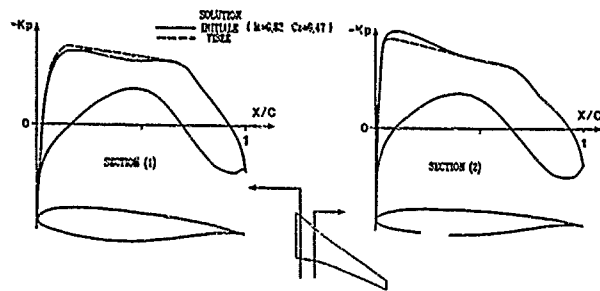


Fig.9 : Optimisation en mode quasi-inverse. Répartitions de pression visées dans deux sections.

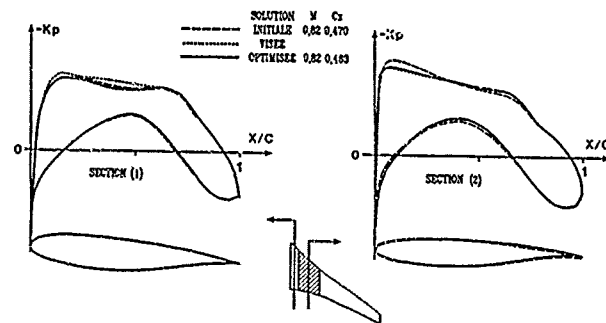


Fig.10 : Optimisation en mode quasi-inverse. Première étape : modification de la zone (2).

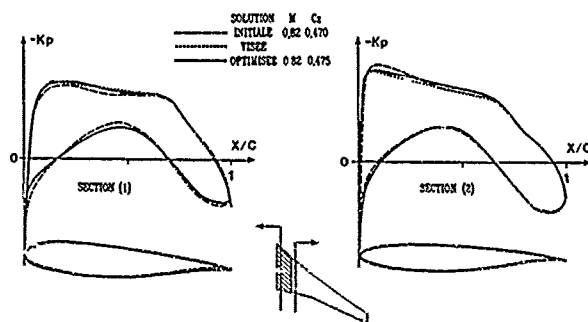


Fig.11 : Optimisation en mode quasi-inverse. Deuxième étape : modification de la zone (1).

LIGNES ISO-NOMBRE DE MACH EXTRADTM $\Delta M=0,02$

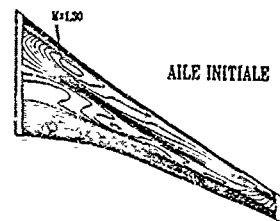


Fig.12 : Optimisation de la partie interne d'une aile d'avion de transport. Calculs de vérification. $M = 0,82$, $C_z = 0,47$.

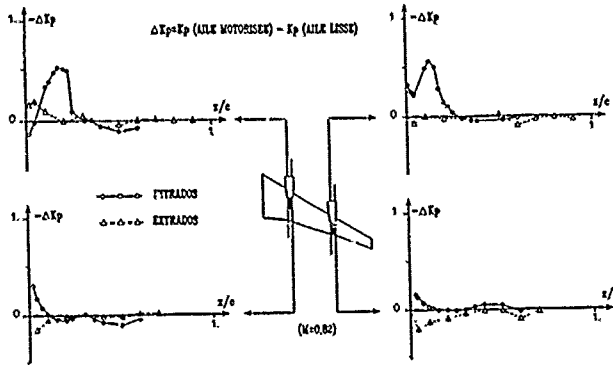


Fig 13 : Effet de l'installation motrice sur les pressions de l'aile d'un quadricopteur. Mesures en soufflerie.

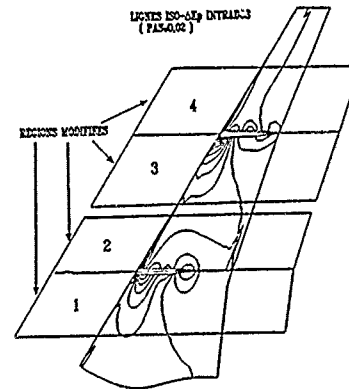


Fig 14 : Optimisation d'une aile de quadricopteur tenant compte de l'effet de l'installation motrice. Définition des régions à modifier d'après des résultats de calculs "singularités".

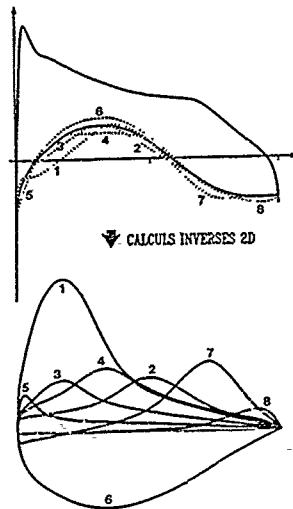


Fig 15 : Exemples de fonctions de modification géométrique.

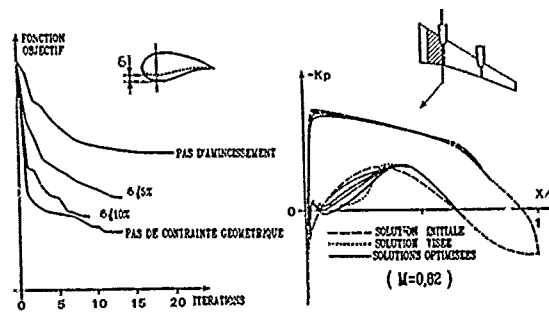


Fig 16 : Optimisation d'une aile de quadricopteur. Objectif : répartition de pression intrados. Contrainte géométrique sur la diminution δ de l'épaisseur à $x/c = 0,20$. Six fonctions de modification intrados.

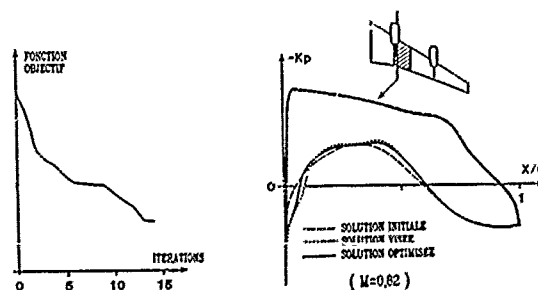


Fig 17 : Optimisation d'une aile de quadricopteur. Objectif : répartition de pression intrados. Pas de contrainte. Six fonctions de modification intrados.

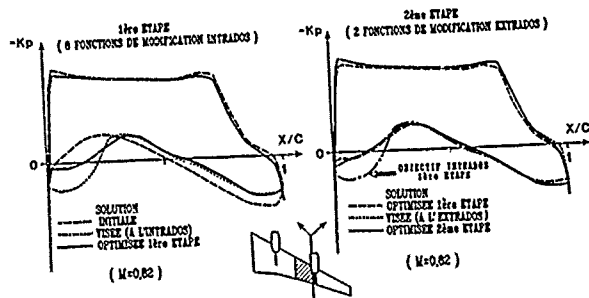


Fig.18 : Optimisation d'une aile de quadricopteur. Objectif : répartition de pression. Pas de contrainte.

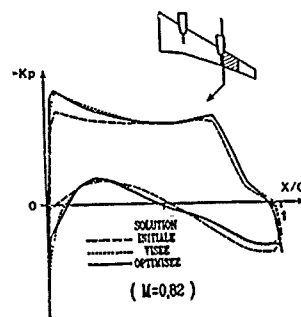
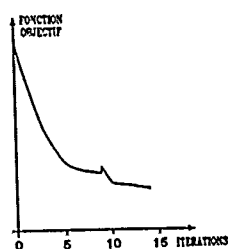


Fig.19 : Optimisation d'une aile de quadricopteur. Objectif : répartition de pression intrados et extrados. Pas de contrainte. Douze fonctions de modification.

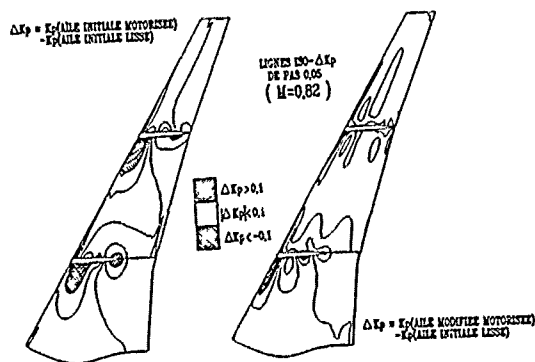


Fig.20 : Perturbation par l'installation moutrice par rapport au champ de pression intrados de l'aile lisse initiale. Calculs singularités.

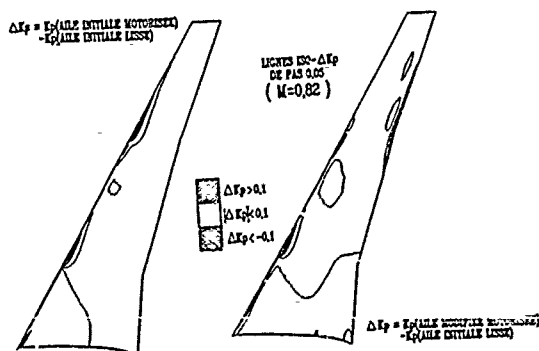


Fig.21 : Perturbation par l'installation moutrice par rapport au champ de pression extrados de l'aile lisse initiale. Calculs singularités.

AERODYNAMIC DESIGN VIA CONTROL THEORY*

by

Professor Antony Jameson
128 Broadmead
Princeton
NJ 08540
United States

1. Introduction and historical survey

Computers have had a twofold impact on the science of aerodynamics. On the one hand numerical simulation may be used to gain new insights into the physics of complex flows. On the other hand computational methods can be used by engineers to predict the aerodynamic characteristics of alternative designs. Assuming that one has the ability to predict the performance, the question then arises of how to modify the design to improve the performance. This paper is addressed to that question.

Prior to 1960 computational methods were hardly used in aerodynamic analysis. The primary tool for the development of aerodynamic configurations was the wind tunnel. Shapes were tested and modifications selected in the light of pressure and force measurements together with flow visualization techniques. Computational methods are now quite widely accepted in the aircraft industry. This has been brought about by a combination of radical improvements in numerical algorithms and continuing advances in both speed and memory of computers.

If a computational method is to be useful in the design process, it must be based on a mathematical model which provides an appropriate representation of the significant features of the flow, such as shock waves, vortices and boundary layers. The method must also be robust, not liable to fail when parameters are varied, and it must be able to treat useful configurations, ultimately the complete aircraft. Finally reasonable accuracy should be attainable at reasonable cost. Much progress has been made in these directions [1-10]. In many applications where the flow is unseparated, including designs for transonic flow with weak shock waves, useful predictions can be made quite inexpensively using the potential flow equation [1-4]. Methods are also available for solving the Euler equations for two- and three-dimensional configurations up to a

* Reprinted from the proceedings of the 12th IMACS World Congress on Scientific Computation held in Paris in July 1988.

complete aircraft [5-10]. Viscous simulations are generally complicated by the need to allow for turbulence: while the Reynolds averaged equations can be solved by current methods, the results depend heavily on the choice of turbulence models.

Given the range of well proven methods now available, one can distinguish objectives for computational aerodynamics at several levels:

- 1) Capability to predict the flow past an airplane or important components in different flight regimes such as take-off or cruise, and off design conditions such as flutter.
- 2) Interactive design calculations to allow rapid improvement of the design.
- 3) Automatic design optimization.

Substantial progress has been made toward the first objective, and in relatively simple cases such as an airfoil or wing in inviscid flow, calculations can be performed fast enough that the second objective is within reach. The third objective has also been addressed for various special cases. In particular it has been recognized that the designer generally has an idea of the kind of pressure distribution that will lead to the desired performance. Thus it is useful to consider the problem of calculating the shape that will lead to a given pressure distribution. Such a shape does not necessarily exist, unless the pressure distribution satisfies certain constraints, and the problem must therefore be very carefully formulated: no shape exists, for example, for which stagnation pressure is attained over the entire surface.

The problem of designing a two dimensional profile to attain a desired pressure distribution was first studied by Lighthill, who solved it for the case of incompressible flow by conformally mapping the profile to a unit circle [11]. The speed over the profile is

$$q = \phi_0/h \quad (1.1)$$

where ϕ is the potential for flow past a circle, and h is the modulus of the mapping function. The solution for ϕ is known for incompressible flow. Let q_d be the desired surface speed. Then the surface value of h can be obtained by setting $q = q_d$ in equation (1.1), and since the mapping function is analytic, it is uniquely determined by the value of h on the boundary. A solution

exists for a given speed q_∞ at infinity only if

$$\frac{1}{2\pi} \oint q d\theta = q_\infty \quad (1.2)$$

and there are additional constraints on q if the profile is required to be closed.

Lighthill's method was extended to compressible flow by McFadden [12]. Starting with a given shape, and a corresponding mapping function $h^{(0)}$, the flow equations can be solved for the potential $\phi^{(0)}$, which now depends on $h^{(0)}$. A new mapping function $h^{(1)}$ is then determined by setting $q = q_d$ in equation (1.1), and the process is repeated. In the limiting case of zero Mach number the method reduces to Lighthill's method, and McFadden gives a proof that the iterations will converge for small Mach numbers. He also extends the method to treat transonic flow through the introduction of artificial viscosity to suppress the appearance of shock waves, which would cause the updated mapping function to be discontinuous. This difficulty can also be overcome by smoothing the changes in the mapping function. Such an approach is used in a computer program written by the author for Grumman Aerospace. It allows the recovery of smooth profiles that generate flows containing shock waves, and it has been used to design improved blade sections for propellers [13]. A related method for three dimensional design was devised by Garabedian and McFadden [14]. In their scheme the steady potential flow solution is obtained by solving an artificial time dependent equation, and the surface is treated as a free boundary. This is shifted according to an auxiliary time dependent equation in such a way that the flow evolves toward the specified pressure distribution.

Another way to formulate the problem of designing a profile for a given pressure distribution is to integrate the corresponding surface speed to obtain the surface potential. The potential flow equation is then solved with a Dirichlet boundary condition, and a shape correction is determined from the calculated normal velocity through the surface. This approach was first tried by Tranen [15]. Volpe and Melnik have shown how to allow for the constraints that must be satisfied by the pressure distribution if a solution is to exist [16]. The same idea has been used by Henne for three-dimensional design calculations [17].

The hodograph transformation offers an alternative approach to the design of airfoils in

transonic flows. Garabedian and Korn achieved a striking success in the design of airfoils to produce shock-free transonic flows by using the method of complex characteristics to solve the equations in the hodograph plane [18]. Another design procedure has been proposed by Giles, Drela and Thompkins [19], who write the two-dimensional Euler equations for inviscid flow in a streamline coordinate system, and use a Newton iteration. An option is then provided to treat the surface coordinates as unknowns, while the pressure is fixed.

Finally, Hicks and Henne have explored the possibility of meeting desired design objectives by using constrained optimization [20]. The configuration is specified by a set of parameters, and any suitable computer program for flow analysis is used to evaluate the aerodynamic characteristics. The optimization method then selects values of these parameters that maximize some criterion of merit, such as the lift-to-drag ratio, subject to other constraints such as required wing thickness and volume. In principle this method allows the designer to specify any reasonable design objectives. The method becomes extremely expensive, however, as the number of parameters is increased, and its successful application in practice depends heavily on the choice of a parametric representation of the configuration.

The purpose of this paper is to propose that there are benefits in regarding the design problem as a control problem in which the control is the shape of the boundary. A variety of alternative formulations of the design problem can then be treated systematically by using the mathematical theory for control of systems governed by partial differential equations [21]. Suppose that the boundary is defined by a function $f(x)$, where x is the position vector. As in the case of optimization theory applied to the design problem, the desired objective is specified by a cost function I , which may, for example, measure the deviation from a desired surface pressure distribution, but could also represent other measures of performance such as lift and drag. The introduction of a cost function has the advantage that if the objective is unattainable, it is still possible to find a minimum of the cost function. Now a variation in the control δf leads to a variation δI in the cost. It is shown in the following sections that δI can be expressed to first order as an inner product of a gradient function g with δf :

$$\delta I = (g, \delta f)$$

Here g is independent of the particular variation δf in the control, and can be determined by

solving an adjoint equation. Now choose

$$\delta l = -\lambda g$$

where λ is a sufficiently small positive number. Then

$$\delta l = -\lambda(g, g) < 0$$

assuring a reduction in l . After making such a modification, the gradient can be recalculated and the process repeated to follow a path of steepest descent until a minimum is reached. In order to avoid violating constraints, such as a minimum acceptable wing thickness, the steps can be taken along the projection of the gradient into the allowable subspace of the control function. In this way one can devise design procedures which must necessarily converge at least to a local minimum, and which might be accelerated by the use of more sophisticated descent methods. While there is a possibility of more than one local minimum, the cost function can be chosen to reduce the likelihood of difficulties caused by such a contingency, and in any case the method will lead to an improvement over the initial design. The mathematical development resembles in many respects the method of calculating transonic potential flow proposed by Bristeau, Pironneau, Glowinski, Periaux, Perrier and Poirier, who reformulated the solution of the flow equations as a least squares problem in control theory [4].

In order to illustrate the application of control theory to design problems in more detail, the following sections present design procedures for three examples. Section 2 discusses the design of two dimensional profiles for compressible potential flow when the profile is generated by conformal mapping. This leads to a generalization of the methods of Lighthill and McFadden. Section 3 discusses the same problem when the flow is governed by the inviscid Euler equations. Finally, Section 4 addresses the three dimensional design problem for a wing, assuming the flow to be governed by the inviscid Euler equations. The procedures which are presented require the solution of several partial differential equations at each step. The question of the most efficient discretization of these equations is deferred for future investigation.

2. Design for potential flow using conformal mapping

Consider the case of two dimensional compressible inviscid flow. In the absence of shock waves an initially irrotational flow will remain irrotational, and we can assume that the velocity vector \mathbf{q} is the gradient of a potential ϕ . In the presence of weak shock waves this remains a fairly good approximation. Let ζ , T and S denote vorticity, temperature and entropy. Then according to Crocco's Theorem, vorticity in steady flow is associated with entropy production through the relation

$$\mathbf{q} \times \zeta + T \nabla S = 0$$

Thus, the introduction of a potential is consistent with the assumption of isentropic flow, and shock waves are modelled by isentropic jumps. Let p , ρ , c and M be the pressure, density, speed of sound and Mach number q/c . Then the potential flow equation is

$$\nabla \cdot \rho \nabla \phi = 0 \quad (2.1)$$

where the density is given by

$$\rho = \left\{ 1 + \frac{\gamma-1}{2} M_\infty^2 (1-q^2) \right\}^{1/\gamma-1} \quad (2.2)$$

while

$$p = \frac{\rho^\gamma}{\gamma M_\infty^2}, \quad c^2 = \frac{\gamma p}{\rho} \quad (2.3)$$

Here M_∞ is the Mach number in the free stream, and the units have been chosen so that p and q have the value unity in the far field. Equation (2.2) is a consequence of the energy equation in the form

$$\frac{c^2}{\gamma-1} + \frac{q^2}{2} = \text{constant}$$

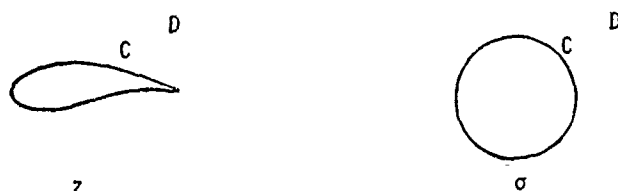


Figure 1

Suppose that the domain D exterior to the profile C in the z plane is conformally mapped onto the domain exterior to a unit circle in the σ plane as sketched in Figure 1. Let R and θ be polar coordinates in the σ plane, and let r be the inverted radial coordinate $1/R$. Also let h be the modulus of the derivative of the mapping function

$$h = \left| \frac{dz}{d\sigma} \right|$$

Now the potential flow equation becomes

$$\frac{\partial}{\partial \theta} (\rho \phi_\theta) + r \frac{\partial}{\partial r} (r \rho \phi_r) = 0 \quad \text{in } D \quad (2.4)$$

where the density is given by equation (2.1), and the circumferential and radial velocity components are

$$u = \frac{r \phi_\theta}{h}, \quad v = -\frac{r^2 \phi_r}{h} \quad (2.5)$$

while

$$q^2 = u^2 + v^2 \quad (2.6)$$

The condition of flow tangency leads to the Neumann boundary condition

$$v = \frac{1}{h} \frac{\partial \phi}{\partial r} = 0 \quad \text{on } C \quad (2.7)$$

In the far field the potential is given by an asymptotic estimate, leading to a Dirichlet boundary condition at $r = 0$ [2].

Suppose that it is desired to achieve a specified velocity distribution q_d on C . Introduce the cost function

$$I = \frac{1}{2} \int_C (q - q_d)^2 d\theta \quad (2.8)$$

The design problem is now treated as a control problem where the control function is the mapping modulus h , which is to be chosen to minimize I subject to the constraints defined by the flow equations (2.2 - 2.7).

A modification δh to the mapping modulus will result in variations $\delta\phi$, δu , δv and $\delta\rho$ to the potential, velocity components and density. The resulting variation in the cost will be

$$\delta I = \int_C (q - q_d) \delta q d\theta \quad (2.9)$$

where on C $q = u$. Also

$$\delta u = r \frac{\delta\phi_\theta}{h} - u \frac{\delta h}{h}, \quad \delta v = r^2 \frac{\delta\phi_r}{h} - v \frac{\delta h}{h}$$

while according to equations (2.2) and (2.6)

$$\frac{\partial\rho}{\partial u} = -\frac{\rho u}{c^2}, \quad \frac{\partial\rho}{\partial v} = -\frac{\rho v}{c^2}$$

Hence

$$\begin{aligned} \delta\rho &= -\frac{\rho}{c^2} (u\delta u + v\delta v) \\ &= \rho \frac{r^2}{c^2} \frac{\delta h}{h} - \frac{\rho}{c^2} \frac{r}{h} (u\delta\phi_\theta + vr\delta\phi_r) \end{aligned}$$

It follows that $\delta\phi$ satisfies

$$L\delta\phi = -\frac{\partial}{\partial\theta} (\rho M^2 \phi_\theta \frac{\delta h}{h}) - r \frac{\partial}{\partial r} (\rho M^2 r \phi_r \frac{\delta h}{h})$$

where

$$L \equiv \frac{\partial}{\partial \theta} \left\{ \rho \left(1 - \frac{v^2}{c^2} \right) \frac{\partial}{\partial \theta} - \frac{\rho uv}{c^2} r \frac{\partial}{\partial r} \right\} + r \frac{\partial}{\partial r} \left\{ \rho \left(1 - \frac{v^2}{c^2} \right) r \frac{\partial}{\partial r} - \frac{\rho uv}{c^2} \frac{\partial}{\partial \theta} \right\} \quad (2.10)$$

Then if ψ is any periodic differentiable function which vanishes in the far field

$$\int_D \frac{\psi}{r^2} L \delta \phi \, dS = \int_D \rho M^2 \nabla \phi \cdot \nabla \psi \frac{\delta h}{h} \, dS \quad (2.11)$$

where dS is the area element $r dr d\theta$, and the right hand side has been integrated by parts.

Now we can augment equation (2.9) by subtracting the constraint (2.11). The auxiliary function ψ then plays the role of a Lagrange multiplier. Substituting for δq and integrating the term

$$\int_C (q - q_d) r \frac{\delta \phi}{h} \theta \, d\theta$$

by parts, we obtain

$$\delta I = \int_C (q - q_d) q \frac{\delta h}{h} \, d\theta - \int_C \delta \phi \frac{\partial}{\partial \theta} \left[\frac{q - q_d}{h} \right] \, d\theta - \int_D \frac{\psi}{r^2} L \delta \phi \, dS + \int_D \rho M^2 \nabla \phi \cdot \nabla \psi \frac{\delta h}{h} \, dS$$

Now suppose that ψ satisfies the adjoint equation

$$L\psi = 0 \quad \text{in } D \quad (2.12)$$

with the boundary condition

$$\frac{\partial \psi}{\partial r} = \frac{1}{\rho} \frac{\partial}{\partial \theta} \left[\frac{q - q_d}{h} \right] \quad \text{on } C \quad (2.13)$$

Then integrating by parts

$$\int_D \frac{\psi}{r^2} L \delta \phi \, dS = - \int_C \rho \psi_r \delta \phi \, d\theta$$

and

$$\delta I = - \int_C (q - q_d) q \frac{\delta h}{h} \, d\theta + \int_D \rho M^2 \nabla \phi \cdot \nabla \psi \frac{\delta h}{h} \, dS \quad (2.14)$$

Here the first term represents the direct effect of the change in the metric, while the area integral represents a correction for the effect of compressibility.

Equation (2.14) can be further simplified to represent δI purely as a boundary integral because the mapping function is fully determined by the value of its modulus on the boundary. Set

$$\log \frac{dz}{d\sigma} = f + i\beta$$

where

$$f = \log \left| \frac{dz}{dr} \right| = \log h$$

and

$$\delta f = \frac{\delta h}{h}$$

Then f satisfies Laplace's equation

$$\Delta f = 0 \quad \text{in } D$$

and if there is no stretching in the far field, $f \rightarrow 0$. Thus

$$\Delta f = 0 \quad \text{in } D$$

and $\delta f \rightarrow 0$ in the far field.

Introduce another auxiliary function P which satisfies

$$\Delta P = \rho M^2 \nabla \phi \cdot \nabla \psi \text{ in } D \quad (2.15)$$

and

$$P = 0 \text{ on } C \quad (2.16)$$

Then the area integral in equation (2.14) is

$$\int_D \Delta P \delta f \, dS = \int_C \delta f \frac{\partial P}{\partial r} \, d\theta - \int_D P \Delta \delta f \, dS$$

and finally

$$\delta I = \int_C g \delta f \, d\theta \quad (2.17)$$

where

$$g = \frac{\partial P}{\partial r} - (q - q_d)q \quad (2.18)$$

This suggests setting

$$\delta f = -\lambda g$$

so that if λ is a sufficiently small positive number

$$\delta I = -\lambda \int_C g^2 \, d\theta < 0$$

Arbitrary variations δf cannot, however, be admitted. The condition that $f \rightarrow 0$ in the far field, and also the requirement that the profile should be closed, imply constraints which must be

satisfied by f on the boundary C . Suppose that $\log\left(\frac{dz}{d\sigma}\right)$ is expanded as a power series

$$\log\left(\frac{dz}{d\sigma}\right) = \sum_{n=0}^{\infty} \frac{c_n}{\sigma^n} \quad (2.19)$$

where only negative powers are retained because otherwise $\frac{dz}{d\sigma}$ would become unbounded for large σ . The condition that $f \rightarrow 0$ as $\sigma \rightarrow \infty$ implies

$$c_0 = 0$$

Also the change in z on integration around a circuit is

$$\Delta z = \oint \frac{dz}{d\sigma} d\sigma = 2\pi i c_1$$

so the profile will be closed only if

$$c_1 = 0.$$

On C equation (2.19) reduces to

$$f_C + i \beta_C = \sum_{n=0}^{\infty} (a_n \cos n\theta + b_n \sin n\theta) + i \sum_{n=0}^{\infty} (b_n \cos n\theta - a_n \sin n\theta)$$

Thus a_n and b_n are the Fourier coefficients of f_C , and these constraints reduce to

$$a_0 = 0, \quad a_1 = 0, \quad b_1 = 0$$

In order to satisfy these constraints we can project g on to the admissible subspace for f_C

by setting

$$\tilde{g} = g - A_0 - A_1 \cos \theta - B_1 \sin \theta \quad (2.20)$$

where

$$\begin{aligned} A_0 &= \frac{1}{2\pi} \int_C g d\theta \\ A_1 &= \frac{1}{\pi} \int_C g \cos \theta d\theta \\ B_1 &= \frac{1}{\pi} \int_C g \sin \theta d\theta \end{aligned} \quad (2.21)$$

Then

$$\int_C (g - \tilde{g}) \tilde{g} d\theta = 0$$

and if we take

$$\delta I = -\lambda \tilde{g}$$

it follows that to first order

$$\delta I - \lambda \int_C g \tilde{g} d\theta = -\lambda \int_C (\tilde{g} + g - \tilde{g}) \tilde{g} d\theta = -\lambda \int_C \tilde{g}^2 d\theta < 0$$

If the flow is subsonic this procedure should converge toward the desired speed distribution since the solution will remain smooth, and no unbounded derivatives will appear. If, however, the flow is transonic, one must allow for the appearance of shock waves in the trial solutions, even if q_d is smooth. Then $q - q_d$ is not differentiable. This difficulty can be circumvented by a more sophisticated choice of the cost function. Consider the choice

$$I = \frac{1}{2} \int_C \left[\lambda_1 S^2 + \lambda_2 \left(\frac{dS}{d\theta} \right)^2 \right] d\theta \quad (2.22)$$

where λ_1 and λ_2 are parameters, and the periodic function $S(\theta)$ satisfies the equation

$$\lambda_1 S - \lambda_2 \frac{d^2 S}{d\theta^2} = q - q_d \quad (2.23)$$

Then

$$\begin{aligned}
 \delta I &= \int_C (\lambda_1 S \delta S + \lambda_2 \frac{dS}{d\theta} \frac{d}{d\theta} \delta S) d\theta \\
 &= \int_C S (\lambda_1 \delta S - \lambda_2 \frac{d^2}{d\theta^2} \delta S) d\theta \\
 &= \int_C S \delta q d\theta
 \end{aligned}$$

Thus S replaces $q - q_d$ in the previous formulas, and if one modifies the boundary condition (2.13) to

$$\frac{\partial \psi}{\partial r} = \frac{1}{\rho} \frac{\partial}{\partial \theta} \left[\frac{S}{h} \right] \text{ on } C \quad (2.24)$$

the formula for the gradient becomes

$$g = \frac{\partial p}{\partial r} - Sq \quad (2.25)$$

instead of equation (2.18). Then one modifies f by a step $-\lambda \tilde{g}$ in the direction of the projected gradient as before.

The final design procedure is thus as follows. Choose an initial profile and corresponding mapping function f . Then

- 1) Solve the flow equations (2.2 - 2.7) for ϕ, u, v, q, ρ .
- 2) Solve the ordinary differential equation (2.23) for S .
- 3) Solve the adjoint equation (2.12) for ψ subject to the boundary condition (2.24).
- 4) Solve the auxiliary Poisson equation (2.15) for P .

5) Evaluate

$$g = \frac{\partial P}{\partial \Gamma} - S q$$

on C , and find its projection \tilde{g} onto the admissible subspace of variations according to equations (2.20) and (2.21).

6) Correct the boundary mapping function f_C by

$$\delta f = -\lambda \tilde{g}$$

and return to step 1.

3. Design for the Euler equations using conformal mapping

This section treats the case of two dimensional compressible flow where the potential flow equation is replaced as a mathematical model by the inviscid Euler equations. Let p, ρ, u, v, E and H denote the pressure, density, Cartesian velocity components, total energy and total enthalpy. For a perfect gas

$$p = (\gamma - 1) \rho \left\{ E - \frac{1}{2} (u^2 + v^2) \right\} \quad (3.1)$$

and

$$\rho H = \rho E + p \quad (3.2)$$

where γ is the ratio of specific heats. The Euler equations may then be written as

$$\frac{\partial w}{\partial t} + \frac{\partial f}{\partial x} + \frac{\partial g}{\partial y} = 0 \quad (3.3)$$

where x and y are Cartesian coordinates, t is the time coordinate and

$$w = \begin{bmatrix} \rho \\ \rho u \\ \rho v \\ \rho E \end{bmatrix}, \quad f = \begin{bmatrix} \rho u \\ \rho u^2 + p \\ \rho u v \\ \rho u H \end{bmatrix}, \quad g = \begin{bmatrix} \rho v \\ \rho v u \\ \rho v^2 + p \\ \rho v H \end{bmatrix} \quad (3.4)$$

As in the previous section, suppose that the domain D exterior to the profile C in the z plane is mapped conformally onto the domain exterior to a unit circle in the σ plane (see Figure 1). Assume also that the outer boundary B of the domain is very far from the profile. Let the derivative of the mapping function be

$$\frac{dz}{d\sigma} = h e^{i\beta} \quad (3.5)$$

Also let r and θ be polar coordinates in the σ plane, where in this case it is more convenient to take r as the true radial coordinate denoted by R in the previous section, and θ is measured in the clockwise direction. Define the rotation parameters

$$c = \cos(\beta - \theta), \quad s = \sin(\beta - \theta) \quad (3.6)$$

and rotated velocity components

$$\begin{bmatrix} U \\ V \end{bmatrix} = \begin{bmatrix} s & -c \\ c & s \end{bmatrix} \begin{bmatrix} u \\ v \end{bmatrix} \quad (3.7)$$

Then the Euler equations become

$$\frac{\partial}{\partial t} (rh^2 w) + \frac{\partial}{\partial \theta} (hF) + \frac{\partial}{\partial r} (rhG) = 0 \quad (3.8)$$

where

$$w = \begin{bmatrix} \rho \\ \rho U \\ \rho V \\ \rho E \end{bmatrix}, \quad F = \begin{bmatrix} \rho U \\ \rho U u + sp \\ \rho U v - cp \\ \rho U H \end{bmatrix}, \quad G = \begin{bmatrix} \rho V \\ \rho V u + cp \\ \rho V v + sp \\ \rho V H \end{bmatrix} \quad (3.9)$$

Then the flow is determined as the steady state solution of equations (3.8) and (3.9), subject to

the flow tangency condition

$$V = 0 \quad \text{on } C \quad (3.10)$$

At the far field boundary B conditions can be specified for incoming waves, while outgoing waves are determined by the solution.

In contrast to the case of potential flow, the pressure is not determined solely by the speed, and assuming that one wishes to control the surface pressure distribution, a suitable cost function is

$$I = \frac{1}{2} \int_C (p - p_d)^2 d\theta \quad (3.11)$$

where p_d is the desired pressure. A modification to the mapping function will influence equations (3.8) and (3.9) through changes δh and $\delta\beta$ in both the modulus and argument of $\frac{dz}{d\sigma}$, finally leading to a variation in the cost function

$$\delta I = \int_C (p - p_d) \delta p d\theta \quad (3.12)$$

where δp is the variation of the pressure.

Now the mapping variations cause variations in the rotation parameters

$$\begin{aligned} \delta s &= c\delta\beta, & \delta c &= -s\delta\beta \\ \delta(hs) &= s\delta h + hc\delta\beta, & \delta(hc) &= c\delta h - hs\delta\beta \end{aligned} \quad (3.13)$$

Define the Jacobian matrices

$$\begin{aligned} A &= \frac{\partial f}{\partial w}, & B &= \frac{\partial g}{\partial w} \\ C &= sA - cB, & D &= cA + sB \end{aligned} \quad (3.14)$$

Then the variation δw in w satisfies

$$\frac{\partial}{\partial \theta} (hC \delta w) + \frac{\partial}{\partial r} (rhD \delta w) = -\frac{\partial}{\partial \theta} (F \delta h + hG \delta \beta) - \frac{\partial}{\partial r} r(G \delta h - hF \delta \beta) \quad (3.15)$$

Also

$$\delta V = 0 \quad \text{on } C \quad (3.16)$$

At the outer boundary there will be no variation in characteristic variables corresponding to incoming waves. If we take the outer boundary B at a fixed radius, incoming waves correspond to negative eigenvalues of D . Suppose that D is represented as $T \Lambda T^{-1}$, where Λ is a diagonal matrix containing its eigenvalues, and the columns of T are eigenvectors of D . Define

$$\delta \tilde{w} = T^{-1} \delta w$$

and $\delta \tilde{w}^-$ as the components of $\delta \tilde{w}$ corresponding to negative eigenvalues of T . Then

$$\delta \tilde{w}^- = 0 \quad \text{on } B \quad (3.17)$$

Since δw satisfies the constraint (3.15), we can replace equation (3.12) by

$$\begin{aligned} \delta I = & \int_C (p - p_d) \delta p d\theta - \iint_D \psi^T \left\{ \frac{\partial}{\partial \theta} (hC \delta w) + \frac{\partial}{\partial r} (rhD \delta w) \right\} dr d\theta \\ & - \iint_D \psi^T \left\{ \frac{\partial}{\partial \theta} (F \delta h + hG \delta \beta) + \frac{\partial}{\partial r} r(G \delta h - hF \delta \beta) \right\} dr d\theta \end{aligned} \quad (3.18)$$

where the vector ψ is a Lagrange multiplier, and the superscript T denotes the transpose. Suppose that ψ is the steady state solution of the adjoint equation

$$\frac{\partial \psi}{\partial t} - C^T \frac{\partial \psi}{\partial \theta} - rD^T \frac{\partial \psi}{\partial r} = 0 \quad \text{in } D \quad (3.19)$$

At the outer boundary B conditions can be specified for incoming waves, corresponding to positive

eigenvalues of $D^T = T^{-1T} \Lambda T^T$. Define

$$\tilde{\psi} = T^T \psi$$

and $\tilde{\psi}^+$ as the components of $\tilde{\psi}$ corresponding to positive eigenvalues of D . Then we can set

$$\tilde{\psi}^+ = 0 \quad \text{on } B \quad (3.20)$$

If we integrate equation (3.18) by parts the contribution

$$\int_B r h \psi^T D \delta w d\theta = \int_B r h \tilde{\psi} \Lambda \delta \tilde{w} d\theta$$

vanishes because of the complementary boundary conditions (3.17) and (3.20) satisfied by $\delta \tilde{w}$ and $\tilde{\psi}$ at the outer boundary. If δh and $\delta \beta$ decay fast enough in the far field the contribution

$$\int_B r (G \delta h - h F \delta \beta) d\theta$$

will also be negligible. Thus we find that

$$\delta I = \int_C (p - p_d) \delta p d\theta + \int_C \psi^T (h D \delta w + G \delta h - h F \delta \beta) d\theta + J$$

where

$$J = \iint_D \left\{ (F^T \psi_\theta + G^T \psi_r) \delta h + (G^T \psi_\theta - F^T \psi_r) h \delta \beta \right\} dr d\theta \quad (3.21)$$

Also

$$h D \delta w + G \delta h - h F \delta \beta = \mathcal{L}(hG) = h \begin{bmatrix} 0 \\ c \delta p \\ s \delta p \\ 0 \end{bmatrix} + p \begin{bmatrix} 0 \\ \delta(hc) \\ \delta(hs) \\ 0 \end{bmatrix}$$

Thus using the relations (3.13)

$$\delta I = \int_C (p - p_d) \delta p d\theta + \int_C (c\psi_2 + s\psi_3) \delta p h d\theta + \int_C p(c\psi_2 + s\psi_3) \delta h d\theta - \int_C p(s\psi_2 - c\psi_3) \delta \beta h d\theta + J$$

Now let ψ satisfy the boundary condition

$$h(c\psi_2 + s\psi_3) = -(p - p_d) \quad \text{on } C \quad (3.22)$$

Then

$$\delta I = - \int_C (p - p_d) p \frac{\delta h}{h} d\theta - \int_C (s\psi_2 - c\psi_3) p h \delta \beta d\theta + J \quad (3.23)$$

Finally we can use the fact that the mapping function is fully determined by its boundary value to reduce J to a boundary integral. Set

$$\log \frac{dz}{d\sigma} = f + i\beta$$

where

$$f = \log \left| \frac{dz}{d\sigma} \right| = \log h$$

and

$$\delta f = \frac{\delta h}{h}$$

Also f and β separately satisfy Laplace's equation

$$\Delta f = 0, \quad \Delta \beta = 0$$

and jointly they satisfy the Cauchy Riemann equations

$$f_\theta = r\beta_r, \quad \beta_\theta = -rf_r$$

Let the auxiliary function P satisfy the equation

$$\Delta P = h(F^T \psi_\theta + G^T r \psi_r) \quad \text{in } D \quad (3.24)$$

and the boundary condition

$$P = 0 \quad \text{on } C \quad (3.25)$$

Also let the auxiliary function Q satisfy the equation

$$\Delta Q = h(G^T \psi_\theta - F^T r \psi_r) \quad \text{in } D \quad (3.26)$$

and the boundary condition

$$\frac{\partial Q}{\partial r} = hp(s\psi_2 + c\psi_3) \quad \text{on } C \quad (3.27)$$

Then

$$\begin{aligned} J &= \iint_D (\Delta P \delta f + \Delta Q \delta \beta) dr d\theta \\ &= \int_C \left\{ \delta f \frac{\partial P}{\partial r} + hp(s\psi_2 + c\psi_3) - Q \frac{\partial}{\partial r} \delta \beta \right\} d\theta \\ &= \int_C \left\{ \delta f \frac{\partial P}{\partial r} + hp(s\psi_2 + c\psi_3) - Q \frac{\partial}{\partial \theta} \delta f \right\} d\theta \end{aligned}$$

Thus finally

$$\delta I = \int_C g \delta f d\theta \quad (3.28)$$

where

$$g = \frac{\partial P}{\partial r} + \frac{\partial Q}{\partial \theta} - (p - p_d)p \quad (3.29)$$

As in the previous section, an appropriate modification of f is

$$\delta f = -\lambda \tilde{g}$$

where \tilde{g} is the projection of g onto the admissible subspace of variations defined by equations (2.20) and (2.21), and λ is a sufficiently small positive number. Then

$$\delta I = -\lambda \int_C \tilde{g}^2 d\theta < 0$$

If the flow is transonic, shock waves are likely to be formed, and again it may be desirable to use a more sophisticated cost function to produce a smooth shape change. In this case we can set

$$I = \frac{1}{2} \int_C \left[\lambda_1 S^2 + \lambda_2 \left(\frac{dS}{d\theta} \right)^2 \right] d\theta \quad (3.30)$$

where λ_1 and λ_2 are positive parameters, and the periodic function $S(\theta)$ satisfies the equation

$$\lambda_1 S - \lambda_2 \frac{d^2 S}{d\theta^2} = p - p_d \quad (3.31)$$

Then

$$\begin{aligned} \delta I &= \int_C \left(\lambda_1 S \delta S + \lambda_2 \frac{dS}{d\theta} \frac{d}{d\theta} \delta S \right) d\theta \\ &= \int_C S \left(\lambda_1 \delta S - \lambda_2 \frac{d^2}{d\theta^2} \delta S \right) d\theta \\ &= \int_C S \delta p d\theta \end{aligned}$$

Thus S replaces $p - p_d$ in the previous formulas. If one modifies the boundary condition (3.22) to

$$h(c\psi_2 + s\psi_3) = -S \quad \text{on } C \quad (3.32)$$

the formula for the gradient becomes

$$g = \frac{\partial P}{\partial r} + \frac{\partial Q}{\partial \theta} - Sp \quad (3.33)$$

instead of equation (3.29), and an appropriate modification of f is again $-\lambda \tilde{g}$.

The final design procedure using the Euler equations is thus as follows. Choose an initial profile and corresponding mapping function f . Then

- 1) Solve the flow equation (3.8) for w by integrating to a steady state.
- 2) Solve the ordinary differential equation (3.31) for S .
- 3) Solve the adjoint equation (3.19) with the boundary conditions (3.20) and (3.32) for ψ by integrating to a steady state.
- 4) Solve the auxiliary Poisson equations (3.24) and (3.26) for P and Q .
- 5) Evaluate

$$g = \frac{\partial P}{\partial r} + \frac{\partial Q}{\partial \theta} - Sp$$

on C , and find its projection \tilde{g} onto the admissible subspace of variations according to equations (2.20) and (2.21).

- 6) Correct the boundary mapping function f_C by

$$\delta f = -\lambda \tilde{g}$$

where $\lambda > 0$, and return to step 1.

4. Wing design using the Euler equations

In order to illustrate further the application of control theory to aerodynamic design problems, this section treats the case of three-dimensional wing design, again using the inviscid Euler equations as the mathematical model for compressible flow. In this case it proves convenient to denote the Cartesian coordinates and velocity components by x_1, x_2, x_3 and u_1, u_2, u_3 , and to use the convention that summation over $i = 1$ to 3 is implied by a repeated index i . The three-dimensional Euler equations may then be written as

$$\frac{\partial w}{\partial t} + \frac{\partial f_i}{\partial x_i} = 0 \quad (4.1)$$

where

$$w = \begin{bmatrix} \rho \\ \rho u_1 \\ \rho u_2 \\ \rho u_3 \\ \rho E \end{bmatrix} \quad (4.2a)$$

and

$$f_1 = \begin{bmatrix} \rho u_1 \\ \rho u_1^2 + p \\ \rho u_1 u_2 \\ \rho u_1 u_3 \\ \rho u_1 E \end{bmatrix}, \quad f_2 = \begin{bmatrix} \rho u_2 \\ \rho u_2 u_1 \\ \rho u_2^2 + p \\ \rho u_2 u_3 \\ \rho u_2 E \end{bmatrix}, \quad f_3 = \begin{bmatrix} \rho u_3 \\ \rho u_3 u_1 \\ \rho u_3 u_2 \\ \rho u_3^2 + p \\ \rho u_3 E \end{bmatrix} \quad (4.2b)$$

Also

$$p = (\gamma - 1) \rho \left(E - \frac{u_i^2}{2} \right), \quad \rho H = \rho E + p \quad (4.3)$$

Consider a transformation to coordinates X_1, X_2, X_3 where

$$H_{ij} = \frac{\partial x_i}{\partial X_j}, \quad J = \det(H), \quad H_{ij}^{-1} = \frac{\partial X_i}{\partial x_j} \quad (4.4)$$

The Euler equations can now be written as

$$\frac{\partial W}{\partial t} + \frac{\partial F_i}{\partial X_i} = 0 \quad (4.5)$$

where

$$W = Jw, \quad F_i = J \frac{\partial X_i}{\partial x_j} f_j \quad (4.6)$$

Define the contravariant velocity vector

$$\begin{bmatrix} U_1 \\ U_2 \\ U_3 \end{bmatrix} = H^{-1} \begin{bmatrix} u_1 \\ u_2 \\ u_3 \end{bmatrix} \quad (4.7)$$

Then

$$F_i = J \begin{bmatrix} \rho U_i \\ \rho U_i u_1 + \frac{\partial X_i}{\partial x_1} p \\ \rho U_i u_2 + \frac{\partial X_i}{\partial x_2} p \\ \rho U_i u_3 + \frac{\partial X_i}{\partial x_3} p \\ \rho U \end{bmatrix} \quad (4.8)$$

Assume now that the new coordinate system conforms to the wing in such a way that the wing surface B_w is represented by $X_2 = 0$. Then the flow is determined as the steady state solution of equation (4.5) subject to the flow tangency condition

$$U_2 = 0 \quad \text{on } B_w \quad (4.9)$$

At the far field boundary, conditions can be specified for incoming waves as in the two-dimensional case, while outgoing waves are determined by the solution.

Suppose now that it is desired to control the surface pressure by varying the wing shape. It is convenient to retain a fixed computational domain. Variations in the shape then result in

corresponding variations in the mapping derivatives defined by H. Introduce the cost function

$$I = \frac{1}{2} \iint_{B_w} (p - p_d)^2 dX_1 dX_3 \quad (4.10)$$

where p_d is the desired pressure. A variation in the shape will cause a variation δp in the pressure and consequently a variation in the cost function

$$\delta I = \iint_{B_w} (p - p_d) \delta p dX_1 dX_3 \quad (4.11)$$

Since p depends on w through the equation of state (4.3), the variation δp can be determined from the variation δw . Define the Jacobian matrices

$$A_i = \frac{\partial f_i}{\partial w}, \quad C_i = H_{ij} A_j \quad (4.12)$$

Then

$$\frac{\partial}{\partial X_i} (\delta F_i) = 0 \quad (4.13)$$

where

$$\delta F_i = C_i \delta w + \delta \left(J \frac{\partial X_i}{\partial x_j} \right) f_j \quad (4.14)$$

and for any differentiable vector ψ

$$\int_D \frac{\partial \psi^T}{\partial X_i} \delta F_i dv = \int_{\text{boundaries}} n_i \psi^T \delta F_i ds \quad (4.15)$$

where n_1, n_2 and n_3 are the components of a unit vector normal to the boundary. On the wing surface B_w , $n_1 = n_3 = 0$ and it follows from equation (4.9) that

$$\delta F_2 = J \begin{bmatrix} 0 \\ \frac{\partial X_2}{\partial x_1} \delta p \\ \frac{\partial X_2}{\partial x_2} \delta p \\ \frac{\partial X_2}{\partial x_3} \delta p \\ 0 \end{bmatrix} + p \begin{bmatrix} 0 \\ \delta(J \frac{\partial X_2}{\partial x_1}) \\ \delta(J \frac{\partial X_2}{\partial x_2}) \\ \delta(J \frac{\partial X_2}{\partial x_3}) \\ 0 \end{bmatrix} \quad (4.16)$$

Suppose now that ψ is the steady state solution of the adjoint equation

$$\frac{\partial \psi}{\partial t} - C_i^T \frac{\partial \psi}{\partial X_i} = 0 \quad \text{in } D \quad (4.17)$$

At the outer boundary incoming characteristics for ψ correspond to outgoing characteristics for δw . Consequently, as in the two-dimensional case, one can choose boundary conditions for ψ such that

$$n_i \psi^T C_i \delta w = 0$$

If the coordinate transformation is such that $\delta(JH^{-1})$ is negligible in the far field, the only remaining boundary term is

$$-\int_{B_w} \psi^T \delta F_2 dX_1 dX_3$$

Let ψ satisfy the boundary condition

$$J(\psi_2 \frac{\partial X_2}{\partial x_1} + \psi_3 \frac{\partial X_2}{\partial x_2} + \psi_4 \frac{\partial X_2}{\partial x_3}) = -(p - p_d) \quad \text{on } B_w \quad (4.18)$$

Then, since it follows from equation (4.17) that

$$\int_D \frac{\partial \psi^T}{\partial X_i} C_i \delta w dV = 0$$

we find that

$$\delta I = \int_D \frac{\partial \psi^T}{\partial X_i} \delta \left[J \frac{\partial X_i}{\partial x_j} \right] f_j dV - \int_{B_w} \left\{ \psi_2 \delta \left[J \frac{\partial X_2}{\partial x_1} \right] + \psi_3 \delta \left[J \frac{\partial X_2}{\partial x_2} \right] + \psi_4 \delta \left[J \frac{\partial X_2}{\partial x_3} \right] \right\} p dX_1 dX_3 \quad (4.19)$$

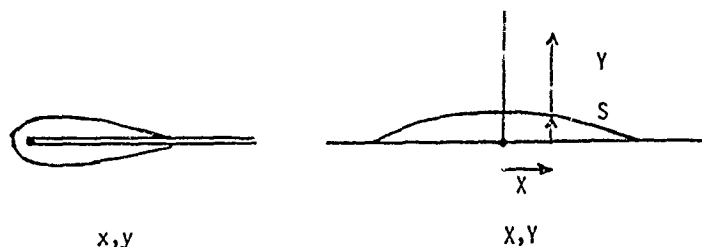


Figure 2

A convenient way to treat a wing is to introduce sheared parabolic coordinates through the transformation

$$x = \frac{1}{2} \left\{ X^2 - (Y + S(X, Z))^2 \right\}$$

$$y = X(Y + S(X, Z))$$

$$z = Z$$

Here x, y, z are Cartesian coordinates, and X and $Y+S$ correspond to parabolic coordinates generated by the mapping

$$x + iy = \frac{1}{2} (X + i(Y + S))^2$$

at a fixed span station Z . The surface $Y=0$ is a shallow bump corresponding to the wing surface, with a height $S(X, Z)$ determined by the equation

$$X + iS = \sqrt{2 (x_g + iy_g)}$$

where $x_g(z)$ and $y_g(z)$ are coordinates of points lying in the wing surface. We now treat $S(X, Z)$ as

the control.

In this case

$$H = \begin{bmatrix} X - (Y+S)S_X & -(Y+S) & -(Y+S)S_Z \\ Y+S + XS_X & X & XS_Z \\ 0 & 0 & 1 \end{bmatrix}$$

while

$$J = X^2 + (Y+S)^2$$

and

$$H^{-1} = \frac{1}{J} \begin{bmatrix} X & Y+S & 0 \\ -(Y+S+XS_X) & (X-(Y+S)S_X) & -JS_Z \\ 0 & 0 & J \end{bmatrix}$$

Also

$$\delta J = 2(Y+S) \delta S$$

and

$$\delta(JH^{-1}) = \begin{bmatrix} 0 & \delta S & 0 \\ -(\delta S + X\delta S_X) & -(\delta S S_X + (Y+S)\delta S_X) & -(\delta J S_Z + J\delta S_Z) \\ 0 & 0 & 1 \end{bmatrix}$$

Inserting these formulas in equation (4.19) we find that the volume integral in δI is

$$\begin{aligned} & \int_D \psi_X^T \delta S f_1 dV \\ & - \int_D \psi_Y^T \left\{ (\delta S + X\delta S_X) f_1 + (\delta S S_X + (Y+S)\delta S_X) f_2 + (\delta J S_Z + J\delta S_Z) f_3 \right\} dV \\ & + \int_D \psi_Z^T \delta J dV \end{aligned}$$

where S and δS are independent of Y . Therefore, integrating over Y , the variation of the cos

function can be reduced to a surface integral of the form

$$\delta I = \iint_B (P(X,Z) \delta S + Q(X,Z) \delta S_X + R(X,Z) \delta S_Z) dX dZ$$

Also the shape change will be confined to a bounded region of the X-Z plane, so we can integrate by parts to obtain

$$\delta I = \iint_B (P - \frac{\partial Q}{\partial X} - \frac{\partial R}{\partial Z}) \delta S dX dZ$$

Thus to reduce I we can choose

$$\delta S = -\lambda (P - \frac{\partial Q}{\partial X} - \frac{\partial R}{\partial Z})$$

where λ is sufficiently small and non-negative.

In order to impose a thickness constraint we can define a baseline surface $S_0(X,Z)$ below which $S(X,Z)$ is not allowed to fall. Now if we take $\lambda = \lambda(X,Z)$ as a non-negative function such that

$$S(X,Z) + \delta S(X,Z) \geq S_0(X,Z)$$

Then the constraint is satisfied, while

$$\delta I = - \iint_B \lambda (P - \frac{\partial Q}{\partial X} - \frac{\partial R}{\partial Z})^2 dX dZ \leq 0$$

5. Conclusion

The purpose of the last three sections is to demonstrate by representative examples that control theory can be used to formulate computationally feasible procedures for aerodynamic design. The cost of each iteration is of the same order as two flow solutions, since the adjoint equation is of comparable complexity to the flow equation, and the remaining auxiliary equations could be solved quite inexpensively. Provided, therefore, that one can afford the cost of a moderate number of flow solutions, procedures of this type can be used to derive improved designs. The approach is quite general, not limited to particular choices of the coordinate transformation or cost function, which might in fact contain measures of other criteria of performance such as lift and drag. For the sake of simplicity certain complicating factors, such as the need to include a special term in the mapping function to generate a corner at the trailing edge, have been suppressed from the present analysis. Also it remains to explore the numerical implementation of the design procedures proposed in this paper.

References

1. Murman, E.M. and Cole, J.D., "Calculation of Plane Steady Transonic Flows", AIAA Journal, Vol. 9, 1971, pp. 114-121.
2. Jameson, A., "Iterative Solution of Transonic Flows Over Airfoils and Wings, Including Flows at Mach 1", Comm. Pure. Appl. Math, Vol. 27, 1974, pp. 283-309.
3. Jameson, A. and Caughey, D.A., "A Finite Volume Method for Transonic Potential Flow Calculations", Proc. AIAA 3rd Computational Fluid Dynamics Conference, Albuquerque, 1977, pp. 35-54.
4. Bristeau, M.O., Pironneau, O., Glowinski, R., Periaux, J., Perrier, P., and Poirier, G., "On the Numerical Solution of Nonlinear Problems in Fluid Dynamics by Least Squares and Finite Element Methods (II). Application to Transonic Flow Simulations", Proc. 3rd International Conference on Finite Elements in Nonlinear Mechanics, FENOMECH 84, Stuttgart, 1984, edited by J. St. Doltsinis, North Holland, 1985, pp. 363-394.
5. Jameson, A., Schmidt, W., and Turkel, E., "Numerical Solution of the Euler Equations by Finite Volume Methods Using Runge-Kutta Time Stepping Schemes", AIAA Paper 81-1259, AIAA 14th Fluid Dynamics and Plasma Dynamics Conference, Palo, Alto, 1981.
6. Ni, Ron Ho., "A Multiple Grid Scheme for Solving the Euler Equations", AIAA Journal, Vol. 20, 1982, pp. 1565-1571.
7. Pulliam, T.H. and Steger, J.L., "Recent Improvements in Efficiency, Accuracy and Convergence for Implicit Approximate Factorization Algorithms", AIAA Paper 85-0360, AIAA 23rd Aerospace Sciences Meeting, Reno, January 1985.
8. McCormack, R.W., "Current Status of Numerical Solutions of the Navier-Stokes Equations", AIAA Paper 85-0032, AIAA 23rd Aerospace Sciences Meeting, Reno, January 1985.

9. Jameson, A., Baker, T.J. and Weatherill, N.P., "Calculation of Inviscid Transonic Flow Over a Complete Aircraft", AIAA Paper 86-0103, AIAA 24th Aerospace Sciences Meeting, Reno, January 1986.
10. Jameson, A., "Successes and Challenges in Computational Aerodynamics", AIAA Paper 87-1184-CP, 8th Computational Fluid Dynamics Conference, Hawaii, 1987.
11. Lighthill, M.J., "A New Method of Two Dimensional Aerodynamic Design", ARC, Rand M 2112, 1945.
12. McFadden, G.B., "An Artificial Viscosity Method for the Design of Supercritical Airfoils", New York University Report C00-3077-158, 1979.
13. Taverna, F., "Advanced Airfoil Design for General Aviation Propellers", AIAA Paper 83-1791, 1983.
14. Garabedian, P. and McFadden, G., "Computational Fluid Dynamics of Airfoils and Wings", Proc. of Symposium on Transonic, Shock, and Multidimensional Flows, Madison, 1981, Meyer, R., ed., Academic Press, New York, 1982, pp. 1-16.
15. Tranen, J.L., "A Rapid Computer Aided Transonic Airfoil Design Method", AIAA Paper 74-501, 1974.
16. Volpe, G. and Melnik, R.E., "The Design of Transonic Aerofoils by a Well Posed Inverse Method", Int. J. Numerical Methods in Engineering, Vol. 22, 1986, pp. 341-361.
17. Henne, P.A., "An Inverse Transonic Wing Design Method", AIAA Paper 80-0330, 1980.
18. Garabedian, P.R. and Korn, D.G., "Numerical Design of Transonic Airfoils", Proc. SYNSPADE 1970, Hubbard, B., ed., Academic Press, New York, 1971, pp. 253-271.
19. Giles, M., Drela, M. and Thompkins, W.T., "Newton Solution of Direct and Inverse Transonic Euler Equations", AIAA Paper 85-1530, Proc. AIAA 7th Computational Fluid Dynamics Conference, Cincinnati, 1985, pp. 394-402.
20. Hicks, R.M. and Henne, P.A., "Wing Design by Numerical Optimization", AIAA Paper 79-0080, 1979.
21. Lions, Jacques Louis, "Optimal Control of Systems Governed by Partial Differential Equations", translated by S.K. Mitter, Springer Verlag, New York, 1971.

OPTIMIZATION OF AERODYNAMIC DESIGNS USING COMPUTATIONAL FLUID DYNAMICS*

D. H. HUDDLESTON
Sverdrup Technology, Inc./AEDC Group
Arnold AFB, TN 37389 USA

and
C. W. MASTIN
Department of Mathematics and Statistics
Mississippi State University, MS 39762 USA

ABSTRACT

An aerodynamic design optimization technique which couples direct optimization algorithms with the analysis capability provided by appropriate computational fluid dynamics (CFD) programs is presented. This technique is intended to be an aid in designing the aerodynamic shapes and test conditions required for the successful simulation of aircraft engine inlet conditions in a ground test environment. However, the method is applicable to other aerodynamic design problems. The approach minimizes a nonlinear least-squares objective function which may be defined in a region remote to the geometric surface being optimized. In this study, finite-difference Euler and Navier-Stokes codes were applied to obtain the objective function evaluations, although the optimization method could be coupled with any CFD analysis technique. Results are presented for a NACA0012 airfoil, convergent/divergent nozzles, and a planar, supersonic forebody simulator design.

NOMENCLATURE

B	= Jacobian approximation
F_p	= Least squares objective function
$g_i^p(u)$	= Bernstein basis function
J	= Jacobian matrix of R with respect to P
M	= Total number of design parameters
M_x	= Mach number component along the x-axis
M_y	= Mach number component along the y-axis
M_z	= Mach number component along the z-axis
N	= Total number of residual components
N_r	= Total number of reference plane grid points
N_c	= Total number of parameter constraints
P	= Design parameter vector
P_i	= Design parameter
P_T	= Total pressure
r_i	= Least-squares residual component
R	= Least-squares residual vector
t	= NACA0012 airfoil thickness parameter
T	= Total temperature
ΔP	= Computed change in design parameters
x	= NACA0012 airfoil axial coordinate
x_n	= Position vectors of Bezier control points
$x(u)$	= Bernstein-Bezier polynomial
$x(u,v,w)$	= Three-dimensional Bezier polynomial
$y(x)$	= Function which defines a NACA0012 airfoil

1.0 INTRODUCTION

During the past three decades Computational Fluid Dynamics (CFD) has emerged as a discipline which allows the analysis of many previously intractable problems in fluid mechanics. Although CFD is still in a stage of rapid growth and development, it is already being widely used to enhance the aerodynamic design process (Ref. 1). The most common contribution of CFD in aerodynamic design has been to provide direct analyses of existing or proposed design configurations as a means of evaluating the design's utility. Coupling numerical optimization methods with the versatile analysis capability afforded by modern CFD techniques offers the potential to allow many aerodynamic designs to be optimized relative to specified design criteria in a fashion heretofore impossible. The objective of this paper is to present a coupled CFD/nonlinear optimization method which is being developed for application to aerodynamic design problems. This is accomplished through the optimization of selected design parameters by minimizing a nonlinear least squares objective function. The technique presented is applicable in both two and three dimensions and in principle could be coupled with any appropriate CFD technique.

Aerodynamic design optimization utilizing CFD has been the subject of several recent papers. An inverse design capability was implemented into an Euler code by Zannetti and Pandolfi (Ref. 2). A similar capability was implemented into a thin-layer Navier-Stokes code by Yang and Ntone (Ref. 3). Design

*The research reported herein was performed by the Arnold Engineering Development Center (AEDC), Air Force Systems Command. Work and analysis for this research were done by personnel of Sverdrup Technology, Inc./AEDC Group, operating contractor of the AEDC propulsion test facilities. Further reproduction is authorized to satisfy the needs of the U. S. Government.

optimizations have been performed by utilizing a family of base designs to define basis functions from which the optimum design can be determined (e.g., Vanderplaats (Ref. 4), Barger and Moltra (Ref. 5), and Pittman (Ref. 6)). Madabhushi, Levy, and Pincus (Ref. 7) coupled a spatially parabolized Navier-Stokes code with a quasi-Newton optimization algorithm for application to subsonic duct design. Jenkins and Hatfield (Ref. 8) coupled a method-of-characteristics flow solver with the Hooke and Jeeves pattern-search optimization algorithm to aid in the design of supersonic turbine stators. Each of these techniques was successfully applied to the class of design problem for which they were developed. However, the aerodynamic range of applicability can be extended if nonlinear optimization is coupled with a general purpose Euler/Navier-Stokes solver.

The aerodynamic design optimization problem which motivated this work is illustrated in Fig. 1. This figure depicts an inlet-engine compatibility test within a generic ground test facility designed to evaluate the performance of an integrated propulsion system. In this problem the indicated forebody simulator must be designed in conjunction with the free-jet flow properties (total pressure, total temperature, Mach number, and flow angle). The design requirement is to produce a flow field entering the engine inlet in the free-jet installation which is very similar to that which would be encountered in flight (Ref. 9). The underlying premise is that it is irrelevant, to the engine/inlet combination, from whence the conditions came as long as an adequate match exists. The aerodynamicist must specify a forebody simulator geometry and free-jet fluid properties which produce, within design tolerance, the desired fluid dynamic state at the region of interest. The fluid properties are specified at a reference plane upstream of the engine inlet, hereafter referred to as the inlet reference plane (RP).

This optimization problem possesses several interesting features in that: (1) the flow-field constraints are imposed at a location away from the geometric surface which is being optimized, (2) some free-jet fluid properties must be optimized, (3) discontinuous or localized high gradient behavior may occur within the design space (e.g., shocks or onset of separated flow), and (4) a history of prior similar designs does not exist. These characteristics preclude the direct application of techniques previously developed since the fluid dynamic analysis requirements indicate that the optimization algorithm be coupled to a three-dimensional Navier-Stokes code or an Euler code.

For this design problem, the fluid dynamic state is completely specified at the RP and an objective function can be defined at the RP which measures the error norm between the desired fluid dynamic properties and the fluid properties computed for a particular design point. The design requirement is to minimize this highly nonlinear objective function with respect to identified design parameters to yield the optimal design. The error norm was selected to be a least-squares deviation between the target flow-field variables and the values computed for a given design point. The least-squares form was selected because: (1) the method is very versatile, (2) extensive literature is available on general nonlinear least-squares minimization, and (3) efficient Newton and quasi-Newton methods are well documented for the nonlinear least-squares problem.

Application to a complete three-dimensional forebody simulator design (FBS) has not yet been achieved, but simpler examples demonstrating development of key features of the design process are presented. The examples presented include a NACA0012 airfoil, a two-dimensional and a three-dimensional convergent/divergent nozzle, and a planar, supersonic, forebody simulator.

2.0 NUMERICAL TECHNIQUE

2.1 CFD Analysis

A typical free-jet test envelope can range from low subsonic flow to moderately high supersonic flows with the free-jet nozzle potentially inclined at high angles of attack relative to the test article. The appropriate aerodynamic analysis for the motivating problem is thus a complex, three-dimensional, flow-field computation necessitating the application of an Euler code or a Navier-Stokes code to produce an accurate simulation.

In this study all of the CFD analyses were performed by application of PARC, a general purpose, finite difference Euler/Navier-Stokes CFD code (Ref. 10) which applies a diagonalized version of the Beam and Warming algorithm to solve the governing partial differential equations. The PARC code has been applied extensively at the Arnold Engineering Development Center (AEDC) and elsewhere to analyze a variety of complex internal and external fluid mechanics problems (Ref. 11). This particular CFD code was selected because of its robustness, ease of use, and reliability. It produces consistent and repeatable flow simulations in the sense that small perturbations to design parameters are accurately reflected in the flow-field solution. All of the computational grids utilized herein were generated by application of the INGRID code developed by Soni (Ref. 12).

2.2 Optimization Algorithm

The nonlinear least-squares minimization is formulated as follows: Let the residuals $r_1(P_1, \dots, P_M)$, $i = 1, 2, \dots, N$, be functions of M design parameters. The design parameters may be geometric, fluid dynamic, or both. To minimize r_i , in the least-squares sense, values for the parameters, P_j , are found which minimize:

$$F(P_1, P_2, \dots, P_M) = \sum_{i=1}^N [r_i(P_1, P_2, \dots, P_M)]^2 \quad (1)$$

where r_i denotes the difference between the N specified reference plane quantities and corresponding N computed quantities associated with the M parameters. This sum can be written in vector form as $R(P)^T R(P)$ where $R(P)$ is a vector with components r_i which are functions of the parameters P_j .

The residuals are comprised of differences between fluid dynamic properties at the reference plane (RP). The set of variables used herein to define the RP fluid state is: (1) RP total pressure, $P_{T,RP}$, (2)

RP total temperature, T_{TP} , and (3) RP directional Mach number, $M_{x_{rp}}$, $M_{y_{rp}}$, and $M_{z_{rp}}$. In two dimensions one Mach number component is eliminated. Variable constraints are imposed by addition of barrier functions, such as the inverse function (Ref. 13), added to the objective function. Thus, the expression RTR becomes:

$$R^T R = \sum_{i=1}^{N_r} \left[(P_{T_{rp}} - P_T)_i^2 + (T_{T_{rp}} - T_T)_i^2 + (M_{x_{rp}} - M_x)_i^2 + (M_{y_{rp}} - M_y)_i^2 + (M_{z_{rp}} - M_z)_i^2 \right] + \sum_{j=1}^{N_c} \phi_j^2 \quad (2)$$

where N_r is the number of geometrically distinct reference plane points, ϕ_j represents the barrier functions, and N_c is the number of parameter constraints. Since each term in Eq. (2) contains five residual components for each i , in order to put this in the form of Eq. (1), $N = 5N_r + N_c$ must hold. In Eq. (2) the subscript rp denotes the specified RP values while unsubscripted values denote RP values computed for a particular trial design (set of design parameters). Quantities in Eq. (2) are normalized by appropriate reference quantities to produce target RP values of order one.

A popular and efficient algorithm for minimizing the nonlinear least-squares form of Eq. (1) is the Gauss-Newton method (Ref. 13) or one of its variants such as Hartley's modified Gauss-Newton method (Ref. 14). Applying the Gauss-Newton method to minimize Eq. (1) yields an optimization algorithm of the form:

$$J^T J \Delta P = J^T R \quad (3)$$

where J denotes the $M \times N$ matrix of R with respect to P . Equation (3) defines an M by M system of equations which is used to compute the change, ΔP , in each of the M design parameters, P_j . To apply this algorithm, J is evaluated by a finite difference approximation to obtain the partial derivative of each residual component with respect to each design parameter. This requires $M + 1$ function evaluations to compute the M partials for each residual. Since a CFD solution is used to obtain each function evaluation, determination of this Jacobian is by far the most expensive part of the algorithm.

An extension of this algorithm is Broyden's quasi-Newton method (Ref. 13). Broyden's extension modifies the standard Gauss-Newton method by approximating the Jacobian, J , at the $k + 1$ iteration from the Jacobian and other data available at iteration k rather than recomputing J directly. Broyden's method is given by:

$$B^T B \Delta P = B^T R \quad (4)$$

where the Jacobian approximation, B , is updated at iteration $k + 1$ according to:

$$B_{k+1} = B_k + \frac{(\Delta R_k - B_k \Delta P_k) \Delta P_k^T}{\Delta P_k^T \Delta P_k} \quad (5)$$

and B_0 is obtained by an initial finite difference approximation to the Jacobian. Application of the Gauss-Newton algorithm requires $M + 1$ function evaluations for each iteration while Broyden's extension requires $M + 1$ function evaluations for the first iteration but only one evaluation for subsequent iterations. Because of the expense of evaluating the objective function, a line search was not employed unless the computed variable change failed to reduce the objective function. Following Hartley (Ref. 14), a quadratic polynomial was applied whenever a line search was used.

3.0 RESULTS

3.1 NACA0012 Airfoil

A NACA0012 airfoil was used as a simple example to illustrate aerodynamic optimization in the presence of separated flow. This is a common airfoil which has been extensively analyzed and is defined by:

$$y(x) = 5t(0.2969x^3 - 0.126x - 0.3516x^2 + 0.2843x^3 - 0.1015x^4) \quad (6)$$

where the parameter, t , determines the maximum airfoil thickness. For the NACA0012 airfoil, the thickness parameter is specified as 0.12.

The PARC CFD code was used to define the target RP properties by computing the laminar flow field about this airfoil, subject to the indicated boundary conditions indicated in Fig. 2. A Reynolds number, based on chord length, of 10^6 was specified which produced a flow field with an attached boundary layer (Fig. 3). Defining the target profile numerically assured that an absolute global minimum existed within the design space. The RP was located at the airfoil trailing edge and extended to the boundary of the computational domain, although the influence of the body was minimal approximately two chord lengths into the domain. The desired RP properties were then used to form the nonlinear least-squares objective function, defined by Eq. (2), which was minimized by application of Broyden's algorithm.

Enhancement of CFD analysis capability per se is not the purpose of this research. Thus, no special effort was made to produce a highly accurate CFD simulation. For this simple problem, however, the PARC code simulation was consistent with results obtained by others (e.g., Jameson and Mavriplis (Ref. 15)). Each simulation was examined to assure that the flow-field solution, particularly at the RP, was converged to minimize the adverse influence of temporal variations upon the design space Jacobian. In

this example, the PARC solution was converged until the norm of RP conservation variables was constant to eight significant figures.

The design parameter (airfoil thickness) was doubled as an initial guess to begin the optimization. This value was selected since the contour subject to the stated boundary conditions produced a flow field which was highly separated (Fig. 4) in contrast to the attached target solution (Fig. 3). As noted, the reference plane was placed at the trailing edge of the airfoil passing through the region of separated flow.

For this example the correct optimum was located, by Broyden's algorithm, within 0.1 percent in six iterations requiring seven function evaluations. Figure 5 compares the target geometric profile with the initial guess profile, the first iteration profile, and the optimal profile as determined by Broyden's algorithm. Figures 6 and 7 show the reduction of the objective function and the convergence history of the design parameter, t , versus iteration number, respectively. As evidenced by these figures, the Broyden's algorithm isolated the global minimum quite efficiently. The optimum was located within 1 percent in four iterations and was isolated within 0.1 percent in six iterations.

3.2 Inviscid Planar Converging/Diverging Nozzle

An inviscid, planar, converging/diverging nozzle (Fig. 8) was used to illustrate optimization of multiple design parameters of diverse type. The design variables for this problem were inflow total pressure, inflow total temperature, and the nozzle wall contour. The simultaneous variation of inlet total conditions and nozzle wall contour is not necessarily representative of a typical nozzle design problem, but this example was constructed because simultaneous variation of free-jet total conditions and a variable geometry is required for the motivating forebody simulator design problem.

The wall contour was a three-parameter Bernstein-Bezier polynomial (Ref. 16) defined as follows:

$$x(u) = \sum_{i=0}^n \frac{n!}{(n-i)!i!} u^i (1-u)^{n-i} x_i, \quad 0 \leq u \leq 1 \quad (7)$$

where $x_0, x_1, x_2, \dots, x_n$ denote the position vectors of the $n+1$ geometric control points. The Bezier parameterization was used because it provides a high degree of variability for a given number of design parameters relative to other parametric representations. This is an important feature for the forebody simulator design problem. The Bezier parameters were located axially at the inlet plane, the midpoint, and the exit plane, as indicated in Fig. 8. The exit plane control point was held constant while the first two parameters were allowed to vary during the optimization. These two geometric parameters, combined with the nozzle inlet total temperature and the nozzle inlet total pressure, produced a total of four design parameters. Since the design parameters are of different type, each was normalized by a reference value yielding nominal parameter values of unity. Geometric parameters were nondimensionalized by the nozzle exit plane half-height. Inflow total pressure and total temperature were nondimensionalized by the target total pressure and total temperature, respectively.

Broyden's quasi-Newton algorithm was again applied in this example. For the first iteration, the Jacobian was approximated by a one-sided finite difference of each of the N residuals. A sensitivity analysis was performed to determine a step size for the geometric parameters in the finite difference approximation which yielded accurate partial derivatives. The parameter sensitivity study was especially important when applying Broyden's algorithm, since the performance of quasi-Newton algorithms is dependent upon the accuracy with which the Jacobian is initially approximated.

A target solution was defined by selecting the Bezier parameters to produce a nominal 2:1 area ratio nozzle and applying PARC to analyze the configuration. The exit pressure was selected to be well below second critical to assure supersonic flow in the divergent portion of the nozzle. This solution was used to define RP properties providing the data necessary to form the least-squares problem. As an initial guess, the inflow height and the nozzle throat height parameters were reduced such that the nozzle area ratio approximately doubled and the geometric throat was shifted forward. The target inflow total temperature and total pressure parameters were doubled for the initial guess. The disparity between the target design and the initial guess is illustrated by comparing the centerline Mach number profiles for the target design and for the initial guess (Fig. 9). As can be seen, the exit target Mach number is nominally 50 percent below the initial guess with a corresponding variation within the rest of the nozzle. Again, no special effort was made to produce a highly accurate CFD simulation, although results for the target nozzle configuration agree well with one-dimensional theory as indicated by comparing the computed centerline Mach number with one-dimensional theory (Fig. 10).

Broyden's quasi-Newton algorithm was applied and converged to the correct answer in four iterations which required nine function evaluations. Typical convergence of the RP properties is illustrated in Fig. 11, which shows RP Mach number profiles for various design iterations. The reduction in the objective function is illustrated in Fig. 12. During the optimization, inflow total conditions converged to within 1 percent of the correct value in one iteration. This is because, for this inviscid example, pressures and temperatures scale linearly with the specified total conditions. Thus, the objective function varies linearly with these parameters and rapid convergence was expected for these parameters since a Gauss-Newton type algorithm was applied. As is well known, for an optimization problem in which the objective function is linear in all of the parameters, the Gauss-Newton algorithm converges to the exact solution in one iteration. The geometric parameters converged more slowly but still at an acceptable rate. The convergence of the full geometry defined by the individual parameters is illustrated in Fig. 13, which shows the iterative variation of the nozzle wall contour.

3.3 Inviscid Three-Dimensional Nozzle

A three-dimensional, rectangular nozzle (Fig. 14) was used to demonstrate that the nonlinear least-squares optimization method is applicable in three dimensions. The nozzle geometry and interior grid were defined by a three-dimensional Bezier polynomial represented by:

$$x(u,v,w) = \sum_{i=0}^p \sum_{j=0}^q \sum_{k=0}^r x_{ijk} g_i^p(u) g_j^q(v) g_k^r(w) \quad (8)$$

Here x_{ijk} denotes the position vectors of the control points, $g_i^p(u)$, $g_j^q(v)$, and $g_k^r(w)$, are Bernstein basis functions of degree p , q , and r , respectively, while u , v , and w are parameters ranging from 0 to 1 (Ref. 15). The Bernstein basis function, $g_i^p(u)$, was defined by:

$$g_i^p(u) = \frac{p!}{(p-i)!i!} u^i (1-u)^{p-i}; i = 0, 1, \dots, p \quad (9)$$

and the other basis functions were analogously defined.

Four control points were specified at each of five axial planes such that each axial cross section was rectangular. The design parameters were two coefficients, P_1 and P_2 , which implicitly determined the distance between the control points in the 'y' and 'z' directions at the mid-plane (Fig. 14). The target geometry corresponded to values of unity for each parameter which produced a nozzle with a nominal exit to throat area ratio of 2.5. Total conditions were specified at the nozzle inlet and a static pressure below second critical was selected at the nozzle exit which provided supersonic flow development in the divergent portion of the nozzle. This geometry and these boundary conditions produced a flow with a nominal exit Mach number of 2.5 when analyzed by application of the Euler version of the PARC code.

For an initial guess, the design parameters P_1 and P_2 were set equal to 2.0 and 2.5, respectively, which produced a high area ratio nozzle with a nominal exit Mach number of 5.8. Unlike the target nozzle, which was square at each axial cross section, the initial guess geometry had a square cross section at the inflow plane, which transitioned to a rectangular cross section at the mid-plane, and then transitioned again to a square at the exit plane. The large difference in exit flow conditions for the initial guess was imposed to illustrate that the initial guess flow field does not necessarily need to closely resemble the desired optimum to obtain acceptable results. The difference in the flow fields for the target and initial guess nozzles is illustrated by comparing the centerline Mach number profiles for the two designs (Fig. 15).

A sensitivity analysis on the geometric design parameters indicated that the objective function partial derivatives were very sensitive to parameter step size because of nonlinear effects and numerical error inherent in the objective function evaluations. Although the most stable step size determined was applied, Broyden's algorithm did not converge to the global minimum. However, the Gauss-Newton algorithm was successfully applied and the optimum was reached in six iterations requiring eighteen function evaluations. Figure 16 illustrates the RP convergence by comparing RP Mach number profiles along the y axis for various iterations. The achieved reduction in objective function and the design parameter convergence is depicted in Figs. 17 and 18, respectively.

3.4 Inviscid Supersonic Planar Forebody Simulator

A two-dimensional analog to the motivating design problem was constructed as shown in Fig. 19. PARC was applied to compute the target flow variables inviscidly at the indicated reference plane. The five design parameters shown in Figure 19 were then perturbed to initialize the optimization. For this case, the variable geometry was defined parametrically as a Bezier curve Eq. (7) with four independent parameters. One additional design parameter was introduced by allowing the Mach number to vary at the inflow plane. For the initial guess, the Mach number parameter was increased by 50 percent and the geometric parameters were reduced by 10 to 70 percent. This produced quite different flow fields in the RP region due, primarily, to the difference in shock structure and shock strength.

As with the three-dimensional nozzle, a sensitivity analysis indicated that objective function partial derivatives were very sensitive to parameter step size and, consequently, Broyden's algorithm was not applied. The Gauss-Newton algorithm was applied, and convergence was obtained in five iterations requiring 31 function evaluations. However, the maximum Mach number deviation was less than 1 percent after only two optimization steps requiring 13 function evaluations which, for many applications, may be adequate. A comparison of the reference plane Mach number profiles for the initial guess, the target solution, and the final converged solution is made in Fig. 20, which shows excellent agreement between the target and final solutions. Figure 21 is a plot of the objective function value versus design iteration number which illustrates the rate at which the minimum was located. Figure 22 depicts the convergence history for each of the five design parameters. Figure 23 further illustrates convergence to the correct FBS geometry by comparing FBS contours at various iterations.

4.0 CONCLUSIONS

A direct optimization technique (coupling an existing Euler/Navier-Stokes solver with efficient nonlinear least-squares minimization algorithms) has been developed for and applied to representative aerodynamic design problems. It was demonstrated by example that the Euler/Navier-Stokes CFD simulations were reliable enough for use in coupling with Newton based optimization algorithms. In fact, for two examples presented a quasi-Newton algorithm was successfully applied.

To date, this research has evaluated the feasibility of coupling nonlinear optimization methods with CFD. Existing Gauss-Newton and quasi-Newton optimization algorithms were employed with minimal modifications and encouraging results were obtained. Although the quasi-Newton algorithm was not

successful in all examples, it was significantly more efficient when applicable. Alternating between the two algorithms may be a more efficient strategy if a reliable switching criteria can be determined. Because of the ultimate intended application, the optimization algorithms were coupled with an Euler/Navier-Stokes CFD code which makes the function evaluations computationally expensive. However, the same technique could be coupled with a less complex CFD technique for design problems in which an Euler/Navier-Stokes simulation is not required.

The approach described provides the designer with a potentially powerful tool to assist in many designs for which a measure of design quality (objective function) can be adequately defined. Because of the flexibility afforded by current CFD codes, this technique can be applied to virtually any steady-state aerodynamic optimization problem for which the selected CFD code is capable of providing a reliable aerodynamic analysis. However, because of the computational expense due to the multiple CFD simulations the technique will most likely be restricted to aerodynamic configurations such as the noted FBS design for which satisfaction of the design criteria is of great importance and simple alternative design methods do not exist.

5.0 REFERENCES

1. Chapman, D. R. "Computational Aerodynamics Development and Outlook." *AIAA Journal*, Vol. 17, No. 12, December 1979, pp. 1293-1313.
2. Zannetti, L. and Pandolfi, M. "Inverse Design Technique for Cascades." NASA CR 3836, November 1984.
3. Yang, T. and Ntone, F. "Viscous Compressible Flow Direct and Inverse Computation with Illustration." NASA CR 175037, January 1986.
4. Vanderplaats, G. N., "An Efficient Algorithm for Numerical Airfoil Optimization." AIAA Paper No. 79-0079, January 1979.
5. Barger, R. L., and Moitra, A. "On Minimizing the Number of Calculations in Design-by-Analysis Codes." NASA TP 2706, June 1987.
6. Pittman, J. L. "Supersonic Airfoil Optimization." *Journal of Aircraft*, Vol. 24, No. 12, December 1987, pp. 873-880.
7. Madabhushi, R. K., Levy, R., and Pincus, S. M. "Design of Optimum Ducts Using an Efficient 3-D Viscous Computational Flow Analysis." Proceedings of the Second International Conference on Inverse Design Concepts and Optimization in Engineering Sciences ICIDES-II, October 1987, pp. 147-166.
8. Jenkins, R. M. and Hatfield, J. A. "Direct Optimization Method for Estimation of Supersonic Flow Turbine Stator Profiles." *Journal of Propulsion*, Vol. 4, No. 6, December 1988, pp. 580-585.
9. Matz, R. J. "Investigations of Free-Jet Test Requirements and Techniques with Emphasis on the Adaptable Jet Stretcher," AEDC-TR-80-35 (AD-A098710), April 1981.
10. Cooper, G. K. "Toward a General Purpose Navier-Stokes Code." Abstracts of the First World Congress on Computational Mechanics, Vol. I, Austin, Texas, September 22-26, 1986.
11. Phares, W. J., Cooper, G. K., Swafford, T. W., and Jones, R. R. "Application of Computational Fluid Dynamics to Test Facility and Experimental Design," AIAA Paper 86-1733, AIAA/ASME/SAE/ASEE 22nd Joint Propulsion Conference, Huntsville, Alabama, 1986.
12. Soni, B. K. "Two- and Three-Dimensional Grid Generation for Internal Flow Applications of Computational Fluid Dynamics." AIAA Paper 85-1520, AIAA 7th Computational Fluid Dynamics Conference, Cincinnati, Ohio, 1985.
13. Scales, L. E., *Introduction to Non-Linear Optimization*, Springer-Verlag, New York, 1985.
14. Hartley, H. O. "The Modified Gauss-Newton Method for the Fitting of Nonlinear Regression Functions by Least Squares." *Technometrics*, Vol. 3, 1961, pp. 269-280.
15. Jameson, A. and Mavriplis, D. "Finite Volume Solution of the Two-Dimensional Euler Equations on a Regular Triangular Mesh." *AIAA Journal*, Vol. 24, No. 4, April 1986, pp. 611-618.
16. Faux, I. D. and Pratt, M. J. *Computational Geometry for Design and Manufacture*, Ellis Horwood Limited, Chichester, West Sussex, England, 1985.

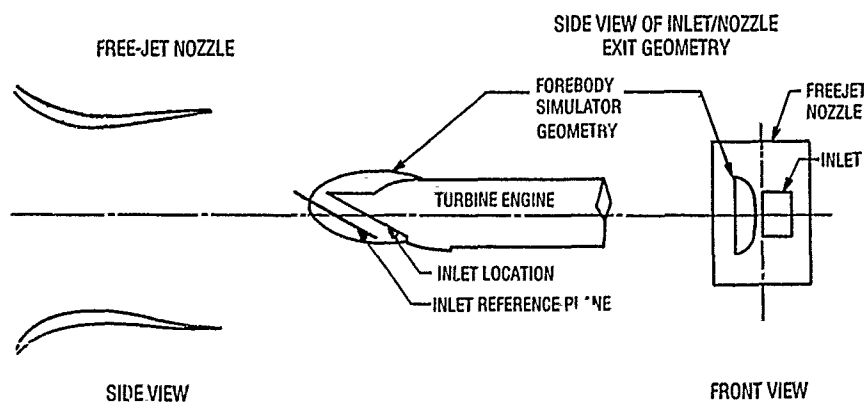


Fig. 1. Generic forebody simulator configuration.

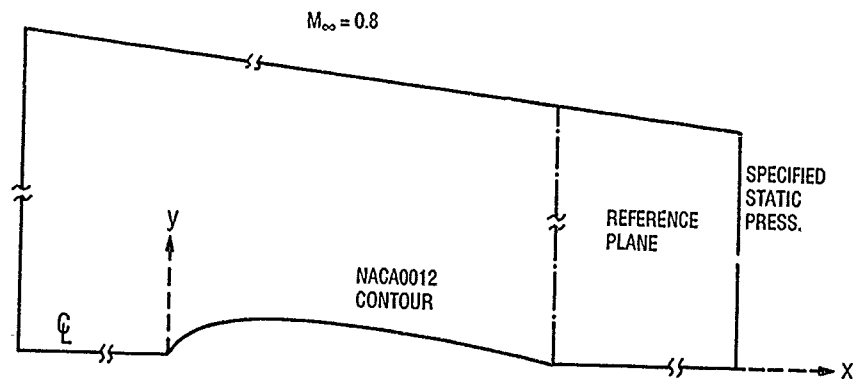


Fig. 2. Viscous airfoil test case.

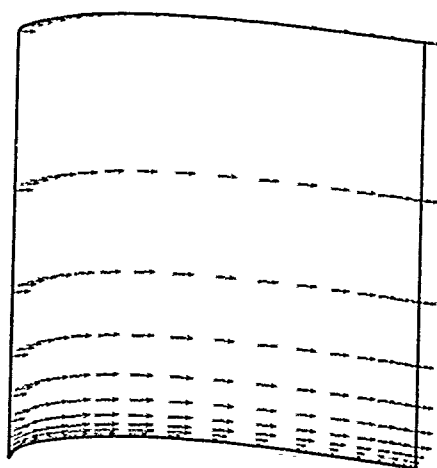


Fig. 3. Viscous airfoil target velocity field.

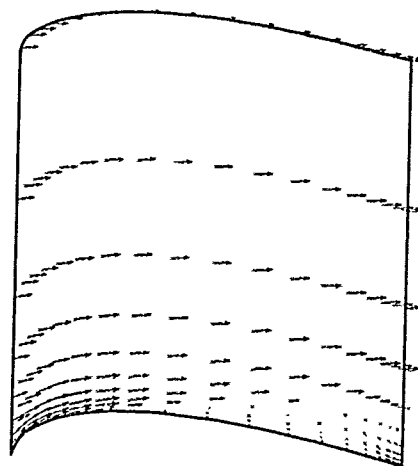


Fig. 4. Viscous airfoil initial guess velocity field.

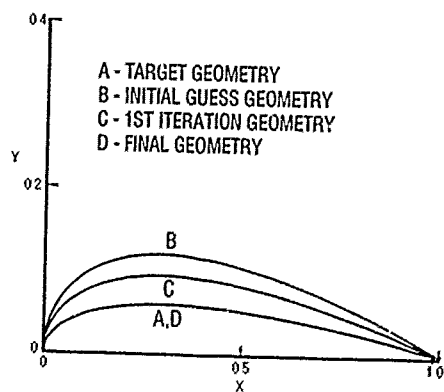


Fig. 5. Viscous airfoil contour variation.

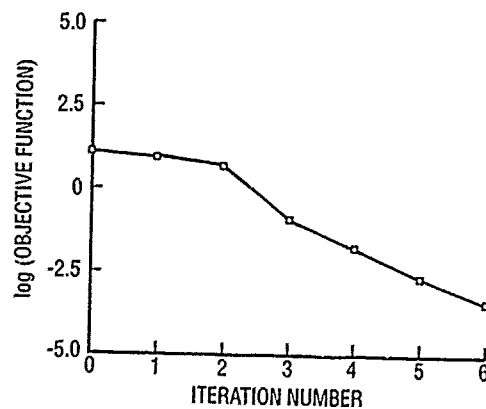


Fig. 6. Viscous airfoil objective function reduction.

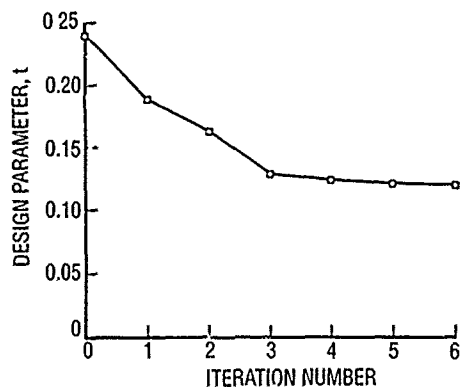


Fig. 7. Viscous airfoil design parameter convergence.

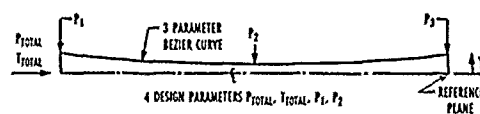


Fig. 8. Planar nozzle test case.

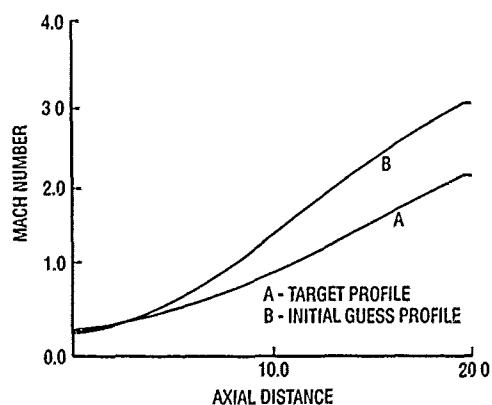


Fig. 9. Planar nozzle centerline Mach number distribution.

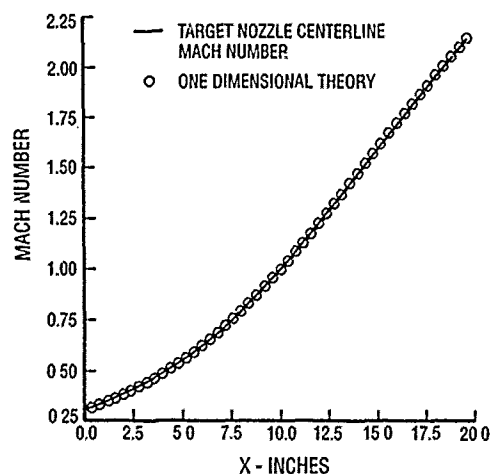


Fig. 10. Planar nozzle centerline Mach number.

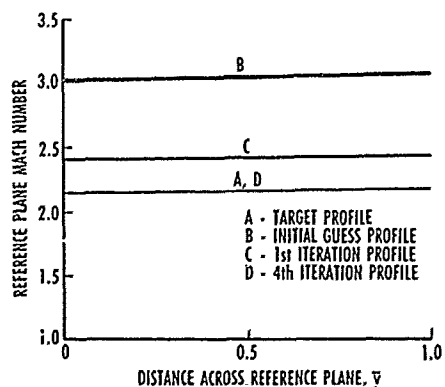


Fig. 11. Planar nozzle RP Mach number profiles.

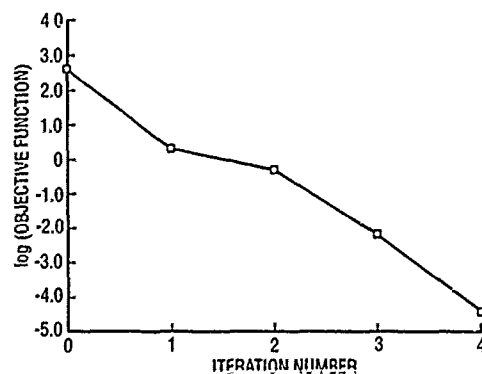


Fig. 12. Planar nozzle objective function reduction.

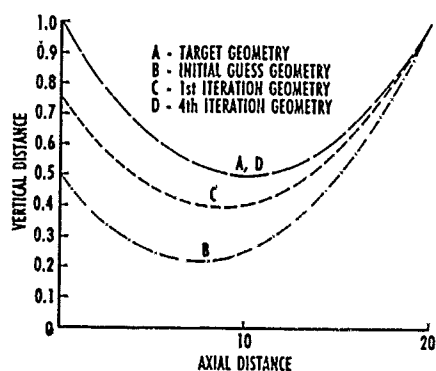


Fig. 13. Planar nozzle wall contour variation.

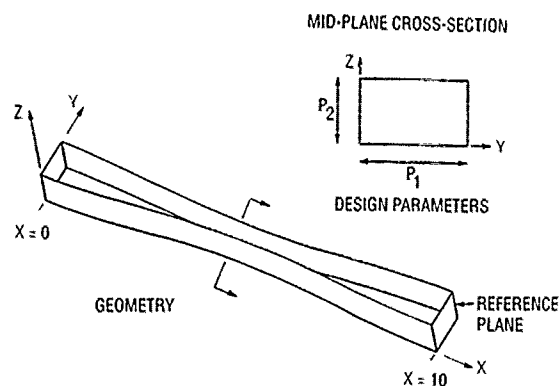


Fig. 14. 3-D nozzle test case.

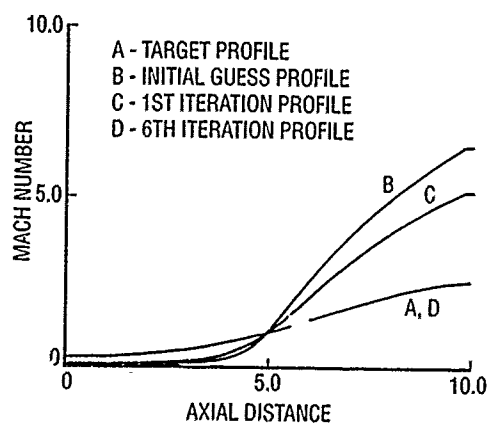


Fig. 15. 3-D nozzle centerline Mach number contours.

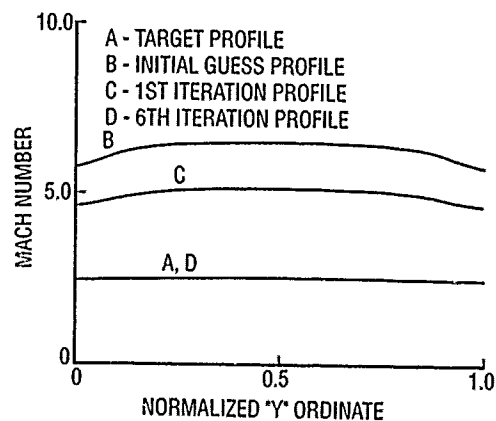


Fig. 16. 3-D nozzle RP Mach number variation.

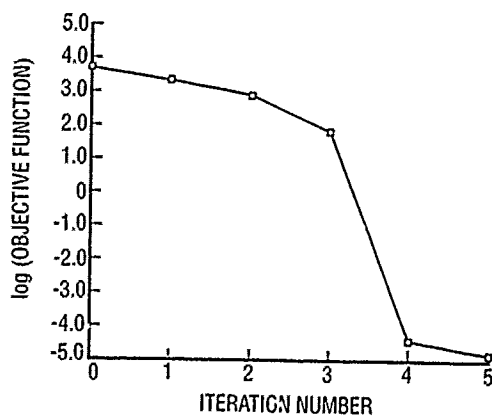


Fig. 17. 3-D nozzle objective function reduction.

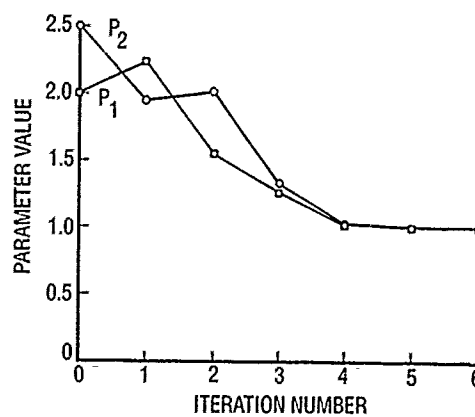


Fig. 18. 3-D nozzle parameter convergence.

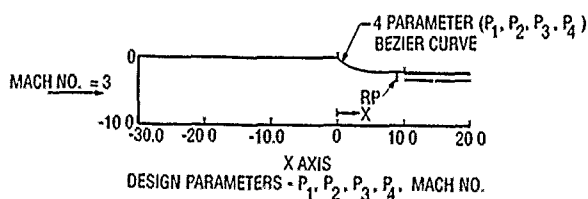


Fig. 19. Planar supersonic forebody simulator optimization.

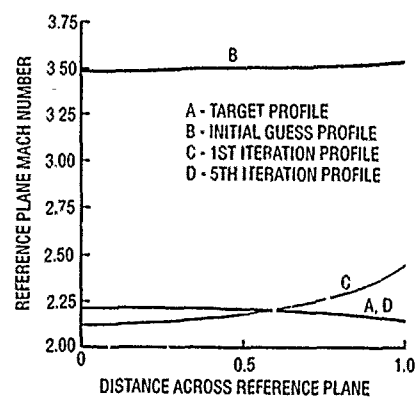


Fig. 20. Supersonic forebody simulator RP Mach number profiles.

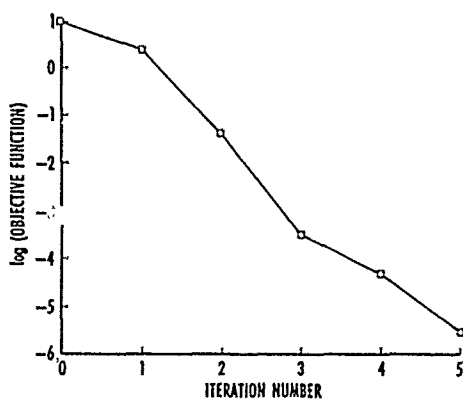


Fig. 21. Supersonic forebody simulator objective function reduction.

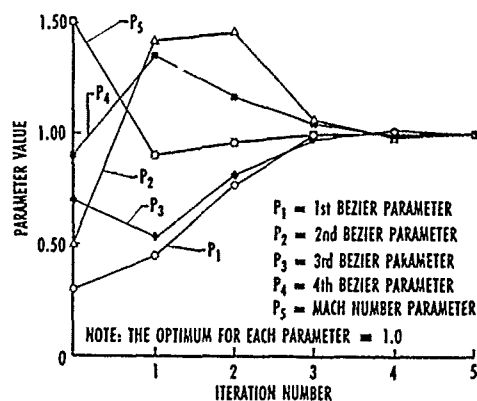


Fig. 22. Supersonic forebody simulator parameter convergence.

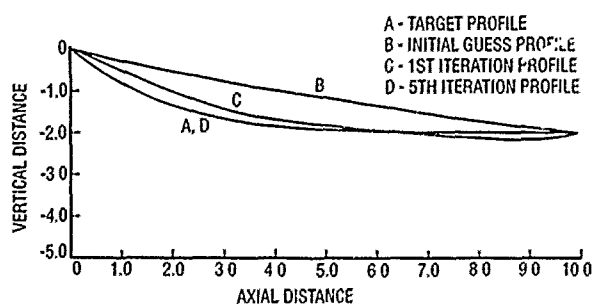


Fig. 23. Supersonic forebody simulator contour variation.

SPECIALISTS' MEETING
ON
COMPUTATIONAL METHODS FOR AERODYNAMIC DESIGN (INVERSE) & OPTIMIZATION
22-23 May 1989
LOEN, NORWAY

Prof. J. Slooff

Good afternoon everybody. As you will have noticed there are two remaining points on our agenda this afternoon. One is the Technical Evaluator's remarks and the other is the Round Table Discussion. The first one, The Technical Evaluator's remarks, is a one-man show, if you like, but each of you is invited, of course, to participate in the Round Table Discussion that will follow afterwards.

I think the Technical Evaluator has the toughest job of all of us. He is supposed to listen carefully to each of the individual papers, so he cannot allow himself to dose off or have some sunshine outside. In addition to that he has to digest the information in a very short time project it against his own framework of thinking, assess the picture that he gets this way, and communicate that assessment. I am glad that we have found Mr. Preston Henne from Douglas Aircraft Company to act as the Technical Evaluator of this meeting. I am very glad for two reasons. First because he is somebody from industry, and all of the methods that we are developing should have at least as the ultimate goal that they are of some use for industry to improve their products. So that is a very good reason to ask somebody from industry to evaluate a conference like this. The second reason why I am very pleased with Mr. Preston Henne is that he himself has been active in design methods. I think he was the one that developed the first three-dimensional transonic inverse method and apart from that he has a lot of experience also in numerical optimization and other types of design problems and techniques.

Mr. Henne is currently Manager of Program Engineering of the MD90 at Longbeach in California. I invite him to please take the mike and give us his remarks.

Mr. Henne

I would like to thank the AGARD Fluid Dynamics Panel for inviting me to come and be the Technical Evaluator. It is an honor for me to do that. It is a pleasure to be here in this kind of environment. For those of you that don't know me, Joop has given a good introduction. I have been working in the aerodynamic design area for about 20 years. My wife thinks that since I have been doing that for 20 years and I have an overgrowth of gray hair that I must be an expert in something. I have been involved in CFD in application for design problems, for airfoils, wings, propulsion system installations. In this conference I feel like I am in my element because I have done both a design method or two, 2-D and 3-D, and I have done numerical optimization in one form or another. Consequently, I felt pretty comfortable in taking on the role of a Technical Evaluator.

Coming to the conference I debated as to whether or not I wanted to be a good guy or a bad guy. I had made the decision to be a good guy. Unfortunately, that decision has waned in two days so I am probably going to turn out to be a bad guy. So let me apologize beforehand if I might be a little bit too harsh. Don't take it personally. I will probably make some critical comments about some of the work and hopefully we can still be friends and walk away from here that way.

Let me start off by congratulating the AGARD Fluid Dynamics Panel for recognizing the need for a conference like this. I think that it is long overdue and I hope that an activity like this can continue. I think that it is important. I want to make some points along the way. I have identified six things that I want to make sure come across. The first point is that I have a question. That question is, "why is it that the area of design methods has lagged the analysis methods to the point it has?" I would like to hear some discussion of that in the Round Table session. I think that that would be a question to tackle. I think that it has lagged too much, being one that has seen the power of design methods doing things useful for a product line. I am concerned that we are missing opportunities with the lag that we have between the analysis method and design methods. So that is point 1.

I would like to compliment Joop and the staff at NLR for their early work in inverse designs. I think that they had some foresight at NLR and they initiated a lot of work a few years ago. In the mid-70's at McDonnell Douglas we had a distinct opportunity when Terry Traenen worked for us. He produced what I felt to be a first successful two-dimensional transonic design method. He has been recognized for that as being the father of the Traenen method. In seeing that applied to a number of design problems in the mid-70's, I took and then extended his approach to three dimensions, which is the example that Joop mentioned. In that process I recognized the power and the capability that such a procedure provides you over an above just simply cutting and trying. Unfortunately, I think it takes a personal exposure like that to really drum up the enthusiasm. I presented an AIAA paper on that three-dimensional method in 1980. In the audience was Paul Ruppert and apparently at that time at Boeing no such methods existed or they were unsuccessful. His approach afterwards was, "well, we don't really need an inverse, because we can just run enough direct solutions to make sure that we get the right answer". I was a bit taken aback by that, but I see in recent publications Paul has taken a little bit different tack. Apparently they now have invented a 3-d inverse, nearly 10 years later, and it sounds like it is the greatest thing since SEX. I think that it takes a personal experience to see that and understand what an inverse method can really do for you. That may be one of the reasons that the development of design methods like that has lagged the development of the direct solution.

As a result of that kind of a position, I feel that in today's environment there is a need for both, which is my second point. There is every bit as much need for design method as for an analysis method. It is like a few years ago someone in CFD said that they were going to get rid of all the wind tunnels. Well, that hasn't happened, you need them both. In the computational area you need both design and analysis. They really do complement each other.

Before I came here I wrote down what I thought were some standard classifications of methods that fall in a design method category. The classifications I came up with were what I would call⁽¹⁾ true inverse, where you simply specify a pressure with no a priori knowledge of any aerodynamic surface, and compute a surface; that is what I would call true inverse. We also have⁽²⁾ a fictitious gas scheme. I would call the approach that Terry Traenen and I used⁽³⁾ the transpiration integration, if you will, and I think Joe Voipe's is essentially similar to that. We have⁽⁴⁾ residual correction methods. We have⁽⁵⁾ an Euler scheme in which you iterate streamlines if you have a streamline coordinate system. We have⁽⁶⁾ parametric optimization.

To that grouping of categories, I would like to make two more points. Relative to fictitious gas, my point is, why do it? I think fictitious gas is a waste of time. I think the use of the fictitious gas model is academic at best. In order to be a real design method you have to be capable of changing the entire aerodynamic surface. A restriction of that capability constrains the designer, and you are not going to get the best answer. Fictitious gas is one of those methods that is in that category. Another point to be made is relative to parametric optimization. I have done methods using numerical optimization. I also developed one using evolution theory, which also was in a paper presented today but did not get discussed, so I was disappointed in that. I am skeptical about numerical optimization or parametric optimization. I think that the name numerical optimization is a misnomer, in fact I think that the name is incorrect. It ought to be called parametric improvement because you are never guaranteed that you have the optimum. All you would have to do is to introduce an additional parameter and you've introduced the uncertainty that you haven't found the optimum. Until you have infinite set, you are just improving the configuration, you are really not optimizing. Unfortunately this afternoon probably convinced me I ought to be a bad guy because Mr. Bock managed to take my two points and combine them both into one solution using a numerical optimization scheme combined and driving a fictitious gas scheme, which I find amazing.

I went through the publications and I must have missed one, because I counted 21. I tried to group them by categories as to where they fell. This is a little bit biased because it is divided up into inverse methods and optimization methods. Part of this distribution was fixed from the onset. In terms of true inverses by my reckoning, and there were five that I couldn't classify, there were none presented, which I find interesting but not surprising. In fictitious gas I think that three authors quoted the use of fictitious gas in one form or another; the transpiration integration, I think three authors utilized that; residual correction - three; streamline iteration - I think one showed the results for that, and in the parametric optimization there were six that I saw as clear parametric improvement schemes, if you will. The part of this that I find a little disconcerting is that 4 papers of that 21 paper set verified what they had done with some sort of a test. The other 17 were more or less an academic exercise, and the proof that they had gone in the right direction, that they had gotten the right sign on the change, really was not shown. So I would offer up a challenge that we need to do a little bit better job in validating or at least correlating that what we are doing in the design method really is appropriate. I asked several times what the drag sensitivity was, for example. Until you take your method and show what its drag accuracy is in terms of a large sample with a standard deviation on your drag calculation compared to some measurements, I don't believe you are justified in using drag in your optimization scheme or in your inverse design. If you have done that and you can show that the change that you are making is above the error band, then you ought to be willing to spend money on that configuration. You ought to be able to spend a lot of money because you are justified. If you are down in the error band, I defy you to commit a lot of money to an improved configuration. It is a sure career-limiting move to do that. The fifth point I would like to make is simply that you need statistical correlation before you can really justify the use in a design environment, that is, in a production environment where you are going to spend a lot of money.

Let me point out some highlights of the Conference. I was glad to see Tony Jameson brought into the program because I think in the last year he has sort of taken on the design problem and offered a fresh look at it. In his own way he has once again brought a more formal math basis to a problem while at the same time not losing sight of the goal, trying to do something of a very practical nature. So I think his presentation was very timely, his insertion into the program was a very good one. I hope that his approach will be pursued not only by him, but will be picked up by others in the industry, in government, research agencies, and schools, universities, etc. A number of people have followed his flow codes, his direct solutions. I hope that there is an interest by others in his approach because it is usually pretty firm.

I would like to point out what I thought were some other good works. Mr. Borges, for example, I think at least did a thorough job in getting all the way through to a hardware validation. I am not sure his method is the most sophisticated, but at least he took it all the way through a hardware validation, and I would like to commend him for that. The same thing is true of Mr. Reneaux even though he used the numerical optimization or a parametric optimization, I am a little skeptical of, he did show an improved airfoil section validated by tests. He showed in the validation or in the original computational design an improvement in drag divergence Mach number. I happen to know for the methods he is talking about the increment in drag divergence Mach number that he was seeking between the two configurations is well above the error band for that method. I know ' the method is capable of discriminating to levels of increment much lower than that. So I think that he was justified in doing the test and his results verified that, so a commendation is deserved. Almost a commendation, I thought he was going to get one, to Mr. Van Egomond from NLR. I thought he finally was going to come to the point of driving a design method with a parametric description of the pressure in which he drove the parameters with the numerical optimization. I thought he was going to do that, but he really didn't. Sort of a not quite commendation goes also to Dr. Malone. He had the greatest title in which he was doing inverse Navier-Stokes work. As it turns out all he is really looking for is attached flow, so I question why on earth you would run 12,000 iterations to do an attached flow problem, sounds like a great deal of overhead for a practical design situation.

I will close with my last point. The sixth point I would like to make is that I think that there are enough independent agencies, authors, developers, in this area now where perhaps AGARD ought to

contemplate a contest, maybe an airfoil design contest, if you will. Perhaps analogous to the Holst airfoil analysis set that was run at NASA Ames a couple years ago. With that I thank you for being here to listen to me.

Prof. J. Slooff

Thank you very much, Preston, for your very to the point and no doubt to some people provocative remarks. Thank you for that in particular because I think that it will help me in trying to get a vivid Round Table Discussion.

Before we go into that, I should point out that this is going to be recorded and printed in the conference proceedings, but don't be afraid. You will have a written account of what you said before it is published and you will be asked to correct it if you like. So please, before you speak give your name and affiliation clearly.

What I would like to do now is perhaps first give the opportunity to react on what Mr. Henne has said. Perhaps after that we can have some remarks, comments or questions with respect to some individual papers for which there was no time during the question period after the particular paper. Maybe at the end we can try to make some sort of a wrap-up where we perhaps might try to evaluate the different limitations and possibilities of the various approaches and that may perhaps help us in setting out directions for the future. Who would like to answer some of the questions or comments of Mr. Henne?

Dr. W. Schmidt

Based on your comments I would like to come back to two points; one is the fictitious gas and the second one is the numerical improvement procedure. Now as far as fictitious gas is concerned, I would say it needs your own experience to really get the best out of it. I cannot agree with your statement, especially because I, quite some years ago, had a very interesting experience by using it, although my initial position was very similar to yours. It turns out that if you use fictitious gas as it stands, with the additional shape functions that are being built in to modify the airfoil in those areas where the fictitious gas is not working, then this approach is very, very attractive. There are examples of design airfoils that are flying and you might be quite amazed by seeing that. Secondly, if you use this type of approach in combination with a driving mechanism that is giving you a chance to mix the different things that otherwise are very difficult to handle via an optimization method, then this is extremely powerful. I would still say that it is beyond our understanding what is the best pressure distribution. Those methods will give you something that is good on pressure and on shape because you can get something immediately that can be manufactured. If you don't do that, if you prescribe pressure, and I have done this actually myself sometime around the mid-70's on small disturbance methods, as you might know, you very often end up with shapes that are not closed or were very funny and very difficult to manufacture. I would still say that the type of method by mixing different things, and the fictitious gas is nothing else but a shape function or a pressure function or whatsoever, you can end up with very, very good tools.

Prof. J. Slooff

Thank you Wolfgang. I made a note here of a very interesting remark that Mr. Henne gave us. I will repeat it since he mumbled away a little bit at that particular point in time, I think he didn't dare to say it out very loudly, but it kind of struck me. He said, "3-d inverse methods are the greatest thing since SEX". I thought he was going to talk about numerical cohabitation in his next statement, but fortunately he didn't.

There is one other point that I noted myself which I think Mr. Van Egmond is probably eager to answer. I think that you misunderstood what he was doing, he was in fact using numerical optimization to drive pressure distribution shape function parameters to get to an optimized pressure distribution, but presumably Mr. Van Egmond wants to say something to that himself.

Mr. Van Egmond

In fact I did not quite understand what your criticisms were. What we try to do is to use optimization techniques to drive pressure distributions to some kind of improved design. You need of course additional constraints and some design experience so to say, in order to stay within feasible pressure distributions. But once having defined those distributions, and we have to see this in combination with the NLR inverse calculation methods for the geometry, as target distributions we can finally calculate new geometries but still we have to incorporate geometry constraints in order to keep the geometry within reasonable limits.

Mr. P. Henne

The example you gave for the Liebeck airfoil I believe was like that. Did you also drive the transonic pressure distribution through what I would call an inverse code and the code created the airfoil? You did. OK then I will take my "almost" away and I'll give you an accolade. I think that that approach has distinct possibilities.

Prof. J. Slooff

I would like to get a little comment on his remark on error bands. I think that in principle he is absolutely correct, but there is a "but" to it I think, particularly in situations where one is trying to improve upon existing configurations, existing airfoils, wings, that are not too far away from the configuration that you may expect to end up with. In that case you may hope that, although perhaps you have an absolute accuracy in your drag prediction say of 5 counts or something, your relative accuracy, on an incremental basis, may be somewhat better than those 5 counts. In such a case minimizing drag as a criteria for optimization is perhaps not absolutely hopeless. Would you care to say something to that?

RTD-4

Mr. P. Henne

There is a tendency to want to say that just because my method can't get an absolute drag value, I can still use it incrementally. It is still a very dangerous proposition to do that. I have gone after 5 counts, identified by methodology that was no more accurate than 5 counts, spent what would be a small personal fortune on a wind tunnel model and had the increment come out to be zero. Speaking from some bitter experience it is still dangerous to do that.

Prof. J. Slooff

That is not too bad though; it could have been negative, I presume.

Alright, any other comments on the Technical Evaluator's remarks. Yes Mr. Deponte.

Mr. De Ponte

About the comment of testing and certifying programs, I think one of the reasons to have this meeting is to bring together people so that one could make some work and some others will go on continuing and testing and so on. I don't think it is a good reason to say that some methods were not tested. Because if it is unknown to other people, it cannot be tested.

Prof. J. Slooff

Thank you for that comment. Anybody like to say something? How about John Malone?

Dr. J. Malone

I think that your point was that I didn't have a separated flow problem in the paper. That is a valid point. There will be one coming, there is work on one now. That third problem actually wasn't trivial, it was a problem that Mr. Narramore had tried to solve with our existing potential flow inverse, the one that can't design a leading edge. When he reanalyzed the different designed shapes, he was never able to match the target pressures. So that was sort of a blind test in his mind of the algorithm. Yes, normally just for a shocked case, you wouldn't want to use a Navier-Stokes code. The second point of developing the methodology was to get us complete airfoil contours with compressibility effects and while we were at it, let's go ahead and try for strong viscous effects, too.

Mr. P. Henne

Then I will consider yours a progress report. Is that fair?

Dr. J. Malone

Yes, I guess so. A reasonable amount of progress, I think.

Mr. P. Henne

Let me add a comment to that. I would hope that sometime in the future, I don't know if it's in my career or not, but I hope sometime in the near future we really do get to the point of doing design with Navier-Stokes. There is a whole area of application there when you talk about design, not in terms of aerodynamic efficiency, but in terms of airplane development and design, perhaps structurally more than anything else, where separated flows are important. Obviously they are important for a military application in terms of manoeuvring requirements, but even in the commercial business there is an entire regime where massive separation exists and if we could only calculate it and design for it, we could probably do a lot better job in the airplane design. I was hoping when I came that you would show us a case like that and you didn't quite make it.

Mr. W. Schmidt

Preston, just following up this point you just made. Do you think there is any single-point design in industry, and if not, what I assume you will say, can you think of any design method other than using numerical optimization that can produce multiple point designs?

Mr. P. Henne

That is a tough box to get out of. The answer to the first question is obviously that a real design problem is a multi-point design problem. We have successfully done multi-point design problems without a numerical optimization scheme using just an inverse. You simply end up looking at the multiple points. So that is maybe a poor man's driver on the inverse. But nevertheless, you can do it that way. That is why I think that the combination of a numerical driver in front of the pressure distribution which you then impose on the design method has some possibilities.

Prof. J. Slooff

I intend to come back to that issue somewhat later, but I have a proposition to open the lid of the box you threw yourself into. But before that let me ask if there is anybody else who would like to say something, either as a reaction to what Mr. Henne said or questions or comments on any of the individual papers we had during the past two days. If not, perhaps you will permit me to put a messy viewgraph that I made during coffee break on the projection machine.

VIEWGRAPH

	direct	inverse	direct num. optzn.	constrained inverse num. optzn.	optimal control
control over aero					
C_L	-	+	+))	+	+
C_D ^{*)}	-	(+)	+))	(+)	+
C_M	-	+	+))	+	+
C_p	-	+	+))	+	+
multi-point capability	+	-	+	+?	+
control over geo	+	-	+))	+	?
uniqueness / ill. posedness	+	+/-	???)	+/?	+/?
comp. effort (relative)	1	10	100 ^{*)} (n = 10)	10 ⁺	10 ⁺

*) subject to choice of
 • objective function, constraints
 • number of variables

■) accuracy crucial for success !

What I tried to do here is to make some sort of a crude evaluation of the possibilities of various approaches, where I have distinguished between 1) direct or analysis type methods, 2) pure inverse type methods, what I call direct numerical optimization, 4) an approach that I call constrained inverse numerical optimization and, I added a new one, 5) the optimal control type of approach that Jameson introduced, at least in my world yesterday. I also have put here a list of what I think are requirements that an aerodynamic designer would like to have some control over. Control over the aerodynamics in one thing. I would say that in any practical case you will have to deal with multiple design requirements in the aerodynamic sense. However, the designer also wants control over the geometry for several reasons, the most important one being that the aerodynamic shape should accommodate a structure of sufficient strength and stiffness. He will also have requirements with respect to the computational effort involved. Finally there is an aspect that can be of rather decisive practical importance in some cases but which is of a very fundamental mathematical nature; that is the question of uniqueness of the problem that is being posed, or the question of whether the problem is not an ill-posed one in the mathematical sense.

We now look at the various types of methods that we have. It is clear that with direct methods only, we have no direct control at all over the aerodynamics, but of course we have full control over the geometries. We can come up with a shape and compute the aerodynamic characteristics as good as the physics and numerics of the code will allow.

With pure inverse methods we have almost the opposite situation. There we have fairly good control over the aerodynamics. For instance, we have direct control over pressure distribution and through that on lift and pitching moment, but no direct control over drag. We only have an indirect control over drag because it will be connected in some way to the pressure distribution. However, there is no guarantee that a transonic flow will be shockless. Even if you specify a pressure distribution that does not have any shock waves on the surface you may still have the shock waves hanging in the flow field, as we have seen these last two days. That is one example of why you don't have full control over drag.

With inverse methods, the uniqueness or ill-posedness of the problem pops up already in some sense. Not so much in 2-d, where if you satisfy the closure condition and the regularity condition near the stagnation point at the leading edge there's not too much of a problem. But in 3-d many people have had the experience that a 3-d inverse problem may not be well posed. That is, there may be several solutions with greatly differing geometry producing almost the same pressure distribution and that is always a bad situation for any numerical scheme.

Direct numerical optimization has almost all these possibilities combined, at least in principle, I think. But there the result depends in particular on things like the choice of the objective function, the choice of the constraints and the number of variables. These determine the amount to which one does really have direct control over the aerodynamics and to a certain extent perhaps also over the geometry. Directly related to that in my point of view is the question of uniqueness or ill-posedness of the problem. That in my experience also depends strongly on what you define as your objective function and what you define as the constraints. The more open you leave your definition of the objective function, the larger I guess will be the risk that you do not really have a unique solution.

In the constrained inverse numerical optimization type of approach one first derives a target pressure distribution by driving parameters that describe the pressure distribution; for instance, like Mr. Van Igmond did, through minimizing the drag subject to constraints on lift and pitching moment and an average pressure or suction level that can be related to thickness. Then you can put that target pressure distribution into an inverse method and come up with a shape that will produce that target pressure distribution. In my opinion it is absolutely necessary to have geometric constraints in the inverse problem for two reasons: to have the control over the geometry since otherwise you might still end up with a geometry that no structural engineer is going to accept, but also to help you in removing any problems associated with uniqueness or ill-posedness of the problem. I don't pretend that we fully understand how and when this constrained inverse 3-d procedure really does have a unique solution, but our experience is that with geometrical constraints you do not have too many problems of that sort.

If we go to optimal control, I think that shares most of the advantages and disadvantages of the constrained inverse numerical optimization technique, but I think it is being done on a much more elegant, a mathematically much more well-founded basis. I would very much like to see more developments along this line.

If you look at the relative computational efforts of these various schemes and I call the computational effort of one direct flow solution as unity, then one might say that generally in a transonic inverse case something of the order of 10 iterations, a computational effort of about 10 times that of an analysis method, is required. For direct numerical optimization, it depends pretty much, of course, on the number of free parameters that one has. For a number of free parameters of about 10, in my impression, we already have a computational effort of about 100 relative to this measure here. Constraining the inverse numerical optimization requires only slightly more computational effort than the pure inverse. The same in my appreciation is the case for the optimal control. Adding that up all together I think that constrained inverse numerical optimization and optimal control approaches are worthwhile investigating further and perhaps that should help us in setting out our future directions.

One final remark on drag that has been mentioned before. It is not just numerical accuracy in the sense of how accurate you can integrate, for instance, pressure or skin friction which is crucial for drag minimization. It is also important to try to find other means of getting values of drag; particular it is interesting to be able to separate drag into its basic viscous, wave drag and induced drag components. I have seen one example where that has been used successfully and that was the example by Monsieur Destarac, which I think was a very good example of the necessity that one has to be smarter than just integrating pressures and skin frictions in order to get better accuracy for drag.

I would like to leave it at that and hopefully some of you may want to comment on this further.

Mr. W. Schmidt

I think what you said with the slide you showed us is fully correct if you talk about inviscid flow, and essentially what you are showing is inviscid flow. However, if you look into viscous, real life flow, then I think that I don't see any reason or any way to specify pressure distribution. You actually should specify skin friction or shape parameter or things like this and then based on an inverse boundary layer method get pressures, then based on that pressure get shapes. If you do that as an inverse design method, you do the viscous case. If you do this inverse design method then the figures you are quoting on efficiency won't work, and the consistency is a big question also and the largest question to me is imagination because I have no idea of how skin friction or shape parameter should look like in a three-dimensional shape as a prescribing parameter.

Prof. J. Slooff

First of all let me say that the constrained inversed-numerical optimization approach has been done with viscous effects. It is my appreciation that a similar thing can be done in the optimal control approach that Jameson suggested. As to shape factors and skin friction, the inverse numerical optimization procedure does have the possibility in principle to handle these because in a target pressure distribution optimization approach, you are using boundary layer codes there is no reason why you couldn't specify skin friction as part of the objective function if you would like to do so.

I guess we are all getting tired and the scenery and sunshine are too inviting outside. Let me finish with thanking you all for your participation to this meeting which I personally feel was quite successful; I thank all the authors for their work and their contributions; the audience for participating in the discussions; and the Technical Evaluator in particular for his interesting and stimulating remarks. I would like to finish by asking Derek Peckham to do the official closing procedure.

Mr. D. Peckham

We will be doing a full official closing procedure on Thursday after the end of our second meeting but it seemed to be wrong not to have some closing remarks today now that we have come to the end of our first specialist meeting. I would like to thank the chairman of the Program Committee for this first meeting, Professor Slooff, and his Program Committee for organizing this meeting and the members of his Program Committee who acted as session chairmen. Joop has already thanked the authors for their excellent presentations and for keeping to their allotted times which I think is very important in these procedures and I would like to add my thanks to his. Some of you will be leaving tonight or tomorrow after this first meeting so on your behalf may I thank the Norwegian authorities for their excellent organization and to Mrs. Inge Hoff, Mayor of Stryn commune for her welcoming remarks on Monday. Also, may I wish those of you who are leaving, a safe journey home.

REPORT DOCUMENTATION PAGE			
1. Recipient's Reference	2. Originator's Reference	3. Further Reference	4. Security Classification of Document
	AGARD-CP-463	ISBN 92-835-0542-5	UNCLASSIFIED
5. Originator	Advisory Group for Aerospace Research and Development North Atlantic Treaty Organization 7 rue Ancelle, 92200 Neuilly sur Seine, France		
6. Title	COMPUTATIONAL METHODS FOR AERODYNAMIC DESIGN (INVERSE) AND OPTIMIZATION		
7. Presented	and discussions held at the Specialists' Meeting of the Fluid Dynamics Panel in Loen, Norway, 22-23 May 1989.		
8. Author(s)/Editor(s)	Various		9. Date March 1990
10. Author's/Editor's Address	Various		11. Pages 336
12. Distribution Statement	This document is distributed in accordance with AGARD policies and regulations, which are outlined on the Outside Back Covers of all AGARD publications.		
13. Keywords/Descriptors	<p>Computation Fluid dynamics Design Aerodynamic characteristics/ Optimization; Transonic airfoils;</p> <p>Navier Stokes equations; Turbine blades; Lift surfaces/foils; Airfoils - Compressor/turbines; Turbomachinery intakes/ducts; Numerical analysis. (E2C) - Meetings</p>		
14. Abstract	<p>Computational Fluid Dynamics (CFD) play an increasingly important role in the aerodynamic design of flight vehicles. The main reasons for this are the rapid developments in computer hardware and solution algorithms in combination with the increasing requirements (and potential) for improving aerodynamic quality and reducing design cycle time and cost.</p> <p>This meeting focused on those CFD-based methods which address the problem of design for given aerodynamic characteristics in a direct sense. Examples are "inverse" methods which provide the detailed geometry required to generate a given pressure distribution and methods utilizing numerical optimization techniques to obtain the geometry that minimizes, subject to constraints, a given aerodynamic objective function such as drag, load distribution, etc.</p> <p>Twenty-three papers were ordered into 4 sessions:</p> <ul style="list-style-type: none"> - Invited and Survey Papers (3 papers) - Inverse Methods & Airfoils and Wings (5 papers) - Inverse Methods - Turbomachinery (6 papers) - Numerical Optimization Techniques (9 papers) <p>These proceedings also contain the Round Table Discussion conducted at the conclusion of the meeting.</p>		

<p>AGARD Conference Proceedings No.463 Advisory Group for Aerospace Research and Development, NATO COMPUTATIONAL METHODS FOR AERODYNAMIC DESIGN (INVERSE) AND OPTIMIZATION Published March 1990 336 pages</p> <p>Computational Fluid Dynamics (CFD) play an increasingly important role in the aerodynamic design of flight vehicles. The main reasons for this are the rapid developments in computer hardware and solution algorithms in combination with the increasing requirements (and potential) for improving aerodynamic quality and reducing design cycle time and cost.</p> <p>P.T.O.</p>	AGARD-CP-463	AGARD-CP-463	<p>AGARD Conference Proceedings No.463 Advisory Group for Aerospace Research and Development, NATO COMPUTATIONAL METHODS FOR AERODYNAMIC DESIGN (INVERSE) AND OPTIMIZATION Published March 1990 336 pages</p> <p>Computational Fluid Dynamics (CFD) play an increasingly important role in the aerodynamic design of flight vehicles. The main reasons for this are the rapid developments in computer hardware and solution algorithms in combination with the increasing requirements (and potential) for improving aerodynamic quality and reducing design cycle time and cost.</p> <p>P.T.O.</p>	AGARD-CP-463
<p>AGARD Conference Proceedings No.463 Advisory Group for Aerospace Research and Development, NATO COMPUTATIONAL METHODS FOR AERODYNAMIC DESIGN (INVERSE) AND OPTIMIZATION Published March 1990 336 pages</p> <p>Computational Fluid Dynamics (CFD) play an increasingly important role in the aerodynamic design of flight vehicles. The main reasons for this are the rapid developments in computer hardware and solution algorithms in combination with the increasing requirements (and potential) for improving aerodynamic quality and reducing design cycle time and cost.</p> <p>P.T.O.</p>	AGARD-CP-463	AGARD-CP-463	<p>AGARD Conference Proceedings No.463 Advisory Group for Aerospace Research and Development, NATO COMPUTATIONAL METHODS FOR AERODYNAMIC DESIGN (INVERSE) AND OPTIMIZATION Published March 1990 336 pages</p> <p>Computational Fluid Dynamics (CFD) play an increasingly important role in the aerodynamic design of flight vehicles. The main reasons for this are the rapid developments in computer hardware and solution algorithms in combination with the increasing requirements (and potential) for improving aerodynamic quality and reducing design cycle time and cost.</p> <p>P.T.O.</p>	AGARD-CP-463

<p>This meeting focused on those CFD-based methods which address the problem of design for given aerodynamic characteristics in a direct sense. Examples are "inverse" methods which provide the detailed geometry required to generate a given pressure distribution and methods utilizing numerical optimization techniques to obtain the geometry that minimizes, subject to constraints, a given aerodynamic objective function such as drag, load distribution, etc.</p> <p>Twenty-three papers were ordered into 4 sessions:</p> <ul style="list-style-type: none"> — Invited and Survey Papers (3 papers) — Inverse Methods — Airfoils and Wings (5 papers) — Inverse Methods — Turbomachinery (6 papers) — Numerical Optimization Techniques (9 papers) <p>These proceedings also contain the Round Table Discussion conducted at the conclusion of the meeting.</p> <p>Papers presented and discussions held at the Specialists' Meeting of the Fluid Dynamics Panel in Loen, Norway, 22—23 May 1989.</p> <p>ISBN 92-835-0542-5</p>	<p>This meeting focused on those CFD-based methods which address the problem of design for given aerodynamic characteristics in a direct sense. Examples are "inverse" methods which provide the detailed geometry required to generate a given pressure distribution and methods utilizing numerical optimization techniques to obtain the geometry that minimizes, subject to constraints, a given aerodynamic objective function such as drag, load distribution, etc.</p> <p>Twenty-three papers were ordered into 4 sessions:</p> <ul style="list-style-type: none"> — Invited and Survey Papers (3 papers) — Inverse Methods — Airfoils and Wings (5 papers) — Inverse Methods — Turbomachinery (6 papers) — Numerical Optimization Techniques (9 papers) <p>These proceedings also contain the Round Table Discussion conducted at the conclusion of the meeting.</p> <p>Papers presented and discussions held at the Specialists' Meeting of the Fluid Dynamics Panel in Loen, Norway, 22—23 May 1989.</p> <p>ISBN 92-835-0542-5</p>
<p>This meeting focused on those CFD-based methods which address the problem of design for given aerodynamic characteristics in a direct sense. Examples are "inverse" methods which provide the detailed geometry required to generate a given pressure distribution and methods utilizing numerical optimization techniques to obtain the geometry that minimizes, subject to constraints, a given aerodynamic objective function such as drag, load distribution, etc.</p> <p>Twenty-three papers were ordered into 4 sessions:</p> <ul style="list-style-type: none"> — Invited and Survey Papers (3 papers) — Inverse Methods — Airfoils and Wings (5 papers) — Inverse Methods — Turbomachinery (6 papers) — Numerical Optimization Techniques (9 papers) <p>These proceedings also contain the Round Table Discussion conducted at the conclusion of the meeting.</p> <p>Papers presented and discussions held at the Specialists' Meeting of the Fluid Dynamics Panel in Loen, Norway, 22—23 May 1989.</p> <p>ISBN 92-835-0542-5</p>	<p>This meeting focused on those CFD-based methods which address the problem of design for given aerodynamic characteristics in a direct sense. Examples are "inverse" methods which provide the detailed geometry required to generate a given pressure distribution and methods utilizing numerical optimization techniques to obtain the geometry that minimizes, subject to constraints, a given aerodynamic objective function such as drag, load distribution, etc.</p> <p>Twenty-three papers were ordered into 4 sessions:</p> <ul style="list-style-type: none"> — Invited and Survey Papers (3 papers) — Inverse Methods — Airfoils and Wings (5 papers) — Inverse Methods — Turbomachinery (6 papers) — Numerical Optimization Techniques (9 papers) <p>These proceedings also contain the Round Table Discussion conducted at the conclusion of the meeting.</p> <p>Papers presented and discussions held at the Specialists' Meeting of the Fluid Dynamics Panel in Loen, Norway, 22—23 May 1989.</p> <p>ISBN 92-835-0542-5</p>

AGARD

NATO OTAN

7 rue Ancelle • 92200 NEUILLY-SUR-SEINE
FRANCE

Telephone (1)47.38.57.00 • Telex 610 176

**DISTRIBUTION OF UNCLASSIFIED
AGARD PUBLICATIONS**

AGARD does NOT hold stocks of AGARD publications at the above address for general distribution. Initial distribution of AGARD publications is made to AGARD Member Nations through the following National Distribution Centres. Further copies are sometimes available from these Centres, but if not may be purchased in Microfiche or Photocopy form from the Sales Agencies listed below.

NATIONAL DISTRIBUTION CENTRES

BELGIUM

Coordonnateur AGARD — VSL
Etat-Major de la Force Aérienne
Quartier Reine Elisabeth
Rue d'Evere, 1140 Bruxelles

CANADA

Director Scientific Information Services
Dept of National Defence
Ottawa, Ontario K1A 0K2

DENMARK

Danish Defer
Ved Idraetsp
2100 Copenl

FRANCE

O.N.E.R.A.
29 Avenue
92320 Chât

GERMANY

Fachinform
Physik, Ma
Karlsruhe
D-7514 Eg

GREECE

Hellenic A
Air War C
Scientific
Dekelia A
Dekelia, /

ICELAND

Director
c/o Flugrad
Reykjavik

ITALY

Aeronautica Militare
Ufficio del Delegato Nazionale all'AGARD
3 Piazzale Adenauer
00144 Roma/EUR

LUXEMBOURG

See Belgium

NETHERLANDS

Netherlands Delegation to AGARD
National Aerospace Laboratory, NLR
Kluyverweg 1
2629 HS Delft

NORWAY

Norwegian Defence Research Establishment
Attn: Biblioteket
P.O. Box 25



National Aeronautics and
Space Administration

Washington, D.C.
20546

**SPECIAL FOURTH CLASS MAIL
BOOK**

Postage and Fees Paid
National Aeronautics and
Space Administration
NASA-451

Official Business
Penalty for Private Use \$300



12 001 AGARD 44390041250026712
DEPT OF DEFENSE
DEFENSE TECHNICAL INFORMATION CENTER
DTIC-FDAC
CAMERON STATION BLDG 5
ALEXANDRIA VA 223046145

UNITED STATES

National Aeronautics and Space Administration (NASA)
Langley Research Center
M/S 180
Hampton, Virginia 23665

THE UNITED STATES NATIONAL DISTRIBUTION CENTRE (NASA) DOES NOT HOLD
STOCKS OF AGARD PUBLICATIONS, AND APPLICATIONS FOR COPIES SHOULD BE MADE
DIRECT TO THE NATIONAL TECHNICAL INFORMATION SERVICE (NTIS) AT THE ADDRESS BELOW.

SALES AGENCIES

National Technical
Information Service (NTIS)
5285 Port Royal Road
Springfield
Virginia 22161, USA

ESA/Information Retrieval Service
European Space Agency
10, rue Mario Nikis
75015 Paris, France

The British Library
Document Supply Centre
Boston Spa, Wetherby
West Yorkshire LS23 7BQ
England

Requests for microfiche or photocopies of AGARD documents should include the AGARD serial number, title, author or editor, and publication date. Requests to NTIS should include the NASA accession report number. Full bibliographical references and abstracts of AGARD publications are given in the following journals:

Scientific and Technical Aerospace Reports (STAR)
published by NASA Scientific and Technical
Information Branch
NASA Headquarters (NIT-40)
Washington D.C. 20546, USA

Government Reports Announcements (GRA)
published by the National Technical
Information Services, Springfield
Virginia 22161, USA



Printed by Specialised Printing Services Limited
40 Chigwell Lane, Loughton, Essex IG10 3TZ

ISBN 92-835-0542-5